Chemostratigraphic Investigation of Early Carboniferous Tuffs and Limestones from the Irish Midlands Based on Geochemical and Geochronological Fingerprinting

PhD Thesis

2021

Hilde Anna Koch

Trinity College Dublin
Coláiste na Tríonóide, Baile Átha Cliath
The University of Dublin

Declaration

I declare that this thesis has not been submitted as an exercise for a degree at this or any other university and it is entirely my own work.

I agree to deposit this thesis in the University's open access institutional repository or allow the library to do so on my behalf, subject to Irish Copyright Legislation and Trinity College Library conditions of use and acknowledgement.

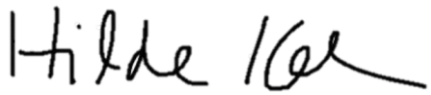

Hilde Anna Koch

Summary

The timing of mineralisation of the Irish Zn-Pb ore field is currently poorly understood. It can be improved by more accurate stratigraphic correlations of the Carboniferous (Mississippian Subsystem) host rocks (Heckel and Clayton, 2006; Richards, 2013). The position of altered volcanic ash layers in relation to the carbonate-hosted Zn-Pb deposits of Ireland makes them key potential isochronous marker horizons and thus provide possibilities to supplement the relatively coarse biostratigraphic resolution for these rocks. The purpose of this study is to establish a geochemical tephrostratigraphy for the Irish Midlands, which will refine the regional Mississippian stratigraphy and its relationship to the timing of mineralisation of Irish Zn-Pb deposits.

Special emphasis is placed on the use of high-precision trace element geochemistry to test whether small, but significant, differences in bulk tuff chemistry can survive alteration and be used as a correlation tool. However, the study undertakes a multi-proxy approach, integrating bulk-rock geochemistry with apatite high-precision trace element and U-Pb zircon age data. The sampling is regional, and was undertaken in active (Navan) and abandoned (Lisheen and Rapla) mines or prospects (Stonepark and Slievedart) across the Irish Midlands. Seventy-nine tuff samples were powdered and chemically analysed for 51 trace elements, using high-precision solution quadrupole ICP-MS. Only 18 and 14 of the mineralogically separated samples contained zircon and apatite grains, respectively. Available grains were dated by U-Pb LA-ICP-MS. Apatite grains were analysed for 23 trace element abundances and for U-Pb ages to ensure they represented Early Carboniferous phenocrysts.

Six different discrete eruptions or eruption sequences, which led to the deposition of volcanic ashes in the Irish Midlands, are identified using whole-rock Ti, Nb, Y, Al, Hf, Ta, La, Pr, Sm, Gd, Dy, Er, Yb concentrations in the modified *matchogram* approach of Marx et al. (2005). Each of the tuff layers in Navan, the Rathdowney Trend and Slievedart also exhibit unique and reproducible trends in REE+Y diagrams and share a similar parental magma composition. These results are supported by apatite trace element and U-Pb zircon age data, which have a supposedly more robust tephrochronological potential (Sell and Samson, 2011a; Harvey, 2014; Nicklen et al., 2015). Thus, the combination of the *matchogram* and bulk-rock trace element fingerprinting is a viable basis for the tuff identification and correlation as geochemical differences are significant enough to cause compositional separation. Importantly, alteration effects or mineralisation do not seem to preclude the use of selected bulk-rock trace element data as a chemostratigraphic tool. Although samples from the Stonepark area show contradictory results in bulk-rock *vs* apatite trace element data, the newly developed multi-proxy approach can be ideally applied to similar geological settings worldwide, to resolve stratigraphic relationships.

All tuff samples from Navan, the Rathdowney Trend and nine out of eleven samples from Slievedart indicate an evolved magma composition. The volcanic centre for the evolved ashes is most likely in Ireland. However, the Limerick volcanic region is a possible source area for two sand-grade tuffs from Slievedart (samples Slievedart_3471/4_HK 237 and Slievedart_3470/15 _HK 238), which have an intermediate magma composition. U-Pb zircon ages, ranging from 350 Ma to 345 Ma, show that tuff samples were deposited in the Tournaisian and Early Viséan. This work also suggests, that the Tournaisian-Viséan boundary in Slievedart should be moved close to the tuffs in the Kilbryan Limestone Formation. Furthermore, this study supports the time-equivalence of the New Thin Bedded Unit in Tara Deep and the Tober Colleen Formation in Navan West. The Slievedart tuffs show that they are influenced by mineralisation, which implies an epigenetic origin of the sediment-hosted mineralisation of the underlying Zn-Pb deposit, which took place later than 347 Ma, which is the minimum age of dated ashes, while the timing of mineralisation in the other three study sites remains unclear.

The possibility of utilising Sr isotope stratigraphy and trace element patterns as a secondary chemostratigraphic tool depends on available geomaterials. Brachiopods from Irish Mississippian limestones proved to be most suitable. Furthermore, the newly introduced *in situ* sampling technique employs the laser ablation unit as a milling device. Ahead of laser micro-sampling, potential sampling targets are mapped by LA-ICP-MS for their trace element distributions. Sampled material will be subsequently analysed using a quadrupole ICP-MS. This approach will improve Sr isotope data as it provides high-spatial resolution sampling (down to 2 x 2 µm) of clean fossil material, devoid of the surrounding matrix and alteration.

Acknowledgements

First, I want to thank Prof. Balz Kamber, who offered me to work on this project and his trust in me for looking after adorable Charlie and the house in his absence.

Special thanks to Prof. David Chew, who adopted me when I became an orphan after Balz moved to Australia. Without Dave's great support this thesis would not have the quality it has now.

I highly appreciate the time and thoughts my examiners Emma Tomlinson and John Murray invested in this thesis, which significantly improved this work.

I also want to thank the wonderful administrative and technical team at Trinity College Dublin – Colin, Cora, Foteini, Frances, Francis, Leona, Maura, Noel, Paul and Sarah. Your help was always highly appreciated. It was a pleasure to be part of the fantastic step challenge team, involving Cora, Francis and Maura.

Sincere thanks to Michael Philcox for providing tuff samples, interesting discussions and ideas. Rob Blakeman and Paul Henry from Boliden Tara Mines and Mark Holdstock from Group Eleven are thanked for further tuff samples and/or accompanying stratigraphic information.

I also want to thank the whole Geology Department for five fantastic years, namely Adri, Aodhán, Brendan, Chris, Claire, Dave, Elliot, Eoghan, Erica, Fermin, Foteini, George Sevastopulo, Ian Sanders, James, Lingli, Lucy, Lydia, Maria-Teresa, Micha, Niamh, Siobhán, Tadhg, Thomas, Weimu and Zoe. It was an honour to be your Minister for Fun for over four years. George, you will be sorely missed in the department! It was a pleasure meeting you and attending the International Congress on the Carboniferous and Permian together.

I wish to thank the iCRAG researchers and the operational team for providing a great research platform. Furthermore, I want to express my gratitude to SFI and iCRAG funding bodies for financially supporting my research.

I feel very lucky that I am surrounded by my Irish family in Dublin, who I can always rely on. I would not have liked to miss a single second spending with you. It was always so much craic. I have so many memorable moments with you, which I will never forget in my life. Josune, Magali, Sara, Philip and Victor, you are the best! Your friendship is forever appreciated.

I also wish to thank my parents Marianne and Joachim and my siblings Karl, Frieda, Lea and Stachys for not constantly asking about the progress of the thesis ☺ but also for the support and believing in me. Further, the Brodbeck family - Cilli and Guenne, for discovering our adopted country together and Marci, Nina and Samu for great company especially during lockdown and delicious Kaesspaetzle.

I will never forget the great adventures I had with my friends, who came to visit me in Ireland, most notably Bea, Hanna, Elke, Juls, Lutz, Mela, Korti and Chrischi.

Also a big thank you to the Kuadri Dublin Chacarron for intense flunkyball matches and roof terrace gatherings and simply everybody I met during this journey and brightened up the everyday PhD life.

Saving the best until last, THANK YOU Mauri for being part of my life. You are the most relaxed person on earth I know. You showed that it is possible doing a PhD while still enjoying life.

SLÁINTE

Table of Contents

Summary ..... **I**

Acknowledgements ..... **III**

Abbreviations and Symbols ..... **XII**

1 Introduction **1**

1.1 Tephrostratigraphy and Tephrochronology 2

1.1.1 Terminology – Tephra *vs* Tuff 2

1.1.2 Tephrostratigraphy 3

1.1.3 Tephrochronology 4

1.2 Mississippian Time Scale 4

2 The Stratigraphic Setting of Irish Carboniferous Tuffs **8**

2.1 Introduction 8

2.2 Irish Mississippian Stratigraphy 11

2.3 Mineralisation 12

2.4 Volcanism 14

2.5 Irish Tuffs 17

2.6 Navan Area 19

2.6.1 Main Mine Area 19

2.6.1.1 Sample Locations – Navan East & West 21

2.6.2 Tara Deep 24

2.6.2.1 Sample Locations – Tara Deep 25

2.7 Rathdowney Trend 29

2.7.1 Lisheen 29

2.7.2 Rapla 31

2.7.3 Sample Locations – Rathdowney Trend 31

2.8 Stonepark Area 36

2.8.1 Sample Locations – Stonepark Area 38

2.9 Slievedart Area 41

2.9.1 Sample Locations – Slievedart Area 43

3 Tuff Description **46**

3.1 Macroscopic Observations 46

3.2 Microscopic Observations 49

4 Bulk-Rock Geochemistry of Irish Volcanic Ash Layers 51

4.1 Introduction 51

4.2 Methods 52

4.2.1 Bulk-Rock Analyses 52

4.2.1.1 Sample Preparation 52

4.2.1.2 Digestion 52

4.2.1.3 Analytical Set-Up 53

4.2.1.4 Data Reduction Protocol 54

4.2.1.4.1 Internal Drift Correction and Internal Precision 55

4.2.1.4.2 Background Correction 55

4.2.1.4.3 External Drift Correction 55

4.2.1.4.4 Blank Correction 56

4.2.1.4.5 Oxide Correction 56

4.2.1.4.6 Calibration 57

4.2.1.5 Analytical Precision 57

4.2.1.5.1 Precision and Accuracy 57

4.2.1.5.2 Reliability of the Digestion Method 58

4.2.1.5.3 Reproducibility of Tuff Digestions 59

4.2.2 The *Matchogram* Approach 60

4.2.2.1 Background 60

4.2.2.2 Method 61

4.2.3 Ratios and Normalisation 64

4.3 Results 64

4.3.1 Trace Elements which were Mobile during Weathering (Mg, Rb, Sr, Ba) 65

4.3.2 Trace Elements which were Immobile during Weathering (Al, Ti, Y, Zr, Nb, Sn, Hf, Ta, Th, REE) 66

4.3.2.1 REE+Y 69

4.3.3 Elements Affected by the Marine Depositional Environment (Ca) and Mineralisation (Zn, Cd, Tl, Pb) 71

4.3.4 Elements with Shale Characteristics (Sc, V, Cr, Co, Ni, Cs, U) 73

4.4 Discussion 75

4.4.1 Identifying Devitrified Volcanic Ashes 76
4.4.2 Processes that might Change Tephra Composition 81
4.4.2.1 Transport Distance and Mineral Segregation 81
4.4.2.2 Alteration as a Key to Identifying the Depositional Environment 83
4.4.2.3 Alteration during Diagenesis 87
4.4.2.4 Reworking and Redeposition 88
4.4.2.4.1 Degree of Reworking 89
4.4.2.4.2 Admixture of Sediments and Detrital Grains 90
4.4.2.5 Mineralisation 91
4.4.2.6 Digestion Set-Up 94
4.4.3 Tuff Composition 94
4.4.3.1 REE Diagrams 96
4.4.3.2 Geochemical Twins 99
4.4.3.3 Source Magma Chemistry - Discrimination Diagrams 101
4.4.3.4 Summary – Tuff Composition 102
4.4.4 Tuff Correlations 103
4.4.4.1 Navan Area 104
4.4.4.1.1 Tara Deep 104
4.4.4.1.2 Navan East & West 106
4.4.4.1.3 Tara Deep *vs* Navan East & West 107
4.4.4.2 Rathdowney Trend 108
4.4.4.2.1 Lisheen 108
4.4.4.2.2 Rapla 109
4.4.4.2.3 Lisheen *vs* Rapla 109
4.4.4.3 Stonepark Area 112
4.4.4.4 Slievedart Area 114
4.4.4.5 Cross-Correlations 116
4.5 Conclusions 116
4.6 Future Work 119
4.6.1 Clay Fraction *vs* Phenocrysts 119
4.6.2 Digestion Method 119
4.6.3 Mineralogy - XRD 119

5 LA-ICP-MS U-Pb Zircon Geochronology and Apatite Trace Element Characterisation 120

5.1 Introduction 120

5.2 Method 121

5.2.1 U-Pb Zircon Geochronology 121

5.2.1.1 Wetherill Concordia Diagram 122

5.2.1.1.1 Pb Loss 122

5.2.1.1.2 Inherited Grains 123

5.2.1.1.3 Common Pb Contamination 123

5.2.1.2 Age Determinations 124

5.2.2 U-Pb Apatite Geochronology 126

5.2.2.1 Common Pb Correction 127

5.2.2.2 Tera-Wasserburg U-Pb Concordia Diagram 127

5.2.2.3 Age Determinations 128

5.2.3 Zircon and Apatite Separation 129

5.2.4 Analytical Technique - Zircon 130

5.2.4.1 Data Reduction 131

5.2.4.2 Age Calculations 132

5.2.4.2.1 Standards 132

5.2.5 Analytical Technique - Apatite 133

5.2.5.1 Data Reduction – U-Pb Apatite Ages 135

5.2.5.2 Age Calculations 136

5.2.5.2.1 Standards 137

5.2.5.3 Data Reduction – Trace Elements 138

5.3 Results 138

5.3.1 U-Pb Zircon Ages 138

5.3.1.1 Tara Deep 140

5.3.1.2 Navan East & West 141

5.3.1.3 Rathdowney Trend 141

5.3.1.4 Stonepark Area 143

5.3.1.5 Slievedart Area 145

5.3.2 Zircon Morphology 147

5.3.3 U-Pb Apatite Ages 150
5.3.3.1 Navan 150
5.3.3.2 Rathdowney Trend 150
5.3.3.3 Stonepark Area 150
5.3.3.4 Slievedart Area 150
5.3.4 Trace Elements 154
5.3.4.1 Standards 154
5.3.4.2 Tuff Samples 156
5.3.4.3 Inter-Grain Variability of Element Concentrations 157
5.3.5 Apatite Morphology 158
5.4 Discussion 160
5.4.1 Whole-Rock Geochemical Data as a Tool to Predicting Apatite and Zircon Yield . 160
5.4.2 Zircon - U-Pb Age Data 164
5.4.2.1 Navan 164
5.4.2.2 Rathdowney Trend 166
5.4.2.3 Stonepark Area 167
5.4.2.4 Slievedart Area 168
5.4.2.5 Cross-Correlation 171
5.4.3 Zircon Trace Elements 175
5.4.4 Zircon Morphology as an Indicator of Inheritance? 175
5.4.5 Apatite Morphology 176
5.4.6 Apatite U-Pb Age Data 176
5.4.7 Apatite -Trace Element Characterisation 177
5.4.7.1 Parental Magma Characterisation 177
5.4.7.2 Correlation Tool 186
5.5 Conclusions 187
6 Integrated Results from the Bulk-Rock, Zircon and Apatite Analyses 191
6.1 Navan 191
6.2 Rathdowney Trend – Lisheen & Rapla 193
6.3 Stonepark 195
6.4 Slievedart 196
6.5 Location of the Volcanic Centre 198

6.6 Eruption History of Irish Early Carboniferous Tuffs 201

7 Strontium Isotope Stratigraphy as a Secondary Stratigraphic Tool using Carbonates from the Irish Mississippian – a Pilot Study Introducing a Novel *In Situ* Laser-Sampling Technique 206

7.1 Introduction 206
7.2 Geological Setting 210
7.3 Wet Chemistry 211
7.3.1 Method 211
7.3.1.1 Milling 212
7.3.1.2 Trace Element Chemistry and Analyses 212
7.3.1.3 Strontium Isotope Chemistry and Analyses 212
7.3.2 Results 213
7.3.2.1 Results – Trace Elements 213
7.3.2.2 Results – Sr Isotopes 214
7.3.3 Discussion 214
7.3.3.1 Acetic *vs* Nitric Acid 215
7.3.3.2 Identification of Contaminants 215
7.3.3.3 Chemostratigraphic Correlations 220
7.3.3.4 Sr Isotopic Correlations 225
7.4 *In Situ* Sampling 228
7.4.1 Experiment Design 229
7.4.1.1 Elemental Maps 229
7.4.1.2 Sampling 230
7.4.1.3 Examination of Sample Volume 230
7.4.1.4 Laser as a Sampling Tool - Theory 231
7.4.2 Sample Volume 233
7.4.2.1 Spot Size 235
7.4.2.2 Scan Speed 235
7.4.2.3 Repetition Rate 236
7.4.2.4 Fluence 237
7.4.2.5 Flow Rate 238
7.4.2.6 Particle Size and Sample Material 239
7.4.2.7 Elemental Fractionation 239

7.4.3 Future Work 240

7.5 Conclusions 241

8 Conclusions 243

9 Appendices 245

9.1 Appendix 1 – Solution ICP-MS Bulk-Rock Geochemistry Data 246

9.2 Appendix 2 – LA-ICP-MS Geochemistry Data 256

9.3 Appendix 3 - Bulk-Rock Geochemistry Data of Limestones and Fossils 279

References 282

Abbreviations and Symbols

ABL	Argillaceous Bioclastic Limestone
AGV-2	andesite, rock reference material from the USGS
ARIS	Aerosol Rapid Introduction System
BC	Boulder Conglomerate
BCR	basalt, rock reference material from the USGS
BEC	background equivalent concentration
BHVO-2	basalt, rock reference material from the USGS
BIR	basalt, rock reference material from the USGS
BMM	Ballynamona Member
BMU	Boudin Mudstone Unit
BSE	backscattered-electron
CA-ID-TIMS	Chemical Abrasion Isotope-Dilution Thermal Ionisation Mass Spectrometry
Cf	Carboniferous foraminifera zone
CHARAC	CHArge-and Radius-Controlled
CL	cathodoluminescence
CN	chondrite normalised
CoDA	compositional data
cps	counts per seconds
FAD	First appearance datum
FG	Fingal Group
GeoReM	Geological and Environmental Reference Materials
GSJ	Geological Survey of Japan
GSSP	Global Stratotype Section and Point
GTS	Geological Time Scale
HCl	hydrochloric acid
HF	hydrofluoric acid
HFSE	high field strength element
HNO_3	nitric acid
HREE	heavy rare earth elements; gadolinium to lutetium
IAG	International Association of Geoanalysts
ICP-MS	inductively coupled plasma mass spectrometry
ICP-Q-MS	inductively coupled quadrupole mass spectrometry
iCRAG	Irish Centre for Research in Applied Geosciences

JA-2	andesite, Japanese rock reference material
JA-3	andesite, Japanese rock reference material
JLs-1	limestone, Japanese rock reference material
KB	Kilbryan Limestone Formation
KRVF	Knockroe Volcanic Formation
KSVF	Knockseefin Volcanic Formation
LA-ICP-MS	laser ablation inductively coupled plasma mass spectrometry
LG	Lough Gur Formation
LILE	large-ion lithophile element
LREE	light rare earth elements; lanthanum to samarium
Ma	million years
MC-ICP-MS	Multi collector inductively coupled plasma mass spectometry
MFZ	Mississippian Foraminiferal Zone
Milli-Q water	deionised water
MS	Micritic Sequence
MSWD	mean square of the weighted deviates
MuQ	Mud from Queensland; shale standard
n	number of grains
NARC	North American Shale Composite; shale standard
NIST	National Institute of Standards and Technology
NMU	Nodular Micrite Unit
OP	Oakport Limestone Formation
OU-6	Penrhyn Slate, shale standard
PAAS	Post-Archaean Australian Shale, shale standard
PEEK	polyetherketone
pers.comm.	personal communication
Pb_C	common lead
REEs	rare earth elements
REE+Y	rare earth elements plus yttrium
SB	Sedimentary Breccia
SBMU	Sub-Bottom Marker Unit
SCO-1	Cody Shale, shale standard
SD	Standard deviation
SEM	scanning electron microscope
SIS	Strontium Isotope Stratigraphy

SP	Shaley Pales
SWEX	south-west extension
TAS	total alkali *vs* silica
TCF	Tober Colleen Formation
TBU	Thin Bedded Unit
TIMS	Thermal Ionisation Mass Spectrometer
UCC	Upper Continental Crust
UCD	University College Dublin
UCM	Upper Calcarenite Member
UDL	Upper Dark Limestone Formation
UDM	Upper Dark Marker
ULSU	Upper & Lower Shaley Units
USGS	United States Geological Survey
UWLU	Upper Wavy Laminated Unit
W-2	diabase, rock reference material from the USGS
WAL	Waulsortian Limestone Formation
WLI	White light interferometer
P	density
σ	sigma
Σ_D	sum of absolute deviates
ΣREE	total concentration of rare earth elements
%RSD	percentage relative standard deviation

Chapter 1:

Introduction

Zinc is the fourth most consumed metal globally after iron, aluminium and copper, with an annual production of about 12 million tonnes (e.g. Thomas, 2018; Tolcin, 2021) . Over 60% of the Zn produced annually is used to galvanise steel to protect it from rust and corrosion. Galvanisation can extend the lifetime of steel and iron products by more than 50 years and thus contributes to sustainability performance. Global Zn inventories reached a multi-year low in 2020, although 30% of global annual Zn production originates from recycled or secondary Zn. New economically viable Zn deposits are difficult to find.

However, the ores hosted in the Carboniferous carbonates in the Irish Midlands constitute the highest concentration of Zn per square kilometre on the planet (Singer, 1995). Zinc-lead orebodies include the extremely large Navan deposit, the biggest Zn resource in Europe (Ashton et al., 2015) and about the fifth largest in the world, as well as Tynagh, Silvermines, Galmoy and Lisheen along with a number of currently sub-economic deposits and prospects (Pallas Green (Minco-Xstrata), Stonepark (Teck Ireland Ltd—Connemara Mining Company Plc) and Kilbricken (Belmore–Lundin) (Redmond, 2010)). The ores recovered from Irish mines are typically clean and easy to process, which keeps the processing costs low and minimises impact on the environment. The overall aim in Ireland is to discover further high-grade Zn deposits to ensure a sustainable future.

Therefore, a thorough understanding of the regional geology of existing mines and exploration targets is crucial, as this knowledge enables efficient exploration on well characterised deposits and prospects. To be able to resolve the origin and geological context of these Irish-type Zn-Pb stratabound deposits requires accurate stratigraphical correlations within the host rocks. However, presently the biostratigraphy of the Mississippian (Tournaisian and Viséan) limestones of the Irish Midlands is not tied to a finely resolved geochronological framework (Wilkinson and Hitzman, 2015). Determination of the absolute age of alteration and mineralisation in the Irish deposits, as in many other carbonate-hosted base metal deposits worldwide, has been hampered by the absence of minerals suitable for radiometric dating. Thus, there are still uncertainties about the timing of mineralisation and faulting relative to the age of the host strata.

However, volcanic ash layers have been observed both above and below known zinc ore horizons in central Ireland. Volcanic ash deposits often can serve as excellent marker horizons as they may form isochronous layers, which can often be traced for hundreds of kilometres

(e.g. Gudmundsson et al., 2012; Lane et al., 2013; Watson et al., 2016). Geochemical characterisation of individual tephra layers has been used widely in correlation and provenance studies and therefore the position of the Irish tuffs makes them potential chemostratigraphic markers (e.g. Jensen et al., 2014; Huff, 2016; Huang et al., 2018; Pointon et al., 2018). If they can be used for precise regional correlations, they can contribute to an increased understanding of the genesis of the Irish Zn-Pb deposits, which ultimately supports exploration for new deposits. This work provides a tephrostratigraphic framework using a combined multi-proxy geochemical approach, which includes bulk-rock trace element geochemistry, U-Pb zircon geochronology and apatite trace element characterisation of these Mississippian ash horizons. Following construction of this tephrostratigraphic framework, the ashes are also linked to their potential volcanic centres. Furthermore, the potential of enclosing limestone deposits as a secondary correlation tool is investigated. Therefore, micritic limestones, brachiopods, corals and crinoids are evaluated for their preservation potential of primary seawater signals by interrogating their trace element and Sr isotopic compositions, while also introducing a novel *in situ* laser ablation sampling technique.

1.1 Tephrostratigraphy and Tephrochronology

Tephrostratigraphy and tephrochronology are chemostratigraphic and dating techniques (respectively) employed to constrain the precise stratigraphic position and geochronological age of volcanic ashes.

Tephrostratigraphic studies use the geochemical composition of the volcanic ashes to arrange sampled tephra into single or several discrete and time-ordered stratigraphic sequences, while tephrochronology provides absolute isotopic age data.

1.1.1 Terminology – Tephra *vs* Tuff

'*Tephra is fragmental material produced by explosive volcanic eruptions, regardless of magma composition, fragment size or the emplacement mechanism*': Sigurdur Thórarinsson, Icelandic volcanologist.

Tephra is derived from the Greek word τεφρα meaning ashes, and was introduced by Sigurdur Thórarinsson in his 1944 doctoral thesis. Tephra may be transported over large distances by wind or water before it is deposited as distinct layers either subaerially or subaqueously. The chemical composition of tephra is often locally and temporally variable.

Tephra terminology is based on the grain size of the material which represents more than 50% of the total volume. The smallest fraction of tephra is called ash (< 2 mm Ø), followed by lapilli (2 mm – 64 mm Ø) and volcanic bombs/blocks (> 64 mm Ø) (Fisher, 1966).

Recent volcanic ash is typically made up of volcanic glass, phenocrysts and amorphous clays (e.g. Kawano and Tomita, 2001). Volcanic ash, which is lithified into solid rock following deposition is called a tuff.

In general, with increasing age and degree of alteration, tephra deposits, which contain fresh volcanic glass, grade into glass-free, clay-bearing bentonites when they are altered in an aqueous environment, either after subaqueous or subaerial transport, where the type of clay materials depends on the nature of the particular depositional environment (Bohor et al., 1979; Bohor and Triplehorn, 1993). Ross and Shannon (1926) defined the term 'bentonite' as 'a rock composed essentially of a crystalline clay-like mineral formed by the devitrification and the accompanying chemical alteration of a glassy igneous material, usually a tuff or volcanic ash'. Although the samples in this study fit into this definition and can thus be classified as bentonites, only the term 'altered volcanic ash' or tuff are used herein.

Whenever several tuff samples from several drill cores form one distinct tuff band, it is referred to a tuff layer, while a tuff horizon is defined as a regionally correlatable tuff layer.

1.1.2 Tephrostratigraphy

Given that the age and chemistry of a tuff layer may be consistent across the entire ash horizon and that the tuffs themselves may have been dispersed over very wide areas (up to 1000’s of kilometres), volcanic ashes can be unique isochronous stratigraphic markers with very wide correlation potential (e.g. Jensen et al., 2014). Therefore, tephrostratigraphy can represent an invaluable stratigraphic correlation tool over large areas and can provide high-resolution correlations to supplement biostratigraphic records. The conventional practice in tephrostratigraphy is to employ the major-element composition of volcanogenic glass as a correlation tool (Lowe, 2011). However, in most cases, especially in pre-Cenozoic ash falls, the tuffs are likely to be affected by secondary alteration and devitrification, which can alter the original glass composition (Cerling et al., 1985; McHenry, 2005). In some cases, volcanic ashes are completely devitrified and altered to clay minerals. As a result, successful geochemical correlation of highly altered ash beds by bulk chemical composition is difficult because these processes may significantly reduce or modify differences in the original chemical compositions of the ash beds (Samson et al., 1995). However, many tephrochstratigraphical studies have relied on the use of chemical analysis of bulk ash samples as a method of identifying individual ash layers on a regional scale (e.g. Kolata et al., 1987; Haynes, 1994; Inanli et al., 2009).

1.1.3 Tephrochronology

Although diagenetically altered volcanic ash layers are comprised predominantly of clay minerals, they often contain a small amount of coarser phenocrysts that include (often euhedral) zircon, apatite, biotite, sanidine and quartz, which are inferred to be original volcanic phenocrysts. More recently, ash beds have been successfully correlated on a continental scale by *in situ* analysis of these mineral phases, in sequences which were reasonably well biostratigraphically constrained (Goldman et al., 1994; Emerson et al., 2004; Mitchell et al., 2004).
Apatite and zircon can have a diagnostic trace element composition, as they often reflect late stage crystallisation in the host magma (e.g. Bowring et al., 1998), thus providing a geochemical fingerprint for each volcanogenic bed. The minor and trace element contents of apatite have been successfully used for stratigraphic correlation purposes in heavily altered Palaeozoic tephra (Samson et al., 1995; Emerson et al., 2004; Mitchell et al., 2004; Carey et al., 2009). However, both, apatites and zircons are also amenable to uranium-lead dating, with zircons in particular providing high-precision age data. Thus, if the tuff horizons contain either zircon or apatite, they can be used as age markers within the stratigraphy (tephrochronology). When the age of one distinct ash layer is determined, it can be applied directly to all correlatives identified by chemostratigraphic approaches, as tephra layers are erupted over very short periods (hours or days to a maximum of weeks to a few months), and thus represent an instantaneous layer on a geological timescale (Lowe, 2011).

1.2 Mississippian Time Scale

The Carboniferous is divided into the older Mississippian and younger Pennsylvanian subsystems. The Mississippian is further sub-divided into the Tournaisian, Viséan and Serpukhovian stages. The Tournaisian and Viséan are called after the Belgian towns of Tournais and Visé, respectively, while the youngest stage is named after the city of Serpukhov in Russia. Currently, only the base of the Tournaisian and Bashkirian (youngest Pennsylvanian stage) are fully ratified Global Stratotype Section and Points (GSSPs) (Paproth et al., 1991; Lane et al., 1999). The GSSP for the base of the Viséan (Devuyst et al., 2003; Richards, 2009) is defined and has been ratified by the International Commission on Stratigraphy, but the final publication on the base Viséan GSSP has yet to be published. The GSSP for the base of the Tournaisian Stage (Devonian/Carboniferous boundary), has been defined in bed 89 in La Serre section, Montagne Noire, southern France (Paproth et al., 1991), based on the conodont species *Siphonodella praesulcata* and *Siphonodella sulcata* in the global timescale, although the first appearance of *S. sulcata* is already in bed 85. The Tournaisian-Viséan boundary is determined at the base of bed 83 of the Pengchong section in Guangxi, south China by the first appearance of the benthic

foraminifera *Eoparastaffella simplex*, within an evolutionary sequence from *Eoparastaffella ovalis* (Devuyst et al., 2003). The Tournaisian lasted from 359.3 ± 0.3 (2σ) to 346.7 ± 0.4 (2σ) Ma, corresponding to a duration of 12.6 Ma. The Viséan is the longest stage in the Phanerozoic and lasted 16.4 Ma from 346.7 ± 0.4 (2σ) to 330.3 ± 0.4 (2σ) Ma. The first appearance datum (FAD) of the conodont *Lochriea ziegleri* is currently regarded as the most useful biomarker to define the base of the succeeding Serpukhovian Stage (e.g. Nemyrovska and Samankassou, 2005; Nemyrovska, 2017), although it still needs official approval from the Subcommission on Carboniferous Stratigraphy and the International Commission on Stratigraphy (Richards, 2013). The GSSP for the base of the Bashkirian Stage is defined near the northern end of the Arrow Range, in Arrown Canyon, United States, based on the first appearance of *Declinognathodus noduliferus* s.l. (Lane et al., 1999). The base of the Bashkirian is dated at 323.4 ± 0.4 (2σ) Ma and coincides with the Mississippian – Pennsylvanian boundary. The bases of the Moscovian, Kasimovian and Gzhelian stages are at 315.2 ± 0.4 (2σ) Ma, 307 ± 0.4 (2σ) Ma and 303.7 ± 0.4 (2σ) Ma, respectively. Specific biomarkers are not defined yet for these three stages. However, different task groups currently discuss potential stratotype candidates (Aretz et al., 2020). The age of the stage boundaries are taken from the Geological Time Scale 2020 (GTS2020; Aretz et al., 2020).

This study focuses only on the Western European Mississippian substages. They are mainly based on the successions in Belgium and Britain. The Belgian Tournaisian and Viséan substages are well characterised. The Tournaisian in Belgium is divided into two subgroups, the Hastarian and Ivorian, followed by the Viséan subgroups, termed the Moliniacian, Livian and Warnantian. The Hastarian coincides with the base of the Mississippian subsystem and correlates *inter alia* with the Mississippian foraminiferal zone (MFZ) 1-3 and the lower part of MFZ4 (Devuyst and Hance, in Poty et al., 2006). The base of the following Ivorian substage corresponds to the appearance of the conodont *Polygnathus communis carina* (Hance et al., 2006) and comprises the upper part of MFZ4 as well as MFZ5 to MFZ8 (Devuyst and Hance, in Poty et al., 2006). The Ivorian – Moliniacian boundary coincides with the base of the Viséan subsystem. The Moliniacian, the Livian and Warnantian are equivalent to the MFZ9-11, MFZ12 and MFZ13-15 of Devuyst and Hance (in Poty et al., 2006), respectively.

The British substages have not been refined since their definition by George et al. (1976) and the only regional substage in the Tournaisian of Britain and Ireland is the Courceyan, with a stratotype at the Old Head of Kinsale in County Cork, Ireland (George et al., 1976). The base of this substage is defined using the base of the *Vallatisporites verrucsus-Retusotriletes incohatus (VI)* miospore zone, which almost coincides with the Devonian-Carboniferous boundary (Clayton et al., 1974). The Viséan Stage in Britain and Ireland is represented by five substages; the Chadian, Arundian,

Holkerian, Asbian and Brigantian. However, the lower part of the Chadian is part of the Tournaisian Stage, while the upper part belongs to the Viséan. Riley (1990) proposed to use the term 'late Chadian' where strictly Viséan-aged strata can be recognised. Another suggestion is to use the term 'Lower Viséan' for the oldest part of the Viséan until a substage is defined, which share the same GSSP as the base of the Viséan (Sevastopulo and Wyse Jackson, 2009). Waters et al. (2011) amongst others push to redefine the base of the Chadian to agree with the base of the Viséan. The Arundian starts with the first lithological change below the appearance of the foraminifer family Archaediscidae (George et al., 1976). Riley (1993) suggested that the Chadian-Arundian boundary can be equated to the boundary between the *Fascipericyclus-Ammonellipsites* and *Bollandites-Bollandoceras* ammonoid biozones, which was acknowledged by Waters et al. (2011). The Arundian lasts until the first lithological change below the diagnostic Holkerian fauna composed of the corals *Axophyllum vaughani* and *Lithostrotion vorticale*, the brachiopods *Davidsonia carbonaria, Composita ficoides*, and *Linoprotonia corrugatohemispherica*, the foraminifers *Archaediscus* spp. of the *A. concavus* stage and paleotextularidiids (George et al., 1976). Waters et al. (2011) indicated the Arundian-Holkerian boundary coincides with the base of the Carboniferous foraminiferal biozone 5 (Cf5), which also equates to the base of MFZ12.

In general, biostratigraphy shows a potential resolution of 10 000 to 50 000 years over time spans on the order of 50 to 100 Ma (Sadler, 2004), but the highest practically obtainable resolution typically lies between 0.5 and 1 Ma (Veizer et al., 1999). At present, the internal sub-boundaries of the Carboniferous System can be determined with an accuracy between 0.8 and 2.5 Ma. Thus, the use of the local biostratigraphy is limited in the area of interest. However, there are several studies on the Irish Carboniferous that have aimed to improve the biostratigraphical resolution, resulting in over 35-40 zones detected in the Carboniferous using foraminifera, conodonts and ammonoids (Kalvoda et al., 2011; Sevastopulo and Barham, 2014; Fallon and Murray, 2015).

Forty-seven radiometric dates are used in the GTS2020, which refine the stratigraphic resolution for the Carboniferous Period, although the Mississippian is less well characterised (only eleven high-precision U-Pb dates) compared to the Pennsylvanian (36 high-precision U-Pb dates) (ages are listed in Table 23.2 in Aretz et al., 2020). Reliable age data for the Tournaisian are based mainly on work in the Donets basin (e.g. Davydov et al., 2010; George Sevastopulo, 2020, pers. comm.), while the base of the various regional substages (Arundian, Holkerian, Asbian and Brigantian) are more uncertain due to a lack of age data (Aretz et al., 2020). However, Davydov et al. (2010) determined an age of 342.01 ± 0.1 (2σ) Ma for the base of the MFZ12 zone in the Donets Basin, which equates to the base of the Livian substage. So far, radiometric data for the Belgian Tournaisian and Viséan stage boundaries and their substages are not used in the

GTS2020. An available absolute age from a bentonite from the base of the Livian type section indicates a comparably younger age of 341.2 ± 0.11 (2σ) Ma (Pointon et al., 2021) for the base of the Livian and thus shows that further work to establish reliable Carboniferous boundaries is necessary.

Herein, the Belgian Tournaisian and the Irish Viséan substages including the term 'Lower Viséan' as suggested by Sevastopulo and Wyse Jackson (2009) are used for stratigraphic descriptions. Thus, the substages match the Western European regional stage boundaries and the biostratigraphic resolution for the Mississippian of Western Europe is provided below.

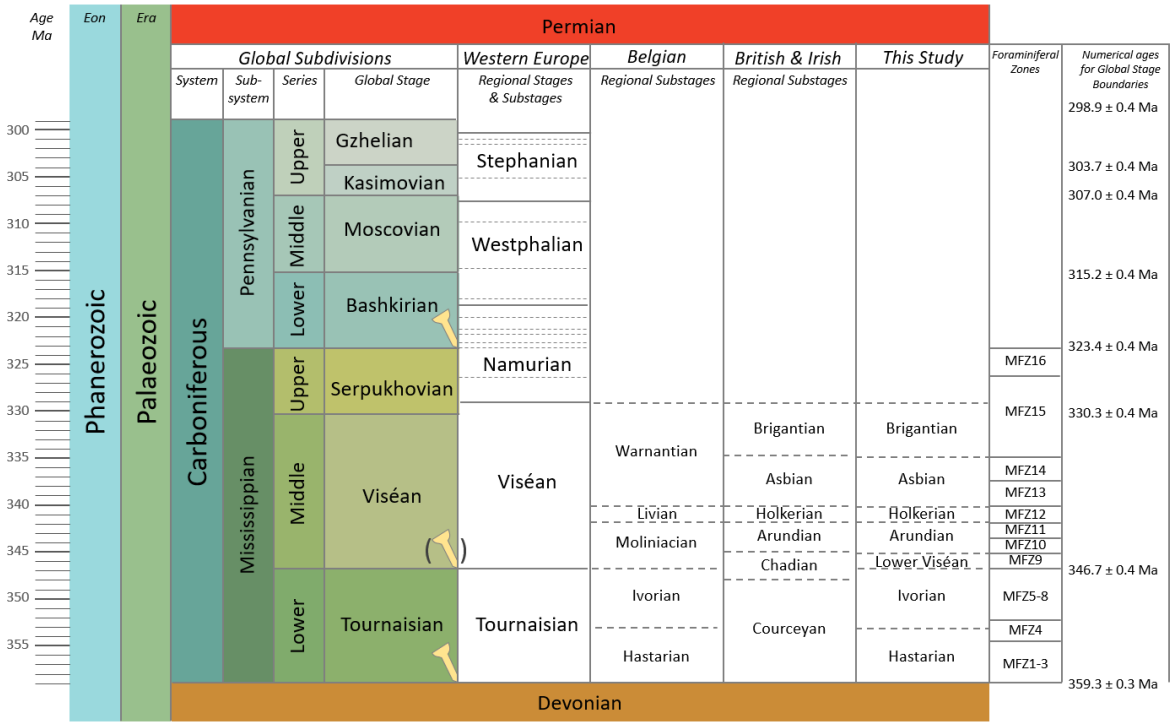

Figure 1-1: The geological time scale for the Carboniferous Period. International chronostratigraphic subdivisions are shown in colour, following the colour composition by J.M.Pellé (Bureau de Recherches Géologiques et Minières, France). Regional stages of Western Europe are labelled, while its substages are indicated by dashed lines. Mississippian Belgian, British and Irish regional substages are also presented. The substages employed in this study follow the Belgian Tournaisian divisions and the Viséan divisions suggested by Sevastopulo and Wyse Jackson (2009). Foraminiferal zones for Western Europe are taken from Devuyst and Hance in Poty et al. (2006). Numerical ages (in Ma) are taken from the Stratigraphic Geological Time Scale 2020 (GTS2020; Aretz et al., 2020). Global Stratotype Section and Points (GSSPs) are indicated by yellow pins. The Viséan GSSP is already ratified while the final publication remains outstanding and is therefore shown in brackets.

Chapter 2:

The Stratigraphic Setting of Irish Carboniferous Tuffs

2.1 Introduction

This chapter provides a general outline on the Irish Mississippian (Tournaisian and Viséan successions, followed by a more detailed description of the sampled areas. These areas are around existing mines or prospects, and are named Navan, Lisheen and Rapla (Rathdoweny trend), Stonepark and Slievedart in this thesis (Figure 2-1).

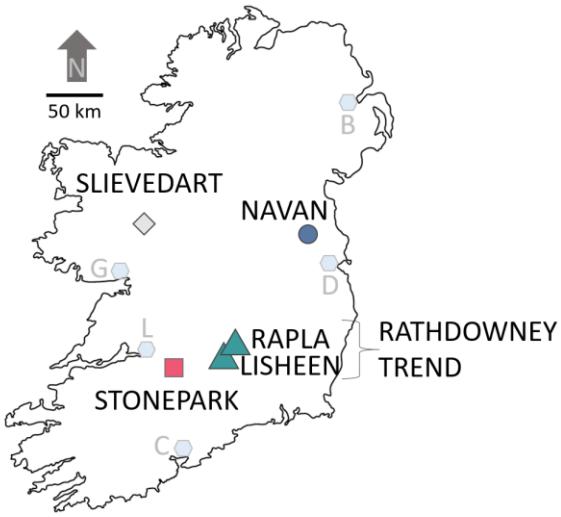

Figure 2-1: The four sample locations, named Navan, Lisheen and Rapla (Rathdowney Trend), Stonepark and Slievedart. Irish cities (blue hexagons; Belfast (B), Cork (C), Dublin (D), Galway (G), and Limerick (L)) are provided for reference.

This geological outline starts in the Early Palaeozoic, when present-day northwest Ireland and Scotland formed part of Laurentia (Golonka, 2000; Golonka, 2002; Ford and Golonka, 2003; Golonka et al., 2003), while southeastern Ireland, England, Wales, northern Germany, the Ardennes in Belgium and northern France formed part of Avalonia (McKerrow et al., 1991; Golonka, 2009). Laurentia, Baltica and Avalonia were originally separated by the Iapetus Ocean (Figure 2-2A-D). During the Late Ordovician (490 Ma), Avalonia started drifting northwards. It then collided with Baltica, followed by the collision with Laurentia at around c. 425 Ma, which coincided with the initial closure of the Iapetus Ocean (Figure 2-2A-F). Collision was complete by c. 390 Ma ago and the continents of Baltic, Avalonia and Laurentia together formed the continent of Laurussia; also called Euramerica (Ziegler, 1989) (Figure 2-2E-H). In Ireland and Britain, all the

orogenic phases associated with the closure of the Iapetus Ocean are termed the Caledonian orogenic cycle (490 – 390 Ma). Ever since then, Ireland has been one landmass (Figure 2-2F).

The Variscan orogeny followed on from the Caledonian orogenic cycle, whereby an ocean to the south of Laurussia (the Rheic Ocean) was subducted during the Devonian and Carboniferous periods, resulting in the formation of the Variscan belt (Figure 2-2G, H). During the Early Carboniferous (the Mississippian), Ireland lay in tropical latitudes (Figure 2-2G, H). A marine transgression, which took place from the Late Devonian through to the Viséan deposited northward-migrating, progressively deeper marine carbonate sequences throughout Ireland (Philcox, 1984; Sevastopulo and Wyse Jackson, 2009) (Figure 2-3A, B). By the Viséan, Ireland had become the location of a shallow-water carbonate shelf (Figure 2-3B). The transgression was accompanied by regional N-S to NNW-SSE directed extension (Gawthorpe et al., 1989; Fraser and Gawthorpe, 1990; Johnston et al., 1996; Fraser and Gawthorpe, 2003), which formed several regionally extensive Mississippian basins (Worthington and Walsh, 2011) (Figure 2-3C). The Tournaisian sequences have been sub-divided by Philcox (1984) into the following four stratigraphic provinces: the Limerick Province, North Midlands Province, Dunmore Province and the Kildare Province (Figure 2-3C).

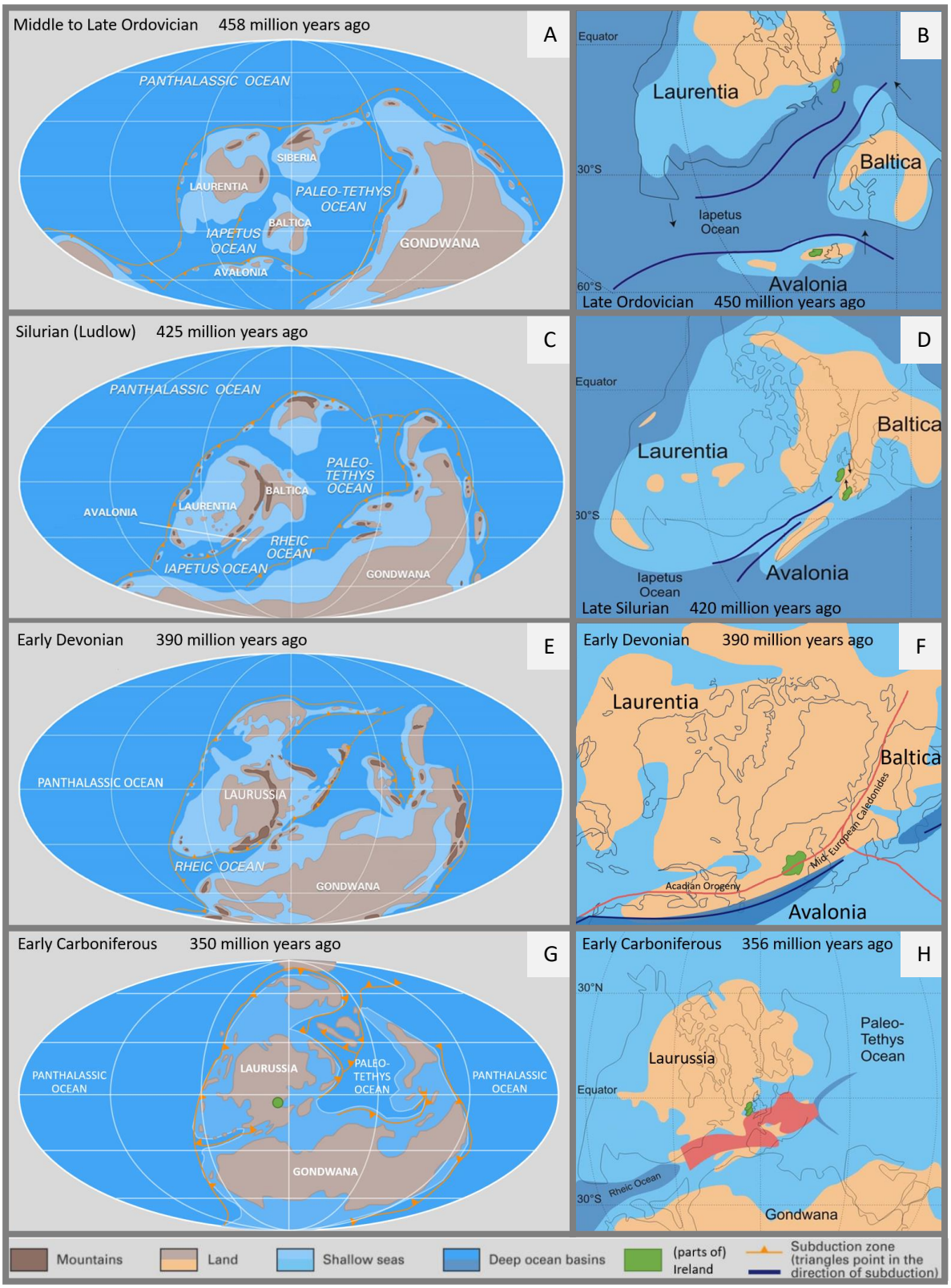

Figure 2-2 A – H) Paleogeographic reconstructions from the Middle Ordovician to the Early Carboniferous. B), D), F), H) show the location of Ireland during this same interval. Present-day coastlines are indicated in grey for reference. The red line in F) shows the Iapetus suture after the collision of Avalonia and Laurentia which built the Caledonian orogeny, which coincides with the amalgamation of the northern and the southern halves of Ireland. The red band in H) indicates the Variscan orogenic belt. A), C) and E) are adapted after Scotese, 2001; B) and D) are adapted after Chew (2009) and Doepke (2017); F) is adapted after Scotese (2001) and Woudloper (2008); G) is adapted after Mikuláš et al. (2017) and Isaacson et al. (2008); H) is adapted after Chew (2009), McKerrow and Scotese (1990), Doepke (2017).

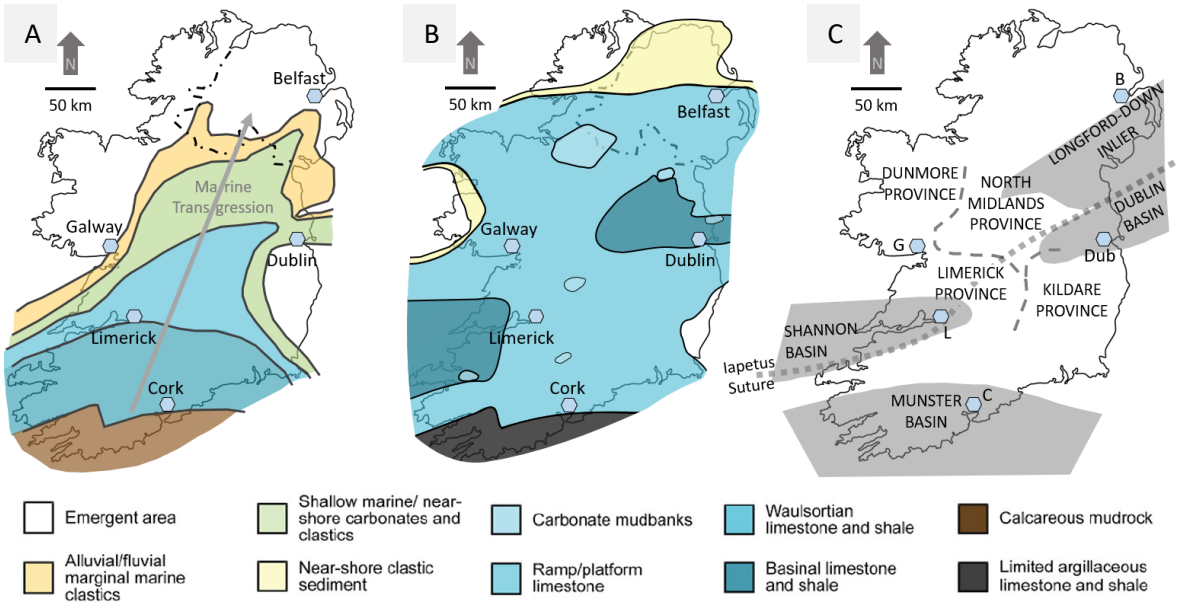

Figure 2-3: The northward-migrating Carboniferous marine transgression in Ireland. A) and B) show the depositional environment in the mid Tournaisian and mid-late Viséan, respectively. C) shows the major tectonic features, which were developed during the Early Carboniferous (Dublin Basin, Munster Basin, Shannon Basin, Longford-Down Inlier) as well as the postulated position of the Iapetus Suture (420 Ma), which is the remnant of what was once the Iapetus Ocean. Tentative boundaries of the four stratigraphic provinces (Kildare Province, Limerick Province, Dunmore Province, North Midlands Province) are adapted from Philcox (1984). Irish cities (blue hexagon) are listed for reference: Belfast (B), Cork (C), Dublin (Dub), Galway (G), and Limerick (L). A) and B) are from Barham (2010).

2.2 Irish Mississippian Stratigraphy

A simplified cross-section of the Irish Mississippian stratigraphy is outlined in Figure 2-4. The Lower Palaeozoic basement to the Irish Carboniferous consists largely of Ordovician and Silurian sedimentary, volcanic and intrusive rocks, many of which are remnants of the former Iapetus Ocean. These were deformed and weakly metamorphosed during the Caledonian orogenic cycle (Wilkinson and Hitzman, 2015). The exceptions are in the northern parts of Ireland where the basement is Dalradian metasediments. In the four study areas, the Old Red Sandstone facies, a terrigenous clastic red bed succession, lies unconformably on the eroded Ordovician or Silurian basement. This facies is partly Devonian and partly Ivorian (Lisheen and Stonepark), or Ivorian (Navan and Slievedart) in age, and is primarily composed of fluvial deposits (e.g. Graham, 2009). The Old Red Sandstone facies migrated gradually northwards, away from the Munster Basin, preceding transgression in the Early Carboniferous (Sevastopulo and Wyse Jackson, 2001).

The Old Red Sandstone is typically conformably overlain by the first Tournaisian marine sediments, which marks the beginning of the northward migrating marine transgression from the South Munster Basin (Figure 2-3A) across the southern margin of the Laurussian continent (Mallon, 1997). In the Limerick Province, the oldest rocks of this marine section are a transitional succession of sandstone, limestones and shales (Philcox, 1984) and are referred to as the Lower Limestone Shale Group (e.g. Somerville et al., 1992; Pracht and Somerville, 2015) (Figure 2-4). This group can neither be observed in the northern region of the Dunmore Province, nor in the North

Midlands Province (Figure 2-3C). The lateral equivalent of the Lower Limestone Shale Group to the north are the basal sequences of the Navan Group (Philcox, 1984), although many publications simply refer to the Navan Group in total (e.g. figure 4 in Wilkinson and Hitzman, 2015). The Navan Group reflects initial marine sedimentation in shallow to peritidal environments (Philcox, 1984; Braithwaite and Rizzi, 1997) (Figure 2-4). More open-marine conditions were then established as far north as the northernmost part of the Dunmore Province (Pracht and Somerville, 2015). This resulted in deposition of the Ballysteen Limestone Formation (which is commonly termed Argillaceous Bioclastic Limestone, ABL) in the Limerick Province, the Ballysteen Group (similar concept) in the Dunmore Province, or the Malahide and Slane Castle Formations (North Midlands Province), which all represent similar ramp facies (Philcox, 1984; Jones et al., 1988; Strogen et al., 1996). This widespread carbonate facies was then followed by deposition of the Waulsortian Limestone Formation throughout all provinces (e.g. Lees and Miller, 1995; Figure 2-4), marking the end of the Early Carboniferous transgression. The Waulsortian Limestone Formation is composed of massive micritic limestones and a number of coalesced mudbanks. In the Viséan (Lower Viséan to Brigantian), carbonate sedimentation continued; likely in shallow water. This led to the development of a widespread supra-Waulsortian shallow-water platform (e.g. Strogen et al., 1996; Morris et al, 2003). However, the facies distribution from Lower Viséan through to Asbian times was controlled by strong differential tectonic subsidence. For example in the Dublin Basin, it led to the deposition of deep-water calcareous shales and carbonate turbidites, whereas the Shannon Basin was a complex depocentre by mid-late Viséan, with late Viséan carbonate mound development fringed by shallow water carbonate platforms (Murray, 2010; Somerville et al., 1992; Strogen et al., 1996) (Figure 2-3A-B). Recent drilling further west has revealed thick mass-transport deposits and sedimentary breccias within deep-water turbidites, similar to Navan (Dr. Michael Philcox, 2020, pers. comm.).

2.3 Mineralisation

The ore deposits in the Irish Orefield are restricted to two stratigraphic units, which were deposited during the Mississippian. Their distribution results from the progressive SW-to NE marine transgression (Wilkinson and Hitzman, 2015). These include the deeper marine Waulsortian Limestone Formation in southern and central Ireland (e.g. the Silvermines, Lisheen, Galmoy, Ballinalack and Tynagh deposits) (Hitzman and Large, 1986; Phillips and Sevastopulo, 1986; Hitzman, 1995; Hitzman and Beaty, 1996; Johnston, 1999; Wilkinson et al., 2003) and the shallow marine Navan Group of north-central Ireland (Navan Deposit) (Ashton et al., 2000; Fallick et al., 2001) (Figure 2-4). Circulating hydrothermal solutions transported and precipitated tens of millions of tonnes of Zn and Pb metal in the form of sulphides (typically galena and sphalerite) in

these carbonates. The ores hosted in the Carboniferous limestones in the Irish Midlands constitute the highest concentration of Zn per square kilometre on the planet (Singer, 1995). The majority of the Zn–Pb mineralisation in Ireland has classically been described as Irish-type (Hitzman and Beaty, 1996). Irish-type mineralisation has many similarities with Mississippi Valley-type mineralisation, occurring as massive strata-bound bodies at the base of the first non-argillaceous carbonate within a marine transgressive sequence. The observed low angle faults and slides in the Navan (Ashton et al., 2015) and Lisheen deposits (Carboni et al., 2003; Fusciardi et al., 2003) confirm a close spatial and temporal relationship between tectonism and sedimentation in the developing Carboniferous basins (Wilkinson and Hitzman, 2015). The presence of mineralised clasts with truncated laminae within early Viséan debris flows as well as the occurrence of Zn-Pb mineralisation in well-bedded limestone of late Tournaisian to Viséan age is clear evidence that mineralisation in Navan was active during the late Tournaisian to at least the early Arundian, spanning a timeframe of around 10 Ma (Ashton et al., 1992; Ford, 1996; Altinok, 2005; Ashton et al., 2015). This timeframe is consistent with interpreted ages for the Lisheen mine (Wilkinson et al., 2011; Hnatyshin et al., 2015). Detailed observations show that normal faults have an important control on the local distribution of mineralisation (Fusciardi et al., 2003). Two broad genetic models have been proposed for the Irish-type mineralisation. The first proposes a partly syn-sedimentary origin with mineralisation happened at or near the seafloor (Andrew, 1986; Wilkinson et al., 2005), while the second contends that mineralisation is entirely epigenetic and that mineralisation occurred at depth (> 800 m) (Hitzman and Beaty, 1996; Peace and Wallace, 2000; Reed and Wallace, 2001; Hitzman et al., 2002; Reed and Wallace, 2004). While uncertainty exists in the timing of mineralisation relative to the age of the host strata, it is clear that normal faults exert an important control on the mineralisation with most known Irish deposits located in the hanging wall of normal faults i.e., Lisheen and Galmoy (Hitzman et al., 2002). There is clear geological evidence that ore at Lisheen (Carboni et al., 2003) and at Navan (Ashton et al., 2015) is then cut by reverse faults related to subsequent Variscan tectonic inversion. This implies that mineralisation had ceased prior to Variscan deformation at c. 300 Ma (Wartho et al., 2006). However, difficulty in interpreting the origin of the Irish mineralisation arises partly from the coincidence of both extensional and compressional features within the deposits. Across Ireland, Carboniferous faulting is strongly influenced by reactivated late Silurian to early Devonian Caledonian structures, which is most evident in the wide Iapetus Suture Zone (Figure 2-3C; Phillips et al., 1976). There is general acceptance that the Caledonian NE-SW structural grain was inherited by later Carboniferous faulting (Phillips et al., 1976; Phillips and Sevastopulo, 1986; Johnston et al., 1996).

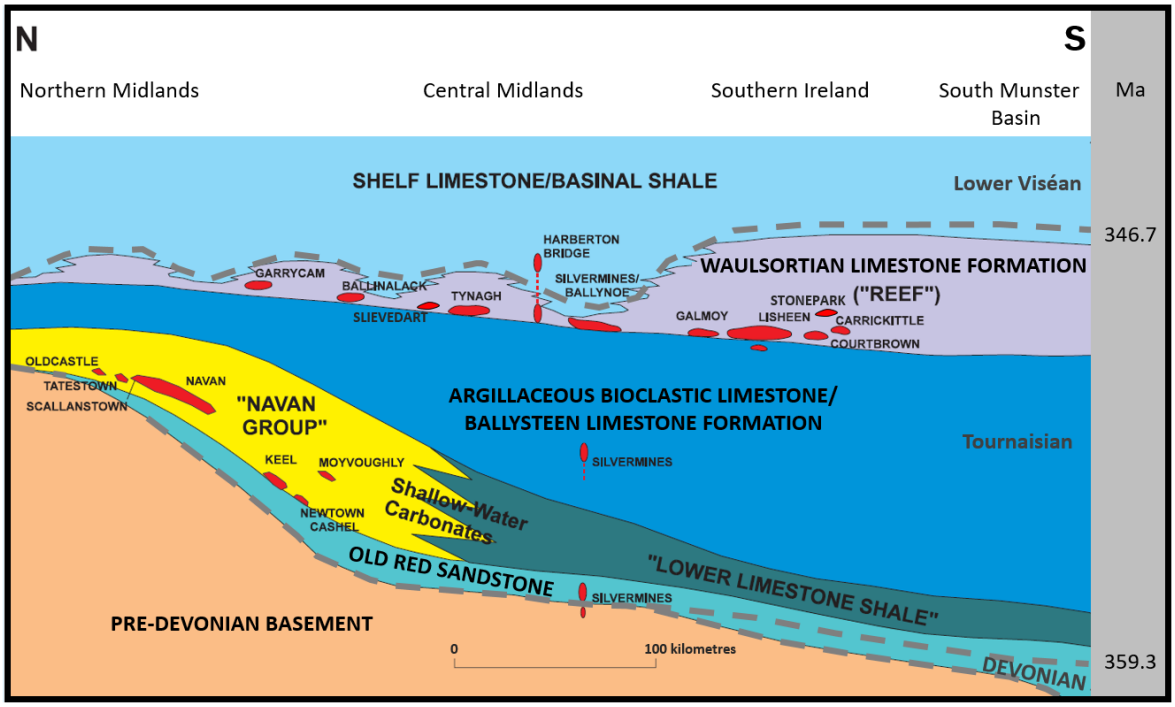

Figure 2-4: Simplified geological profile across the Irish Midlands and Munster Basin showing the stratigraphic location of mineralisation in red. The dashed grey lines represent surfaces of similar age. Straight line across the top of shelf limestone/basinal shale is not isochronous. Modified from an EMD report.

2.4 Volcanism

By the latest Devonian-Early Carboniferous, subduction of the Rheic ocean initiated on the southern margin of Laurussia led to the formation of a back-arc system. This subduction zone as well as the main Variscan collision zone (or Variscan belt), lasted until early Permian times, and is associated with intensive partial melting and voluminous granitoid magmatism (e.g. Burda and Gawęda, 2009; Schulmann et al., 2009). Based on similar tectonic histories and rock types, the emerging Variscan belt (Figure 2-2G, H; Figure 2-5) can be subdivided into three major zones, named the Rhenohercynian, Saxothuringian and Moldanubian zones (Figure 2-5). The oldest Variscan magmatism occurred between 370 and 340 Ma within the Saxothuringian Zone (Odenwald, Northern Vosges and Northern Black Forest), in the Central Bohemian Batholith and along the Alpine Front (Finger et al., 1997) (Figure 2-5). These granitoid bodies are mainly felsic tonalites and granodiorites (Finger et al., 1997). Subsequent Early Carboniferous (c. 340 Ma) granitoid magmatism is represented by deformed peraluminous granites in the southeastern Bohemian Massif (Finger et al., 1997) (Figure 2-5). The most voluminous Variscan magmatic activity took place between 340 and 310 Ma. This is represented by S-type and high-K I-type granitoid within the Moldanubian unit, particularly in the Southern Vosges, Southern Black Forest and Southern Bohemian Massif (Finger et al., 1997) (Figure 2-5).

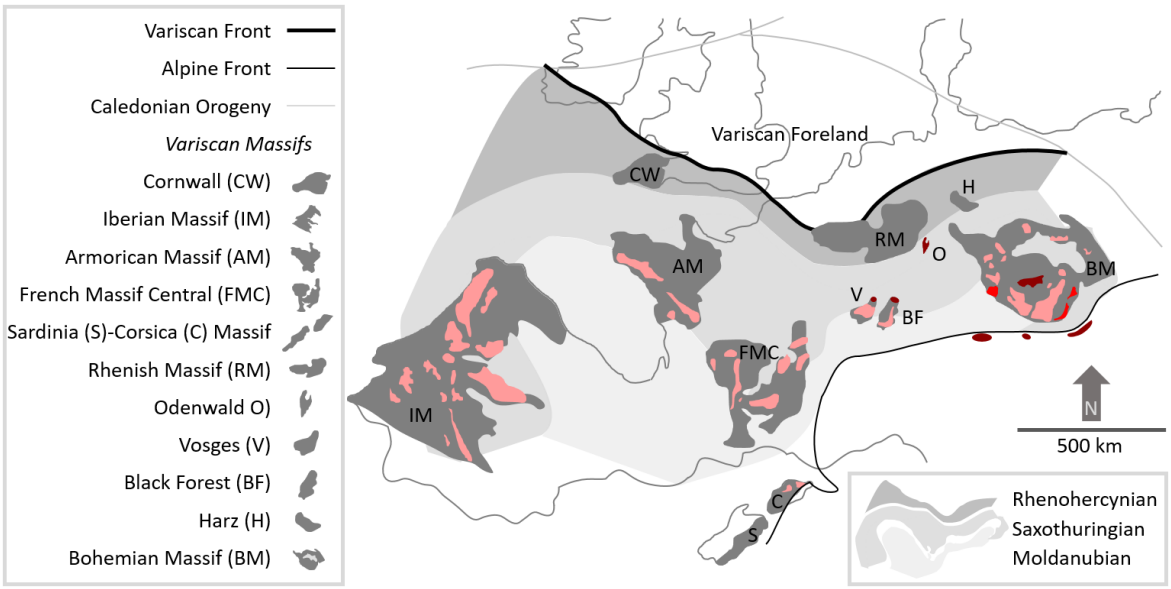

Figure 2-5: The Variscan mountain belt is the area between the Variscan front (thick black line) and the Alpine front (thin black line). The Variscan orogenic belt is divided into three major zones, the Rhenohercynian (dark grey area), the Saxothuringian (medium grey area) and the Moldanubian (bright grey area) zones. The very dark grey areas within the three zones represent the European Variscan massifs. The pastel red, bright red and dark red areas are granitic rocks of the Variscan Orogeny with intrusion ages between 370 to 340 Ma (after Finger et al., 1997), 340 Ma (after Finger et al., 1997) and 340 to 320 Ma respectively (after Franke, 1989; Martínez et al., 1990; Franke, 1992; Neubauer and Raumer, 1993; Carron et al., 1994; Ledru et al., 1994). Present-day coastlines are indicated in light grey for reference. The Caledonian suture is indicated as a thin grey line. Structural subdivision of the European Variscan Belt is from Franke (1992). The legends are framed by grey boxes.

During this time, most of Ireland and Britain was situated outside of the internal Variscan orogenic belt, in the Variscan foreland (Figure 2-5; Figure 2-6). Crustal thinning as a result of back-arc extension related to the Variscan subduction zone to the south led to the development and emplacement of volcanic centres and intrusions across Ireland, Scotland and the English Midlands (Woodcock and Strachan, 2012). While the Early Carboniferous magmatic rocks of the internal Variscides are predominantly felsic to intermediate composition, Tournaisian and Viséan magmatic activity in Britain and Ireland was largely of mafic, within-plate alkaline character (Timmerman, 2004).

At Croghan Hill in central Ireland, on the margin of the Dublin Basin (Figure 2-6A), accumulation of coarse tuffs, agglomerates and ankaramite (feldspar-free basalt) flows occur within early Viséan limestones (McConnell and Philcox, 1994; Strogen et al., 1996; Gatley et al., 2004; Timmerman, 2004). Two ages have been obtained from Croghan Hill, including an ^{40}Ar-^{39}Ar amphibole age of 345 ± 3 Ma from a basalt/ankaramite (M. J. Timmerman, unpublished data) and an Arundian age for vitric tuffs and ankaramites (Strogen et al., 1996). Five biotite megacrysts from Croghan Hill, Clare Castle and Dungolman River have yielded a Rb-Sr iochron age of 351 ± 21 Ma (Van den Berg, 2005), while a Sm-Nd garnet age from a xenolith from Clare Castle yielded an age of 341 ± 2 Ma interpreted as recording the age of intrusion (Daly et al., 1993). Two extrusive volcanic units have been reported in Ulster close to Omagh (Asbian flow-banded andesite; Sevastopulo and Wyse Jackson, 2009) and close to Ballycastle (Brigantian basaltic flows overlain by tuffs; Wilson et al.,

1966; Mitchell, 2004), while there is also volcanic activity in Killary Harbour (the late Viséan, mildly alkaline basaltic Logmor Dyke; Mitchell and Mohr, 1987) (Figure 2-6A).

More voluminous volcanism occurred in the Limerick volcanic region during Viséan times. The volcanic centres of these more primitive eruptions are focused on the east-west trending Limerick Syncline, which is a pull apart basin (Strogen, 1983), approximately 25 km long and 15 km wide and located on the edge of the Shannon Basin (Figure 2-6A). At least three volcanic centres (Boughilbreaga, Knockroe and Knockanea) on the northern limb and three volcanic centres (Knockderk, Rathfooroge, Kilteely) on the southern limb are associated with the Knockroe Volcanic Formation (Figure 2-6A) (Somerville et al., 1992). These centres are positioned on north-east trending lineaments and migrated from west-southwest to north-northeast over time (Somerville et al., 1992). The Knockroe Volcanic Formation is late Chadian to early Arundian (c. 344 Ma) in age (Figure 2-6A), and comprised of mildly evolved alkaline basalts, olivine-basalt (hawaiites) and trachytes (Strogen, 1988; Somerville et al., 1992). The volcanism began with explosive alkali basalt eruptions that produced laterally extensive green coloured vitric and volcanic ash layers, followed by massive alkali basalt lava flows. The final eruptions comprised trachyandesite flows and tuffs as well as intrusions of trachyte dykes (Strogen, 1983; Sevastopulo and Wyse Jackson, 2009).

Volcanic activity in the Limerick region recommenced in the early Asbian (c. 335 Ma), forming mafic flows (ankaramitic and limburgitic (similar to basalt without feldspar)), tuffs and ankaramitic (variety of basanite) dykes and plugs of the Knockseefin Volcanic Formation (Strogen, 1983; Strogen, 1988; Somerville et al., 1992). This Asbian volcanic centre is in the middle of the Limerick Syncline at Knockseefin (Somerville et al., 1992) (Figure 2-6A).

Minor occurrences of volcanic rocks in the Limerick Volcanic Region include, for example, Lower Viséan tuffs around Golden (Archer et al., 1996), Arundian-aged basic tuffs of the Subulter Volcanic Formation (Hudson and Philcox, 1964), Asbian tuffs at Mitchelstown (Shearley, 1988), Asbian intrusions of ankaramite at Gortdrum (Sevastopulo and Wyse Jackson, 2009) and Brigantian basaltic, coarse tuffs and flows of the Turret Volcanic Member, south of Tulla (Schultz and Sevastopulo, 1965; Lewis, 1986; Sleeman and Pracht, 1999) (Figure 2-6A; numbered one to five).

Volcanism in Limerick was similar in style and timing to magmatic and volcanic activity in Britain. Tournaisian magmatic rocks in Britain include the Cockermouth, Birrenswark and Kelso volcanic rocks in the NW England, Midland Valley of Scotland and the Northumberland Basin, respectively (Figure 2-6B) and have mainly a transitional, mildly alkaline to tholeiitic composition (MacDonald and Walker, 1984; Timmerman, 2004), which characterises all of the Tournaisian and Viséan volcanism of northern Britain (Macdonald, 1976). No radiometric ages exist for these rocks, but

Monaghan and Pringle (2004) suggest an age of 352 ± 1.4 Ma based on the dating of a nearby trachyte intrusion. In SW England pyroclastics and alkaline flows erupted in the late Tournaisian (Faulkner, 1989), followed by pillow basalts and cross-bedded tuffs, which could be related to a vent intrusion (347 ± 4 Ma; Kirton, 1981) near Usk in SE Wales (Figure 2-6B).

The Clyde Plateau Volcanic Formation in the Midland Valley of Scotland (Figure 2-6B) represents the largest volume (3000 km^2; Francis, 1991) of Viséan magmatic rocks in Britain and Ireland, which comprises mainly of ankaramites to trachytes and rhyolites (Smedley, 1988; Francis, 1991; Phillips and MacPherson, 1996). The southern Clyde Plateau Volcanic yield an age of 335 ± 2 Ma to 329.2 ± 1.4 Ma (Monaghan and Pringle, 2004). The Garleton Hills Volcanic Formation (c. 342 Ma; Monaghan and Pringle, 2004) and Arthur's Seat Volcanic Formation (Figure 2-6B) occur in the eastern part of the Midland Valley and is *inter alia* composed of basaltic lavas, tuffs, agglomerates, phonolitic or basaltic intrusions (Smedley, 1986; Browne et al., 1999). The Derbyshire basalts in central England (Figure 2-6B) consist of several eruptive sequences (alkaline-tholeiitic basalts) of Asbian to Brigantian in age (Walters and Ineson, 1981). Volumetrically minor Viséan eruptions occurred in the West Midlands of England and SW England producing the Little Wenlock (olivine) basalt (Brigantian; Hamblin et al., 1995) and Tintagel Volcanic Formation (basalts, volcaniclastics and sills; mid-Viséan; Timmerman, 2004), respectively (Figure 2-6B). There are also small, but very well exposed basaltic volcanic rocks of the early to mid Brigantian Scarlett Volcanic Formation in the south of the Isle of Man in the Irish Sea (Dickson et al., 1987).

2.5 Irish Tuffs

Tournaisian tuffs are volumetrically insignificant and have no known source (Sevastopulo and Wyse Jackson, 2009). To date, thin, very fine-grained volcanogenic clay bands which occur within Tournaisian (c. 359 to 346 Ma) argillaceous bioclastic limestones (= Ballysteen Limestone Formation), close to the base of the Waulsortian Limestone Formation are only known from the Lisheen area and to the south-east of the Devilsbit Mountains (Hitzman et al., 1992; Shearley et al., 1996) (Figure 2-6A). However, in the Stonepark area (Figure 2-6A), up to three tuff horizons have been recently detected in the Ballysteen Limestone Formation, just below the Waulsortian Limestone Formation.

In the northern Midlands (Figure 2-6A) most of the known tuffs are found either in the upper part of the Waulsortian Limestone Formation or just above its top (Philcox, 1984). In some cores, two or rarely three tuff horizons are present within a few tens of metres (Philcox, 2016; unpublished report). Most of these tuffs are probably Ivorian in age (Sevastopulo and Wyse Jackson, 2009; Philcox, 1984). In addition, a younger (Arundian), geochemically distinct tuff has been sometimes encountered (Philcox, 2016; unpublished report). Tuffs which are visually similar to the clay bands

in the Ballysteen Limestone Formation are found in probably early Viséan carbonate turbidite deposits above the Navan ore deposit. Furthermore, in the Navan area (Tara Deep; Figure 2-6A), a distinctive tuff forms a unique marker horizon, probably early Viséan in age (Philcox, 2016; unpublished report). This Marker Tuff is visually distinctive because it is inter-laminated with mudstone usually over an interval of c. 60 to 90 cm. Two or three other tuffs have been intersected just below this Marker Tuff.

Four tuff horizons have been identified just above the Waulsortian Limestone Formation within the Kilbryan Limestone Formation, which is late Tournaisian to earliest Viséan in age. One tuff layer occurs in the early Viséan (MFZ9) Oakport Limestone Formation within the Dunmore Province in the Slievedart area (Figure 2-6A). The age of both formations are based on Pracht and Somerville (2015).

Thin clay bands of Brigantian age occur around Lough Allen (not shown in Figure 2-6) (Brandon and Hodson, 1984; Legg et al., 1998).

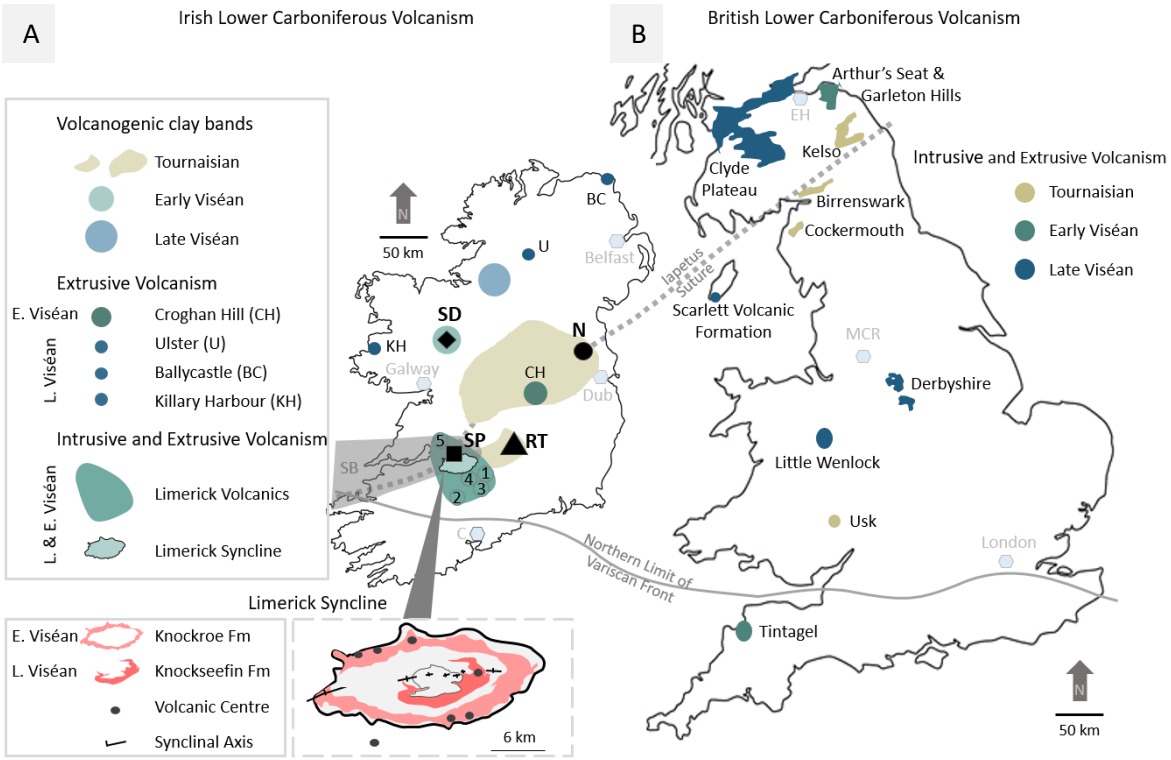

Figure 2-6 A) Schematic distribution of Mississippian volcanic rocks in Ireland modified after Sevastopulo and Wyse Jackson (2009). Geologic map of the Limerick Syncline is modified after the Geological Survey of Ireland's 1:100 000 Bedrock Geology map. Tournaisian tuffs which occur within the Ballysteen Limestone Formation are observed within the small beige area, while the Tournaisian northern Midlands tuffs (large beige area) occur either within the Ballysteen Limestone, the Waulsortian Limestone or in the Tober Colleen Formation. The tuff layers which were sampled for this study are restricted to four areas, which are highlighted in black; N=Navan; RT=Rathdowney Trend; SD=Slievedart; SP=Stonepark. The general area where reported intrusive and extrusive rocks from the Limerick Volcanics occur is shown in green. The occurrences are labelled one to five, either indicating the volcanic member/formation or their location; 1=Turret Volcanic Member; 2=Subulter Volcanic Formation; 3=Mitchelstown; 4=Golden; 5=Gortdrum. Irish cities (blue hexagons; C=Cork, Dub=Dublin) and the Shannon Basin (SB) are provided for reference. B) The map of Britain with locations of Early Carboniferous magmatic activity modified after Guion et al. (2000) and Stephenson (2003). The Little Wenlock, Usk and Tintagel volcanics are shown larger than their true extent for clarity and are thus indicated as circles. British cities (blue hexagons) are provided for reference: Edinburgh (EH) and Manchester (MCR).

2.6 Navan Area

Boliden Tara Mines operates the largest Zn mine in Europe at Navan, County Meath, Ireland. The Navan Zn-Pb orebody is located 1 km west of Navan (approximately 50 km northwest of Dublin), towards the northern margin of the Dublin Basin (e.g. Figure 2-7A). The main deposit was discovered in 1970 and has been in production since 1977. Five extensions southwest of the Main Orebody were discovered between 1991 and 2012 (Ashton et al., 2015). In 2012, a potential new satellite deposit was found, called Tara Deep. Since then, more than 90 holes have been drilled and additional seismic lines have been shot and processed, which highlighted several new target areas for exploration (Ashton et al., 2018).

2.6.1 Main Mine Area

The Navan deposit lies on the northern flank of a heavily faulted, northeast-trending anticlinal structure on the southern margin of the Lower Palaeozoic Longford-Down inlier (Ashton et al. 1986), within the North Midlands Province (Figure 2-7A).

The following stratigraphy of the Navan area is illustrated on Figure 2-7B. In the mine area, deformed Lower Palaeozoic (Ordovician and Silurian) basement rocks are unconformably overlain by the Red Beds, a unit of basal Tournaisian fluviatile sedimentary rocks. The Red Beds are followed by the Navan Group, which was deposited in the Tournaisian. The first unit of the Navan Group are the Mixed Beds, comprising the Laminated Beds (thinly bedded dark argillaceous siltstone and mudstone) and the Muddy Limestone (well-bedded argillaceous and crinoidal limestone) = Liscartan Formation of Strogen et al., 1990. The second unit is the Pale Beds (Philcox, 1984; = Meath Formation of Strogen et al., 1990 and Sevastopulo and Wyse Jackson, 2009), which are predominantly carbonate. They are sub-divided by a number of distinctive sandstone, siltstone and shale layers, which form marker horizons (Philcox, 1984). The Lower Pale Beds comprise the Micrite Unit, in which a prominent dolomitic horizon, the 5 Lens Dolomite is developed. The Middle Pale Beds consist of micro-conglomerate and calcarenite and is followed by the Upper Pale Beds (heterogeneous package of various calcarenites). These beds are separated by a particularly well-defined horizon of dark shale, termed the Upper Dark Marker. Most of the mineralisation at Navan (> 97%) occurs as seven stratabound lenses within these Pale Beds of Tournaisian age. These are numbered upwards from five to zero, followed by the letter U, and refer to the Pale Beds marker horizons (Philcox, 1984). In the main mine area, mineralisation may be vertically continuous over up to 80 m (Ashton et al., 2015). The uppermost unit of the Navan Group is the Shaley Pale Limestones (Shaley Pales; = Moathill Formation of Strogen et al., 1990). They are mainly made up of thinly bedded argillite and grainstone. The oldest rocks of the Navan Group, the Laminated Beds, were deposited in an intertidal to shallow marine environment

(Strogen et al., 1990; McNestry and Rees, 1992; Rizzi, 1992) and shallow marine lagoons (Anderson, 1990; Rizzi, 1992). There was then a rapid change from shallow water to a higher energy environment characterised by shallow-shelf, sub-tidal, intertidal and supratidal facies (Strogen et al., 1990; McNestry and Rees, 1992; Rizzi and Braithwaite, 1996). The Shaley Pales represent a deeper water depositional environment than the Pale Beds (Philcox, 1984; Philcox, 1989).

The Tournaisian Ballysteen Limestone Formation (dark, well-bedded, crinoidal argillaceous limestone) overlies the Shaley Pales (McConnell et al., 2001; Morris et al., 2003; Gatley et al., 2004) (= Slane Castle Formation of Strogen et al., 1990) and passes upwards and diachronously into the Waulsortian Limestone Formation (mudbank facies micritic limestone; = Feltrim Limestone Formation of Jones et al., 1988), which is irregularly developed. Both formations form the Cruicetown Group (Rees, 1992). This group is followed by the Tober Colleen Formation (dark calcareous mudstones), which is Ivorian (in the basin) to Lower Viséan (basin margin) in age (Sevastopulo and Wyse Jackson, 2009) and represents the lowest beds in the Fingal Group. An erosion surface, which was probably formed during the late Tournaisian as a result of a low-angle gravity slide complex separates the Cruicetown and Fingal groups (Boyce et al., 1983; Philcox, 1989; Ashton et al., 1992). This collapse is interpreted to be footwall degradation promoted by the Navan Fault (Ashton et al., 2015). The Boulder Conglomerate (Late Tournaisian to Lower Viséan; Sevastopulo and Wyse Jackson, 2009), which represents syn-depositional debris flows, represents the final stage of the gravity slide event. This submarine mass wastage removed a significant thickness (> 300 m) of strata. As a result, the Boulder Conglomerate rests above the Waulsortian Limestone Formation to the north-west of the mine and cuts progressively deeper levels into the Lower Palaeozoic, unconformably lying on truncated Navan and Cruicetown group beds (Ashton et al., 1992; Ashton et al., 2015). The Boulder Conglomerate is the lowest unit of the Fingal Group and comprises chaotic, polymict clasts with material from the underlying Pale Beds, Shaley Pales and Waulsortian Limestone Formation. Although the Boulder Conglomerate generally lies directly on the erosion surface, it can occur as multiple horizons within the Tober Collen Formation (Ashton et al., 2015). Upwards, the Boulder Conglomerate and the Tober Colleen Formation pass into the Upper Dark Limestone Formation (= Lucan Formation). These two formations are also part of the Fingal Group. The Upper Dark Limestone Formation is a thick sequence of dark, well-bedded limestones, typically calc-turbidites, which makes up the main infill of the Dublin Basin (Ashton et al., 2015). The Upper Dark Limestone Formation represents several stratigraphic units of late Tournaisian to Viséan age; The lowermost unit is called the Thin Bedded Unit and is preferentially developed where the erosion surface has cut deepest into the underlying rocks. It is followed by the Boudin Mudstone Unit, Sub-Bottom Marker Unit, Upper &

Lower Shaley Units, Micritic Sequence and Units A-D. Importantly, the base of the Thin Bedded Unit is diachronous, due to infill of the irregular erosion surface on the northwest side of the mine area.

The succession at Navan is offset by a series of major east-northeast- and northeast-trending growth faults of late Courceyan-Chadian age (e.g. Andrew and Ashton, 1985; Ashton et al., 1986). Many structures were subsequently inverted by reverse and wrench tectonism of probable Variscan age (Ashton et al., 2015).

Lithostratigraphic units of the main mine area together with their formation descriptions and estimated formation thicknesses are summarised in Table 2-1.

2.6.1.1 Sample Locations – Navan East & West

All sample names in this study are composed of three parts and are written as follows; location_drill core number_lab ID. When appropriate, only the lab ID is used. Five drill cores were sampled outside the Tara Deep area, also referred to as Navan East & West (Figure 2-7C; Table 2-2). Drill core N-2412 was drilled in the main mine area, which is 3 km to the NW of Tara Deep, whereas drill holes N-2411 and N-2441 are 8 km to the west (close to Athboy) and 11 km to the NW (close to Kells) of Tara Deep, respectively (Figure 2-7C). Two drill cores come from 0.8 km to the NE (N-2317) and 1.8 km to the ENE (N-2376) of Tara Deep (Figure 2-7C). Two samples were taken from the same tuff layer within the Waulsortian Limestone Formation (samples Navan West_N-2411_HK 125 and Navan West_N-2411_HK 126), while sample Navan West_N-2441_HK 169 was deposited within the Waulsortian equivalent (Figure 2-7D). Another three tuff samples (Navan West_N2441_HK 155, Navan West_N2441_HK 156 and Navan West_N-2441_HK 157) were taken from the Tober Colleen Formation, where samples HK 156 and 157 stem from the same horizon (Figure 2-7D). One sample each was sampled from the Sub-Bottom Marker Unit (Navan East_N-2317_HK 117), Micritic Sequence (Navan West_N-2412_HK 128) and Unit B (Navan East_N-2376_HK 227) (Figure 2-7D).

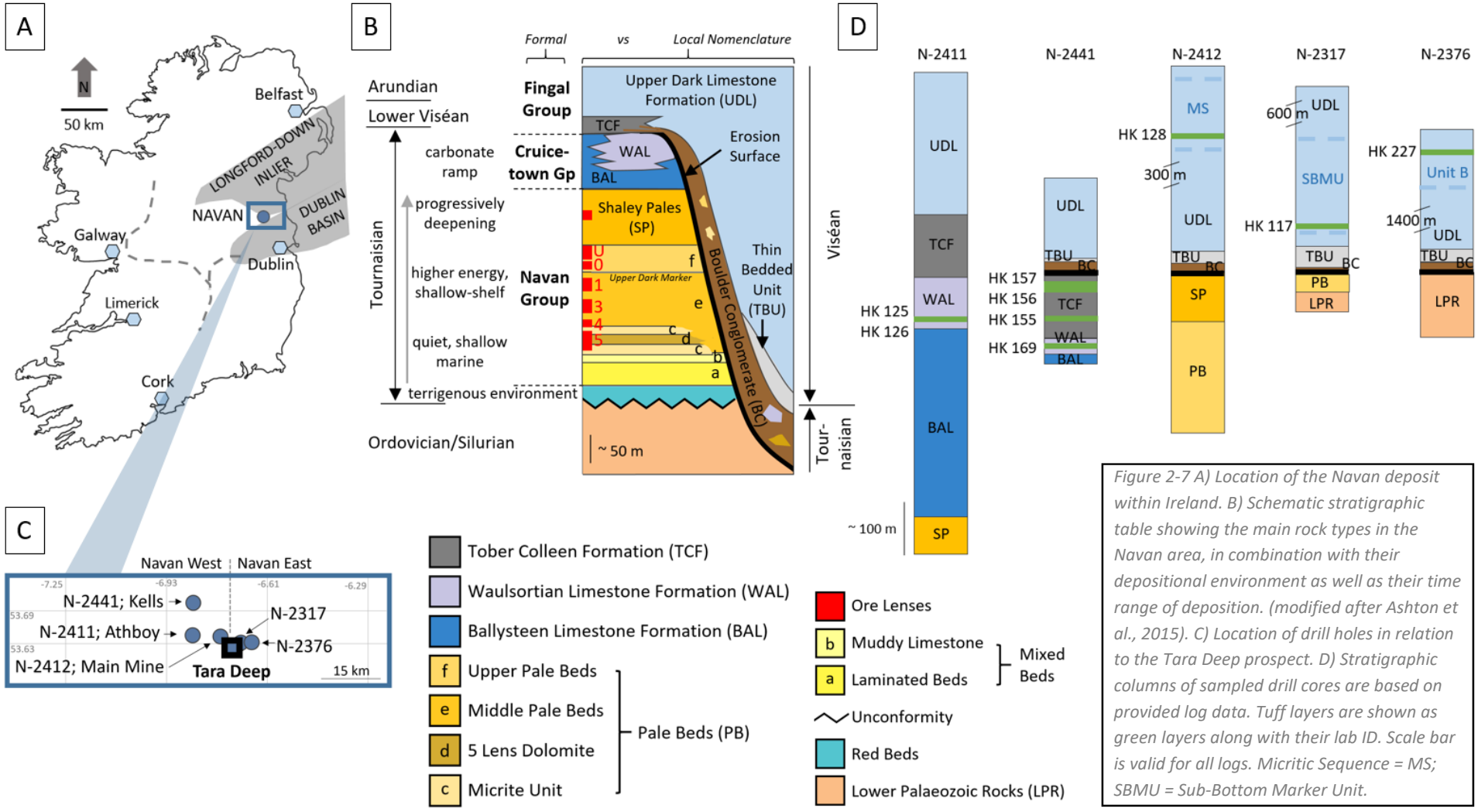

Figure 2-7 A) Location of the Navan deposit within Ireland. B) Schematic stratigraphic table showing the main rock types in the Navan area, in combination with their depositional environment as well as their time range of deposition. (modified after Ashton et al., 2015). C) Location of drill holes in relation to the Tara Deep prospect. D) Stratigraphic columns of sampled drill cores are based on provided log data. Tuff layers are shown as green layers along with their lab ID. Scale bar is valid for all logs. Micritic Sequence = MS; SBMU = Sub-Bottom Marker Unit.

Table 2-1: Lithostratigraphic units of the main mine are listed in stratigraphic order, showing the oldest unit on bottom row. Formation descriptions are taken from Ashton et al. (2015) Thicknesses are estimated based on fig. 3 in Ashton et al. (2015).

Lithostratigraphic Unit	Formation Description	Formation Thickness
Thin Bedded Unit	Thinly interbedded mudstones and fine calcarenites	Up to 20 m
Boulder Conglomerate	One debris-flow polymict breccia-conglomerate. It comprises chaotic, polylmict, limestone-dominated clasts originated from Pale Beds, Shaley Pales and Waulsortian Limestone Formation	< 1m to > 50 m Clasts up to 8 m across
Upper Dark Limestone Formation	Dark calcareous mudstone with well-bedded turbiditic grainstones, wackestones and rudstones	Several 100s m
Tober Colleen Formation	Dark calcareous mudstones	30 m
Waulsortian Limestone Formation	Mudbank facies micritic limestone	60 m
Ballysteen Limestone Formation	Dark, well-bedded, crinoidal argillaceous limestone	90 m
Shaley Pales	Thinly bedded argillite and grainstone	90 m
Upper Pale Beds	Heterogeous package of locally dolomitised, sandy, bioclastic, oolitic, and silty calcarenite	40 m
Middle Pale Beds	Variable bioclastic and oolitic grainstone horizons with significant limestone micro-conglomerate and thin silty and shaley calcarenite	90 m
5 Lens Dolomite	Dolomite	Some 10s m
Micrite Unit	Micritic limestone	45
Muddy Limestone	Dark, well-bedded argillaceous and crinoidal limestone	10 m
Laminated Beds	Thinly bedded, often bioturbated, dark argillaceous siltsone and mudstone	40 m
Red Beds	Impure red sandstone and polymict pebble conglomerates	30 m

Table 2-2: Samples are separated based on their sampling location into Navan West and Navan East. The total amount of samples taken from the same drill core is indicated by the sum of samples (ΣSamples). Tuff# refers to a specific sample within the drill core with Tuff# = 1 being the stratigraphically lowest tuff horizon, while letters (A and B) point out that one tuff horizon was sampled at different levels, A being the stratigraphically lowest sample; MS=Micritic Sequence; SBMU= Sub-Bottom Marker Unit; TCF=Tober Colleen Formation; UDL=Upper Dark Limestone Formation; WAL=Waulsortian Limestone Formation.

NAVAN							
	Sample ID			ΣSamples - Tuff#	Depth (m)	Strat. level	Location	Sample #
	Location	Drill core	Lab ID					
W	Navan West_N-2441_HK 169			4 – 1	321.7	WAL Equivalent	53.7033, -6.8461	35
E	Navan West_N-2411_HK 125			2 – 1B	500.5	Waulsortian	53.6437, -6.8478	36
	Navan West_N-2411_HK 126			2 – 1A	501.55	Waulsortian	53.6437, -6.8478	37
S	Navan West_N-2441_HK 155			4 – 2	276.75	TCF	53.7033, -6.8461	38
	Navan West_N-2441_HK 156			4 – 3A	216.75	TCF	53.7033, -6.8461	39
T	Navan West_N-2441_HK 157			4 – 3B	216.45	TCF	53.7033, -6.8461	40
	Navan West_N-2412_HK 128			1	156	UDL - MS	53.6437, -6.7583	41
EA	Navan East_N-2317_HK 117			1	1038.5	UDL - SBMU	53.6306, -6.7011	42
ST	Navan East_N-2376_HK 227			1	65.4	UDL - Unit B	53.6294, -6.6856	43

2.6.2 Tara Deep

Tara Deep was identified 2 km south of the main mine at Navan Figure 2-8A. The following section describes the Tara Deep area in more detail. Most of the information is taken from Ashton et al. (2018). A schematic stratigraphic table is displayed in Figure 2-8B. Tara Deep is located on the footwall side of the major ENE-striking Navan fault. Between the south-west extension of the main mine (SWEX) and Tara Deep are further major faults, called the E, P and G faults. The Red Beds, Laminated Beds and Muddy Limestone are generally similar to those at Navan, while only the units of the Lower (Micrite Unit and 5 Lens Dolomite) and Middle (Dolomitised Calcarenites) Pale Beds are observed. The latter are more prominently developed compared to the main mine area. The Pale Beds pass upwards into a lithology termed the Pale Beds Breccia-Conglomerate whose origin is currently poorly understood. It is made up of variably brecciated and fractured calcarenites and calcisiltites in a similar or more argillaceous matrix material. This lithotype is not recognised in the main mine area, while the Upper Pale Beds, Shaley Pales, Ballysteen Limestone and the Waulsortian Limestone formations, observed in the main mine, cannot be observed as autochthonous material in Tara Deep. They appear to have been removed during Chadian (most likely late Tournaisian) extension and gravity sliding or due to a facies change. Furthermore, none of the marker horizons identified in the main mine are recognised in Tara Deep. Although the Lower and Middle Pale Beds in Tara Deep are locally overlain by allochthonous slide units of Upper Pale Beds, Shaley Pales or Argillaceous Bioclastic Limestones, they are generally covered by the Boulder Conglomerate.

In the main Navan deposit there is only one single polymict breccia-conglomerate (the Boulder Conglomerate), while at least four additional individual lenses occur in Tara Deep within the Thin Bedded Unit. This unit, consisting of alternating beds of the Thin Bedded Unit and lenses of polymict breccias is defined as a new unit, called the New Thin Bedded Unit. Each lens is comprised primarily of reworked clasts of Pale Beds, Shaley Pales and Waulsortian Limestone Formation. They are termed Sedimentary Breccias and are separated by appreciable sections of the Thin Bedded Unit (Figure 2-8C). The New Thin Bedded Unit is split into Thin Bedded Unit 1 to Thin Bedded Unit 4 (Dr. Michael Philcox, 2020, pers. comm.; Figure 2-8C). This new unit is probably comparable temporally to the Tober Colleen Formation elsewhere (Dr. Michael Philcox, 2020, pers. comm). Figure 11 in Ashton et al., (2018) implies an even younger depositional age for the New Thin Bedded Unit of Lower Viséan to mid Arundian.

A new marker horizon, a distinct tuffaceous horizon was found in Thin Bedded Unit 1, which is immediately below the uppermost conglomerate; Sedimentary Breccia 1 (Figure 2-8C). This Marker Tuff is not seen closer to the main mine area. Sometimes more tuff horizons occur in Thin Bedded Unit 2 to Thin Bedded Unit 4 (which are stratigraphically lower than Thin Bedded Unit 1;

Figure 2-8C). The Boulder Conglomerate and Thin Bedded Unit thicken from < 20 m in SWEX, to several hundred meters to the southeast across the Tara Deep area. The New Thin Bedded Unit is overlain by the Boudin Shales, which are part of the Upper Dark Limestone Formation. The other various units of the Upper Dark Limestone Formation are generally thicker than at the Navan deposit. The lithostratigraphic units mentioned above, formation descriptions and estimated formation thicknesses are summarised in Table 2-3.

Besides the mineralisation occurring in the basal Pale Beds, which contribute around 90% of the total resource in Tara Deep, there are mineralised Pale Beds conglomerates within the Boulder Conglomerate near the hanging walls of the G and S faults in the NW zone. Based on the stratigraphic position, mineralisation at Tara Deep and at the Navan deposit appears to be of similar age. Post-diagenetic evidence from the Pale Beds and Boulder Conglomerate in the main mine area indicates that base-metal mineralisation postdates the deposition of the Boulder Conglomerate. The replacement of similar conglomerates by base-metal sulphide mineralisation in Tara Deep supports the hypothesis that mineralisation at Navan is entirely epigenetic in nature. As laminated pyrite appears in the New Thin Bedded Unit, it is possible that the mineralisation continued over a longer period at Tara Deep compared to the main mine area. No significant mineralisation is known in the Ballysteen Limestone and Waulsortian Limestone formations at Navan, despite their important role as host rocks to mineralisation in other Irish Zn-Pb deposits (Ashton et al., 2015). However, both units are either poorly developed or have been removed across most of the mine area anyway.

2.6.2.1 Sample Locations – Tara Deep

A schematic cross-section is shown in Figure 2-8C to demonstrate the variable occurrence of the tuff layers within the Tara Deep prospect. Several samples from the Tara Deep prospect are taken from 'daughter' drill holes, which splay off from their original ('mother') drill hole. Therefore, names of sampled drill cores are distributed between mother drill hole locations (blue circles) (Figure 2-8D). These twenty-two drill cores (comprising 34 samples) were collected within an area of 0.5 km^2 (Figure 2-8D). All samples were taken from within the New Thin Bedded Unit. The Marker Tuff is encountered in most drill cores from Tara Deep, whereas the other tuffs (Upper and Lower tuffs) are rarely found. Thus, twenty-two samples of this study are from the Marker Tuff, while only four and eight samples are Upper and Lower Tuffs, respectively (Table 2-4). One shale sample (sample HK 164) was deliberately sampled from a drill core for comparison purposes, which is situated within the 0.5 km^2 Tara Deep area (N-2406) and was deposited in the New Thin Bedded Unit.

Table 2-4 shows all drill cores along with corresponding sample IDs, number of sampled tuff horizons, sampling depths, stratigraphic level, location (coordinates) and sample number.

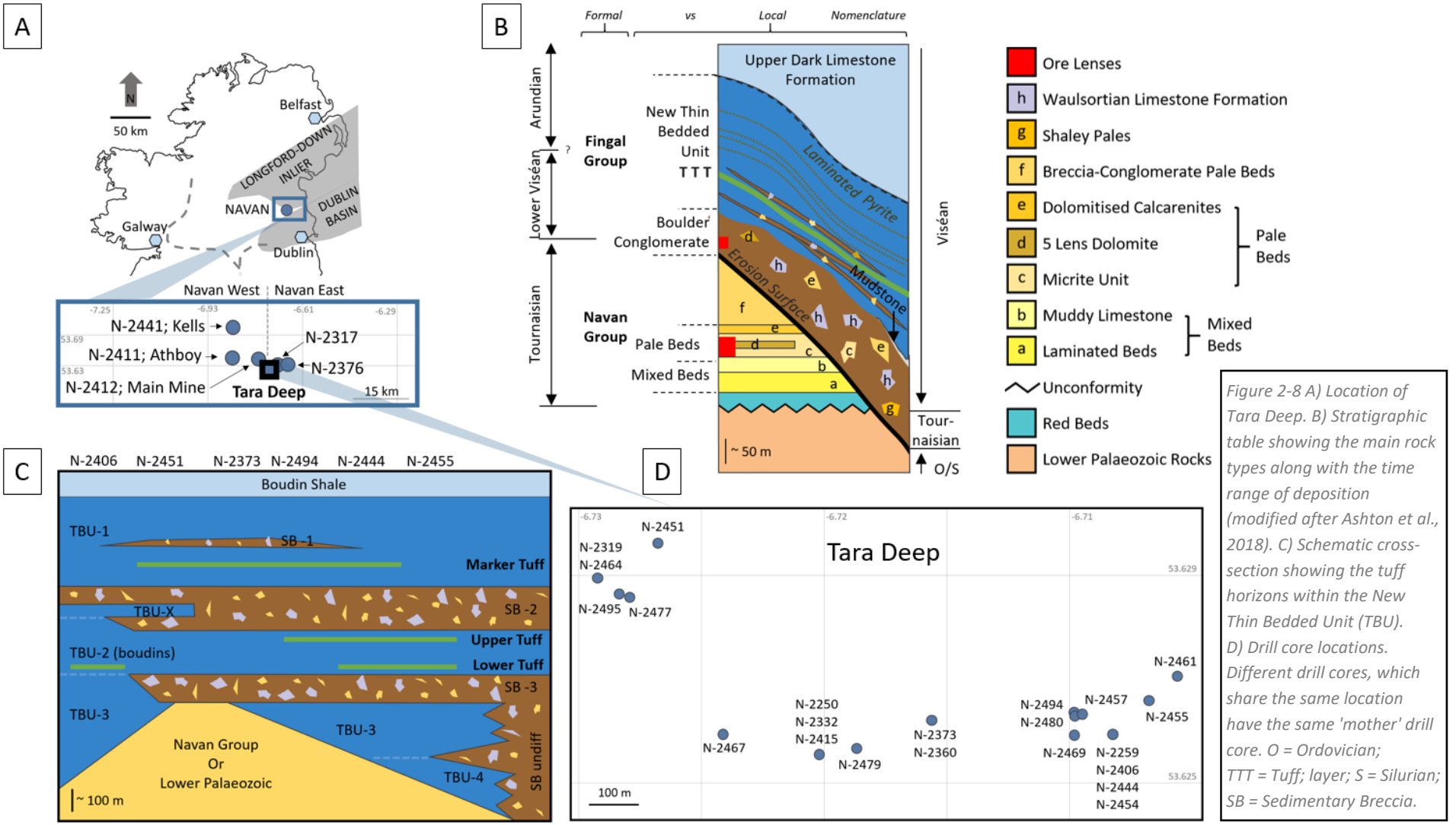

Figure 2-8 A) Location of Tara Deep. B) Stratigraphic table showing the main rock types along with the time range of deposition (modified after Ashton et al., 2018). C) Schematic cross-section showing the tuff horizons within the New Thin Bedded Unit (TBU). D) Drill core locations. Different drill cores, which share the same location have the same 'mother' drill core. O = Ordovician; TTT = Tuff; layer; S = Silurian; SB = Sedimentary Breccia.

Table 2-3: Lithostratigraphic units, observed in Tara Deep are listed in stratigraphic order, showing the oldest unit in the bottom row. Formation descriptions are taken from Ashton et al. (2018). Formation thicknesses are estimated based on fig. 2 in Ashton et al. (2018).

Lithostratigraphic Unit	Formation Description	Formation Thickness
Upper Dark Limestone Formation	Dark calcareous mudstone with well-bedded turbiditic grainstones, wackestones and rudstones	Several 100s m
New Thin Bedded Unit	Alternating beds of thinly bedded calcisiltites, argillites, calcarenites and lenses of plymict breccias as seen in the Boulder Conglomerate	Several 100s m
Boulder Conglomerate	Up to four individual lenses in argillaceous matrix Each lens is mainly comprised of clasts from the Pale Beds and Waulsortian Limestone Formation	80 m
Pale Beds Breccia Conglomerate	Calcarenites and calcisiltites, variably brecciated and fractured Matrix material is either similar or more argillaceous	135 m
Middle Pale Beds	Dolomitised Calcarenites	10 m
5 Lens Dolomite	Dolomite	Several 10s m
Micrite Unit	Micritic limestone	45 m
Muddy Limestone	Dark, well-bedded argillaceous and crinoidal limestone	25 m
Laminated Beds	Thinly bedded, often bioturbated, dark argillaceous siltsone and mudstone	40 m
Red Beds	Impure red sandstone and polymict pebble conglomerates	30 m

Table 2-4: The sample ID comprises three parts; the location, drill core number and lab ID. The total amount of samples taken from the same drill core is indicated by the sum of samples (ΣSamples). Tuff# refers to a specific sample within the drill core with Tuff# = 1 being the stratigraphically lowest tuff horizon, while letters (A, B, C and D) point out that one tuff horizon was sampled at different levels, A being the stratigraphically lowest sample; TBU=Thin Bedded Unit.

	Sample ID	ΣSamples - Tuff#	Depth (m)	Strat. Level		Location	Sample #
	Location Drill core Lab ID						
TARA DEEP	Tara Deep_N-2250_HK 115	1	1072.8	TBU-1	Marker Tuff	53.6259, -6.7214	1
	Tara Deep_N-2259_HK 116	1	898.7	TBU -1	Marker Tuff	53.6264, -6.7128	2
	Tara Deep_N-2319_HK 118	1	1385	TBU-1	Marker Tuff	53.6291, -6.7278	3
	Tara Deep_N-2332_HK 122	4 – 1A	1117.5	TBU-1	Marker Tuff	53.6259, -6.7214	4
	Tara Deep_N-2332_HK 121	4 – 1B	1117.45	TBU-1	Marker Tuff	53.6259, -6.7214	5
	Tara Deep_N-2332_HK 120	4 – 1C	1116.95	TBU-1	Marker Tuff	53.6259, -6.7214	6
	Tara Deep_N-2332_HK 119	4 – 1D	1116.9	TBU-1	Marker Tuff	53.6259, -6.7214	7
	Tara Deep_N-2360_HK 245	1	1036.1	TBU -1	Marker Tuff	53.6266, -6.7181	8
	Tara Deep_N-2373_HK 130	2 – 1A	961.35	TBU-1	Marker Tuff	53.6266, -6.7181	9
	Tara Deep_N-2373_HK 114	2 – 1B	961.25	TBU-1	Marker Tuff	53.6266, -6.7181	10
	Tara Deep_N-2415_HK 161	1	1115.15	TBU-1	Marker Tuff	53.6259, -6.7214	11
	Tara Deep_N-2444_HK 163	4 – 3A	938.27	TBU-1	Marker Tuff	53.6264, -6.7128	12
	Tara Deep_N-2444_HK 162	4 – 3B	937.72	TBU-1	Marker Tuff	53.6264, -6.7128	13
	Tara Deep_N-2451_HK 186	1	1299.60	TBU-1	Marker Tuff	53.6297, -6.7261	14
	Tara Deep_N-2457_HK 232	1	885.7	TBU-1	Marker Tuff	53.6267, -6.7136	15
	Tara Deep_N-2464_HK 196	1	1407.7	TBU-2	Marker Tuff	53.6291, -6.7278	16
	Tara Deep_N-2467_HK 247	1	1267	TBU -1	Marker Tuff	53.6264, -6.7242	17
	Tara Deep_N-2477_HK 234	1	1478	TBU-1	Marker Tuff	53.6288, -6.7272	18
	Tara Deep_N-2479_HK 235	1	1028	TBU-1	Marker Tuff	53.6261, -6.7203	19
	Tara Deep_N-2480_HK 236	1	887	TBU-1	Marker Tuff	53.6266, -6.7139	20
	Tara Deep_N-2494_HK 251	3 – 2A	1117.9	TBU-1	Marker Tuff	53.6267, -6.7139	21
	Tara Deep_N-2494_HK 250	3 – 2B	1115.4	TBU-1	Marker Tuff	53.6267, -6.7139	22
	Tara Deep_N-2444_HK 158	4 – 2	989.2	TBU-2	Upper Tuff	53.6264, -6.7128	23
	Tara Deep_N-2455_HK 228	2 – 2	939.6	TBU-2	Upper Tuff	53.6270, -6.7117	24
	Tara Deep_N-2461_HK 230	2 – 2	967	TBU-2	Upper Tuff	53.6274, -6.7108	25
	Tara Deep_N-2494_HK 252	3 – 1	1212.7	TBU-2	Upper Tuff	53.6267, -6.7139	26
	Tara Deep_N-2406_HK 166	2 – 1A	966.5	TBU-2	Lower Tuff	53.6264, -6.7128	27
	Tara Deep_N-2406_HK 165	2 – 1B	966.4	TBU-2	Lower Tuff	53.6264, -6.7128	28
	Tara Deep_N-2444_HK 159	4 – 1	1048.2	TBU-2	Lower Tuff	53.6264, -6.7128	29
	Tara Deep_N-2454_HK 170	1	1010	TBU-2	Lower Tuff	53.6264, -6.7128	30
	Tara Deep_N-2455_HK 229	2 – 1	981	TBU-2	Lower Tuff	53.6270, -6.7117	31
	Tara Deep_N-2461_HK 231	2 – 1	1011.55	TBU-2	Lower Tuff	53.6274, -6.7108	32
	Tara Deep_N-2469_HK 233	1	996	TBU-2	Lower Tuff	53.6264, -6.7139	33
	Tara Deep_N-2495_HK 248	1	980.6	TBU-2	Lower Tuff	53.6288, -6.7269	34
	Tara Deep_N-2406_HK 164	1	950.1	TBU-2	Shale	53.6264, -6.7128	44

2.7 Rathdowney Trend

The Lisheen Zn-Pb-Ag deposit and the Rapla prospect are located in County Tipperary in southeast-central Ireland, along the Rathdowney Trend (Figure 2-9A). The Rathdowney Trend is a 40-km-long transtensional dextral relay-ramp system of Tournaisian-Viséan age, which is parallel to that of the underlying NE-ENE- trending Caledonian structural grain (Johnston et al., 1996; Worthington and Walsh, 2011; Bonson et al., 2012; Torremans et al., 2018; Kyne et al., 2019). The majority of the mineralisation occurs in the hanging wall within a hydrothermal dolomite breccia located at the base of the Waulsortian Limestone Formation, namely the Waulsortian mudbank complex of late Tournaisian age (Philcox, 1984; Hitzman and Beaty, 1996; Wilkinson and Hitzman, 2015). The ore deposits (Lisheen, Galmoy and Rapla) are controlled by the segmented Lisheen normal fault system, which partly defines the Rathdowney Trend (Johnston et al., 1996).

2.7.1 Lisheen

The Lisheen deposit was discovered in 1990 by an Ivernia West - Chevron Mineral Corporation of Ireland joint venture. Production followed in 1999 (Hitzman et al., 2002). The Lisheen mine was the second largest Irish base metal deposit after the Navan deposit and the largest example of the Waulsortian complex-hosted subtype of Irish-type deposits (Hitzman and Beaty, 1996). Mine activity stopped in 2015.

The Devonian and Mississippian succession at Lisheen is similar to that recognised elsewhere in south-central Ireland such as in the Limerick Province (Shephard-Thorn, 1961; Brück et al., 1979; Philcox, 1984; Sevastopulo and Wyse Jackson, 2009). The following stratigraphic descriptions and ages are, if not stated otherwise, taken from Hitzman et al. (2002) and George et al. (1976), Lippolt and Hess (1985), Leeder and McMahon (1988), respectively. The stratigraphy of the mine area is shown in Figure 2-9B. It commences with Silurian metasedimentary basement rocks. The Devonian (Famennian) Old Red Sandstone is a terrigenous clastic red bed succession, which lies unconformably on the eroded basement. This succession is followed by the basal, inter-tidal to fully marine Carboniferous limestone and mudstones, the Lower Limestone Shale Group (e.g. Somerville et al., 1992; Somerville and Strogen, 1992; Pracht and Somerville, 2015). The Lower Limestone Shale Group comprises the Mellon House (mixed shale, sandstone and limestone), Ringmoylan Shale (thinly interbedded, dark shale and skeletal limestone) and Ballyvergin Shale (laminae of non-calcareous shale, siltstone and fine sandstone) formations. Some studies include an additional unit, consisting of interbedded bioclastic limestone and calcareous shale, at the top of the Lower Limestone Shale Group: the Ballymartin Limestone Formation (e.g. Somerville and Jones, 1985 and Hitzman et al., 2002 *vs* Archer et al., 1996). The Ballyvergin Shale and parts of the Ballymartin Limestone formations contain microflora of PC biozonal age (Clayton et al., 1980;

Sevastopulo and Wyse Jackson, 2009) and were thus deposited in the Hastarian. The Lower Limestone Shale Group is overlain by the marine Ballysteen Limestone Formation, a sequence characterised by shaley, bioclastic limestones, often termed the Argillaceous Bioclastic Limestone (or ABL), in the mine area. The Ballysteen Limestone Formation comprises the Lower Calcarenite Member, the Lisduff Oolite, the Upper Calcarenite Member and the Nodular Micrite Unit. Sometimes there is no distinction between the Upper Calcarenite Member and Nodular Micrite Unit in logging sheets and together they are named S-ABL. The Nodular Micrite Unit is approximately 20 m thick and contains up to two tuff horizons. The upper tuff horizon occurs at depths of 8.5-13.5 m from the top of the Nodular Micrite Unit, and the lower tuff horizon occurs some 3 m below this (Fusciardi et al., 2003). The Ballysteen Limestone Formation spans the Ivorian *Pseudopolygnathus multistriatus and Polygnathus mehli* conodont biozones (Sevastopulo and Wyse Jackson, 2009). The main facies of the overlying Waulsortian Limestone Formation were most likely also deposited in the Tournaisian (Ivorian) as the youngest Waulsortian limestones in the Midlands are of late Tournaisian age with some local Lower Viséan occurrences (Sevastopulo and Wyse Jackson, 2009). The micritic main facies of the dolomitised Waulsortian Reef Formation is termed the Biomicrite and Veines Bleues Unit. It is covered by the late Ivorian Upper Wavy Laminated Unit (crinoidal micrite), which is in turn overlain by the post-Waulsortian late Ivorian to Lower Viséan Crosspatrick Formation (Sevastopulo and Wyse Jackson, 2009). The Crosspatrick Formation is the youngest unit preserved in the Lisheen area consisting of mildly argillaceous, cherty biocalcarenite. This unit is often followed in south-central Ireland by shallow-water carbonates of the Aghmacart Formation, containing Lower Viséan (MFZ9) aged foraminifera (Sevastopulo and Wyse Jackson, 2009). Lithostratigraphic units, formation descriptions and thicknesses are also shown in Table 2-5.

Three strata-bound pyritic ore bodies are hosted at the base of the dolomitised Waulsortian Limestone Formation (Wilkinson and Hitzman, 2015). These are the Main, Derryville and Bog zones, controlled by four major east-west-striking normal faults of the Lisheen fault system (Killoran, Derryville, Bog and Barnalisheen faults) (> 150 m offset) (Hitzman et al., 2002). A minor proportion of ore is hosted in the hanging-wall and footwall sides of the major faults within the Lisduff Oolite Member (of the Ballysteen Limestone Formation). Hitzman et al. (2002, and references therein) as well as Wilkinson and Hitzman (2015) suggest that mineralisation at Lisheen occurred at least 10 Ma after the deposition of the Waulsortian host rocks. This is supported by Hnatysin et al. (2015) who assume that Zn-Pb mineralisation at Lisheen most likely developed during the later depositional stages of the Waulsortian Limestone Formation, or during the deposition of the overlying Crosspatrick Formation at a depth of no more than 200 m below the palaeoseafloor.

2.7.2 Rapla

The Rapla prospect is located 20 km northeast of the Main Zone of the Lisheen mine, near the former Galmoy Zn-Pb mine (Figure 2-9A). Rapla exhibits a similar stratigraphic sequence to that seen in Lisheen mine (Figure 2-9B). One major difference is the presence of a faulted contact between the Waulsortian Limestone Formation and the argillaceous limestones of the Ballysteen Limestone Formation, which is not observed in the Lisheen area (Riegler and McClenaghan, 2017). The overall displacements of the four major normal faults of the Lisheen fault system, observed across the three deposits within the Rathdowney Trend, gradually decline from 220 m in the western side of Lisheen to 130 m at Galmoy, and 130 m at Rapla (Kyne et al., 2019). This change is more typical for individual normal faults than for relay ramp systems, which are accommodated by strong displacement transfer between segments (Kyne et al., 2019).

2.7.3 Sample Locations – Rathdowney Trend

Seventeen tuff samples in total come from the Rathdowney Trend. Sixteen samples were taken from 13 different drill cores, along with one mine sample. Six of these samples are from Rapla and eleven are from Lisheen (Figure 2-9C, D). Rapla and Lisheen are 16 km apart. The tuff horizons from Rapla and Lisheen were sampled within regions 0.5 km^2 and 9 km^2 in area respectively (Figure 2-9E, F). According to logging data, the regional Mississippian stratigraphy can host up to five tuff horizons in one drill core. However, during sampling a maximum of two tuff horizons were identified and sampled in three different drill cores - one in the Lisheen area (LK-1915) and two in the Rapla area (3312-62; 3667-04). The remaining drill cores had only one obvious tuff layer (Figure 2-9C, D). All drill cores along with corresponding sample IDs (consist of three parts: location_drill core number_lab ID), number of sampled tuff horizons, sampling depths, stratigraphic level, location (coordinates) and sample# are listed in Table 2-6.
The allocation of the sixteen tuff layers to their respective stratigraphic units is based on logging data from the company (Figure 2-9C, D). Two tuff layers were sampled in the Upper Calcarenite Member (Rapla_3667-04_HK 185 and Rapla_3312-62_HK 217), a further eight tuffs were taken from the Nodular Micrite Unit (Lisheen_LK-1722_HK 180, Lisheen_LK-1874_HK 214, Lisheen_LK-0669_HK 215, Lisheen_LK-1915_HK 216, Lisheen_LK-1585_HK 218, Lisheen_LK-1915_HK 220, Lisheen_LK-1773_HK 221, Rapla_3312-78_HK 184), two tuffs (Lisheen_LK-2180_HK HK 181 and Lisheen_LK-1040_HK 182) are assigned to the S-ABL (either Upper Calcarenite Member or Nodular Micrite Unit) and one tuff was deposited close to the boundary of the Upper Calcarenite Member and Nodular Micrite Unit (Rapla_3667-04_HK 223). One tuff was sampled in the Waulsortian Limestone Formation (Lisheen_LK-1432_HK 219), the remaining two tuff horizons Rapla_3312-54_HK 222 and Rapla_3312-62_HK 183 were deposited above the Waulsortian Limestone Formation within the Upper Wavy Laminated Unit and the Crosspatrick Formation, respectively.

Sample number seventeen (Lisheen_mine sample_HK 203), also referred to as the ‘Green Tuff’, was taken from an underground face, when the Lisheen mine was still operating. Approximately 6 kg of this particularly well-developed, c. 5 cm thick tuff layer was sampled.

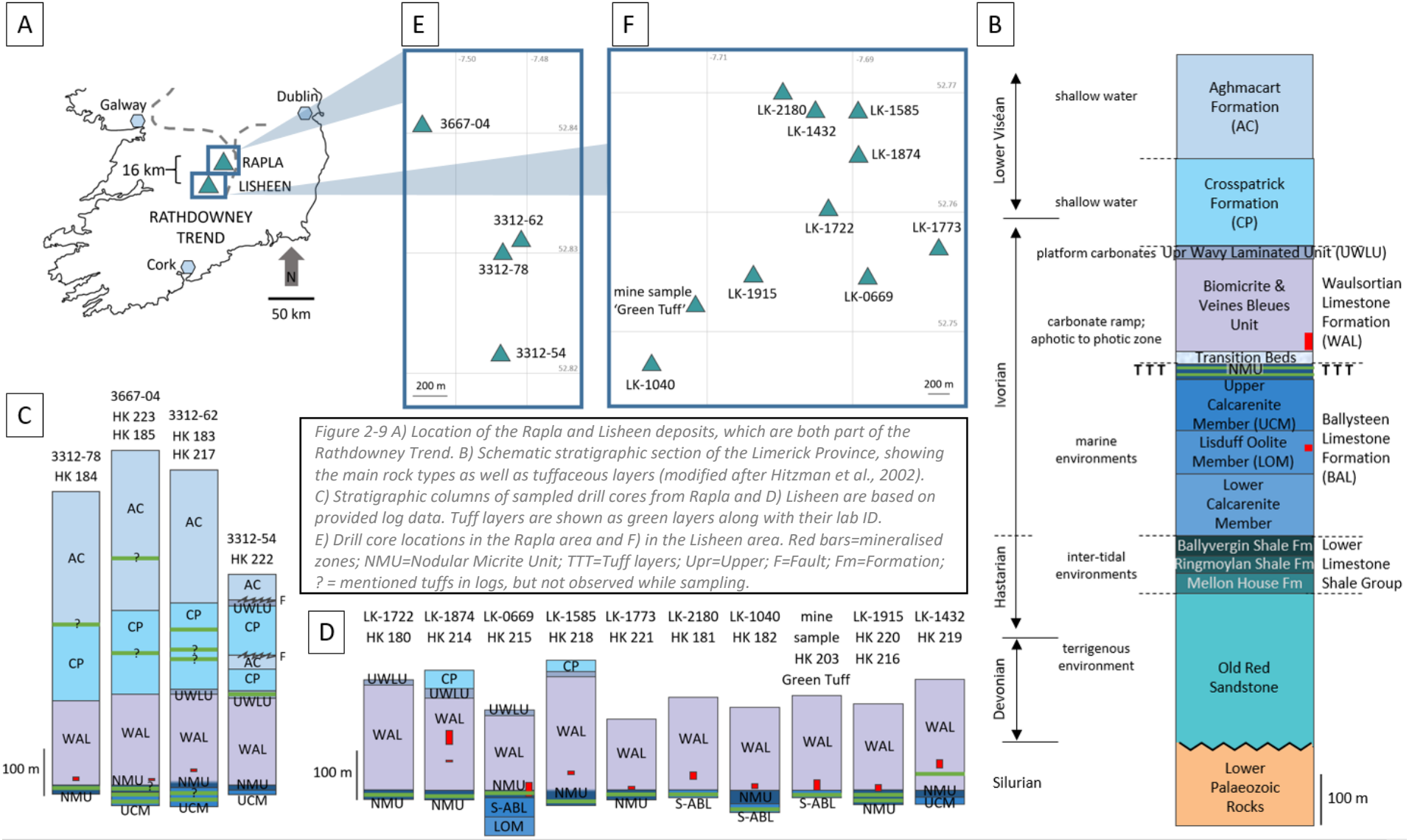

Figure 2-9 A) Location of the Rapla and Lisheen deposits, which are both part of the Rathdowney Trend. B) Schematic stratigraphic section of the Limerick Province, showing the main rock types as well as tuffaceous layers (modified after Hitzman et al., 2002). C) Stratigraphic columns of sampled drill cores from Rapla and D) Lisheen are based on provided log data. Tuff layers are shown as green layers along with their lab ID. E) Drill core locations in the Rapla area and F) in the Lisheen area. Red bars=mineralised zones; NMU=Nodular Micrite Unit; TTT=Tuff layers; Upr=Upper; F=Fault; Fm=Formation; ? = mentioned tuffs in logs, but not observed while sampling.

Table 2-5: Lithostratigraphic units of the Limerick Province in the Lisheen and Rapla areas are listed in stratigraphic order, showing the oldest unit in the bottom row. Formation descriptions and thicknesses are taken from Sevastopulo and Wyse Jackson (2009) and from Fig. 3 in Hitzman et al. (1992), respectively.

Lithostratigraphic Unit	**Formation Description**	**Formation Thickness**
Aghmacart Formation	Daek, fine-grained, peloidal limestone	>200 m
Crosspatrick Formation	Medium- to coarse- grained, mildly argillaceous, cherty biocalcarenite	170 m
Upper Wavy Laminated Unit	Also called cover facies. Consists of stylolitic crinoidal micrite. Wavy laminated texture due to the presence of very thin, pale grey argillites and argillaceous partings	15-20 m
Biomicrite and Veines Bleues Unit	Several coalesced mudbanks, which consists of Flank facies: crinoidal micrites, occasionally argillaceous laminae that result in a wavy laminated texture Core facies: light – to medium-grey micritic limestone Basal facies: interlayered laminated Biomicrite, mildly argillacous crinoidal micrite and encrinitic calcarenite	170 – 210 m
Nodular Micrite Unit	Argillaceous biocalcarenites	20 m
Upper Calcarenite Member	Argillaceous biocalcarenites	110 m
Lisduff Oolite	Mildly argillacous, medium- to coarse-grained oobiosparite and oosparite	80 m
Lower Calcarenite Member	Argillaceous biocalcarenites	130 m
Ballymartin Formation	Interbedded limestone and shale	50 m
Ballyvergin Shale Formation	Non-calcareous grey-green shale with laminae of siltsone and fine sandstone	6 m
Ringmoylan Shale Formation	Thinly interbedded dark shale and subordinate skeletal limestone	35 m
Mellon House formation	Mixed shale, sandstone and limestone	20 m
Old Red Sandstone	Clastic red bed succession	c. 300 m

Table 2-6: Tuff samples from Lisheen and Rapla from 13 different drill cores along with corresponding sample IDs, sampling depths, number of sampled horizons, location (coordinates) and stratigraphic levels. The amount of sampled tuff layers within one drill core is indicated by the sum of samples (ΣSamples), whereas Tuff# shows from which horizon the specific sample was taken from with Tuff# = 1 being the stratigraphically lowest tuff horizon. Fm = Formation, M. = Member, NMU = Nodular Micrite Unit; spl = sample, UCM = Upper Calcarenite Member, Upr Wavy Lam Unit = Upper Wavy Laminated Unit, WAL = Waulsortian Limestone Formation.

	Sample ID			ΣSamples –Tuff#	Depth (m)	Stratigraphic level	Location	Sample #
	Location	Drill core	Lab ID					
LISHEEN	Lisheen_LK-0669_HK 215			1	180.2	Nodular Micrite Unit	52.7538, -7.6882	45
	Lisheen_LK-1585_HK 218			1	282.7	Nodular Micrite Unit	52.7678, -7.6893	46
	Lisheen_LK-1722_HK 180			1	241.3	Nodular Micrite Unit	52.7595, -7.6937	47
	Lisheen_LK-1773_HK 221			1	171.9	Nodular Micrite Unit	52.7566, -7.6784	48
	Lisheen_LK-1874_HK 214			1	267.7	Nodular Micrite Unit	52.7638, -7.6892	49
	Lisheen_LK-1915_HK 216			2 - 1	207.5	Nodular Micrite Unit	52.7541, -7.7035	50
	Lisheen_LK-1915_HK 220			2 - 2	203.3	Nodular Micrite Unit	52.7541, -7.7035	51
	Lisheen_LK-2180_HK 181			1	210.8	Nodular Micrite Unit	52.7695, -7.6997	52
	Lisheen_LK-1040_HK 182			1	176.9	Nodular Micrite Unit	52.7468, -7.7178	53
	Lisheen_mine spl_HK 203			N/A	N/A	Nodular Micrite Unit	52.7513, -7.7119	54
	Lisheen_LK-1432_HK 219			1	208.6	WAL	52.7679, -7.6951	55
RAPLA	Rapla_3312-62_HK 217			2 - 1	727	Upper Calcarenite M.	52.8307, -7.4852	56
	Rapla_3667-04_HK 185			2 - 1	726.2	Upper Calcarenite M.	52.8375, -7.4950	57
	Rapla_3667-04_HK 223			2 - 2	724	boundary UCM/NMU	52.8375, -7.4950	58
	Rapla_3312-78_HK 184			1	655.1	Nodular Micrite Unit	52.8298, -7.4869	59
	Rapla_3312-54_HK 222			1	369	Upr Wavy Lam Unit	52.8237, -7.4871	60
	Rapla_3312-62_HK 183			2 - 2	381.8	Crosspatrick Fm	52.8307, -7.4852	61

2.8 Stonepark Area

Group Eleven Resources Corporation currently manages the Stonepark project, which is considered highly prospective for economic Irish-zinc lead deposits. It is located in County Limerick, south-central Ireland, 10 km southeast of Limerick City and 5 km next to Glencore plc's Pallas Green deposit, an undeveloped zinc project (Figure 2-10A). The Stonepark prospect was initially discovered during a joint venture between Teck Ireland and Connemara Mining in 2007. Drilling by Teck Ireland Ltd has intersected mineralisation at three main Zn-Pb zones (Stonepark, Stonepark North and Stonepark West).

The Stonepark area is part of the Limerick Province. Although only part of the stratigraphic succession has been intersected during drilling, the whole section is outlined in Figure 2-10B and is detailed below. If not stated otherwise, the following information is taken from a technical report on the Stonepark project written by Gordon et al. (2018). Lithological units are widely occurring and laterally persistent in the carbonate-dominated Limerick Province (Philcox, 1984; Somerville et al., 1992). Where present (e.g. 20 km to the northeast of Stonepark), the Lower Palaeozoic basement is typically comprised of complexly folded and faulted Silurian metasedimentary rocks. The Old Red Sandstone (Devonian to earliest Carboniferous) unconformably overlies the basement rocks. These deposits are non-marine alluvial and fluvial sedimentary rocks (Graham, 2009) and crop out 10 km to the southwest. The marine transgressive sequence of the Mississippian rocks starts with the Lower Limestone Shale Group. Similar to the situation in the Rathdowney Trend, the Lower Limestone Shale Group was deposited in the early Courceyan (Hastarian) and is subdivided into the Mellon House, the Ringmoylan Shale and the Ballyvergin Shale formations (Sevastopulo and Wyse Jackson, 2009). The Ballymartin Limestone Formation succeeds these units and is included in the Lower Limestone Shale Group (Somerville and Jones, 1985). It was probably deposited in a carbonate ramp setting (Somerville and Strogen, 1992) and is the lowest unit that has been intersected during drilling in the Stonepark area. The lithology and age of the Lower Limestone Shale Group is already described in the previous section 2.7.1. The following Ballysteen Formation is sub-divided into the Knockainy Limestone and the Ballynamona members. The Ballynamona Member is formerly known as the Transition Unit (Strogen, 1988). The Knockainy Limestone Member is composed of bedded to thickly bedded argillaceous biosparites, while the Ballynamona Member is split into three separate units, which are made up of argillaceous wackestone, argillaceous limestone and nodular micritic limestone, respectively. The stratigraphically highest unit is informally also called Wavy Nodular Limestone or Nodular Micrite Unit, which frequently contains pale-green volcanic tuff bands. The Ballysteen Limestone Formation is overlain by relatively pure carbonate mudbank facies of the Waulsortian Limestone Formation (Lees and Miller, 1995). The

Waulsortian Limestone Formation comprises a mound complex composed of stacked mounds, which may be separated by argillaceous beds, referred to as Waulsortian equivalent facies. The variably dolomitised Waulsortian Limestone Formation is conformably overlain by the Lough Gur Formation which is composed predominantly of cherty bioclastic mudstones. The Lough Gur Formation is up to 100 m thick in places where it fills depressions created in the irregular topographic surface of the Waulsortian Limestone Formation carbonate mounds and is equivalent to the Crosspatrick Formation in the Rathdowney Trend (Somerville et al., 1992). It contains Ivorian (Cf4α1) and Lower Viséan (Cf4α2) foraminiferal fauna (Somerville et al., 1992). The Lower Viséan to early Arundian (345 – 339 Ma) Knockroe Volcanic Formation of alkali basalt, syenitic and trachytic composition overlies the Lough Gur Formation (Somerville et al., 1992; Sevastopulo and Wyse Jackson, 2009). Locally the fine-grained water-lain tuffs and basaltic lava flows of the former are interbedded with limestones at the top of the latter. In the Stonepark area, a number of basaltic diatreme-like breccia pipes with associated alkali basalt dikes and mafic sills of the Knockroe Volcanic Formation are located on the east and west margins of the prospect area, younging from west to east. Overlying the Knockroe Volcanic Formation, the stratigraphy is dominated by shallow-water oolites and non-argillaceous limestones of the Herbertstown Limestone Formation, whose age is late Arundian to early Asbian (e.g Somerville et al., 1992; Water et al., 2011). The Herbertstown Limestone Formation is succeeded with the volcanic rocks of the Asbian Knockseefin Volcanic Formation, which is dominantly comprised of ankaramitic and limburgitic lava flows with subordinate tuff breccias and vitric tuffs (Sevastopulo and Wyse Jackson, 2009). The Herbertstown limestones interfingers with both the Knockseefin and Knockroe volcanics. The well-bedded pale-grey grainstones of the Asbian to probably Brigantian Dromkeen Limestone Formation conformably overly the Knockseefin Volcanic Formation (Strogen, 1988). Lithostratigraphic units of the Stonepark area together with their formation descriptions and estimated formation thicknesses are summarised again in Table 2-7.

The structure of the Stonepark area is dominated by the east-west trending Limerick Syncline. There is also a subtle anticline to the north of the Limerick Syncline, which strikes approximately north-east and plunges gently to the south-west (Figure 2-10A). No major normal faults that offset the Waulsortian Limestone Formation have been delineated at Stonepark (McCusker and Reed, 2013).

Multiple zones of Zn–Pb mineralisation have been identified at Stonepark, occurring in strata-bound lenses. The bulk of the sulphide bodies defined to date occurs some tens of metres above the base of the Waulsortian Limestone Formation, whereas the mineralisation in the Rathdowney Trend is almost entirely at the immediate base of the same lithostratigraphic unit. Ore bodies occur specifically on the northern limb of the aforementioned anticline.

The Shannon Basin was the site of significant volcanic activity in the Early Carboniferous (Strogen, 1983). Unlike other Irish-type deposits, Zn-Pb mineralisation in the Limerick province is intimately associated with these igneous rocks. Although the Stonepark mineralisation lies along strike to the west of Glencore's Pallas Green deposits, no large faults which could act as conduits for the introduction of the mineralising fluids are observed, unlike in Lisheen and Navan (Hitzman and Beaty, 1996). Therefore it has been proposed that the intrusive rocks could have provided a mechanism for the introduction of the mineralising fluids (McCusker and Reed, 2013).
The relative timing of mineralisation is similar to that described at Silvermines (Reed and Wallace, 2004) and Navan (Peace and Wallace, 2000). The mineralisation post-dates the intrusion of the of the Lower Viséan to early Arundian Knockroe Volcanic Formation (Timmerman, 2004). The mineralisation is most likely epigenetic in origin and was emplaced at depths of at least 800 m (McCusker and Reed, 2013). However, the relationship between base metal mineralisation and Early Carboniferous magmatism is not well understood and needs further research (Wilkinson and Hitzman, 2015).

2.8.1 Sample Locations – Stonepark Area

Sample names consist of three parts: location_drill core number_lab ID. Eight tuff layers occur in Mississippian successions in four different drill cores from the Stonepark area, county Limerick, south-west Ireland (Figure 2-10A, C). One tuff layer (Stonepark_G11-450-02_HK 210) is identified in drill core 450-02, two tuff horizons occur in both drill cores 2638-01 (Stonepark_G11-2638-01_HK 197 and Stonepark_G11-2638-01_HK 198) and 2654-01 (Stonepark_G11-2654-01_HK 211 and Stonepark_G11-2654-01_HK 212) and three tuff layers (Stonepark_2638-02_HK 207, Stonepark_2638-02_HK 208 and Stonepark_2638-02_HK 209) are observed in drill core 2638-02 (Table 2-8, Figure 2-10C). The maximum distance between the drill cores is 22.5 km (Figure 2-10B). Seven tuff horizons occur in the highest stratigraphic unit (Nodular Micrite Unit used herein) of the Ballynamona Member, whereas one tuff layer (Stonepark_G11-2654-01_HK 211) is separated by the Waulsortian Limestone Formation from these samples and was deposited in the stratigraphically higher Lough Gur Formation.

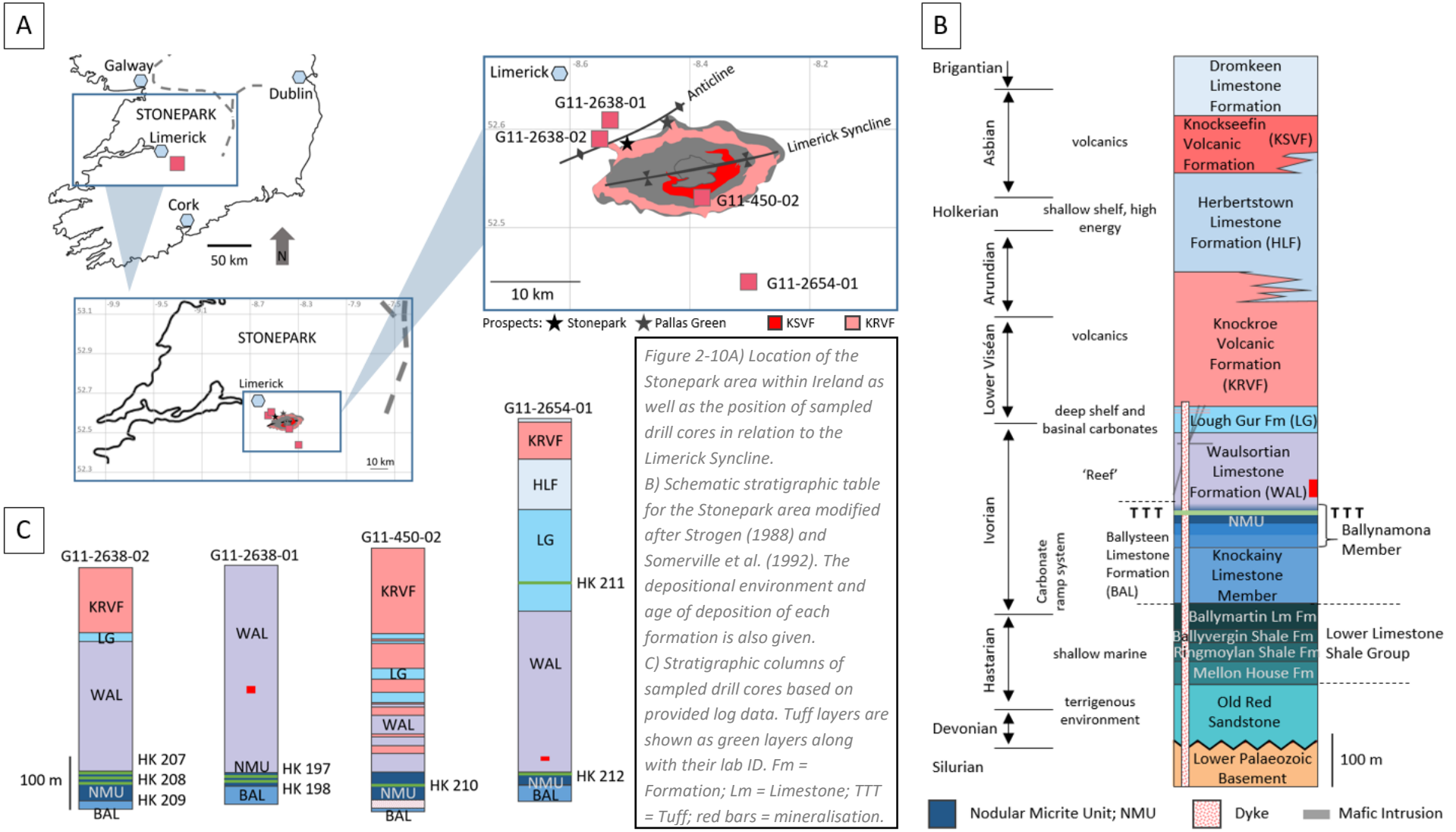

Figure 2-10A) Location of the Stonepark area within Ireland as well as the position of sampled drill cores in relation to the Limerick Syncline. B) Schematic stratigraphic table for the Stonepark area modified after Strogen (1988) and Somerville et al. (1992). The depositional environment and age of deposition of each formation is also given. C) Stratigraphic columns of sampled drill cores based on provided log data. Tuff layers are shown as green layers along with their lab ID. Fm = Formation; Lm = Limestone; TTT = Tuff; red bars = mineralisation.

Table 2-7: Lithostratigraphic units of the Stonepark area are listed in stratigraphic order, showing the oldest unit in the bottom row. Formation descriptions are taken from Strogen (1988), Sevastopulo and Wyse Jackson (2009) and Gordon et al. (2018). Formation thicknesses are the same like in table 7.1 in Gordon et al. (2018).

Lithostratigraphic Unit	Formation Description	Formation Thickness
Dromkeen Limestonen Formation	Well-bedded paly-grey grainstones	0 – 320 m
Knockseefin Volcanic Formation	Ankaramitic and limburgitic lava flows, subordinate tuff breccias and vitric tuffs	0 – 500 m
Herbertstown Limestone Formation	Coarse grainstones, oolites and non-argillacous limestones	190 – 500 m
Knockroe volcanic Formation	Complex package of volcaniclastic sediments, lavas and igneous intrusions of alkali basalt, syenitic and trachytic composition	250 – 550 m
Lough Gur Formation	Dark-grey to black cherty argillaceous wackestones	50 – 100 m
Waulsortian Limestone Formation	Mound complex composed of stacked mounds, sheets or tabular bodies, made up of massive to poorly bedded biomicrite wackestone	140 – 440 m
Ballynamona Member	Three units: - Nodular micritic limestones and shales; frequently cherty (formally named Ballynash; informally called Nodular Micrite Unit) - Argillaceous limestones - -Dark, well-bedded argillacous wackestones	190 m
Knockainy Limestone Member	Bedded to thickly bedded slightly argillaceous biosparite	
Ballymartin Formation	Thinly interbedded paly-grey muddy limestone and dark-grey calcareous shales	45 m
Ballyvergin Shale Formation	Non-calcareous grey-green shale with laminae of siltsone and fine sandstone	6 m
Ringmoylan Shale Formation	Thinly interbedded dark-grey to black calcareous shale and subordinate skeletal limestone	30 m
Mellon House formation	Mixed calcareous shales, grey fine-grained sandstones and dark-grey laminated siltstones	40 m
Old Red Sandstone	Pale to white calcareous sandstone with black mudstone specks	Base not seen

Table 2-8 Tuff horizons from drill cores 2638-01, 2638-02, 2654-01 and 450-02 along with corresponding sample IDs, sampling depths, number of sampled horizons, stratigraphic levels and sample location (coordinates). The amount of sampled tuff layers within one drill core is indicated by the sum of samples (ΣSamples), whereas Tuff# shows from which horizon the specific sample was taken from with Tuff# = 1 being the stratigraphically lowest tuff horizon.

	Sample ID			ΣSamples - Tuff#	Depth (m)	Stratigraphic level	Location	Sample #
	Location	Drill core	Lab ID					
STONEPARK	Stonepark_G11-2638-01_HK 198			2 - 1	405.6	Nodular Micrite Unit	52.5961, -8.5394	62
	Stonepark_G11-2638-01_HK 197			2 - 2	400	Nodular Micrite Unit	52.5961, -8.5394	63
	Stonepark_G11-2638-02_HK 209			3 - 1	420.8	Nodular Micrite Unit	52.5801, -8.5583	64
	Stonepark_G11-2638-02_HK 208			3 - 2	400.7	Nodular Micrite Unit	52.5801, -8.5583	65
	Stonepark_G11-2638-02_HK 207			3 - 3	399.8	Nodular Micrite Unit	52.5801, -8.5583	66
	Stonepark_G11-450-02_HK 210			1	453.4	Nodular Micrite Unit	52.5196, -8.3839	67
	Stonepark_G11-2654-01_HK 212			2 - 1	743.5	Nodular Micrite Unit	52.4377, -8.3081	68
	Stonepark_G11-2654-01_HK 211			2 - 2	376	Lough Gur Formation	52.4377, -8.3081	69

2.9 Slievedart Area

Minco Exploration Limited presently holds a range of high quality exploration targets in the Slievedart Block (Blaney, 2019). The area, referred to as the Slievedart area in this study, lies in County Galway, western Ireland, close to Dunmore in the Dunmore Province (Philcox, 1984) (Figure 2-11A). Due to distinct lateral facies changes, which occurred especially during the Viséan, Pracht and Somerville (2015) sub-divided the area into four successions: The Dunmore-Ballymoe (Central and NE Galway), Lough Corrib (West Galway), Craughwell-Burren (South and SW Galway) and Loughrea (SE Galway) successions. The Loughrea and Craughwell - Burren successions contain Tournaisian sequences where direct correlations with the formations seen in the Limerick Province can be made. These formations are part of the Lower Limestone Shale Group and are only present in the two southern successions in the Dunmore Province and mark a transitional unit of sandstone, limestone and shale. The succeeding late Tournaisian Ballysteen Limestone Formation is developed throughout the whole area, while there was a localised development of the deeper water Waulsortian Limestone Formation. The overlying Viséan marine successions are distinct between the four successions. However, the northern part of the region is dominated by shallow-water limestones, which form the beginning of an extensive carbonate platform, called the Galway-Roscommon Shelf (e.g. Morris et al., 2003; Long et al., 2005).

As all the investigated drill cores are taken from the Dunmore-Ballymoe succession, only details of this succession, which is also regarded as the standard succession for most of the Galway-Roscommon Shelf (see Morris et al., 2003), is outlined here (Figure 2-11B). The Dunmore-Ballymoe succession is initially terrestrial in the earliest Tournaisian, before becoming entirely marine for the duration of the Tournaisian and Viséan. The oldest Mississippian formation is a basal siliciclastic unit of late Tournaisian (Ivorian; CM miospore biozone age), termed the Boyle Sandstone Formation (Caldwell, 1959; Morris et al., 2003). These continental red-bed sediments pass directly up to a late Tournaisian (Ivorian) marine succession, locally called the Moathill Formation, which is part of the Navan Group (Morris et al., 2003; Somerville and Waters, 2011). It was deposited on a nearshore, shallow-water shelf and is made up of an alternation of bioclastic limestone, calcareous sandstone and mudstone (Pracht and Somerville, 2015). The Moathill Formation is followed by open marine limestones of the late Tournaisian (Ivorian) Ballysteen Limestone Formation. It was mostly deposited on an offshore shelf and is about 35 m thick around Dunmore. The overlying Waulsortian Limestone Formation does not occur everywhere on the carbonate platform. Around Dunmore, 45 m of the massive, deep-water distal ramp micritic Waulsortian limestone is recorded (Morris et al., 2003; Pracht and Somerville, 2015). The late Tournaisian age of the Waulsortian Limestone in the Slievedart area was determined using very limited foraminiferal and conodont data (Sevastopulo, 1982; Pracht et al., 2004). Where the

Waulsortian limestone is absent, a Waulsortian equivalent unit is present. It is differentiated from the overlying Kilbryan Limestone Formation by its higher proportion of limestone to mudstone (Pracht and Somerville, 2015). The Kilbryan Limestone Formation was deposited in a moderately deep-water shelf/mid ramp setting and can sometimes be laterally equivalent with the Waulsortian Limestone Formation (Morris et al., 2003; Pracht and Somerville, 2015). There are no age-diagnostic microfossils in the Kilbryan Limestone Formation. However, due to its stratigraphic position it is considered to be of latest Tournaisian to earliest Viséan in age (Pracht and Somerville, 2015). This unit is composed of argillaceous bioclastic limestones and it sometimes contains two thin green clay bands, that have been interpreted as altered volcanic ashes (Philcox, 1984; Morris et al., 2003) (Figure 2-11C) and form regional isochronous marker horizons between drill holes (Pracht and Somerville, 2015). In 2019, a 'sand-grade tuff' and a fourth thin clay band were discovered by Michael Philcox (Figure 2-11C). The boundary between the Kilbryan Limestone Formation and the overlying 140 m thick (Morris et al., 2003) Oakport Limestone Formation is gradational (Pracht and Somerville, 2015). The Lower Viséan age of the latter unit is well constrained using six different key foraminifers (*Eoparastaffella simplex, Pseudodolituotubella, Brunsia, Pseudoammodiscus, Eblanaia michoti* and *Eostaffella*, as well as the alga *Koninckopora* sp. and *Luteotubulus* (Pracht and Somerville, 2015). The Oakport Limestone Formation was deposited in a shallow-water shelf setting and is succeeded by the Arundian Ballymore Limestone Formation, a fine-grained argillaceous limestone, which was developed in a moderately deep-water shelf/mid ramp setting (Caldwell, 1959; Pracht and Somerville, 2015). Both of these shallow-water limestones, as well as the overlying Holkerian Croghan Limestone Formation, interpreted as a slightly deeper-water shelf limestone, form the Galway-Roscommon Shelf (Morris et al., 2003; Sevastopulo and Wyse Jackson, 2009; Pracht and Somerville, 2015). Lithostratigraphic units, formation descriptions and thicknesses of the Slievedart area are also listed in Table 2-9.
The structures in the Slievedart area are controlled by reactivation of existing Caledonian faults within the underlying basement, resulting in a series of northeast-southwest trending folds (Blaney, 2019). Small Mississippian and Lower Palaeozoic horst blocks separate a series of south- to southeast-dipping graben structures, which are known as the Castlerea and Slievedart Inliers (Blaney, 2019).
Mineralisation is hosted by the Waulsortian Limestone Formation or stratigraphic equivalent rocks and is slightly offset from the main faults (Blaney, 2019). While there is either little or no zinc-lead mineralisation, pyrite occurs as massive bands up to 50 cm thick in the northern part of the Slievedart Block. Boliden Tara Mines proposed that the mineralisation could be related to a larger mineralising system, which developed to the south of the block and was controlled by major structures.

2.9.1 Sample Locations – Slievedart Area

Eleven samples are available from two drill cores from the Slievedart area, county Roscommon, north-west Ireland (Figure 2-11A;Table 2-10). Drill hole 3470/15 was drilled 3 km west of Dunmore. The second drill hole 3471/4 is located 5.6 km to the south-east of the first drill hole (Figure 2-11B).

Sample names are composed of three parts: location_drill core number_lab ID. When appropriate, only the lab ID is used. Four thin tuff layers from drill core 3470/15 and five tuff horizons from drill core 3471/4 are encountered within the Kilbryan Limestone Formation. The tuffs in drill core 3470/15 appear at 223.3 m (Slievedart_3470/15_HK 190 = tuff one), 212 m (Slievedart_3470/15_HK 189 = tuff two), 207.9 m (Slievedart_3470/15_HK 237 = tuff three) and 200.5 m (Slievedart_3470/15_HK 188 = tuff four). Tuff one (Slievedart_3471/4_HK 194), tuff two (Slievedart_3471/4_HK 195), tuff three (Slievedart_3471/4_HK 238) and tuff four (Slievedart_3471/4_HK 193 / Slievedart_3471/4_HK 192) in drill core 3471/4 were deposited with similar stratigraphic separation as tuffs one to four in drill core 3470/15 (450.6 m, 436.5 m, 428.1 m and 419.2/419.1 m, respectively; Figure 2-11C). As samples HK 192 and 193 are found within a vertical interval of 10 cm, both tuff horizons are treated as tuff four. One thin tuff layer occurs in both drill cores in the overlying Oakport Limestone Formation at 136.6 m (Slievedart_3470/15_HK 187) and 328.6 m (Slievedart_3471/4_HK 191). Thus, all sampled tuff layers were deposited above the Waulsortian Limestone Formation.

The location and the stratigraphic column of drill core 1680/2 is shown as well as the U-Pb zircon age data of Pointon (2012) are shown in Figure 2-11C.

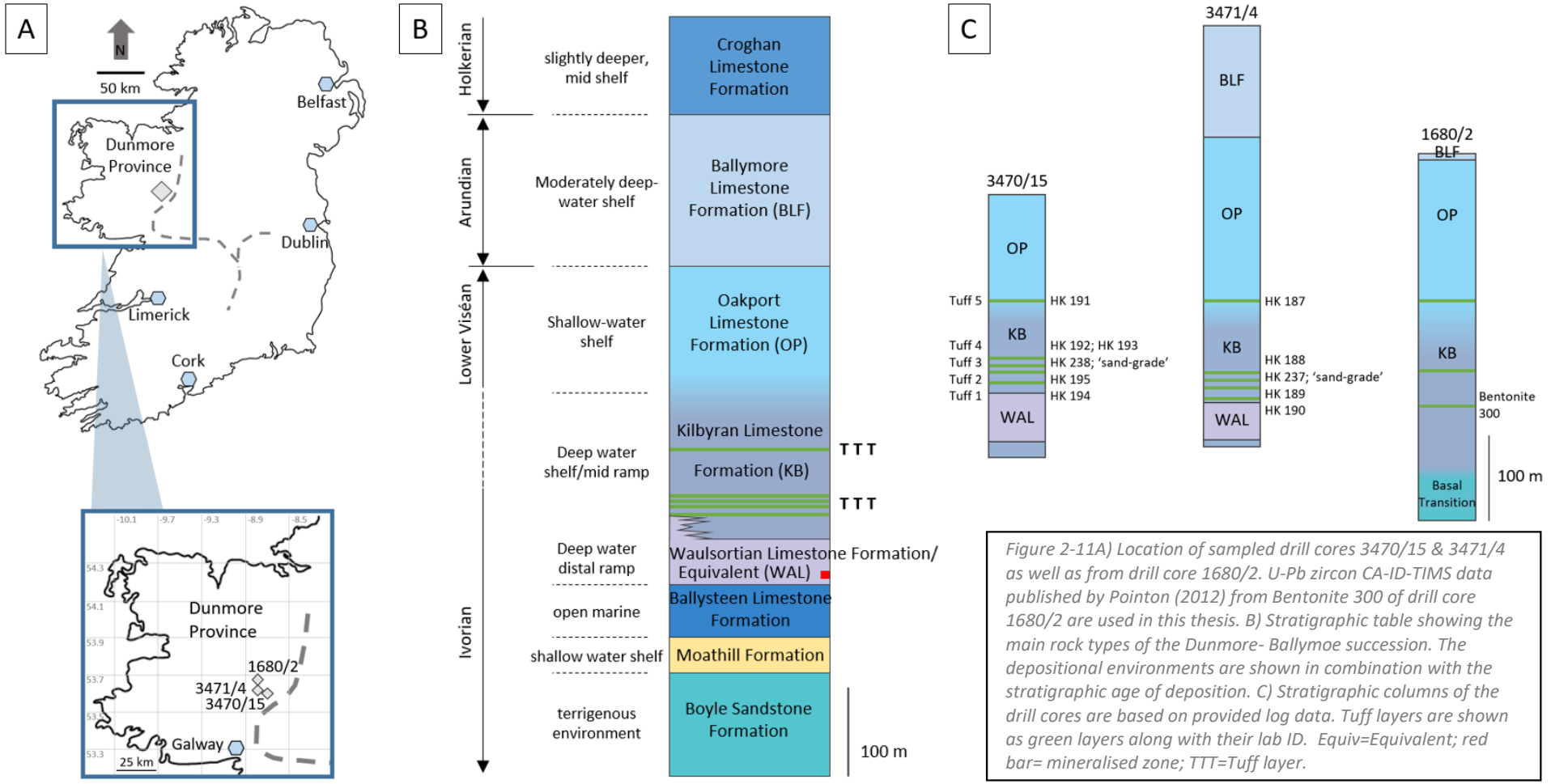

Figure 2-11A) Location of sampled drill cores 3470/15 & 3471/4 as well as from drill core 1680/2. U-Pb zircon CA-ID-TIMS data published by Pointon (2012) from Bentonite 300 of drill core 1680/2 are used in this thesis. B) Stratigraphic table showing the main rock types of the Dunmore- Ballymoe succession. The depositional environments are shown in combination with the stratigraphic age of deposition. C) Stratigraphic columns of the drill cores are based on provided log data. Tuff layers are shown as green layers along with their lab ID. Equiv=Equivalent; red bar= mineralised zone; TTT=Tuff layer.

Table 2-9: Lithostratigraphic units of the Slievedart area are listed in stratigraphic order, showing the oldest unit in the bottom row. Formation descriptions and thicknesses are taken from Pracht and Somerville (2015), and references therein.

Lithostratigraphic Unit	Formation Description	Formation Thickness
Croghan Limestone Formation	Dark-grey, well-bedded, fine grained argillaceous limestone with frequent bioturbation	> 77 m
Ballymore Limestone	Dark-grey well-bedded and nodular fine-grained argillaceous limestone, alternating with light grey coarse-grained limestone	Up to 225 m
Oakport Limestone Formation	Light-grey, massive, coarse-grained bioclastic limestone, occasionally intervals of dark-grey fine-grained fenestral lime mudstone, thick-bedded and massive	Up to 140 m
Kilbryan Limestone Formation	Dark-grey, fine-grained argillaceous bioclastic limestone alternating with minor mudstone and some chert nodules	Up to 185 m
Waulsortian Limestone Formation	Pale-grey, massive limestone forms large mud-mounds with stromatactid cavities Waulsortian equivalent: Thinly-bedded, fine-grained nodular limestone and shale	Up to 500 m
Ballysteen Limestone Formation	Light-grey and dark-grey, fine-grained argillaceous bioclastic limestones, alternating with calcareous mudstone	Up to 168 m
Moathill Formation	Alternation of bioclastic limestone, grey calcareous sandstone and mudstone	c. 15 m
Boyle Sandstone Formation	Grey sandstone	Up to 105 m

Table 2-10: Tuff horizons from drill cores 3470/15 and 3471/4 along with corresponding sample IDs, sampling depths, number of sampled horizons, stratigraphic levels and sample locations (coordinates). The amount of sampled tuff layers within one drill core is indicated by the sum of samples (ΣSamples), whereas Tuff# shows from which horizon the specific sample was taken from with Tuff# = 1 being the stratigraphically lowest tuff horizon.

	Sample ID			ΣSamples -Tuff#	Depth (m)	Stratigraphic level	Location	Sample #
	Location	Drill core	Lab ID					
SLIEVEDART	Slievedart_3470/15_HK 190			5 - 1	223.3	Kilbryan Limestone	53.6125, -8.79	70
	Slievedart_3471/4_HK 194			5 - 1	450.6	Kilbryan Limestone	53.5914, -8.7142	71
	Slievedart_3470/15_HK 189			5 - 2	212.0	Kilbryan Limestone	53.6125, -8.79	72
	Slievedart_3471/4_HK 195			5 - 2	436.5	Kilbryan Limestone	53.5914, -8.7142	73
	Slievedart_3470/15_HK 237			5 - 3	207.9	Kilbryan Limestone	53.6125, -8.79	74
	Slievedart_3471/4_HK 238			5 - 3	428.1	Kilbryan Limestone	53.5914, -8.7142	75
	Slievedart_3470/15_HK 188			5 - 4	200.5	Kilbryan Limestone	53.6125, -8.79	76
	Slievedart_3471/4_HK 193			5 - 4	419.2	Kilbryan Limestone	53.5914, -8.7142	77
	Slievedart_3471/4_HK 192			5 - 4	419.1	Kilbryan Limestone	53.5914, -8.7142	78
	Slievedart_3470/15_HK 187			5 - 5	136.6	Oakport Limestone	53.6125, -8.79	79
	Slievedart_3471/4_HK 191			5 - 5	329.0	Oakport Limestone	53.5914, -8.7142	80

Chapter 3:

Tuff Description

This chapter covers macroscopic and microscopic descriptions of the tuff samples from the four study sites. Figure 3-1A-AL shows drill core as well as close-up and thin-section images from a representative suite of samples.

3.1 Macroscopic Observations

The tuff bands are typically fine-grained, so not show evidence of grading. The tuffs are lithified and moderately indurated, presumably due to minor Variscan burial and heating. In contrast, Carboniferous tuffs in northern Ireland, where the degree of Variscan thermal maturation is very low, are putty-like (e.g. Serpukhovian tuffs, located a short distance beneath the base of the Pendleian British & Irish substage (= base of the Namurian Western European substage) in Cuilcagh Mountain, County Leitrim; Pointon, 2012, p. 127). Sometimes it is possible to sample the tuff layer as a continuous 'disc' in drill core (Figure 3-1C, I, J, U, W), while mostly they can only be sampled in smaller pieces (up to 2 cm) (Figure 3-1D, F, H, K, N, T, AB, AC). The hardness of the discs and pieces varies between soft (can easily be powdered using a pestle and mortar) to hard (hammer necessary to produce small pieces before being powdered using a TEMA). Many samples investigated in this study fell apart while sampling, which is characteristic of highly altered samples. The Marker Tuff from Tara Deep and most tuffs from the Rathdowney Trend and Slievedart are generally greyish green to medium grey. The Lower and Upper Tuffs from Tara Deep are dark grey to black and the tuffs from Stonepark are beige. However, samples from within the same stratigraphic unit can also have varying hardness and colour. The grain size of the samples is typically between clay and silt-grade with the exception of the third tuff layer in Slievedart (samples Slievedart_3470/15_HK 237 and Slievedart_3471/4_238), which can be classified as sand-grade (Figure 3-1AE-AL).

Many of the tuffs occur as discrete layers. For example, in Tara Deep, two or rarely three tuff horizons are present within a few tens of metres. The stratigraphically lowest tuff is called the Lower Tuff, followed by the Upper Tuff and the Marker Tuff. The Upper and the Lower Tuffs as well as the tuffs in the Rathdowney Trend, in Stonepark and Slievedart occur as distinct tuff layers (Figure 3-1O, Q, X, Y, AD). However, the Marker Tuff in Tara Deep was deposited as thin bands (0.1 to 5 cm), which are inter-laminated with calcareous mudstone bands over an interval of c. 60 to 250 cm (Figure 3-1A, B). Details on each tuff sample are listed in Table 3-1.

Table 3-1: Thickness, colour, hardness, type of occurrence, lower and upper contacts to host lithologies of the Irish Mississippian tuff samples are outlined herein. The thickness of samples one to 22 refers to the total thickness of the so-called Marker Tuffs, which are inter-laminated tuff bands with calcareous mudstones. The thickness of sampled tuff bands is provided along with their colour and hardness. Sample # corresponds to sample # in Tables 2-2, 2-4, 2-6 and 2-8, where more detailed sample information (depth, stratigraphic level and sample coordinates) can be found. N/A: no data available.

	Sample ID Location_Drill core_Lab ID	Thick-ness (cm)	Colour, Hardness, Characterisations	Lower contact	Upper Contact	Sample #
	Tara Deep_N-2250_HK 115	N/A	Dark grey, mainly soft platy pieces, ø 1 cm across, some hard pieces	N/A	N/A	1
	Tara Deep_N-2259_HK 116	N/A	Medium grey, soft, pieces ø 5 mm	N/A	N/A	2
	Tara Deep_N-2319_HK 118	N/A	Medium grey-green, hard pieces ø 2cm across	N/A	N/A	3
	Tara Deep_N-2332_HK 122	60	Light grey, soft, one disc, 2-3 mm thick, falls apart in platy pieces	sharp	sharp	4
	Tara Deep_N-2332_HK 121	60	Light grey, soft, one disc, 2-3 mm thick, falls apart in platy pieces	sharp	sharp	5
	Tara Deep_N-2332_HK 120	60	Light grey, soft, disc, 2-3 mm thick, contains lots of mica	sharp	sharp	6
	Tara Deep_N-2332_HK 119	60	Medium grey, 2 mm thick disc, falls apart in relatively hard pieces	sharp	sharp	7
	Tara Deep_N-2360_HK 245	N/A	Green-grey, soft, platy pieces, ø 5 mm surface	N/A	N/A	8
	Tara Deep_N-2373_HK 130	40	Green, 0.5 cm thick disc, falls apart in hard pieces ø 2cm across	sharp	sharp	9
	Tara Deep_N-2373_HK 114	40	Medium grey-green, 2.5 cm total thickness, falls apart in several discs, soft and hard pieces	sharp	Sharp	10
	Tara Deep_N-2415_HK 161	N/A	green, hard, 5 cm thick, broken in several big blocky pieces, thin bands of black shale	sharp	sharp	11
	Tara Deep_N-2444_HK 163	30	Greenish, Soft disc, 2cm thick, contains thin shale band	sharp	sharp	12
	Tara Deep_N-2444_HK 162	30	Greenish, Soft disc, 0.5 cm thick	sharp	sharp	13
	Tara Deep_N-2451_HK 186	N/A	Dark grey, mainly soft with some hard pieces up to 3 cm long	N/A	N/A	14
	Tara Deep_N-2457_HK 232	70	Medium grey, several hard flat discs, fall apart in platy pieces	N/A	N/A	15
	Tara Deep_N-2464_HK 196	N/A	Medium grey-green, hard flat pieces, ø 3 cm across	N/A	N/A	16
	Tara Deep_N-2467_HK 247	180	Medium grey, several hard discs, fall apart in platy pieces	N/A	N/A	17
	Tara Deep_N-2477_HK 234	50	Medium grey-green, several hard flat discs, fall apart in platy pieces	N/A	N/A	18
	Tara Deep_N-2479_HK 235	100	Medium grey, hard pieces ø 2cm across	N/A	N/A	19
	Tara Deep_N-2480_HK 236	70	Medium grey, several hard discs, fall apart in platy pieces	N/A	N/A	20
	Tara Deep_N-2494_HK 251	250	Medium grey, soft platy pieces ø 1 cm	N/A	N/A	21
	Tara Deep_N-2494_HK 250	250	Medium grey, soft, platy pieces ø 1 cm	N/A	N/A	22
	Tara Deep_N-2444_HK 158	1	Dark grey, soft, flat pieces ø 5 mm across	N/A	N/A	23
	Tara Deep_N-2455_HK 228	5	Dark grey, flat pieces ø 1 cm	N/A	N/A	24
	Tara Deep_N-2461_HK 230	10	Medium grey-greenish, hard disc, 5 mm thick with 1mm thick shale band, falls apart in in platy pieces	N/A	N/A	25
	Tara Deep_N-2494_HK 252	N/A	Dark grey-black, hard pieces ø 3 cm	N/A	N/A	26
	Tara Deep_N-2406_HK 166	20	Greenish, soft disc, 0.2 cm thick, falls apart in platy pieces	sharp	sharp	27
	Tara Deep_N-2406_HK 165	20	Greenish, hard pieces ø 1 cm within 5 cm mix with shale	sharp	sharp	28
	Tara Deep_N-2444_HK 159	10	N/A	N/A	N/A	29
	Tara Deep_N-2454_HK 170	2	Dark grey, hard flat pieces ø 3 mm across	sharp	gradational	30
	Tara Deep_N-2455_HK 229	N/A	Dark grey, flat pieces ø 1 cm	N/A	N/A	31
	Tara Deep_N-2461_HK 231	N/A	Dark grey, soft, pieces ø 2 mm	N/A	N/A	32

	Tara Deep_N-2469_HK 233	30	Dark grey, hard pieces ø 3 mm	N/A	N/A	33
	Tara Deep_N-2495_HK 248	N/A	Dark grey, flat pieces ø 1 cm across	N/A	N/A	34
	Navan West_N-2441_HK 169	N/A	Medium grey, hard pieces ø 3 mm	N/A	N/A	35
	Navan West_N-2411_HK 125	105	green, soft, small pieces ø 3 mm	sharp	sharp	36
	Navan West_N-2411_HK 126	105	green, soft, small pieces ø 3 mm	sharp	sharp	37
	Navan West_N-2441_HK 155	N/A	Medium grey, hard pieces, pieces ø 2 cm	N/A	N/A	38
	Navan West_N-2441_HK 156	35	Green, soft, flat pieces ø 1 cm across	sharp	gradational	39
	Navan West_N-2441_HK 157	35	green, hard solid disc, 1cm thick	sharp	gradational	40
	Navan West_N-2412_HK 128	N/A	Bright grey, soft	N/A	N/A	41
	Navan East_N-2317_HK 117	> 20	Grey-green, soft 2 mm thick disc, falls apart in platy soft pieces, part of interlaminated tuff	Sharp	sharp	42
	Navan East_N-2376_HK 227	N/A	Bright grey-greenish, soft, pieces ø 3 cm	N/A	N/A	43
	Lisheen_LK-0669_HK 215	3	Green, one disc with black shale band, soft	gradational	sharp	45
	Lisheen_LK-1585_HK 218	2	Dark green, soft	sharp	sharpish	46
	Lisheen_LK-1722_HK 180	7.5	Grey-greenish, hard pieces ø 3 cm	sharp	sharp	47
	Lisheen_LK-1773_HK 221	1	medium grey, was very swollen, crushed, hard pieces ø 1 cm	N/A	N/A	48
	Lisheen_LK-1874_HK 214	3	Dark green to black, hard pieces ø 5 mm	sharp	sharp	49
	Lisheen_LK-1915_HK 216	1	Medium grey, crushed, hard pieces ø 2 mm	sharp	sharp	50
	Lisheen_LK-1915_HK 220	0.5	Medium grey, crushed, several thin, hard discs	sharp	sharp	51
	Lisheen_LK-2180_HK 181	2	Light grey-green, soft	sharp	gradational	52
	Lisheen_LK-1040_HK 182	1	Green, soft pieces ø 5 mm across	sharp	gradational	53
	Lisheen_mine sample_HK 203	N/A	Medium grey, crushed, hard pieces ø 2 mm to 10 cm	N/A	N/A	54
	Lisheen_LK-1432_HK 219	1	Dark green, one hard disc with two shale bands	sharp	sharp	55
	Rapla_3312-62_HK 217	1	Grey, soft	sharp	sharp	56
	Rapla_3667-04_HK 185	0.6	grey, several thin, soft discs, pyritic	sharp	gradational	57
	Rapla_3667-04_HK 223	3	Medium grey, soft parts with thin hard discs	sharp	sharp	58
	Rapla_3312-78_HK 184	2	Bright green, crushed, several hard pieces ø 5 mm	sharp	sharp	59
	Rapla_3312-54_HK 222	6	Soft, yellow coloured at the outside of the core; bright grey in the inside; specks of pyrite	sharp	sharp	60
	Rapla_3312-62_HK 183	9	Medium grey with black shale band, soapy, soft and hard pieces ø 1 cm	sharp	gradational	61
	Stonepark_G11-2638-01_HK 198	N/A	Green, hard, blocky pieces, ø 2 cm	N/A	N/A	62
	Stonepark_G11-2638-01_HK 197	N/A	Green-yellowish, hard, blocky pieces , ø 2 cm	N/A	N/A	63
	Stonepark_G11-2638-02_HK 209	1	Light grey-green, hard solid disc	sharp	sharp	64
	Stonepark_G11-2638-02_HK 208	1.5	Green-beige, hard solid disc	sharp	sharp	65
	Stonepark_G11-2638-02_HK 207	1	Green-beige, hard solid disc	sharp	sharp	66
	Stonepark_G11-450-02_HK 210	N/A	Light grey, hard, blocky pieces up to 4 cm across	N/A	N/A	67
	Stonepark_G11-2654-01_HK 212	N/A	Medium grey, pieces up to 3 cm	N/A	N/A	68
	Stonepark_G11-2654-01_HK 211	N/A	Medium-dark grey, blocky pieces up to 3 cm across	N/A	N/A	69
	Slievedart_3470/15_HK 190	7	Medium grey, hard pieces ø 1.5 cm	sharp	gradational	70
	Slievedart_3471/4_HK 194	11	Medium grey, hard pieces, ø 5 mm	sharp	gradational	71
	Slievedart_3470/15_HK 189	1.5	Medium grey-greenish, soft, falls apart in flat pieces ø 2 cm	gradational	gradational	72
	Slievedart_3471/4_HK 195	N/A	Medium grey-greenish, soft, falls apart in flat pieces ø 1 cm	N/A	N/A	73
	Slievedart_3470/15_HK 237	4	Hard solid piece, internally graded	sharp	gradational	74
	Slievedart_3471/4_HK 238	5	Hard solid piece, internally graded	sharp	gradational	75
	Slievedart_3470/15_HK 188	5	Medium grey, soft pieces ø 1 cm	sharp	gradational	76
	Slievedart_3471/4_HK 193	3	Medium grey-green, hard platy pieces ø 2 cm	sharp	sharp	77

	Slievedart_3471/4_HK 192	1.5	Green, hard platy pieces ø 2 cm across	sharp	sharp	78
	Slievedart_3470/15_HK 187	N/A	Medium grey, soft pieces ø 2 mm	N/A	N/A	79
	Slievedart_3471/4_HK 191	3	Medium grey, soft pieces, ø 3 mm,	gradational	gradational	80

3.2 Microscopic Observations

For most of the samples, it was not possible to make conventional thin sections. Therefore, resin pucks are made first from the tuff fragments, which binds the sample together and then thin sections are made out of these pucks. A fine-grained, clay matrix was generally noted in photomicrographs, while there is no evidence for volcanic phenocrysts or remnants of unaltered volcanic glass (Figure 3-1D, F, H, K, N, T, AB, AC). The lack of volcanogenic glass in these samples can be explained by their high degree of alteration and their age. Ancient volcanic glass is relatively rare, especially in rocks older than the Paleogene (Hamilton, 1992). There were some textures, which could be vitroclastic, but iron staining makes it difficult to see. Samples Slievedart_3470/15_HK 237 and Slievedart_3471/4_HK 238 (the coarse, sand-grade tuffs from Slievedart in the Kilbryan Limestone Formation) are an exception (Figure 3-1AE-AL). They consist mainly of angular and equigranular pale feldspar grains, which have an average size of 0.25 mm with minor biotite embedded in a fine -grained matrix. Opaque minerals are interstitial. However, overall, petrological approaches are of limited value. Therefore, this study focuses on geochemical methods for fingerprinting these highly weathered and altered ash layers.

Figure 3-1A-AL) Drill core close-up photographs and photomicrographs from representative tuff samples of this study. A) B) L) Drill core picture of green altered ash beds, separated by calcareous mudstone bands in a carbonate section. O) Q) X) Y) AD) AE) AL) Drill core picture of single, discrete ash layers within a carbonate host rock. C) I) J) U) W) close-up photographs of tuffs, which could be sampled as continuous 'discs', whereas E) G) M) P) R) S) V) Z) and AA) show samples which could only be sampled as separate pieces. D) F) H) K) N) T) AB) and AC) are photomicrographs (plane-polarised light) showing an iron-altered, very fine-grained clay matrix. AF) AG) AI) and AJ) are photomicrographs of a sand-grade tuff (plane polarised light), while AH) and AK) show the same photomicrographs under cross-polarised light. The length of the scale bar is 4.5 cm for drill core images, 1 cm for close-up photographs and 1.5 mm for photomicrographs.

Chapter 4:

Bulk-Rock Geochemistry of Irish Volcanic Ash Layers

4.1 Introduction

The most commonly used technique for fingerprinting volcanic ash layers employs major-element compositions of volcanogenic glass as a correlation tool (Lowe, 2011). As an example, volcanic ash from a recent eruption (1990) consists of 70-80% of volcanic glass, 20-25% of phenocrysts and c. 5% of amorphous clays (Kawano and Tomita, 2001). However, in some cases, especially in pre-Cenozoic ash falls, volcanic ashes are completely devitrified and altered to clay minerals. As a result, only the remaining phenocrysts (see Chapter 5), clay minerals or bulk-rock geochemistry can be employed for geochemical correlations.

Volcanic ash horizons are typically considered as having been emplaced geologically instantaneously. However, the stratigraphic distribution of ash beds is controlled by primary factors such as eruption volume, proximity to volcanic centres, strength, direction of winds and mineral sorting (e.g. Wilson and Walker, 1987; Walker, 1971). Furthermore, ash layers are also affected by various pre-, syn- and post-depositional processes including reworking and mixing due to waves, currents, storm events, sediment dilution, condensation and bioturbation and diagenesis (Straeten, 2004; Hong et al., 2008). This affects both the lateral continuity and chemical homogeneity of volcanic ashes. The whole-rock chemistry of ashes is also more susceptible to chemical modification than its constituent phenocrysts. However, many tephrochronology / tephrostratigraphy studies employ chemical analysis of highly altered bulk ash samples as a method for identifying individual ash layers on a regional scale and reveal promising results (e.g. Huff, 1983; Kolata et al., 1987; Hints et al., 2008; Kiipli et al., 2010; Siir et al., 2015; Hong et al., 2016; Huff, 2016). Thus, this study also employs a bulk-rock geochemical approach to fingerprint Irish volcanic ashes, along with the use of apatite phenocrysts to characterise the source magma of the tuffs (see Chapter 5).

As only the primary source (i.e. magma chamber) signal is of importance for fingerprinting and subsequently correlating volcanic ashes, it is crucial to focus on elements whose abundance primarily reflects the magma source. Therefore, the selected tracer elements need to behave conservatively during transport and deposition and should be immune to post-depositional element mobility caused by weathering, solution/precipitation or other redox processes.

This study employed solution inductively coupled plasma quadrupole mass spectrometry (ICP-Q-MS) for trace element analyses of the tuff samples to obtain precise and accurate data for 51 trace elements, which were used to chemically characterise and subsequently differentiate between different tuff horizons and assign them to possible volcanic centres (sources). At the same time, the selected element suite should also allow for regional correlation within the four regional study areas, namely Navan, Lisheen, Stonepark and Slievedart (see Chapter 2). Tuff samples are characterised by comparing the patterns of elemental abundance between the samples using a new method, called the *matchogram*, where the degree of similarity can be quantified by calculating the difference in the relative abundance of suitable elements.

4.2 Methods

This section is comprised of two parts. The first part deals with the analyses of tuff whole-rock samples, including the preparation and digestion steps, the analytical protocol and analytical precision. The second part outlines the methods used to treat and present the geochemical data for correlation purposes.

4.2.1 Bulk-Rock Analyses

The tuff horizons are sampled from 4.5 cm diameter drill cores, while the stratigraphic thickness of the tuff layers varies between a few mm and 10 cm. Solution ICP-Q-MS was chosen for trace element analyses of the tuff samples due to the limited amount of sample material available and the expected low chemical variability between samples. This approach utilised here means only 100 mg of powdered material, or less, was needed to obtain precise and accurate data for 51 trace elements present at a ng/g concentration level (see section 9.1) as the method has very low detection limits.

4.2.1.1 Sample Preparation

As very small sample sizes were employed, the sample needed to be processed to a very fine size fraction to avoid any 'nugget' effects. Therefore, half of each sample was crushed using an anvil and hammer to generate rock chips up to 3 x 3 mm in size. The resulting rock chips were then powdered either in an agate ball mill or an agate disc mill to create a representative powder sample. Reagents were prepared from a stock of in-house triply distilled concentrated HF, HNO_3 or HCl and then diluted with ultra-pure Milli-Q water.

4.2.1.2 Digestion

Powdered samples (100 mg each) were transferred into pre-cleaned 30 ml Teflon vessels and then digested in a HF-HNO_3 (1:3) mixture at 150°C on a hotplate for 72 hrs. During the digestion, the beakers were agitated twice within 24 hrs. The digested solution was then

evaporated at 110°C, which liberates volatile fluorides such as silicon tetrafluoride, and then sequentially attacked with concentrated HCl and HNO_3 in order to remove excess F and convert any insoluble fluorides that may have formed during digestion. First, the samples were dissolved overnight using 1.5 ml of concentrated HCl in the sealed vessels at 160°C. Next, 1 ml of concentrated HNO_3 was added and immediately dried down to convert produced chlorides into nitrates. This step was conducted twice. Finally, the samples were dissolved in 2 ml concentrated HNO_3 and diluted to a c. 3.5 M HNO_3 sample solution using ultra-pure Milli-Q water. To equilibrate the solution, the beakers were put on a hotplate overnight at 120°C. Stock solutions were prepared by adding Milli-Q water to the sample solution to produce a 100 g gravimetric sample to solution ratio of 1:1 000 of c. 0.3 M HNO_3 in a pre-cleaned (acid-leached) 125 ml polypropylene bottle. For analysis, a 2 g gravimetric mixture of the stock solution, an internal standard mixture and 0.3 M HNO_3 was produced, giving a 1:20 000 final sample dilution. The internal standard mixture contained elemental and enriched isotopes (^{6}Li, Re, Rh, Bi and ^{235}U) covering the full mass range of ionisation potentials and analysed elements. The internal standard enables corrections for matrix-related signal suppression and analytical drift.

The United States Geological Survey (USGS) reference materials BHVO-2 (basalt), the Japanese reference materials JA-2 (andesite) and JLs-1 (limestone), and one rock reference material from the International Association of Geoanalysts (OU-6, slate) were used as quality control standards for the digestion process and treated the same way as the Carboniferous tuff samples, W-2a (mafic rock standard from the USGS) and the procedural blank. W-2a (diabase) is used as both the calibration and monitor solution. Procedural blanks are introduced to detect potential contamination during the digestion process. The procedural blanks were empty beakers that were processed the same way as all other samples.

The basalt standards BCR-2, BHVO-2 and BIR-1, the andesite reference materials AGV-2 and JA-2 are used as in-house standards. They were prepared and digested separately and serve as quality control standards to monitor the external precision and accuracy of the analytical set-up.

4.2.1.3 Analytical Set-Up

Trace element analyses were performed at Trinity College Dublin, Ireland using a Thermo Scientific iCAP ICP-Q-MS. The aliquots were introduced to the ICP-Q-MS with an Elemental Scientific (ESI) SC-2 DX autosampler equipped with a microFAST injection system. Ideally, the analysed samples are diluted so that the samples and standards are in the same concentration range as the on-board cross calibration corrections cannot fully account for the non-linear offset between pulse and analogue detector counting modes. Prior to analysis, the instrument was also tuned to maximise sensitivity across the target analyte range while maintaining a CeO^{+} production

rate < 3%. Oxide and dimer production rates on elements with isobaric interferences were tested using pure solutions of Ba+Nd and Dy, and natural isotope ratios of $^{6}Li/^{7}Li$ and $^{235}U/^{238}U$ were measured using a natural rock standard (Geological Survey of Japan (GSJ) rock reference standard JA-3) that was not spiked with the internal standard ahead of the main experiment.

The solution ICP-Q-MS experiment analyte list for sessions involving unknowns typically included the following isotopes: ^{7}Li, ^{9}Be, ^{25}Mg, ^{26}Mg, ^{27}Al, ^{31}P, ^{43}Ca, ^{44}Ca, ^{45}Sc, ^{49}Ti, ^{51}V, ^{53}Cr , ^{54}Fe, ^{55}Mn, ^{59}Co, ^{60}Ni, ^{65}Cu, ^{66}Zn, ^{71}Ga, ^{75}As, ^{84}Sr, ^{85}Rb, ^{86}Sr, ^{87}Sr, ^{89}Y, ^{90}Zr, ^{91}Zr, ^{93}Nb , ^{98}Mo, ^{111}Cd, ^{115}In, ^{120}Sn, ^{121}Sb, ^{133}Cs, ^{135}Ba, ^{139}La, ^{140}Ce, ^{141}Pr, ^{146}Nd, ^{149}Sm, ^{151}Eu, ^{159}Tb, ^{160}Gd, ^{161}Dy, ^{165}Ho, ^{167}Er, ^{169}Tm, ^{172}Yb, ^{175}Lu, ^{178}Hf, ^{181}Ta, ^{184}W, ^{204}Pb, ^{205}Tl, $^{206,207,208}Pb$, ^{232}Th, and ^{238}U. The sample run sequence of Eggins et al. (1997) was applied with the modifications described in Kamber et al. (2003) and Babechuk et al. (2010). The sequence started with the analysis of 0.3 M HNO_3, followed by instrument blanks, procedural blanks, calibration solutions (10 000, 30 000 and 50 000-fold dilutions of USGS mafic rock standard W-2a), in-house rock reference standards, experimental standards and samples. The run finished with another set of calibration solutions (20 000, 40 000 and 60 000 - fold dilutions of W-2a). All solutions, blanks, standards and samples were spiked with the internal standard mixture. Samples were analysed in blocks of 5-7, bracketed by repeated analysis of a monitor solution, such that the monitor solution was analysed approximately every 40 minutes over the course of the experiment. The 20 000-fold dilution of the calibration solution W-2a is also used as the monitor solution in this study. The sample order of tuff unknowns started with samples with expected low-level concentrations of elements known to have poor washout times (e.g. Nb and Ta) to avoid carryover signal between samples. Each sample was analysed in three independent cycles of c. 30 sweeps through the analyte mass range. The total analysis time for one sample was c. 8-10 min. For the analysis of 18 - 36 unknown samples, the typical run time was between 3 and 7 hrs.

In total, 94 samples, including tuff samples, tuff sample replicates and a shale sample, were analysed in seven different analytical sessions.

4.2.1.4 Data Reduction Protocol

Raw ICP-Q-MS signals are given in counts per seconds (cps), which reflects the detected strength of the ion signal from the analysed solutions. To transpose the acquired raw counts into element concentrations, data reduction was performed using an in-house Excel spreadsheet, containing the following steps.

4.2.1.4.1 Internal Drift Correction and Internal Precision

The internal standard solution was used to correct for ionisation and sensitivity variations, which results in internal drift during the course of one analytical run, such as matrix dependent signal suppression. The internal standard mixture contains multiple elemental standards (Re, Rh, Bi) and enriched isotopes (^{6}Li, ^{235}U), which are spaced at appropriate intervals through the entire mass spectrum (ideally about 20 mass units apart). The drift correction normalises the signal intensity of each element in a sample (in cps) to the pure internal standard solution analysed at the beginning of the experiment and linearly interpolates for analyte masses between internal standard masses to account for signal and ionisation variation between samples, while also scaling the internal standard signal intensity between individual sample runs to account for internal drift during sample measurement. For the enriched isotopes ^{6}Li and ^{235}U, it is also necessary to account for their natural abundance prior to internal drift correction. For each sample, the raw count signal of ^{7}Li and ^{238}U and the natural isotope ratios of ^{6}Li/^{7}Li and ^{235}U/^{238}U in the unspiked natural granodioritic rock reference standard JA-3 measured at the beginning of the analytical session, is used to determine the natural ^{6}Li and ^{235}U abundance in the sample, which is subsequently subtracted from the ^{6}Li raw counts or ^{235}U raw counts. The elemental standards (e.g. Re, Rh, Bi) contain all isotopes in their natural abundances. Therefore, there is no possibility to apply corrections for these elemental standards, but it should be noted that this is not necessary, as their concentrations in the internal standard solution are overwhelmingly higher than their concentrations in natural samples.

4.2.1.4.2 Background Correction

The background correction accounts for background signals, which occur during analyses due to the analytical set-up. It was undertaken by subtracting the average raw counts of the 0.3 M HNO_3, spiked with the internal standard, which was analysed at the beginning of the experiment. The background correction was applied for all samples, which were run during the experiments, including blanks, calibration and monitor solutions, standards, unknown samples. If the result was a negative value, the number was replaced by a zero.

4.2.1.4.3 External Drift Correction

Internal standard corrections cannot remove all sensitivity differences, particularly in the low- to mid- mass range (between ^{6}Li and Rh). Therefore, residual drift is corrected for using an external monitor of instrumental drift measured across the analytical session. Monitor solutions ideally have a matrix representative of the unknowns being analysed, to monitor differences in ionisation behaviour between the monitor and the samples they bracket. The monitor solution is measured repeatedly at intervals every 5-7 samples, allowing for a linear interpolation of the drift

across the analytical session. In all experiments a 1: 20 000 dilution of USGS reference material W-2a was used as this external drift monitor.

To evaluate the extent of instrumental drift, monitor solutions were inspected in a spreadsheet and a given element of each monitor was ratioed to the same element in the previous monitor analysis. These ratios were then examined visually to determine if the fluctuations represented true instrumental drift or were the result of anomalous measurements. In general, any ratios outside the range of 0.95 and 1.05 (± 5%) are investigated. Anomalous ratios were corrected by taking the average of the ratio of a given element before and after the outlier. If the ratios for all elements in a similar mass range evolve in a similar fashion then true elemental drift is present and corrected for. Thus, neighbouring isotope masses should have similar correction factors. The external drift correction is scaled by the relative distance of the unknowns from the respective bracketing monitor solution, with the corrections weighted more heavily the closer the sample is to the monitor solution (i.e. a form of lever correction). No correction was applied for blank solutions and the first monitor solution, since these represent the instrument conditions before any matrix is introduced to the plasma.

4.2.1.4.4 Blank Correction

Contamination during the digestion process was detected by the procedural blank. These procedural blank contributions were removed from the sample signals by subtracting the product of the procedural blank signal with its dilution factor.

4.2.1.4.5 Oxide Correction

Masses ^{71}Ga, ^{135}Ba, ^{146}Nd, ^{151}Eu, ^{159}Tb, ^{160}Gd, ^{161}Dy, ^{167}Er, ^{178}Hf and ^{181}Ta were measured in pure, matrix-free Ba+Nd and Dy solutions ahead of the main experiment to estimate i) oxide production of Ba interfering on Eu, Nd oxides on Tb, Gd, Dy and Er and Dy isotopes on Hf and Ta; ii) the production of Nd dimers on Ga and iii) to monitor isobaric interference of Dy on Gd. These results, as well as the ion signals of Ba, Ce, Nd, Sm, Eu, Tb, Gd, Dy and Ho from the main experiment, were subsequently used for the oxide/hydroxide and isobaric interference correction following Ulrich et al. (2010) on ^{71}Ga, ^{151}Eu, ^{159}Tb, ^{160}Gd, ^{161}Dy, ^{165}Ho, ^{167}Er, ^{169}Tm, ^{172}Yb, ^{175}Lu, ^{178}Hf, ^{181}Ta and ^{184}W. The final calculations also include oxide production rates, which were calculated during annual determinations of pure solutions, scaled to the measurement conditions of the current analytical session using the measured NdO^+/Gd^+ ratio.

4.2.1.4.6 Calibration

Instrument calibration was routinely performed using the well characterised USGS natural rock standard W-2a. W-2a was analysed six times in each analytical session, using six different dilution factors, ranging between 10 000 and 60 000. The dilution factors ideally cover the full range of ion signals encountered in all unknown solutions, which then results automatically in a calibration curve for each element, which spans the final element concentrations. That calibration curve is subsequently used to get the calibration factor. The following steps are necessary to receive the calibration factor for one element, which is then repeated to obtain the calibration factors for any element of interest. The first step is to compare the calculated dilution factors of analysed W-2a samples to published W-2a element values (see Appendix 1, Table A1 - 1) for each considered element. This ratio was subsequently divided by the ion signal of corresponding element. These steps were conducted for each dilution, resulting in six calibration factors, whose average is the final calibration factor. The final element concentrations were obtained by multiplying the ion signal of the element of interest with corresponding dilution and calculated calibration factor. This procedure had to be undertaken for every element in each sample.

4.2.1.5 Analytical Precision

Instrumental and procedural blanks are smaller than 0.001 ng/g for nearly all elements except for Zn and Cr (up to 0.04 ng/g and 0.015 ng/g, respectively), possibly related to minor contamination issues associated with reusing test tubes. To determine the limits of detection for each element, background equivalent concentrations (BEC) were calculated by dividing the signal of the internal standard solution (in cps) by the signal of the sample. The BEC is smaller than 0.001 ng/g for most elements except for Sc, Cr, Fe, Co, Ni, Cu, Mo, Cd, In, Sn Sb, Ba and W, whose values can go up to 0.35 ng/g in some experiments, while BECs for P can reach 0.7 ng/g. Thus, the background concentrations were small and should not influence the element concentrations of the analysed samples.

Internal precision was calculated using the average of the three measurement cycles (already corrected for internal drift). The percentage relative standard deviation (%RSD) is typically better than 2% for each element.

4.2.1.5.1 Precision and Accuracy

The USGS basalt standards BCR-2 (n=5), BHVO-2 (n=8), BIR-1 (n=6) and the andesite reference material AGV-2 (n=5), as well as the Japanese andesite reference standard JA-2 (n=6), were run as unknown solutions. Although these standards, also called in-house standards, were prepared separately to the experimental standards, they still follow the same digestion protocol. These in-house standards were analysed in every experiment and deployed as quality control standards to monitor the external precision and accuracy of the analytical method and data

reduction protocol. External precision was measured as the %RSD for multiple analyses of the reference materials listed above. Analyses were carried out over a time period of 36 months. The long-term reproducibility was smaller than 3% for 38 out of 51 analysed elements. Sample bias is the difference between an analytical determination of a material and its accepted reference value (Bainbridge, 1985). As those 38 elements from the five different reference rock standards were comparable to the Geological and Environmental Reference Materials (GeoReM) preferred values (a randomly distributed sample bias < 4%), the data set also demonstrates very good accuracy. Long-term averages for multiple digestions and analyses of the rock reference standards BCR-2, BHVO-2, BIR-1, AGV-2 and JA-2 are listed in Table A1 - 1 in Appendix 1, along with the preferred W-2a calibration values and accepted reference material values listed in GeoReM. For Be, Mg, Al, P, Ti, V, Cu, Zn, As, Cd, Sb, W and Pb the %RSD was between 3 and 10% (see Appendix 1, Table A1 - 1).

Stock solutions from nine randomly chosen tuff samples from this study were diluted and analysed twice during two different experiments. Comparing both runs for the same sample, elevated %RSDs were mainly observed for Be, Mg, P, Mn, Zn, As, Cd and W, while the %RSDs for all other elements were < 3% (see Appendix 1, Table A1 - 2). Sample HK 119 seems to be an exception, which has 27 elevated %RSDs in total.

The higher %RSDs of Cd, Sn, Sb, W and Pb can be explained by their heterogeneous distribution in the standards (e.g. Weis et al., 2006; Kamber and Gladu, 2009), while the elevated %RSDs of Cr and Zn could be caused by minor contamination during the digestion process as both elements show elevated concentrations in the procedural blanks. Other elements (e.g. Be and Cd) have low abundances in the calibration standard W-2a and thus cannot be analysed with sufficient precision in unknowns.

4.2.1.5.2 Reliability of the Digestion Method

The experimental standards are used to test the reliability of the preparation and digestion method. Therefore, at least two of the reference standards BHVO-2 (basalt), JA-2 (andesite) and OU-6 (slate) were digested and treated in an identical fashion as each batch of samples. The internal and external precision, as well as the accuracy, were comparable to the quality control in-house rock standards, which were prepared separately, indicating that there were no issues associated with sample digestion (see Appendix 1, Table A1 - 3).

4.2.1.5.3 Reproducibility of Tuff Digestions

The tuffs contain the mineral zircon, which is a very resistant phase in acid digestion. As it is important that samples are completely digested prior to analysis, high-pressure digestions like microwave or 'bomb' digestions are often employed to ensure complete dissolution of such resistant phases (e.g. Eggins et al., 1997). However, Marx and Kamber (2010) were able to prove throughout a comparative study using high-pressure bomb and hotplate digestion experiments, that even though there are clear deficiencies in Zr, Hf, Cr and Ti relative to the bomb-digested analyses, the offset is sufficiently systematic that reproducible analyses can still be obtained. Therefore, the reproducibility of element abundances was assessed from digestions and analyses of two randomly chosen unknown samples in this study (Rapla_3312-78_HK 184, Nodular Micrite Unit and Rapla_3667-04_HK 223, Upper Calcarenite Member/Nodular Micrite Unit), which were repeated twice, using the same hotplate beaker digestion described earlier that does not completely dissolve zircon. This approach facilitates detection of possible digestion or analytical issues affecting the reproducibility, which cannot be detected by repeated analysis of the USGS or GSJ standards due to the imperfect matrix match between those reference standards and the unknown samples.

Sample HK 223 showed deviations less than 3% except for Al, As, Rb, Mo, Cd, Sb and Pb, whereas sample HK 184 displayed elevated deviations for the same elements plus Be, Mg, P, Sc, Ti, V, Fe, Zn, Sn and Ta (see Appendix 1, Table A1 - 4). The element list which exhibits elevated deviations is very similar to those obtained during analysis of the primary and secondary quality control standards. Therefore, keeping in mind that concentrations for the HREE, Zr and Hf are an under-estimate, the digestion method shows good reproducibility and also homogeneity of the sample powder, especially for sample HK 184.

4.2.2 The *Matchogram* Approach

The treatment and protocols for the correlation of geochemical data have received a lot of attention in the literature in recent years. Many researchers use combinations of binary scatter plots (bi-plots) and spider diagrams to discriminate between samples or to propose correlations. Other workers have developed further statistical approaches, such as simple correlation coefficients or multivariate methods using discriminant function analysis, principal component analysis and kernel density estimates (Begét et al., 1991; Pollard et al., 2006; Pouget et al., 2014; Ramsey et al., 2015).

Along with binary diagrams, the approach of Marx et al. (2005) was employed with modifications in this study. Their approach was originally developed to provenance dust samples from New Zealand using ultra-high-precision trace element chemistry, calculating the composition of mixtures of potential source end-members and subsequently comparing those mixtures to the dust chemistries. In this study the geochemical characterisation and correlation of the tuff layers relies on determining the difference in concentration of an appropriate suite of elements between two samples. Whenever this method is used, it is referred to as the *matchogram*. The section below describes the use of the *matchogram* in more detail.

4.2.2.1 Background

Volcanic ash or tuff is provenanced by comparing the pattern of elemental abundances in a sample suite. If the volcanic ash or tuff suite is of similar composition, then correlation relies on detecting small differences in relative trace element composition to fingerprint the different volcanic ashes/tuffs. This approach requires highly precise and accurate data because of the potential small extent of chemical variability. The trace element data produced by solution ICP-Q-MS are well suited to this approach as that method has very low detection limits yielding precise and accurate data, given as concentrations (e.g. wt%, µg/g or ng/g) which represent proportions of the total sum (100 wt%). Such data are called compositional data, as the sum of all elements in one sample is always constant and more importantly, these elemental abundances are intrinsically correlated - as some elements increase in concentration, others must decrease. Hence the absolute concentrations of all elements will be affected if the sample is contaminated (e.g. dilution by carbonate), whereas elemental ratios will only change if they involve an element present in the contaminant. Hence, relevant information is more likely being contained in the element ratios than in absolute concentrations (Figure 4-1).

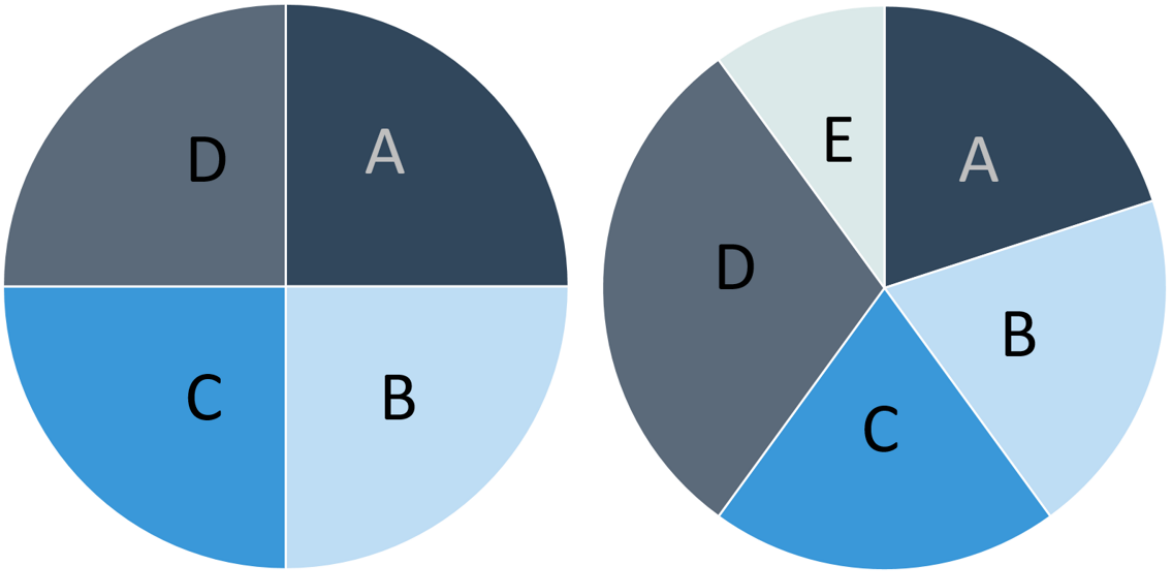

Element	wt%
A	25
B	25
C	25
D	25
E	0
Total	100

Ratios					
A/B	1	B/C	1	C/D	1
A/C	1	B/D			
A/D	1				

sample 1 – pure tuff

Element	wt%
A	20
B	20
C	20
D	30
E	10
Total	100

Ratios							
A/B	1	B/C	1	C/D	2/3	D/E	3
A/C	1	B/D	2/3	C/E	2		
A/D	2/3	B/E	2				
A/E	2						

sample 2 – contaminated tuff

Figure 4-1: Sample 1 is a hypothetical pure tuff, whose composition is made up equally of four different elements (A, B, C, D). Sample B once had the same composition as sample 1 but was contaminated by elements D and E, which leads to a shift of their absolute concentrations. As element D was also present in the contaminated material, its concentration increased, while there is a decrease in A, B and C. The ratios of A/B and A/C are the same in the pure tuff and in the contaminated sample.

As the Irish Carboniferous tuff layers are very thin and were originally deposited in marine environments, there is a risk of contamination by either interbedded carbonates (limestones or shales), which can lead to a dilution of the tuff sample and subsequently change the original tuff composition. In the case of compositional data, Aitchison (1982, 1986) suggested the transformation of element concentrations to log-ratio space to avoid incorrect measures of spread and co-dependence and at the same time bypassing the asymmetry of normal ratios.

4.2.2.2 Method

A worked example of the method is illustrated in Table 4-1 using a set of four different samples with element E as the common denominator and four different elements, which are compared between the samples. To eliminate the co-dependence of possible carbonate contamination on the original tuff composition, the first step towards the additive log-ratio transformation is performed, which makes use of one component as the common denominator (Table 4-1, panel 'Step 1'). Therefore, each element of the sample gets divided by its Ca concentration, which is chosen as the 'inert' denominator. Calcium is an appropriate denominator in this study as pure calcium carbonate contains 40.04 wt% of Ca while other elements only occur

as minor trace elements. Thus, minor contamination by carbonates has the biggest impact on the overall Ca concentration of an original tuff composition, leading to a shift in all other element concentrations towards lower values (Table 4-1, panel 'original concentration'). The following step compensates for the effects of carbonate dilution and thus, translocates all elements back to their 'original', non-diluted values. This is achieved by multiplying the normalised values from the previous step with a constant multiplier (total number of chosen elements), divided by the sum of all normalised values from the same sample (Table 4-1, panel 'Step 2'). That new value (the y-value in the panel 'Step 2' in Table 4-1) is now the same for tuffs which share the same eruption history and hence geochemistry, independent of their degree of contamination. Subsequently, the y-value of each element from sample_A is normalised to the y-value of the corresponding element in sample_B to compare these samples against each other. Instead of using log-ratios to bypass the asymmetry of normal ratios as suggested by Aitchison (1982, 1986), the y-value of chosen element of sample_A serves once as the numerator and once as the denominator before both results are summed and divided by two to produce the symmetrical ratio (Table 4-1, panel 'Step 3'). The benefit of the introduced term *symmetrical ratio*s is the independence use of numerators and denominators within a ratio. A perfect fit for a given element is indicated by a value of one. Each elemental comparison value is then subtracted by one. The values of all chosen elements are added to generate the sum of absolute deviates (Σ_D) and a perfect match between every chosen element between two samples would be zero (Table 4-1, 'Step 4'), which means that the concentration of every element between a pair of samples is identical. The closer the Σ_D for two samples is to zero, the more likely they have the same chemical composition, and thus share the same eruption history.

Table 4-1: Hypothetical matchogram illustrating the similarity between two tuff samples while correcting for possible sample contaminations or dilutions. The sum of absolute deviates, which is calculated in step four should be zero if two samples match perfectly. The further away they are from zero, the less likely they share a common eruption history. Sample one, sample two and sample three are the same tuffs, while sample four represents a different tuff. Original element concentrations of samples one to three are different due to their varying carbonate contamination. Step one and two corrects for the carbonate contamination. Therefore, the y-values, which represent the non-contaminated equivalent to the original concentrations are the same for sample one, sample two and sample three. Calculating the absolute deviation between sample one and sample two as well as between sample one and sample three results in a value of zero, which shows a common origin. Sample four shows different y-values, as well as a sum of deviation of 0.75, indicating a different eruption history compared to samples one to three.

	Sample 1 Tuff One	Sample 2 Contaminated Tuff One	Sample 3 Contaminated Tuff One	Sample 4 Tuff Two
ORIGINAL CONCENTRATION	wt%	wt%	wt%	wt%
Element A	30	25	13	10
Element B	30	25	13	40
Element C	25	21	11	20
Element D	10	8	4	15
E; inert denominator	5	20	60	15
Total	100	100	100	100
Step 1 - RATIOS USING ELEMENT E AS COMMON DENOMINATOR				
A/E = X1	6	1.26	0.21	0.67
B/E = X2	6	1.26	0.21	2.67
C/E = X3	5	1.05	0.18	1.33
D/E = X4	2	0.42	0.07	1
$\Sigma_{ratios\ X1,\ X2,\ \ldots,\ Xn}$	19	4	2.33	5.67
Step 2 - TRANSLOCATION TO NON-CONTAMINATED VALUE Y				
Y1	1.26	1.26	1.26	0.47
Y2	1.26	1.26	1.26	1.88
Y3	1.05	1.05	1.05	0.94
Y4	0.42	0.42	0.42	0.71
Step 3 - COMPARISON OF ELEMENTAL ABUNDANCE BETWEEN TWO SAMPLES				
	SAMPLE 1 – SAMPLE 2	SAMPLE 1 – SAMPLE 3	SAMPLE 1 – SAMPLE 4	
Z1	1	1	1.5	
Z2	1	1	1.1	
Z3	1	1	1.0	
Z4	1	1	1.1	
Step 4 - SUM OF ABSOLUTE DEVIATES				
	SAMPLE 1 – SAMPLE 2	SAMPLE 1 – SAMPLE 3	SAMPLE 1 – SAMPLE 4	
Σ_D	0	0	0.75	

4.2.3 Ratios and Normalisation

In general, immobile elements were chosen for fingerprinting altered tuff samples. However, immobile elements typically get relatively enriched in altered tuff samples relative to their parent material when mobile elements are lost (regardless of the element mobility process involved). Reworking, redeposition and transport can potentially also increase the concentrations of immobile elements. Similar to the earlier discussion on the effects of dilution, ratios of immobile components were used in bivariate plots in this study in order to assess the original composition of source magmas, as the ratios of immobile components should remain unaffected by element mobility (Kiipli et al., 2007; Özdamar et al., 2014; Siir et al., 2015; Göncüoglu et al., 2016).

Normalisation to a given reference material does not affect the information content of data. However, normalisation of rare earth element (REE) concentrations of natural materials against those of a natural reference system eliminates the Oddo-Harkins effect (elements with even atomic number > elements with uneven atomic number during nucleosynthesis in supernovae) and leads to a smooth REE patterns (Masuda, 1962; Coryell et al., 1963). Furthermore, when an appropriate reference material is employed it serves as a useful comparison to visually detect patterns of elemental enrichment or depletion in samples and are invaluable in igneous petrogenesis studies. A C1 chondritic meteorite (representative of Bulk Earth) and the post-Archaean upper continental crust (representative of shale) are commonly used in such normalisation diagrams (Bau et al., 2018). However, if the normaliser is similar to the investigated sample, fine-scale variability in the trace element composition can become more apparent and can highlight similar chemical characteristics (i.e. each normalised trace element yields a value close to unity) or accentuate anomalies (i.e. significant deviations form unity). To highlight the differences between samples using this form of normalisation, the y-axis of diagrams is shown on a linear scale rather than on a log-scale when appropriate.

4.3 Results

In the following sections, only chemical elements which were proven useful / diagnostic in the bulk-rock discussion section (section 4.4), are presented, while all trace element analyses are reported in Appendix 1, Table A1 - 5, along with selected elemental ratios. The trace element data of the shale sample are also listed in the same table and shown in Figure 4-2 to Figure 4-6 for comparison.

As it is known that only immobile trace elements should be used for fingerprinting highly weathered tuff layers, data are grouped according to their expected behaviour into mobile and immobile elements. Particular emphasis is also placed on Ca as well as on Pb, Zn, Cd and Tl

content, as the tuff layers were deposited in a marine carbonate environment close to known areas which exhibit base-metal mineralisation. Arsenic, U, Cr, Co, Sc, V, Ni and Cs are used to distinguish the tuff from an incorporated shale component, thus they are also briefly mentioned. The samples are grouped according to the four sampling sites, beginning with samples from Navan, followed by samples from the Rathdowney Trend, Stonepark and Slievedart. Within each sampling site, the tuff samples are subdivided by their stratigraphic occurrence based on the drill core logs.

The sample numbers in the plots correspond with the sample numbers in Table A1 - 5 (Appendix) and in Table 2-2, Table 2-4, Table 2-6 and Table 2-8 in Chapter 2, where detailed sample information is provided. Sample names in this study are composed of three parts: location_drill core number_lab ID. Only the lab ID is used when appropriate, but especially in provided figures.

4.3.1 Trace Elements which were Mobile during Weathering (Mg, Rb, Sr, Ba)

Magnesium, Rb, Sr and Ba concentrations for all tuff samples are plotted in Figure 4-2. Magnesium concentrations for samples from Tara Deep and Navan vary between 0.8 and 2 wt%, while samples from the Rathdowney Trend show the biggest spread in concentration, ranging from 1.1 to 3.2 wt%, followed by samples from Slievedart (0.9 – 2.3 wt%). Tuff samples from Stonepark, which were deposited within the Nodular Micrite Unit define a cluster with Mg values between 1 and 1.4 wt%, while the tuff samples from the Lough Gur Formation have a Mg content of 2.2 wt%. The Rb content of the tuff samples from the four areas are all between 83 and 402 µg/g. Most samples have Sr concentrations around 100 µg/g. Only six samples from the Thin Bedded Unit 2 (Tara Deep), two samples from the Kilbryan Limestone Formation (Slievedart) and one sample each from the Tober Colleen Formation (Navan West), Nodular Micrite Unit (Rapla) and Crosspatrick Formation (Slievedart) have Sr contents above 200 µg/g. While Ba concentrations are generally below 500 µg/g, two samples from the New Thin Bedded Unit 2 (Tara Deep) one sample from the Tober Colleen Formation (Navan West), three samples from the Nodular Micrite Unit (Lisheen) and two samples from the Kilbryan Limestone Formation (Slievedart) are between 991 and 2231 µg/g.

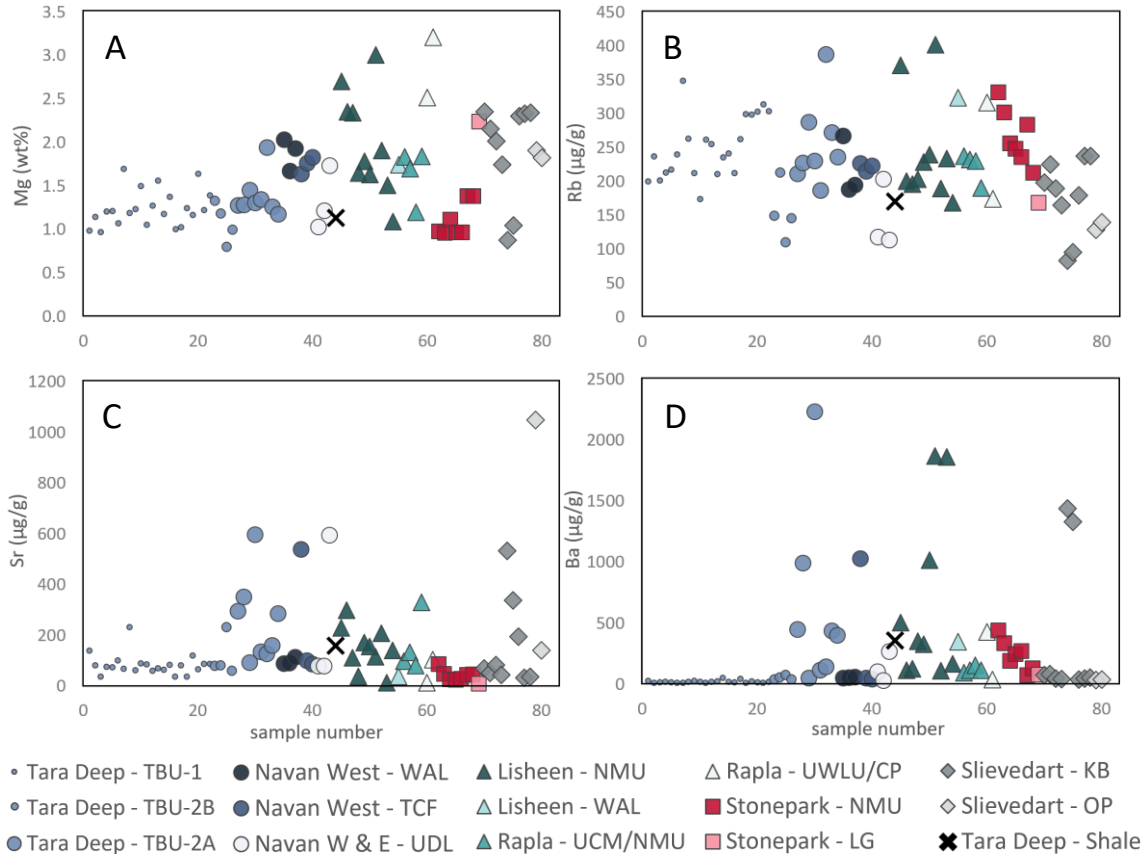

Figure 4-2: Magnesium (A), Rb (B), Sr (C) and Ba (D) concentrations for all Irish Mississippian tuff samples processed during this study. These four elements are mobile during weathering and alteration. Sample numbers correspond with sample numbers listed in Table A1 - 5, Appendix 1. Analysed shale sample is shown for comparison. CP = Crosspatrick Formation, KB = Kilbryan Limestone Formation, LG = Lough Gur Formation, NMU = Nodular Micrite Unit, OP = Oakport Limestone Formation, TBU = Thin Bedded Unit, TCF = Tober Colleen Formation, UCM = Upper Calcarenite Member, UDL = Upper Dark Limestone Formation, UWLU = Upper Wavy Laminated Unit, WAL = Waulsortian Limestone Formation.

4.3.2 Trace Elements which were Immobile during Weathering (Al, Ti, Y, Zr, Nb, Sn, Hf, Ta, Th, REE)

Figure 4-3 shows Al, Ti, Y, Zr, Nb, Sn, Hf, Ta and Th concentrations for all tuff samples from this study. All but ten samples are within ± 4 wt% (absolute) of the median Al concentration (11.2 wt%) of the tuff samples from the four areas. Two tuff samples from Tara Deep, one from Navan, three from the Rathdowney Trend and three from Stonepark are enriched in Al (15.3 – 24.6 wt%), while one sample from Tara Deep is depleted in Al (6.4 wt%). Titanium concentrations are between 0.1 and 0.32 wt% for all tuff samples, which were deposited in the Thin Bedded Unit 1 (Tara Deep), Navan and in the Lough Gur Formation (Stonepark), and for most samples from Lisheen (15/17) and Slievedart (9/11). The remaining samples yield a Ti content between 0.32 and 0.72 wt%. Three out of six samples from Navan East & West, 13 out of 17 samples from the Rathdowney Trend, three out of eight samples from Stonepark and four out of eleven samples from Slievedart have Th concentrations between 6.4 and 32.2 µg/g, while the Th content of all other samples is above 39.1 µg/g with an average of 63.8 µg/g. Tin concentrations of samples, which were deposited within Thin Bedded Unit 1 (Tara Deep) all plot within 10.2 and 24.1 µg/g,

while the remaining samples have a big spread, ranging from 0.5 to 49.1 µg/g. The average Y, Zr, Nb, Hf and Ta concentration for samples from Tara Deep is 250, 2971, 299, 64.1 and 18.1 µg/g, respectively and thus higher compared to the averages of the samples from Navan, the Rathdowney Trend, Stonepark and Slievedart, which are 108, 1365, 134, 35 and 12.1 µg/g, respectively. Fourteen of these 46 samples plot within the Y, Zr, Hf, Nb and Ta concentration range of the Tara Deep samples. These samples are mostly from Navan East, Navan West, Stonepark and Slievedart for the latter two elements.

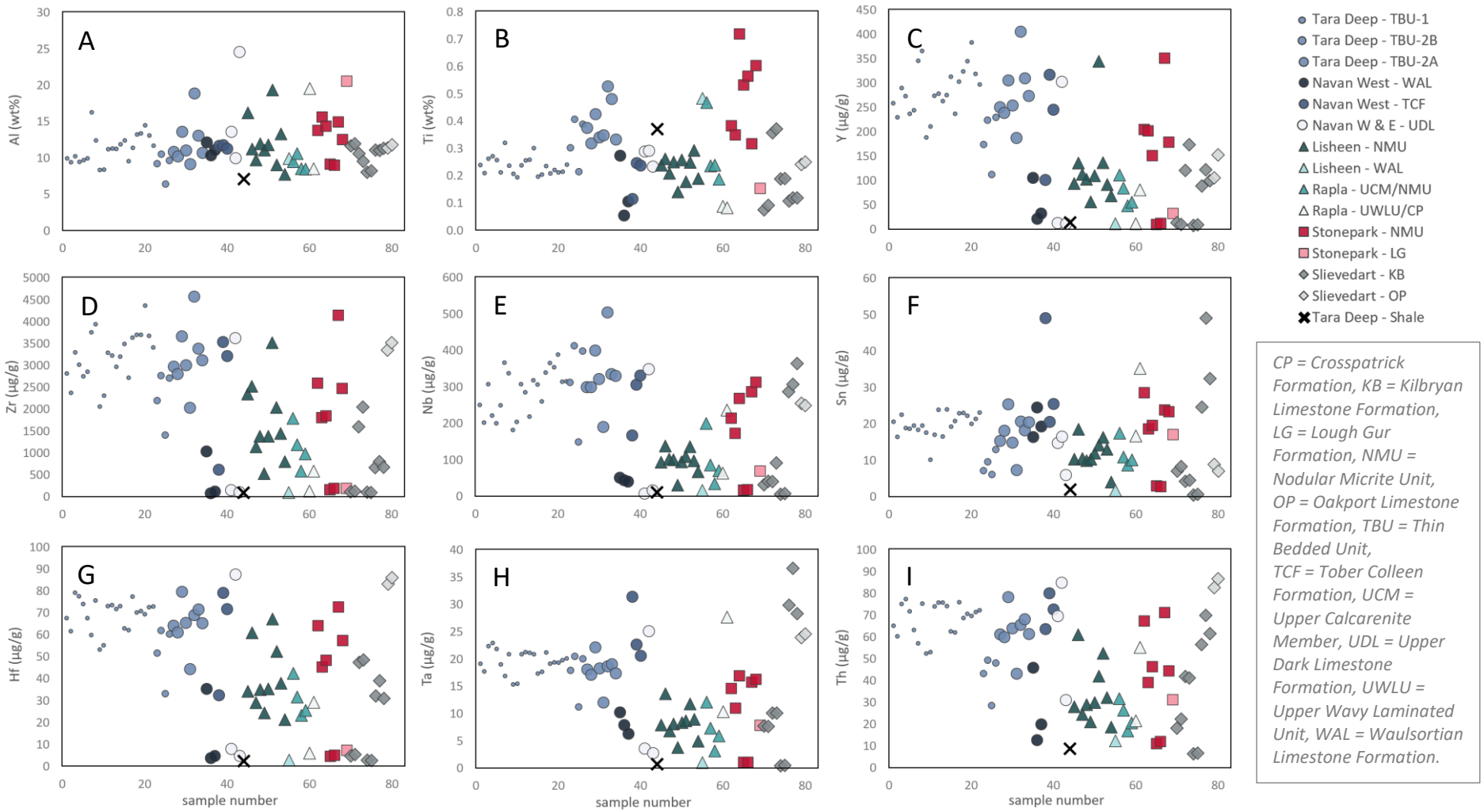

Figure 4-3: Trace element concentrations in wt% or µg/g of nine immobile elements during weathering and alteration for all Irish Mississippian tuff samples processed during this study. A) Aluminium B) Ti C) Y D) Zr E) Nb F) Sn G) Hf H) Ta and I) Th concentrations. Sample numbers correspond with sample numbers listed in Table A1 - 5, Appendix 1. Analysed shale sample is shown for comparison.

4.3.2.1 REE+Y

Rare earth element plus Y concentrations (REE+Y) from the Tara Deep samples range between 634 and 2156 µg/g, with an average of 1165 µg/g, while all other tuff samples have an average of 435 µg/g with REE+Y concentrations between 48 and 1285 µg/g. REE+Y concentrations for all analysed samples are shown in Figure 4-4A.

Whole-rock REE+Y abundances are normalised to chondritic values from McDonough and Sun (1995). All but four samples (Navan West_N-2441_HK 169, Waulsortian Limestone Formation; Stonepark_G11-2638-01_HK 197 and Stonepark_G11-450-02_HK 210, both Nodular Micrite Unit; Slievedart_3471/4_HK 193, Kilbryan Limestone Formation) show an enrichment in chondrite normalised light rare earth element (LREE; La-Sm) compared to the heavier counterparts (Gd-Lu), which are referred to as heavy REEs (HREEs) ($La_{CN}/Lu_{CN} > 1$; Figure 4-4B). All other samples from all four areas show a La_{CN}/Lu_{CN} ratio between 1.48 and 11.6, with the exception of samples Stonepark_G11-2638-02_HK 207 and Stonepark_G11-2638-02_HK 208, whose La_{CN}/Lu_{CN} values are up to 18.6 and 17.8, respectively (Figure 4-4B). The Eu anomaly is calculated using the equation of Bau et al. (2018); Eu anomaly=$Eu_{CN}/Eu^{*}=(Eu_{CN})/(0.5*Sm_{CN}+0.5*Gd_{CN})$.

The Eu anomaly of 77 out of the 79 analysed tuff samples is negative ranging between 0.06 and 0.55, while samples Slievedart_3470/15_HK 237 and Slievedart_3471/4_HK 238 have a positive Eu anomaly of 1.14 and 1.02, respectively (Figure 4-4B).

The La_{CN} - Sm_{CN} (4 to 1319) against Gd_{CN} - Lu_{CN} (-74 to 107) plot summarises the basic topology of the chondrite-normalised REE+Y patterns (Figure 4-4C), with five trends recognised:

1) The Navan samples in particular are characterised by a steeper slope in LREE compared to HREE, while both slopes are declining; however, this trend is also seen in selected samples from Lisheen, Stonepark and Slievedart.
2) Two Navan samples (Navan West_N-2441_HK 155, Tober Colleen Formation; Navan West_N-2441_HK 169, Waulsortian Limestone Formation), three Lisheen samples (Lisheen_LK-1773_HK 211, Lisheen_LK-1915_HK 220 and Lisheen_LK-2180_HK 181, Nodular Micrite Unit), three Rapla samples (Rapla_3312-62_HK 217, Rapla_3667-04_HK 223, Upper Calcarenite Member/Nodular Micrite Unit; Rapla_3312-62_HK 183, Crosspatrick Formation), four Stonepark samples (Stonepark_G11-2638-01_HK 198, Stonepark_G11-2638-02_HK 209, Stonepark_G11-2638-02_HK 208 and Stonepark_G11-2638-02_HK 207, Nodular Micrite Unit) and three Slievedart samples (Slievedart_3471/4_HK 194, Slievedart_3470/15_HK 188 and Slievedart_3471/4_HK 192, Kilbryan Limestone Formation) differ from the previous grouping by having a positive slope in HREE.

3) One Stonepark sample (Stonepark_G11-2638-01_HK 197, Nodular Micrite Unit) and one Slievedart sample (Slievedart_3471-4_HK 193, Kilbryan Limestone Formation) reveal a steeper slope in the HREE compared to LREE, a negative slope in LREE and a positive slope in HREE.
4) One Stonepark sample (Stonepark_G11-450-02_HK 210, Nodular Micrite Unit) has a steeper slope in the HREE compared to the LREE and a positive slope in both.
5) One Rapla sample (Rapla_3312-78_HK 184, Nodular Micrite Unit) and one Slievedart sample (Slievedart_3470/15_HK 187, Oakport Limestone Formation) have a steeper slope in the HREE and a negative slope in LREE and HREEs.

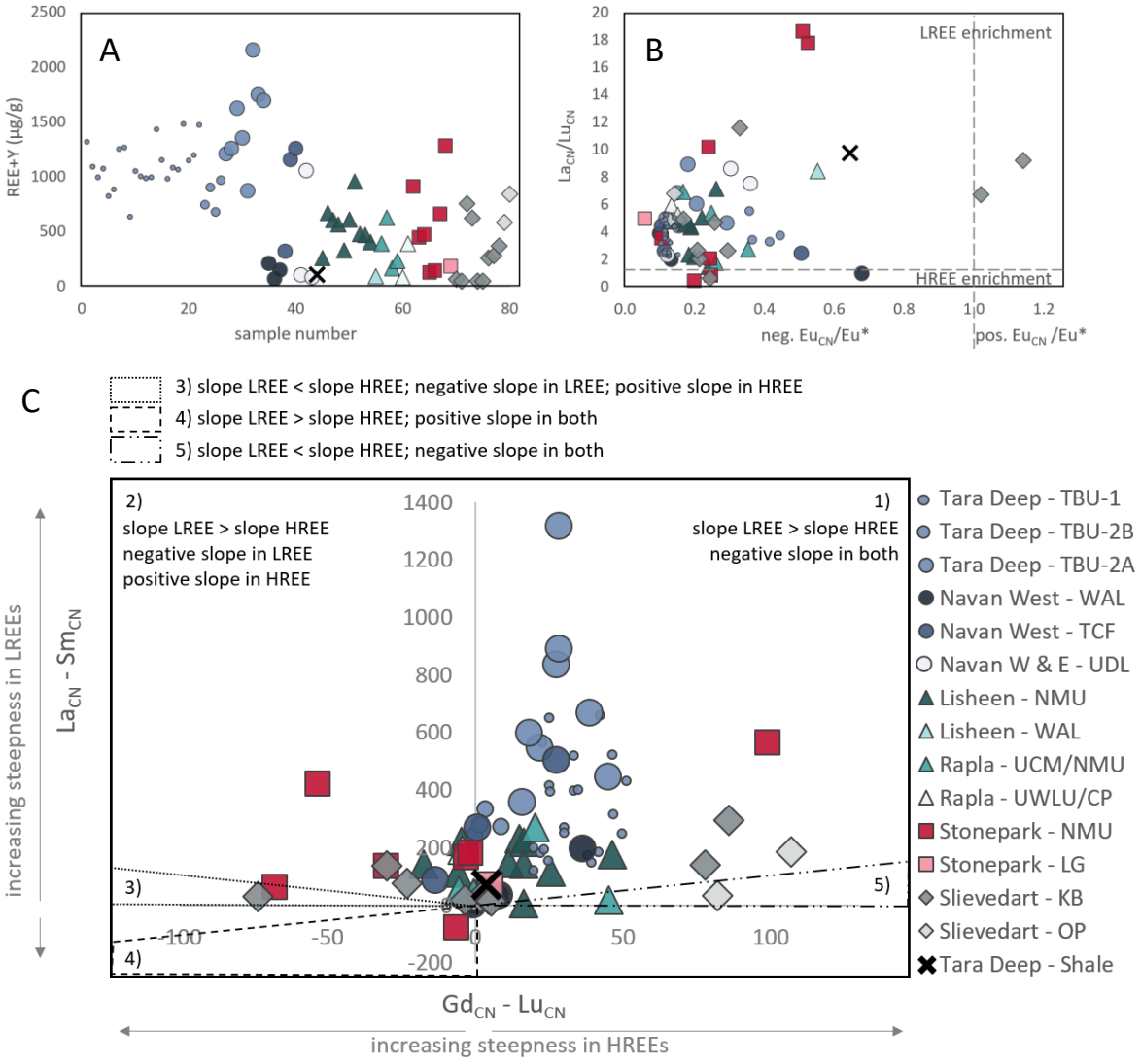

Figure 4-4: A) REE+Y concentrations and B) Eu anomaly vs La_{CN}/Lu_{CN} biplots for all analysed Irish Mississippian tuff samples processed during this study. C) Summary plot for REE elements for the 79 tuff samples from this study using La_{CN}-Sm_{CN} vs Gd_{CN}-Lu_{CN}. Chondrite values are taken from McDonough and Sun (1995). Shale is shown for comparison (black cross). CP = Crosspatrick Formation, KB = Kilbryan Limestone Formation, LG = Lough Gur Formation, NMU = Nodular Micrite Unit, OP = Oakport Limestone Formation, TBU = Thin Bedded Unit, TCF = Tober Colleen Formation, UCM = Upper Calcarenite Member, UDL = Upper Dark Limestone Formation, UWLU = Upper Wavy Laminated Unit, WAL = Waulsortian Limestone Formation.

4.3.3 Elements Affected by the Marine Depositional Environment (Ca) and Mineralisation (Zn, Cd, TI, Pb)

The range in Ca concentrations in the Navan area is smallest for Thin Bedded Unit 1, ranging between 0.2 and 3.1 wt%, followed by tuff samples from the Upper Dark Limestone Formation (1 - 3.8 wt%) and the Tober Colleen Formation (0.9 – 5.5 wt%) (Figure 4-5A). The biggest scatter can be observed in the Nodular Micrite Unit of samples from the Rathdowney Trend. Their Ca concentration ranges between 1.5 and 11.2 wt%, while the Ca content of the remaining samples varies from 0.1 to 4.7 wt% (Figure 4-5A).

Zinc, Cd, TI and Pb concentrations for all tuff samples from this study are presented in Figure 4-5B-E. The tuff samples from Tara Deep and the Tober Colleen Formation (Navan area) yield the lowest Zn concentrations, which do not exceed 27 µg/g. The Zn contents of remaining samples from Navan, and five samples from the Stonepark area are up to 71 µg/g. Most tuff samples from Lisheen (12/17) and Slievedart (9/11) show concentrations between 17 and 199 µg/g. Four samples from the Rathdowney Trend, three samples from Stonepark and two samples from Slievedart have Zn values between 332 and 954 µg/g, while one sample from Lisheen has the highest Zn concentration of the data set, which is 2.5 times higher (2422 µg/g) compared to next highest Zn concentration. Cadmium concentrations for all but two samples are between 0.1 and 1.5 µg/g with one sample from the Rathdowney Trend and one sample from the Slievedart area having Cd contents of 6.6 and 3.3 µg/g, respectively. Most samples across the four sampling areas have Pb concentrations below 70 µg/g, while three samples from the Rathdowney Trend, two samples from Stonepark and five samples from Slievedart yield Pb concentrations up to 255 µg/g. One sample from Lisheen has a Pb concentration of 7583 µg/g, which is roughly 30 times higher than average. Thallium concentrations are below 17 µg/g for all samples except for one sample from Tara Deep (Thin Bedded Unit 2) and four samples from the Rathdowney Trend, whose TI content ranges between 32 and 50 µg/g.

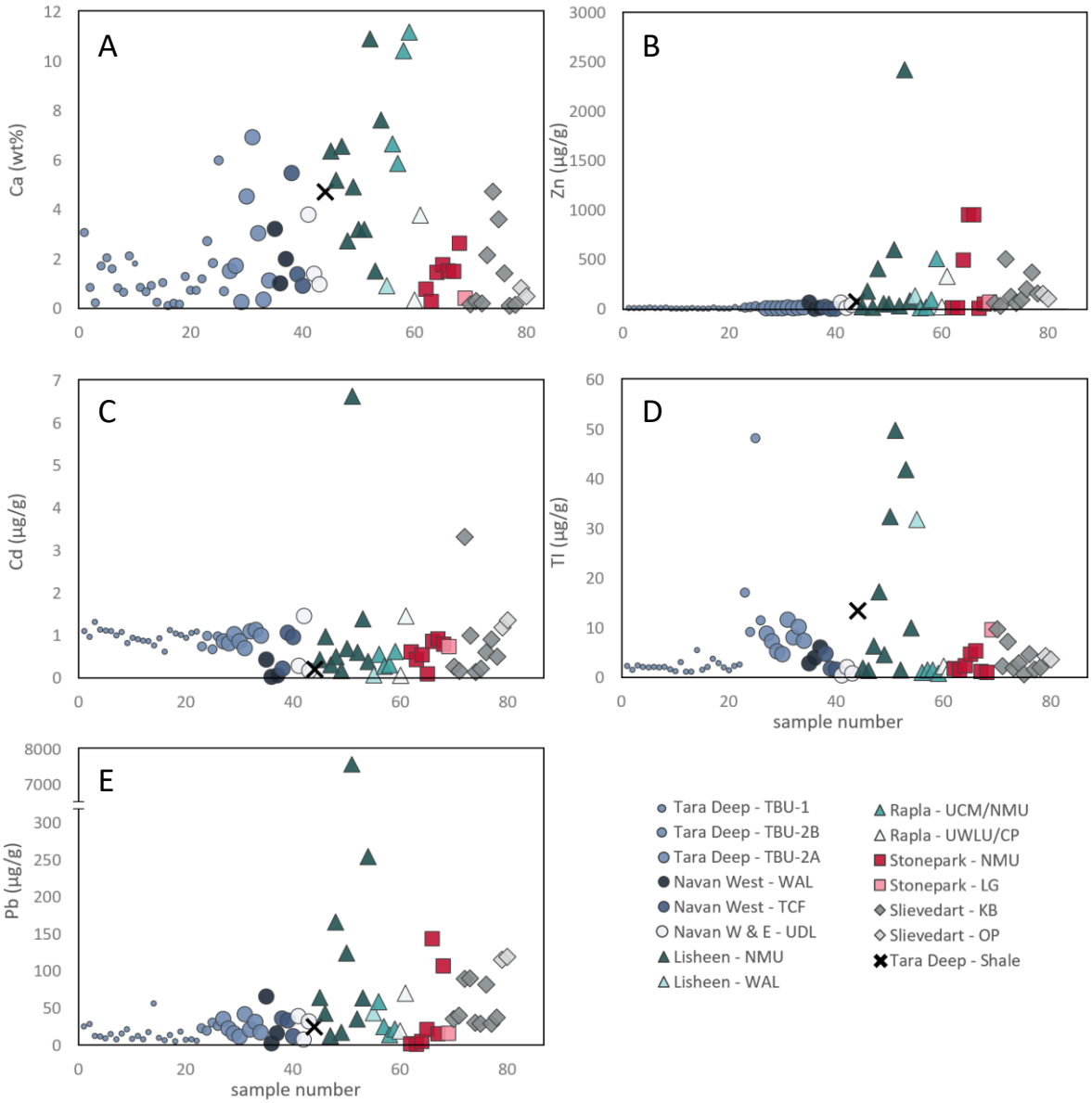

Figure 4-5: Calcium (A), Zn (B), Cd (C), Tl (D) and Pb (E) concentration for Irish Mississippian tuff samples processed during this study. Sample numbers correspond with sample numbers listed in Table A1 - 5, Appendix 1. Analysed shale sample is shown for comparison. CP = Crosspatrick Formation, KB = Kilbryan Limestone Formation, LG = Lough Gur Formation, NMU = Nodular Micrite Unit, OP = Oakport Limestone Formation, TBU = Thin Bedded Unit, TCF = Tober Colleen Formation, UCM = Upper Calcarenite Member, UDL = Upper Dark Limestone Formation, UWLU = Upper Wavy Laminated Unit, WAL = Waulsortian Limestone Formation.

4.3.4 Elements with Shale Characteristics (Sc, V, Cr, Co, Ni, Cs, U)

Figure 4-6A-G shows the Sc, V, Cr, Co, Ni Cs and U content of tuff samples from this study. Scandium and V concentrations for all samples range between 1.2 to 15.9 µg/g and 1.6 to 83.39 µg/g, respectively. The average Cr content for these samples is 16 µg/g, with three samples yielding exceptionally high values of 103 µg/g (Rathdowney Trend), 113 and 113.3 µg/g (Stonepark). Cobalt concentrations for samples from Tara Deep, Navan and Slievedart are below 17 µg/g, from Stonepark below 49 µg/g and from the Rathdowney Trend below 106 µg/g. Tuff samples from Tara Deep have the lowest Ni concentrations and vary between 8.6 and 37.3 µg/g, while samples from Navan and Stonepark reach values up to 128 µg/g, followed by samples from Stonepark and the Rathdowney Trend, which have maximum values of 367 and 386 µg/g, respectively. The average Cs content of samples from Thin Bedded Unit 1 in Tara Deep is 186 ± 83 µg/g, while the remaining samples from Tara Deep and Navan have a big spread, ranging between 19 and 530 µg/g. Samples from the Rathdowney Trend, Stonepark and Slievedart have a Cs average of 23 ± 10 µg/g. Uranium concentrations from samples from Navan range between 5.9 and 21.7 µg/g, while most of the other samples yield a U content between 1.1 and 13.4 µg/g. One sample from the Rathdowney Trend and one sample from Stonepark have a U content of 31 and 35 µg/g, respectively.

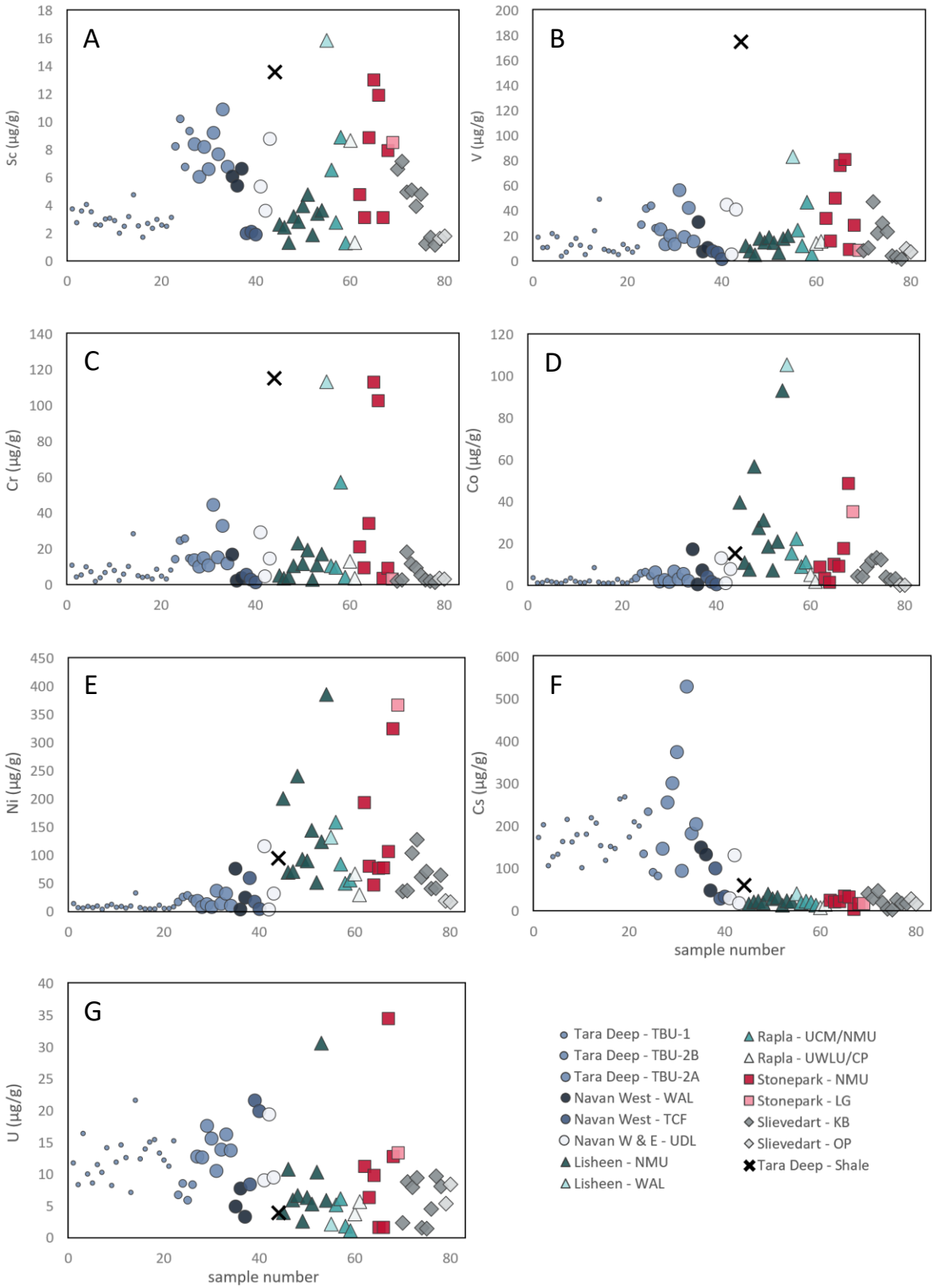

Figure 4-6: Scandium (A), V (B), Cr (C), Co (D), Ni (E), Cs (F) and U (G) concentration for Irish Mississippian tuff samples processed during this study. Sample numbers correspond with sample numbers listed in Table A1 - 5, Appendix 1. Analysed shale sample is shown for comparison. CP = Crosspatrick Formation, KB = Kilbryan Limestone Formation, LG = Lough Gur Formation, NMU = Nodular Micrite Unit, OP = Oakport Limestone Formation, TBU = Thin Bedded Unit, TCF = Tober Colleen Formation, UCM = Upper Calcarenite Member, UDL = Upper Dark Limestone Formation, UWLU = Upper Wavy Laminated Unit, WAL = Waulsortian Limestone Formation.

4.4 Discussion

Elements selected for provenancing volcanic ash or tuff need to reflect the primary magma composition (e.g. Huff et al., 2016; Kiipli et al., 2017; Hong et al., 2019). The data need to be carefully interrogated, filtered and interpreted as tuff layers are often highly weathered, and may have been recrystallised, devitrified and hydrated. These processes lead to the replacement of siliceous glass shards to clay minerals, which occurs extremely rapidly compared to other water/rock interactions as volcanic glass is highly reactive in the presence of water (Zielinski, 1982; Zielinski, 1985; Christidis, 1998; Arslan et al., 2010). During water/rock interaction, the mobile elements are reallocated, whereas highly immobile elements in the bulk-rock sample should still reflect the original composition of the volcanic ash/tuff and can be subsequently used for correlation purposes (tephrostratigraphy) and interpreting the chemistry of the parental source magma. Major elements like Si, Al, Na, K, Mg, Ca and Fe are usually depleted in the ash due to the mobility of these elements during weathering and diagenesis (Winchester and Floyd, 1977; Zielinski, 1985; Christidis, 1998; Spears et al., 1999; Ross and Bédard, 2009). Thus, emphasis should be placed on the interpretation of immobile trace element data. It is generally accepted that the high field strength elements (HFSE: Hf, Zr, Ti, Nb, Ta, Th and U) remain stable during alteration, whereas large ion lithophile elements (LILE: Ba, Cs, Eu, K, Rb, Sr, Pb) are more soluble and thus comparatively mobile in diagenetic environments (Nesbitt, 1979; Wray, 1995). However, their systematics in a sample are still useful to monitor diagenetic processes and the degree of weathering. Rare earth elements show intermediate degree of mobility in aqueous systems. Nevertheless, the mobility and solubility of any given element depends on the environmental pH, salinity, and redox conditions (Zielinski, 1985; Christidis, 1998; Kiipli et al., 2010). Thus, the elements selected for ash fingerprinting have to be carefully evaluated and a small degree of mobility and hence variability may be encountered at any sample site.

However, even the most immobile elements within an ash or tuff layer (i.e. those that are most likely unaffected by weathering or alteration) can be modified and influenced by secondary processes like mineral segregation during transport (i.e. during eruption), reworking and redeposition processes, and subsequent admixtures (incorporation) of detrital material such as accessory minerals (Kiipli et al., 2017; Hong et al., 2019). The depositional environment and burial history can also control the behaviour of immobile elements within a sample (Hong et al., 2019). As the detailed mechanisms and rate-controlling factors for the alteration of volcanic ashes in natural environments are not fully understood, careful characterisation of samples has to be undertaken first. Therefore, volcanic ash *vs* shale samples have to be identified first before processes like transport distance, alteration and reworking that might change the tephra composition are addressed. This study also investigates if these processes affect the tephra

composition differently between the four sample sites, and if they can be possibly used for local correlations. Subsequently, a robust suite of elements is selected for regional correlation and magma source typing of the Irish Mississippian tuff samples in this study.

4.4.1 Identifying Devitrified Volcanic Ashes

Tuff horizons are commonly not visually distinctive from host (enclosing) sedimentary rocks, especially shales. Recent volcanic ash is typically a mixture of volcanic glass (70–80%), phenocrysts (20-25%) and amorphous clays (c. 5%) (Kawano and Tomita, 2001). While the presence of volcanic glass particles is clear evidence for a volcanic origin, devitrification in altered volcanic ashes and tuffs makes unambiguous identification difficult (Weaver, 1963). Nevertheless, euhedral phenocrysts like apatite, biotite, quartz, sanidine and zircon can indicate a probable volcanic origin (Weaver, 1963; Smith, 1967; Bohor et al., 1979) (see section 5.4.4). In addition, trace element geochemistry can be used to distinguish volcanic products from visually similar siliciclastic units, such as shales. However, there is no prescribed definitive suite of elements which can be applied to unambiguously distinguish tuff horizons from their surrounding shales. As one of the first goals of the data interrogation is to detect differences between shale and tuff samples, all uncertain, but suspected tuff samples are compared with a suite of shale normalisation values. Consequently all samples which following normalisation display sub-horizontal trends around unity (between 0.5 and 1.5) for a 'shale-diagnostic' group of elements are unlikely to have a substantial volcanic component and can be excluded from the sample suite. The Post-Archaean Australian Shale (PAAS), the North American Shale Composite (NARC), Cody Shale (SCO-1), Penrhyn Slate (OU-6) and Mud from Queensland (MuQ) are widely used for normalisation purposes. They are referred to and used as ‘reference shales’ within this study. The sample set for PAAS is taken from Taylor and McLennan (1985), besides Tm and Lu, which is taken from Pourmand et al. (2012). North American Shale Composite values are mainly taken from Gromet et al. (1984) with the REE+Y using the values of McLennan (1989). Values for SCo-1, OU-6 and MuQ are taken from Govindaraju (1989), Kane (2004) and Kamber et al. (2005), respectively. As shale standards effectively represent the trace element composition of the average Post-Archaean upper continental crust, the upper continental crust values (UCC) from McLennan (2001) are considered as well. A shale sample from this study, sample Tara Deep_N-2406_HK 164 from the Navan area was also employed as a representative shale sample, and its values along with the five 'reference shales' and UCC described above are listed in Table 4-2.
Yttrium, Zr, Nb, Sn, Cs, Hf, Ta, Th, U and the REEs (excluding Eu) appear to be elements, which are clearly enriched in most tuff samples compared to the shale normalisation values. Using this element list in the *matchogram* approach (see section 4.2.2 for details), the 'reference shales' can clearly be distinguished from the samples of this study. The same result was obtained either using

Cr, Zn, Y, Zr, Nb, Cs, Tb, Hf, Ta, Pb, Th, U or Cr, Co, Zn, Y, Zr, Nb, Tb, Hf, Ta, Pb, Th, U, which are both frequently used element combinations. The shale sample from this study (sample Tara Deep_N-2406_HK 164) correlates well with the 'reference shales', especially when using the latter element combination. When comparing the REE+Y concentrations of the reference shale samples with the unknown tuff samples using the *matchogram* approach, only samples Lisheen_LK-1432_HK 219 and Rapla_3667-04_HK 223 can be confidently grouped with the ‘reference shale’ samples. Zhou et al. (2000) use the characteristics of Sc, Ti, V, Cr, Co, Ni, Eu, Th and U to distinguish tuff layers, which were deposited in coal (tonsteins) and claystones. Using this set of elements in comparison to the 'reference shales', samples Tara Deep_N-2461_HK 230, Rapla_3667-4_HK 223 and Stonepark_G11-2638-02_HK 207 can be possibly assigned as a shale sample.

Table 4-2: Selected elemental concentrations for various shales, which are widely used for normalisation purposes (Upper Continental Crust - UCC, Post-Archaean Australian Shale - PAAS, Mud from Queensland - MuQ, North American Shale Composite - NASC, Cody Shale - SCO1 and Penrhyn Slate - OU-6) as well as for the Mississippian shale of this study (Tara Deep_N-2406_HK 164). Concentrations are given in µg/g and are arranged by atomic number.

Sample ID	UCC[1]	PAAS[2]	MuQ[3]	NASC[4]	SCO-1[5]	OU-6[6]	HK 164
Al	80400	100714	91612	89389	72300	108230	71123
Sc	14	18	16	15	11	23	14
Ti	4100	4796	8153	4200	4000	5935	3701
V	107	103	120		131	130	175
Cr	83	130	65	125	68	71	115
Co	17	18	22	26	11	29	15
Ni	44	59	32	58	27	40	95
Zn	71		73		103	111	70
Y	22	28	32	27	26	28	14
Zr	190	194	199	200	160	174	93
Nb	12	19	15		11	14	11
Sn	6	4	3		4	3	2
Cs	5			5	8		61
La	30	43	33	32	30	33	22
Ce	64	91	71	73	62	77	39
Pr	7	10	8	8	7	8	5
Nd	26	35	33	33	26	30	17
Sm	5	6	7	6	5	6	3
Eu	1	1	2	1	1	1	1
Gd	4	5	6	5	5	5	3
Tb	1	1	1	1	1	1	0
Dy	4	5	6	6	4	5	2
Ho	1	1	1	1	1	1	1
Er	2	3	3	3	3	3	2
Tm	0	0	1	1	0	0	0
Yb	2	3	3	3	2	3	2
Lu	0	0	0	0	0	0	0
Hf	6	4	5	6	5	5	2
Ta	1	1	1	1	1	1	1
Pb	17	23	20		31	29	25
Th	11	16	11	12	10	11	9
U	3	3	3	3	3	2	4
La_{CN}/Sm_{CN}	4	4	3	4	4	3	4
Gd_{CN}/Lu_{CN}	1.47	1.37	1.60	1.34	1.67	1.46	1.40
Eu anomaly	1	1	1	1	1	1	1
ΣREE+Y	168	231	207	200	173	203	110
TiO_2/Al_2O_3	0.05	0.04	0.08	0.04	0.05	0.05	0.05

[1]McLennan (2001); [2]Taylor and McLennan (1985), Pourmand et al. (2012); [3]Kamber et al. (2005); [4]Gromet et al. (1984), McLennan (1989); [5]Govindaraju (1989); [6]Kane (2004)

Detrital clay minerals are formed during the weathering and erosion of pre-existing bedrock. As very minor amounts of REEs go into solution prior to deposition, detrital clays in a shale or claystone should record and retain a shale REE pattern in marine environments (Fleet, 1984; McLennan, 1989). The chondrite-normalised La/Sm and Gd/Lu ratios of the 'reference shales' are listed in Table 4-2 and are between 3.08 and 4.2 and between 1.3 and 1.7, respectively (grey field in Figure 4-7A), indicating larger fractionation within the LREEs compared to the HREEs. Samples HK 119, 233 and 248 (Tara Deep) and HK 219 (Lisheen) plot very close to the 'shale field' on a plot of chondrite-normalised La/Sm *vs* Gd/Lu ratios (Figure 4-7A). Negative Eu_{CN} anomalies of the 'reference shales' are between 0.6 and 0.7, while the REE+Y concentrations range between 168 and 231 µg/g (grey field in Figure 4-7B). On a Eu_{CN}/Eu^{*} *vs* REE+Y biplot, only sample HK 169 (Navan) plot within the 'shale field' defined by the reference shales (Figure 4-7B).

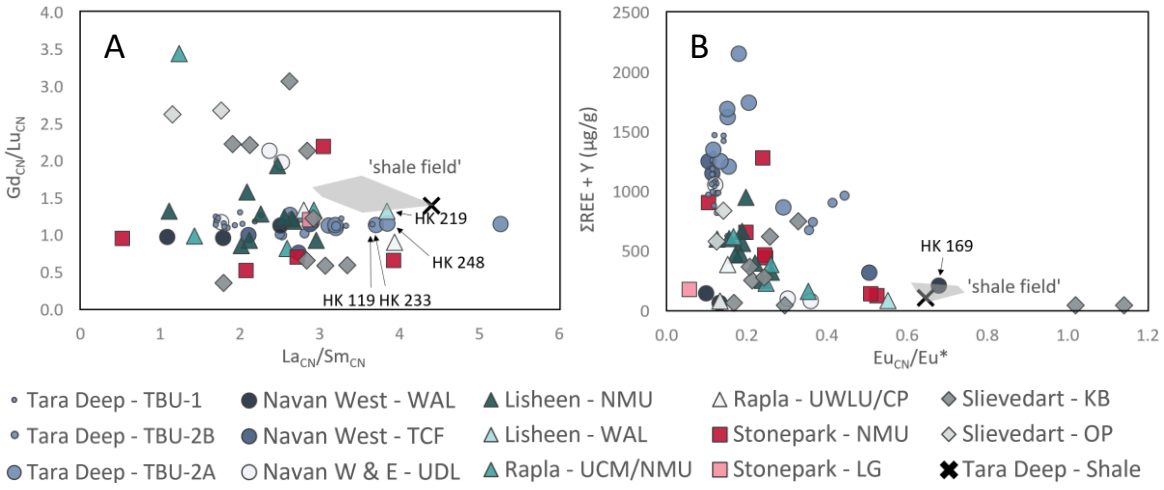

Figure 4-7: A) La_{CN}/Sm_{CN} vs Gd_{CN}/Yb_{CN} biplot and B) Eu anomaly (Eu_{CN}/Eu^{*}) vs the sum of REE+Y content of all analysed tuff samples of this study. Widely used shale samples as well as the analysed shale of this study (see Table 4-2) plot within the grey field, termed the 'shale field'. C1 chondrite values are taken from McDonough and Sun (1995). Analysed shale sample is shown for comparison. Full sample names are listed in Tables 2-2, 2-4, 2-6 and 2-8. CP = Crosspatrick Formation, KB = Kilbryan Limestone Formation, LG = Lough Gur Formation, NMU = Nodular Micrite Unit, OP = Oakport Limestone Formation, TBU = Thin Bedded Unit, TCF = Tober Colleen Formation, UCM = Upper Calcarenite Member, UDL = Upper Dark Limestone Formation, UWLU = Upper Wavy Laminated Unit, WAL = Waulsortian Limestone Formation.

Thirteen tuff samples show a sub-horizontal pattern (Navan: HK 125, 126, 128, 227; Rathdowney Trend: HK 219, 222; Stonepark: HK 207, 208, 211; Slievedart: HK 190, 194, 237, 238) on a PAAS-normalised REE+Y diagram (Figure 4-8A). When taking into account solely REE+Y concentrations, all of the aforementioned samples plus samples HK 169 (Navan), HK 184 and 223 (Rapla) have comparable REE+Y contents (< 250 µg/g) to the 'reference shale' samples (Figure 4-8B).

Although Ti and Al are relatively immobile during weathering, Pellenard et al. (2003) were able to distinguish shales and bentonites based on the TiO_2/Al_2O_3 ratio. The TiO_2/Al_2O_3 ratio of shales were lower than 0.06, whereas bentonites showed values higher than 0.06. However, while most of the reference shale data set has TiO_2/Al_2O_3 ratios between 0.04 and 0.06, most of the tuff samples from this data set reveal ratios lower than 0.04 (Figure 4-8C). TiO_2/Al_2O_3 ratios from only

six tuff samples are comparable to shales, namely HK 217 and 219 (Lisheen) as well as samples HK 207, 208, 209 and 212 from Stonepark (Figure 4-8C).

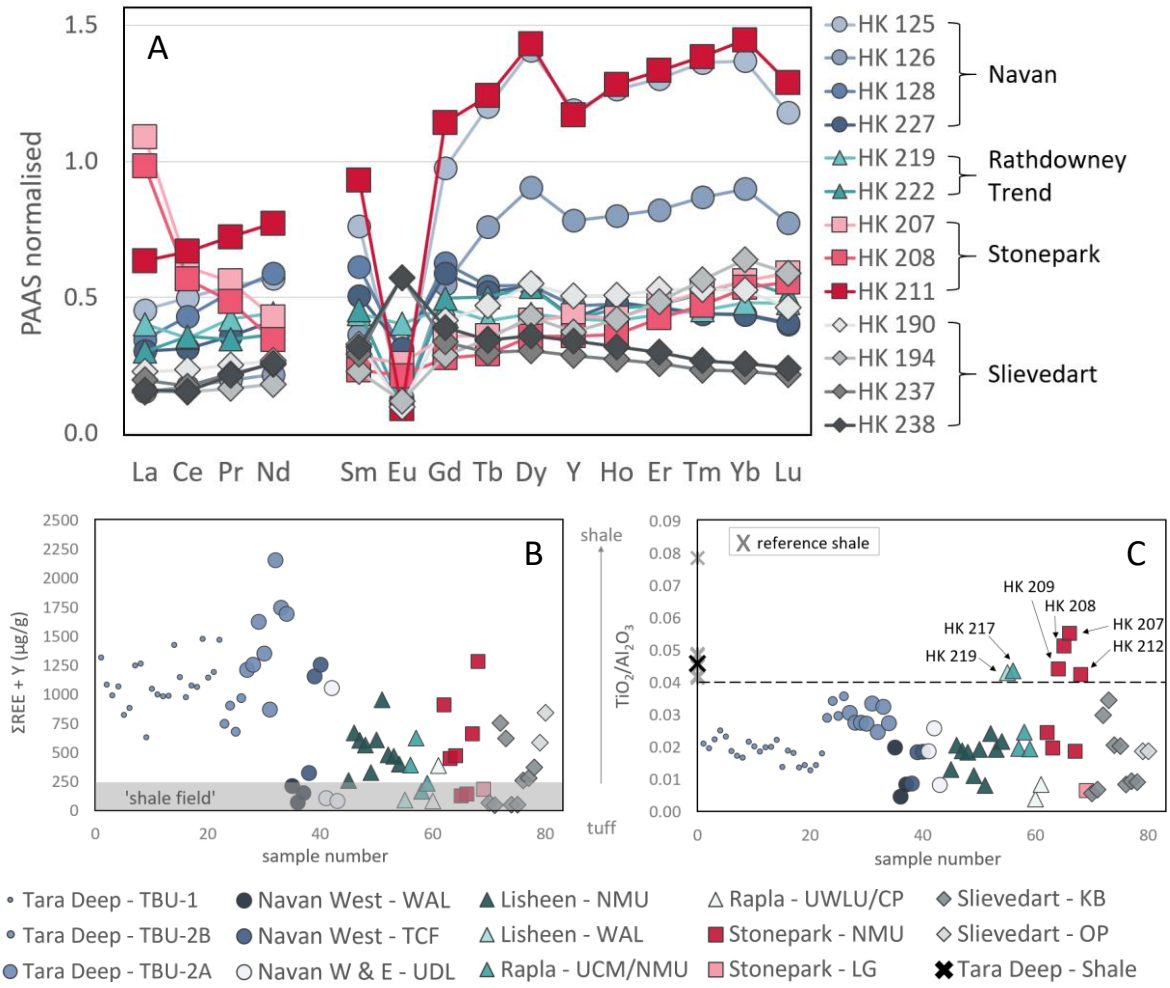

Figure 4-8: A) Post-Archaean Australian Shale (PAAS) normalised REE+Y biplot, showing the 13 Mississippian samples from this data set, which reveal a shale-like trend/signature. B) The sum of REE+Y concentrations and C) TiO_2/Al_2O_3 ratios of all analysed tuffs of this study. Shale samples, which are listed in Table 4-2 plot within the grey box in B) and above the dashed line in C). Sample numbers correspond with sample numbers listed in Tables 2-2, 2-4, 2-6 and 2-8. Full sample names are also shown in those tables. CP = Crosspatrick Formation, KB = Kilbryan Limestone Formation, LG = Lough Gur Formation, NMU = Nodular Micrite Unit, OP = Oakport Limestone Formation, TBU = Thin Bedded Unit, TCF = Tober Colleen Formation, UCM = Upper Calcarenite Member, UDL = Upper Dark Limestone Formation, UWLU = Upper Wavy Laminated Unit, WAL = Waulsortian Limestone Formation.

Thus, based on the classification systems and suite of elements employed, none of the tuff samples consistently group within the 'reference shale' fields, indicating that the samples are indeed tuffs (or in some cases tuffs with a minor detrital component) rather than sedimentary shales. It cannot be resolved if the detrital component originates from the adjacent shale from sampling or from mud which got incorporated during the deposition of the ash. Only sample Lisheen_LK-1432_HK 219 shows a thin shale band within the tuff layer, indicating the former. The other tuff samples with minor shale characteristics are also not especially thin layers (see Table 3-1), which potentially increases the risk of contaminating the tuff sample with surrounding shale. Thus, it may be most likely that these samples incorporated a higher mud content during their deposition.

4.4.2 Processes that might Change Tephra Composition

4.4.2.1 Transport Distance and Mineral Segregation

Prior to deposition of volcanic ash particles, they can experience physical sorting during transport, especially over large distances, as more dense minerals will be deposited closer to the volcanic centre (Pell et al., 1997) and the further-transported material becomes correspondingly depleted in these phases (Marx and Kamber, 2010). Besides aeolian fractionation, marine sorting can also remove lighter ash during aqueous deposition (Clayton et al., 1996; Pellenard et al., 2003). Both processes can thus cause fractionation of immobile elements, especially for those elements incorporated in dense ('heavy') accessory minerals like Zr, Hf and the HREE in zircon, Y in garnet and monazite and Sn in cassiterite (Summa and Verosub, 1992; Wray, 1995; Pellenard et al., 2003; López et al., 2005). Therefore, samples deposited at varying distances from the volcanic centre can exhibit differences in whole-rock trace element chemistry. Ideally, elements, which are significantly affected by mineral sorting should not be used for regional correlations.

Samples from this study mainly consist of clay minerals. The only 'heavy' minerals, which were observed in the samples under a binocular microscope are zircon and apatite. Zircon ($ZrSiO_4$) is a zirconium orthosilicate. Besides Zr and Hf, it is a host for significant fractions of the HREE (Hoskin and Schaltegger, 2003; Claiborne et al., 2006). As Zr and Hf behave nearly identically, zircons are essentially a zircon-hafnon solid solution (e.g. Heaman et al., 1990; Belousova et al., 2002b; Hoskin and Schaltegger, 2003; Bea et al., 2006). Thus, if the Zr, Hf and REE content of the tuff samples is strongly controlled by the abundance of zircon, there should be a strong positive correlation between these elements. The whole sample set reveals a linear positive trend between Zr and Hf (Figure 4-9A) and between Zr and HREE (not shown) (R^2 = 0.9045 and 0.8763, respectively). This trend can also be observed in the tuff samples occurring in the Thin Bedded units of Tara Deep (R^2 = 0.7083), in the Rathdowney Trend (R^2 = 0.527) and in Slievedart (R^2 = 0.7639), using Hf/Zr and HREE/Zr biplots, while the Stonepark samples reveal rather a cluster than a linear correlation (Figure 4-9B-E). Samples from Navan East & West show a large spread (Figure 4-9B; small diagram). Thus, tuff samples from Tara Deep, the Rathdowney Trend and Slievedart seem to be strongly affected by their zircon contents.

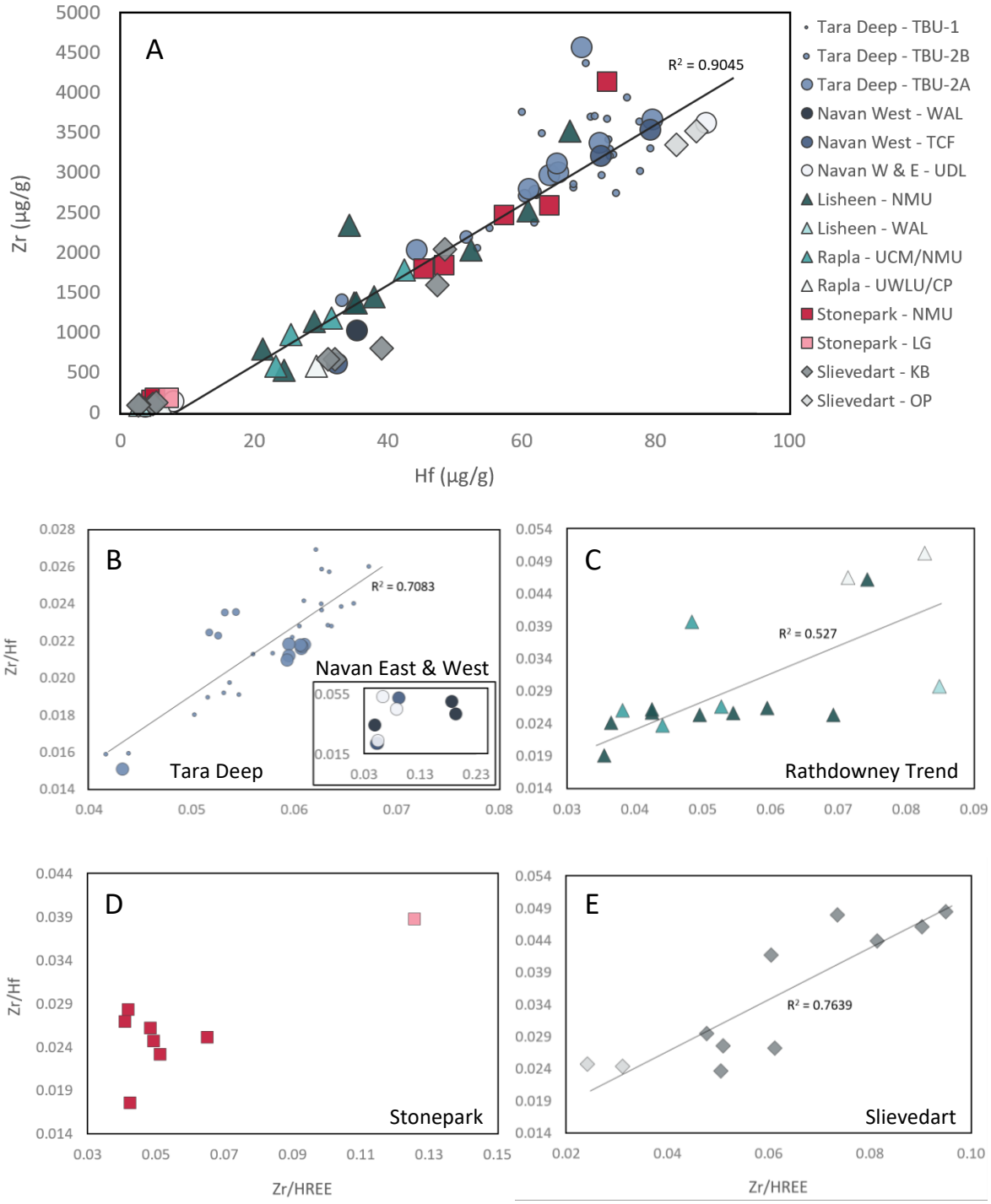

Figure 4-9: A) Zr (µg/g) vs Hf (µg/g) biplots as well as Zr/HREE vs Zr/Hf biplots of Mississippian tuff samples from B) Navan (split into Tara Deep and Navan East & West), C) Rathdowney Trend, D) Stonepark, and E) Slievedart along with the coefficient of determination (R^2). CP = Crosspatrick Formation, KB = Kilbryan Limestone Formation, LG = Lough Gur Formation, NMU = Nodular Micrite Unit, OP = Oakport Limestone Formation, TBU = Thin Bedded Unit, TCF = Tober Colleen Formation, UCM = Upper Calcarenite Member, UDL = Upper Dark Limestone Formation, UWLU = Upper Wavy Laminated Unit, WAL = Waulsortian Limestone Formation.

Furthermore, most of the samples from Tara Deep and two samples from the Slievedart area (Slievedart_3470/15_HK 187 and Slievedart_3471/4_HK 191; Oakport Limestone Formation) show the highest Zr, Hf and HREE concentrations (Figure 4-9A), potentially indicating the closest proximity to the volcanic centre among the four study sites. However, the tuff samples from this

study can neither be separated based on their sampling site, nor according to their stratigraphic occurrence using the applied Zr *vs* Hf or Zr/Hf *vs* Zr/HREE diagrams (Figure 4-9).
One potential reason could be the mixing of ash with marine sediments during transport. This process can also alter Zr, Ti, Nb and Y concentrations because of the admixture of inherited accessory minerals (Clayton et al., 1996; Straeten, 2004) from the surrounding shales (Pellenard et al., 2003). Zircons for example do not only occur as primary crystals from the magma in the deposited ash, but can also be present as a (reworked) detrital phase in siliciclastic sediments (see section 4.4.2.4.2). Alternatively, the relative depletions and enrichments could also stem from incomplete digestion of heavy minerals. As nearly no zircon grains could be found in tuff samples from Tara Deep (despite having the highest Zr and Hf concentrations), these samples could contain more metamict zircons, while samples from Stonepark and Slievedart are dominated by higher quality zircons that are less easily digested by the hotplate method (see section 4.4.2.6).

4.4.2.2 Alteration as a Key to Identifying the Depositional Environment

Alteration and devitrification of volcanic ashes takes place after their deposition. Thus, the conditions for the alteration/devitrification vary according to the facies-specific conditions under which the ash layers were deposited (Summa and Verosub, 1992; Clayton et al., 1996; Straeten, 2004; Hong et al., 2017). As the composition of the pore waters in which the tephra layer was altered can be facies-dependant (Summa and Verosub, 1992), the bulk-rock geochemistry of the sample may reveal a facies-dependant pattern and allow local correlations. During the devitrification of volcanic glass to authigenic clay minerals, leaching of alkalis and silica takes normally place concurrently with the uptake of Mg, Fe, and Ca (Caballero et al., 1992; Arslan et al., 2010). This may cause significant changes in the bulk geochemistry of the ash or tuff, especially with respect to mobile elements like K and Mg (Zielinski, 1985; Christidis, 1998; Huff, 2016). Some studies have discovered that the types of authigenic clay minerals vary among different facies and can generate spatial variations in the types of authigenic clay minerals and the bulk chemistry of ash beds (Kramer et al., 2001; Grevenitz et al., 2003; Hong et al., 2019). In contrast, other studies have only observed modifications on the crystal-chemical characteristics but not necessarily changes in the trace element composition due to the depositional environment (Ddani et al., 2005). However, since the tuff layers of this study were deposited during a marine transgression, it may be possible to see the influence of the changing depositional facies on the subsequent geochemical signature of the altered volcanic ash. Ashes which were deposited in deep water can experience more intensive chemical weathering compared to those laid down in shallow water environments (Hong et al., 2016).

Titanium oxide and Al_2O_3 are generally considered to be the most chemically immobile components of ash during weathering, transport, diagenesis and metamorphism, although small-

scale mobility has been observed (Slack and Stevens, 1994; Laviano and Mongelli, 1996; McHenry, 2009; Kiipli et al., 2017). However, their concentrations can be increased when fresh ashes are devitrified to authigenic clay minerals. Therefore, the TiO_2/Al_2O_3 ratios exhibit facies-dependence (Shen, 2014; Hong et al., 2017). Deep-marine and shallow marine ash beds cannot be distinguished from each other (0.006 to 0.089) but differ compared to lacustrine horizons (0.019-0.17) and paludal (marsh-like) ash beds (0.15-0.224) (Hong et al., 2019).

Furthermore, the Al_2O_3 and MgO concentration of volcanic ash layers can also be used to assign volcanic ashes to their depositional environment (Hong et al., 2019). Aluminium has low mobility under most environmental conditions, although the solubility of Al increases below pH 5.5 and above pH 8, (Shiller and Frilot, 1996). Thus, there can be small differences between different depositional environments. Velde and Brusewitz (1982) and Ddani et al. (2005) assign the alteration of felsic volcanic ashes (now preserved as authigenic silicates) to the depositional environment in which they were modified. The Al_2O_3 content of samples from deep- and shallow-marine, lacustrine, and mixed marine-terrestrial/paludal facies primarily fall between 15 and 30 wt% with no obvious difference between the four environments. However, in the marine environment, Mg incorporated into the clay minerals of felsic ash beds commonly comes from sediment porewaters (Arslan et al., 2010), which results in a 15-fold increase in the Mg content (Zielinski, 1985). Thus compared to mixed marine-terrestrial, paludal, and lacustrine facies, ash beds which were deposited in marine facies have notably higher Mg contents, although shallow marine (1.84-4.14 wt% MgO) and deep marine (1.32-4.9 wt% MgO) environment cannot be distinguished (Hong et al., 2019).

Consequently, Hong et al. (2019) devised a facies-dependant diagenetic alteration diagram based on MgO, Al_2O_3 and TiO_2 contents. Tuff samples with MgO/Al_2O_3 ratios higher than 0.056 plot in the shallow and deep marine field, whereas samples having a MgO/Al_2O_3 ratio of less than 0.056 are either in the mixed marine-terrestrial, paludal, and lacustrine field, depending on their TiO_2/Al_2O_3 ratios (Figure 4-10) (Hong et al., 2019). All samples from this study bar one (Stonepark_G11-2638-01_HK 197), have MgO/Al_2O_3 and TiO_2/Al_2O_3 ratios higher than 0.056 and lower than 0.089, respectively (Figure 4-10). Thus, most tuff samples can be allocated to either a shallow or deep marine depositional environment. While the Stonepark samples nearly span the full range of TiO_2/Al_2O_3 ratios within this data set, they show the lowest MgO/Al_2O_3 ratios (Figure 4-10). Tuff samples from Navan, the Rathdowney Trend and Slievedart cannot confidently be distinguished, although there is a tendency for tuff samples from Navan to have the next lowest MgO/Al_2O_3 ratios after the Stonepark tuffs, followed by samples from the Rathdowney Trend and Slievedart (Figure 4-10).

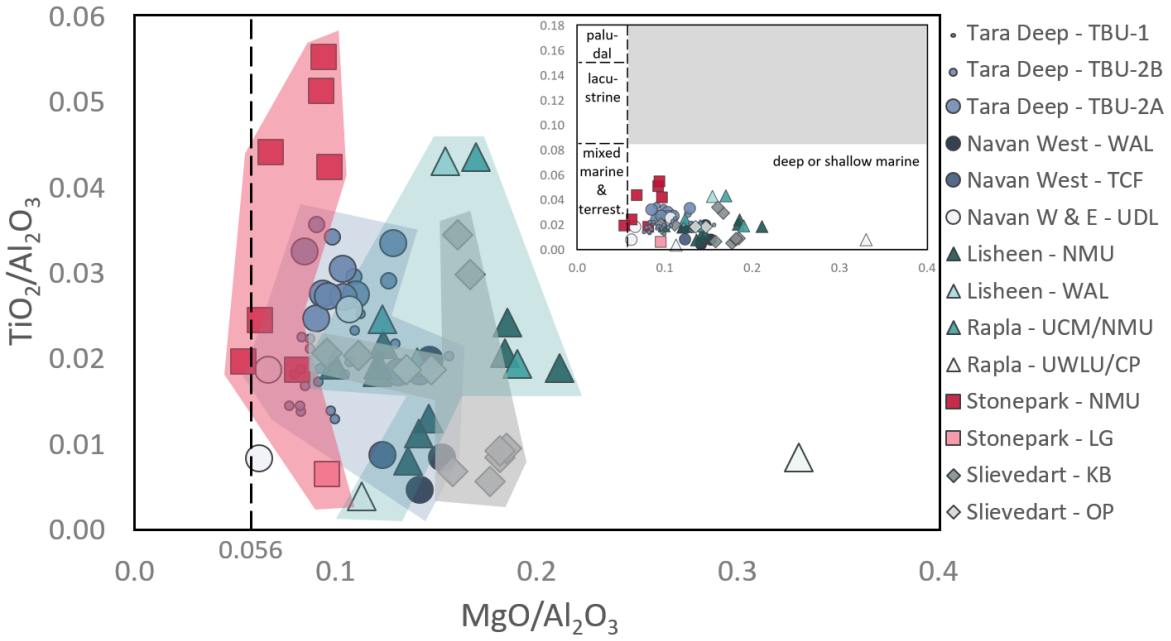

Figure 4-10: MgO/Al_2O_3 vs TiO_2/Al_2O_3 covariation plot of Irish Mississippian tuffs, which chemically distinguishes samples based on their different depositional environment into marine, terrestrial, lacustrine and paludal. All samples but one (Stonepark_G11-2638-01_HK 197) plot in the deep or shallow marine field. CP = Crosspatrick Formation, KB = Kilbryan Limestone Formation, LG = Lough Gur Formation, NMU = Nodular Micrite Unit, OP = Oakport Limestone Formation, TBU = Thin Bedded Unit, TCF = Tober Colleen Formation, UCM = Upper Calcarenite Member, UDL = Upper Dark Limestone Formation, UWLU = Upper Wavy Laminated Unit, WAL = Waulsortian Limestone Formation.

The development of Ce anomalies in tuff samples can potentially be used to differentiate between terrestrial and marine depositional environments. Cerium could be locally enriched or depleted in the sediment, as Ce^{4+} may be fractionated relative to the trivalent REEs under oxic conditions (German and Elderfield, 1990; Chen et al., 2015). A significant positive Ce anomaly can indicate alteration in a terrestrial (non-marine) depositional environment, whereas a negative Ce anomaly is frequently developed in marine ashes or tuffs (Kubanek and Zimmerle, 1986). The absence of significant Ce anomalies within most of the tuff samples (Figure 4-11A) could imply that the porefluids of the tuff samples did not achieve equilibrium with seawater. This could explain why there are also no characteristic Ce anomalies for each sampling site. However, two samples from Tara Deep (HK 234 & HK 236; both deposited in the Thin Bedded Unit 1) and one sample from the Lisheen area (HK 220; Nodular Micrite Unit) show positive Ce anomalies, suggesting a terrestrial depositional environment, while two samples from Stonepark show notable negative Ce anomalies (HK 207 & HK 208; both deposited in the Nodular Micrite Unit), implying deposition in a marine environment (Figure 4-11A). The positive Ce anomaly for samples HK 234, 236 and 220 is most likely the result of a different geochemical process as neither of the three samples reveal a terrestrial origin in Figure 4-10, nor is it expected based on their stratigraphic occurrence. The Thin Bedded Unit as well as the Nodular Micrite Unit were deposited during an ongoing marine transgression.

Finally, mobile elements are also environmentally sensitive elements, as they can vary as a function of depositional facies. It is generally accepted that Ba, Rb and Sr are highly mobile during alteration and weathering. On a Ba/Rb *vs* Sr/Rb biplot, it is possible to distinguish some tuff samples according to their stratigraphic position/region albeit with some outliers (Figure 4-11B).

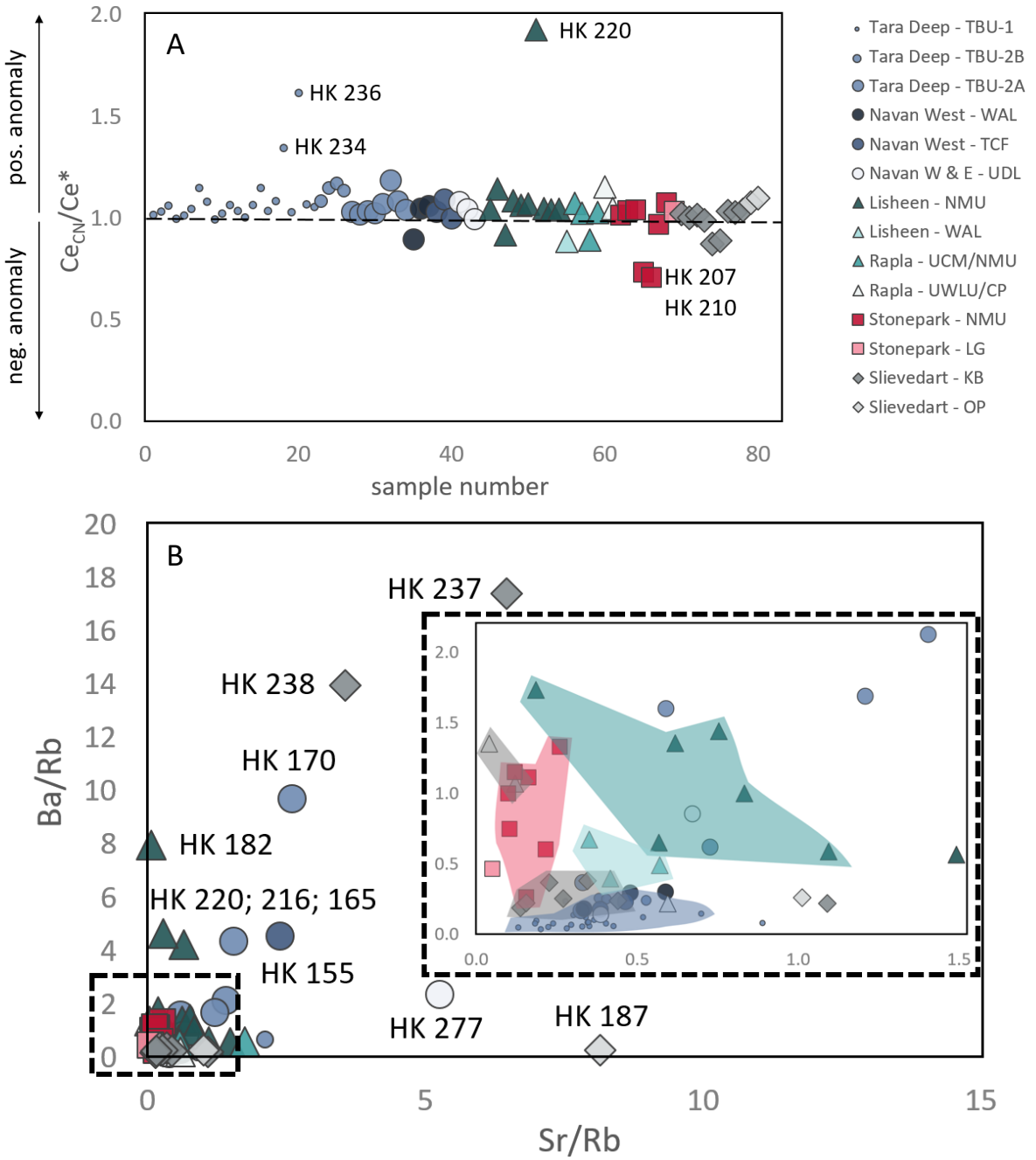

Figure 4-11: A) Ce anomaly of Irish Mississippian tuff samples. Ce anomalies are calculated by using C1 normalised concentrations of Ce and its neighbouring elements La and Pr: $Ce_{CN}/Ce^* = Ce_{CN}/(0.5La_{CN} + 0.5Pr_{CN})$. C1 chondrite values are taken from McDonough and Sun (1995). B) Ba/Rb vs Sr/Rb biplot, grouping tuff samples according to their stratigraphic level. Blue shaded area = samples within the Thin Bedded Unit 1 and 2 (Tara Deep), dark green shaded area = samples within the Nodular Micrite Unit (Rathdowney Trend), bright green shaded area = samples within the Waulsortian Limestone Formation (Rathdowney Trend), red shaded area = samples within the Nodular Micrite Unit (Stonepark area), dark grey = samples within the Kilbryan Limestone Formation (Slievedart area), bright grey area = samples within the Oakport Limestone Formation (Slievedart area). Sample numbers correspond with sample numbers listed in Tables 2-2, 2-4, 2-6 and 2-8. Full sample names are shown in these tables as well. CP = Crosspatrick Formation, KB = Kilbryan Limestone Formation, LG = Lough Gur Formation, NMU = Nodular Micrite Unit, OP = Oakport Limestone Formation, TBU = Thin Bedded Unit, TCF = Tober Colleen Formation, UCM = Upper Calcarenite Member, UDL = Upper Dark Limestone Formation, UWLU = Upper Wavy Laminated Unit, WAL = Waulsortian Limestone Formation.

However, independent of the geochemical proxy employed, the depositional environment backs up the unequivocal sedimentary evidence for a marine environment, with subtle differences in the proxy signature between the four sampling sites as well as their stratigraphic position (Figure 4-10, Figure 4-11A, B). While the lithostratigraphical units are quite laterally persistent in the carbonate-dominated Limerick Province (Philcox, 1984; Somerville et al., 1992; Sevastopulo and Wyse Jackson, 2009) in which tuff samples from the Rathdowney Trend and Stonepark area occur, the Midlands Province (Navan area) is characterised by more significant lateral facies variation (Philcox, 1984; Strogen and Somerville, 1984). The Dunmore province (Slievedart area) is controlled by the development of a broad shelf (Pracht and Somerville, 2015).

4.4.2.3 Alteration during Diagenesis

Alteration of volcanic ash may take place through chemical weathering, burial diagenesis, contact metamorphism, hydrothermal activity and, when deposited in surface environments, percolating groundwater (Hong et al., 2019). Mobile elements can provide information on alteration processes and the diagenetic conditions. It is generally accepted that Ba, Rb and Sr are highly mobile. Barium is usually hosted in feldspars and biotite, and Rb is mainly incorporated in micas and K-feldspar. During weathering, these silicates release Rb and Ba very quickly (Renock et al., 2016). Thus, the Rb and Ba concentration in ash beds is mainly dependant on adsorption by clay minerals (Nesbitt and Markovics, 1980; Hodson, 2002). Ddani et al. (2005) observed strong depletion of Rb, Ba and, to a lesser extent, Sr in all of their sample suite. To evaluate the mobility of Sr, Rb and Ba (and hence the extent of weathering), they are normalised to an immobile element in the data set (Ti and Al). Both of these particular elements were employed in this study for comparison.

Considering all six ratios (Rb/Al, Sr/Al, Ba/Al, Rb/Ti, Sr/Ti and Ba/Ti), most of the samples lie within the same range and thus appear to have experienced similar degrees of alteration, with no major distinctions between the four study sites or their stratigraphic position (Figure 4-12A is representative for all ratios). Samples Navan West_N-2441_HK 155, Slievedart_3470/15_HK 187, Slievedart_3470/15_HK 237 and Slievedart_3471/4_HK 238 exhibit the most consistent enrichment of Rb, Sr and Ba in Al and Ti normalised biplots. Thus, these four samples are most likely less weathered compared to the rest of the sample set (Figure 4-12A).

A negative Eu anomaly of 0.86 is typical of felsic igneous rocks (Kramer et al., 2001) (Figure 4-12B), whereas intensively chemically weathered sediments have lower values, ranging from 0.53 to 0.62 (Hong et al., 2013). Applying this observation to the Mississippian tuff samples of this study, all samples except two from the Slievedart area (Slievedart_3470/15_HK 237 and Slievedart_3471/4_HK 238), would have undergone intense chemical weathering, characterised by alteration of feldspar (Figure 4-12B). This result partly confirms the aforementioned trend on

Figure 4-12A. Samples Slievedart_3470/15_HK 237 and Slievedart_3471/4_HK 238 are the least weathered on both plots; while samples Navan West_N-2441_HK 155, Navan West_N-2441_HK 169, Lisheen_LK-1432_HK 219, Stonepark_G11-2638-02_HK 208 and Stonepark_G11-2638-02_HK 209 are less weathered compared to the other samples on Figure 4-12B. Sample Slievedart_3470/15_HK 187 shows the same degree of weathering as the majority of samples on Figure 4-12B, despite having a high Sr/Al ratio (Figure 4-12A).

Consequently, samples from different sample sites and stratigraphic levels show similar alteration behaviour on the diagrams employed and are therefore not useful for local correlations.

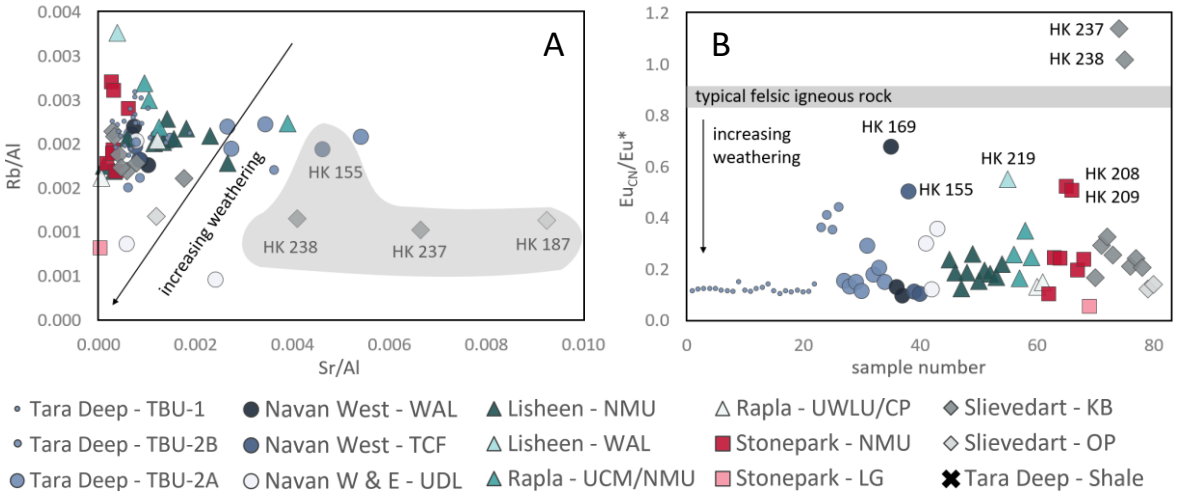

Figure 4-12A) Al-normalised biplot of the mobile elements Sr and Rb of the Irish Mississippian tuff samples. This diagram is representative for all Al and Ti normalised Rb, Sr and Ba biplots of the tuff samples. Samples within the grey shaded area are consistently the least weathered in these biplots. B) Degree of chemical weathering based on the Eu anomaly. Sample numbers correspond with sample numbers listed in Tables 2-2, 2-4, 2-6 and 2-8. Full sample names are shown in the same tables. CP = Crosspatrick Formation, KB = Kilbryan Limestone Formation, LG = Lough Gur Formation, NMU = Nodular Micrite Unit, OP = Oakport Limestone Formation, TBU = Thin Bedded Unit, TCF = Tober Colleen Formation, UCM = Upper Calcarenite Member, UDL = Upper Dark Limestone Formation, UWLU = Upper Wavy Laminated Unit, WAL = Waulsortian Limestone Formation.

4.4.2.4 Reworking and Redeposition

Reworking and redeposition can result in mixing of the original volcanic ash with variable amounts of the underlying carbonate sediments (including muds), which can lead to relative enrichments or dilutions by elements. Thus, reworking and redeposition of ash layers can significantly modify the immobile element concentrations. This effect can be especially pronounced for ash beds deposited in terrestrial and high-energy marine environments which suffer from subaerial erosion and riverine transport or are close to subaqueous currents (Naish et al., 1993; Straeten, 2004) or to *in situ* admixture through bioturbation. Based on sedimentary facies information supported by tuff chemistry (Figure 4-10), the Irish Mississippian tuffs from this study were deposited in a shallow or deep marine environment during an ongoing transgression. Thus, reworking, redeposition or dilution effects cannot be ruled out.

4.4.2.4.1 Degree of Reworking

The combination of TiO_2/Al_2O_3 with MgO/Al_2O_3 ratios can allow for the recognition of the facies-dependence of a sample (see section 4.4.2.2). Samples of this study cannot be distinguished according to their sample location based purely on the TiO_2/Al_2O_3 ratios (Figure 4-10). Thus, samples were either deposited in very similar environments, or their TiO_2 and Al_2O_3 contents were not influenced by the surrounding facies. Assuming the latter, these concentrations can also be used for detecting syn-depositional physical reworking processes, as reworking can enhance the TiO_2 content of samples and thus its TiO_2/Al_2O_3 ratios (Dai et al., 2017; Hong et al., 2019). TiO_2/Al_2O_3 values smaller than 0.055 probably still reflect unreworked ash, while values between 0.055 and 0.14 could indicate weakly reworked and redeposited samples with values higher than 0.14 show strong reworking and modification (Hong et al., 2019). Eu_{CN}/Eu^* values between 0.53 and 0.8 of already reworked samples shows further evidence of their reworked character (e.g. Hong et al., 2019). Based on that work, the samples from this data set were most likely not strongly influenced by reworking processes as they all displayTiO_2/Al_2O_3 ratios ≤ 0.055 (Figure 4-13). Furthermore, this diagram does not reveal any local correlations.

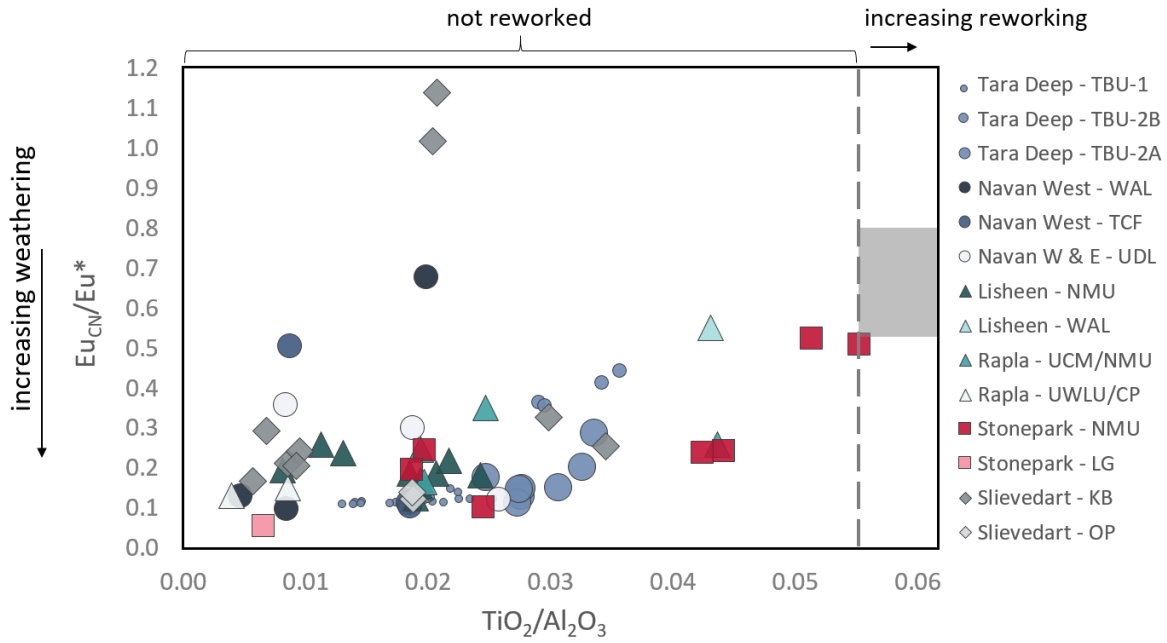

Figure 4-13: Degree of reworking using the TiO_2/Al_2O_3 ratio of Irish Mississippian tuff samples. Values < 0.005 indicate no reworking (left of dashed vertical line), while values between 0.005 and 1.4 refer to increasingly reworked samples (right of dashed line). Eu_{CN}/Eu^* values between 0.53 and 0.8 of already reworked ashes can confirm the reworked character of samples (grey field). CP = Crosspatrick Formation, KB = Kilbryan Limestone Formation, LG = Lough Gur Formation, NMU = Nodular Micrite Unit, OP = Oakport Limestone Formation, TBU = Thin Bedded Unit, TCF = Tober Colleen Formation, UCM = Upper Calcarenite Member, UDL = Upper Dark Limestone Formation, UWLU = Upper Wavy Laminated Unit, WAL = Waulsortian Limestone Formation.

4.4.2.4.2 Admixture of Sediments and Detrital Grains

The deposition of volcanic ash in a carbonate environment can lead to the reworking of the ash and consequently to carbonate contamination as seen by Batchelor and Jeppsson (1999). They justified the low REE concentrations of one ash sample with the large proportion of Ca, which diluted the absolute abundance of all other elements. In addition, carbonate phases and minerals formed in marine environments generally reflect the very low REE signatures of seawater (Desprairies and Bonnot-Courtois, 1980; Rollinson, 1993; Wray, 1995). This data set does not show an obvious correlation between high Ca concentrations and low REE concentrations (Figure 4-14). Thus, carbonate contamination does not seem to be significant. However, samples from the Rathdowney Trend show higher Ca concentrations than samples from Navan and Stonepark, while most of the samples from Slievedart show the lowest Ca contents (Figure 4-14).

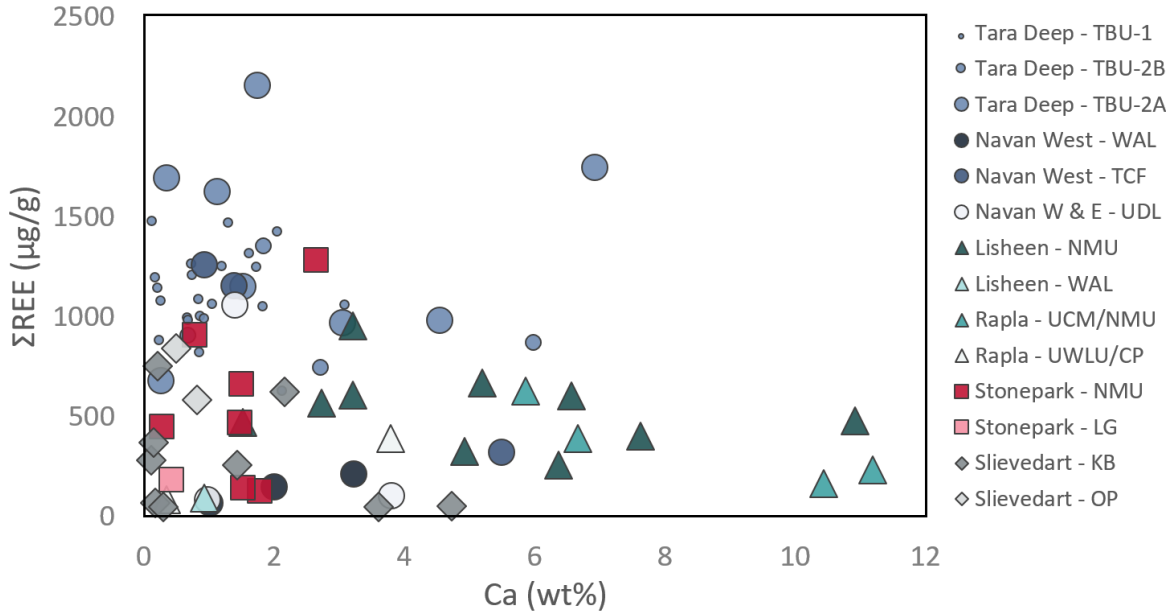

Figure 4-14: ΣREE (µg/g) vs Ca (wt%) biplot of Irish Mississippian tuff samples. These samples do not show carbonate contamination as there is no obvious negative correlation between Ca and REE concentrations. However, samples from the Rathdowney Trend have highest Ca contents, followed by samples from the Stonepark, Navan and Slievedart area. CP = Crosspatrick Formation, KB = Kilbryan Limestone Formation, LG = Lough Gur Formation, NMU = Nodular Micrite Unit, OP = Oakport Limestone Formation, TBU = Thin Bedded Unit, TCF = Tober Colleen Formation, UCM = Upper Calcarenite Member, UDL = Upper Dark Limestone Formation, UWLU = Upper Wavy Laminated Unit, WAL = Waulsortian Limestone Formation.

If the overall percentage of shale within the sampled material is high, the composition of the sample should be closer to that of the 'reference shale' than to the other tuffs. The REE+Y concentration of 16 samples are within the range of the REE+Y content of the 'reference shales' (Figure 4-8B). Thirteen out of the 16 samples also show a subhorizontal pattern when normalised to PAAS (Figure 4-8A) Thus, there is the possibility that these samples are shales or tuffs with a significant shale component, or were strongly contaminated/diluted by the surrounding shales during sampling while the remaining samples from this study are 'clean' tuff samples.

To circumvent the effects of the dilution of bulk-rock trace elements in volcanic ashes by enclosing sediments, the geochemistry of primary phenocrysts like apatite can be used for fingerprinting altered volcanic ash layers (e.g. Summa and Verosub, 1992; see Chapter 5). However, reworking and redeposition can also lead to the admixture of detrital grains into the original ash layers. For example, zircons can be transported, deposited and preserved as detrital zircon grains before finally becoming admixed into existing ash layers. As mentioned before, zircon is a significant host of Ce, Hf, Th, U and HREE (Bea, 1996; Belousova et al., 2002b; Hoskin and Schaltegger, 2003). The Irish Mississippian tuff samples analysed here display a strong correlation between HREE, Hf and Zr concentrations (Figure 4-9A-E). Thus, these elements seem to be controlled by zircon. However, these plots cannot differentiate between volcanic and detritally sourced zircons. Subsequently, it remains unclear the extent to which the whole-rock data is influenced by detrital grains, as this cannot be determined from elemental ratios. However, the morphology of phenocrysts or accessory minerals in ash beds can provide some information regarding the degree of abrasion and reworking (Hong et al., 2019), as it is more likely that rounded mineral grains have been concentrated by reworking, whereas euhedral minerals indicate derivation from a primary volcanic (magmatic) source, with relatively minimal levels of transport. Although this method provides only qualitative results, if a mineral separate is available it does give a first order indication of the presence of detrital zircon. Most zircons investigated in this study are euhedral to subhedral with sometimes one or two pyramidal terminations (see section 5.3.2). Based on TiO_2/Al_2O_3 ratios (Figure 4-13), Ca/ΣREE biplots (Figure 4-14) and the morphology of the zircon grains, it is likely that the sampled tuff layers were thus not significantly affected by reworking processes.

4.4.2.5 Mineralisation

Mineralisation in the Irish orefield occurs mainly at two different stratigraphic levels, the shallow marine Navan Group of north-central Ireland (Navan area) and in the deeper marine Waulsortian Limestone Formation in southern and central Ireland (e.g. in the Lisheen, Rapla, Stonepark and Slievedart area). While the Navan and Lisheen deposits are both highly mineralised areas, the Stonepark and Slievedart locations recently became exploration targets and are treated as highly prospective (see sections 2.6 to 2.9). The most abundant minerals in the Irish orefield are galena (PbS) and sphalerite ((Zn,Fe)S). Common trace elements in sphalerite are Cd, Mn, Ga, Ge and In (100s to 1000s of µg/g), while galena can incorporate Ag, Bi and Sb, Sn and TI at high concentrations. The tuff samples examined in this study occur either above or below these mineralised areas, and are thus plotted on Al-normalised Pb *vs* TI, Zn *vs* Cd and Pb *vs* Zn biplots (Figure 4-15A-C) to evaluate possible sample contaminations by Zn and/or Pb-bearing minerals or circulating hydrothermal fluids, which are associated with the mineralisation. Positive linear

correlations between these ratios as well as positive anomalies in Zn and Pb in tuff samples of this study are indicators if samples are influenced by mineralisation.

Sample Lisheen_LK-1915_HK 220 has an exceptionally high Pb/Al as well as an elevated TI/Al ratio (Figure 4-15A), indicating that this sample may contain galena. Another eight samples from Navan and Lisheen (Tara Deep, Thin Bedded Unit 2: HK 158, 229, 230, 252; Lisheen, Nodular Micrite Unit: HK 182, 203, 216, 221; Lisheen, Waulsortian Limestone Formation: HHK 219) have elevated TI/Al values with sample Tara Deep_N-2461_HK 230 having an extremely high TI/Al ratio (Figure 4-15A). As the high TI/Al values do not coincide with high Pb/Al ratios, they are likely not caused by galena mineralisation. The remaining samples cluster together, while some samples from Slievedart show a positive correlation between Pb/Al and TI/Al (HK 192, 193, 194, 237, 188, 189; Kilbryan Limestone Formation; highlighted in grey in Figure 4-15A), pointing towards a weak influence on these samples by galena.

While samples Lisheen_LK-1040_HK 182, Lisheen_LK-1773_HK 221, Rapla_3312-78_HK 184, Stonepark_G11-2638-02_HK 207, Stonepark_G11-2638-02_HK 208, Stonepark_G11-2638-02_HK 209 and Slievedart_3471/4_HK 193 show only elevated Zn/Al values, samples Lisheen_LK-1915_HK 220, Rapla_3312-62_HK 183 and Slievedart_3470/15_HK 189 show enhanced Zn/Al as well as Cd/Al ratios (Figure 4-15B). Only some Slievedart samples from the remaining sample set show a positive correlation in these ratios (HK 194, 190, 237, 238, 192, 188; Kilbryan Limestone Formation; highlighted in grey in Figure 4-15B). Thus, samples Lisheen_LK-1915_HK 220, Rapla_3312-62_HK 183 and Slievedart_3470/15_HK 189 and the aforementioned Slievedart samples are most likely more influenced by sphalerite mineralisation compared to the remaining samples of the data set.

Overall, sample Lisheen_LK-1915_HK 220 seems to be most affected by mineralisation as it has very high Pb/Al as well as Zn/Al values. Samples HK 182, 183, 184, 221 (Rathdowney Trend), HK 207, 208, 209 (Stonepark) and HK 184 and 193 (Slievedart) have only elevated Zn/Al values while sample HK 203 (Lisheen) has an enriched Pb/Al ratio (Figure 4-15C).

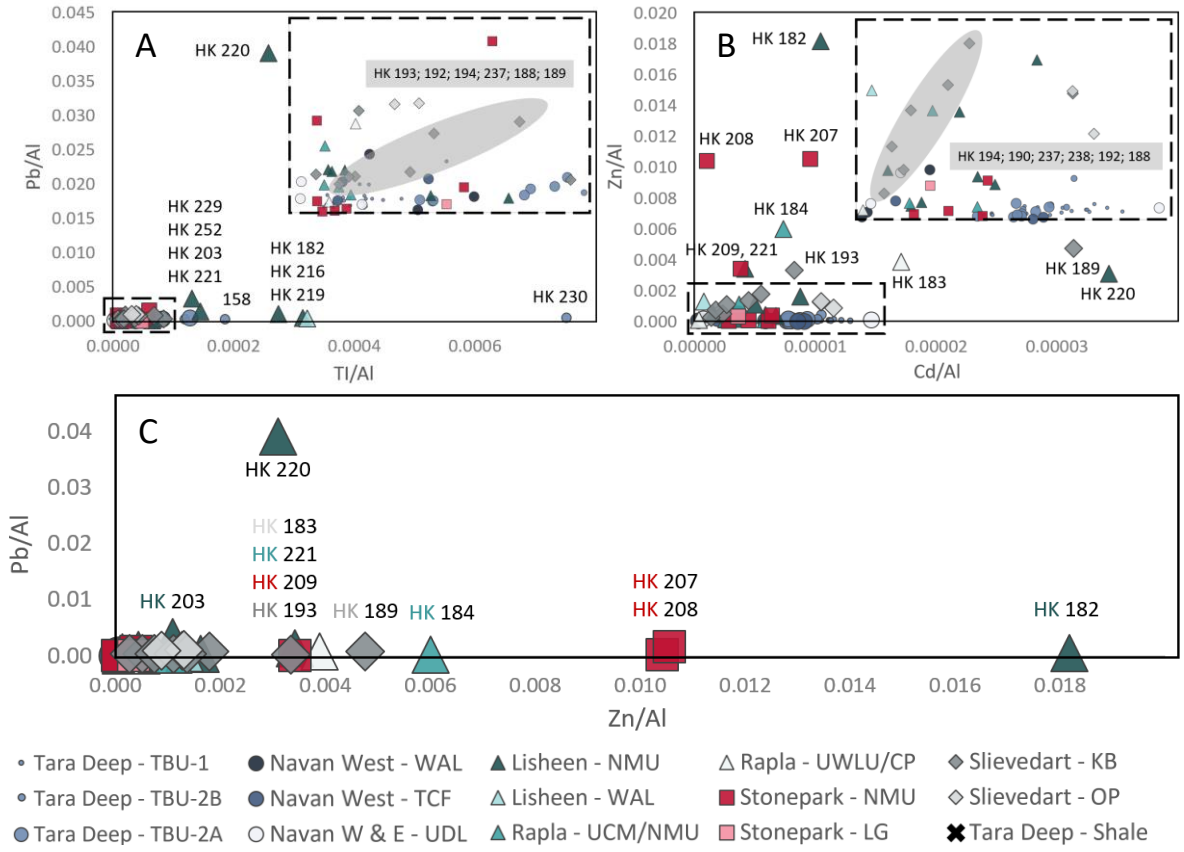

Figure 4-15: Influence of mineralisation on Mississippian tuff samples from Navan, Lisheen, Stonepark and Slievedart in Ireland. A) Pb/Al vs Tl/Al, B) Zn/Al vs Cd/Al and C) Pb/Al vs Zn/Al biplots. Labelled samples either show an enrichment in Pb, Zn, Tl or Cd. Grey shaded areas in A) and B) highlight samples from the Slievedart area, which show a strong positive correlation in Pb/Al vs Tl/Al and Zn/Al vs Cd/Al space. C) While sample HK 203 and 220 show an enrichment in Pb, samples HK 182, 207, 208, 184, 189, 183, 221, 209 and 193 reveal elevated values in Zn. Full sample names are shown in Tables 2-2, 2-4, 2-6 and 2-8. CP = Crosspatrick Formation, KB = Kilbryan Limestone Formation, LG = Lough Gur Formation, NMU = Nodular Micrite Unit, OP = Oakport Limestone Formation, TBU = Thin Bedded Unit, TCF = Tober Colleen Formation, UCM = Upper Calcarenite Member, UDL = Upper Dark Limestone Formation, UWLU = Upper Wavy Laminated Unit, WAL = Waulsortian Limestone Formation.

Thus, it appears the samples from the Navan area are influenced least by mineralisation, followed by tuffs from the Stonepark area. Although significant mineralisation is not known in the Slievedart area, in total eight (HK 188, 189, 190, 192, 193, 194, 237, 238) out of eleven samples show a linear correlation on Pb/Al *vs* Tl/Al or Zn/Al *vs* Cd/Al biplots (Figure 4-15A, B), suggesting that samples contain either minor Zn- or Pb-bearing phases. Mineralisation had likely had the biggest impact on tuffs from the Rathdowney Trend as six out of fifteen samples exhibit evidence for either Zn or Pb mineralisation (Figure 4-15C; HK 220 >> HK 182 >> HK 184 > HK 183 > HK 221 > HK 203).

In general, samples cannot be separated according to their sampling location or depositional environment based on the ratios employed. However, the Tara Deep samples taken from the Thin Bedded Unit 1 show consistently lower Tl/Al and higher Cd/Al ratios compared to samples deposited in Thin Bedded Unit 2 (Figure 4-15A, B).

4.4.2.6 Digestion Set-Up

Elements which are not fully recovered during digestion should not be used for fingerprinting. Therefore, it is important that samples are completely digested prior to analysis. The most difficult phase to digest in the Irish Mississippian tuff samples in this study is zircon. Zircon requires high-pressure attack with HF-HNO_3 for complete elemental recovery (Marx and Kamber, 2010). If it cannot be assured that zircon is completely digested, Zr, Hf and HREE concentrations, which occur in high abundance in zircon, should not be used. However Marx and Kamber (2010) managed to produce coherent Zr/Hf data, using hotplate digestions. Furthermore, hotplate digestions are quicker, less dangerous and more cost-effective to run. Thus, all samples from this study were digested using the hotplate method as opposed to high-pressure bomb digestions. Two samples, which were digested and analysed twice using the hotplate method, produced consistent Zr, Hf and HREE data (see section 4.2.1.5.3). Therefore, it can be assumed that the degree of digestion of zircon in these two aliquots of the samples was similar. However, zircons from different samples could still undergo different digestion rates, dependant on the state of the zircons. Metamict (radiation-damaged) zircons contain more porosity and micro-fractures (Marx and Kamber, 2010). Thus, they are more easily attacked by acid and therefore release more Zr, Hf and REEs compared to more pristine zircons that have a higher chance of surviving transport but are less easily digested by the hotplate method. The relatively high Zr, Hf and HREE concentrations in samples from Navan, which is accompanied by a lack of zircons in mineral separates (see Table 5-2) could be explained by the higher amount of metamict zircons in comparison to samples from the other sampling areas. These zircons could represent small, broken up metamict fragments that went undetected during mineral picking. The small fragments would have a larger surface to volume ratio and are thus dissolved easier. Overall, the variations in REE contents is then caused by differing digestion rates as opposed to the primary magma composition.

However, the influence of the digestion set-up can only be established with confidence by direct comparison between high-pressure bomb *vs* hotplate beaker digestions of the tuff samples.

4.4.3 Tuff Composition

The most common method of chemically classifying volcanic rocks is the total alkali (Na_2O + K_2O)-silica (SiO_2) (TAS) diagram introduced by Le Bas et al. (1986). But it has long been recognised that theTAS diagram is not robust for altered volcanic rocks due to the mobility of alkali elements during weathering and alteration (e.g. Winchester & Floyd, 1977; Pearce, 1996). However, the original tuff composition can be estimated using other approaches.

Igneous zircon for example is most common in intermediate to Si-saturated compositions and least common in less Si-saturated rocks (Hoskin and Schaltegger, 2003). The presence of

magmatic zircon (as opposed to inherited) in the mineral separates thus implies an intermediate to Si-saturated source magma.

The Al_2O_3 contents of intermediate to felsic source magmas are generally between 15 to 25 wt% (Wedepohl, 1978), while the MgO content of evolved magmas is typically between 0.4 and 1.8 wt% (Le Maitre, 1976). This suggests an evolved magma composition for most samples of this study as they exhibit Al_2O_3 and MgO concentrations between 15 - 30 and 1 – 4 wt%, respectively. However, it should be noted that the devitrification of rhyolitic ash to montmorillonite results in a 15-fold increase in the Mg content (Zielinski, 1985), as discussed in section 4.4.2.2.

Although the TiO_2/Al_2O_3 ratios can be used for the recognition of the facies-dependence of a sample (see section 4.4.2.2*)* and as an indicator for the degree of reworking (see section 4.4.2.4.1), it is most commonly used to determine the parent magma chemistry of volcanic ash layers (Le Maitre, 1976). The TiO_2/Al_2O_3 ratios of samples from this data set seem neither be influenced by their depositional environment, nor by reworking, which is in agreement with the general view that these two elements are the most chemically immobile components of volcanic ash. Thus, the TiO_2/Al_2O_3 ratios of ash beds from this study should also be inherited from their source magma. Low ratios of TiO_2/Al_2O_3 (in between 0.004 and 0.022) can suggest a silicic magma composition, while relatively high ratios indicate intermediate (0.022 to 0.055) to mafic (0.055 to 0.14) source magmas (Le Maitre, 1976; Spears and Kanaris-Sotiriou, 1976). The TiO_2/Al_2O_3 ratios of all tuff samples from this study indicate a felsic to intermediate composition (TiO_2/Al_2O_3 = 0.004 – 0.055) of these samples (Figure 4-16).

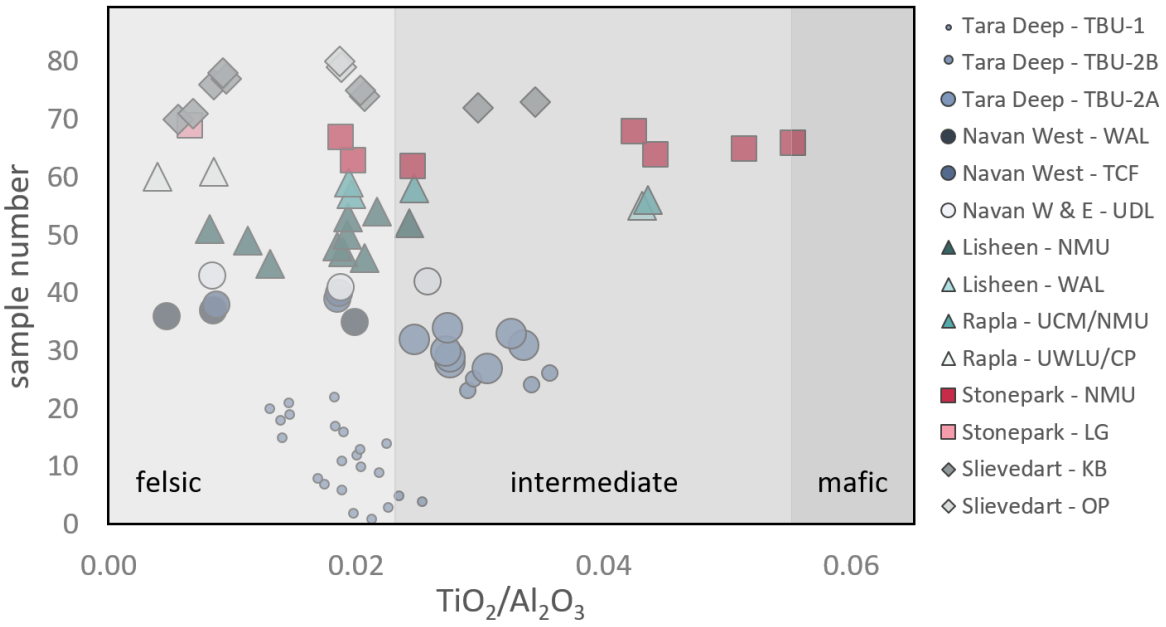

Figure 4-16: TiO_2/Al_2O_3 ratios of Irish Mississippian tuff samples. TiO_2 and Al_2O_3 are commonly considered as highly immobile elements. Thus, their ratios reflect the mafic, intermediate and felsic source magmas with TiO_2/Al_2O_3 values of 0.14, 0.055 and 0.022, respectively (Le Maitre, 1976). Tuff samples, which plot in the bright grey field, show a felsic character, in the medium grey field an intermediate character and in the dark grey field a mafic character. Fields are based on Le Maitre (1976). Sample numbers correspond with sample numbers listed in Tables 2-2, 2-4, 2-6 and 2-8. CP = Crosspatrick Formation, KB = Kilbryan Limestone Formation, LG = Lough Gur Formation, NMU = Nodular Micrite Unit, OP = Oakport Limestone Formation, TBU = Thin Bedded Unit, TCF = Tober Colleen Formation, UCM = Upper Calcarenite Member, UDL = Upper Dark Limestone Formation, UWLU = Upper Wavy Laminated Unit, WAL = Waulsortian Limestone Formation.

The use of REE diagrams, Zr/Hf, Nb/Ta and Y/Ho ratios (geochemical 'twins') as well as source discrimination diagrams is discussed below.

4.4.3.1 REE Diagrams

Normalised REE diagrams are widely used for geochemical characterisation as they are conservative tracers of petrogenetic processes (e.g. Rollinson, 1993). In general, terrestrial weathering mobilises only small amounts of REEs as supergene chemical processes, as well as transport and deposition, which operate under oxic conditions, do not change REE distributions and therefore neither the Eu relative to other REEs (Zielinski, 1982; Sverjensky, 1984; McLennan, 1989; Püspöki et al., 2008).

Chondrite-normalised LREE enrichments and relatively flat HREEs are frequently observed in evolved magmas as well as in felsic volcanic rocks (e.g. Moghazi, 2003; Calarge et al., 2006; Ersoy et al., 2008; Kacmaz, 2016). Furthermore, Eu anomalies are generally inherited from the parent magma and therefore can serve as important markers for the volcanic source (MacRae et al., 1992; Wray, 1995; He et al., 2014). Negative Eu anomalies ($Eu_{CN}/Eu^* < 1$) are characteristic of silicic igneous rocks (Bohor and Triplehorn, 1993), while also indicating highly evolved, sub-alkaline magma sources. Early fractional crystallisation of plagioclase in the source magma results

in the removal of Eu from the residual liquid. Europium can be incorporated into feldspars during crystallisation owing to its presence as Eu^{2+} in reducing magmas (Zielinski, 1982). Dependant on the degree of plagioclase crystallisation, the negative Eu anomaly in chondrite-normalised REE patterns of igneous rocks is variable. The larger the Eu anomaly, the more evolved was the parent magma. Typical felsic igneous rocks have Eu anomalies around 0.86 (Kramer et al., 2001).
The REE distributions from 73 out of 79 Mississippian tuff samples of this study are all characterised by enrichments in LREE compared to HREE ($La_{CN}/Lu_{CN} > 1$), relatively flat HREE profiles (Gd_N/Lu_{CN} around 1) and negative Eu anomalies (0.06 - 0.67) (Figure 4-17A-J) and thus support a felsic character for these samples. Only samples HK 169 (Navan, Waulsortian Limestone Formation), HK 197, 210 (Stonepark, Nodular Micrite Unit), and HK 193 (Slievedart, Kilbryan Limestone Formation) are slightly enriched in HREE (Figure 4-17A, K), while samples HK 237 and 238 (Slievedart, Kilbryan Limestone Formation) show positive Eu anomalies (1.02 and 1.14, Figure 4-17A, J).

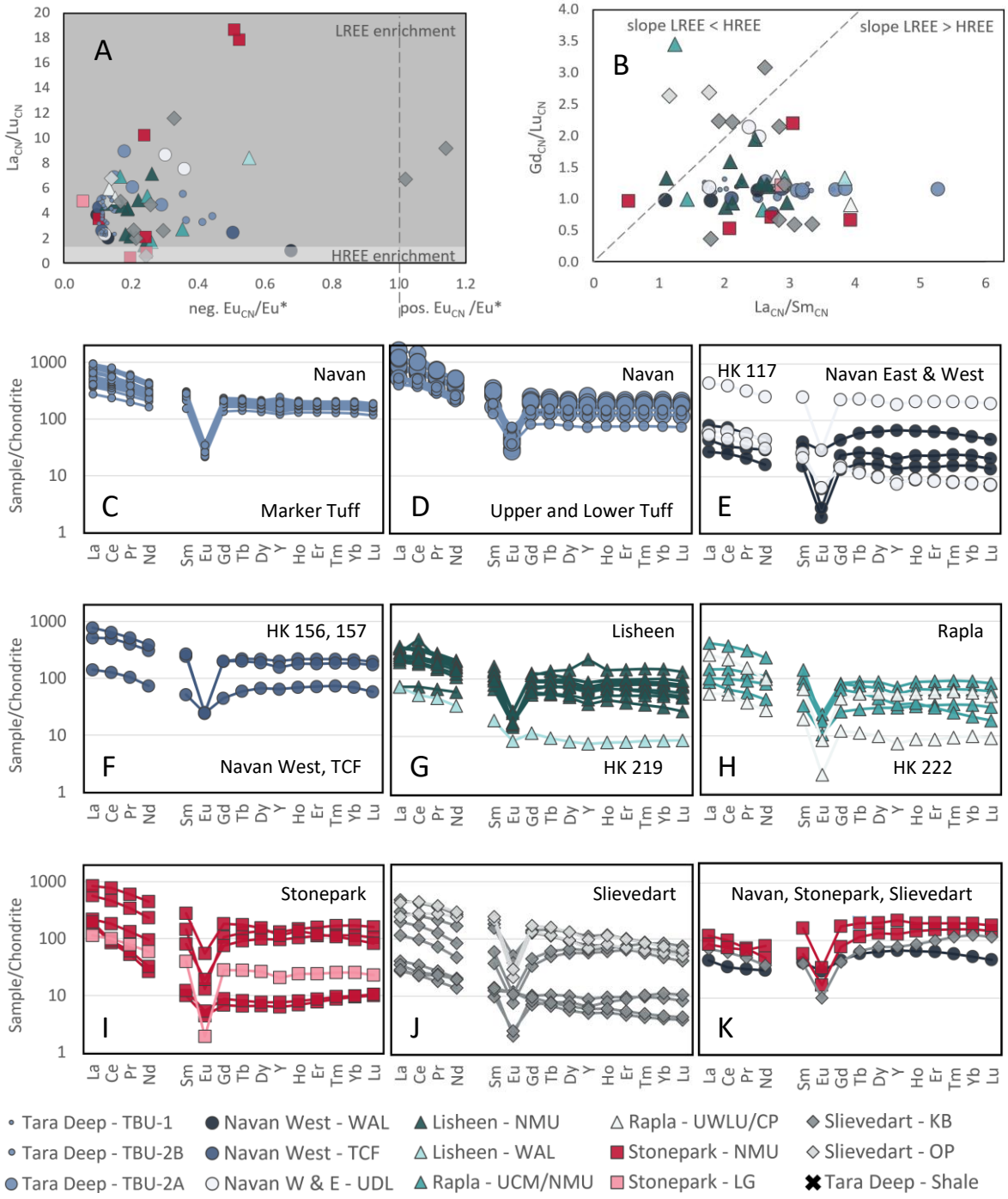

Figure 4-17: Rare earth element plots of Irish Mississippian tuffs. A) La_{CN}/Lu_{CN} vs Eu anomaly biplot. Tuff samples, which plot within the dark grey and bright grey areas are enriched in LREEs ($La_{CN}/Lu_{CN} > 1$) or HREEs ($La_{CN}/Lu_{CN} < 1$), respectively. Left of the dashed line are samples with negative Eu anomalies, while samples right of the dashed line have positive Eu anomalies. B) Tuff samples with similar REE patterns plot close together on a La_{CN}/Sm_{CN} vs Gd_{CN}/Lu_{CN} diagram. C-J) C1-chondrite normalised REE diagrams with an enrichment in LREE relative to HREE and K) an enrichment in HREE relative to LREE from Navan, Slievedart and Stonepark. Normalised abundances are plotted on a logarithmic scale in order of atomic number (Z) with the exception of Y (inserted between Dy and Ho). As Pm does not form stable or long-lived isotopes and only occurs in traces in natural materials, there is a gap in the REE spectrum. The REE data are normalised to the C1 chondrite values taken from McDonough and Sun (1995). Full sample names are shown in Tables 2-2, 2-4, 2-6 and 2-8. CP = Crosspatrick Formation, KB = Kilbryan Limestone Formation, LG = Lough Gur Formation, NMU = Nodular Micrite Unit, OP = Oakport Limestone Formation, TBU = Thin Bedded Unit, TCF = Tober Colleen Formation, UCM = Upper Calcarenite Member, UDL = Upper Dark Limestone Formation, UWLU = Upper Wavy Laminated Unit, WAL = Waulsortian Limestone Formation.

Thus, most samples have a significantly lower Eu anomaly than expected from typical felsic igneous rocks, with a median of 0.16 (Figure 4-17A). This could indicate that samples were either crystallised from a very highly evolved magmatic source or that the Eu anomaly of these samples was enhanced by intense weathering, which can also lower Eu anomalies (see section 4.4.2.3).

The positive Eu anomalies and the chondrite-normalised LREE enrichment patterns from samples Slievedart_3470/15_HK 237 and Slievedart_3471/4_HK 238 are contradictory as they point towards both an evolved and basic magma chemistry. However, the relative enrichment of LREE to HREE can be influenced by mineral segregation during transport as minerals such as zircon, which host the HREE, are denser than those that host the LREE such as apatite (Marx and Kamber, 2010). At the same time, apatite gets fully dissolved during hotplate digestions, releasing LREE, while HREE can be retained in partly dissolved zircons (see section 4.4.2.6). Thus, samples HK 237 and 238 could have been crystallised from a mafic source and were deposited at a reasonable distance from the volcanic centre. This is a plausible scenario, as no zircons but numerous apatites were found in mineral separates from both samples (see sections 5.3.1.5 and 5.3.3.4).

4.4.3.2 Geochemical Twins

Geochemical 'twins' like Zr/Hf, Nb/Ta and Y/Ho have identical charge and similar ionic radius. Thus, if a geochemical system is characterised by CHArge-and-RAdius-Controlled (CHARAC) trace element behaviour, twin pairs should retain their respective chondritic ratio (Bau, 1996). Basic to intermediate igneous rocks show Y/Ho, Zr/Hf and Nb/Ta ratios close to the chondritic ratios (28, 34 and 18 respectively) and plot within the CHARAC fields as defined by Bau (1996) and discussed by Atanasova et al. (2020). Y/Ho and Zr/Hf fields are based on 48 international igneous geostandards and range from $24 < Y/Ho < 34$ and $26 < Zr/Hf < 46$, respectively. The Nb/Ta field ranges between 14 and 20 (Atanasova et al., 2020). Highly evolved magmas, aqueous solutions like seawater and their precipitates often show non-chondritic twin ratios and plot well outside the CHARAC field, showing a significant decrease in Y/Ho and Zr/Hf ratios (Bau, 1996). This implies that no large fractionation is expected during mantle melting and fractional crystallisation in most magmatic systems among geochemical twins. Thus, these twin elements can be used to verify whether igneous rocks have a basic to intermediate or felsic origin or if they have been modified by silicate melts or aqueous fluids (Jochum et al., 1989; Bau and Dulski, 1995; Bau, 1996). Furthermore, Bau (1996) observed that shale samples plot around chondritic Y/Ho and Zr/Hf ratios, including the 'reference shales' (not shown in this study) and the shale sample (Tara Deep_N-2406_HK 164; Figure 4-18A-D), analysed within this study.

As incorporation of detrital zircon can have a strong influence on Zr and Hf abundances in tuff samples (see sections 4.4.2 and 4.4.2.4.2), focus is placed on Y/Ho and Nb/Ta ratios. Twenty tuff

samples from Navan, two from Lisheen, seven from Stonepark, and one from Slievedart plot within the CHARAC field, indicating a basic composition of the source magma, while samples HK 119, 231 and 236 from Tara Deep as well as sample HK 220 from Lisheen plot outside the CHARAC ranges for both ratios (Figure 4-18A-D). The remaining samples (49 in total) plot within the CHARAC range for Y/Ho, but outside the CHARAC Nb/Ta range or vice versa, indicating both a mafic to intermediate and felsic source magma composition (Figure 4-18A, B, C, D). Thus, only samples from Stonepark from the Nodular Micrite Unit plot consistently within the CHARAC field, which is indicative of a basic to intermediate magma composition (Figure 4-18C), although the REE+Y patterns for five out of seven samples support an evolved character of the source magma (Figure 4-17A, I). This contradictory result for the majority of the sample set is probably caused by the non-CHARAC behaviour of Y, Ho, Nb and Ta in the source magma and hence alternative approaches to characterising the source chemistry are explored. These diagrams do not allow for distinguish samples according to their sample location or stratigraphic occurrence and thus prevent local correlations.

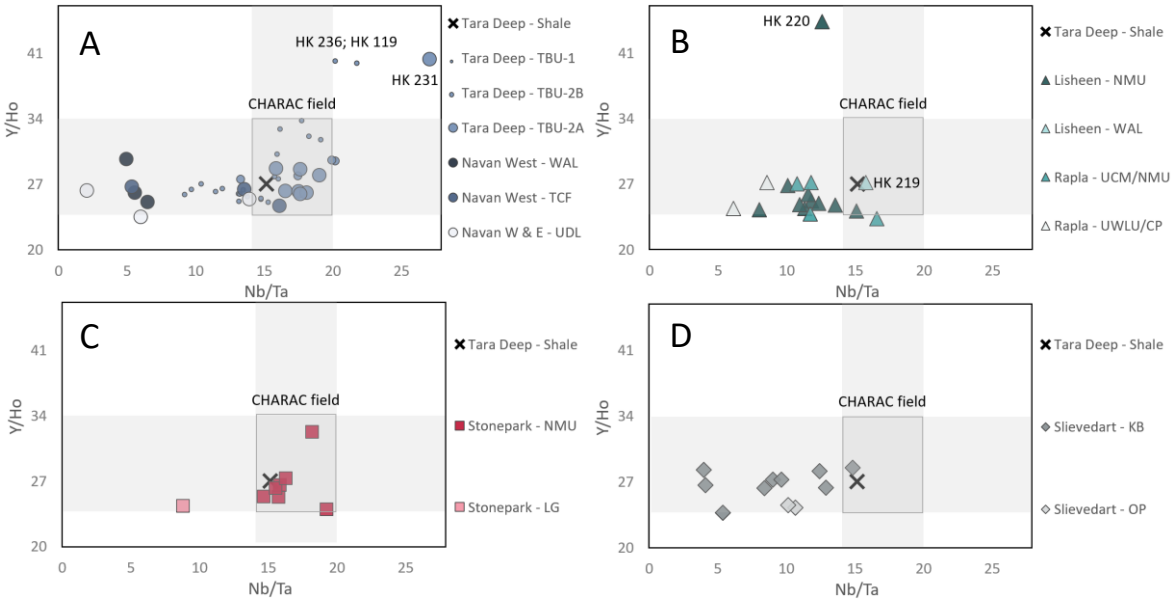

Figure 4-18: Y/Ho vs Nb/Ta biplots of Irish Mississippian tuffs, separated into the different study areas. A) Navan area; B) Rathdowney Trend; C) Stonepark area; D) Slievedart area. Grey shaded areas indicate the CHARAC range for Y/Ho and Nb/Ta values, while the framed field is called the CHARAC (CHArge-and-RAdius-Controlled) field, defined from Bau (1996). Basic to intermediate volcanic rocks normally retain their chondritic values and are expected to plot within the CHARAC field. Full sample names are shown in Tables 2-2, 2-4, 2-6 and 2-8. CP = Crosspatrick Formation, KB = Kilbryan Limestone Formation, LG = Lough Gur Formation, NMU = Nodular Micrite Unit, OP = Oakport Limestone Formation, TBU = Thin Bedded Unit, TCF = Tober Colleen Formation, UCM = Upper Calcarenite Member, UDL = Upper Dark Limestone Formation, UWLU = Upper Wavy Laminated Unit, WAL = Waulsortian Limestone Formation.

4.4.3.3 Source Magma Chemistry - Discrimination Diagrams

Geochemical discrimination diagrams provide visual classification of rocks where direct petrogenetic and geological observations are either not possible as samples are highly weathered (see Chapter 3) or available.

Traditionally, such diagrams have employed major elements like Si, Al, Na, K, Mg, Ca and Fe but they should only be used to classify fresh or slightly altered volcanic material due to the mobility of these elements during weathering and diagenesis (Winchester and Floyd, 1977; Zielinski, 1985; Spears et al., 1999; Ross and Bédard, 2009). Therefore, the Winchester and Floyd diagram uses four immobile elements; Zr, Ti, Nb and Y, for the characterisation of the source magma where the magmatic sample may have been altered (Winchester and Floyd, 1977). The Zr/TiO_2 and Nb/Y ratios increase from basic to more evolved (acidic) and from sub-alkalic to alkali compositions, respectively. Because of the mobility of Y (Christidis, 1998), the estimation of the alkaline character (Nb/Y) could be overestimated and therefore should be regarded as a maximum estimate for the alkalinity of the original ash layers, whereas the diagram provides a more reliable indication of the basic character of the protolith (Zr/TiO_2).

Sixty-six samples plot either in the rhyolite, comendite-pantellerite, phonolite or in the upper part of the trachyte field, which all represent an evolved magma composition (Figure 4-19). Ten tuff samples can be assigned either to the lower part of the trachyte field (Navan West_N-2411_HK 126, Tober Colleen Formation; Lisheen _3312-54_HK 222, Upper Wavy Laminated Unit; Stonepark_G11-2654-01_HK 211, Lough Gur Formation; Slievedart_3470/15_HK 190 and Slievedart_3471/4_HK 194, both Kilbryan Limestone Formation), the rhyodacite/dacite (Navan West_N-2412_HK 128, Upper Dark Limestone Formation) or trachyandesite field (Navan West_N-2411_HK 125, Tober Colleen Formation; Navan East_N-2376_HK 227, Upper Dark Limestone Formation; Slievedart_3450/15_HK 237 and Slievedart_3471/4_HK 238, Kilbryan Limestone Formation), which all suggest intermediate source compositions (Figure 4-19). Samples Lisheen_LK-1432_HK 219 (Waulsortian Limestone Formation), Stonepark_G11-2638-02_HK 207 and Stonepark_2638-02_HK 208 (Nodular Micrite Unit) have an alkali basaltic composition, indicating a basic to intermediate magma composition (Figure 4-19). These three samples also exhibit CHARAC behaviour (Figure 4-18B, C), which additionally points towards a basic magma source for the samples.

Thus, according to the Winchester and Floyd diagram, 66 tuff samples have an evolved magma composition, ten tuff samples an intermediate composition and three tuff samples a basic to intermediate composition with all samples showing an alkaline character (Figure 4-19).

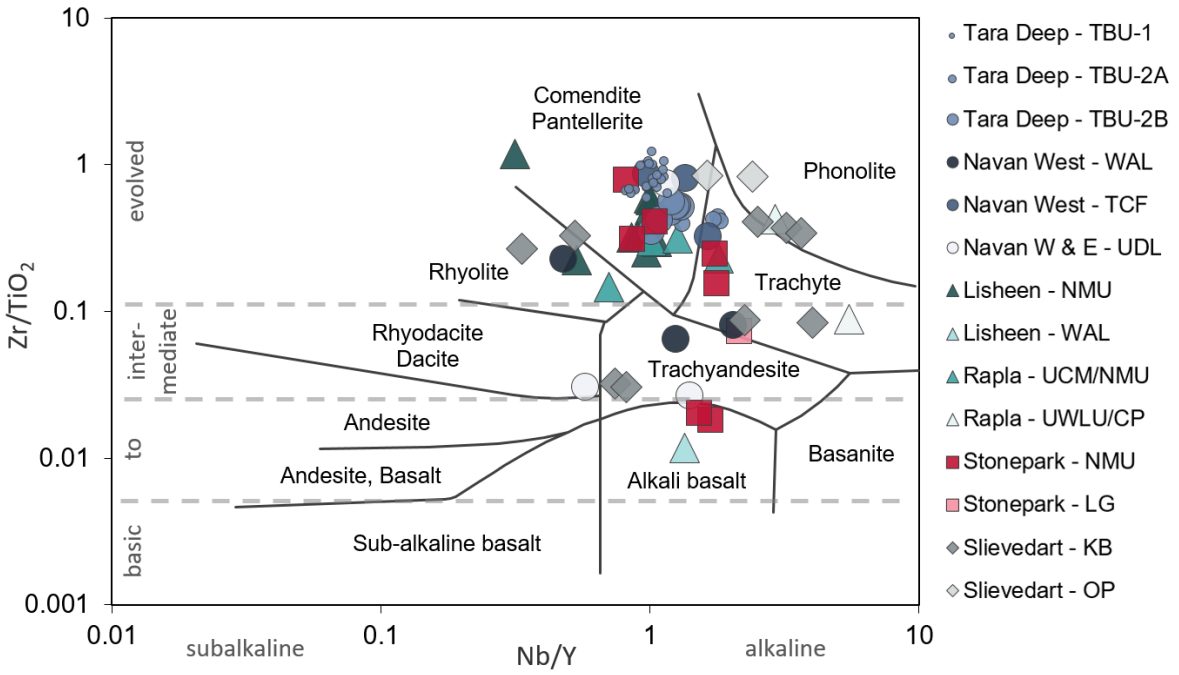

Figure 4-19: Source magma discrimination diagram after Winchester and Floyd (1977). Sixty-three tuff samples from Navan, the Rathdowney Trend, Stonepark and Slievedart reveal an evolved magma composition, while the remaining 13 samples plot within fields, which are either indicative of intermediate or basic to intermediate magma compositions. However, all samples reveal an alkaline character. CP = Crosspatrick Formation, KB = Kilbryan Limestone Formation, LG = Lough Gur Formation, NMU = Nodular Micrite Unit, OP = Oakport Limestone Formation, TBU = Thin Bedded Unit, TCF = Tober Colleen Formation, UCM = Upper Calcarenite Member, UDL = Upper Dark Limestone Formation, UWLU = Upper Wavy Laminated Unit, WAL = Waulsortian Limestone Formation.

4.4.3.4 Summary – Tuff Composition

All samples show a felsic to intermediate composition in a TiO_2/Al_2O_3 diagram (Figure 4-16), while 74 out of 79 samples show REE patterns, which are indicative of evolved magmas (Figure 4-17A-J). Using the Winchester and Floyd (1977) discrimination plot, 66, ten and three tuff samples plot in the evolved, intermediate and basic to intermediate fields, respectively (Figure 4-19). The majority of the samples from Navan, the Rathdowney Trend and Slievedart show inconsistent results in the Y/Ho and Nb/Ta plots (Figure 4-18). Summarising, samples from Navan, the Rathdowney Trend and Slievedart have most likely an evolved magma composition with the exception of samples Slievedart_3470/15_HK 237 and Slievedart_3471/4_HK 238 (both from the Kilbryan Limestone Formation), which show a less evolved character in the REE patterns and in the Winchester and Floyd discrimination plot (Figure 4-17A-J, Figure 4-19). Apatite trace element data confirm this result (see Chapter 5). Samples from Stonepark show contradictory results. While all samples show CHARAC behviour on the Y/Ho *vs* Nb/Ta diagram, which is expected from samples which crystallised from a mafic to intermediate magma source (Figure 4-18C), only two of these samples (Stonepark_G11-2638-01_HK 197 and Stonepark_G11-450-02_HK 210) show REE+Y patterns, which confirm a basic magma source (Figure 4-17K). At the same time, only samples Stonepark_G11-2638-0_HK 207 and Stonepark_G11-2638-02_HK 208 are among the sample, which show the least evolved magma compositions on the TiO_2/Al_2O_3

(Figure 4-16) and Winchester & Floyd diagrams (Figure 4-19), while the remaning samples imply an evolved magma source.

4.4.4 Tuff Correlations

Besides characterising and geochemically fingerprinting sampled tuffs, their potential for chemostratigraphic correlations are investigated following the *matchogram* approach as described in section 4.2.2. The sum of absolute deviates (Σ_D) determines whether two samples share the same eruption history, with $\Sigma_D = 0$ being a perfect match. Increasing deviation from zero implies a decreasing probability that the compared samples stem from the same ash horizon. Commonly employed elements in correlation studies of weathered volcanic ash horizons are Zr, Ti, Nb, Y, Al, Hf, Ta and REEs (e.g. Christidis, 1998; Pellenard et al., 2003; Ddani et al., 2005; Hong et al., 2016). To minimise the impact of selecting the entire REE suite in the pool of elements, only seven REEs (La, Pr, Sm, Gd, Dy, Er, Yb) are chosen for this study and applied in the first *matchogram*. The suite of elements for the second *matchogram* is based on Kiipli et al. (2017) and employs Al, Nb, Ti, Zr, Sn, Ta, Hf and Th. Although Zr concentrations are controlled by the zircon abundance in a sample and are possibly influenced by differing digestion rates or zircon incorporation, the results from both *matchograms* are nearly identical when Zr is excluded and Zr is incorporated in the *matchograms*. In the following, the Σ_D values are based on the first sample suite, while the Σ_D values of the second suite, which uses the same element list as Kiipli et al. (2017), are not shown as they show the same overall trend.

Samples from the same tuff horizon can only be correlated if they show small chemical variation in the chosen element suite, which results in small Σ_D values between tuff samples from that horizon (Figure 4-20; Σ_D(sample 1) ≈ Σ_D(sample 2) ≈ Σ_D(sample 3) ≈ 0).

If several tuff layers occur within an area, it is a requirement that the chemical heterogeneity within a tuff horizon across the basin is minor while at the same time there is a significant difference in the chemistry between tuff layers up and down the section (Figure 4-20; Σ_D(Tuff 1) >> Σ_D(Tuff 2) >> Σ_D(Tuff 3)). The fine-scale homogeneity within a tuff layer can be tested where tuff layers are thick enough to be sampled several times at slightly different levels (e.g. every 1 or 2 cm). The Σ_D value obtained is classified as the 'cut-off Σ_D value' for that specific tuff horizon (Figure 4-20). If it was possible to sample more levels of the same tuff horizon, the largest chemical difference between two samples (= biggest Σ_D value) is chosen as the 'cut-off Σ_D value'. This value is representative for the chemical homogeneity within a tuff horizon. As different volcanic eruptions have different chemical compositions and eruption dynamics, the homogeneity of tuff layers can vary. Thus, the 'cut-off Σ_D value' can also differ between different tuff horizons.

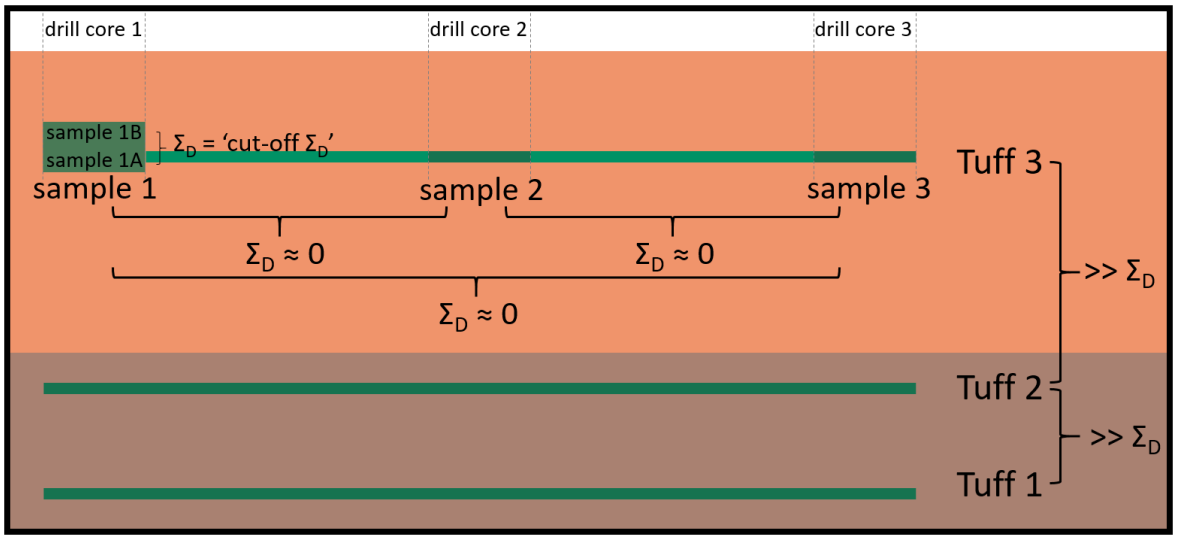

Figure 4-20: Hypothetical example of the use of the sum of deviation (Σ_D) in tuff correlation (tephrostratigraphic) studies. If Σ_D is close to zero between different samples, they were most likely deposited from the same volcanic event and represent one laterally equivalent horizon (Tuff 3). If two tuff samples show high Σ_D values, they probably stem from different tuff horizons (e.g. Tuff 1 vs Tuff 2 or Tuff 2 vs Tuff 3). The Σ_D value from two samples taken from the same tuff horizon are normally very close to zero and this value is called the 'cut-off Σ_D value'. This value is representative for the chemical homogeneity within a tuff horizon.

4.4.4.1 Navan Area

The tuff correlations in the Navan area are split into two sections. Tuff samples which were deposited in Tara Deep are investigated first, followed by tuff samples from Navan East & West.

4.4.4.1.1 Tara Deep

Five tuff layers from five different drill cores from the Navan area were examined for their chemical homogeneity, as these tuff layers were thick enough to be sampled between two and four times at slightly different stratigraphic levels. Four samples were taken from the Marker Tuff of drill core N-2332 and two samples each from the Marker Tuff of drill cores N-2373, N-2444 and N-2494 as well as from the Lower Tuff of drill core N-2406. The 'cut-off Σ_D value' for samples taken from the Marker Tuff is 3.05 (Σ_D(N-2332_HK 119, top tuff)-(N-2332_HK 121, 2nd lowest tuff)), while the Lower Tuff in Thin Bedded Unit 2 was very homogenous with a 'cut-off Σ_D value' of 0.1. Twenty-two samples of the Marker Tuff from Tara Deep from 16 different drill cores were available for correlation studies. The Σ_D values range between 0.06 and 3.3, which is in good agreement with obtained 'cut-off Σ_D value' for the Marker Tuffs (= 3.05), indicating a common volcanic source for all analysed samples (Figure 4-21).

Four samples from the Upper Tuff and eight samples from the Lower Tuff reveal Σ_D values up to 1.93 and 2.74, respectively (Figure 4-21). Hence, the heterogeneity of the Lower Tuff samples in between drill cores is bigger than indicated by the 'cut-off Σ_D value' of 0.1. However, when comparing the three tuff horizons (Marker Tuff, Lower Tuff and Upper Tuff), they reveal Σ_D values between 0.11 and 4.52 (Figure 4-21). Thus, tuff samples, which were sampled within one tuff

horizon are almost indistinguishable from samples taken from the stratigraphically adjacent tuff horizons.

Some drill cores contained two or even all three tuff horizons. These tuff horizons can also not be distinguished based on the Σ_D values of the samples. As the tuff horizons are clearly distinct based on the presence of significant amounts of intervening strata (Figure 4-21), it is likely that the heterogeneity of each tuff horizon is naturally greater than the chemical heterogeneity between different tuff horizons in Tara Deep. The three tuff horizons may share the same volcanic source, whose magma chemistry did not change and erupted three times in different time intervals. The primary chemical pattern could also have been changed by secondary processes like weathering or alteration, although there are no indications that the tuff samples were influenced by Zn or Pb mineralisation (see section 4.4.2.5).

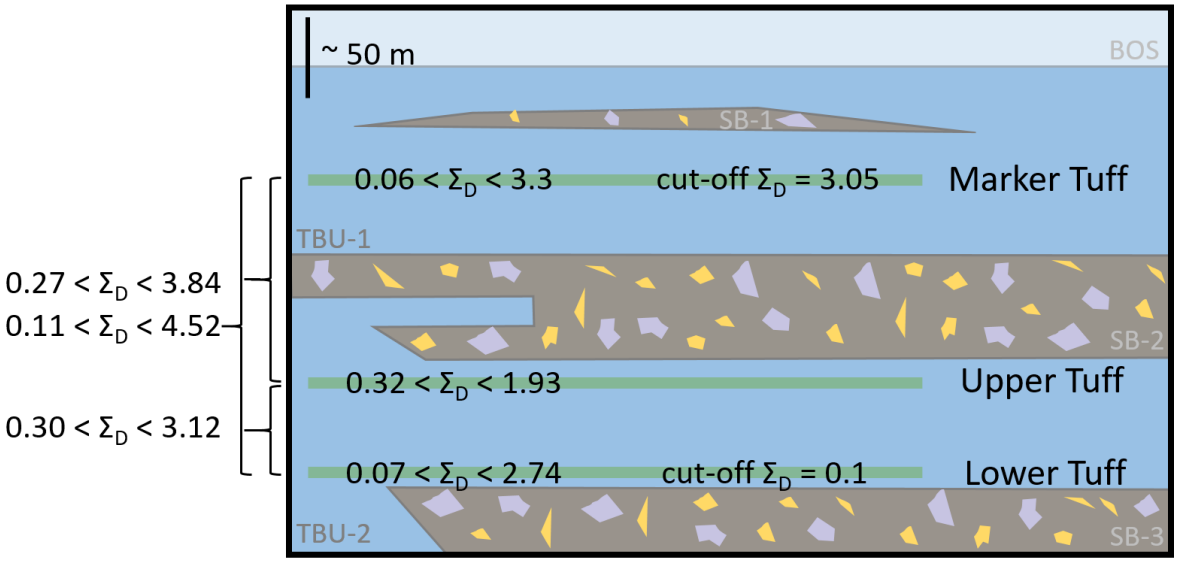

Figure 4-21: Sum of deviation (Σ_D) values for geochemical correlation of tuff horizons from Tara Deep. The Lower, Upper and Marker tuffs cannot be distinguished based on the Σ_D values. BOS = Boudin Shale, SB = Sedimentary Breccia, TBU = Thin Bedded Unit.

4.4.4.1.2 Navan East & West

Two tuff horizons from Navan West could be sampled twice. Samples HK 156 and 157 were taken from the highest tuff layer of drill core N-2441 (Tober Colleen Formation) and reveal a 'cut-off Σ_D value' of 0.82, while the 'cut-off Σ_D value' of samples HK 125 and 126 (N-2411, Waulsortian Limestone Formation) is 1.21 (Figure 4-22).

The two different tuff samples, which were sampled from two different tuff horizons from the same drill core (N-2441) within the Tober Colleen Formation, can clearly be separated based on their Σ_D value, which are 4.62 (HK 155 *vs* 156) and 6.18 (HK 155 *vs* 157), and thus, significantly higher than the 'cut-off Σ_D value' of samples HK 156 and 157 (0.82) (Figure 4-22). Another tuff in drill core N-2441 (HK 169), which was deposited in the carbonate mudbank facies of the Waulsortian Limestone Formation can also be separated from sample HK 155 (Σ_D = 1.98) (Figure 4-22). Hence the tuffs in this region appear to be distinguishable.

Two samples taken from two different drill cores in the Waulsortian Limestone Formation yield Σ_D values of 3.0 (HK 169 *vs* HK 126) and 4.41 (HK 169 *vs* HK 125) and thus significantly higher than the 'cut-off Σ_D value' of samples HK 125 and 126, which is 1.21 (Figure 4-22). Thus, most likely, these two samples do not share a common volcanic source and were deposited during two different volcanic events.

The three samples, which were deposited within the Fingal Group but in slightly different sub-units can also be separated based on their Σ_D values, which are 3.54 between samples HK 227 and HK 128, 6.6 between sample HK 117 and HK 227 and 8.82 between samples HK 117 and HK 128 (Figure 4-22).

These Σ_D values would imply that seven different eruption phases must have taken place, which all led to the deposition of a tuff horizon, which could only be found in one drill core each (Figure 4-22). However, there is also the possibility that samples HK 125, 126, 128, 169 and 227 have a strong clay/silt (shale) component due to their sub-horizontal PAAS normalised REE patterns and low REE concentrations (Figure 4-8A, B), and the variation in Σ_D values is due to variable clay, silt or shale incorporation.

Further work is also necessary to investigate the intensity of volcanic activity in this region and related extent of ash deposition. Samples Navan West_N-2411_HK 125 and Navan West_N-2411_HK 126 for example can also be separated from sample Navan West_N2441_HK 155 (Σ_D = 1.69 (HK 155 *vs* 125); Σ_D = 2.73 (HK 155 *vs* 126)). Although no tuff horizon was observed within the Tober Colleen Formation in drill core N-2411, there is the possibility that after its deposition, the tuff layer in this specific area was removed through sedimentary reworking. The Tober Colleen Formation is developed above the Waulsortian Limestone Formation (see section 2.6.1), which is irregularly developed in the Navan area. It consists of locally well developed micritic limestone

mudbank, crinoidal flank and transition facies (Ashton et al., 2015), which led to a hummocky surface on the seafloor with lots of intra-mound slopes. Boulder beds, which are products of debris flows are observed within the Tober Colleen Formation (Sevastopulo and Wyse Jackson, 2009), which suggests sediment remobilisation and reworking and proves that this facies is sedimentologically active. Therefore, it is plausible that volcanic ash could have deposited on stratigraphically highs, but could then have washed downslope into the hollows and valleys between mounds.

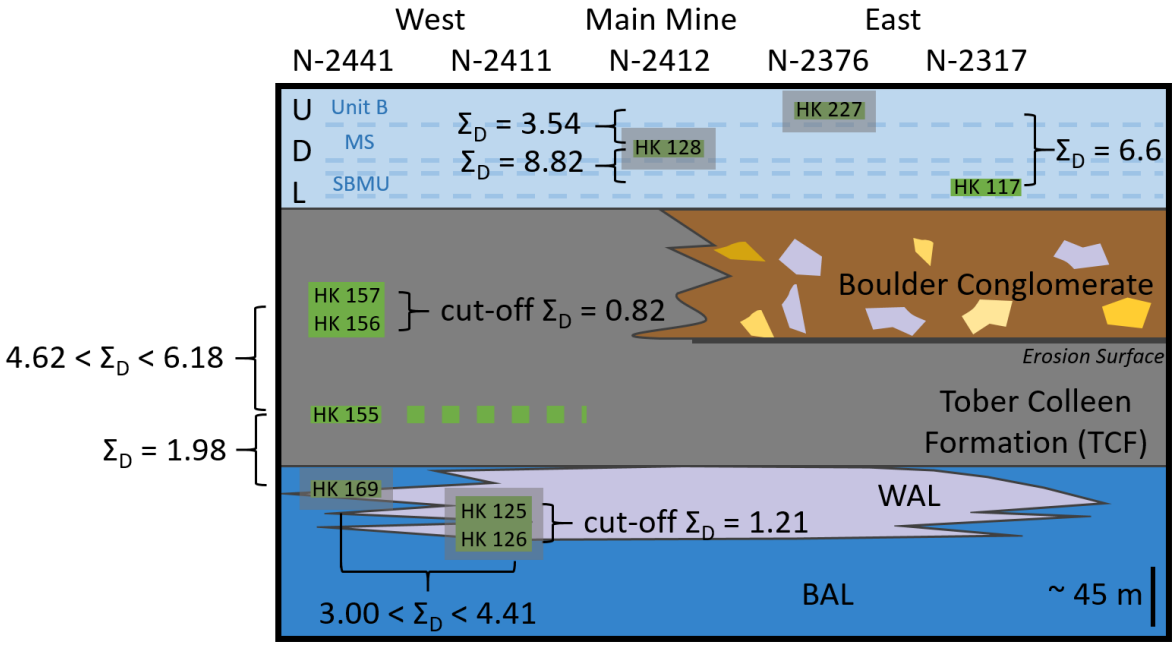

Figure 4-22: Sum of deviation (Σ_D) for chosen tuff samples from the Navan area from five different drill cores. The closer Σ_D is to zero, the more likely the samples share the same eruption history. Grey highlighted samples share characteristics of shale samples. BAL = Ballysteen Limestone Formation, MS – Micritic Sequence, SBMU = Sub-Bottom Marker Unit, UDL = Upper Dark Limestone Formation, WAL – Waulsortian Limestone Formation.

4.4.4.1.3 Tara Deep *vs* Navan East & West

Σ_D values of most samples in between Tara Deep and Navan East & West is > 3.00 and thus indicate no cross-correlations of these samples (geochemically). Cross – correlations of samples from Tara Deep and samples Navan West_N-2412_HK 128 and Navan East_N-2376_HK 227 are also not expected due to the different stratigraphic occurrence of these samples. Samples from Tara Deep were most likely deposited in the Lower Viséan, while samples Navan West_N-2412_HK 128 and Navan East_N-2376_HK 227 are presumably younger (Arundian to Holkerian) (see section 2.6). However, > 80% of tuff samples from Tara Deep and samples Navan East_N-2317_HK 117, Navan West_N-2441_HK 156 and Navan West_N-2441_HK 157 show Σ_D values < 2.68, implying a common volcanic centre. Sample Navan East_N-2317_HK 117 occurs in the Sub Bottom Marker Unit of the Fingal Group in Navan East, which is early Viséan in age. The Tober Colleen Formation, which is the host rock of samples HK 156 and 157 has a diachronous distribution and can be much younger on the margin of the Dublin basin (Viséan) than its

lithological equivalent in the basin (Tournaisian) (Ashton et al., 2015). Thus, the stratigraphic occurrence of these ash layers support a common eruption history, assuming ash layers HK 156 and 157 deposited in the Tober Colleen Formation are Lower Viséan in age. Furthermore, the tuff bands from the Marker Tuff and from sample Navan East_N-2317_HK 117 have a similar appearance in drill cores as both are interlaminated with calcareous mudstones (Figure 3-1A, B, L).

4.4.4.2 Rathdowney Trend

As the Rathdowney Trend consists of both the Lisheen and Rapla study areas, they are approached separately.

4.4.4.2.1 Lisheen

Ten tuff samples, which were taken from nine different drill cores from Lisheen were either assigned to the Nodular Micrite Unit or the S-ABL (equivalent ABL facies). The S-ABL is not formally defined. Some core loggers did not distinguish between the Upper Calcarenite Member and Nodular Micrite Unit and therefore both units are sometimes subsumed under the term S-ABL.

Σ_D values of samples HK 216, 182, 218 and 221 from this stratigraphic level at Lisheen range within 0.08 – 1.67. Samples HK 180, 181, 203 and 214 have Σ_D values of 0.61 – 1.92 (Figure 4-23). These samples, which could be split into two groups were most likely deposited during two different volcanic events, as Σ_D values between both groups are up to 3.66 (Figure 4-23). Furthermore, both groups contain samples from the Nodular Micrite Unit and the S-ABL. Thus, the S-ABL in these particular drill cores can be assigned as the Nodular Micrite Unit based on the tuff geochemistry. However, although samples HK 215 and 220 also occur within the Nodular Micrite Unit and are chemically similar to some of the above mentioned samples, they do not match properly to either group. Thus, this tuff horizon probably consists of four tuff layers, which were probably deposited during four separate events or as part of an eruption sequence. The mineralisation of five samples from this horizon by either Pb (HK 203) or Zn (HK 182, 184, 221) or both (HK 220), does not seem to affect the elements employed for correlation between these tuff layers (Figure 4-23).

Tuff sample HK 219 was taken from the Waulsortian Limestone Formation. As it is in a different stratigraphic unit compared to the other samples, higher Σ_D values between this sample and the rest of the sample set is expected. All samples do indeed show high Σ_D values (3.2-11.38), indicating a different eruption based on trace element geochemistry. As sample HK 219 shows strong chemical similarities to shale (Figure 4-7; Figure 4-8), there is the possibility that this sample does not have a volcanic origin. Additionally, none of the remaining drill cores from

Lisheen have a tuff layer in the Waulsortian Limestone Formation carbonate mound facies (Figure 4-23), which supports this hypothesis.
Overall, this method works well for the Lisheen region. The chemical similarity of samples HK 215 and 220 to some other samples cannot be conclusively clarified, but the results imply four separate tuff layers in the Nodular Micrite Unit, probably as part of an eruption sequence with only slightly changes in the chemical composition of the source magma between eruptions.

4.4.4.2.2 Rapla

Samples HK 185 and 217 were taken from the Upper Calcarenite Member and have a Σ_D value of 2.03, while sample HK 184 was sampled within the overlying Nodular Micrite Unit and has Σ_D(HK 184-185) = 4.73 and Σ_D(HK 184-217) = 3.59 (Figure 4-23). Therefore, sample HK 184 can be distinguished from samples HK 185 and 217. Sample HK 223 was taken from the boundary of the Upper Calcarenite Member and Nodular Micrite Unit. Its Σ_D value is closest to sample HK 184 (Σ_D = 1.23), followed by sample HK 217 (Σ_D = 3.52) and sample HK 185 (Σ_D = 5.17) (Figure 4-23). Thus, samples HK 185 and 217 were most likely deposited within the Upper Calcarenite Member as part of the same eruption. This volcanic event was followed by a later eruption, which produced a second ash layer within the Nodular Micrite Unit (samples HK 184 and 223).
Sample HK 183, which occurs within the Crosspatrick Formation, is separated by four different stratigraphic units from samples HK 217 and 185 and by three different units from samples HK 184 and 223. Although the chemical difference between sample HK 183 and the four aforementioned samples is minor to moderate, it can still be separated based on its Σ_D values, which are between 3.09 and 8.39.
However, sample HK 222, which was deposited in the Upper Wavy Laminated Unit (part of the Waulsortian Limestone Formation) can be clearly distinguished from samples HK 184, 185, 217 and 223, which occur in the Upper Calcarenite Member or Nodular Micrite Unit (Σ_D=10.54-12.55) and from sample HK 183 (Σ_D=10.32; Crosspatrick Formation) (Figure 4-23). As sample HK 222 shows REE concentrations similar to shale (Figure 4-8A, B), there is the possibility that it is in fact a shale, instead of a tuff. Thus, samples HK 185 and 217 were deposited first, followed by samples HK 184 and 223. Samples HK 185 and 223 were taken from the same drill core (3667-04), and are separated by 2 m of intervening limestone. Finally sample HK 183 was deposited. Due to the stratigraphic position of sample HK 183, it was deposited much later than samples HK 185 and 217, although there is only a small chemical difference between these samples.

4.4.4.2.3 Lisheen *vs* Rapla

The results from the Lisheen and Rapla area showed that tuff samples within the Rathdowney Trend can be assigned to the same layer if Σ_D values are < 2. There are two different layers in the Nodular Micrite Unit in Lisheen, which can be distinguished based on their Σ_D values

of < 2. One tuff layer includes samples HK 182, 216, 218 and 221, while the second layer incorporates samples HK 180, 181, 203 and 214. Sample HK 185 from Rapla can be correlated with samples HK 180, 181, 218 and sample HK 217 can be correlated with samples HK 180, 182, 203, 214, 216, 218, 221 from Lisheen, respectively. Thus, samples HK 185 and 217, which define a single layer in Rapla can both be matched with some samples from Lisheen tuff layer one and with some samples from Lisheen tuff layer two. However, based on the stratigraphic position of the samples, the Rapla layer cannot correlate with both tuff layers in Lisheen, as Rapla samples HK 185 and 217 were deposited in the Upper Calcarenite Member, which is stratigraphically older than the host formation of both Lisheen layers (Figure 4-23). Thus, it appears that perhaps as many as seven different volcanic eruptions occurred, which lead to the deposition of one ash layer in the Upper Calcarenite Member, followed by five ash layers in the Nodular Micrite Unit and one ash layer within the Crosspatrick Formation, where none of the ash layers can be correlated between Rapla and Lisheen. It seems likely that there were neither ash deposits in the carbonate mudbank facies of the Waulsortian Limestone Formation nor in the Upper Wavy Laminated Unit of the same formation, as samples HK 219 and 222 show an affinity to shale (grey highlighted samples on Figure 4-23). Zinc and/or Pb mineralisation does not affect the element suite used for the correlations.

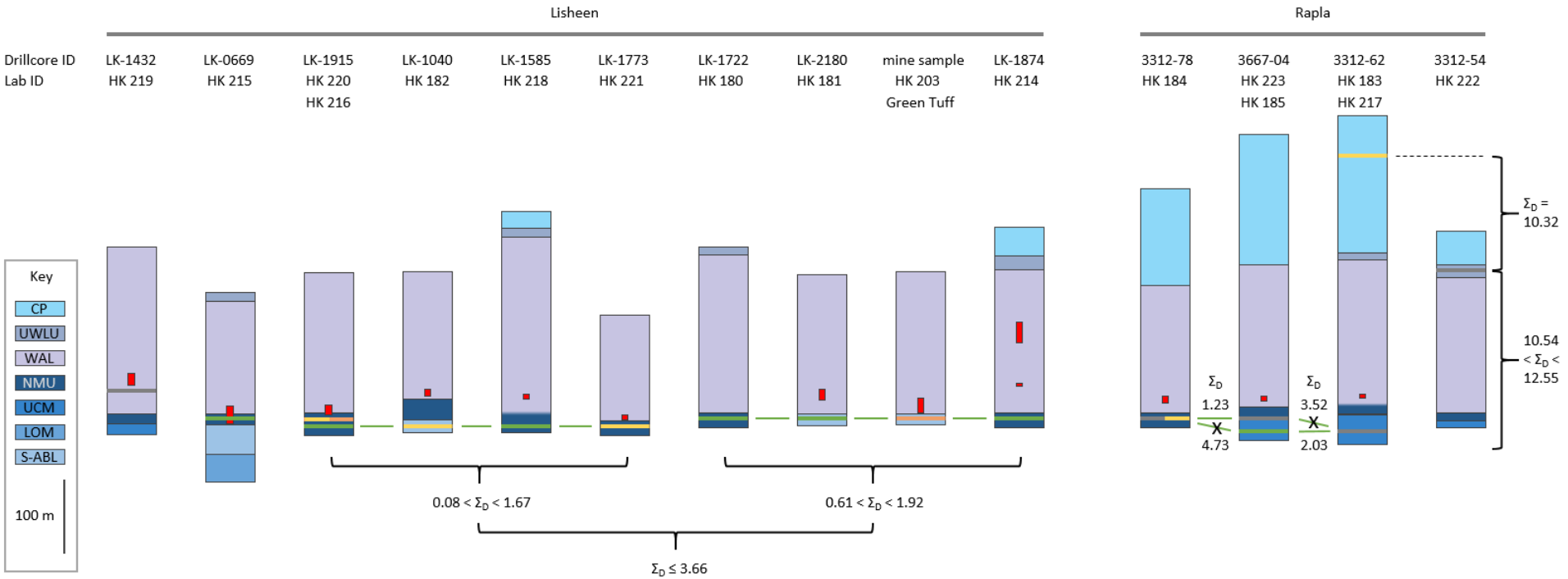

Figure 4-23: Σ_D values of samples taken in the Rathdowney Trend. The closer Σ_D is to zero, the more likely the samples share the same eruption history. Samples which are linked with a thin green line have all low Σ_D values and thus share possibly a volcanic source. Green lines which are crossed out indicate that Σ_D values between two samples are too high and thus do no match geochemically. Samples HK 183, 215, 219, 220 and 222 cannot be matched with any sample from this study site. The distance (stratigraphically) between samples HK 220 and 216, between samples HK 223 and 185 and between samples HK 217 and 183 is 4 m, 2 m and 345.5 m, respectively. Samples, which are highlighted in grey, orange or yellow show shale-like patterns in some diagrams, are possibly influenced by galena or sphalerite mineralisation, respectively. Complete stratigraphic columns are shown in Figure 2-9. Full sample names are listed in Table 2-6. CP = Crosspatrick Formation, LOM = Lisduff Oolite Member; NMU = Nodular Micrite Unit; S-ABL = S-Argillaceous Bioclastic Limestone; UCM = Upper Calcarenite Member, UWLU = Upper Wavy Laminated Unit, WAL = Waulsortian Limestone Formation, red bars=mineralised zones.

4.4.4.3 Stonepark Area

Samples HK 197, 198, 207, 208, 209, 210 and 212 were taken within the Nodular Micrite Unit. Three samples (HK 207, 208 and 209) occur in drill core 2638-02. Samples HK 207 and 208 are 1 m apart and show a Σ_D value of 0.22, indicating very similar source chemistries, while the difference to sample HK 209 (11 and 10 m apart, respectively) is quite large with values of 6.53 Σ_D(HK 207-209) and 6.65 Σ_D(HK 208-209) (Figure 4-24). Thus, the influence of Zn mineralisation on these samples did not homogenise their chemical patterns as they can still be separated. Samples HK 197 and 198 are 5 m apart in drill core 2638-01 and reveal a Σ_D value of 1.79, while samples HK 210 and 212 were taken from the only tuff layers within the Nodular Micrite Unit (Figure 4-24). Most Σ_D values between samples HK 197, 198, 209, 210 and 212 are between 1.31 and 4.0, except between samples HK 210 and 198 (Σ_D=8.78) and samples HK 197 and 212 (Σ_D=8.78) (Figure 4-24). These noticeable differences in Σ_D values in between some samples from this tuff horizon could be indicative of small-scale chemical heterogeneity. However, this ash horizon also contains two samples from the same drill core, which are 5 m apart (sample HK 197 and 198). Their occurrence as well as the differences in magma chemistry can be probably better explained by pulsing eruptions with small changes in magma chemistry. Precise correlation between drill cores cannot be fully reconstructed, probably due to the natural chemical heterogeneity of the source magma. However, more samples are necessary to confirm this theory.

The Σ_D values between samples HK 207 and 208 and these five samples is constantly high (5.24 to 7.96; Figure 4-24). Thus, there is the possibility that a second and third eruption took place after the first eruption sequence finished, which led to the deposition of two further tuff layers (samples HK 208 and 207), which are 10 and 11 m apart from the first tuff horizon. The similar chemistry of both samples show a constant magma source chemistry.

Sample HK 211 occurs in the Lough Gur Formation and is 367.5 m stratigraphically above sample HK 212. Both samples are taken from drill core 2654-01 and are separated by the Waulsortian Limestone Formation. However, the Σ_D values between the samples from the first tuff horizon (samples HK 197, 198, 209, 210 and 212) and sample HK 211 vary between 2.83 and 8.11, while the difference between samples HK 207 and 208 and sample HK 211 is 6.28 and 6.74, respectively (Figure 4-24). Thus, sample HK 211 shows a slightly different magma chemistry and could be deposited above the Waulsortian Limestone Formation during a fourth volcanic event. Alternatively, samples HK 207, 208 and 211 could have a non-volcanic origin or at least a strong shale component as they show flat shale normalised REE+Y patterns as well as REE concentrations within the range of shales (Figure 4-7, Figure 4-8).

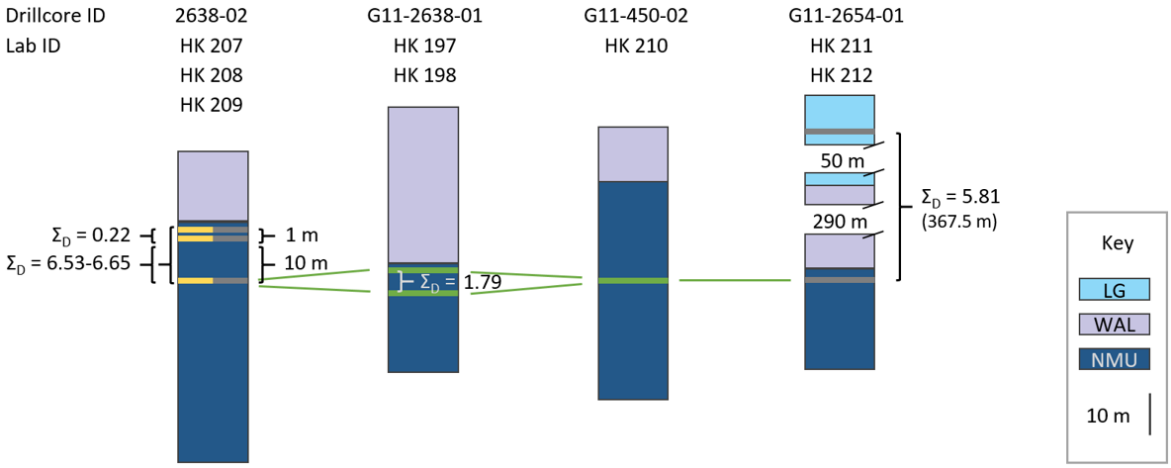

Σ_D	HK 197	HK 198	HK 207	HK 208	HK 209	HK 210	HK 212	HK 211
HK 197	0	1.79	7.93	7.96	3.87	3.82	6.22	8.11
HK 198		0	5.96	6.06	2.92	8.78	3.38	4.18
HK 207			0	0.22	6.53	7.14	5.24	6.28
HK 208				0	6.65	7.54	5.81	6.74
HK 209					0	1.49	1.31	2.83
HK 210						0	4.00	4.56
HK 212							0	5.81
HK 211								0

Figure 4-24: The table shows Σ_D values of all samples occurring in the Stonepark area. The closer Σ_D is to zero, the more likely the samples share the same eruption history. Samples HK 207, 208 and 209 are influenced by Zn mineralisation and are highlighted in yellow, while grey highlighted samples show similarities to shales. Samples HK 209, 197, 198, 210 and 212 have Σ_D values smaller than 5.24 and could be part of the same volcanic sequence, which produced several tuff layers. These samples are linked with a green thin line. The Σ_D values of samples HK 207, 208 and 211 are mainly larger than 5.81 when comparing to the four aforementioned samples and therefore do not match geochemically. They most likely represent three additional tuff horizons in the Stonepark area. However, these three samples plus sample HK 212 also show shale-like patterns in some elements. LG = Lough Gur Formation, NMU = Nodular Micrite Unit, WAL = Waulsortian Limestone Formation.

4.4.4.4 Slievedart Area

The homogeneity of one tuff layer was tested using samples HK 192 and 193 as they are only 10 cm apart and regarded as one tuff layer (see section 2.9.1). These two samples show a Σ_D value of 0.9 (Figure 4-25A), indicating minor heterogeneity within the tuff layer.
Tuffs one, three, four and five can be correlated based on their relative position of the tuff layers between drill core 3470/15 and 3471/4, but also show the smallest Σ_D values within the Slievedart tuff sample data set (Figure 4-25A, B, dark grey cells). The difference in Σ_D values with any other tuff sample is at least double (Figure 4-25B). Subsequently, the homogeneity within a tuff horizon as well as the large chemical variation between the tuff horizons from the same drill cores allow the confident allocation of the ash samples to four different ash horizons. The only exemption is tuff two. The Σ_D value between samples HK 189 and 195 is 3.79 and thus bigger than Σ_D value between samples HK 189 and 191 (Figure 4-25B, bright grey cells). Thus, the tuff samples in the Slievedart area indicate two different eruptive sequences with either three or four horizons in the lower eruption sequence, while the second eruption only produced one ash layer (Tuff 5). Zinc-lead mineralisation in some samples does not influence the correlations (Figure 4-25A).

A

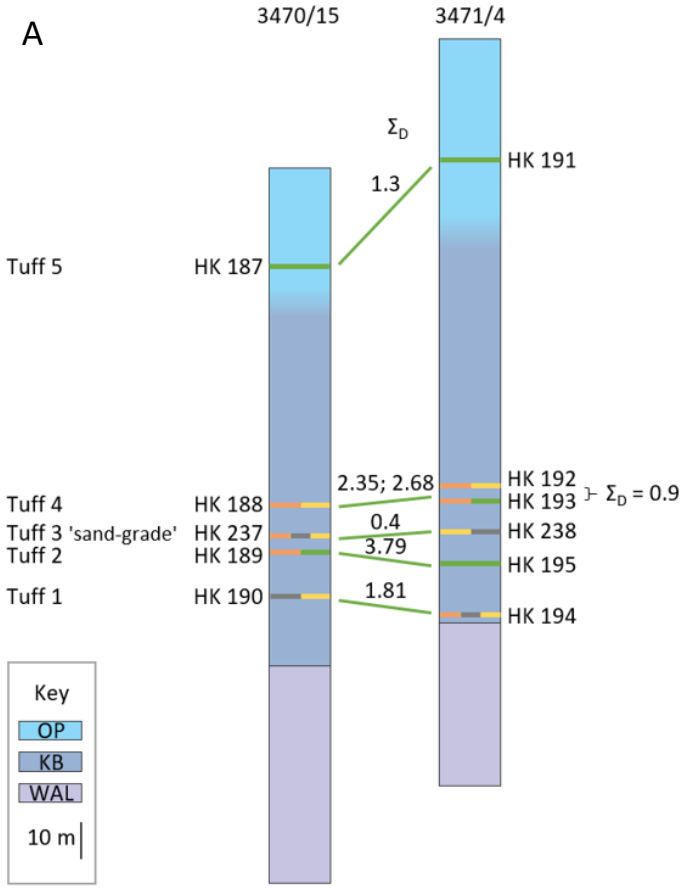

B

Σ_D	*HK 190*	*HK 194*	*HK 189*	*HK 195*	*HK 237*	*HK 238*	*HK 188*	*HK 192*	*HK 193*	*HK 187*	*HK 191*
HK 190	0	1.81	6.07	9.35	11.56	11.09	5.47	5	7.65	4.7	5.19
HK 194		0	8.09	5.22	12.66	12.1	3.74	4.44	6.74	5.91	6.9
HK 189			0	3.79	4.61	4.89	8.91	6.87	7.36	3.72	2.03
HK 195				0	5.57	5.28	3.53	9.85	10.67	4.7	4.2
HK 237					0	0.4	12.18	11.82	12.56	8.26	6.42
HK 238						0	11.59	11.15	12.11	8.38	6.41
HK 188							0	2.35	2.68	6.71	7.62
HK 192								0	0.9	5.58	4.04
HK 193									0	7.86	5.84
HK 187										0	1.33
HK 191											0

Figure 4-25: Σ_D values of Mississippian tuff samples occurring in the Slievedart area. The closer Σ_D is to zero, the more likely the samples share the same eruption history. A) Occurrence of tuff layers in drill cores 3470/15 and 3471/4. The tuff one samples are the stratigraphically lowest samples, while the tuff five samples are stratigraphically highest. Samples which are influenced by Pb or Zn or show shale-like patterns are highlighted in orange, yellow and grey, respectively. B) Dark grey shaded cells show smallest Σ_D values between any taken tuff samples in the Slievedart area, which can be assigned to tuff layers from the same stratigraphic position between the two drill cores, suggesting four different eruptions. Light grey shaded cells indicate that the Σ_D value of samples HK 189 and 191 is smaller compared to the Σ_D value of samples HK 189 and 195. Thus, although samples HK 189 and 195 appear at the same stratigraphic level in the two drill cores, they cannot be clearly correlated based on their Σ_D values. Full sample names are listed in Table 2-10. KB = Kilbryan Limestone Formation, OP = Oakport Limestone Formation, WAL = Waulsortian Limestone Formation.

4.4.4.5 Cross-Correlations

The Σ_D value, which determines if two samples can be correlated and thus stem from the same volcanic eruption is < 3.3 for Marker Tuffs, < 2.74 for the Lower Tuffs and < 1.93 for the Upper Tuffs in Tara Deep and < 1.21 and < 0.82 for samples taken within the Waulsortian Limestone and Tober Colleen formations, respectively. Samples from the Rathdowney Trend are assigned to the same tuff layer or horizon if their Σ_D values were < 2.03. Tuff samples from the Stonepark area revealed slightly greater chemical heterogeneity within a tuff horizon, which result in Σ_D cut-off values around 3.8. Slievedart samples which can be allocated to the same tuff layer are chemically very homogeneous with Σ_D cut-off values < 1.81. Based on these observations and the stratigraphic position of the samples there are likely ten different tuff layers across the four study sites.

However, when all tuff samples from one tuff horizon in one area are compared with all tuff layers from a second region, the Σ_D cut-off values are usually large, implying cross correlations between the four regions are not possible.

4.5 Conclusions

Eight different classification diagrams were used to examine the volcanic origin of the 79 samples of this study. None of the samples could be unambiguously determined as shale, although twenty-one samples showed shale-like geochemical patterns (e.g. see Figure 4-7 and Figure 4-8). The geochemical evidence that samples were deposited in a shallow or deep marine environment (Figure 4-10) is consistent with the unequivocal sedimentary evidence for marine deposition during the Tournaisian and Viséan. The samples were most likely not strongly influenced by reworking processes, besides samples Navan West_N-2441_HK 169 and Lisheen_LK-1432_HK 219, which have Eu anomalies implying reworked samples (Figure 4-13, Figure 4-14). Samples from the four study sites show a similar degree of weathering (Figure 4-12). However, the lack of glass shards, the general condition of the samples and the strong negative Eu anomalies (Figure 4-12B) potentially indicate a strong degree of weathering.

Tuff samples from Tara Deep and Slievedart seem to have the strongest correlation between Zr, Hf and the HREE with samples from Tara Deep having the highest Zr concentrations (Figure 4-9A-E). Due to the minor amount of reworking during the deposition of the tuff samples, the trend is most likely caused by primary zircon phenocrysts as opposed to detritally incorporated grains. However, as no zircons were found in most samples from Navan, the high Zr, Hf and HREE content may be associated with small metamict fragments that were more easily digested.

Six out of fifteen samples from the Rathdowney Trend exhibit strong evidence for either Zn or Pb mineralisation with two samples from Lisheen showing either highest Zn or Pb concentrations

(Figure 4-15). A minor influence of mineralisation on the tuff samples is found in the Slievedart area, followed by the Stonepark and Navan area (Figure 4-15).

Following correlations are based on the *matchogram* method, using Zr, Ti, Nb, Y, Al, Hf, Ta, La, Pr, Sm, Gd, Dy, Er, Yb. Tuff samples from Tara Deep, which were either assigned as Marker Tuff, Upper Tuff or Lower Tuff cannot be distinguished from each other (Figure 4-21) and were most likely erupted from a highly evolved magma source (Figure 4-17A-D, Figure 4-19). Samples Navan East_N-2317_HK 117, Navan West_N-2441_HK 156 and Navan West_N-2441_HK 157 can be correlated with samples from Tara Deep. Their chemical compositions also match (Figure 4-19). This supports that the Tober Colleen Formation and the lower units of the Fingal Group in Navan East & West and the New Thin Bedded Unit in Tara Deep could be time-equivalent. Five samples (HK 125, 126, 128, 169 and 227) taken from Navan East & West show both shale - and tuff - like patterns. Assuming all samples are tuffs, they have all different chemical patterns (Figure 4-17E, Figure 4-19) and cannot be cross-correlated to samples from Tara Deep. Tuffs from the Rathdowney Trend were deposited as a result of seven different volcanic events. The first tuff layer was deposited within the Upper Calcarenite Member in Rapla, followed by five discrete tuff horizons in the Nodular Micrite Unit either in Lisheen or in Rapla. The final tuff layer was deposited in the Crosspatrick Formation at Rapla. All samples show a REE+Y pattern typical of an evolved source magma (Figure 4-17) and plot either in or near the comendite/pantellerite field (Figure 4-19). Samples HK 219 and 222 were taken within the carbonate mudmound facies and the Upper Wavy Laminated Unit of the Waulsortian Limestone Formation and are both more likely shales than tuffs (Figure 4-7A, Figure 4-8). These two samples are also the only samples in the Rathdowney Trend, which reveal different REE patterns (Figure 4-17G, H) and plot away from the other samples on the Winchester and Floyd discrimination diagram (Figure 4-19). Five out of eight samples were taken within the Nodular Micrite Unit in the Stonepark area and were most likely deposited successively as part of a prolonged magmatic event. Two tuff samples were taken 10 m above these five samples and were deposited as part of two independent volcanic eruptions as was sample Stonepark_G11-2654-01_HK 211, which occurs within the Crosspatrick Formation. The determination of the source magma chemistry is not straightforward as different diagrams provide different results for the same samples (e.g. Figure 4-17I, K, Figure 4-19). The tuff samples in the Slievedart area indicate two different eruptive sequences. The first led to the deposition of four tuff horizons in the Kilbryan Limestone Formation while the second phase produced one ash layer within the Oakport Limestone Formation. The five tuff layers from similar stratigraphic levels can also be separated based on their chemical composition (Figure 4-19). A continuous differentiation of the magma chemistry from tuff one to tuff five can be excluded. However, there is the possibility that the magma chamber evolved in between tuff one and two from a trachytic

to a rhyolitic composition, while there was a second differentiation series, evolving from a trachyandesitic start to a phonolitic end composition (Figure 4-26).

The mineralisation of some samples from the Rathdowney Trend, Stonepark and Slievedart area does not seem to influence the correlations.

Overall, 77 out of 79 tuff samples have an evolved to intermediate composition (Figure 4-10, Figure 4-17, Figure 4-18, Figure 4-19), while samples Slievedart_3470/15_HK 237 and Slievedart_3471/4_HK 238 have a slightly less evolved source magma, indicated by a positive Eu anomaly (Figure 4-17J) and comparably low Nb/Y and Zr/TiO_2 ratios (Figure 4-19).

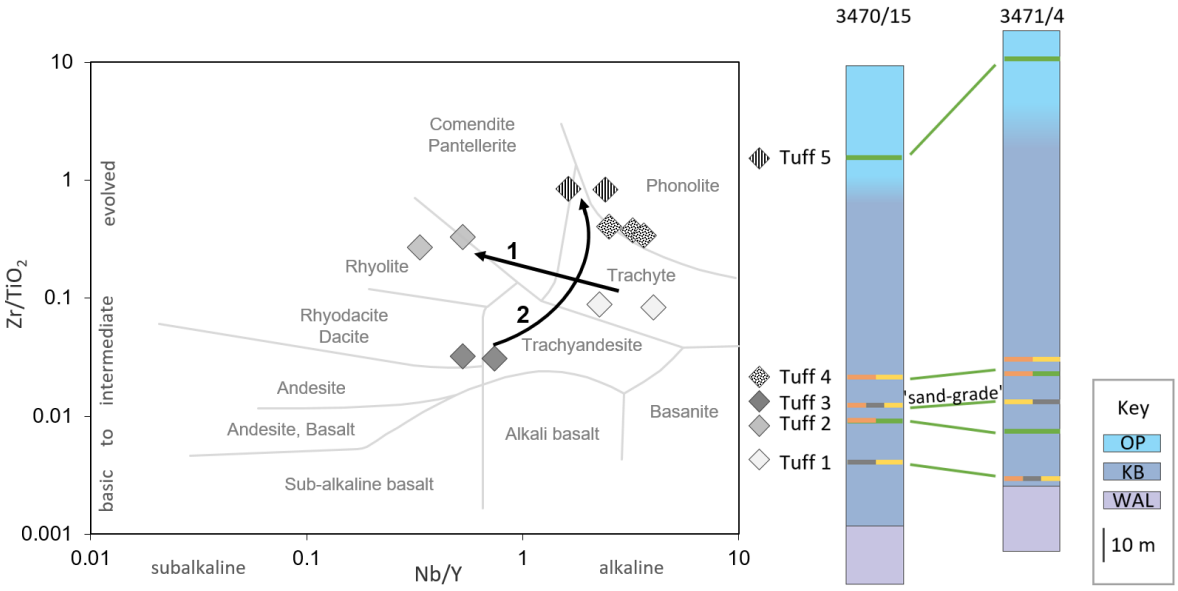

Figure 4-26: Eleven Mississippian tuff samples from Slievedart are plotted on the source magma discrimination diagram after Winchester and Floyd (1977). Tuffs one to five from two different drill cores can be distinguished based on their composition. It is possible that the magma source evolved between eruption one and two, first producing a trachytic ash, followed by a rhyolitic ash composition, visualised by the black arrow. A second differentiation path is indicated by the second black arrow. It started with a trachyandesitic magma and finished with a comenditic/pantelleritic/phonolitic magma composition, producing tuffs three to five.

4.6 Future Work

4.6.1 Clay Fraction *vs* Phenocrysts

To minimise the influence of phenocrysts and accessory minerals on the overall REE and trace element content, phenocrysts and accessory minerals could be separated from the bulk-rock in a clay and heavy mineral fraction. Some studies propose that the composition of the clay fraction, which is formed *in situ* from volcanic glass during devitrification is less likely influenced by heavy minerals through reworking and, thus, preserves the source-magma composition more reliably compared to bulk-rock data (Clayton et al., 1996; Laviano and Mongelli, 1996; Hong et al., 2019).

4.6.2 Digestion Method

To confirm, that produced trace element data are reliable, at least five samples from each sample location should be randomly picked and analysed using high-pressure bomb digestions. Subsequently, produced element ratios should be within the same range.

4.6.3 Mineralogy - XRD

The mineralogy of tuff samples, especially the different type of clay minerals, can be used to identify the volcanic origin of ash layers (Kiipli et al., 2008).

Chapter 5:

LA-ICP-MS U-Pb Zircon Geochronology and Apatite Trace Element Characterisation

5.1 Introduction

Tephra deposits from a single volcanic eruption can be widely dispersed over terrestrial and marine environments (e.g. Alloway et al., 2007; Matthews et al., 2012; Engwell et al., 2012). Where datable magmatic phenocrysts are present, the ash layer should yield the same age from dispersed sampling localities, assuming xenocrysts/detrital contamination and daughter isotope loss can be accounted for. Zircon and apatite phenocrysts are commonly employed to obtain high-precision ages of volcanic eruptions.

Uranium-lead zircon dating by laser ablation inductively coupled plasma mass spectrometry (LA-ICP-MS) is now a rapid and routine analytical technique (Spencer et al., 2016). Laser ablation of the sample produces an aerosol, which is introduced into a mass spectrometer with typically He used as a carrier gas. Due to the high-temperature argon plasma source of the mass spectrometer, the sample aerosol is vaporised, atomised and ionised. The ions get accelerated and are detected by the detector (typically a dual-stage discrete dynode electron multiplier for a quadrupole inductively coupled plasma mass spectrometry (ICP-MS) which filters ions according to their mass/charge ratios) and reported in counts per second (cps). During a series of data reduction steps, the raw isotope data of unknowns and age standards are processed to yield U-Pb ages.

Zircon ($ZrSiO_4$) is usually the mineral of choice for U-Pb geochronology as it is chemically and mechanically very stable. It is commonly preserved intact in diagenetically altered tuff layers even when other phenocrysts, such as sanidine and biotite, have undergone alteration. It yields very reliable U–Pb age information due to its low Pb diffusivity, typically high U concentrations (which substitutes for Zr^{4+}) and minimal incorporation of common Pb in its crystal structure during crystallisation, generating high initial parent (U) to daughter (Pb) ratios.

In sediments, apatite is more likely to represent first-cycle detritus compared to the polycyclic behaviour of zircon as it is mechanically less stable than zircon and is chemically unstable in weathering profiles, particularly in the presence of acidic meteoric water (e.g. Morton & Hallsworth, 1999, and references therein; Dickinson & Gehrels, 2009). Apatite LA–ICP-MS U–Pb

dating is more challenging than zircon dating as apatite typically yields lower U, Th and radiogenic Pb concentrations and higher common Pb to radiogenic Pb ratios, although common Pb in apatite age standards can now be corrected for (e.g. Chew et al., 2011; Thomson et al., 2012; Chew et al., 2014).

In a best-case scenario, precision of U-Pb LA-ICP-MS apatite dates is typically limited to c. 2% (2RSD) on an Early Carboniferous age, compared to 0.75% (2RSD) for U-Pb LA-ICP-MS zircon ages. Although zircons typically yield more precise U-Pb ages than apatite, they also have some disadvantages as a geochronometer: zircon does not occur in every crustal rock; it is most common in igneous rocks of intermediate to Si-saturated composition and less common in silica-undersaturated and peralkaline igneous lithologies (Watson, 1979; Hoskin and Schaltegger, 2003). Furthermore, it is still challenging to link zircon to its parent rock type based on variations in Hf, Y, REE, Th and U. Several studies have shown that zircon trace elements cannot necessarily be used to 'blindly' determine parental liquid compositions in detrital zircon studies (Hoskin and Ireland, 2000; Wilde et al., 2001; Hoskin and Schaltegger, 2003), whereas other publications could distinguish individual zircons from different sources and could recognise zircons from certain rock types (Chyi, 1986; Heaman et al., 1990; Belousova et al., 2002b). However, the trace element partition coefficients in igneous apatite are typically more sensitive to changes in magmatic conditions. The trace element chemistry of detrital apatite can therefore provide an effective link to the parent igneous rock type. Furthermore, unlike zircon, which is generally restricted to igneous rocks of felsic composition, apatite is a nearly ubiquitous accessory phase in igneous rocks of both felsic and mafic composition (Belousova et al., 2002b; Piccoli and Candela, 2002)

Hence, this study presents U-Pb age data for both zircons and apatites from the Irish Mississippian tuff horizons. The zircons are analysed to yield precise U-Pb ages, whereas the apatite grains are primarily used to characterise the source magma chemistry (for grains that yield Early Carboniferous U-Pb apatite ages).

5.2 Method

5.2.1 U-Pb Zircon Geochronology

Uranium-lead geochronology is based on two independent geochronometers, the ^{238}U-^{206}Pb system and the ^{235}U-^{207}Pb system, whose half-lives are 4468 Ma and 704 Ma, respectively. For U-Pb zircon geochronology, zircon incorporates U and Th atoms in its crystal structure at the time of crystallisation but negligible Pb, and thus typically the entire Pb content of zircon is radiogenic in origin. Thus, the calculated dates based on the ^{238}U-^{206}Pb decay and the ^{235}U-^{207}Pb decay schemes within one zircon grain should equal each other, as the parent/daughter ratio changes as a function of time only. This provides the possibility to detect small amounts of open

system behaviour such as Pb loss, inheritance of older material or contamination/incorporation of common Pb, using the concordia diagram of Wetherill (1956).

5.2.1.1 Wetherill Concordia Diagram

The Wetherill concordia diagram is a plot of ^{207}Pb-^{235}U and ^{206}Pb-^{238}U ratios, with each ratio representing a specific age. The concordia curve thus represents the locus of points of ^{207}Pb-^{235}U *vs* ^{206}Pb-^{238}U ratios that have exactly the same age. The shape of the curve is due to the different half-lives of ^{235}U and ^{238}U.

The ^{207}Pb-^{235}U and ^{206}Pb-^{238}U ratios, determined by mass spectrometry have uncertainties, which are associated both with the measurement and also systematic uncertainties such as those associated with the U decay constants (Ludwig, 1980; Davis, 1982; Ludwig, 1998). Thus, a 2σ error ellipse is constructed around each sample point. As there are also small uncertainties in the U decay constants, each point of the concordia curve can be converted to its own error ellipse, which results in the transformation of a line into a band (Miller, 2006). This is generally only visible on highly precise U-Pb isotope dilution thermal ionisation mass spectrometry (ID-TIMS) analyses, as the scale of observation of the concordia curve for more imprecise LA-ICP-MS analyses means the concordia curve appears as a single line.

If a sample plots on top of the concordia curve/band, it is said to be a concordant analysis, otherwise it is referred to a discordant analysis. Data, which plot above the concordia curve/band are reversely discordant, whereas data plotting below are termed normally discordant analyses. Normal discordance is more commonly observed in zircon, whereas reverse discordance is very rare (Mattinson et al., 1996).

Igneous zircon grains, which record the eruption age of a volcanic ash should be represented by the youngest cluster of several concordant analysis on a Wetherill concordia diagram. Zircon grains, whose ellipses are not part of the cluster, most likely experienced residual Pb loss, inheritance of older cores, contamination with common Pb (or a combination of some or all of these processes) and typically result in discordant analyses (e.g. Bowring et al., 2006).

5.2.1.1.1 Pb Loss

Open system behaviour in zircon is most likely due to Pb loss, which is predominantly caused by the passage of Pb from radiation-damaged domains through crystal defects and fractures, as opposed to volume diffusion (Lee et al., 1997; Cherniak and Watson, 2001). In particular, U-rich zones, like the outer rims of zircon grains, are more prone to radiation-induced damage, resulting in a deficiency of Pb. Measured isotopic ratios will fell off the concordia curve, moving either towards the origin ($^{207}Pb/^{235}U = 0$ and $^{206}Pb/^{238}U = 0$) if the Pb loss event is recent, or towards the time of a prior thermal or alteration event, creating a discordant arrays of points

(Figure 5-1). The upper intersect of this line (a discordia regressed through these points) with the concordia curve, can indicate the true concordant age before Pb-loss (Miller, 2006).

5.2.1.1.2 Inherited Grains

The chemical and mechanical robustness of zircon crystals allows them to retain age information from prior geological events. These older zircon grains are called xenocrysts. Xenocrystic zircon grains can be incorporated into magmatic systems by assimilation of the country rock during magma generation, transport and/or eruption, and may remain undissolved in some magmas. The results of this recycling process may be demonstrated and visualised texturally by cathodoluminescence (CL) imaging, showing that older inherited cores (xenocrysts) act as seed nuclei and are overgrown by younger magmatic material (phenocryst rims). Reworking of volcanic ashes during deposition can also lead to the incorporation of pre-existing zircons of significantly older age (i.e. the xenocrysts are effectively detrital contamination). While an entirely inherited xenocryst still appears on the concordia diagram as a concordant analysis (Figure 5-1; purple ellipse and purple grain on concordia) polyphase grains (a xenocryst core plus phenocryst rim) yield an admixture of the two ages, plotting off the concordia curve/band. If there are only two age components and Pb-loss is absent, a mixing line can be defined (Figure 5-1; purple ellipses and green grains with purple cores on discordia). The lower concordia intercept would yield the igneous crystallisation age, while the upper intercept yields the age of the xenocrystic zircon. As it is more likely that xenocrysts of many different ages are present within one sample suite, and which also could have experienced Pb-loss to different degrees, these type of mixing-lines must be interpreted with great caution (Miller, 2006).

5.2.1.1.3 Common Pb Contamination

The assumption that all zircon grains only contain radiogenic Pb (Pb^{*}) produced by the *in situ* decay of U does not always hold. Zircon grains can incorporate non-radiogenic Pb, which is also called initial or common Pb, from micro-inclusions of minerals like apatite, feldspar, sulphides or incorporation of Pb from an external source along fractures (Bowring et al., 2006). Analyses of zircon grains containing a reasonable amount of common Pb plot on a sub-horizontal trend to the right of the concordia curve/band (Figure 5-1).

When abundant in a sample, the amount of common Pb can be measured based on its ^{204}Pb abundance as this Pb isotope is a non-radiogenic Pb isotope. Subsequently, a common Pb correction can be applied. As it is not possible to precisely measure ^{204}Pb in LA-ICP-MS U-Pb geochronology due to the small analyte signal and isobaric interference from ^{204}Hg in the carrier gas, a ^{207}Pb correction is employed (see section 2.2.1) and the isotopic composition of initial common Pb can be obtained either by analysis of cogenetic Pb-bearing, uranium-poor mineral phases such as feldspar, where such phases are present or by iterative Pb evolution models (e.g.

Stacey and Kramers, 1975). Ideally, measured ^{204}Pb signals are low and U-Pb ages are concordant or nearly concordant. In this case, common Pb corrections are not necessary. Otherwise, it has to be examined carefully if a common Pb correction should be applied, as it improves the concordance of the data on the one hand, but adversely affects the precision of the U-Pb dates on the other hand. For the samples of this study, no common Pb correction was applied.

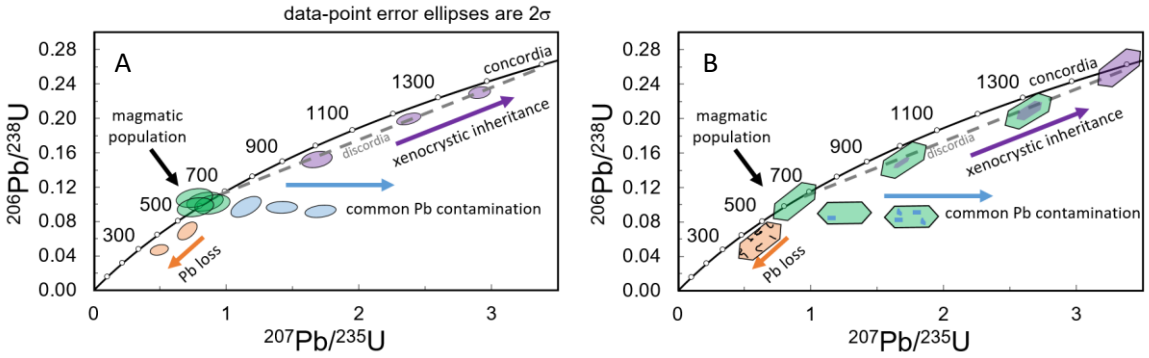

Figure 5-1: A) Schematic illustration of a Wetherill concordia diagram. A magmatic population of zircon grains (green ellipses) plot on the concordia. Analyses of zircon grains which experienced Pb loss (orange ellipse), plot below and to the right of the concordia curve, towards younger ages. Analyses result in an older age as soon as the laser ablation spot hits either parts of an inherited core or a detrital zircon grain (purple ellipses). Sometimes, analyses lie on a discordia, when varying proportions of the same core and overgrowth are analysed. Micro-inclusions can cause common Pb contamination in zircons. Grains incorporating common Pb plot on a sub-horizontal trend to the right of the concordia (blue ellipses). B) Appearance of zircon grains that produce the Wetherill concordia systematics shown in (A) Orange grain with fractures is a radiation damaged zircon grain, which experienced Pb loss. The purple area within the green grain represents an inherited core, while the purple grain is an older detrital zircon. Micro-inclusions (blue areas in green grain) can cause common Pb contamination in zircons.

5.2.1.2 Age Determinations

Concordia and weighted average concordia age diagrams are used to determine the eruption age of the tuff samples. The analytical technique for U-Pb zircon data acquisition is outlined in section 5.2.4. Before the U-Pb zircon data were plotted and calculated using Isoplot v. 3.7 (Ludwig, 2003), the data were examined using an in-house excel spreadsheet, which calculates single grain concordia ages along with 2σ errors and the probability-of-fit. The probability-of-fit is the measure of concordance of a grain. Analyses of zircon grains, which experienced residual Pb loss, are influenced by xenocrysts or incorporation of common Pb result most likely in discordant analyses, which leads to a probability-of-fit of zero. These analyses show dates clearly outside the 2σ error ellipse of the main cluster. Analyses with comparatively large analytical errors, which could be either due to low radiogenic/common Pb (Pb^*/Pb_c) ratios or a poor quality analysis (Bowring et al., 2006) are also excluded from the age determinations.

Using filtered data for age calculations, Isoplot can calculate single-grain concordia ages and their uncertainties. The weighted average (and associated uncertainty) of these single-grain concordia ages from a single population can then be calculated, along with the probability-of-fit of the overall age and the mean square of the weighted deviates (MSWD). The MSWD is used to aid the selection of analytical data for age calculation. It is a statistical parameter, which provides a

measure of the scatter of the data around the mean value and thus the 'coherence' of the data (York 1967, 1968) . An MSWD value of approximately one indicates that the scatter in the data can be attributed to analytical uncertainties alone (Wendt and Carl, 1991; Horstwood, 2008). This either means that there is a single age population of data and the analytical uncertainties are estimated correctly, or that if real age variation is present, it cannot be resolved within the precision of the individual analyses (Kalsbeek and Wendt, 1992). Values much less than one indicates that errors have been overestimated and thus, the scatter in the data is under dispersed (Horstwood, 2008). Data scatter for MSWD values greater than one can be overdispersed, indicating either that analytical uncertainties have been underestimated or that another source of scatter, like two or more populations of data, often called 'geological' scatter, is present (Horstwood, 2008).

However, there is a range of acceptable MSWD values as a function of sample size at 1σ and 2σ (Spencer et al., 2016), which is calculated using the $\sqrt{2/f}$ rule of Wendt and Carl (1991). The range of acceptable MSWD values at 1σ and 2σ is shown in Figure 5-2 and is used for quality control for this study.

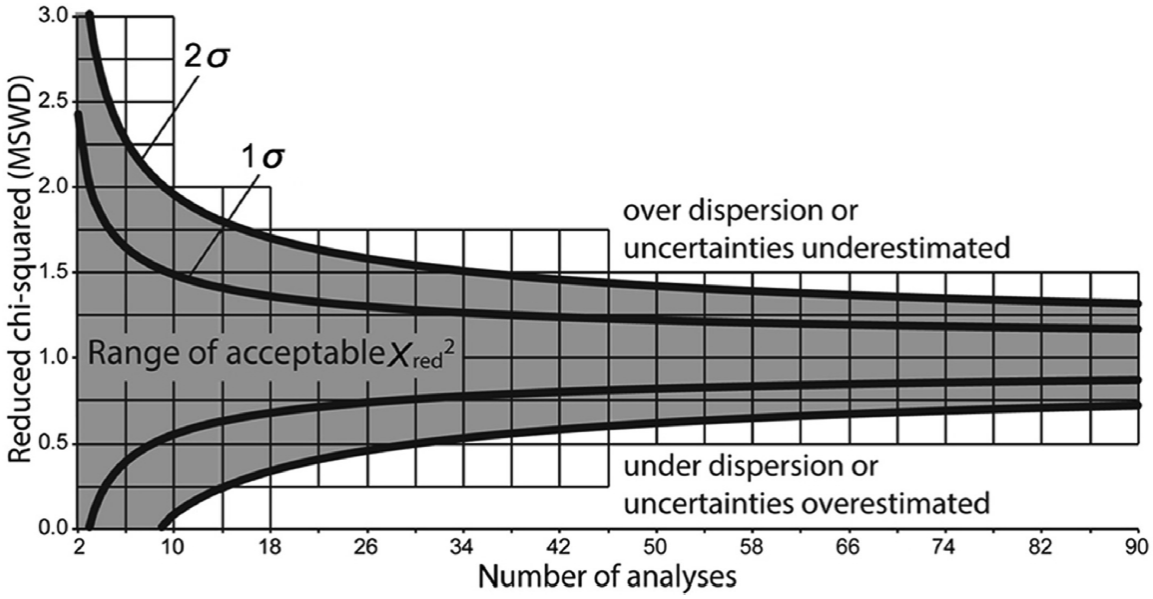

Figure 5-2: The mean square of weighted deviation (MSWD) provides a measure of the data scatter about the weighted mean zircon age for analysed samples. It is calculated using Isoplot v. 3.7 for the Irish Mississippian tuff samples of this study. Dark grey area shows acceptable MSWD values at 1σ and 2σ for a given number of analyses. From Spencer et al. (2016).

Ideally, a relatively large number of zircon dates should be obtained, whose analytical uncertainties (2σ error ellipse) overlap, to get MSWDs and probability-of-fits as close to one as possible. Only then it can confidently concluded that it is one zircon population, which stem from the same volcanic eruption.

Zircon grains can generally be clearly categorised as either primary magmatic grains, inherited grains, grains with big uncertainties, grains that suffered Pb loss or show common Pb

contamination. Incorporating any other zircon grains than primary magmatic grains in final concordia age calculations normally result in MSWD and probability-of-fit values greater than unity (i.e. geological scatter). However, sometimes it is less obvious which grains should be allocated to which category. A small data set with large amounts of ambiguous grains can therefore give different eruption ages, depending on the choice or classification of the zircons, with still reasonable MSWD and probability-of-fit values (see Figure 5-2 for accepted values). This data set was examined carefully and eleven out of 14 datable samples gave unique eruption ages (see section 5.3.1). The remaining three samples allowed the calculation of at least two different concordia ages with reasonable MSWD (0.29 – 2.1) and probability-of-fit values (0.13 – 0.98) for each sample (see Table 5-1). Sample Slievedart_3471/4_HK 194 even allows the calculation of either one or two magmatic populations. The deviations of zircon ages from the same sample is between 0.9 and 2.8 Ma for samples of this study. Calculated ages whose MSWD and probability-of-fit values are closest to unity for both concordia and weighted average mean age calculations are used herein.

Table 5-1: Concordia and weighted mean average U-Pb zircon ages, along with their mean square of weighted deviation (MSWD) and probability-of-fit values. Zircon grain classifications of these samples were ambiguous. Therefore, there are slightly different ages, depending on which zircon grains the calculations were based on. The number of zircon grains which were allocated to a specific group (Pb loss, common Pb input, inheritance, large uncertainties, primary magmatic) are shown as well. Green highlighted samples show best MSWD and probability-of-fit values and are thus used in this study.

Lab ID	Amount of zircons showing					final concordia U-Pb age (Ma)	MSWD	proba-bility-of-fit	weighted mean average age (Ma)	MSWD	proba-bility-of-fit
	Pb loss	common Pb input	inheri-tance	large uncer-tainties	eruption age						
HK 158	0	0	0	4	10	343.6 ± 4.5	0.84	0.66	343.2 ± 4.3	0.61	0.79
HK 158	0	0	0	0	14	346.4 ± 3.9	1.08	0.35	345.6 ± 3.8	1.07	0.38
HK 197	2	1	3	0	10	352.1 ± 3.	0.79	0.73	352.1 ± 3.8	1.3	0.23
HK 197	2	1	5	0	7	350.7 ± 3.3	0.63	0.86	350.8 ± 3.2	1.14	0.33
HK 194	4	6	4	0	8	359.7 ± 3.0	0.68	0.81	359.9 ± 3.9	1.2	0.29
HK 194	1	6	4	0	5	345.6 ± 3.5	0.50	0.87	345.5 ± 3.3	1.0	0.41
					6	361.0 ± 3.2	0.49	0.91	361.2 ± 3.2	0.72	0.61
HK 194	1	6	4	0	6	347.7 ± 3.2	0.88	0.55	346.9 ± 5.3	1.7	0.13
					5	361.9 ± 3.5	0.29	0.98	362.1 ± 3.4	0.36	0.84

5.2.2 U-Pb Apatite Geochronology

U-Pb apatite geochronology is also based on the decay of ^{238}U to ^{206}Pb and ^{235}U to ^{207}Pb, but apatite differs from zircon, in that apatite can accommodate a significant amount of initial Pb (also known as common Pb) in its crystal structure. This, together with low U, Th and Pb concentrations and laser-induced U-Th-Pb fractionation, creates challenges for accurate and precise apatite dating by LA-ICP-MS, compared to dating radiogenic Pb-bearing minerals like zircons. But there is considerable progress in LA-ICP-MS data reduction and matrix-matched standards, which overcomes these problems (e.g. Thomson et al., 2012; Chew et al., 2014). Two

sigma weighted mean uncertainties of 1-2% on Phanerozoic apatites are already achieved (Chew et al., 2011). The main limitations on the accuracy and precision of apatite age determinations is either the lack of a suite of cogenetic apatite grains, which define a well constrained linear array on a concordia diagram, or an inaccurate common Pb correction due to an inappropriate choice of initial Pb isotopic composition, which can be particularly acute for samples with high common Pb / radiogenic Pb ratios (Chew et al., 2011).

5.2.2.1 Common Pb Correction

Due to the incorporation of 'common Pb' as well as radiogenic Pb into the crystal lattice of apatite, apatite data have to be corrected for 'common Pb', which leads to more accurate and precise age determinations. The ^{204}Pb, ^{207}Pb and ^{208}Pb correction methods are commonly employed in the literature (e.g. Williams, 1998) . The ^{204}Pb correction method is normally used for U-Pb dating by high-precision ID-TIMS, as ID-TIMS allows the accurate measurement of ^{204}Pb, which is required. Due to ^{204}Pb interference by ^{204}Hg, it is challenging to get accurate measurements of ^{204}Pb using LA-ICP-MS. From the two remaining correction methods, the ^{207}Pb correction method is more common and is employed in this study. It requires precise measurement of ^{238}U/^{206}Pb and ^{207}Pb/^{206}Pb ratios and an appropriate choice of initial ^{207}Pb/^{206}Pb. When Pb-bearing, U-poor co-generic mineral phases like K-feldspar and plagioclase, which exhibit negligible ingrowth of radiogenic Pb, are present in a sample, the isotopic composition of initial common Pb can be estimated by analysing these mineral phases. Whenever suitable minerals are absent, like in this study, the initial ^{207}Pb/^{206}Pb ratio is typically calculated after the terrestrial Pb isotope evolution model of Stacey and Kramers (1975), using the estimated age of the sample (in this case Early Carboniferous). In both cases an uncertainty of 5% (2σ) is propagated on the initial ^{207}Pb/^{206}Pb ratios to the final age calculation (Chew et al., 2011).
Another method to determine the common Pb component is to use a Tera–Wasserburg concordia diagram on assumed co-genetic apatite grains (see section 5.2.2.3).

5.2.2.2 Tera-Wasserburg U-Pb Concordia Diagram

The Tera-Wasserburg type (Tera and Wasserburg, 1972) concordia diagram visualises, like the Wetherill concordia diagram, the concordance or discordance of a data set. As Tera-Wasserburg diagrams permit optimal visualisation of U-Pb data from low-U and high common Pb phases, it is employed for LA-ICP-MS U–Pb dating of apatite.
The x and y axis of the Tera-Wasserburg concordia diagram are the ^{238}U/^{206}Pb and ^{207}Pb/^{206}Pb ratios respectively, where the ^{207}Pb/^{206}Pb ratios of the concordia curve are determined by knowing the ^{238}U and ^{235}U decay constant and using the natural ^{238}U/^{235}U ratio of 137.88 (Steiger and Jäger, 1977). Samples, whose radiometric ages of the two independent decay schemes, ^{235}U

to ^{207}Pb and ^{238}U to ^{206}Pb are in agreement will plot on the concordia curve, whereas grains, which experienced open system behaviour like Pb loss, resetting events or common Pb incorporation, fall off the concordia.

As apatite grains typically contain a variable amount of common Pb, they will usually plot off the concordia. A suite of co-genetic apatite grains with a large spread in common Pb *vs* radiogenic Pb ratios would define a well constrained linear array (Chew et al., 2011). Where a regression line through these data points hit the y-axis, this determines the initial $^{207}Pb/^{206}Pb$ composition. Grains forming a different population build another linear array, revealing a different common Pb component. However, grains, which are discordant and do not build linear arrays indicate Pb loss or other open system behaviour. If a grain, which is not co-genetic, coincidentally plots on an array, it will be mistakenly regarded as a grain from the same population unless it exhibits some other characteristics (such as a different characteristic trace element chemistry).

5.2.2.3 Age Determinations

Apatite data from a sample are plotted on a Tera-Wasserburg concordia diagram, and if significant variability in U to total Pb (radiogenic plus common Pb) is evident then a linear regression is plotted through these analyses. Where this regression (or discordia) crosses the concordia at its lower intercept, this is interpreted as the age at which the apatite began to accumulate radiogenic Pb, called the lower intercept age. The y-intercept on the $^{207}Pb/^{206}Pb$ axis determines the common Pb-component. The better the spread of the discordant analyses is on the diagram, the more precise will be the intercept age. This approach also assumes that the U–radiogenic Pb data are concordant, which means having the same initial $^{207}Pb/^{206}Pb$ isotopic compositions (in the absence of common Pb) prior to the onset of radiogenic Pb ingrowth. Alternatively the initial isotopic composition can be obtained from the Stacey and Kramers (1975) model for crustal Pb evolution or from co-genetic Pb-bearing, U-poor mineral phases.

The initial common-Pb value for Tera-Wasserburg age calculations for all unknown tuff samples in this study is 0.86. The initial common-Pb values for apatite standards are 0.8681, 0.88198 and 0.8376 for the c. 473 Ma Madagascar, c. 523 Ma McClure and c. 31.44 Ma Durango age standards respectively.

Uranium-lead age determinations, which are based on an in-house excel spreadsheet use a ^{207}Pb-based, offline correction method, and assume an initial Pb composition from Stacey and Kramers (1975).

Thus, final ages are either weighted averages of common Pb corrected ages from an in-house excel-spreadsheet or a Tera-Wasserburg concordia intercept age anchored through common Pb. The MSWD value is used again for quality control of the obtained ages (see section 5.2.1.2; Figure 5-2).

5.2.3 Zircon and Apatite Separation

All zircon and apatite separation and concentration procedures were undertaken using the facilities at the Department of Geology, Trinity College Dublin.

Thirty-six tuff samples were targeted based on their availability and stratigraphic occurrence. Some samples had to be completely crushed to obtain enough material for trace element analyses. If available, a representative amount of samples (> three samples) from each stratigraphic level was chosen. These samples were crushed using a hammer and anvil, before they were lightly disaggregated using a mortar and pestle. Following disaggregation, samples were sieved to 300 µm. The < 300 µm fraction was subsequently processed for zircon and apatite. Samples were then washed several times in a gold pan in water to remove the clay fractions and were then dried in an oven at 40°C. At this stage, samples were ready for magnetic separation using a Frantz LB-1 magnetic separator. Zircon and apatite are routinely selected from the least paramagnetic fraction and further concentrated using sodium-polytungstate (ρ = 2.7-2.8 g/cm^3). This technique separates zircon (ρ = 4.6-4.7 g/cm^3) and apatite (ρ = 3.2 g/cm^3) from the matrix clay minerals that comprise the bulk of the Irish Mississippian tuff samples investigated (e.g. kaolinite ρ = 2.6 g/cm^3; illite ρ = 2.6-2.9 g/cm^3). All the zircon and apatite grains were hand-picked from each sample in alcohol under high magnification using a Nikon SMZ 1500 binocular microscope to ensure that the clearest, most inclusion-free grains were chosen. Subsequently, they were mounted on 2.5 cm diameter epoxy disks and polished to approximately half thickness. Therefore, the surfaces of the grains were polished using a diamond grit, followed by a 6 µm and finally 1 µm polishing paste.

Out of the 36 processed tuff samples, 18 samples yielded zircons and 14 samples yielded apatites (Table 5-2). The best zircon recovery was in samples from the Rathdowney Trend, as all of the investigated samples yielded zircons, whereas the sample yield from Navan samples was much lower, with only 25% of these samples (3/12) yielding zircons. Zircon recovery for samples from the Stonepark area was 62.5% (5/8) and for the Slievedart area 55.6% (5/9).

Twenty-five percent of the investigated samples from the Navan area (3/12), 62.5% (5/8) of the samples from the Stonepark area and 66.67% of the samples from the Slievedart area (6/9) contained at least one apatite grain. Thus, 14 samples in total produced apatite mineral grains of which seven produced a sufficient amount of apatite to permit age calculations.

Table 5-2: The total number of recovered zircon and apatite grains of Irish Mississippian tuff samples along with their stratigraphic position.

	Sample ID	Amount of recovered zircon grains	Amount of recovered apatite grains	Stratigraphic Position
TARA DEEP	_N-2444_HK 163	0	0	TBU-1; Marker Tuff
	_N-2444_HK 162	0	0	TBU-1; Marker Tuff
	_N-2415_HK 161	0	0	TBU-1; Marker Tuff
	_N-2457_HK 232	0	0	TBU-1; Marker Tuff
	_N-2479_HK 235	0	1	TBU-1; Marker Tuff
	_N-2480_HK 236	0	0	TBU-1; Marker Tuff
	_N-2444_HK 158	14	1	TBU-2; Upper Tuff
	_N-2444_HK 159	0	5	TBU-2; Lower Tuff
NAVAN WEST	_N-2441_HK 156	0	0	Tober Colleen Formation
	_N-2441_HK 157	0	0	Tober Colleen Formation
	_N-2441_HK 155	7	0	Tober Colleen Formation
	_N-2441_HK 169	10	0	Waulsortian Equivalent
LISHEEN	_LK-1722_HK 180	29	0	Nodular Micrite Unit
	_LK-1040_HK 182	26	0	Nodular Micrite Unit (S-ABL)
	_mine sample_HK 203	49	0	Nodular Micrite Unit (S-ABL)
	_LK-2180_HK 181	2	0	Nodular Micrite Unit (S-ABL)
RAPLA	_3667-04_HK 185	25	0	Upper Calcarenite Member
STONEPARK	_G11-2654-01_HK 211	35	25	Lough Gur Formation
	_G11-2654-01_HK 212	9	11	Nodular Micrite Unit
	_G11-2638-01_HK 197	16	0	Nodular Micrite Unit
	_G11-2638-01_HK 198	0	0	Nodular Micrite Unit
	_G11-2638-02_HK 207	7	2	Nodular Micrite Unit
	_G11-2638-02_HK 208	12	0	Nodular Micrite Unit
	_G11-2638-02_HK 209	0	1	Nodular Micrite Unit
	_G11-450-02_HK 210	0	8	Nodular Micrite Unit
SLIEVEDART	_3470/15_HK 190	30	3	Kilbryan Limestone Formation
	_3471/4_HK 194	22	6	Kilbryan Limestone Formation
	_3470/15_HK 189	0	0	Kilbryan Limestone Formation
	_3471/4_HK 195	0	0	Kilbryan Limestone Formation
	_3470/15_HK 237	0	22	Kilbryan Limestone Formation
	_3471/4_HK 238	0	21	Kilbryan Limestone Formation
	_3470/15_HK 188	24	0	Kilbryan Limestone Formation
	_3471/4_HK 193	23	1	Kilbryan Limestone Formation
	_3471/4_HK 192	23	0	Kilbryan Limestone Formation
	_3470/15_HK 187	0	1	Oakport Limestone Formation
	_3471/4_HK 191	0	0	Oakport Limestone Formation

5.2.4 Analytical Technique - Zircon

As magmatic zircon commonly shows pronounced internal zoning, polished grain mounts were imaged under a scanning electron microscope (SEM) using backscattered-electron (BSE) and CL imaging prior to LA-ICP-MS analysis. The zoning reflects compositional variations, particularly in trace elements (CL) and major-minor elements (BSE). These textural images serve as a guide for positioning laser spots during LA-ICP-MS analysis with the aim to avoid small inherited cores, mineral and melt inclusions.

All U-Pb and trace element spot analyses were simultaneously acquired using a Teledyne Photon Machines Analyte Excite 193 nm ArF laser-ablation system with a Helex two-volume

ablation cell, coupled to an Agilent 7900 ICP-MS, located in the Centre for Microscopy and Analysis (CMA)/iCRAG lab, Trinity College Dublin, Ireland. Laser ablation was performed using a 24 µm spot, a repetition rate of 15 Hz and a fluence of 2.5 J/cm^2. Ablated material was transported into the ICP-MS by He carrier gas (0.65 l/min), mixed with Ar nebulizer gas (0.7 l/min). A small volume of N_2 (c. 6 ml/min) was added to enhance signal sensitivity and reduce the oxide formation. Thirteen isotopes (^{31}P, ^{47}Ti, ^{49}Ti, ^{91}Zr, ^{175}Lu, ^{178}Hf, ^{202}Hg, ^{204,206,207,208}Pb, ^{232}Th and ^{238}U) were acquired for all U-Pb analyses. The total sweep cycle time was 0.309 s. All instrumental parameters and dwell times are shown in Table 5-3.

Silicate glass standard NIST SRM 612 was used for tuning the mass spectrometer to obtain a Th/U ratio of unity. Four natural zircons were used as standards because of the difficulty in inserting Pb into synthetic crystals. Zircon 91500 (^{206}Pb/^{238}U age = 1062.4 ± 0.4 Ma, 2σ; ^{207}Pb/^{206}Pb age = 1065.4 ± 0.3 Ma, 2σ; Wiedenbeck et al., 1995) was used as the primary standard for U-Pb dating. GZ7 (^{206}Pb/^{238}U age = 530.26 ± 0.05 Ma, 2σ; Nasdala et al., 2018), WRS1348 (^{206}Pb/^{238}U age = 526.26 ± 0.7 Ma, 2σ; Pointon et al., 2012) and Plešovice (^{206}Pb/^{238}U age = 337.13 ± 0.37 Ma, 2σ; Sláma et al., 2008) were treated as unknowns for quality control of the analyses. Conventional standard-sample bracketing was used for data acquisition. Each analytical session started and finished with four analyses of NIST SRM 612 glass standards, followed by zircon 91500, GZ7, WRS1348 and Plešovice, which were analysed five times each. The same block of standards was measured in the middle and at the end of each session. One NIST SRM 612 standard, three 91500, three GZ7, WRS1348 and three Plešovice zircon standards were analysed every 15 unknown zircon grains.

5.2.4.1 Data Reduction

Conventional standard-sample bracketing with matrix-matched natural zircon standards, enables samples to be corrected for elemental mass bias, intra-session analytical drift and downhole isotopic fractionation in Iolite. Gas blank corrections were done first by introducing a baseline, followed by the intra-session analytical drift correction using the 91500 zircon standard (^{206}Pb/^{238}U age = 1062.4 ± 0.4 Ma, 2σ; ^{207}Pb/^{206}Pb age = 1065.4 ± 0.3 Ma, 2σ; Wiedenbeck et al., 1995), which serves as the primary standard. To avoid accidental analysis of titanite, monazite or apatite inclusions, zircon grains with high Ti and P concentrations were discarded. Corrected U-Pb data were then processed using the VizualAge data reduction scheme of the Iolite software package (Paton et al., 2011) with the 91500 zircon standard used as the primary standard. The total beam served as the index channel. Downhole fractionation and instrumental mass discrimination for ^{207}Pb/^{235}U and ^{206}Pb/^{238}U ratios were corrected by normalisation to the 91500 zircon standard. Common Pb correction was not performed due to low ^{204}Pb counts on the mass spectrometer and the concordance or near-concordance of U-Pb ages.

5.2.4.2 Age Calculations

Exported $^{207}Pb/^{235}U$, $^{206}Pb/^{238}U$ and $^{207}Pb/^{206}Pb$ ratios and their associated propagated errors, generated by Iolite, were entered into an in-house excel spreadsheet to calculate single grain ages and the probability of concordance, which facilitates distinguishing of concordant and discordant grains. Subsequently, only the Iolite corrected $^{207}Pb/^{235}U$ and $^{206}Pb/^{238}U$ ratios of concordant grains, which neither suffered Pb loss, nor incorporated common Pb or inherited cores are used for age calculations using the Isoplot program v. 3.75 (Ludwig, 2003). Uncertainty ellipses on the Wetherill concordia diagrams are drawn at the 2σ confidence level. They include decay constant uncertainties. Final concordant ages are also at the 2σ level. The MSWD value and the accompanying probability-of-fit is shown as well. They reflect the equivalence and concordance of the data and thus take the data scatter into account. Weighted age averages are conducted in Isoplot, using the single grain concordia ages from the in-house spreadsheet. Each vertical bar represent dates from single grains of zircon including its 2σ analytical uncertainty, while the uncertainties of the weighted average ages of one population are quoted at the 95% confidence level, which corresponds to 1.96σ. Weighted average ages are shown for comparison and are always within analytical uncertainty of corresponding Wetherill concordia diagrams.
Even with careful zircon selection and preparation, samples still contained zircons which had experienced either Pb-loss, incorporation of common Pb or displayed signs of inheritance. Thus, although exclusively concordant grains were used for age determinations, all grains are plotted on Wetherill concordia and weighted average age diagrams. There are two exceptions; very old inherited grains and grains with very large uncertainty ellipses were not plotted on Wetherill concordia diagrams, which allows showing a more detailed portion of the concordia containing analyses close to the eruption age. All grains employ the same colour code. These are:

- igneous zircon grains, which record eruption ages
- zircon grains which experienced residual Pb loss
- zircon grains with incorporation of common Pb
- xenocrystic / inherited zircon grains

Dark grey bars in weighted average age diagrams represent grains, whose errors were too big and thus were not plotted on the Wetherill concordia diagrams.

5.2.4.2.1 Standards

Zircon ages were obtained during four analytical sessions. Five hundred and twenty-nine analyses on four different zircon standards were conducted (see Appendix 2, Table A2 - 1). The mean concordia ages from the secondary standard Plešovice and WRS1478 varied in between each session, ranging from 335.1 ± 1.2 Ma (2σ, n = 13, MSWD = 0.69) to 338.8 ± 2.8 Ma (2σ, n = 12, MSWD = 0.67) (Figure 5-3A-D) and from 522.8 ± 2.6 Ma (2σ, n = 16, MSWD = 1.03) to

526.9 ± 2.2 Ma (2σ, n = 43, MSWD = 0.43) (Figure 5-3E-H), respectively. Thus, over the whole analytical period, the analysed ages of both secondary standards are within 1% of their recommended ages, which are 337.13 ± 0.37 Ma for Plešovice (Sláma et al., 2008) and 526.26 ± 0.7 Ma for WRS1348 (Pointon et al., 2012). Mean concordia ages of GZ7 for the four sessions are between 534.3 ± 2 Ma (2σ, n = 10, MSWD = 0.53) and 540.1 ± 1.8 Ma (2σ, n = 38, MSWD = 0.53) (Figure 5-3 I-L), which is between 0.8 and 1.8% older than the recommended age of 530.36 ± 0.05 Ma for GZ7 (Nasdala et al., 2018).

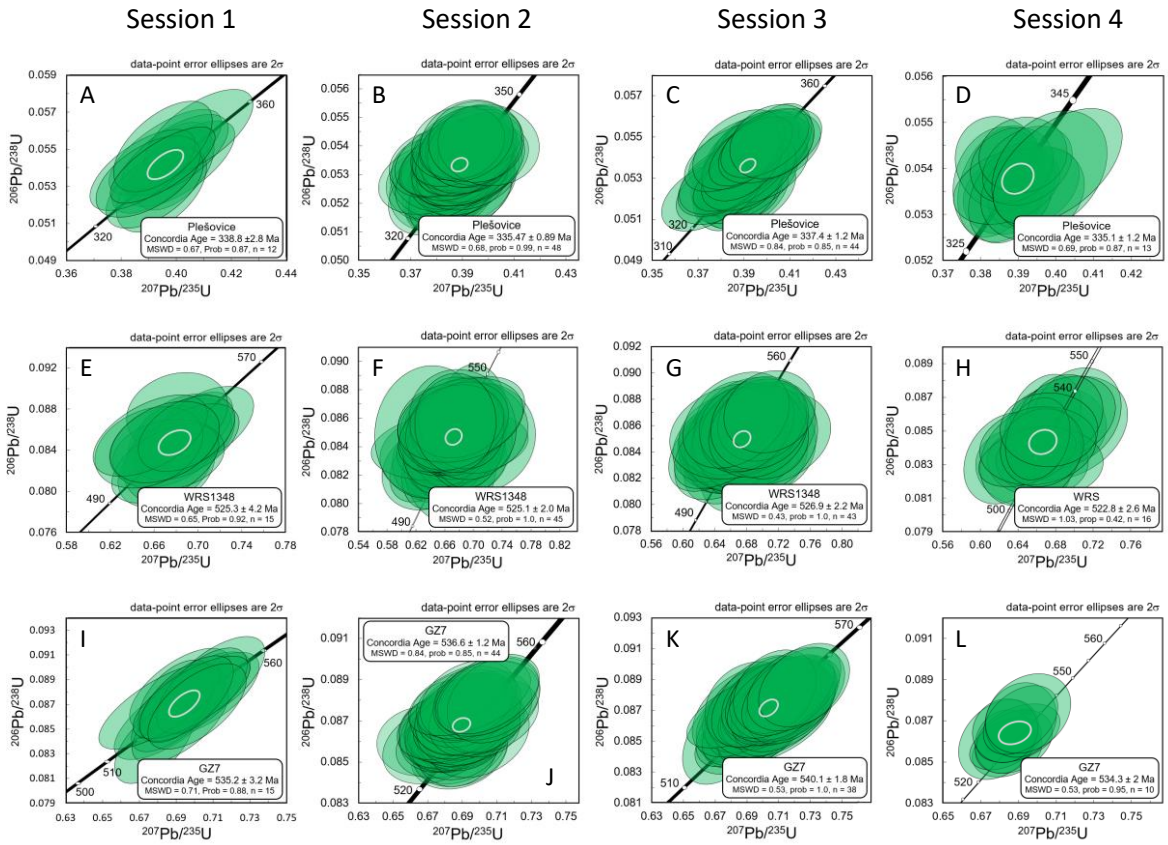

Figure 5-3: Concordia ages from three different zircon standards; Plešovice, megacrysts from an alkaline granulite (A-D), WRS1348, an in-house zircon standard (E-H) and GZ7, a gemstone specimen from a placer deposit (I-L). They were used as secondary standards during four different analytical sessions. The concordant analyses of each zircon standard of each session cluster tightly together. All U-Pb zircon ages are in good agreement with recommended values.

5.2.5 Analytical Technique - Apatite

Examination under CL revealed no obvious chemical zoning. Subsequently, samples were analysed using an Agilent 7900 ICP-MS, in combination with a Teledyne Photon Machines Analyte Excite 193 nm ArF laser-ablation system with a Helex two-volume ablation cell, located in the CMA/iCRAG lab, Trinity College Dublin, Ireland. He carrier gas (0.65 l/min) was split evenly between the sample chamber and the 'cup'. The enhancement of signal sensitivity and the reduction of oxide formation was achieved by adding N_2 (6 ml/min). Ar nebulizer gas (0.7 l/min) was introduced to the sample-gas mixture via an in-house smoothing device.

A total of 29 isotopes were analysed in all apatite grains, which includes ^{43}Ca, ^{202}Hg, common trace elements in apatite (^{35}Cl, ^{51}V, ^{55}Mn, ^{57}Fe, ^{88}Sr, ^{89}Y, ^{90}Zr), the REEs (^{139}La, ^{140}Ce, ^{141}Pr, ^{146}Nd, ^{147}Sm, ^{153}Eu, ^{157}Gd, ^{159}Tb, ^{163}Dy, ^{165}Ho, ^{166}Er, ^{169}Tm, ^{172}Yb, ^{175}Lu) and the six isotopes ($^{204, 206, 207, 208}Pb$, ^{232}Th ^{238}U), commonly employed in U–Th–Pb geochronology. The natural $^{238}U/^{235}U$ ratio of 137.88 was used to calculate ^{235}U. ^{43}Ca was employed as an internal standard for the calibration of analyses for trace element concentrations and ^{202}Hg was used to monitor interferences on the ^{204}Pb peak by ^{204}Hg in the argon gas supply. Laser ablation was performed using a 36 µm laser spot, a 12 Hz laser repetition rate and a fluence of 2.25 J/cm^2. The dwell time on each element is between 0.005 and 0.085 s, resulting in a total sweep cycle time of 0.515 s. Dwell times, machine conditions and protocols are listed in Table 5-3.

Data were collected in conventional standard-sample bracketing mode. Thus, three measurements of NIST SRM 612 glass, followed by four measurements each of the primary Madagascar apatite standard and the secondary standards McClure Mountain and Durango apatite were taken at the beginning, in the middle and at the end of each sample run. One measurement of NIST SRM 612, and three measurements each of the three natural apatite standards Madagascar, McClure and Durango were taken after every 15 analyses of unknown apatite grains as a quality control to monitor and subsequently correct for elemental mass bias, intra-session analytical drift and downhole isotopic fractionation.

Table 5-3: Laser and mass spectrometer conditions and protocols for LA-ICP-MS U-Pb and trace element analyses for Irish Mississippian tuff samples. Samples were analysed in the Centre for Microscopy and Analysis/iCRAG lab in Trinity College Dublin, Ireland.

	Zircon	Apatite
Laser parameters		
Instrument	Photon Machines Analyte ArF Excimer	
Wavelength	193 nm	
Washout	9 s	12 s
Fluence	2.5 J/cm^2	2.25 J/cm^2
energy setpoint	4.5 mJ	4.5 mJ
Shot count	305	300
Laser repetition rate	15 Hz	12 Hz
Spot size (diameter)	24 µm	36 µm
ICP-MS parameters		
Instrument	Agilent 7900	
Plasma RF power	1500 W	
Gas flows		
Carrier gas	0.65 L/min He	
Nebulizer gas	0.7 L/min Ar	
Analysis protocol		
Sampling period (s)	0.309	0.515

Dwell times (s)				
	^{175}Lu ^{178}Hf	0.0075	^{147}Sm	0.0075
	^{31}P ^{47}Ti ^{49}Ti	0.005	^{89}Y ^{139}La ^{140}Ce ^{141}Pr	0.005
	^{91}Zr	0.007	^{146}Nd ^{202}Hg $^{204, 208}$Pb ^{232}Th	0.005
	^{202}Hg	0.01	^{43}Ca ^{90}Zr ^{153}Eu ^{157}Gd ^{159}Tb	0.01
	^{204}Pb ^{208}Pb ^{232}Th	0.018	^{163}Dy ^{165}Ho ^{166}Er ^{169}Tm ^{172}Yb	0.01
	^{238}U	0.045	^{175}Lu	0.015
	^{206}Pb	0.055	^{35}Cl	0.02
	^{207}Pb	0.085	^{51}V ^{55}Mn ^{57}Fe ^{88}Sr ^{238}U	0.075
			$^{206, 207}$Pb	0.085

5.2.5.1 Data Reduction – U-Pb Apatite Ages

Data were reduced using the Iolite software. A baseline was first defined which allows for gas blank corrections. Intra-session instrument drift, which is a change in elemental sensitivity with time is corrected for by introducing a linear fit through all primary reference standards (Madagascar apatite). To ensure that only apatite grains were analysed, ^{43}Ca and ^{90}Zr were monitored, discarding any grains with high ^{90}Zr concentrations.

The corrected isotope data were then processed using VizualAge_UcomPbine, a modified version of the VizualAge data reduction scheme of Petrus and Kamber (2012) for the Iolite software package (Paton et al., 2011), that accounts for the presence of common Pb in the primary age standard materials (Chew et al., 2014). For U-Pb apatite geochronology in this study, the 473.5 ± 0.7 Ma (2σ) U-Pb Madagascar apatite standard (Thomson et al., 2012) was used as the primary reference material and ^{43}Ca as the index channel. All data is corrected for downhole fractionation and for intra-session instrument drift before a ^{207}Pb correction was applied, which allows the correction for common Pb. The fixed initial ^{206}Pb/^{207}Pb ratios used for Madagascar, Durango and McClure are

0.8681, 0.8376 and 0.88198, respectively. An estimated initial $^{206}Pb/^{207}Pb$ ratio of 0.86 ± 0.02 was used for all unknown samples, as this number is a reasonable approximation for the Stacey & Kramers (1975) Pb isotopic composition for the upper crust during the Palaeozoic.

The McClure Mountain apatite ($^{207}Pb/^{235}U$ TIMS age of 523.51 ± 1.47 Ma; Schoene and Bowring, 2006) and Durango apatite (31.44 ± 0.18 Ma; McDowell et al., 2005) were employed as secondary standards and processed as unknowns, which allows the verification and the accuracy of the method in each session and to approximate the behaviour of the unknowns. If resulting ^{207}Pb corrected ages for primary and secondary standards are within published values, the analyses as well as data reduction and analytical session is viewed as successful.

Exported isotopic ratios, which are subsequently used for concordia age and weighted average age calculations are not ^{207}Pb corrected and are listed in Table A2 - 2, Appendix 2.

5.2.5.2 Age Calculations

An in-house excel-spreadsheet calculates the final ^{207}Pb corrected ages for every single apatite grain based on the exported $^{207}Pb/^{206}Pb$ and $^{238}U/^{206}Pb$ ratios and an iterative ^{207}Pb correction using the Stacey and Kramers (1975) crustal Pb-isotope evolution model. Grains, which either reveal age uncertainties > 25% or > 100 Ma at the 2σ level or are well outside the samples' average age were neither included in weighted mean age calculations, nor in anchored Tera–Wasserburg concordia ages, using the Isoplot program v. 3.75 (Ludwig, 2003).

Tera-Wasserburg concordia ages employ the corrected $^{207}Pb/^{206}Pb$ and $^{238}U/^{206}Pb$ ratios, along with their propagated 2σ uncertainties and associated error correlation. The intercept age is calculated by placing a regression line through the initial $^{207}Pb/^{206}Pb$ ratio and multiple data from analysed grains. The initial $^{207}Pb/^{206}Pb$ for McClure, Durango and unknown tuff samples are 0.88198, 0.8376 and 0.86, respectively. Error ellipses in Tera-Wasserburg concordia diagrams are drawn at the 2σ confidence level and include decay constant uncertainties. Anchored Tera-Wasserburg concordia ages are also reported with 2σ uncertainties. On ^{207}Pb-corrected weighted average date plots, each vertical bar represent dates from single grains of apatite including its 2σ analytical uncertainty. These ages are based on the single grain age calculations from the in-house excel-spreadsheet. The uncertainties of the weighted average ages of one population are quoted at the 95% confidence level. Weighted averages of the ^{207}Pb corrected ages are shown for comparison and are always similar to Tera-Wasserburg concordia intercept ages anchored through common Pb (Figure 5-4, Figure 5-12).

Grains treated as a single population on Tera-Wasserburg concordia have MSWD values close to one. To get reasonable MSWD values at 2σ uncertainties, the amount of analysed grains is ideally at least 30 (Figure 5-2). As all samples yielding only a few apatite grains (one to twenty-five), most of them have poor MSWDs and large uncertainties. When it was only possible to obtain one or

two apatite grains, ages were only produced as ^{207}Pb-corrected weighted average ages using the in-house excel spreadsheet and no Tera-Wasserburg intercept ages were calculated.

5.2.5.2.1 Standards

One hundred and thirty-nine analyses were undertaken during two different experiments on the apatite standards Madagascar, McClure and Durango (see Appendix 2, Table A2 - 2). Both, the anchored Tera-Wasserburg intercept age for McClure (501.1 ± 3.8 Ma; 95% conf., n = 16, MSWD = 1.4) and the weighted average age (499.7 ± 4.8 Ma; 95% conf., n = 16, MSWD = 1.6) (Figure 5-4A, B) from the first experiment are slightly beyond the analytical uncertainty and is 4.5% younger than its reference age of 523.5 ± 1.47 Ma (Schoene and Bowring, 2006). Both ages from the second experiment are well within its reference age (Figure 5-4C, D).
The anchored Tera-Wasserburg intercept age for Durango and the weighted average age of the first experiment are 29.8 ± 1 Ma (95% conf., n = 26, MSWD = 1.3) and 29.4 ± 1.1 Ma (95% conf., n = 25, MSWD = 1.8) (Figure 5-4C, D) and thus only 1.47 and 2.43%, respectively, outside analytical uncertainty of the recommended age of McDowell et al. (2005), which is 31.44 ± 0.18 Ma (95% conf.). The anchored Tera-Wasserburg intercept age for Durango of the second experiment is only 0.22 Ma outside analytical uncertainty of the recommended age, while the weighted average age is well within analytical uncertainty of its reference age (Figure 5-4G, H).

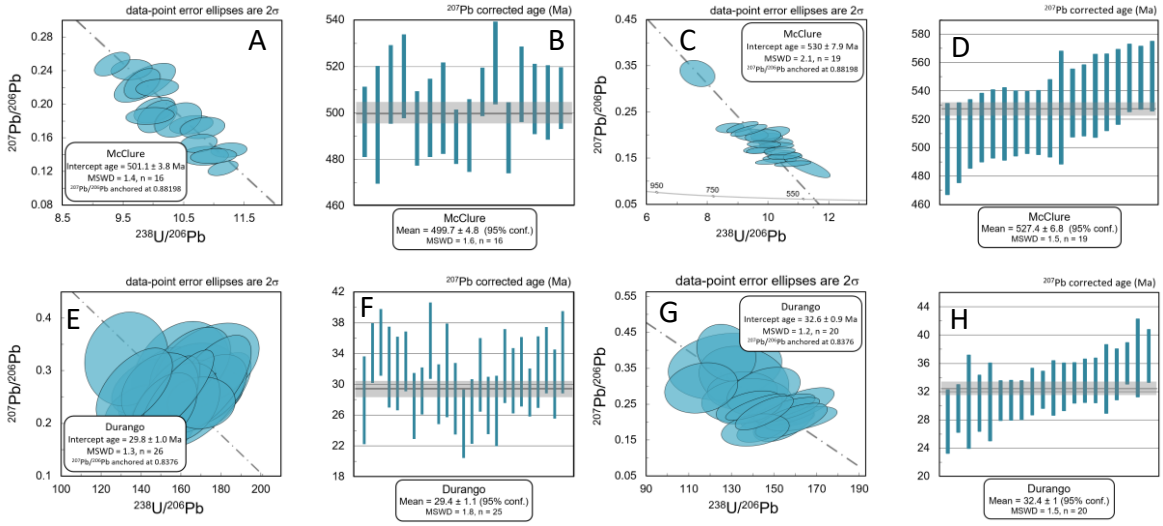

Figure 5-4: Anchored Tera-Wasserburg intercept and weighted average mean ages for McClure (A-D) and Durango (E-H) apatite standards. Bars represent ^{207}Pb-corrected dates from single grains of apatite with uncertainties at 2σ. The horizontal line through the middle of the population represents the weighted average mean. The light grey bar indicates its uncertainty at a 95% confidence level.

5.2.5.3 Data Reduction – Trace Elements

The Iolite Trace Element reduction scheme was applied for trace element analysis. Element concentrations were obtained through calibration of the relative element sensitivities using NIST SRM 612 standard glass as the primary reference material and ^{43}Ca as the index channel. Although glass is not matrix-matched to apatite, the data still serve as a good approximation for the absolute element concentrations of the apatite samples (Chew et al., 2011). The reference data for the NIST SRM 612 calibration standard glass are from Jochum et al. (2011). A crushed aliquot of a well characterised crystal of Durango apatite (e.g. Chew et al., 2016) was used as a secondary standard.

5.3 Results

5.3.1 U-Pb Zircon Ages

Four hundred and fifty-one analyses on 381 zircon grains were undertaken on 18 different tuff samples from four different regions (Navan, Rathdowney Trend, Stonepark, Slievedart) in central Ireland (see Appendix 2, Table A2 - 1). One hundred and eighty-eight grains yielded 16 sample concordia ages (Figure 5-5 to Figure 5-9). Table 5-4 summarises the results for these samples, including MSWD and probability-of-fit values for the calculated concordia ages and the number of magmatic zircons that these ages are based on along with the number of zircons that were discarded due to Pb loss, common Pb contamination, inheritance or large analytical uncertainties. Additionally, it is shown if the calculated U-Pb zircon ages equals the assumed biostratigraphic ages as well as an assessment of the quality of the Irish Mississippian zircon ages.

Table 5-4: Mean square of the weighted deviates (MSWD) and probability-of-fit values for the calculated concordia ages of 18 different tuff samples from Navan, the Rathdowney Trend, Stonepark and Slievedart) are listed along with the number of magmatic zircon and the number of zircons that were discarded due to Pb loss, common Pb contamination, inheritance or large analytical uncertainties. An assessment if the calculated U-Pb zircon ages of the tuff samples match the biostratigraphic age of their host rocks and the quality of the Irish Mississippian zircon ages are shown as well.

	Sample ID		Amount of zircons showing				Final concordia U-Pb age (Ma)	MSWD	Propability-of-fit	Stratigraphic Position	Zircon age equals strat. age?	Quality
		Pb loss	common Pb input	inheritance	Large uncertainty	eruption age						
	_N-2444_HK 158	0	0	0	0	14	346.4 ± 3.9	1.08	0.35	TBU-2; Upper Tuff	yes	good
	_N-2441_HK 155	1	2	1	0	3	348.7 ± 3.0	0.92	0.46	Tober Colleen Formation	yes	bad
	_N-2441_HK 169	0	10	0	0	10	342 ± 2.7	1.03	0.42	Waulsortian Equivalent	no	good
	_LK-1722_HK 180	4	5	7	0	13	344.8 ± 2.1	0.72	0.84	Nodular Micrite Unit	no	good
	_LK-1040_HK 182	6	7	5	0	8	346.6 ± 2.5	0.47	0.95	Nodular Micrite Unit (S-ABL)	no	OK
	_mine sample_HK 203	0	2	11	0	36	349.6 ± 1.5	0.71	0.97	Nodular Micrite Unit (S-ABL)	yes	very good
	_LK-2180_HK 181	0	0	2	0	N/A	N/A	N/A	N/A	Nodular Micrite Unit (S-ABL)	N/A	N/A
	_3667-04_HK 185	0	12	2	0	11	340.1 ± 2.3	0.63	0.9	Upper Calcarenite Member	no	good
	_G11-2654-01_HK 211	5	8	7	0	15	348.2 ± 2.4	0.68	0.9	Lough Gur Formation	yes	good
	_G11-2654-01_HK 212	2	2	1	0	4	350.3 ± 4.3	0.65	0.71	Nodular Micrite Unit	yes	good
	_G11-2638-01_HK 197	2	1	6	0	7	350.7 ± 3.3	0.63	0.86	Nodular Micrite Unit	yes	good
	_G11-2638-02_HK 207	0	0	7	0	N/A	N/A	N/A	N/A	Nodular Micrite Unit	N/A	N/A
	_G11-2638-02_HK 208	0	0	12	0	N/A	N/A	N/A	N/A	Nodular Micrite Unit	N/A	N/A
	_3470/15_HK 190	2	8	1	6	13	358.1 ± 3.0	0.67	0.89	Kilbryan Limestone Formation	no	good
	_3471/4_HK 194_pop 1	1	6	4	0	5	345.6 ± 3.5	0.50	0.87	Kilbryan Limestone Formation	yes	OK
	_3471/4_HK 194_pop 2	1	6	4	0	6	361.1 ± 3.2	0.49	0.91	Kilbryan Limestone Formation	no	OK
	_3470/15_HK 188	0	5	4	8	15	347.2 ± 2.9	0.65	0.92	Kilbryan Limestone Formation	yes	good
	_3471/4_HK 193	2	3	1	0	16	345.4 ± 1.8	0.61	0.95	Kilbryan Limestone Formation	yes	good
	_3471/4_HK 192	3	7	1	0	12	347.7 ± 2.2	0.85	0.67	Kilbryan Limestone Formation	yes	good

5.3.1.1 Tara Deep

Nine tuff samples from Tara Deep were investigated for zircons. The tuff layers from drill cores N-2415 (sample HK 161), N-2457 (sample HK 232), N-2479 (sample HK 235) and N-2480 (sample HK 236) did not yield any zircons. Furthermore, no zircons were found in the first (sample HK 159; Lower Tuff) and third (Marker Tuff; sample HK 163, bottom of layer; sample HK 162, top of layer) tuff layer from drill core N-2444. However, the second tuff horizon (sample HK 158; Upper Tuff, from the New Thin Bedded Unit) yielded a zircon U-Pb concordia age of 346.4 ± 3.9 Ma and a weighted average mean age of 345.6 ± 3.8 Ma (Figure 5-5A - C), which is close to the presently estimated age for the Tournaisian-Viséan boundary (346.7 Ma; e.g. Aretz et al., 2020). However, this age comprises four zircon grains with relatively high analytical uncertainties. Therefore, they can or cannot be included in the age determination. If they are excluded, sample Tara Deep_N-2444_HK 158 yield a concordia age of 343.6 ± 4.5 Ma and a weighted average mean age of 343.2 ± 4.3 Ma (Figure 5-5D, E).

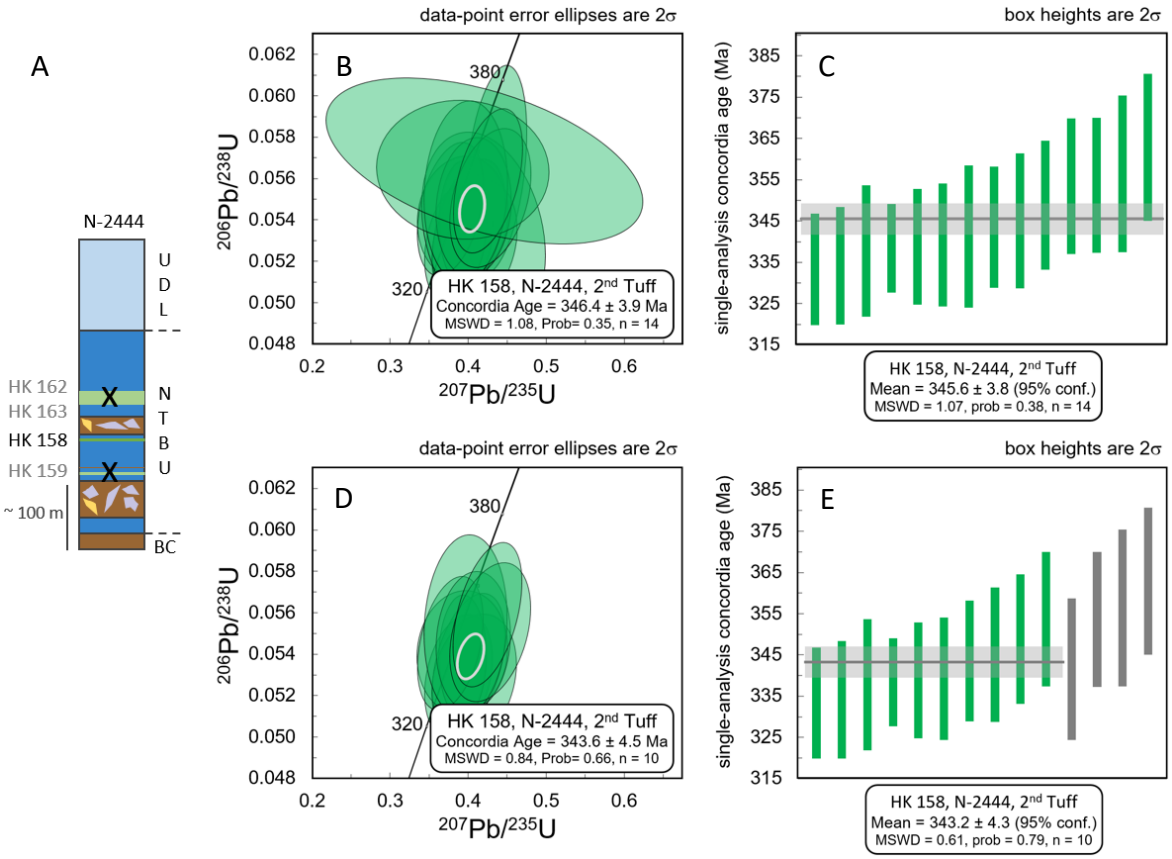

Figure 5-5: A) Stratigraphic position of the tuff samples in drill core N-2444. Samples HK 162, 163 and 159 do not contain zircon grains (tuff layers are crossed out), while 14 zircon grains from sample HK 158, which occurs in the New Thin Bedded Unit (NTBU) could be dated. B) and C) Geochronological ages of the second tuff layer from drill core N-2444 (sample HK 158) from Tara Deep. D) shows Wetherill and E) weighted average mean ages from the same tuff samples, where four zircon grains showing high analytical uncertainties are not included. Green ellipses: magmatic zircon population. Bars represent dates from single grains of zircon with errors at 2σ. Dark grey bars represent zircon grains, with high analytical uncertainties. The horizontal line through the middle of the population represents the weighted average mean. The light grey bar indicates its uncertainty at a 95% confidence level. BC = Boulder Conglomerate, UDL = Upper Dark Limestone Formation.

5.3.1.2 Navan East & West

Three tuff layers were sampled from core N-2441 (Navan West). While neither the top nor the bottom of the third tuff layer contained any zircon (samples HK 156 and 157, respectively), the first (sample HK 169, Waulsortian equivalent) and second (sample HK 155, Tober Colleen Formation) tuff layers could be dated, yielding concordia ages of 342 ± 2.7 Ma and 348.7 ± 3 Ma, respectively (Figure 5-6).

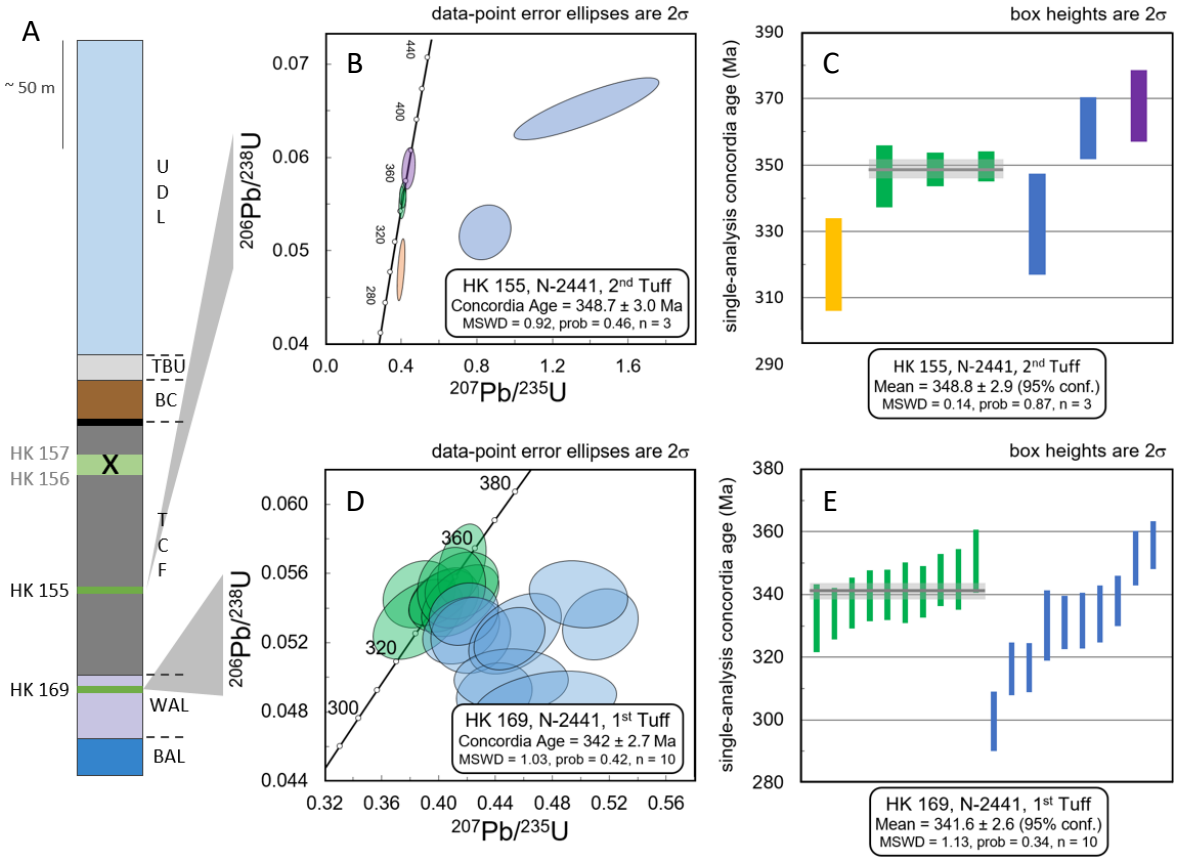

Figure 5-6: A) Stratigraphic position of the tuff samples in drill core N-2441. Samples HK 156 and 157 do not contain zircon grains (tuff layers are crossed out). Samples HK 155 and 169 yield eruption ages. B) Wetherill and C) weighted average mean ages from the second (HK 155; Tober Colleen Formation) and D) Wetherill and E) weighted average mean ages from the first (HK 169; Waulsortian equivalent; C, D) tuff layers from drill core N-2441 (Navan West). Green ellipses and bars: magmatic zircon population; Orange ellipses and bars: zircon grains which suffered Pb-loss; blue ellipses and bars: zircon grains with incorporation of common Pb; purple ellipses and bars: partly inherited cores or fully inherited zircon grains. Bars represent dates from single grains of zircon with errors at 2σ. The horizontal line through the middle of the population (green vertical bars), represents the weighted average mean. The light grey bar indicates its uncertainty at a 95% confidence level. BC = Boulder Conglomerate, BAL = Ballysteen Limestone Formation, TBU = Thin Bedded Unit, UDL = Upper Dark Limestone Formation, WAL = Waulsortian equivalent.

5.3.1.3 Rathdowney Trend

Eleven zircon grains from sample HK 185, a tuff sample from the Upper Calcarenite Member from Rapla, could be dated and they yield a concordia age of 340.1 ± 2.3 Ma (Figure 5-7A B). Two tuff samples from the Nodular Micrite Unit from Lisheen yield concordia ages of 344.8 ± 2.1 Ma (HK 180, Figure 5-7C - D) and 346.6 ± 2.5 Ma (HK 182, Figure 5-7E - F), which are within analytical uncertainty. Sample Lisheen_mine sample_HK 203, also called the 'Green Tuff' was the only sample from an underground face at Lisheen Mine. The tuff layer was deposited

within the Nodular Micrite Unit. Approximately 6 kg of this particularly well-developed tuff layer were sampled underground and it yields a concordia age of 349.6 ± 1.5 Ma (Figure 5-7G – H). This sample is within analytical uncertainty of sample Lisheen_LK-1040_HK 182.

One tuff layer from sample Lisheen_LK-2180_HK 181 (Nodular Micrite Unit) only contained two zircons, which produced ages of 300.63 ± 8.96 Ma and 1034.91 ± 22.97 Ma (Figure 5-7I). They are discordant and outside the average age of sample HK 180, HK 182 and HK 185.

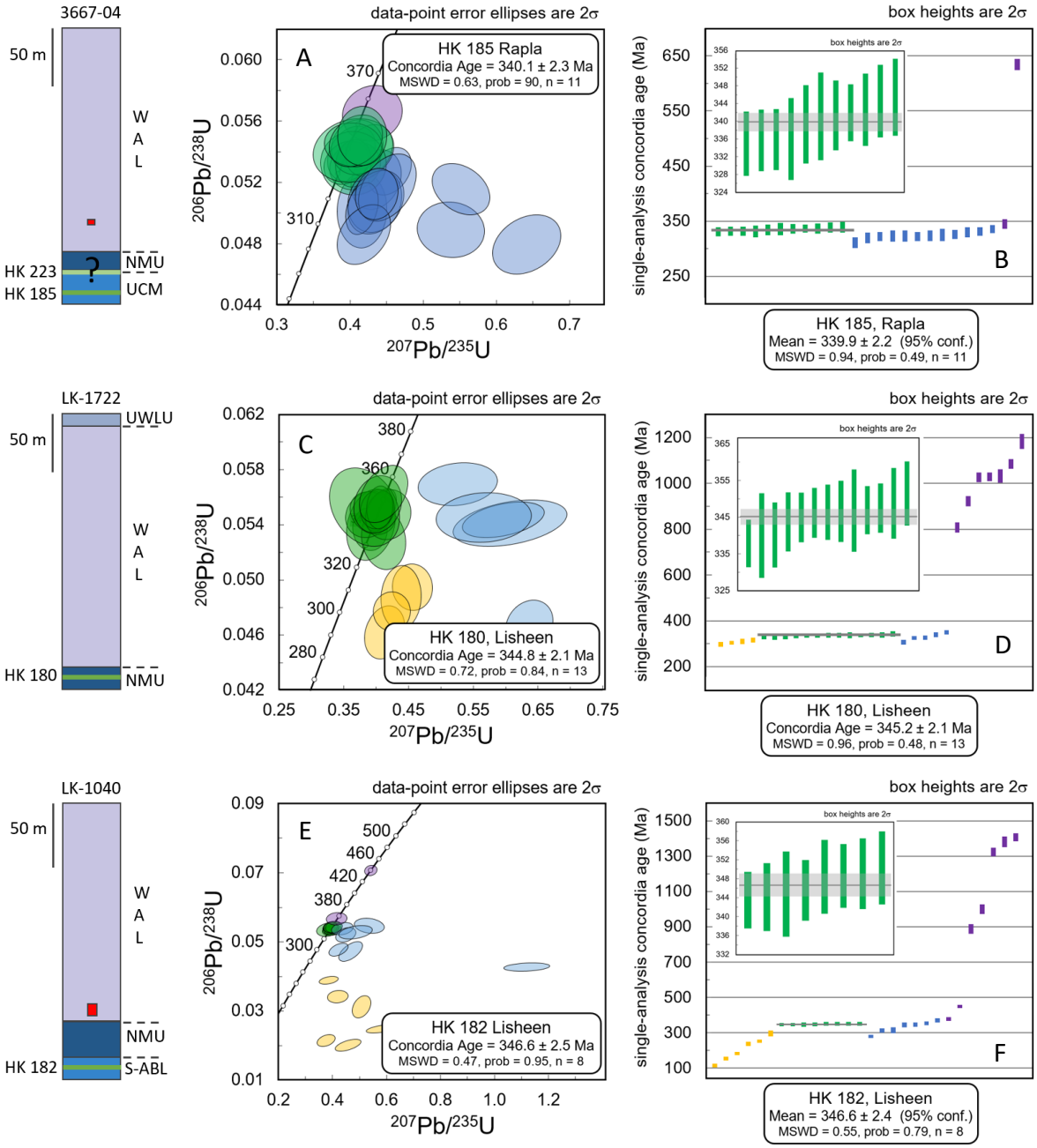

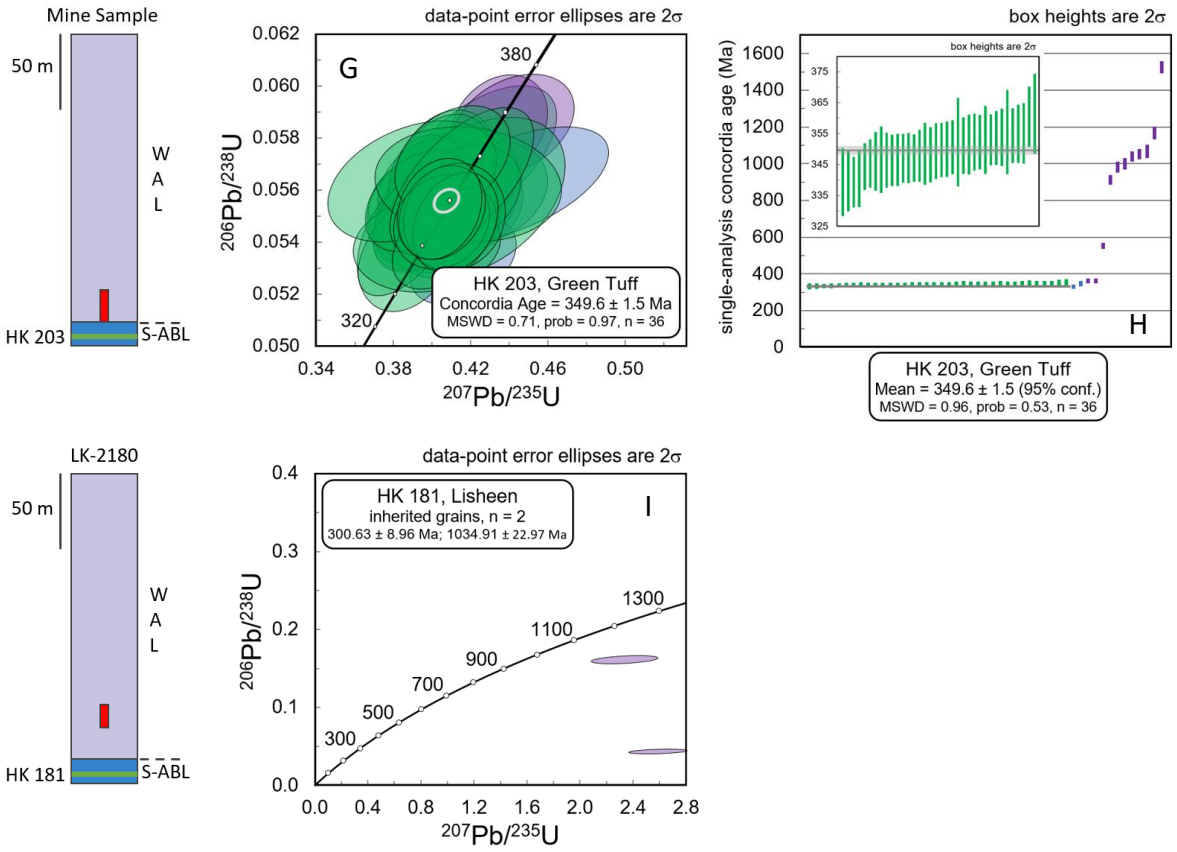

Figure 5-7: Geochronological results for tuff samples from Lisheen and Rapla, in the Rathdowney Trend, Ireland. One tuff sample from Rapla (HK 185; A, B), two tuff samples from Lisheen (HK 180, C, D; HK 182, E, F) and the Green tuff (HK 203, G, H) yields concordia ages between 340.1 ± 2.3 Ma (2σ) and 349.6 ± 1.5 Ma (2σ) and weighted average mean ages between 339.9 ± 2.2 Ma (95% conf.) and 349.6 ± 1.5 Ma (95% conf.). I) Sample HK 181 shows the ages of two inherited grains. The stratigraphic position of dated tuff layers is shown on the left of the corresponding age diagrams. Green ellipses and bars: magmatic zircon population; Orange ellipses and bars: zircon grain, which suffered Pb-loss; blue ellipses and bars: zircon grains with incorporation of common Pb; purple ellipses and bars: partly inherited cores or fully inherited zircon grains. Dark grey bars represent zircon grains, with high analytical uncertainties. Bars represent dates from single grains of zircon with errors at 2σ. The horizontal line through the middle of the population (green vertical bars), represents the weighted average mean. The light grey bar indicates its uncertainty at a 95% confidence level. NMU = Nodular Micrite Unit, UCM = Upper Calcarenite Member, WAL = Waulsortian Limestone Formation.

5.3.1.4 Stonepark Area

Two tuff layers occur in drill core G11-2654-01. The second tuff reveals a concordia age of 348.2 ± 2.4 Ma (HK 211, Lough Gur Formation, Figure 5-8A, B) and the first tuff has a concordia age of 350.3 ± 4.3 Ma (HK 212, Nodular Micrite Unit, Figure 5-8C, D). Thus, they are both within analytical uncertainty. There are two tuff layers in drill core G11-2638-01. Only the second tuff (out of two tuff layers) from drill core 2638-01 contained zircon grains, yielding a concordia age of 350.7 ± 3.3 Ma (HK 197, Nodular Micrite Unit, Figure 5-8E, F). Drill core 2638-02 contained three tuff layers. The first layer did not contain zircon grains. The twelve grains from the second layer (HK 208, Nodular Micrite Unit, Figure 5-8G) and the seven grains from the third layer (HK 207, Nodular Micrite Unit, Figure 5-8H) yielded ages from 421 ± 11 Ma to 1847 ± 40 Ma, which are significantly older age estimates than the majority of the zircon dates from this study. No zircons were found in the only tuff layer occurring in drill core 450-02 (HK 210).

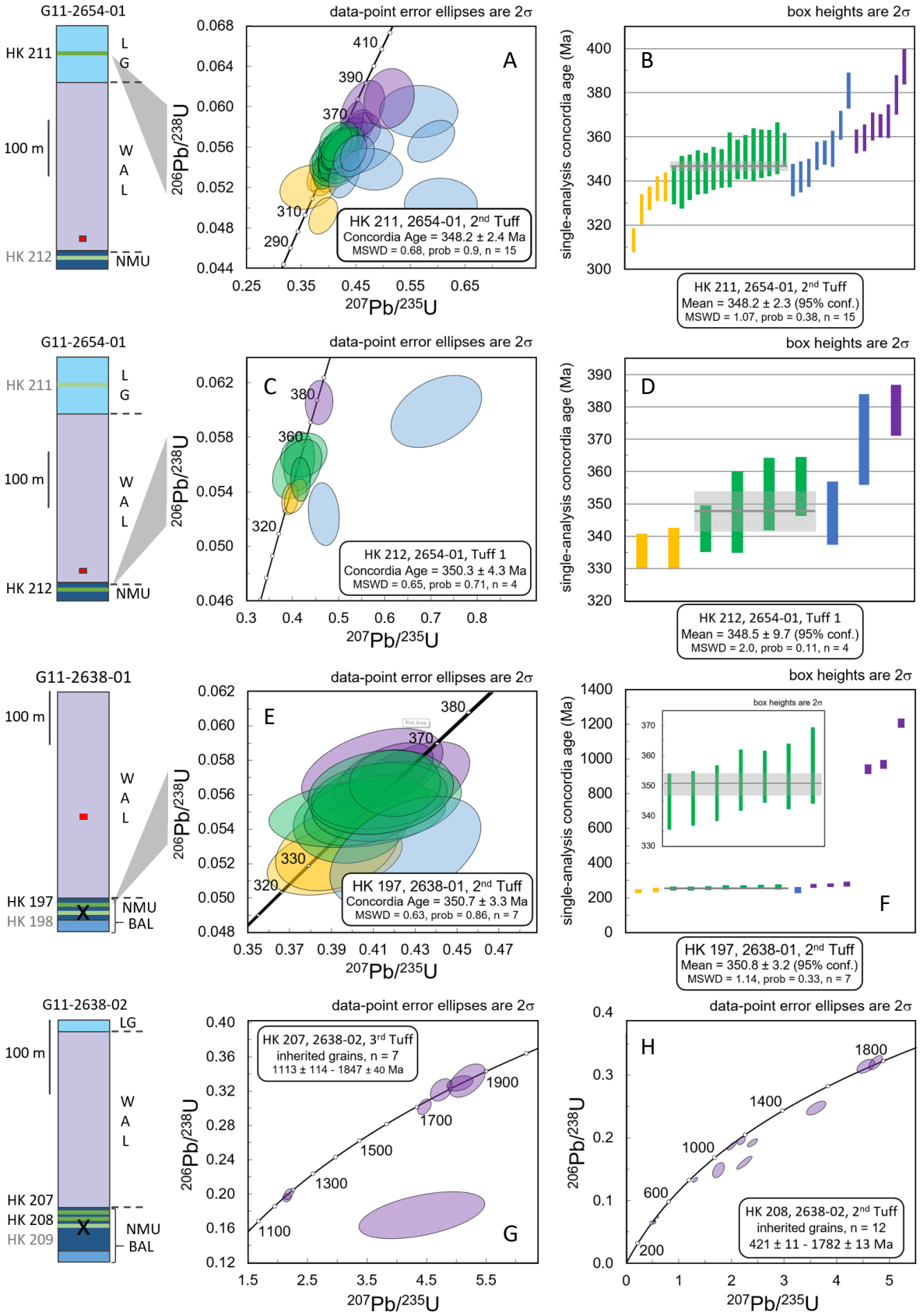

Figure 5-8: Concordia ages and weighted average mean ages from tuff 1 (A, B) and tuff 2 (C, D) from drill core 2654-01 at Stonepark in Limerick. One tuff from drill core 2638-01 revealed eruptive zircon ages (E, F), whereas only inherited grains could be separated from the second (G) and third (H) tuff layer from drill core 2638-2. Stratigraphic position of the dated tuff samples is shown as well. The Nodular Micrite Unite (NMU) is the stratigraphically highest unit of the Ballysteen Limestone Formation (BAL). Tuff layers, which are crossed out did not contain zircon grains. Green ellipses and bars: magmatic zircon population; Orange ellipses and bars: zircon grains which suffered Pb-loss; blue ellipses and bars: zircon grains with incorporation of common Pb; purple ellipses and bars: partly inherited cores or fully inherited

zircon grains. Bars represent dates from single grains of zircon with errors at 2σ. The horizontal line through the middle of the population (green vertical bars), represents the weighted average mean. The light grey bar indicates its uncertainty at a 95% confidence level. WAL = Waulsortian Limestone Formation, red bars = mineralisation.

5.3.1.5 Slievedart Area

No zircons were found in samples HK 189 and 195, which were taken from the second tuff horizon (in the Kilbryan Limestone Formation) in drill core 3470/15 and 3471/4, nor in samples HK 237 and 238. They were taken from the stratigraphically younger tuff layer, which also occur in the Kilbryan Limestone Formation in the same drill cores. Samples HK 191 (3471/4, fifth tuff, Oakport Limestone Formation) and HK 187 (3470/15, fifth tuff, Oakport Limestone Formation) did not contain zircons either.

Zircon grains were found in samples HK 194 (3471/4, first tuff) and HK 190 (3470/15, first tuff), as well as in the fourth tuffs of each drill core; samples HK 192 and HK 193 in drill core 3471/4, and sample HK 188 in drill core 3470/15 (Figure 5-9). Both tuff layers occur within the Kilbryan Limestone Formation. Two concordia ages were obtained from tuff layers within 10 cm for the fourth tuff from drill core 3471/4; both are considered to represent tuff four. Their concordia ages are 345.4 ± 1.8 Ma (HK 193, Figure 5-9A, B) and 347.7 ± 2.2 Ma (HK 192, Figure 5-9 C, D). The concordia age for the fourth tuff from drill core 3470/15 is 347.2 ± 2.9 Ma (HK 188, Figure 5-9I, J). All ages of the fourth tuff are thus within analytical uncertainty. The concordia age of the stratigraphically lowest tuff is 358.1 ± 3.0 Ma for sample Slievedart_3470/15_HK 190 (Figure 5-9K, L). Sample Slievedart_3471/4_HK 194 has two magmatic populations. Population one has a concordia age of 345.6 ± 3.5 Ma (Figure 5-9G, H). The concordia age of population two is 361.0 ± 3.2 Ma (Figure 5-9E, F). Thus, sample HK 190 and population two of sample HK 194 are again within analytical uncertainty.

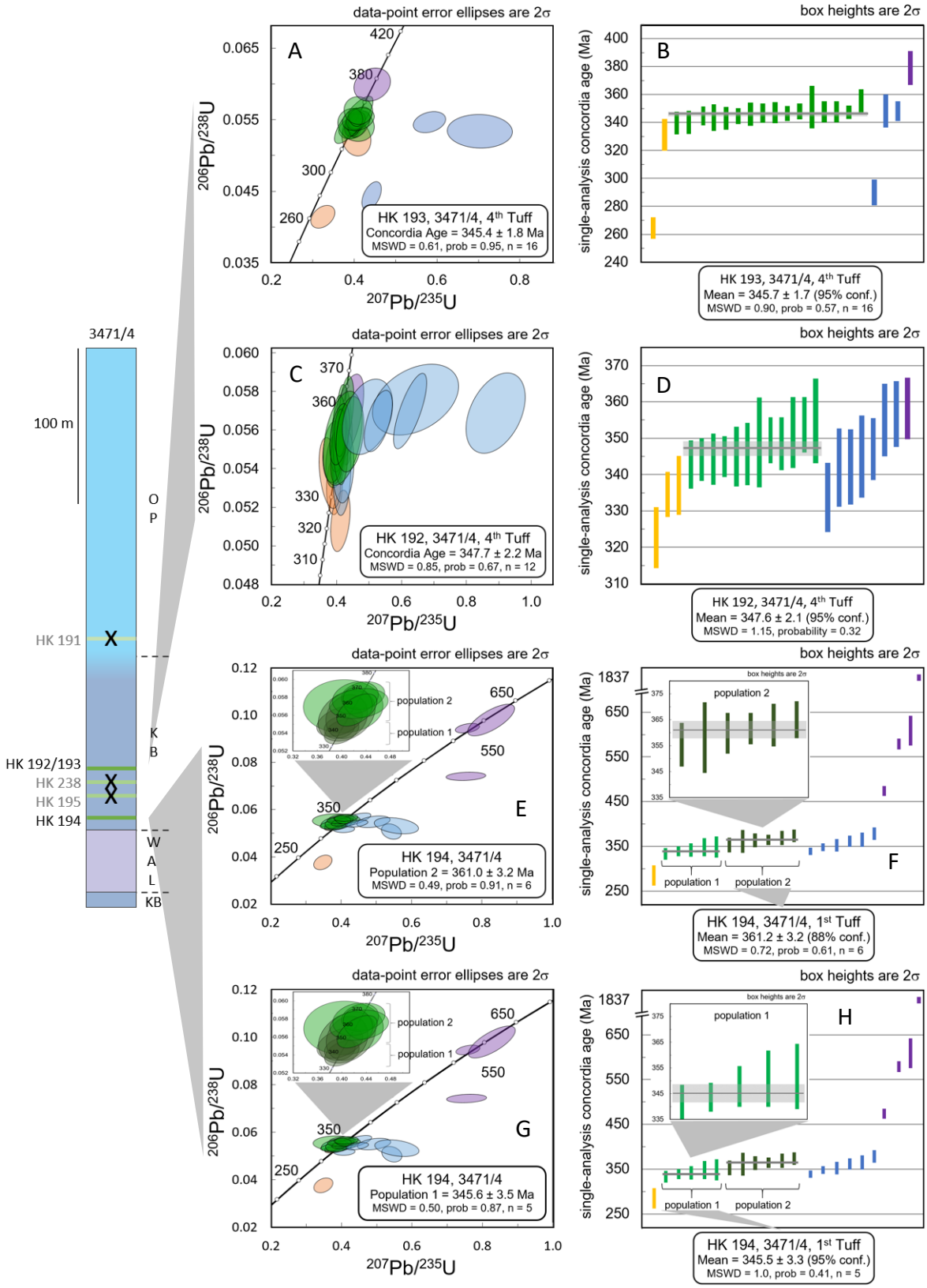
3471/4
100 m
O
P
K
B
W
A
L
KB
HK 191
HK 192/193
HK 238
HK 195
HK 194
data-point error ellipses are 2σ
box heights are 2σ
A
B
C
D
E
F
G
H
206Pb/238U
207Pb/235U
single-analysis concordia age (Ma)
HK 193, 3471/4, 4th Tuff
Concordia Age = 345.4 ± 1.8 Ma
MSWD = 0.61, prob = 0.95, n = 16
HK 193, 3471/4, 4th Tuff
Mean = 345.7 ± 1.7 (95% conf.)
MSWD = 0.90, prob = 0.57, n = 16
HK 192, 3471/4, 4th Tuff
Concordia Age = 347.7 ± 2.2 Ma
MSWD = 0.85, prob = 0.67, n = 12
HK 192, 3471/4, 4th Tuff
Mean = 347.6 ± 2.1 (95% conf.)
MSWD = 1.15, probability = 0.32
population 1
population 2
HK 194, 3471/4
Population 2 = 361.0 ± 3.2 Ma
MSWD = 0.49, prob = 0.91, n = 6
HK 194, 3471/4, 1st Tuff
Mean = 361.2 ± 3.2 (88% conf.)
MSWD = 0.72, prob = 0.61, n = 6
HK 194, 3471/4
Population 1 = 345.6 ± 3.5 Ma
MSWD = 0.50, prob = 0.87, n = 5
HK 194, 3471/4, 1st Tuff
Mean = 345.5 ± 3.3 (95% conf.)
MSWD = 1.0, prob = 0.41, n = 5

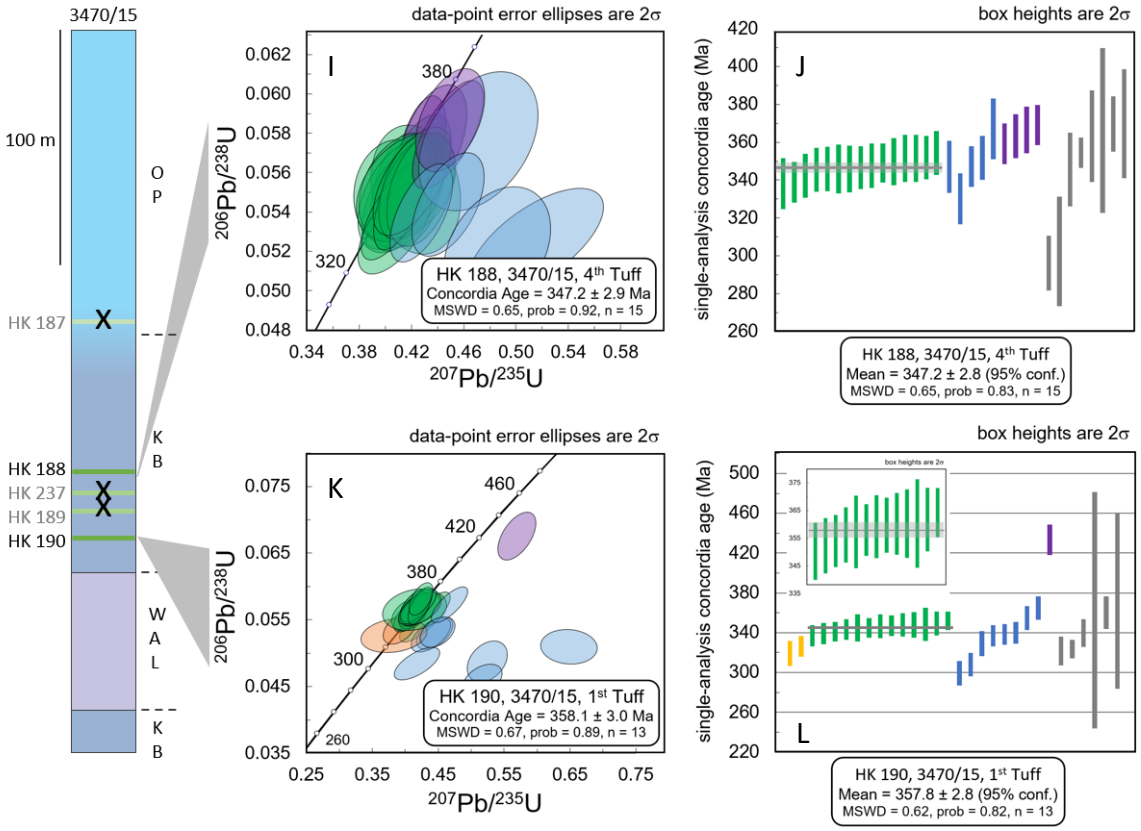

Figure 5-9: Concordia ages and weighted average mean ages from tuff four (A-D) and tuff one (E-H) from drill core 3470/15 and from tuff four (I, K) and tuff one (K, L) from drill core 3470/15 at Slievedart. The fourth tuffs from both drill cores are roughly 346.8 Ma old (A-D, K, L), whereas the stratigraphically lowest tuffs from drill core 3471/4 and 3470/15 yield ages of 361.0 ± 3.2 Ma (E, F), 345.6 ± 3.5 Ma (G, H) and 358.1 ± 3.0 Ma (K, L). Thus, four out of five samples are within analytical uncertainty. Stratigraphic position of the dated tuff samples is also shown. Tuff layers which are crossed out did not contain zircon grains. Green ellipses and bars: magmatic zircon population; Orange ellipses and bars: zircon grains which suffered Pb-loss; blue ellipses and bars: zircon grains with incorporation of common Pb; purple ellipses and bars: partly inherited cores or fully inherited zircon grains. Dark grey bars represent zircon grains, with high analytical uncertainties. Bars represent dates from single grains of zircon with errors at 2σ. The horizontal line through the middle of the population (green vertical bars), represents the weighted average mean. The light grey bar indicates its uncertainty at a 95% confidence level. KB = Kilbryan Limestone Formation, OP = Oakport Limestone Formation, WAL = Waulsortian Limestone Formation.

5.3.2 Zircon Morphology

Overall, the zircons from Irish Mississippian tuff samples in this study typically occur as euhedral to subhedral crystals, comprising a mix of well-developed grains with one or two pyramidal terminations, broken fragments and slightly rounded zircon grains (Figure 5-10). Some grains are clear with no or only few fractures or inclusions, while other grains exhibit many examples of both features (Figure 5-10). Euhedral zircons with doubly terminated pyramids were measured revealing a variation in width between 18 – 91 µm and 50 – 364 µm in length, with aspect ratios of length to width (c/a values) between 1.4 and 6.3 (median = 2.4) across the whole sample suite (Figure 5-11).

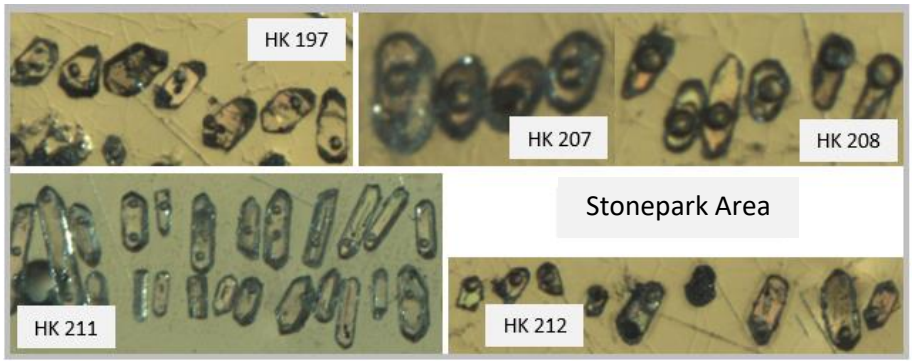

Figure 5-10: Zircons embedded in epoxy resin and polished to approximately half thickness. Only some representative zircons for each sample are shown. The laser analyses conducted on the zircons are the clearly visible circles, which are 24 µm in diameter. The laser spots also serve as scale.

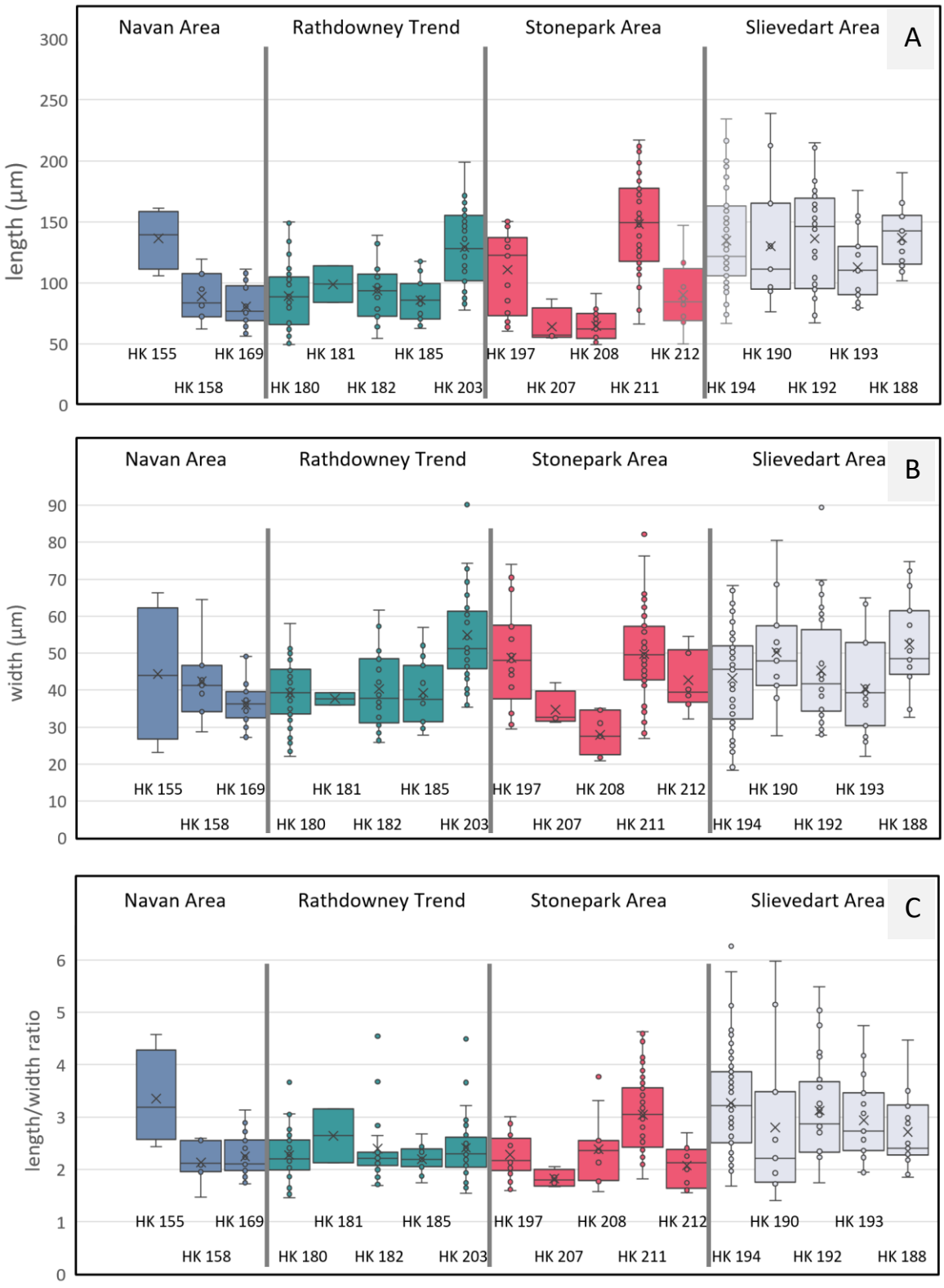

Figure 5-11: Box and whisker plots for the length (A), width (B) and length/width ratio (C) of dated zircon grains for all samples, showing the minimum, lower quartile, median, upper quartile and maximum numbers of the data set for each sample.

5.3.3 U-Pb Apatite Ages

Between one and 25 apatite grains from 14 different tuff samples from four different areas within the Irish Midlands were analysed (see Appendix 2, Table A2 - 2).

5.3.3.1 Navan

Samples HK 158 (Upper Tuff) and HK 235 (Marker Tuff) from Tara Deep contained one apatite each. Their apatite ages were produced using the in-house excel sheet and are 1276.5 ± 34 Ma (2SE, n = 1) and 1641.7 ± 31 Ma (2SE, n = 1), respectively. An anchored Tera-Wasserburg intercept age of 334 ± 39 Ma (2σ; MSWD = 0.85; n = 4) and a weighted mean age of 324 ± 43 Ma (95% conf. level; MSWD = 1.4; n = 4) was obtained for sample HK 159 (Figure 5-12A, B), which is located in the Thin Bedded Unit 2 (Lower Tuff). No apatite grains were found in samples HK 155, 156, 157, 161, 162, 163, 169, 232 and 236.

5.3.3.2 Rathdowney Trend

Tuff samples from Lisheen and Rapla did not yield any apatite grains.

5.3.3.3 Stonepark Area

Samples HK 207, 208 and 209 are located in the Nodular Micrite Unit and were sampled from the same drill core (2638-02; see Figure 2-10C). The former sample is the stratigraphically highest sample and contained two apatite grains, which were dated at 1770.3 ± 92 Ma (2SE, n = 1) and 895.1 ± 23 Ma (2SE, n = 1). Sample HK 208 did not contain any apatite grains, whereas sample HK 209, the third tuff layer reveals one U-Pb apatite age of 315.6 ± 48 Ma (2SE, n = 1).
Five apatite grains from sample HK 210 (located in the Nodular Micrite Unit, see Figure 2-10C), which is the only occurring tuff in drill core 450-02 yields a Tera-Wasserburg lower intercept age of 298 ± 33 Ma (2σ, MSWD = 0.36, n = 5) (Figure 5-12C, D).
Samples HK 211 and 212 which are two successive tuff layers in drill core 2654-01 (and located in the Lough Gur Formation and Nodular Micrite Unit, respectively; see Figure 2-10C), were dated on Tera-Wasserburg concordia with lower intercept ages of 334 ± 15 Ma (2σ, MSWD = 1.9, n = 23) and 334 ± 13 Ma (2σ, MSWD = 1.3, n = 10), respectively (Figure 5-12E- H).
No apatite grains were found in samples HK 197 and 198. Both samples are located in the Nodular Micrite Unit (Figure 2-10C).

5.3.3.4 Slievedart Area

One grain each could be dated from samples HK 187 and 193 from the Slievedart area. Sample HK 187, the stratigraphically highest tuff (located in the Oakport Limestone Formation; see Figure 2-11C) in drill core 3470/15 is 372.6 ± 34 Ma, whereas sample HK 193 (located in the Kilbryan Limestone Formation; see Figure 2-11C), the second highest tuff in drill core 3471/4,

yields a very young age of 12.9 ± 9 Ma. Samples HK 190 (drill core 3470/15) and HK 194 (drill core 3471/4), which are both the stratigraphically lowest tuffs in the Kilbryan Limestone Formation (Figure 2-11C), yield Tera-Wasserburg lower intercept ages of 368 ± 35 Ma (2σ; MSWD = 0.17; n = 3) and 379 ± 28 Ma (2σ; MSWD = 1.9; n = 6), respectively (Figure 5-12I-L).

Samples HK 237 and 238 occur as the third tuff in the Kilbryan Limestone Formation in drill cores 3470/15 and 3471/4, respectively (Figure 2-11C). Twenty-two grains from sample HK 237 and twenty-one grains from sample HK 238 yield intercept ages of 320 ± 40 Ma (2σ, MSWD = 0.57, n =22; Figure 5-12M-N) and 335 ± 51 Ma (2σ, MSWD = 1.8, n =21; Figure 5-12O-P), respectively.

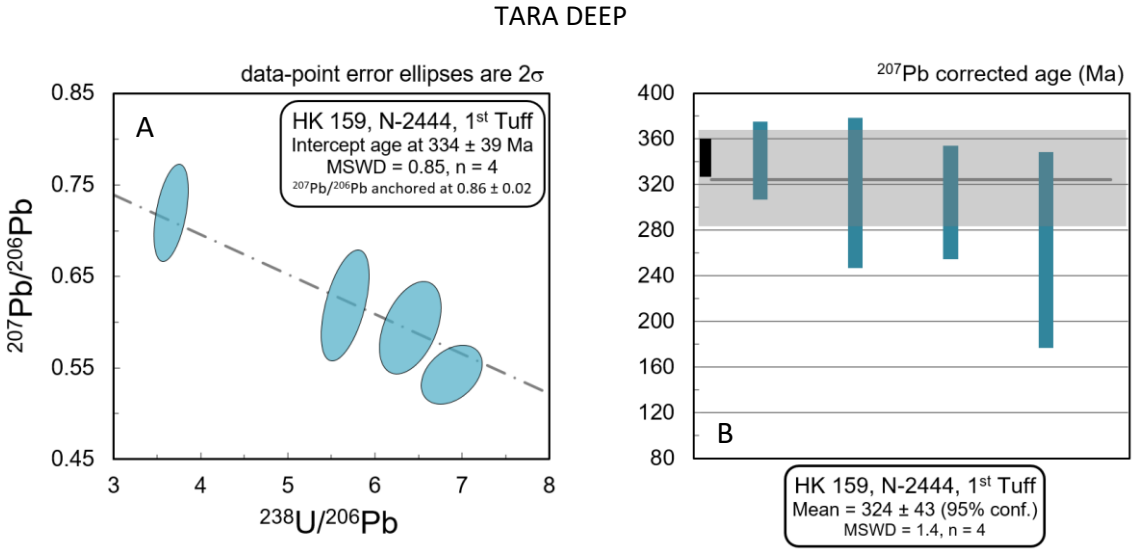

STONEPARK

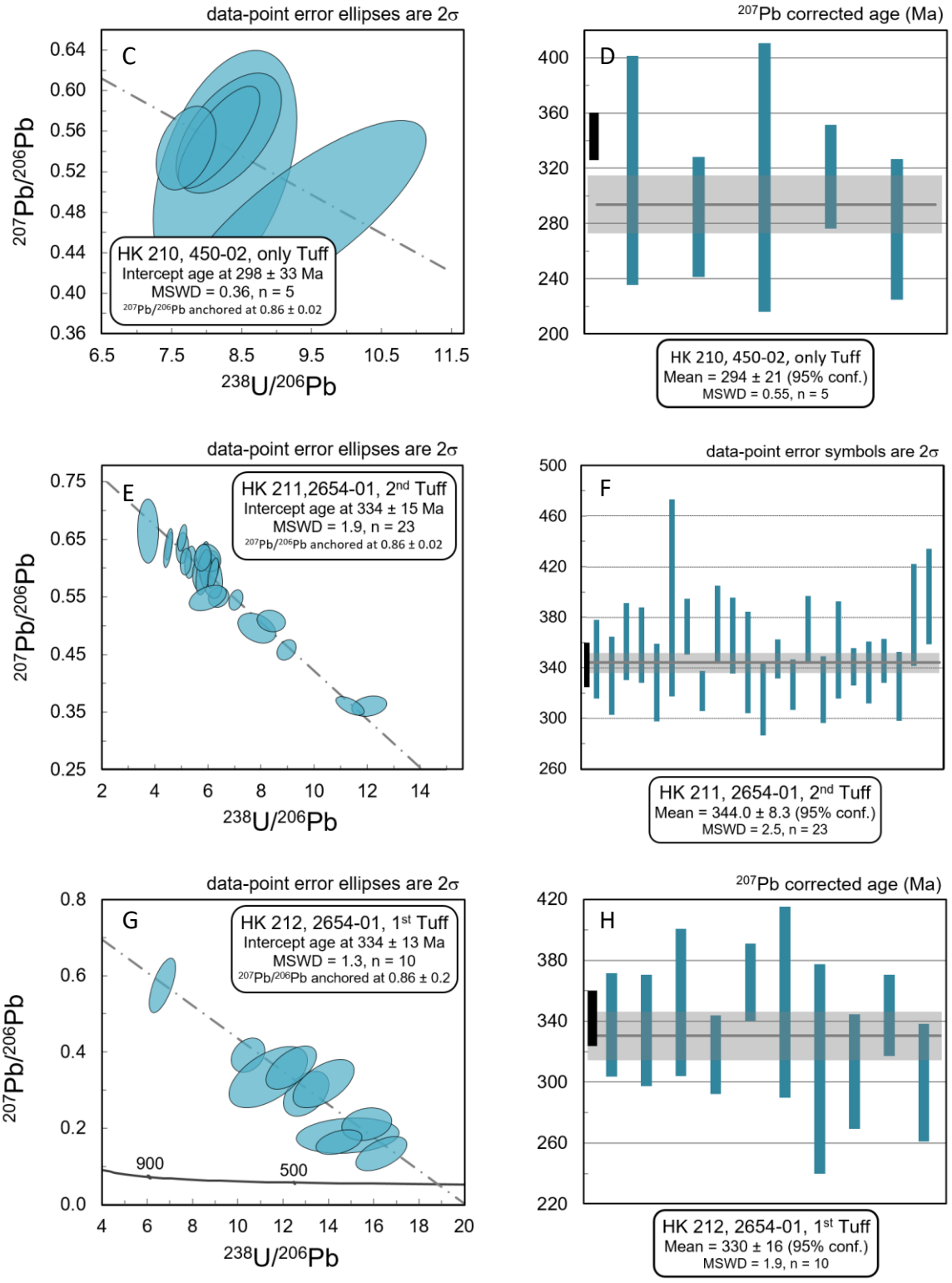
data-point error ellipses are 2σ
C
HK 210, 450-02, only Tuff
Intercept age at 298 ± 33 Ma
MSWD = 0.36, n = 5
207Pb/206Pb anchored at 0.86 ± 0.02
207Pb/206Pb
238U/206Pb
207Pb corrected age (Ma)
D
HK 210, 450-02, only Tuff
Mean = 294 ± 21 (95% conf.)
MSWD = 0.55, n = 5
data-point error ellipses are 2σ
E
HK 211,2654-01, 2nd Tuff
Intercept age at 334 ± 15 Ma
MSWD = 1.9, n = 23
207Pb/206Pb anchored at 0.86 ± 0.02
207Pb/206Pb
238U/206Pb
data-point error symbols are 2σ
F
HK 211, 2654-01, 2nd Tuff
Mean = 344.0 ± 8.3 (95% conf.)
MSWD = 2.5, n = 23
data-point error ellipses are 2σ
G
HK 212, 2654-01, 1st Tuff
Intercept age at 334 ± 13 Ma
MSWD = 1.3, n = 10
207Pb/206Pb anchored at 0.86 ± 0.2
900
500
207Pb/206Pb
238U/206Pb
207Pb corrected age (Ma)
H
HK 212, 2654-01, 1st Tuff
Mean = 330 ± 16 (95% conf.)
MSWD = 1.9, n = 10

SLIEVEDART

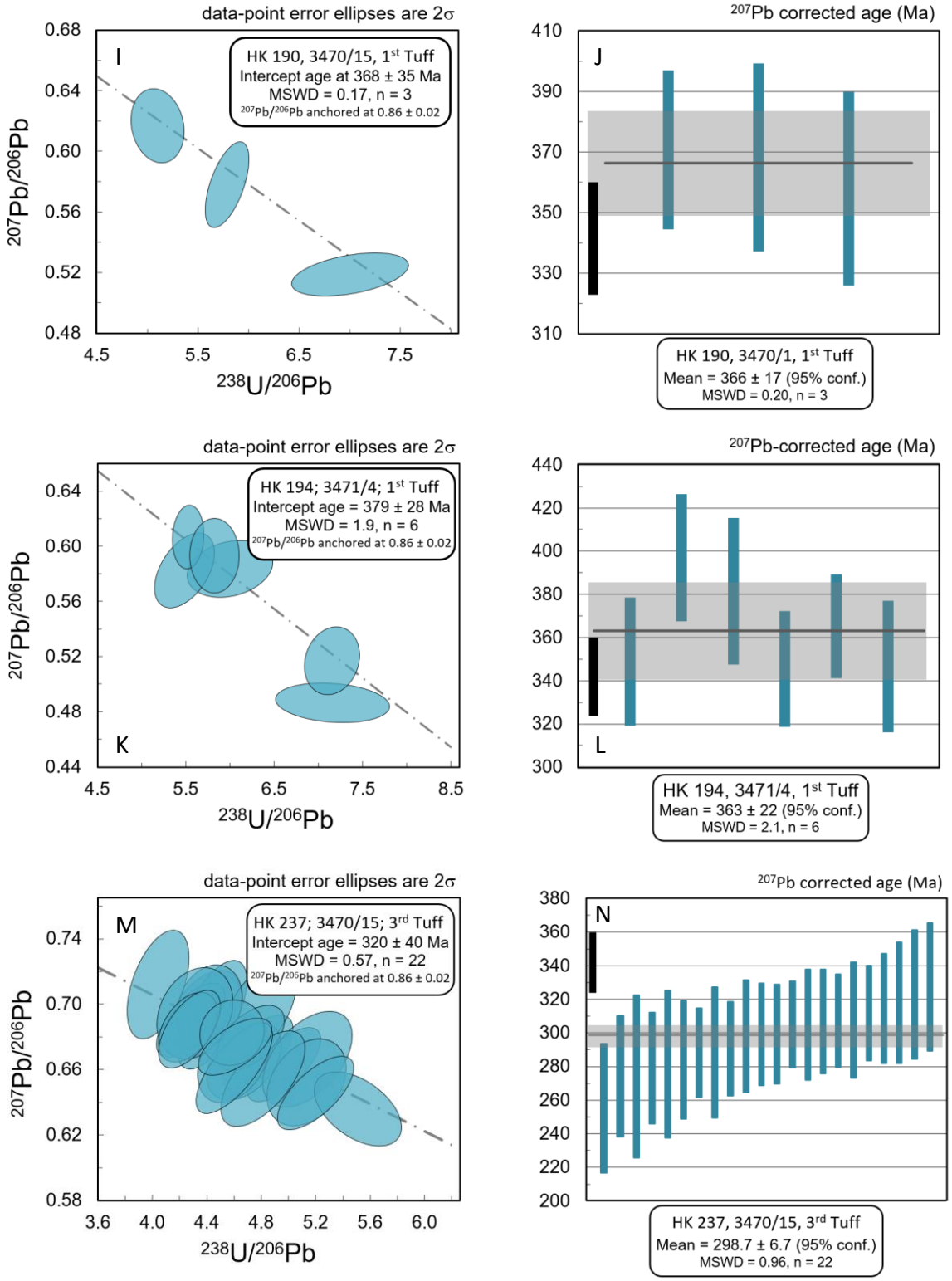
data-point error ellipses are 2σ
I
HK 190, 3470/15, 1st Tuff
Intercept age at 368 ± 35 Ma
MSWD = 0.17, n = 3
207Pb/206Pb anchored at 0.86 ± 0.02
207Pb/206Pb
238U/206Pb
207Pb corrected age (Ma)
J
HK 190, 3470/1, 1st Tuff
Mean = 366 ± 17 (95% conf.)
MSWD = 0.20, n = 3
data-point error ellipses are 2σ
HK 194; 3471/4; 1st Tuff
Intercept age = 379 ± 28 Ma
MSWD = 1.9, n = 6
207Pb/206Pb anchored at 0.86 ± 0.02
K
207Pb/206Pb
238U/206Pb
207Pb-corrected age (Ma)
L
HK 194, 3471/4, 1st Tuff
Mean = 363 ± 22 (95% conf.)
MSWD = 2.1, n = 6
data-point error ellipses are 2σ
M
HK 237; 3470/15; 3rd Tuff
Intercept age = 320 ± 40 Ma
MSWD = 0.57, n = 22
207Pb/206Pb anchored at 0.86 ± 0.02
207Pb/206Pb
238U/206Pb
207Pb corrected age (Ma)
N
HK 237, 3470/15, 3rd Tuff
Mean = 298.7 ± 6.7 (95% conf.)
MSWD = 0.96, n = 22

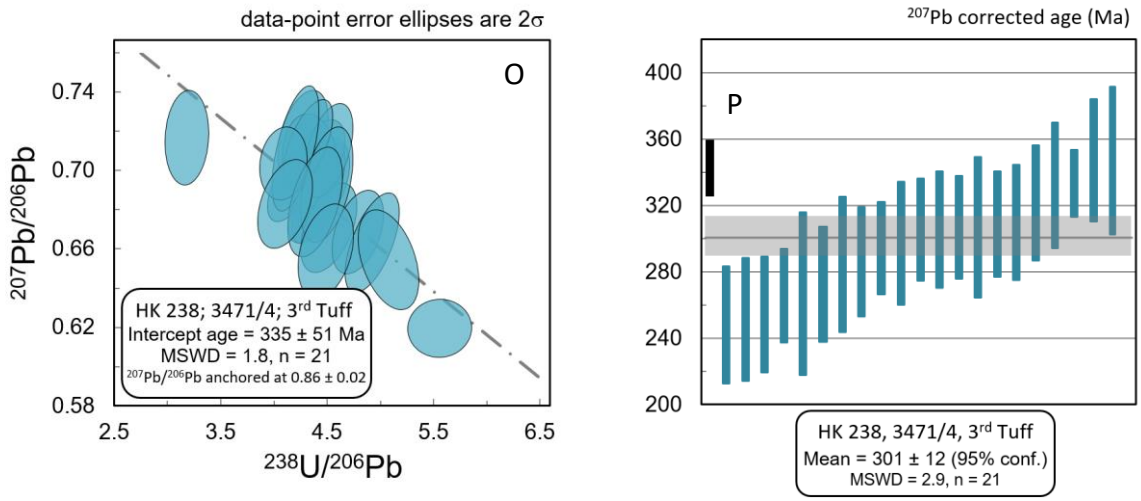

Figure 5-12 A-N: Tera-Wasserburg anchored lower intercept U-Pb apatite ages (A; C; E; G; I; K; M; O) and weighted mean age calculations (B; D; F; H; J; L; N; P) of seven Irish Mississippian tuff samples from this study produced using the software package Isoplot (Ludwig, 2003). A) and B) tuff sample from Tara Deep (Navan area); C) - H) tuff samples from the Stonepark area; I) - P) tuff samples from the Slievedart area. Turquoise bars represent ^{207}Pb-corrected dates from single grains of apatite with errors at 2σ. Black bars span the Early Carboniferous time period. The horizontal line through the middle of the population represents the weighted average mean. The light grey bar indicates its uncertainty at a 95% confidence level.

5.3.4 Trace Elements

Trace element concentrations (V, Mn, Fe, Sr, Y, Zr, Pb, Th, U and REEs) from each analysed apatite grain are listed in Table A2 - 3 (Appendix 2) along with average element concentrations for each sample. The elements were chosen based on their potential to provide information about the magmatic protolith. Only Early Carboniferous (359.3 to 323.4 Ma) apatite U-Pb ages with acceptable uncertainties were included in the average calculations and considered for further trace element correlations; all other analyses were coloured grey in Table A2 - 3, Appendix 2. Element concentrations from grains within the same sample, whose concentrations deviated more than 20% from its median (bold grey in Table A2 - 3, Appendix 2) were also excluded from the data set.

5.3.4.1 Standards

Mao et al. (2016) published between 23 and 250 trace element analyses for V, Mn, Sr, Y, Zr, Pb, Th, U and REEs for the Madagascar and Durango apatite standards respectively. Average Mn, Sr and La concentrations from Durango apatite are within analytical uncertainty of analysed values by Mao et al. (2016). The differences of average element concentrations between the study of Mao et al. (2016) and this study range from 10.8 to 18% for Y, Zr, Ce, Pr, Eu, Gd, Yb, Lu and Th, whereas V, Nd, Sm, Tb, Dy, Ho, Er, Tm, Pb and U concentrations differ between 30 and 48.8% from the average published values. All concentrations, except of V and Mn, obtained during this study are constantly higher compared to data from Mao et al. (2016). This is likely due to trace element variation between different Durango crystals (*cf* Chew et al., 2016).

Average concentrations of most elements from Madagascar apatite are within 20% of the recommended values of Mao et al. (2016). Only Tm concentrations differ by 24.6%. All concentrations from the Madagascar apatite standard, gained during this study, show higher concentrations than the values published by Mao et al. (2016) and is likely due to systematic trace element variations between different crystals of Madagascar apatite.

Sr/Mn ratios and Th/U ratios from each analysed apatite grain from the Durango, Madagascar and McClure standards are displayed in Figure 5-13A. The sum of the REE concentrations of the analysed apatite standards are shown in Figure 5-13B, along with the published average REE concentrations of Durango and Madagascar standards. Chew et al. (2016) published 1758 Durango and 1533 McClure (LA and solution)-ICP-MS trace element data on the same aliquots used in this study. The average published values are within uncertainty of the values obtained in this study (Figure 5-13).

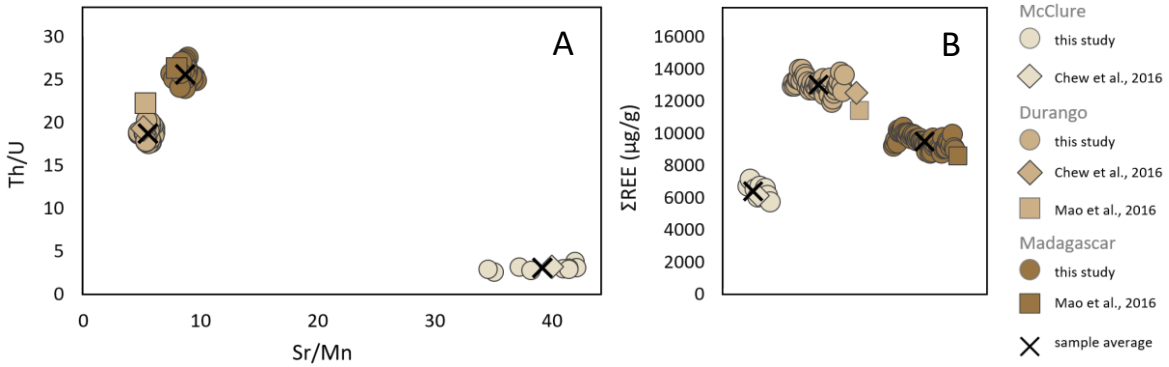

Figure 5-13: Sr/Mn vs Th/U ratios (A) and REE concentrations in µg/g (B) of the three apatite standards Durango, Madagascar and McClure are shown along with their averages (black cross). The average Sr/Mn vs Th/U values and the average sum of the REEs from the publication of Mao et al. (2016) for Durango (brown square) and Madagascar (dark brown square) are shown for comparison as well as the average values from Chew et al. (2016) (diamonds).

5.3.4.2 Tuff Samples

Although it was possible to recover apatite grains from fourteen samples in total (Table 5-2) there are two samples from the Navan area (HK 158, 235), one sample (HK 207) from the Stonepark area and one sample (HK 187) from the Slievedart area, whose apatite ages are either older or younger than Early Carboniferous (see Appendix 2, Table A2 - 3). Therefore, trace element concentrations from these grains are not taken into further consideration. For another two samples (HK 193, Slievedart area; HK 209, Stonepark area), trace element concentrations are only available for one grain each. Due to high inter-grain variabilities in the REE+Y content of the ten apatite grains of sample HK 212 (Stonepark area) (Figure 5-14), only their median REE+Y concentration is shown in diagrams of this study. Furthermore, the amount of available data in each diagram can slightly vary due to different inter-grain variabilities (see section 5.3.4.3). For example there are only two data points available for sample HK 212 in the Sr *vs* Mn biplot (Figure 5-25B) as the Sr and Mn content from only two grains were within 20% of the median value of all grains (n = 10), whereas four data points are plotted in the Fe *vs* Mn diagram (Figure 5-25C) as Mn and Fe concentrations of four out of ten grains were within 20% of its median values (Figure 5-14).

Between three and twenty-three suitable apatite grains are available from samples HK 159 (Navan), HK 210 and 211 (Stonepark) and samples HK 190, 194, 237 and 238 (Slievedart).

The apatite grains have low values of both Th and U (6.2 – 25.2 µg/g Th, 2.2 -14.4 µg/g U) (Figure 5-24B). The Sr/Y and Fe/Mn ratios range between 0.02 - 6.8 (not shown) and 0.4 - 2.2 (Figure 5-25C), respectively. Vanadium, Zr and Pb concentrations show big variations and plot between 0.2 - 30.8 µg/g, 0.4 – 13.9 µg/g and 0.5 – 9.4 µg/g, respectively.

Furthermore, all samples show an enrichment in light rare earth elements (LREE) compared to heavy rare earth elements (HREE) (La/Lu > 1) (Figure 5-26A). However, there are distinct differences in the rare earth elements plus yttrium (REE+Y) profiles of the samples (Figure 5-26C-L). Samples HK 190, 194 and 211 are characterised by a bell-shaped chondrite normalised REE+Y pattern (La_{CN}-Sm_{CN} < 0; Gd_{CN}-Lu_{CN} > 0), with a fairly flat LREE profile (La/Lu = 2.17 – 3.13), a slight depletion of HREE compared to LREE and a strong negative Eu anomaly (0.04 – 0.05) (Figure 5-26A-E). Apatites from samples HK 159 and 210 have very high chondrite normalised differences in La-Sm and Gd-Lu and La/Lu ratios (2420 – 4580, 1171 - 1663 and 18.73 to 24.7, respectively), resulting in steep rightward-declining REE+Y-profiles (Figure 5-26A, B, F, G). These samples also show less pronounced negative Eu anomalies (0.25 – 0.44). The REE+Y profile of samples HK 237 and 238 are similar to samples HK 159 and 210, but less steep with total REE+Y contents between 3436 and 4223 µg/g (Figure 5-26H, I, Figure 5-25D). The sum of the REE+Y concentrations from samples HK 190, 194, 211, 159 and 210 range from 8046 to 16 652 µg/g,

whereas samples HK 193, 209 and 212 are characterised by low REE+Y contents (1324 – 3533 µg/g) (Figure 5-25D). Otherwise, they are markedly different from each other. Sample HK 193 has a steeper slope in the LREEs opposed to the HREEs (La_N-Sm_N > Gd_N-Lu_N) and a weak Eu anomaly (Eu_{CN}/Eu* = 0.7) (Figure 5-26A, B, J). Samples HK 209 and 212 have also a rightward declining chondrite-normalised REE+Y-profile with average La/Lu ratios of 13.13 and 13.56, respectively and positive Eu anomalies (2.82 and 1.38, respectively) (Figure 5-25A, K, L).

5.3.4.3 Inter-Grain Variability of Element Concentrations

Ideally, trace element concentrations of individual apatite grains from one sample should not vary significantly. As magma chamber conditions during the crystallisation of apatite may change, inter-grain variabilities in a single sample can be expected (e.g. Belousova et al., 2001; Bruand et al., 2017). Furthermore, even if all apatite grains from a sample are within uncertainty of the deposition age, there is still the possibility that the sample represents admixtures of Early Carboniferous apatites from the surrounding region. To show the range of concentrations in different apatite grains from the same sample, a median for all analysed apatite grains was calculated first. Subsequently, the percentage of grains, whose trace element concentrations are within 20% of the median value is displayed in Figure 5-14. Inter-grain variations are by far biggest for V, followed by Th, Pb, U and Zr (Figure 5-14). Rare earth element, Y, Fe and Mn concentrations in different apatite grains from the same sample are relatively constant (Figure 5-14). Interestingly, sample HK 212 (Stonepark, Nodular Micrite Unit) displays high inter-grain variability in all elements. In some diagrams only the average element concentration is plotted, as no grains yield elemental values that are within 20% of the median value. Thus, it is questionable which apatite grain from sample HK 212 represents the actual parental magma composition. However, inter-grain variability cannot be determined for samples HK 209 (Stonepark, Nodular Micrite Unit) and HK 193 (Slievedart, Kilbryan Limestone Formation) as only one apatite for each sample could be recovered.

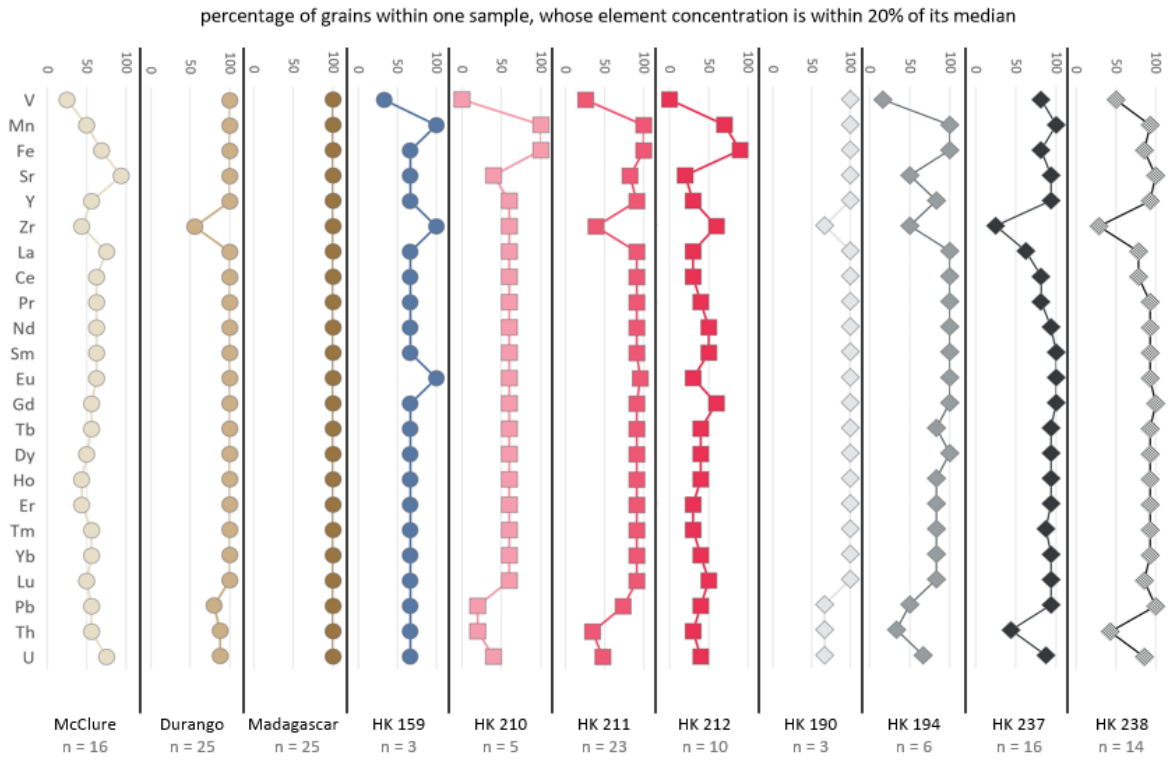

Figure 5-14: Inter-grain variations in trace element concentrations in single apatite crystals from one sample. McClure, Durango and Madagascar are apatite standards, while the HK samples are Irish Mississippian tuffs. n is the amount of total recovered grains, which were either analysed (McClure, Durango, Madagascar) or were within uncertainty of an Early Carboniferous age (HK samples).

5.3.5 Apatite Morphology

The apatite crystals are typically yellowish brown and transparent under reflected light. They are euhedral to subhedral. Most of the elongated apatite grains are fractured and slightly rounded, while some are hexagonal crystals (Figure 5-15).

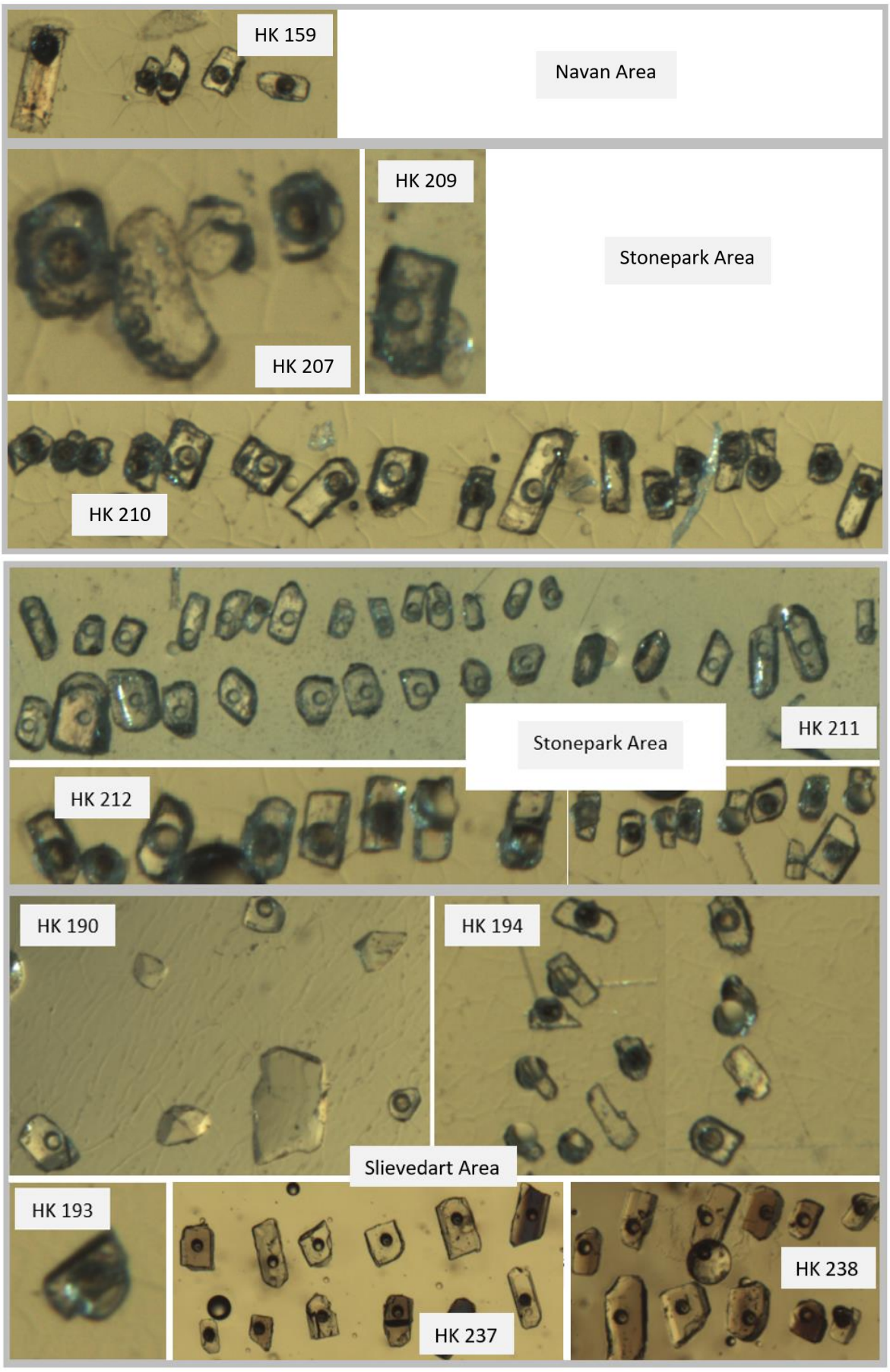

Figure 5-15: Apatite crystals from Irish Mississippian tuffs embedded in epoxy resin and polished to approximately half thickness. The laser analyses conducted on the apatites are the clearly visible circles, which are 36 µm in diameter. The laser spots also serve as scale.

5.4 Discussion

Sometimes, insufficient sample material was available to acquire both whole-rock geochemical and U-Pb apatite and / or zircon data. As obtaining whole-rock geochemical data was prioritised, the whole-rock aliquot was often larger in comparison to volume of sample processed for zircon and apatite separation. Additionally, even when sufficient sample material was available, not all samples contained zircons and apatites, which explains the relatively small data set (see Table 5-2).

5.4.1 Whole-Rock Geochemical Data as a Tool to Predicting Apatite and Zircon Yield

Whole-rock geochemical analyses were conducted on all tuff horizons before these layers were dated by the LA-ICP-MS U-Pb zircon and apatite method (see Chapter 4). As apatite is the predominant P reservoir in magmatic rocks and apatite grains get fully dissolved in the applied hotplate digestion method, it was expected that samples with the highest P concentrations should contain most apatite grains, but there is only a correlation between the P concentration and apatite abundances in the Navan area; no correlation is observed for Stonepark and Slievedart (Figure 5-16).

Equally the same should apply for zircon, as zircon host significant fractions of the whole-rock abundance of Zr. However, zircon grains require high-pressure digestions for complete elemental recovery (Marx and Kamber, 2010). There is no positive correlation between the Zr concentration of a sample and the amount of recovered zircon grains for samples from the Stonepark area (Figure 5-16C) and neither for Navan, the Rathdowney Trend and the Slievedart area, where even the samples with lowest Zr concentrations in the bulk-rock sample contained zircon grains as opposed to the samples with the highest Zr concentrations (Figure 5-16A, B, D). In hotplate digestions, the degree of radiation damage (metamictisation) of the zircons could control digestion rates. Zircons which contain more porosity and micro-fractures are more easily attacked by acid and therefore release more Zr, Hf and REEs compared to more pristine zircons. Thus, there is the possibility that samples from Navan, the Rathdowney Trend and the Slievedart area, which have the highest Zr contents also contained the most radiation-damaged zircon grains. However, no specific pattern could be observed for Stonepark samples (Figure 5-16C).

In summary, the amount of zircons and apatite within a separated sample cannot be reliably predicted based on their Zr and P concentrations, respectively.

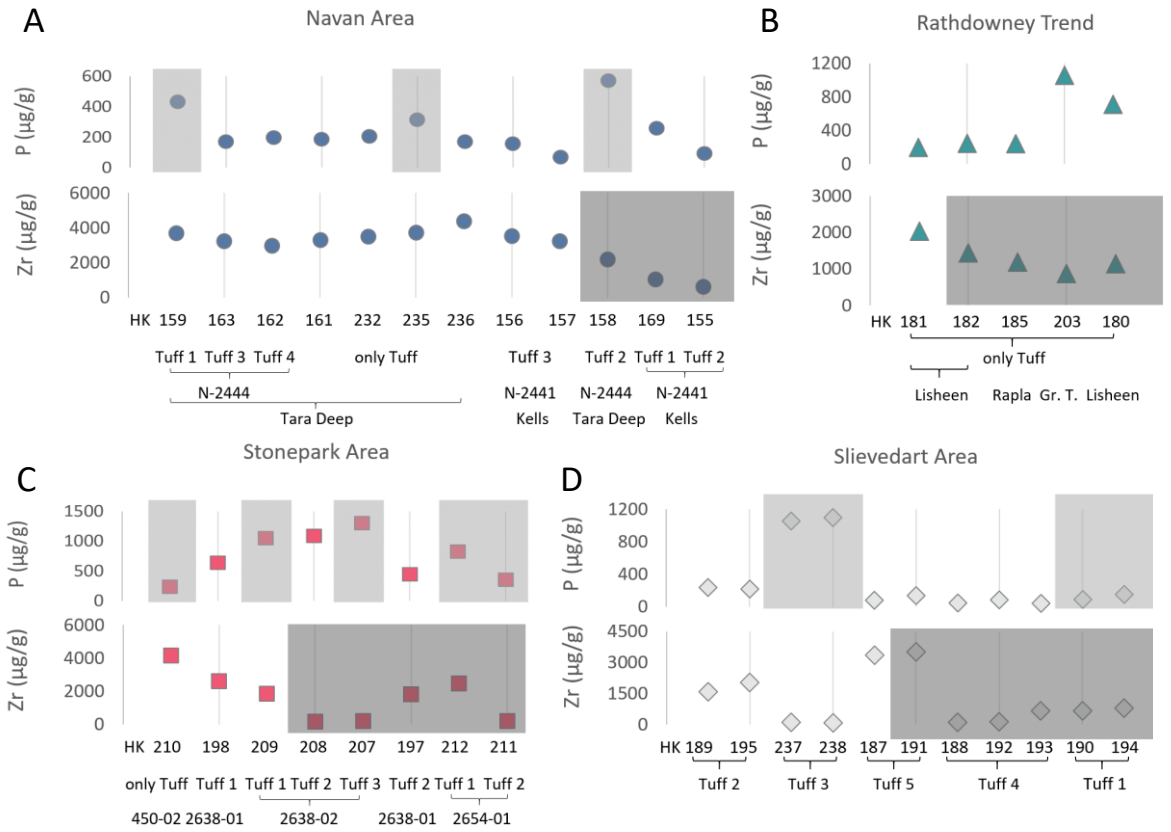

Figure 5-16: Phosphorus and Zr concentrations in µg/g from Irish Mississippian tuffs in relation to the abundance of apatite and zircons, respectively. Bright grey shaded samples contain apatites, whereas dark grey shaded samples contain zircons. A) Navan area, B) Rathdowney Trend; C) Stonepark area; D) Slievedart area.

Whole-rock analyses were undertaken primarily for chemostratigraphic purposes, but also to investigate the composition of the magma from which the (now altered) volcanic ash layers were originally erupted and connect them to potential volcanic centres. However, there is also the potential to connect the varying abundance of zircon grains in different samples to the nature of the tuff layers themselves, as zircons occur predominantly in evolved/felsic magmas. TiO_2/Al_2O_3 ratios between 0.004 and 0.022 can suggest a silicic magma composition, while relatively high ratios indicate intermediate (0.022 to 0.055) to mafic (0.055 to 0.14) source magmas (Le Maitre, 1976; Spears and Kanaris-Sotiriou, 1976). Samples from all four study areas show TiO_2/Al_2O_3 ratios between 0.01 and 0.055, implying felsic to intermediate magma compositions. However, no clear trend between the TiO_2/Al_2O_3 ratio and zircon yield was observed for the Navan, Rathdowney Trend and Stonepark areas (Figure 5-17A, B and C). However, the four most evolved samples (lowest TiO_2/Al_2O_3 ratios) in the Slievedart area are the only tuffs that contained zircons in that region (Figure 5-17D).

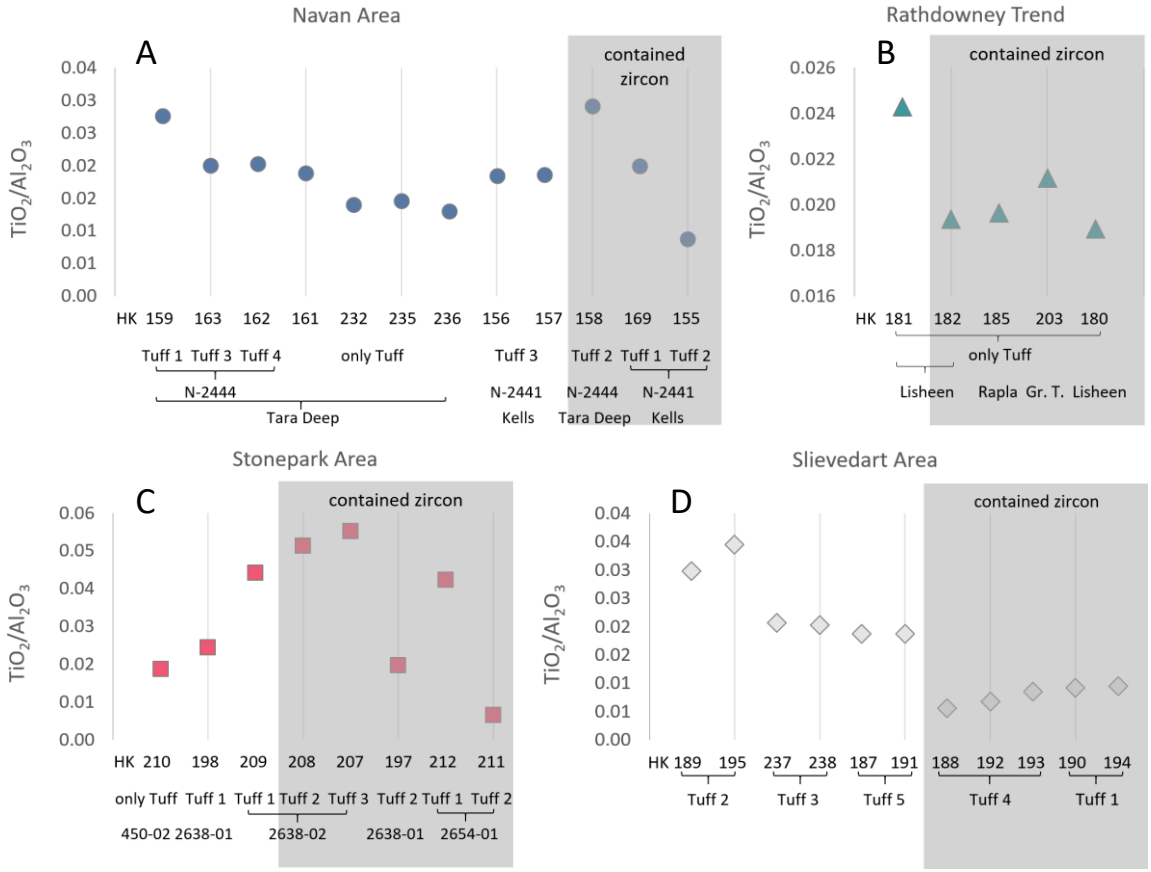

Figure 5-17: TiO_2/Al_2O_3 ratios for all Irish Mississippian tuff samples, which were examined for zircons in this study. Zircon-bearing samples are denoted by a grey box. A) Navan area, B) Rathdowney Trend; C) Stonepark area; D) Slievedart area.

Negative Eu anomalies ($Eu_{CN}/Eu^* < 1$) are characteristic of silicic igneous rocks (Bohor and Triplehorn, 1993), while also indicating highly evolved, sub-alkaline magma sources. The larger the negative Eu anomaly, the more evolved was the parent magma. The samples from Navan and the Rathdowney Trend which have a less pronounced Eu anomaly, contain zircons (Figure 5-18A, B), which is somewhat unexpected. There is no correlation between the whole-rock Eu anomaly (Eu_{CN}/Eu^*) and zircon yield for the Stonepark nor for the Slievedart areas (Figure 5-18C, D).

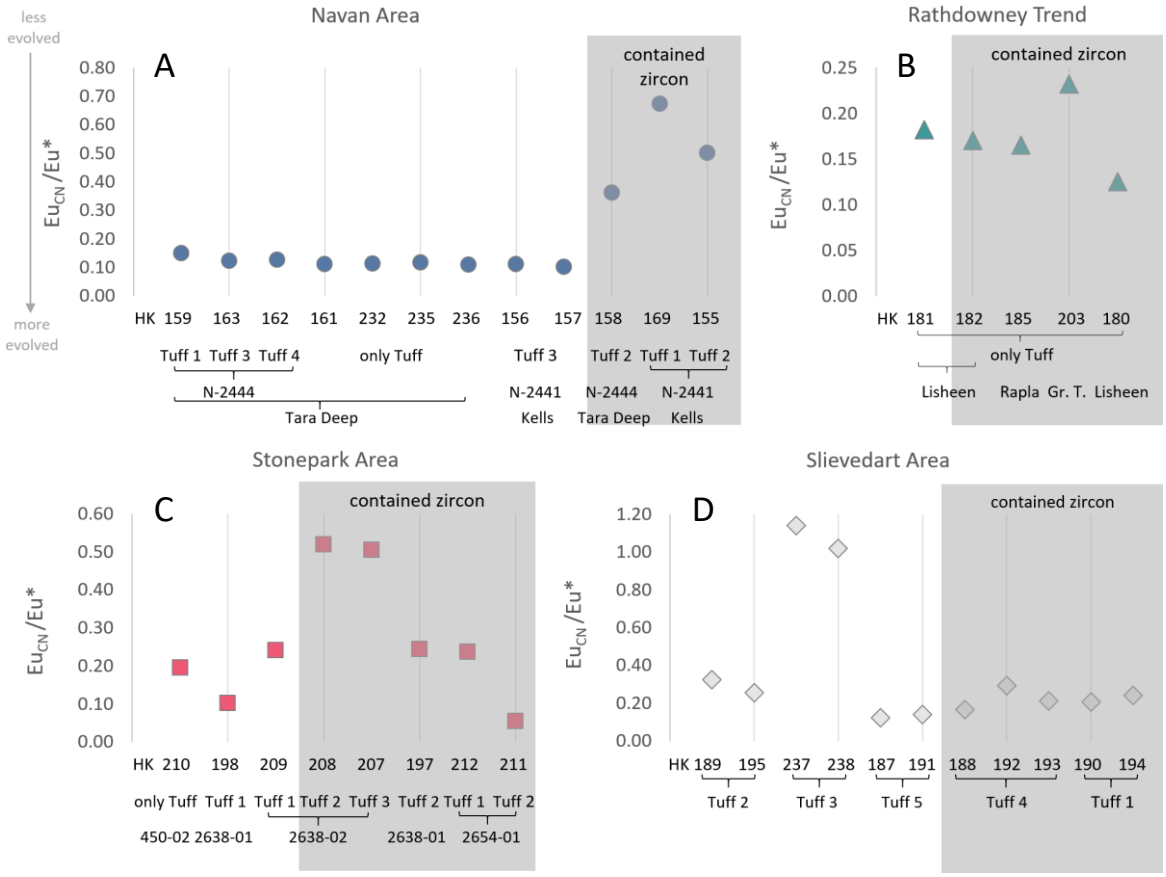

Figure 5-18: Whole-rock Eu anomaly (Eu_{CN}/Eu^*) for all Irish Mississippian tuff samples, which were examined for zircons in this study. Zircon-bearing samples are denoted by a grey box. A) Navan area, B) Rathdowney Trend; C) Stonepark area; D) Slievedart area. Grey arrow points towards values, which indicate a higher evolved parent magma compositions.

The size of the processed samples (see section 5.2.3 for detailed steps) ranged from < 0.01 g to 0.6 g, with five exceptions; HK 161 (0.83 g), HK 203 (25.57 g), HK 195 (2.84 g), HK 237 (5.5 g) and HK 238 (7.8 g) (Figure 5-19A-D). Again, there is no systematic difference between the sample size and zircon yield (Figure 5-19A-D).

There is also no relationship between whole-rock TiO_2/Al_2O_3 ratio, whole-rock Eu anomalies or sample size on the abundance of apatite grains in a sample (not shown).

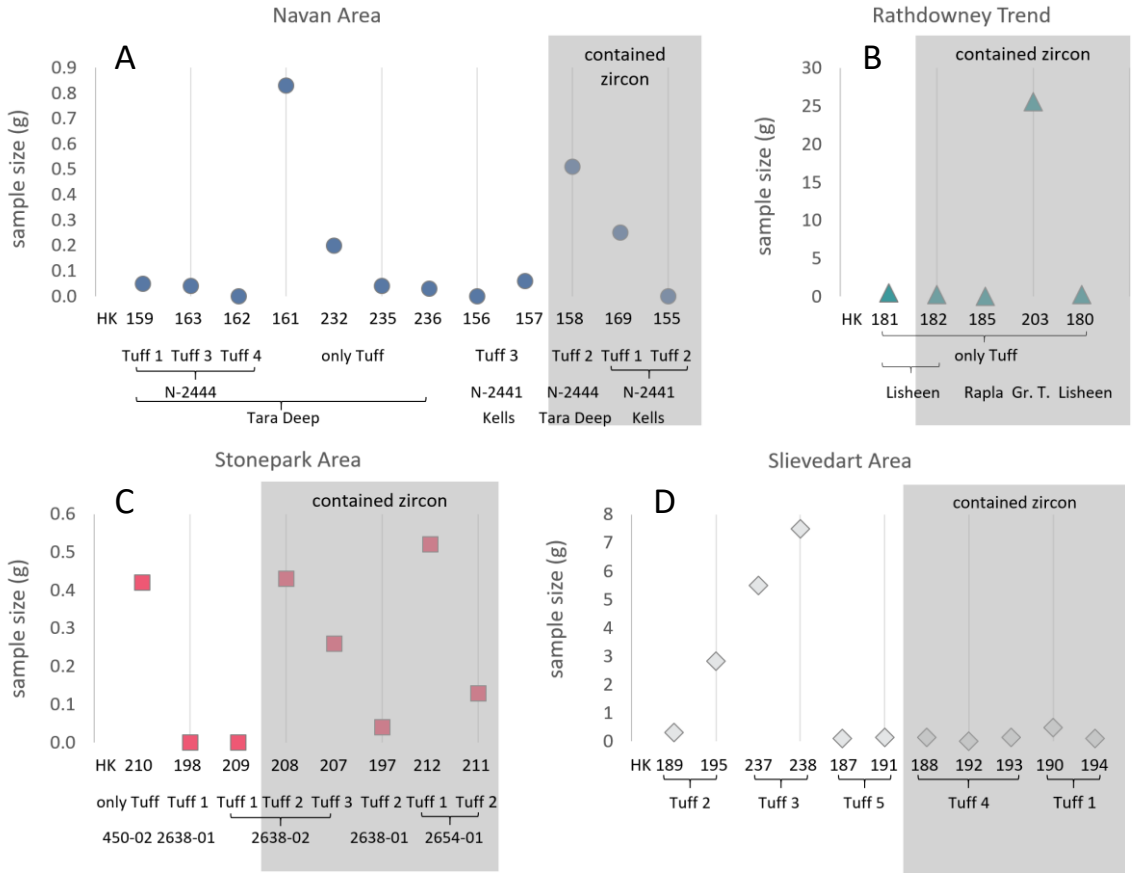

Figure 5-19: Sample size (in g) of the non-magnetic, > 2.7 g/cm³ and < 300 µm fraction of the sampled Irish Mississippian tuffs from this study. Zircon-bearing samples are denoted by a grey box. A) Navan area, B) Rathdowney Trend; C) Stonepark area; D) Slievedart area.

5.4.2 Zircon - U-Pb Age Data

This section discusses the U-Pb zircon ages of the tuff layers in the context of the Early Carboniferous timescale, which is outlined in section 1.2.

5.4.2.1 Navan

Only one out of eight examined tuff samples from Tara Deep yielded zircon grains (see Table 5-2).

There are three tuff layers in drill core N-2444. Only the second tuff layer (sample Tara Deep_N-2444_HK 158) has zircons, which gives a calculated eruption age of 346.4 ± 3.9 (2σ) Ma or 343.6 ± 4.5 (2σ) Ma, depending if the four zircon grains that show large analytical uncertainties were included in the age determination or not (see section 5.3.1.1). The sampled tuff layer occurs in the Early Viséan (Lower Viséan to Arundian) New Thin Bedded Unit of the Fingal Group (Figure 5-20A). Thus, as the age of the zircon population is in agreement with the Lower Viséan, it is most likely that the zircon grains in this sample represent the depositional age of the tuff horizon. The quality of the data is supported by MSWDs of 1.08 or 0.84 (Figure 5-5B, D).

The first and second tuff layers (out of three) from drill core N-2441 are 44.95 m apart (stratigraphically). The first tuff layer (sample HK 169) occurs in the Waulsortian equivalent whereas the second tuff (sample HK 155) was deposited in the overlying Tober Colleen Formation (Figure 5-20B). They yield ages of 342.0 ± 2.7 Ma (sample HK 169) and 348.7 ± 3.0 Ma (sample HK 155), respectively. Thus, their ages are slightly outside analytical uncertainty (c. 1 Ma), with the stratigraphically older sample yielding a younger Viséan age.

The age of sample Navan West_N-2441_HK 169 from the first tuff layer does not match the Tournaisian age of its Waulsortian equivalent host rock. Therefore, this age is most likely erroneous, although the MSWD is 1.03 and thus would normally indicate a reliable age.

Taking the analytical uncertainty of sample Navan West_N-2441_HK 155 into consideration, it ranges from 345.7 to 351.7 Ma and is thus consistent with either the Ivorian or Lower Viséan age of the diachronously distributed Tober Colleen Formation.

The ages of sample Tara Deep_N-2444_HK 158 and sample Navan West_N-2441_HK 155 are also within analytical uncertainty. As these samples occur in laterally equivalent host rocks (New Thin Bedded Unit and Tober Colleen Formation, respectively; Philcox, pers. comm., 2020), there is the possibility that they share the same eruption history (Figure 5-20), assuming the ash was deposited in the Lower Viséan part of the Tober Colleen Formation. However, four out of seven zircon grains from tuff sample Navan West_N-2441_HK 155 displayed either Pb loss (one grain), common Pb contamination (two grains) or inheritance (one grain) (Table 5-4). Therefore, the eruption age was determined using only three zircon grains, resulting in a MSWD of 0.92 for a Wetherill concordia age. However, the MSWD for the weighted average mean age of the same sample was only 0.14 (Figure 5-6C, E). Therefore, the age determined for sample Navan West_N-2441_HK 155 should be interpreted with caution. Further analyses of samples from this tuff layer are necessary to yield more magmatic zircon grains and thus more reliable eruption ages.

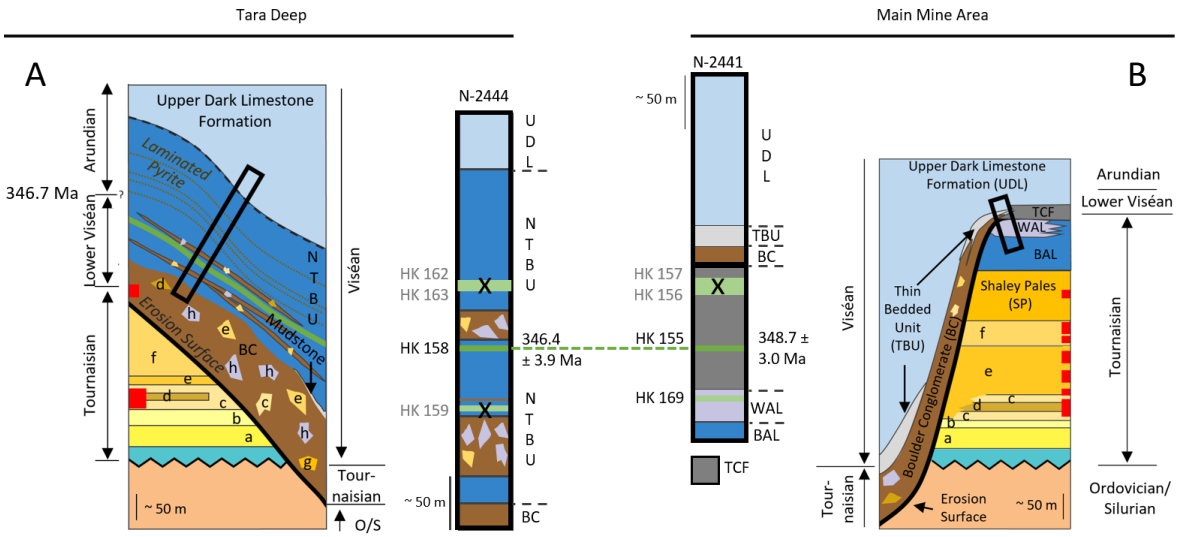

Figure 5-20: A) Simplified stratigraphy of Tara Deep along with drill core N-2444 and the LA-ICP-MS U-Pb zircon age for sample HK 158. B) Simplified stratigraphy of the main mine area along with drill core N-2441. LA-ICP-MS U-Pb zircon ages for samples HK 169 and HK 155 are 342 ± 2.7 Ma and 348.7 ± 3 Ma, respectively. U-Pb zircon ages for sample HK 158 and HK 155 are within uncertainty. Thus, they could be from the same tuff horizon (indicated by green dashed line) and share a common volcanic centre. No zircon grains were found in the tuff layers which are crossed out (marked with an X). BAL = Ballysteen Limestone Formation, BC = Boulder Conglomerate, NTBU = New Thin Bedded Unit, TBU – Thin Bedded Unit, TCF = Tober Colleen Formation, UDL = Upper Dark Limestone Formation, WAL = Waulsortian Limestone Formation. See Figure 2-7B and 2-8B for the full key of the lithostratigraphic units.

5.4.2.2 Rathdowney Trend

Five tuff samples were processed; all yielded zircons but of these only four samples (HK 180, 182, 185, 203) yielded Early Carboniferous U-Pb ages (Figure 5-7). Both zircon grains from sample Lisheen_LK-2180_HK 181 (S-ABL) are well outside the Early Carboniferous time window (ages of 300.63 ± 8.96 Ma and 1034 ± 22.97 Ma) (Figure 5-7I). Thus, sample HK 181 is not discussed further.

Sample Lisheen_LK-1722_HK 180 occurs in the Nodular Micrite Unit, samples Lisheen_LK-1040_HK 182 and Lisheen_mine sample_HK 203 in the S-ABL and sample Rapla_3667-04_HK 185 in the Upper Calcarenite Member (Figure 5-7). These units are part of the Ballysteen Limestone Formation, which was deposited in the Tournaisian. Thus, the youngest expected ages of these tuff layers should not be younger than 346.7 Ma (the Tournaisian-Viséan boundary). Two analysed tuffs from the Rapla and Lisheen area yield U-Pb concordia ages between 340.1 ± 2.3 (2σ) Ma (HK 185) and 344.8 ± 2.1 (2σ) Ma (HK 180). Therefore, these samples record a late Arundian to Asbian age, while sample Lisheen_LK-1040_HK 182 yielded a concordia age of 346.6 ± 2.5 (2σ) Ma, which is exactly the age of the Tournaisian-Viséan boundary. However, sample Lisheen_mine sample_HK 203 shows a Tournaisian age of 349.6 ± 1.5 (2σ) Ma. Thus, only the latter sample reflects clearly the depositional age of the host rock. Sample Lisheen_LK-1040_HK 182 plots at the Tournaisian – Viséan boundary, while samples Lisheen_LK-1722_HK 180 and Rapla_3667-04_HK 185 yield Viséan ages.

It is not very likely that the younger ages are caused by analytical bias, especially because data were obtained during two different analytical sessions. Furthermore, the data are tightly clustered around the assumed eruption age, where Pb loss and inheritance is apparently minimal. Each data set also only showed a single concordant population of zircon grains that allowed the calculation of a concordant age with good MSWDs and probability-of-fits (see Table 5-4). However, the determined age of sample Lisheen_mine sample_HK 203 is based on 36 magmatic zircon grains compared to eight (sample HK 182), eleven (sample HK 185) and 13 (sample HK 180) grains and shows the best values for MSWD and probability-of-fit (Table 5-4). Thus, sample HK 203 shows probably is the most reliable age among the four analysed samples from Lisheen and Rapla. This could imply that there is not enough zircons in a single thin Mississippian tuff horizon in a single drill core to provide a reliable date, while enough zircons could be recovered from the outcrop sample HK 203.

If the younger calculated ages of samples HK 180, 182 and 185 actually reflect the age of their host rocks, the Tournaisian - Viséan boundary has to be moved closer or even within the Nodular Micrite Unit. Subsequently, the Waulsortian Limestone Formation would be early Viséan rather than late Tournaisian in age. Although the Waulsortian Limestone Formation was generally deposited in the late Tournaisian, there are some local Lower Viséan occurrences known in the Irish Midlands (Sevastopulo and Wyse Jackson, 2009). However, biostratigraphy principally governs the placement of regional substage boundaries, while radiometric ages are used to further define these boundaries. Thus, the next step is to examine carefully the biostratigraphy of the Waulsortian Limestone Formation in this area. Only if the biostratigraphy and the ages (which must be confirmed by further analyses, particularly high-precision ID-TIMS work) match, there is the possibility that the Tournaisian - Viséan boundary should be moved.

5.4.2.3 Stonepark Area

Drill core G11-2654-01 contains two datable tuff layers. The first tuff layer (sample HK 212) appears within the Nodular Micrite Unit, which is the stratigraphically highest portion of the Ballynamona Member of the Ballysteen Limestone Formation (see section 2.8.1 and Figure 5-21). The Nodular Micrite Unit is overlain by the Waulsortian Limestone Formation, followed by the Lough Gur Formation, which contains the second tuff layer (sample HK 211) of drill core G11-2654-01 (Figure 5-21). The Nodular Micrite Unit is Ivorian in age, while the Lough Gur Formation is late Ivorian/early Viséan in age. Hence, the Tournaisian-Viséan boundary is within the Lough Gur Formation.

The obtained age for sample HK 212 (350.3 ± 4.3 Ma) is in agreement with the age of the Nodular Micrite Unit, which is the host rock of this tuff layer (Figure 5-21). The age of the second tuff layer in the same drill core (sample HK 211; 348.2 ± 2.4 Ma) is also within analytical uncertainty of the

expected time range for the Lough Gur Formation and thus represents the depositional age of the host rock (Figure 5-21). However, both tuff ages from drill core G11-2654-01 are within analytical uncertainty, although both tuff layers are 367.6 m (stratigraphically) apart, separated by the Waulsortian Limestone Formation. Thus, it seems like the LA-ICP-MS U-Pb zircon dating is not sensitive enough to distinguish individual tuffs by age alone for this area.

Nevertheless, sample HK 197, the second tuff layer from drill core 2638-01, was also deposited within the Nodular Micrite Unit and yields an age of 350.7 ± 3.3 (2σ) Ma, which represents the age of the host rock. Thus, samples HK 197 and 212 share a similar eruption age and possibly the same volcanic centre. All other tuff layers from the Stonepark area, which appear in the Nodular Micrite Unit (HK 198, 207, 208, 209, 210) yielded no zircons.

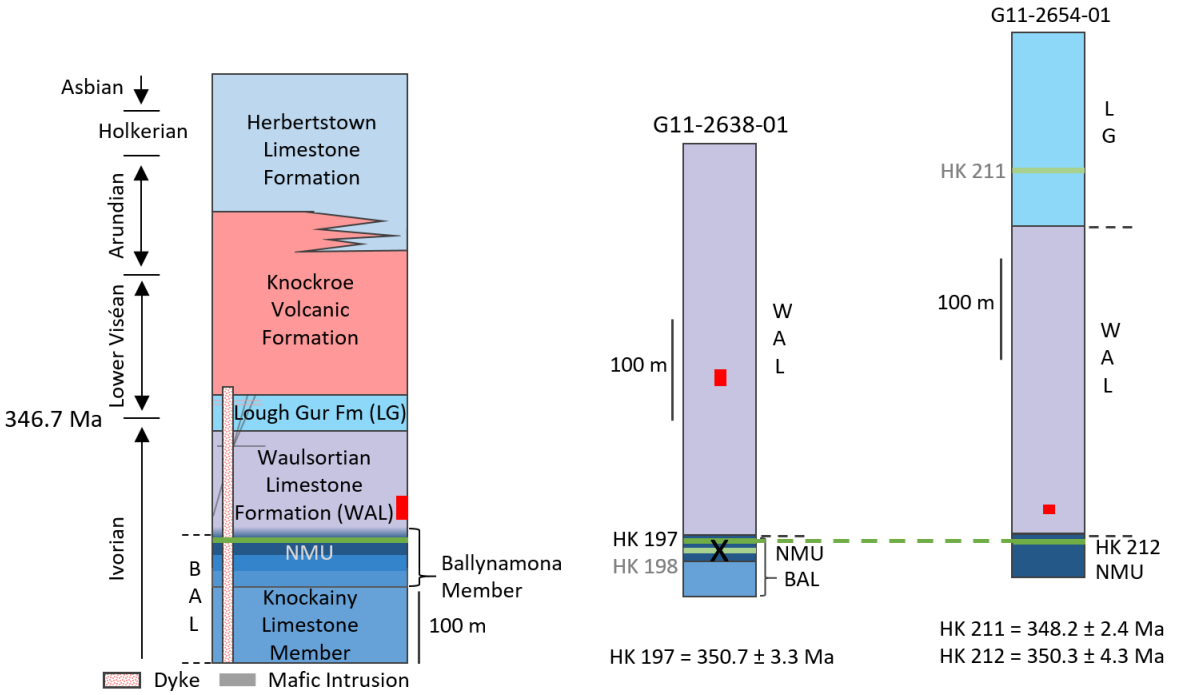

Figure 5-21: Schematic lithostratigraphy of the Stonepark area. See Figure 2-10 for the full stratigraphic table. Drill cores G11-2654-01 and G11-2638-01 yielded three tuff samples (HK 212, 211 and 197), whose LA-ICP-MS zircon ages yielded Early Carboniferous ages, which are consistent with their host rock ages. Zircon ages from samples HK 212 and 197 are within analytical uncertainty. Thus, both tuff layers could share the same eruption centre. No zircon grains were found in the tuff layers which are crossed out (marked with an X). BAL = Ballysteen Limestone Formation, NMU = Nodular Micrite Unit, red bar = mineralisation.

5.4.2.4 Slievedart Area

The age of the Waulsortian Limestone Formation in the Slievedart area is late Tournaisian (Sevastopulo, 1982; Pracht et al., 2004). The Kilbryan Limestone Formation sits either above or can may be in part laterally equivalent to the Waulsortian Limestone Formation (or a Waulsortian equivalent) and does not contain diagnostic microfossils (Pracht and Somerville, 2015). The stratigraphically younger Lower Viséan Oakport Limestone Formation is well constrained *(Pracht and Somerville, 2015)*. Hence, due to its stratigraphic position between the Waulsortian Limestone and the Oakport Limestone formations, the Kilbryan Limestone Formation is

considered to be of late Tournaisian to earliest Viséan age (Pracht and Somerville, 2015) (Figure 5-22).

The first tuff layers are the stratigraphically lowest layers from drill cores 3470/15 and 3471/4 and appear in the Kilbryan Limestone Formation. Sample Slievedart_3471/4_HK 194 has two magmatic populations. It yields a U-Pb LA-ICP-MS zircon age of 345.6 ± 3.5 Ma (population one) and 361.0 ± 3.2 Ma (population two). Only one concordia age could be calculated for sample Slievedart_3470/15_HK 190, which is 358.1 ± 3.0 Ma (Figure 5-9E-H, K, L; Figure 5-22). Thus, the ages of sample HK 190 and the age of population two of sample HK 194 are within analytical uncertainty and coincides with the age of the Devonian-Carboniferous boundary. Although the Kilbryan Limestone Formation could not be dated in this area, the age of the tuff layers should not exceed 346.7 Ma based on the late Tournaisian age of the underlying Ballysteen Limestone or Waulsortian Limestone formations (Sevastopulo, 1982; Pracht et al., 2004). The MSWD and probability-of-fit of both tuff layers are 0.67 and 0.89 (HK 190) and 0.49 and 0.91 (HK 194, population 2) respectively, which supports the reliability of the ages. However, the Waulsortian Limestone Formation in this particular area and the biostratigraphy in NW Ireland in general is not well constrained. The Tournaisian age of the Ballysteen Limestone and Moathill formations are also only based on sparse foraminiferal, algal/cyanobacteria and microproblematica assemblages (Pracht and Somerville, 2015). Nevertheless, it is very unlikely that the Devonian-Carboniferous boundary age lies within the Kilbryan Limestone Formation as the late Tournaisian age of the underlying Boyle Sandstone Formation is well characterised, using spore data (CM Zone) from the type section near Boyle, Co. Roscommon (Caldwell, 1959; Morris et al., 2003). One possibility is that the c. 360 Ma ages represent an older magmatic population that was reworked into the tuffs with sample HK 194 showing a younger magmatic population (population two) and an older inherited magmatic population while sample HK 190 only shows the older original eruption age. Population one of tuff one in drill core 3471/4 yields a concordant zircon age of 345.6 ± 3.5 Ma (MSWD = 0.6, probability-of-fit = 0.87), which is in agreement with the biostratigraphic age of the Kilbryan Limestone Formation. A third drill core (1680/2) is located 5.7 km north of drill core 3470/15 and 9.6 km north-west of drill core 3471/4 (see section 2.9.1 and Figure 2-11). Tuff one and two of drill core 1680/02 occur also in the Kilbryan Limestone Formation at 300.9 m and 263.1 m, respectively. Tuff three is located in the Oakport Limestone Formation at 179.75 m. Uranium-lead zircon chemical abrasion isotope dilution thermal ionisation mass spectrometry (CA-ID-TIMS) data from that first tuff layer from 1680/02 (also called bentonite 300) produced a weighted mean $^{206}Pb/^{238}U$ date of 347.94 ± 0.08 Ma (95% conf., MSWD = 1.5, p = 0.18) (Pointon, 2012). Thus, the published isotopic data supports the age of population one of sample Slievedart_3471/4_HK 194 but diverges significantly with sample Slievedart_3470/15_HK 190 and

population two of sample Slievedart_3471/4_HK 194 (358.7 ± 3.0 Ma (HK 190) and 361.0 ± 3.2 Ma (HK 194, population 2)).

Tuff four layers are the stratigraphically second highest layers in drill cores 3470/15, 3471/4 and 1680/02 and occur in the Kilbryan Limestone Formation. Zircons were only found in tuff four layers in drill core 1680/2 (pers. comm. George Sevastopulo, 2020). The fourth tuff layer in drill core 3470/15 yields a zircon age of 347.2 ± 2.9 Ma (2σ) (HK 188). Tuff layers from drill core 3471/4, which are both considered as equivalent to tuff four due to their proximity within the drill core, are 345.4 ± 1.8 Ma (2σ) (HK 193) and 347.7 ± 2.2 Ma (2σ) (HK 192) old. Thus, all tuff four layers are within analytical uncertainty (Figure 5-22).

Although drill cores 3470/15, 3471/4 and 1680/02 cannot be correlated based on whole-rock trace-element chemistry as trace elements were not determined for drill core 1680/02 due to insufficient sample material, the three drill cores can be correlated on the basis of three volcanogenic clay bands; tuff one, tuff four and tuff five (Mike Philcox and George Sevastopulo, pers. comm., 2020) (Figure 5-22). The stratigraphic thickness of the intervals between these clay bands, especially in drill core 3471/15 and 1680/2, is very similar, which supports a similar depositional history (Figure 5-22). Thus, samples HK 190, 194 and bentonite 300 as well as samples HK 188, 192 and 193 should share the same eruption history. The biostratigraphic position of tuff one from drill core 1680/02 (bentonite 300) is constrained to either the late Mississippian foraminiferal zones (MFZ) 7 or the MFZ8 foraminifera biozones (pers. comm. George Sevastopulo, 2020). Therefore, it is more likely that the high-precision CA-ID-TIMS age of Pointon (2012) and the U-Pb zircon LA-ICP-MS age of population one in sample HK 194 show the real eruption age (average age = 346.77 Ma), while population two of the same sample and sample HK 190 yield slightly too old ages (average age = 359.55 Ma) and likely represent an inherited component. Consequently, tuff one and tuff four layers cannot be distinguished based on their U-Pb zircon ages, although the two tuff layers can be clearly separated stratigraphically. However, these layers also have similar ages close to the Tournaisian – Viséan boundary. Thus, this study suggests that the Viséan in the Slievedart area could begin within the Kilbryan Limestone Formation, 52.2 m and 71.2 m below the Kilbryan Limestone - Oakport Limestone formation boundary in drill core 3470/15 and 3471/4, respectively. If the MFZ8 and 9 can be detected in the limestones enclosing the tuff layers, these drill cores have potential to more precisely constrain the Tournaisian – Viséan boundary in future iterations of the Carboniferous timescale.

In summary, the ages of sample Slievedart_3470/15_HK 190 and population one in sample Slievedart_3471/4_HK 194 are slightly too old for tuff layers within the Kilbryan Limestone Formation as they appear to conflict with published biostratigraphical ages and likely represent

inherited zircon. However, the magmatic population two in sample Slievedart_3471/4_HK 194 and bentonite 300 from Pointon (2012) yield an average eruption age for tuff one of 346.77 Ma and are thus in agreement with the host rock. The mean concordia age of tuff four is 346.76 Ma and is thus within analytical uncertainty of the tuff one ages. Therefore, U-Pb zircon ages of tuff layers within the Kilbryan Limestone Formation cannot be temporally resolved although they can be clearly separated based on their stratigraphic position and whole-rock trace element analyses. However, the age determinations from the tuff layers of the Slievedart area suggest that the Tournaisian-Viséan boundary can be confined and placed between the first and fourth tuff layers of drill cores 3470/15 and 3471/4 and the first and second tuff layer of drill core 1680/2 (Figure 5-22).

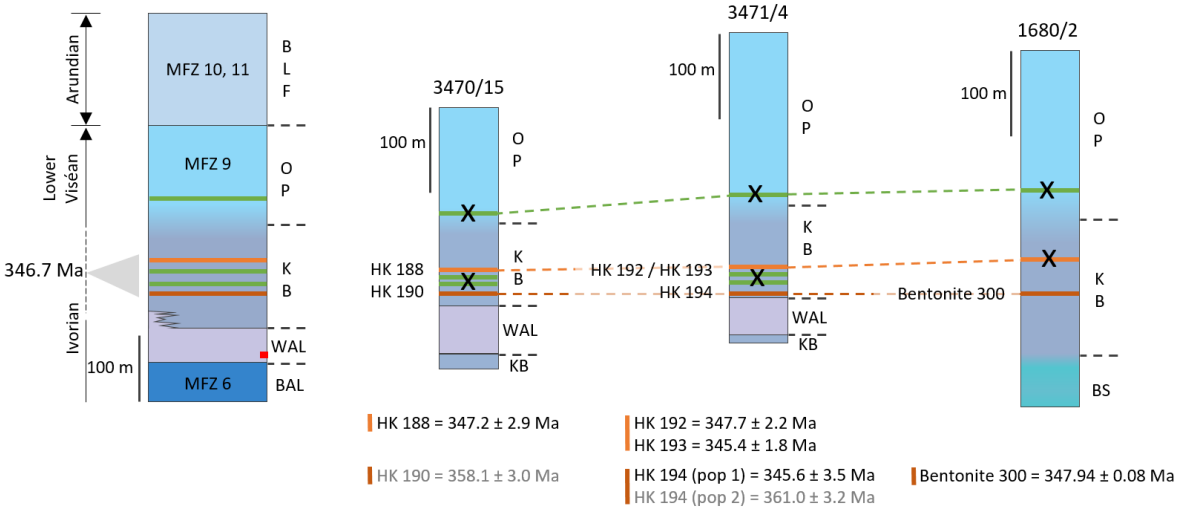

Figure 5-22: Schematic stratigraphy of the Slievedart area. The dark orange, bright orange and bright green tuff layers can be linked in between drill core 3470/15, 3471/4 and 1680/2 based on biostratigraphic data, interval thickness and the overall occurrence within the drill core (personal communication George Sevastopulo, 2020) and is indicated by dashed lines. LA-ICP-MS U-Pb zircon data of sample HK 188, 192, 193, population one (pop 1) of sample HK 194 and bentonite 300 are within analytical uncertainty and are in agreement with host rock ages. Thus, U-Pb zircon age resolution is not fine enough to distinguish tuff layers, occurring within the Kilbryan Limestone Formation. However, this study suggests that the Tournaisian-Viséan boundary can be refined and placed between the occurrence of the dark and bright orange tuff samples, which is indicated by the grey triangle on the left. Calculated ages for samples HK 190 and the second population (pop 2) of sample HK 194 are most likely too old and thus do not represent eruption ages. Ages are therefore written in grey. No zircon grains were found in the tuff layers which are crossed out (marked with an X). Known Mississippian foraminifera zones (MFZ) are taken from Pracht and Somerville (2015). BAL = Ballysteen Limestone Formation, BLF = Ballymore Limestone Formation, BS = Basal Transition, KB = Kilbryan Limestone Formation, OP = Oakport Limestone Formation, WAL = Waulsortian Limestone Formation, red bar = zone of mineralisation.

5.4.2.5 Cross-Correlation

Ash layers, which are deposited from the same volcanic eruption are isochronous, and represent the eruption age. Thus, if several ash layers from the four different areas sampled in this study yield similar ages, they can be potentially linked to the same volcanic centre. At the same time, multiple tuff horizons within one drill core must clearly have different eruption ages. The following ten samples of this dataset show reliable eruption ages: Stonepark_G11-2638-01_HK 197, Stonepark_G11-2654-01_HK 211, Stonepark_G11-2654-01_HK 212, Lisheen_mine sample_HK 203, Slievedart_3471/4_HK 194_pop 1, Slievedart_3470/15_HK 188,

Slievedart_3471/4_HK 192, Slievedart_3471/4_HK 193, Navan West_N-2441_HK 155 and Tara Deep_N-2444_HK 158 (see sections 5.4.2.1 to 5.4.2.4. The median U-Pb zircon age for these tuff layers is 348.0 ± 1.77 (2SD) Ma. If this is used as a reference benchmark, all samples lie very close (within uncertainty) to the median value (Figure 5-23A). Hence, they could stem from the same volcanic centre, and represent a hypothesised extensive volcanic event, which led to the deposition of ash layers across the four study sites: Navan, Tara Deep, Lisheen, Stonepark and Slievedart. However, samples Stonepark_G11-2638-01_HK 197, Stonepark_G11-2654-01_HK 212 and Lisheen_mine sample_HK 203 occur below the Waulsortian Limestone Formation. They show a median eruption age of 350.3 ± 0.45 (2SD) Ma while the remaining seven samples, which were deposited above the Waulsortian Limestone Formation have a median U-Pb zircon age of 347.2 ± 01.18 (2SD) Ma (Figure 5-23A). Thus, both sample sets can be clearly distinguished, suggesting an older eruption around 350.3 Ma ago, which was followed by a younger eruption around 347.2 Ma. These led to the deposition of volcanic ash in Stonepark and Lisheen as well as in Slievedart, Stonepark and Navan, respectively. However, drill core 3471/4 in Slievedart contains two tuff horizons (HK 194 and HK 192/193), which are 31.4 m stratigraphically apart. This implies the occurrence of two different eruption events, which cannot be temporally resolved. As only one tuff horizon of this age is observed in Navan and Stonepark, it is unlikely that the volcanic ashes across the three areas were deposited as part of the same volcanic event, unless the preservation potential for tuffs was higher in Slievedart compared to Navan and Stonepark. Furthermore, while sample Tara Deep_N-2444_HK 158 falls within the median value of the Slievedart tuff ages, the zircon U-Pb age of sample Navan West_N-2441_HK 155 is slightly too old (Figure 5-23A). Certainly the latter age has to be treated with caution and additional age constraints for this tuff layer are recommended as already discussed in section 5.4.2.1. However, the stratigraphical and geographical position of samples Tara Deep_N-2444_HK 158 and Navan West_N-2441_HK 155 suggest simultaneous deposition of these ash layers as a single separate event rather than being part of the Slievedart eruption sequence. The age range for sample Stonepark_G11-2654-01_HK 211 is between 345.8 and 350.6 Ma. Thus, it could be part of either the Stonepark/Lisheen or the Slievedart eruption event. However, only the younger age estimates are reasonable based on its stratigraphic position and this allows grouping this sample together with the four Slievedart samples.

In summary, this dataset suggests a local eruption in the Stonepark and Lisheen area at c. 350.3 Ma ago, whose ash can be seen in drill core G11-2638-01 (sample HK 197) and G11-2654-01 (sample HK 212) in Stonepark and in the mine sample HK 203 in Lisheen (Figure 5-23B, C). Shortly afterwards (c. 346.4 Ma ago), a second local eruption took place in the Slievedart area, producing the ash layers of samples HK 188, HK 192, HK 193 and HK 194 (Figure 5-23B, C). This

eruption event led to the deposition of two datable tuff horizons within the same drill core (tuff one = sample HK 194; tuff four = samples HK 192, 193), whose U-Pb zircon ages cannot be temporally distinguished. There is the possibility that sample Stonepark_G11-2654-01_HHK 211 was part of that same eruption. Whether there was a third volcanic event, which produced another ash layer, which can be traced across Navan West and Tara Deep or if it was part of the Slievedart eruption event has to be confirmed by further analyses.

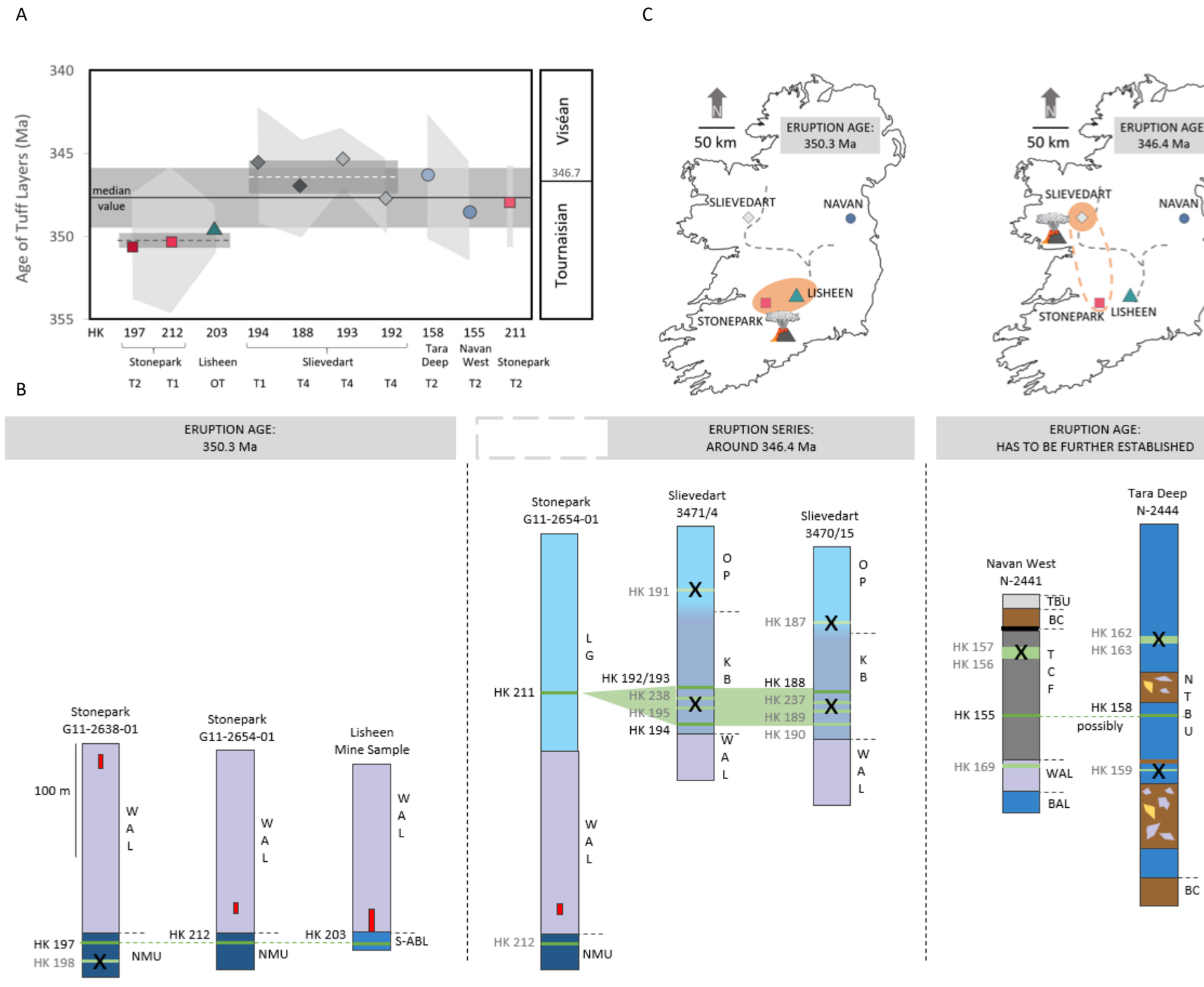

Figure 5-23: Cross-correlation between Irish Mississippian tuff samples from Stonepark (squares), Lisheen (triangles), Slievedart (diamonds) and Navan (circles) that show reliable U-Pb zircon ages. A) The samples' age uncertainty (bright grey shaded area) plot within the two standard deviation (dark grey shaded area) of the median value (grey solid line) of the whole data set. However, the age of samples HK 197 and HK 212 from the Stonepark area and sample HK 203 from Lisheen lie within 2SD of their median value (dark grey dashed line) and can be clearly distinguished from the median value (white dashed line) of the Slievedart samples. Sample Navan West_N-2441_HK 155 plots neither within the median value of the Stonepark and Lisheen nor within the Slievedart samples, while sample Tara Deep_N-2444_HK 158 plots within the median value of theSlievedart samples. Sample Stonepark_2654-01_HK 211 plots within uncertainty of the Slievedart and Navan samples. B) Stratigraphic columns for tuff layers from seven different drill cores is shown. Tuff layers, which share the same eruption age, are either linked with a dashed line or a grey shaded area. The potential eruption age of tuff layers from Stonepark and Lisheen is c. 350.d Ma; the potential eruption age of tuff layers from Slievedart is c. 346.4 Ma. Sample HK 211 is probably part of the same eruption. Sample HK 155 from Navan West and sample HK 158 from Tara Deep share most likely the same volcanic centre. The eruption age has to be confirmed by further analyses. Bright green tuff layers which are marked with a cross did not contain datable zircon grains, while zircons from the remaining bright green tuff layers could be analysed but did not yield reliable U-Pb zircon ages. The name of the sample location and drill core ID is indicated at the top of the log. The lab ID of samples of interest is written in black. See table 2-2, 2-4, 2-6, 2-8 and 2-10 for full sample names. Scale bar is same for all samples. C) The location of deposited ash layers (in orange) when separated by their eruption age. T1 = tuff 1; T2 = tuff 2; OT = only tuff in respective drill core. BAL = Ballysteen Limestone Formation, BC = Boulder Conglomerate, KB = Kilbryan Limestone Formation, NMU = Nodular Micrite Unit, NTBU = New Thin Bedded Unit, OP = Oakport Limestone Formation, TCF = Tober Colleen Formation, TBU = Thin Bedded Unit.

5.4.3 Zircon Trace Elements

Igneous zircons can be distinguished from metamorphic or hydrothermal zircons based on the steeply rising slope from La to Lu with a distinct positive Ce-anomaly and negative Eu-anomaly on chondrite normalised diagrams and Th/U ratios greater than 0.5 (Hoskin and Schaltegger, 2003). However, igneous zircons from different source rocks have very similar REE patterns (Hoskin and Schaltegger, 2003). Also Heaman et al. (1990) showed that zircon from kimberlite, carbonatite and nepheline syenite, mafic and ultramafic samples, felsic samples and basalts could not be distinguished from each other based on Lu, Sc, Th/U and Lu/Sm plots alone. Hoskin and Ireland (2000) confirmed that zircon chemistry is generally not useful as indicators of provenance as the REE chemistries of zircon from a wide range of crustal rock types and tectonic settings exhibit remarkable similarity. Hoskin et al. (2000) also demonstrated that zircon REE characteristics are generally not useful as an indicator of magmatic processes, whereas apatite REE abundances and pattern resembles that of whole-rock composition. More recently, Grimes et al. (2015) showed, that misclassification, especially for small groups of a few grains is very likely and complementary data will be critical to fully characterise parental melt sources for zircon grains. For this reason, trace element analyses were restricted to apatite grains and not conducted on zircon grains for this study. This also enabled more precise U-Pb zircon ages to be obtained as less isotopes have to be measured, which allows longer analyses of each U-Th-Pb isotope.

5.4.4 Zircon Morphology as an Indicator of Inheritance?

The median value for the width of single samples ranges between 36.3 and 54.9 µm, excluding samples Stonepark_G11-2638-02_HK 207 and Stonepark_G11-2638-02_HK 208. The median width for the whole data set is 43.7 µm, whereas the median width for samples HK 207 and 208 is 31.3 µm and 20.8 µm, respectively (Figure 5-11B).

The median length of zircon grains from samples HK 207 is 55 µm and from HK 208 is 49.6 µm. The remaining samples show a median length of the zircon grains between 76.5 to 151 µm. Thus, the median width and median length of zircon grains from samples HK 207 and 208 are smaller compared to the values from the average data set. Mechanical abrasion during sedimentary transport can reduce grain sizes through grain fracturing and rounding (Morton and Hallsworth, 1999). Although zircon grains are generally remarkably mechanically robust, detrital zircon grains can be affected by sedimentary transport (Markwitz and Kirkland, 2018). Although samples HK 207 and 208 yielded zircons, all U-Pb ages indicate inheritance. Thus, even if it is a small data set, the smaller zircon grains in samples HK 207 and 208 potentially confirms that detrital zircon grains are smaller than their pyroclastic counterparts.

Markwitz and Kirkland (2018) showed that sedimentary transportation has less effect on the minor axes of detrital zircon grains compared to the major axes of the grains. Thus, detrital grains should be characterised by lower length to width ratios than grains of pyroclastic origin. Detrital zircons in normal sediments of terrigenous origin showed a length/width ratio around 2, while a pyroclastic zircon population, analysed within the same study showed ratios > 2.5 (Zhou, 1992). The median length to width values of the zircons from 18 out of 20 analysed samples reach from 2.1 to 3.2 (Figure 5-11C), supportive of a pyroclastic origin. Samples HK 207 and 208 have median length/width ratios of 1.8 and 2.3, respectively, which lends credence to a detrital origin for the zircons in sample HK 207.

5.4.5 Apatite Morphology

Rounded apatite crystals would indicate transportation and detrital input. The apatite grains in this study are elongated and hexagonal (Figure 5-15), which more likely indicate a volcanic origin as opposed to detrital incorporation.

5.4.6 Apatite U-Pb Age Data

The apatite U-Pb age data are primarily used in this study to confirm that only Early Carboniferous grains (between 359.3 and 323.4 Ma) are subsequently employed for apatite trace element characterisation. While no sample from the Rathdowney Trend yielded any apatites, one sample from the Navan area (Tara Deep_N-2444_HK 159), four samples from the Stonepark area (Stonepark_G11-2638-02_HK 209, Stonepark_G11-450-02_HK 210, Stonepark_G11-2654-01_HK 211 and Stonepark_G11-2654-01_HK 212) and five samples from the Slievedart area (Slievedart_3470/15_HK 190, Slievedart_3470/15_HK 237, Slievedart_3471/4_HK 193, Slievedart_3471/4_HK 194, and Slievedart_3471/4_HK 238) can be further investigated by trace element characterisation as the age of eight tuff samples (Figure 5-12A, C, E, G, I, K, M, O) as well as single apatite ages (Figure 5-12B, D, F, H, J, L, N, P), are within uncertainty of an Early Carboniferous time window.

5.4.7 Apatite -Trace Element Characterisation

Trace elements which occur in the same volcanic ash horizon are expected to show a single trace element population with small dispersion. Thus, element concentrations from grains within the same sample, whose concentrations are within 20% from its median value were exclusively used for the characterisation and correlation of the Irish tuff horizons (see section 5.3.4.3).

5.4.7.1 Parental Magma Characterisation

The potential for apatite trace element composition to characterise the parental magma chemistry was discovered by Fleischer and Altschuler (1986), using a La/Nd *vs* (La + Ce)/ΣREE discrimination diagram. Based on the (La + Ce)/ΣREE ratios of igneous apatite grains, their source magma was classified as acidic (felsic) (0-65), intermediate-mafic (65-70) or alkaline/ultramafic (> 70) (Figure 5-24A). While all analysed apatites fall into the acidic field, samples Slievedart_3470/15_HK 190, Slievedart_3471/4_HK 194 and Stonepark_G11-2654-01_HK 211 show the lowest values (Figure 5-24A). Further discrimination diagrams, primarily for magmatic apatites, have been developed since then. Dill (1994) introduced the Th-U biplot as a detrital apatite discrimination diagram. The Th/U ratio in apatites is typically lower in felsic igneous rocks compared to mafic granitoids. The depletion of Th relative to U in different types of granites is usually attributed to the crystallisation of monazite, which has a strong affinity for Th and crystallises before apatite in strongly fractionated rocks (Sha and Chappell, 1999). Thus, the lower the Th content and the closer the samples plot to the Th/U = 1:10 ratio, the more evolved was the parent magma from which the apatite crystallised. Apatite grains from samples Slievedart_3470/15_HK 190, Slievedart_3471/4_HK 194, Stonepark_G11-2654-01_HK 211, Slievedart_3470/15_HK 237 and Slievedart_3471/4_HK 238 show the biggest depletion in Th relative to U (Figure 5-25B). Thus, these five samples are more evolved in comparison to the other samples in the data set and samples Slievedart_3470/15_HK 190, Slievedart_3471/4_HK 194 and Stonepark_G11-2654-01_HK 211 are also the most evolved samples on the La/Nd *vs* (La + Ce)/ΣREE discrimination diagram (Figure 5-24A).

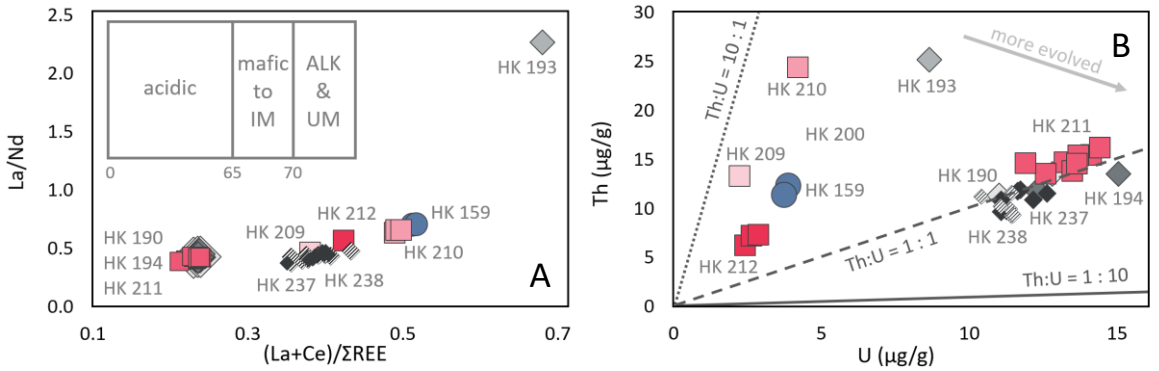

Figure 5-24: A) La/Nd vs (La+Ce)/ΣREE plot from Fleischer and Altschuler (1986) for apatite from Irish Mississippian tuffs. The schematic plot in the top left corner shows the separation into the acidic, mafic to intermediate (IM)/alkaline (ALK) and ultramafic (UM) field. All apatite grains from this study plot in the acidic field. B) Th – U biplot from Dill (1994) for apatite grains from this study. Th/U ratios are > 1 for nearly all grains and vary between 1 (HK 190, 194 and 211) and 6 (HK 209). The dotted, dashed and solid line in the Th vs U diagram show Th-U ratios of 10:1, 1:1 and 1:10, respectively. Symbols indicate the sample location; circles: samples from Navan area; squares: samples from Stonepark area; diamonds: samples from Slievedart area. Full sample names are shown in Tables 2-4, 2-8 and 2-10.

Furthermore, Ce/Y ratios of apatite has been used to define the alkalinity of the host melt (Roeder et al., 1987). Samples having values above 7.7 are considered to represent highly alkaline environments (Batchelor and Jeppsson, 1999). Ce/Y ratios of all samples from this study have values between 0.4 and 5.6, indicating non-alkaline parental magmas (Figure 5-25A). Apatites from ultramafic, feldspar-absent rocks like carbonatites and mantle-derived lherzolites have Ce/Yb ratios over 100 and 200, respectively, whereas apatites in granitoid rocks and granitic pegmatites show Ce/Yb ratios not bigger than 15-20 and mostly < 1, respectively (Belousova et al., 2002a). Samples Slievedart_3470/15_HK 190, Slievedart_3471/4_HK 194 and Stonepark_G11-2654-01_HK 211 show Ce/Yb values between 8.28 and 10.10, whereas the Ce/Yb ratio of remaining samples range within 25 and 72.5 (Figure 5-25A). Thus, the parental magma of all samples had neither an alkaline nor an ultramafic character. However, only the Ce/Yb ratio of samples Slievedart_3470/15_HK 190, Slievedart_3471/4_HK 194 and Stonepark_G11-2654-01_HK 211 is well within that of the highly evolved granitic pegmatites and granitoid rocks. Again these three samples are distinct, as on the La/Nd *vs* (La + Ce)/ΣREE discrimination diagram (Figure 5-24A).

The apatite Sr/Mn ratio is usually low in apatite from highly fractionated melts, close to unity in I-type granitoids and very high in mafic melts. One of the reason is the increase of Mn concentrations up to 1 wt% in apatite from mafic to felsic systems, which coincides with higher Mn contents in apatites occurring in more reduced conditions (Belousova et al., 2001; Belousova et al., 2002b). At the same time there is a decrease in the Sr content of apatites from ultramafic to mafic (several thousand µg/g) towards more felsic systems (tens to several hundred µg/g) (O'Reilly and Griffin, 2000; Belousova et al., 2001; Tang et al., 2012), probably because of the partitioning of Sr into plagioclase, independent on the oxidation state of the crystallisation environment (Belousova et al., 2001). Strontium and Mn abundances in apatite grains from this

study vary between 49 and 1056 µg/g for Sr and between 398 and 2735 µg/g for Mn (Figure 5-24B). On a Sr/Mn biplot, apatite grains from samples Slievedart_3470/15_HK 190, Slievedart_3471/4_HK 194 and Stonepark_G11-2654-01_HK 211 cluster together and plot close to the 1:10 Sr-Mn line as well as samples Tara Deep_N-2444_HK 159 and Stonepark_G11-450-02_HK 210 (Figure 5-25B), indicating felsic parental magma compositions. The apatite grains from samples HK 237 and 238 show the least evolved chemistry, followed by samples HK 193, 209 and 212 (Figure 5-25B).

S-type and felsic I-type granites typically yield apatite crystals with higher Mn and Fe contents than mafic I-type granites (Sell and Samson, 2011b). Apatite grains from samples Slievedart_3470/15_HK 190, Slievedart_3471/4_HK 194 and Stonepark_G11-2654-01_HK 211 show the highest values in both Mn and Fe, followed by samples Tara Deep_N-2444_HK 159, Stonepark_G11-450-02_HK 210, Stonepark_G11-2654-01_HK 212, Stonepark_G11-2638-02_HK 209, Slievedart_3470/15_HK 237, Slievedart_3471/4_HK 238 and Slievedart_3471/4_HK 193 (Figure 5-25C). Thus, based on this discriminant, samples Slievedart_3470/15_HK 190, Slievedart_3471/4_HK 194 and Stonepark_G11-2654-01_HK 211 are the most evolved samples similar to the other plots, whereas sample Slievedart_3471/4_HK 193 is the least evolved sample.

The REE+Y content in igneous apatite grains, which derive either from a mafic or felsic host magma does not differ significantly (e.g. Chu et al., 2009). However, alkali-rich rocks can be distinguished based on their ultra-enriched REE+Y contents (e.g. Zirner et al., 2015; ΣREE+Y in apatite grains can be up to 108 235 µg/g and 85 362 µg/g in phonolitic and agpaitic rocks, respectively). The REE+Y content of samples Tara Deep_N-2444_HK 159, Slievedart_3470/15_HK 190, Slievedart_3471/4_HK 194, Stonepark_G11-450-02_HK 210, Stonepark_G11-2654-01_HK 211, Slievedart_3470/15_HK 237 and Slievedart_3471/4_HK 238 from this study varies between 3436 and 16 652 µg/g, while the average REE+Y content of sample Stonepark_G11-2654-01_HK 212 is 3533 µg/g and the REE+Y concentrations of the two individual apatite grains for Slievedart_3471/4_HK 193 and Stonepark_G11-2638-02_HK 209 yield 1324 and 3009 µg/g, respectively (Figure 5-25D). Thus, their REE+Y content fits to a non-alkaline, mafic or felsic parental magma composition.

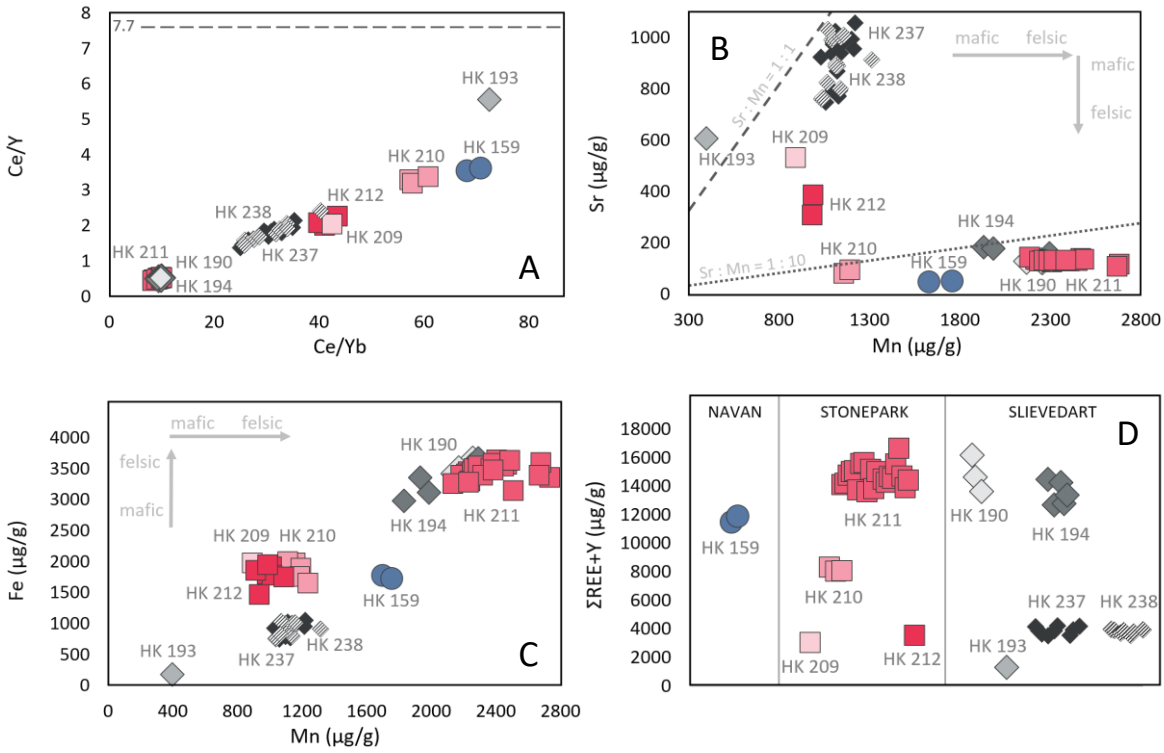

Figure 5-25: Geochemical analysis of apatite grains from Mississippian tuffs analysed in this study. Strontium vs Mn (A), Fe vs Mn (B), Ce/Y vs Ce/Yb (C) biplots and the sum of the REE+Y concentrations (D) are shown for each apatite crystal. All concentrations are in µg/g. Symbols indicate the sample location; circles: samples from Navan area; squares: samples from Stonepark area; diamonds: samples from Slievedart area. Full sample names are shown in Tables 2-4, 2-8 and 2-10.

Besides the REE+Y contents, chondrite normalised REE+Y patterns of apatite also reflects the chemistry of the host-magma composition. Apatites from S-type and felsic I-type granites show generally pronounced depletion of LREE (La to Sm < Gd to Lu), whereas apatites from mafic I-type granites are characterised by strong LREE enrichment (Sha and Chappell, 1999; Belousova et al., 2001; Hsieh et al., 2008). Carbonatites and lherzolite are also enriched in the LREE compared to HREE (Belousova et al., 2002a). The depletion in LREE in apatite in S-type and felsic I-type granitoids is most likely due to the occurrence of monazite, whereas its absence in mafic I-type granitoids leads to an enrichment in these elements (Sha and Chappell, 1999). Apatite grains from ultramafic rocks are even more depleted in HREEs (O'Reilly and Griffin, 2000; Tang et al., 2012).

According to these observations, the apatite REE+Y profiles of the Mississippian tuffs investigated in this study suggest a mafic character of the host magma for six samples as they are characterised by medium (Slievedart_3470/15_HK 237 and Slievedart_3471/4_HK 238; Figure 5-26A, H, I), medium to strong (Tara Deep_N-2444_HK 159, Stonepark_G11-450-02_HK 210; Stonepark_G11-2638-02_HK 209, Stonepark_G11-2654-01_HK 212; Figure 5-26A, F, G, K, L; La/Lu >> 1) and strong (Slievedart_3471/4_HK 193; Figure 5-26A, J; La/Lu >>> 1) LREE enrichments. While the La/Lu ratio is commonly used to show LREE enrichments or depletions, it cannot be used as a direct measure of the REE+Y pattern as they do not pick up bell-shaped

profiles. However, Figure 5-26B illustrates the steepness of the LREE (La_{CN} minus Sm_{CN}) on the x-axis and the steepness of the HREE (Gd_{CN} minus Lu_{CN}) on the y-axis and illustrates, together with Figure 5-26C-E, the bell-shape REE+Y curve of samples Slievedart_3470/15_HK 190, Slievedart_3471/4_HK 194 and Stonepark_G11-2654-01_HK 211, having a steeper slope in the HREE compared to the LREE. Thus, the chondrite REE+Y pattern of these three samples is not typical for a mafic parental magma. Their shape is very similar to that of S-type granitoid apatite, both having low La-Ce ratios and flat chondrite-normalised REE+Y profiles (e.g. Bea and Montero, 1999; Nutman, 2007; Henrichs et al., 2018).

The amplitude of Eu anomalies ($Eu_{CN}/Eu^* = Eu_{CN}/(0.5*Sm_{CN} + 0.5*Gd_{CN})$; Bau et al., 2018) is strongly controlled by the timing and degree of feldspar crystallisation, which concentrate Eu^{2+} from the melt, prior to apatite crystallisation (Samson et al., 1995). When compared to mafic I-type granites, there is strong Eu depletion in apatites from S- and felsic I-type granites (Sha and Chappell, 1999), primarily because feldspar normally crystallises before apatite, while Eu-anomalies vary in apatite in mafic igneous rocks depending on whether apatite crystallises before or after feldspar (Tang et al., 2012). Due to the timing of feldspar crystallisation, Eu anomalies in ultramafic apatite can be either non-existent or very minor (Tang et al., 2012). Europium anomalies can even be mildly positive in feldspar-absent rocks such as lherzolites and carbonatites (e.g. O'Reilly and Griffin, 2000). However, as samples Slievedart_3470/15_HK 190, Slievedart_3471/4_HK 194 and Stonepark_G11-2654-01_HK 211 show more pronounced Eu anomalies compared to samples Tara Deep_N-2444_HK 159, Stonepark_G11-450-02_HK 210 , Slievedart_3470/15_HK 237 and Slievedart_3471/4_HK 238 (Figure 5-26A), the former samples probably crystallised from a more evolved parental melt. Samples Stonepark_G11-2638-02_HK 209 and Stonepark_G11-2654-01_HK 212 show positive Eu anomalies, indicating either an ultramafic magma source or at least a feldspar-absent magma (Figure 5-26A). Although apatite grains from sample Slievedart_3471/4_HK 193 show a weakly negative Eu anomaly (Figure 5-26A, I), the strong LREE enrichment (Figure 5-26A, J) in that sample also points towards a mafic-ultramafic magma source.

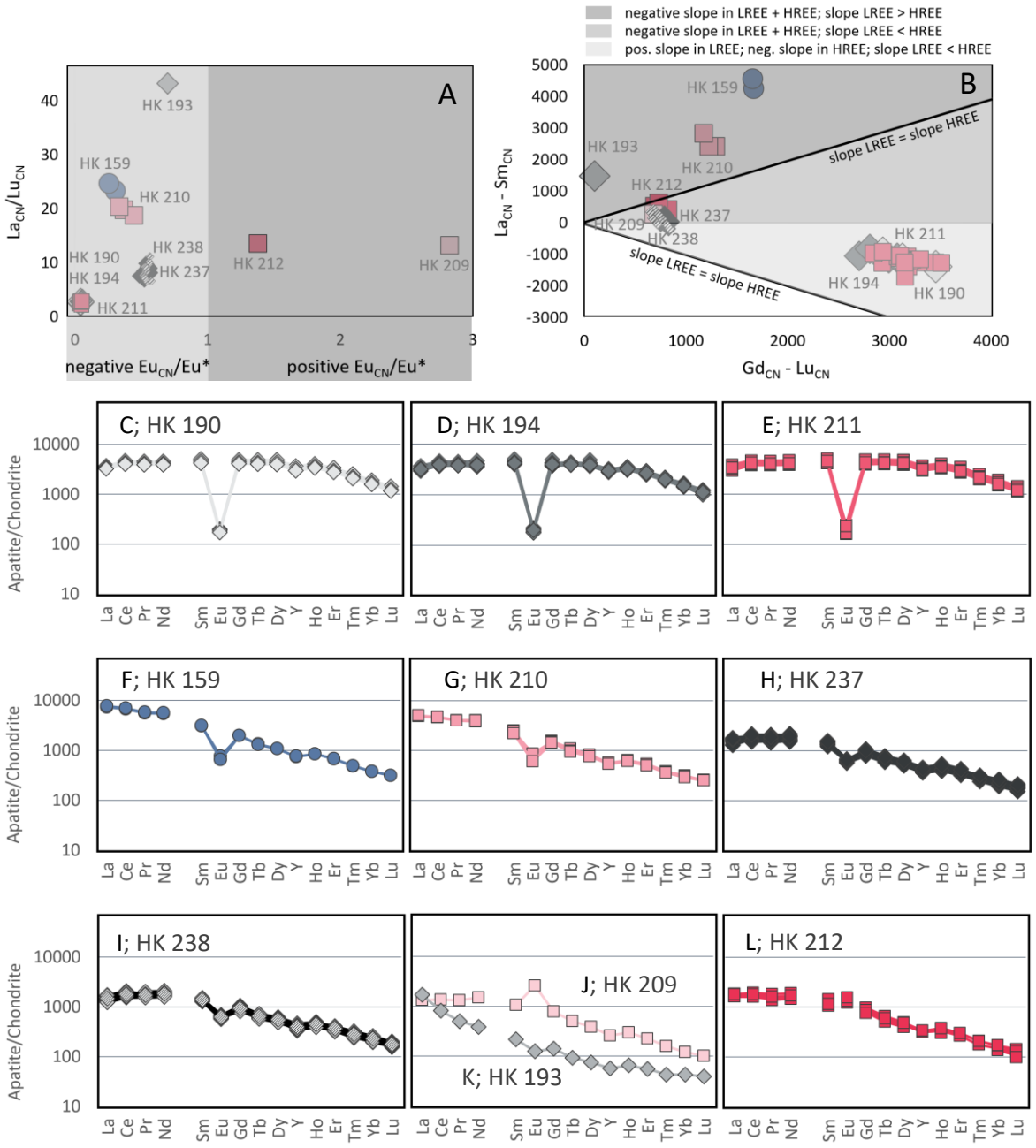

Figure 5-26: Chondrite normalised rare earth element (REE) pattern are shown along with La/Lu, La-Sm, Gd-Lu and Eu anomalies. A) La/Lu vs Eu anomaly (Eu_{CN}/Eu^*) biplot. Chondrite normalised La/Lu ratios are used to show the relative enrichment or depletion of LREE in the parental melt. La/Lu ratios > 1 indicate LREE enrichment, whereas La/Lu ratios < 1 show HREE enrichment. All samples of this study show LREE enrichment. Samples HK 209 and 212 have Eu_{CN}/Eu^* values greater than unity, which corresponds to a positive Eu anomaly, whereas all other samples show negative Eu anomalies ($Eu_{CN}/Eu^* < 1$). B) Differences between La_{CN} and Sm_{CN} values and between Gd_{CN} and Lu_{CN} values represent the degree of LREE and HREE enrichment, respectively. While samples HK 190, 194 and 211 are characterised by a positive slope in LREE ($La_{CN} - Sm_{Cn} < 0$) and a negative slope in HREE ($Gd_{CN} - Lu_{CN} > 0$), all other samples show a negative slope in both, LREE and HREE. C)-L) Chondrite-normalised REE+Y profiles of apatite grains from the nine different apatite bearing samples of this study. All samples are normalised to chondrite values from McDonough and Sun (1995). Full sample names are shown in Tables 2-4, 2-8 and 2-10.

Besides the occurrence of apatite in magmatic systems, apatite can also be found in low-grade metamorphic systems and diagenetic environments. More recently, several studies published apatite trace element data from less common igneous rocks as well as from metamorphic rocks (e.g. Nishizawa et al., 2005; Hsieh et al., 2008; El Korh et al., 2009; Zirner et

al., 2015; Chakhmouradian et al., 2017; Henrichs et al., 2018). Based on the availability of this larger data set, O'Sullivan et al. (2020) provide a classification diagram, which categorises these broad source lithologies of apatite, in contrast to only distinguishing between igneous apatite grains (e.g. Belousova et al., 2001; Belousova et al., 2002b). The classification diagram employs three independent parameters, the ΣLREE (La-Nd), Sr and Y concentrations. Based on the ΣLREE content and the Sr/Y ratios, apatite data get classified into six different groups:

- alkali-rich igneous rocks like syenitic, agpaitic and phonolitic rocks (ALK)
- mafic I-type grantioids and mafic igneous rocks (IM)
- low- and medium-grade metamorphic and metasomatic apatites (LM)
- partial-melts/leucosomes/high-grade metamorphic apatite grains (HM)
- S-type granitoids, felsic granitoids and high aluminium saturation index 'felsic' I-types (S) ultramafic rocks including feldspar-absent rocks like carbonatites, lherzolites and pyroxenites (UM)

The fields are defined using a support vector machine (SVM) on the training (literature) database. Misclassifications based on reruns of the training data set are on average 15%.
The study of O'Sullivan et al. (2020) supports the findings of Belousova et al. (2002a), that Sr *vs* Y biplots provide the clearest distinction of apatites from different rock types, as Sr concentrations decrease with the degree of magmatic fractionation, while Y concentrations increase. However, Sr/Y ratios cannot be used to separate alkali-rich igneous grains and metamorphic grains in detritus. Therefore, O'Sullivan et al. (2020) paired the Sr/Y ratios with a second axis of ΣLREE (La-Nd), which allows the determination of alkali-rich igneous grains by their extremely high LREE-contents.
The approach of O'Sullivan et al. (2020) summarises well the findings of Figure 5-24 to Figure 5-26: Apatite grains from samples Slievedart_3470/15_HK 190, Slievedart_3471/4_HK 194 and Stonepark_G11-2654-01_HK 211 plot in the felsic granitoid (S) field (Figure 5-27), confirming the evolved character of these samples, which was observed in Figure 5-24A and B, Figure 5-25A-D and Figure 5-26A-E. Sample Tara Deep_N-2444_HK 159 plots next to samples Slievedart_3470/15_HK 190, Slievedart_3471/4_HK 194 and Stonepark_G11-2654-01_HK 211 in the felsic granitoid field (Figure 5-27). Although there is a moderate LREE enrichment in sample Tara Deep_N-2444_HK 159 (Figure 5-26A, B, F) implying a mafic character, the majority of the diagrams, especially the Sr *vs* Mn (Figure 5-25B), Fe *vs* Mn (Figure 5-25C) and the REE+Y content (Figure 5-25D), support the felsic character of this sample.
Samples Stonepark_G11-2638-02_HK 209, Stonepark_G11-450-02_HK 210, Stonepark_G11-2654-01_HK 212, Slievedart_3470/15_HK 237 and Slievedart_3471/4_HK 238 plot in the mafic

granitoid-to-mafic igneous rocks (IM) field (Figure 5-27). The medium to strong LREE enrichment (Figure 5-26A, B, G-I, K, L), as well as the pattern observed in the Th *vs* U (Figure 5-24B), Sr *vs* Mn (Figure 5-25B) and the Fe *vs* Mn (Figure 5-25C) biplots supports the more mafic character of samples Stonepark_G11-2638-02_HK 209, Stonepark_G11-450-02_HK 210 and Stonepark_G11-2654-01_HK 212. However, samples Stonepark_G11-2638-02_HK 209 and Stonepark_G11-2654-01_HK 212 plot towards the ultramafic field, whereas sample Stonepark_G11-450-02_HK 210 is close to the felsic granitoid field. The difference in chemistry between these three samples can be explained using their Eu anomalies. While sample Stonepark_G11-2638-02_HK 209 and Stonepark_G11-2654-01_HK 212 show a positive Eu anomaly (Figure 5-26A), which is associated with a mafic to even ultra-mafic character, sample Stonepark_G11-450-02_HK 210 is characterised by a negative Eu-anomaly (Figure 5-26A), suggesting a more evolved character of the parental magma.

Samples Slievedart_3470/15_HK 237 and Slievedart_3471/4_HK 238 plot next to samples Stonepark_G11-2638-02_HK 209 and Stonepark_G11-2654-01_HK 212 in the mafic granitoid-to-mafic igneous rock (IM) field (Figure 5-27). The mafic character of these two samples is supported by their high Sr (Figure 5-25B), but low Fe and Mn contents (Figure 5-25C) as well as their LREE enrichment (Figure 5-26A, H, I).

Sample Slievedart_3471/4_HK 193 is the least evolved sample of the data set and plots on the border between the mafic and the ultramafic field (Figure 5-27). Although the Ce/Yb ratio of this does not support an ultramafic magmatic source (Figure 5-25A), it was the least evolved sample in the Ce/Y *vs* Ce/Yb (Figure 5-25A) and Fe *vs* Mn (Figure 5-25C) biplots. Furthermore, sample Slievedart_3471/4_HK 193 has the lowest REE+Y contents (Figure 5-25D) and the strongest LREE enrichment (Figure 5-26A, I) of all samples in this study confirming its mafic character.

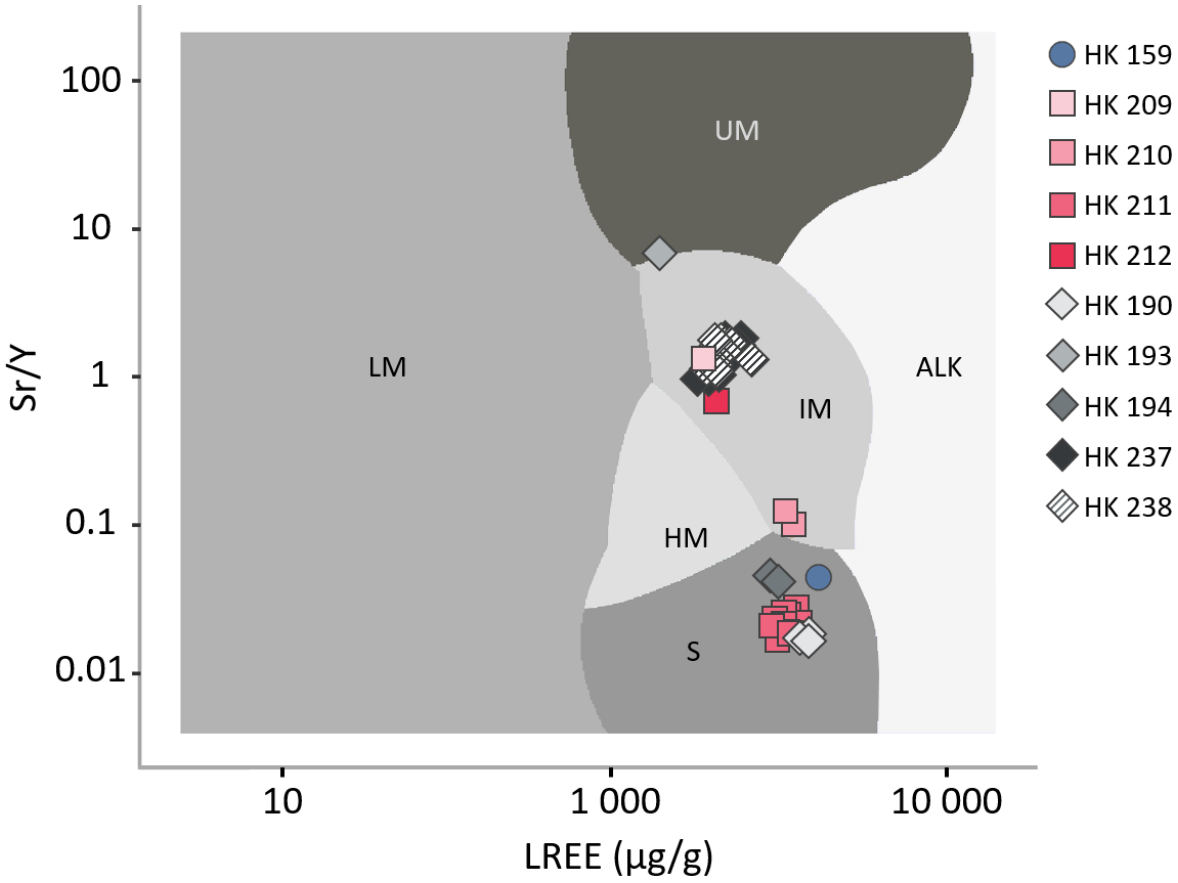

Figure 5-27: Sr/Y vs ΣLREE (La, Ce, Pr, Nd) biplot from O'Sullivan et al. (2020) based on a training (literature) data set and support vector machine (SVM) classification. ALK = alkali-rich igneous rocks; IM = mafic I-type granitoids and mafic igneous rocks; LM = low- and medium-grade metamorphic and metasomatic; HM = partial-melts/leucosomes/high-grade metamorphic; S = S-type granitoids and high aluminium saturation index (ASI) felsic I-types; UM = ultramafic rocks including carbonatites, lherzolites and pyroxenites. Full sample names are shown in Tables 2-4, 2-8 and 2-10.

5.4.7.2 Correlation Tool

Apatite trace element composition can be used to characterise the parental melt from which the grains crystallised, and it is also a useful correlation tool for weathered tephra. Due to the lack of primary glass phases, Samson et al. (1995) employed mainly Mg, Fe, Cl and Sr-isotope apatite chemistry to correlate K-bentonites. Since then, the abundance of Mn, Mg and Cl in apatite phenocrysts has been successfully applied to distinguish different K-bentonite layers (e.g. Emerson et al., 2004; Carey et al., 2009). Sell and Samson (2011a, b) further explored and established that apatite tephrochronology is a powerful correlation tool even in heavily altered K-bentonites using Mg, Cl, Mn, Fe, Ce and Y chemistry. Sell et al. (2015) also proved that apatite in K-bentonite layers exhibit unique reproducible trends over large areas across different depositional and tectonic environments based on those. These studies also confirm that diagenesis (Morton and Hallsworth, 2007) and low-grade metamorphism in the absence of recrystallisation (Lux and Yates, 2009) appear to have minimal effect on the composition of apatite.

On Ce/Y *vs* Ce/Y, Sr *vs* Mn and Fe *vs* Mn biplots, samples Slievedart_3470/15_HK 190, Slievedart_3471/4_HK 194 and Stonepark_G11-2654-01_HK 211 define one discrete cluster, which is clearly separated from the other samples (Figure 5-25A-C). Based on the same diagrams, samples Stonepark_G11-2638-02_HK 209 and Stonepark_G11-2654-01_HK 212 define another discrete population (Figure 5-25A-C). The ash layers from samples Tara Deep_N-2444_HK 159, Slievedart_3471/4_HK 193 and Stonepark_G11-450-02_HK 210 are randomly distributed and cannot be grouped based on their Ce, Y, Yb, Fe, Mn and Sr concentrations (Figure 5-25A-C). Thus, purely based on element concentrations, which are commonly used in literature to correlate ash beds (Mg, Fe, Sr, Mn, Ce, y and Yb), samples Slievedart_3470/15_HK 190, Slievedart_3471/4_HK 194 and Stonepark_G11-2654-01_HK 211 would share the same eruption history. Furthermore, samples Stonepark_G11-2638-02_HK 209 and Stonepark_G11-2654-01_HK 212 would have a common volcanic centre although different to samples Slievedart_3470/15_HK 190, Slievedart_3471/4_HK 194 and Stonepark_G11-2654-01_HK 211. Samples Slievedart_3470/15_HK 237 and Slievedart_3471/4_HK 238 would share a third source, which is unrelated to the other two volcanic centres. Samples Tara Deep_N-2444_HK 159 and Stonepark_G11-450-02_HK 210 do not share a common source, nor can they be assigned to the groupings of samples Slievedart_3470/15_HK 190, Slievedart_3471/4_HK 194 and Stonepark_G11-2654-01_HK 211, nor to the group with samples Stonepark_G11-2638-02_HK 209 and Stonepark_G11-2654-01_HK 212.

5.5 Conclusions

The zircon and apatite yield within each Irish Mississippian tuff sample cannot be predicted based on their Zr and P contents, respectively. The morphology of the zircons and apatite grains indicate a primary magmatic origin as opposed to a detrital origin.

Two out of three tuff layers from the Navan area, which dated by the LA-ICP-MS U-Pb zircon method are late Tournaisian (Navan West_N-2441_HK 155, Tober Colleen Formation, Figure 5-6C, D and early Viséan (Tara Deep_N-2444_HK 158, New Thin Bedded Unit, Upper Tuff, Figure 5-5A, B) in age and are thus in agreement with their relative host rock ages. Further analyses are necessary to see if they share a common volcanic history and if they can be assigned to other volcanic eruptions. The age of sample Navan West_N-2441_HK 169 (Figure 5-6A, B) is most likely erroneous as the calculated age of 342.0 ± 2.7 Ma is too young to match the stratigraphic age of the Waulsortian host rock. The only apatite grains were recovered from sample Tara Deep_N-2444_HK 159 (New Thin Bedded Unit, Lower Tuff, Tara Deep) and these were most likely derived from an evolved magmatic source. The evolved parental magma chemistry from this sample matches the apatite chemistry and the stratigraphic position of tuff one layers (samples Slievedart_3470/15_HK 190 and Slievedart_3471/4_HK 194) from the Slievedart area (Figure 5-20A, Figure 5-22C, Figure 5-27). However, apatite trace element correlation diagrams do not suggest the same source for these samples (Figure 5-24A, B; Figure 5-25A, C; Figure 5-26A, B, C-F, Figure 5-27). Thus, sample Tara Deep_N-2444_HK 159 is most likely not part of the Slievedart eruption event that happened at around 346.4 Ma. Furthermore, as the apatite trace element data of sample Tara Deep_N-2444_HK 159 and sample Stonepark_G11-2654-01_HK 212 are dissimilar (Figure 5-24-Figure 5-27), it cannot be part of the c. 350.3 Ma Stonepark/Lisheen eruption event either. Sample Tara Deep_N-2444_HK 159 can neither be assigned to the potential eruption event that produced the sampled ashes at Navan West_N-2441_HK 155 and Tara Deep_N-2444_HK 158 as sample HK 159 occurs 59 m stratigraphically below sample HK 158 in drill core N-2444 (Figure 5-28D).

Samples Lisheen_LK-1722_HK 180, Lisheen_LK-1040_HK 182, Lisheen_main mine_HK 203 and sample Rapla_3667-04_HK 185 from the Rathdowney Trend could be dated using U-Pb LA-ICP-MS zircon geochronology. However, only the outcrop sample HK 203 (U-Pb zircon age = 349.6 ± 1.5 Ma) reflects the Ivorian age of its host rock, while drill core samples yield younger ages. Thus, the tuff samples taken from drill cores likely do provide not enough zircon to allow for the calculation of accurate concordia ages (i.e. there is not enough zircon to unequivocally distinguish subpopulations characterised by Pb loss, inheritance and common Pb). The composition of the magma chemistry of samples from the Rathdowney Trend cannot be determined due to the lack of apatite grains (Figure 5-28C).

Seven out of eight tuff layers from the Stonepark area are found within the Nodular Micrite Unit (Stonepark_G11-2638-01_HK 197, Stonepark_G11-2638-01_HK 198, Stonepark_G11-2638-02_HK 207, Stonepark_G11-2638-02_HK 208, Stonepark_G11-2638-02_HK 209, Stonepark_G11-450-02_HK 210, Stonepark_G11-2654-01_HK 212), whereas one tuff horizon (Stonepark_G11-2654-01_HK 211) occurs in the stratigraphically younger Lough Gur Formation. Two samples from the Nodular Micrite Unit (Stonepark_G11-2638-01_HK 197 and Stonepark_G11-2654-01_HK 212) and sample Stonepark_G11-2654-01_HK 211 from the Lough Gur Formation contained datable zircons. Data produced by LA-ICP-MS indicate that samples HK 197 and 212 are within analytical uncertainty and Tournaisian in age, which reflects the age of the Nodular Micrite Unit. The zircon age of sample HK 211 is 348.2 ± 2.4 Ma and was thus deposited c. 3 million years after samples HK 197 and 212 (Figure 5-23B, D, G, H, J, K). Apatite trace element concentrations are available for samples Stonepark_G11-2638-02_HK 209, Stonepark_G11-450-02_HK 210, Stonepark_G11-2654-01_HK 211 and Stonepark_G11-2654-01_HK 212. Samples HK 209, 210 and 212, which share the same host rock (Nodular Micrite Unit) have a mafic parental magma chemistry (Figure 5-27). However, sample HK 210 cannot be correlated with another sample from this group, whereas samples HK 209 and 212 can be correlated using Ce/Y *vs* Ce/Yb, Sr *vs* Mn and Fe *vs* Mn biplots (Figure 5-25B, C, D). Apatite grains from sample HK 211 show a highly evolved parental magma composition (Figure 5-25A, B, C; Figure 5-27) and no correlation with sample HK 209, 210 and 212 (Figure 5-24-Figure 5-27). Thus, samples HK 211 and 212, which occur in the same drill core can be distinguished based on zircon U-Pb age data and apatite trace element concentrations. In addition, U-Pb zircon and apatite trace element data indicate a common volcanic centre for samples HK 197, 209 and 212, which have a mafic magma composition and were probably erupted at c.350.3 Ma (Figure 5-28B). Sample Lisheen_main mine_HK 203 could be part of that same eruption as its U-Pb zircon age is within uncertainty of the eruption ages of samples Stonepark_G11-2638-01_HK 197 and Stonepark_G11-2654-01_HK 212 (Figure 5-23B, C).

Five tuff layers are found in two drill cores in the Slievedart area with tuff one being the stratigraphically lowest samples. Both drill cores are 5.6 km apart from each other. Sample Slievedart_3471/4_HK 194 (tuff one) and three tuff four layers (samples Slievedart_3470/15 _HK 188, Slievedart_3471/4_HK 192, Slievedart_3471/4_HK 193) contain zircon grains that cannot be separated from each other based on their U-Pb zircon ages (e.g. Figure 5-23A, D, E). Both tuff one samples (Slievedart_3470/15_HK 190 and Slievedart_3471/4_HK 194), both tuff three samples (Slievedart_3470/15_HK 237 and Slievedart_3471/4_HK 238) and one tuff four sample (Slievedart_3471/4_HK 193) yielded apatite grains. On Ce/Y *vs* Ce/Yb, Sr *vs* Mn and Fe *vs* Mn biplots, using apatite trace element data, tuff one samples Slievedart_3470/15_HK 190 and

Slievedart_3471/4_HK 194 build one distinct cluster, which is clearly distinct from both tuff three samples (HK 237 and 238) and the one tuff four sample (Slievedart_3471/4_HK 193) (Figure 5-25A-C). While tuff one samples HK 190 and 194 have a felsic parental magma composition, tuff three samples HK 237 and 238 have a mafic character and tuff four sample HK 193 has an even less evolved source chemistry (Figure 5-27). As both tuff one layers represent the stratigraphically lowest horizons in their respective drill cores, their stratigraphic position and apatite trace element data support the same origin for this ash layer, yielding an eruption age of c. 345.6 Ma (Figure 5-23A, F, I; Figure 5-24-Figure 5-27; Figure 5-28A). Although U-Pb zircon ages are not available for both tuff three samples, the stratigraphic position, as well as their similar apatite trace element data for both samples, suggest a mafic magma composition (e.g. Figure 5-27) and a slightly younger eruption, which was followed by an even less evolved eruption with an average eruption age of 346.7 Ma, which is the age of the Tournaisian-Viséan boundary (Figure 5-23E; Figure 5-27). Thus, the eruption history in the Slievedart area can be resolved based on apatite trace element data rather than U-Pb zircon ages.

Sample Stonepark_G11-2654-01_HK 211 shares the same apatite chemistry and plots together with samples Slievedart_3470/15_HK 190 and Slievedart_3471/4_HK 194 on correlation diagrams (Figure 5-24-Figure 5-27). Furthermore, the U-Pb zircon ages of sample Stonepark_G11-2654-01_HK 211 and sample Slievedart_3471/4_HK 194 are within analytical uncertainty, supporting a potential link of evolved tuff horizons in between these areas, which are 133 km away from each other (Figure 5-8A, B; Figure 5-9G-J, Figure 5-28C).

Overall, this study demonstrates that the REE+Y, Fe, Mn, Sr, Y, Th and U contents of apatite retain information pertaining to the host magma and can be used as a local correlation tool. The consistent U-Pb zircon and apatite trace element data for samples Stonepark_G11-2638-01_HK 197, Stonepark_G11-2638-02_HK 209, Stonepark_G11-2654-01_HK 212 and Lisheen_mine sample_HK 203 indicate a common mafic source, which erupted c. 350.3 Ma ago and led to the deposition of an ash layer within the Nodular Micrite Unit. Samples Slievedart_3471/4_HK 194 and Stonepark_G11-2654-01_HK 211 show similar eruption ages. They also share, together with sample Slievedart_3470/15_HK 190, a similar apatite trace element patterns and were most likely erupted from the same evolved magma source around 347 Ma ago. This eruption was followed by a mafic eruption, producing an ash layer, which was restricted to the Slievedart area (samples Slievedart_3470/15_HK 237 and Slievedart_3471/4_HK 238). The eruption sequence ended with the deposition of an even less evolved tuff layer, which is so far only detected in Slievedart.

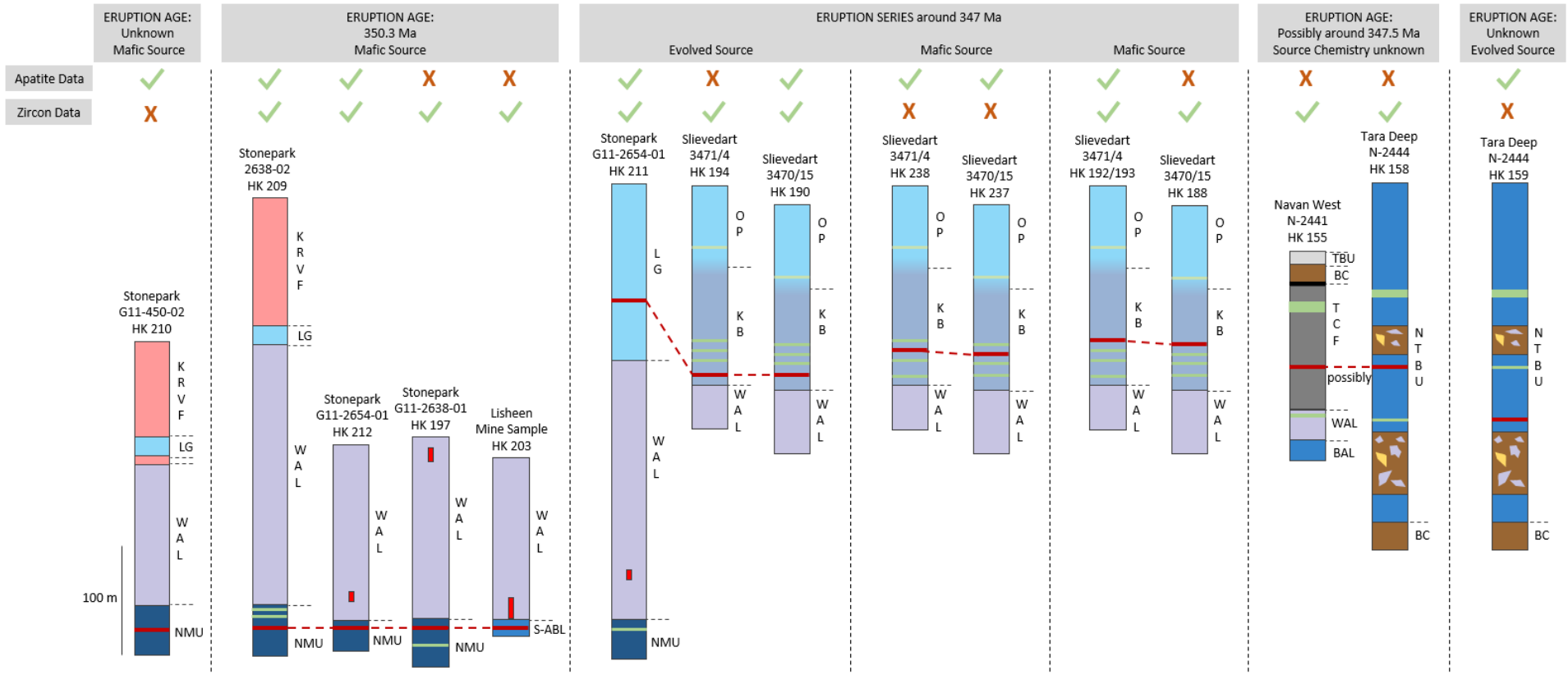

Figure 5-28: Stratigraphic columns of nine different drill cores, whose tuff layers either contained datable zircons, apatite trace element chemistry or both. Availability of data is indicated by either a green tick (reliable age data available) or orange cross (reliable data not available) at the top of each drill core. Samples of interest in respective drill cores are highlighted in red. The name of the sample location, as well as the drill core and lab ID of the highlighted tuff layer is indicated at the top of the logs. Sometimes, only relevant sections of the log are shown; see Figure 2-7 to Figure 2-11 for full logs. Tuff samples which could be correlated are connected with a red dashed line. A) The magmatic source of tuff sample HK 210 was most likely mafic. The eruption age is unknown. B) LA-ICP-MS zircon ages as well as apatite chemistry confirm a common mafic source for samples HK 209, 212, 197 and 203 from Stonepark and Lisheen, which yield an eruption of c. 350.3 Ma. C) Samples HK 211, 194 and 190 share an evolved source, while the source composition for samples HK 188, 192, 193, 237, 238 was mafic. These samples got deposited as part of an eruption series at around 347 Ma. D) The eruption age for samples HK 155 and 158 from Navan West and Tara Deep was possibly around 347.5 Ma with an unknown source composition. D) Only the source chemistry (evolved) is known from sample HK 159 from Tara Deep. Red bars=mineralisation; BAL=Ballysteen Limestone Formation, BC=Boulder Conglomerate, KB=Kilbryan Limestone, KRVF-Knockroe Volcanic Formation, LG=Lough Gur Formation, NMU=Nodular Micrite Unit, NTBU=New Thin Bedded Unit, OP=Oakport Limestone Formation, S-ABL=S-Argillaceous Bioclastic Limestone, TBU=Thin Bedded Unit, TCF=Tober Colleen Formation, WAL=Waulsortian Limestone Formation.

Chapter 6:

Integrated Results from the Bulk-Rock, Zircon and Apatite Analyses

This chapter provides a refined tephrostratigraphic framework for the Irish Mississippian (Tournaisian and Viséan stages) across the four study sites - Navan, Rathdowney Trend, Stonepark and Slievedart. Tuff correlations are based on the newly introduced *matchogram* method, which compares high-precision bulk-rock trace element data between every tuff sample of this study. When two tuffs yield a comparison value (Σ_D) below the threshold for a given region (< 3.3 in Navan, < 2.03 in the Rathdowney Trend, < 3.8 in Stonepark and < 1.81 in Slievedart) then there is a high likelihood that these samples share the same eruption history. These results are complemented by trace element data from apatite grains that yield Early Carboniferous U-Pb apatite ages (i.e. magmatic phenocrysts), high-precision U-Pb zircon ages and the stratigraphic position of investigated tuff samples. Identification and characterisation of tuff samples is only based on bulk-rock trace element data, while parent magma compositions are obtained from the bulk-rock and, where available, apatite trace element data.

6.1 Navan

Three tuff layers are recognised in the New Thin Bedded Unit in Tara Deep based on their stratigraphic position – from oldest to youngest they are the Lower Tuff, the Upper Tuff and the Marker Tuff (Figure 6-1). However, they show similar bulk-rock trace element patterns, suggesting a relatively homogenous and evolved magmatic source. These observations are based on 34 samples, which comprise 22 Marker Tuff samples, four Upper Tuff samples and eight Lower Tuff samples. The only apatite grain from Tara Deep were recovered from sample Tara Deep_N-2444_HK 159 (Lower Tuff), which also suggest an evolved magmatic source. Cross-correlations between Tara Deep and Navan East & West are possible. Based on stratigraphic position and bulk-rock geochemistry, sample Navan East_N-2317_HK 117 was most likely deposited contemporaneously with the Tara Deep Marker Tuff, while samples HK 156 and 157 (top and bottom of the same tuff layer) from the Tober Colleen Formation (Navan West) correlate either with the Upper or Lower Tuff (Figure 6-1). Thus, whole-rock trace element chemistry confirm the assumption from M. Philxoc (pers. comm., 2020) that the New Thin Bedded Unit in Tara Deep and the Tober Colleen Formation in Navan West are time-equivalent.

Sample Navan West_N-2441_HK 155 also occurs in the Tober Colleen Formation and yields a zircon U-Pb concordia age (348.7 ± 3 Ma) that is within the age uncertainty of the Upper Tuff in Tara Deep (sample HK 158; 346.4 ± 3.9 Ma) (Figure 6-1). However, the bulk-rock chemistry of both tuffs do not match. Furthermore, the calculated age of sample Navan West_N-2441_HK 155 has to be treated with caution, as already discussed in section 5.4.2.5. Thus, it is more likely that samples HK 156 and 157 share the same eruption history with either the Upper or the Lower Tuff from Tara Deep than sample Navan West_N-2441_HK 155. It is questionable if the other Navan East & West samples in the Upper Dark Limestone Formation (samples Navan West_N-2412_HK 128 and Navan East_N-2376_HK 227) or in the Waulsortian Limestone Formation (samples Navan West_N-2411_HK 125, Navan West_N-2411_HK 126 and Navan West_N-2441_HK 169) have a volcanic origin, as they show a strong shale component in the bulk-rock geochemical data.

In summary, there are at least three tuff layers in the Navan area. They most likely share a common, highly evolved magma source, which did not fractionate in between the three eruptive sequences. However, there remains the possibility that post-depositional alteration has homogenised the chemistry of the tuff layers. Mineralisation can be ruled out as a potential homogenisation mechanism as tuff samples in the Navan area did not seem to be affected by mineralisation, although there is clear evidence that mineralisation was active in the Chadian (most likely Lower Viséan) to at least the early Arundian (Ashton et al., 1992; Ford, 1996; Altinok, 2005; Ashton et al., 2015). The only reliable U-Pb zircon age for the Navan area is taken from the Upper Tuff in Tara Deep. It yields an eruption age of 346.4 ± 3.9 Ma.

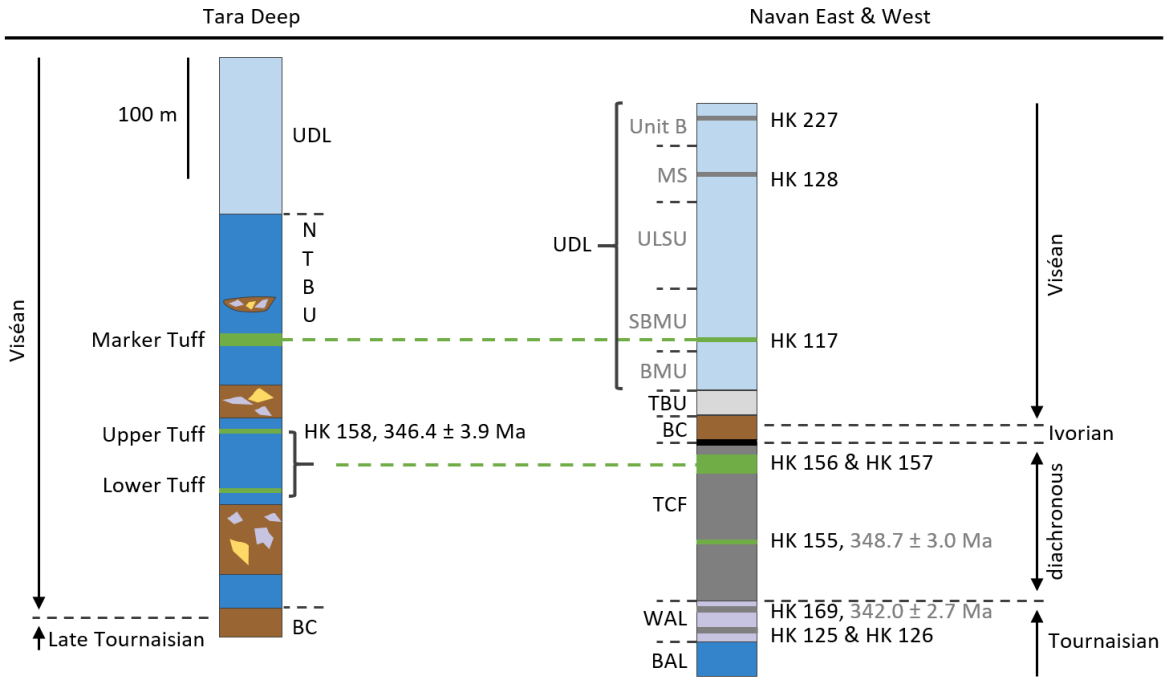

Figure 6-1:Cross-correlation of tuff samples from Tara Deep and Navan East & West, based on matching bulk-rock trace element analyses, U-Pb zircon age data, apatite trace element composition and stratigraphic position. Lithostratigraphic columns are generalised, showing the stratigraphic position of the tuff layers. Note that they do not necessarily occur in the same drill core. Lithostratigraphic thickness is based on drill core N-2444 for Tara Deep and N-2441 for Navan East & West. Scale is same for both columns. The three different tuff layers in Tara Deep (Marker Tuff; Upper Tuff, Lower Tuff) show similar bulk-rock trace element patterns but can be distinguished based on their stratigraphic position. The Marker Tuff from Tara Deep and sample Navan East_N-2317_HK 117 can be correlated based on their bulk-rock chemistry and their stratigraphic position. Samples Navan West_N-2441_HK 156 and 157 are taken from the same tuff layer and can either be correlated with the Upper or Lower Tuff from Tara Deep, while sample Navan West_N-2441_HK 155 shows a different bulk-rock chemistry. Calculated ages for samples Navan West_N-2441_HK 155 and Navan West_N-2441_HK 169 have to be treated with caution as they do not fit within the overall context. All tuff samples show an evolved magma composition. Grey shaded samples (Navan West_N-2411_HK 125, Navan West_N-2411_HK 126, Navan West_N-2212_HK 128, Navan West_N-2441_HK 169, Navan East_N-2376_HK 227) are most likely of non-volcanic origin. BAL=Ballysteen Limestone Formation, BC=Boulder Conglomerate, BMU=Boudin Mudstone Unit; SBMU=Sub-Bottom Marker Unit, UDL=Upper Dark Limestone Formation; ULSU=Upper & Lower Shaley Units; MS=Micritic Sequence, NTBU=New Thin Bedded Unit, TBU=Thin=Bedded Unit, TCF = Tober Colleen Formation, WAL=Waulsortian Limestone Formation.

6.2 Rathdowney Trend – Lisheen & Rapla

Samples from the Rathdowney Trend did not contain apatite grains. Thus, tuff correlations and compositions are based entirely on bulk-rock trace element data. Four different tuff layers are detected in Lisheen in the Nodular Micrite Unit, and all show different bulk-rock trace chemistry (Figure 6-2). Four tuff samples each were taken from two of these layers while only one sample each was taken from the other two tuff layers. There are also three separate tuff layers in Rapla - in the Upper Calcarenite Member, in the overlying Nodular Micrite Unit, and in the Crosspatrick Formation that can be separated based on their trace element chemistry in addition to their stratigraphic position (Figure 6-2). Hence it appears that none of the seven tuff layers can be correlated across from Lisheen to Rapla.

Three samples in Lisheen (Lisheen_LK-1722_HK 180, Lisheen_LK-1040_HK 182 and Lisheen_mine sample_HK 203) and one Rapla sample (Rapla_3667-04_HK 185) could be dated. However, only

one (Lisheen_mine sample_HK 203) yields a reliable zircon age of 349.6 ± 1.5 Ma. Thus, there is the possibility that single tuff layers from drill core do not provide enough zircon grains for reliable age determinations (i.e. there is not enough zircon to unequivocally distinguish subpopulations characterised by Pb loss, inheritance and common Pb), and only the age of the outcrop sample reflects the depositional age of the host rock.

Summarising, the first layer in the Rathdowney Trend was deposited within the Upper Calcarenite Member in Rapla. The five different layers in the Nodular Micrite Unit were probably deposited as part of a volcanic sequence, whose magma chemistry evolved slightly over time. Thus, the ash layers in this tuff package can be chemically distinguished. The U-Pb zircon data of sample Lisheen_mine sample_HK 203 implies an eruption age of 349.6 ± 1.5 Ma for these ashes. The final ash layer was deposited in the Crosspatrick Formation in Rapla. Besides the clear stratigraphic separation between this tuff layer and the previous tuff package, it can also be distinguished based on its trace element chemistry. All samples show an evolved magma composition. Two samples from this area, one in the Waulsortian Limestone Formation (Lisheen_LK-1432_HK 219) and one in the Upper Wavy Laminated Unit (Rapla_3312-54_HK 222) have a strong affinity to shale (Figure 6-2).

Six out of seventeen samples are either influenced by galena or sphalerite mineralisation, which does not seem to influence the potential of bulk-rock chemistry for fingerprinting Irish tuffs. However, as mineralised areas occur above the tuff layers, it cannot be clarified if the Zn-Pb deposits in Lisheen were formed syn- or epigenetically.

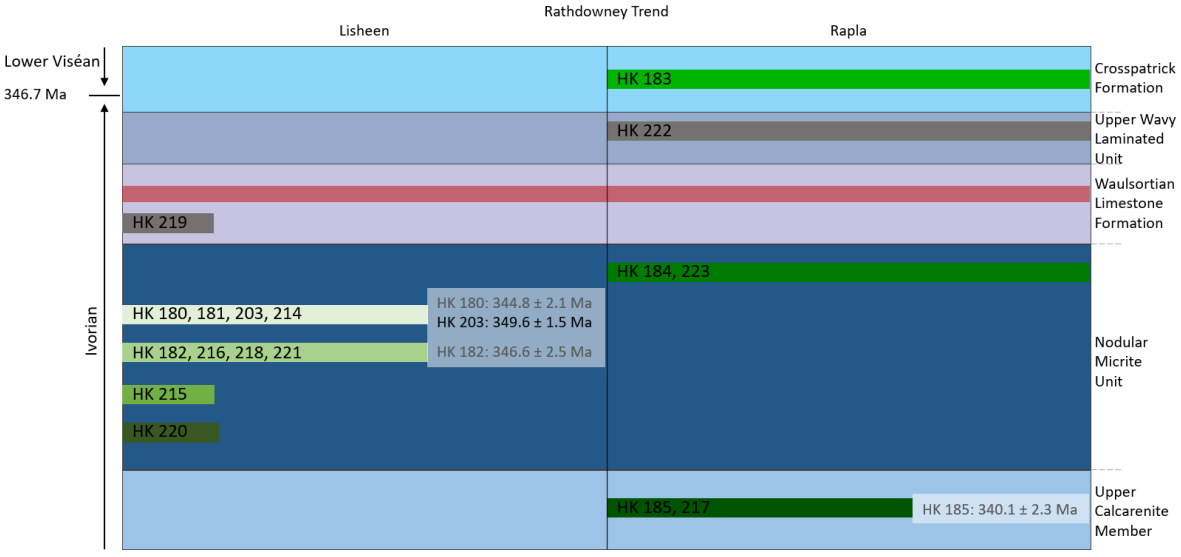

Figure 6-2: Seven different tuff layers are determined within the Rathdowney Trend based on differences in bulk-rock chemistry as well as their stratigraphic positions. The seven bars, which have seven different shades of green represent these seven different layers. Samples Lisheen_LK-1342_HK 219 and LRapla_3312-54_HK 222 have a strong shale component and are thus not considered as tuffs. Sample Lisheen_mine sample_HK 203 provides the only reliable age estimation for the ash layers at 349.6 ± 1.5 Ma. Emphasis was placed on the relative position of the tuff layers in the Rathdowney Trend. The vertical scale does therefore not represent real formation thickness. red bar = mineralised area.

6.3 Stonepark

Five samples (Stonepark_G11-2638-01_HK 197, Stonepark_G11-2638-01_HK 198, Stonepark_G11-2638-02_HK 209, Stonepark_G11-450-02_HK 210, Stonepark_G11-2654-01_HK 212) from the Nodular Micrite Unit share similar bulk-rock trace element systematics and can be correlated (Figure 6-3). Two of these samples (Stonepark_G11-2638-01_HK 197 and Stonepark_G11-2638-01_HK 198,) were taken 5 m stratigraphically apart in the same drill core. Thus, the ash layers were probably deposited during a short lived eruption sequence, building a tuff package of at least two different tuff layers. This tuff package shows the largest chemical heterogeneity compared to other ash layers from the Irish Midlands. Although the samples could be correlated, the source magma chemistry is less certain. Apatite trace element data indicate a mafic composition for samples Stonepark_G11-2638-02_HK 209, Stonepark_G11-450-02_HK 210 and Stonepark_G11-2654-01_HK 212, while bulk-rock data imply either mafic or felsic compositions for the same samples depending on the discrimination schemes employed. Samples Stonepark_G11-2638-01_HK 197 and Stonepark_G11-2654-01_HK 212 could be dated and yield U-Pb zircon ages of 350.7 ± 3.3 Ma and 350.3 ± 4.3 Ma, respectively, which is in agreement with the likely Ivorian age of the host rocks based on biostratigraph(Sevastopulo and Wyse Jackson, 2009). The other two samples from the Nodular Micrite Unit (Stonepark_G11-2638-02_HK 207 and Stonepark_G11-2638-02_HK 208) show a strong shale component in their bulk-rock chemistry, which is supported by an abundance of inherited (as opposed to primary magmatic) zircon grains (Figure 6-3). Sample Stonepark_G11-2654-01_HK 211 from the Lough Gur Formation yields a zircon age of 348.2 ± 2.4 Ma. Hence, it is also within the uncertainty of the likely Ivorian to Lower Viséan biostratigraphic age (Somerville et al., 1992) (Figure 6-3). The apatite chemistry of this sample indicates an evolved source magma. Samples Stonepark_G11-2638-02_HK 207, Stonepark_G11-2638-02_HK 208 and Stonepark_G11-2638-02_HK 209 from the Nodular Micrite Unit show elevated Zn concentrations. Thus, mineralising fluids circulated through that unit after the deposition of the tuff layers, with a maximum age of mineralisation of c. 350 Ma.

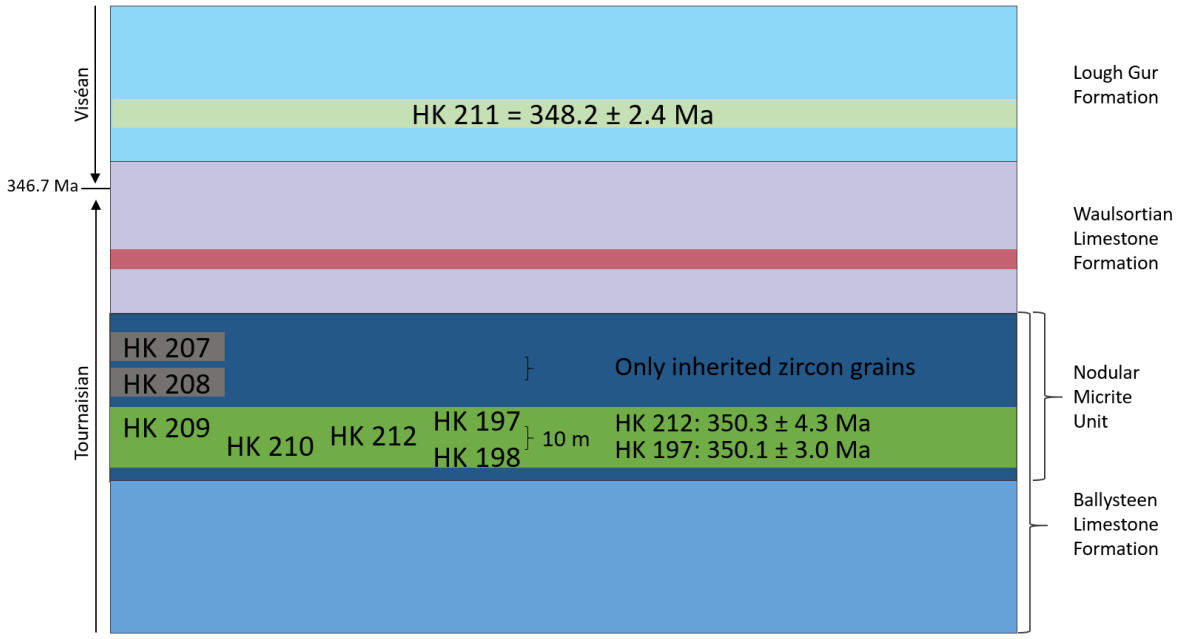

Figure 6-3: Summary of geochemical and geochronological results from the Stonepark area in Limerick. Samples Stonepark_G11-2638-01_HK 197, Stonepark_G11-2638-01_HK 198, Stonepark_G11-2638-02_HK 209, Stonepark_G11-450-02_HK 210, Stonepark_G11-2654-01_HK 212 define a tuff package (thick green bar), which comprises between two and four different tuff layers. This tuff horizon yields a U-Pb zircon age of c. 350 Ma, which is in good agreement with its host rock age. Bulk-rock trace element data of samples Stonepark_G11-2638-02_HK 207 and Stonepark_G11-2638-02_HK 208 show a strong shale component (grey bar). One ash layer was deposited in the Lough Gur Formation (light green bar). Emphasis was placed on the relative position of the tuff layers in Stonepark. The vertical scale does therefore not represent the real formation thickness. red bar = mineralised area.

6.4 Slievedart

The five tuff layers in the Slievedart area either occur in the Kilbryan Limestone or Oakport Limestone formations. These five layers were sampled from two different drill cores: 3470/15 and 3471/4 and they can be clearly separated based on their stratigraphic position (Figure 6-4). Four tuff layers can also be distinguished based on their trace element chemistry. Only the stratigraphically second lowest tuffs (which do not show any shale affinity), cannot be clearly correlated in between both drill cores. The bulk-rock trace element data of tuff layers one, two, four and five show an evolved magma source, indicating two differentiation series, once from a trachytic to rhyolitic composition, followed by an evolution from a trachytic to phonolitic composition (Figure 6-4). Apatite grains, which were recovered from tuff one support the evolved composition of the volcanic source. Uranium-lead zircon ages were obtained from tuff one and tuff four layers. These ages suggest that the four tuff layers from the Kilbryan Limestone Formation were deposited within a very short period of time around 346.4 Ma as the eruption ages from tuff one and tuff four cannot be temporally resolved (Figure 6-4). The second series developed over a longer time, as the fifth tuff layer was deposited in the Oakport Limestone Formation and is at least 64 m apart from the fourth tuff layer. The tuff three layer is coarse (classified as sand-grade) and thus is visually distinct compared to any other tuff layer in this

study. While their bulk-rock data does not unequivocally identify the parent magma composition, the apatite data clearly show a mafic composition.

The Kilbryan Limestone Formation lacks biostratigraphically diagnostic microfossils and is considered to be of late Tournaisian to earliest Viséan age due to its stratigraphic position. Thus, the Tournaisian - Viséan boundary cannot be clearly determined, as indicated by the large grey bar on Figure 6-4. The data from this study (average 347.2 Ma ± 0.99 Ma) and published CA-ID-TIMS data (347.94 ± 0.08 Ma; Pointon, 2012) imply that the Tournaisian-Viséan transition is close to the tuff layers of the Kilbryan Limestone Formation (Figure 6-4).

Tuff one to tuff four layers seem to be influenced by both sphalerite and galena mineralisation, which does not appear to affect the geochemical and geochronological correlation between these layers. Mineralisation in the Slievedart area occurs within the Waulsortian Limestone Formation. As overlying tuff layers are influenced by mineralisation, the deposit was most likely epigenetic in nature as the Waulsortian Limestone Formation host rock was already buried by the Kilbryan Limestone Formation. However, the limestones in both formations can be in part laterally equivalent and may even interfinger in the boreholes of this study, although stratigraphically further down (Figure 2-11C). In any case, mineralisation must have been still ongoing around 347.5 Ma, which is indicated by the tuff ages from this area (this study: average 347.2 Ma ± 0.99 Ma; published age: 347.94 ± 0.08 Ma, Pointon, 2012).

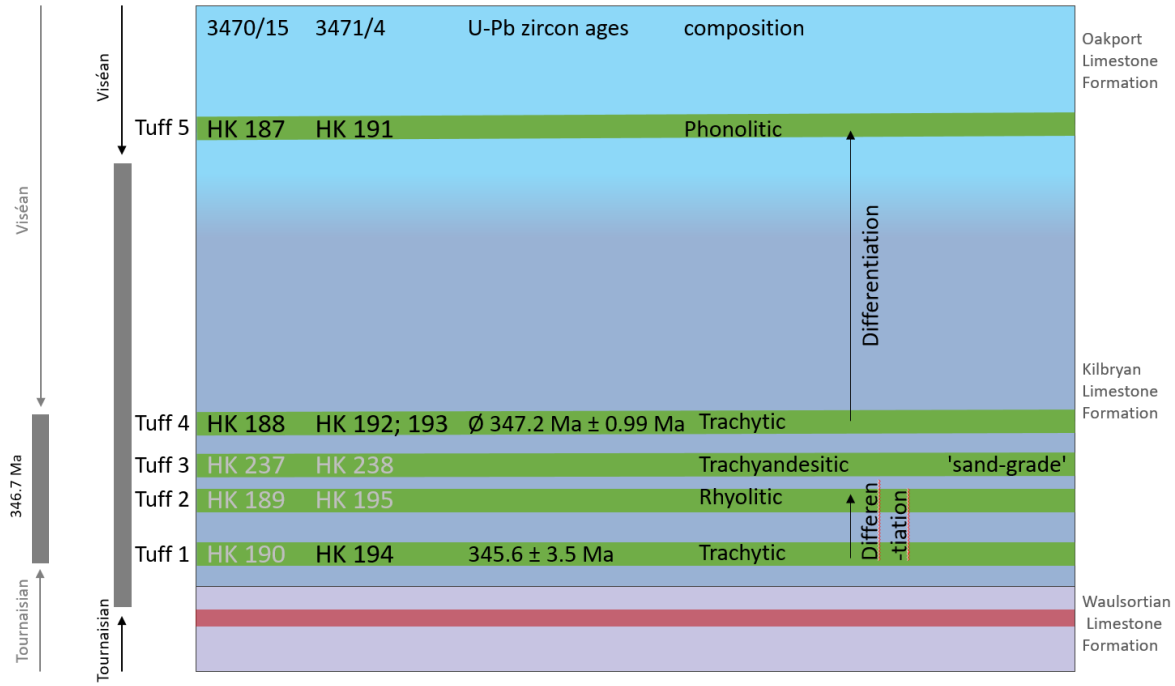

Figure 6-4: Cross-correlation of tuff samples from Slievedart is based on matching bulk-rock trace element analyses, U-Pb zircon age data, apatite trace element chemistry and stratigraphic position. Tuff layers one, three, four and five can be correlated based on their bulk-rock trace element data, their composition and their stratigraphic position. Although samples HK 189 and 195 show a chemical heterogeneity in their bulk-rock trace element data, they can still be correlated based on their composition and stratigraphic position. Reliable U-Pb zircon ages are only available from samples HK 188, 192, 193 and 194 (black font in graph), which cannot be temporally resolved across tuff layers one and four. However, due to the lack of biostratigraphic diagnostic fossils in the area, this study suggests that the Tournaisian-Viséan boundary can be placed based on these ages rather than on biostratigraphy. Emphasis was placed on the relative position of the tuff layers. The vertical scale does therefore not represent the real formation thickness. red bar = mineralised zone.

6.5 Location of the Volcanic Centre

Trace element data indicate an evolved volcanic source for 77 out of 79 tuff samples, while two samples from Slievedart (Slievedart_3470/15_HK 237 and Slievedart_3471/4_HK 238) show a less evolved magma composition. Considering the lack of known outcrops of evolved effusive volcanism within Ireland and Great Britain at the time of ash deposition (see section 2.4 and 2.5), the closest potential source rocks with an evolved magma geochemistry were emplaced within the Variscan mountain belt at c. 1250 km distance of Ireland. Explosive volcanic eruptions can produce huge amounts of fine-grained pyroclastic material. The maximum transport distances of these fine volcanic ashes are difficult to predict. Exceptionally powerful eruptions can produce tephra layers, which are recognisable 1000 km or more from the source (Alloway et al., 2007). The Toba Tuff eruption for example involved c. 2500 km^3 of magma, which was distributed over the Bay of Bengal and the Indian subcontinent and shows primary ashfall units of c. 4 cm thickness, at distances of > 2000 km from the source caldera (Matthews et al., 2012). The same publication reported that reworked ashes of that deposit can be up to c. 3 m in total thickness. Primary ashfalls from the CI eruption, which is the largest known Quaternary eruption in Europe, are dispersed over a 2000 km distance (Engwell et al., 2014). The thickness of these tephra layers are

between 0.2 and 20 cm in a deep sea environment for distal deposition (> 1000 km). The transport distance is influenced by multiple factors like the height of the eruption column, wind strength and direction, grain size, density, shape and surface roughness (e.g. Walker, 1971; Wilson and Walker, 1987). Ash layers are thickest closest to the volcanic centre (Alloway et al., 2007) and show an exponential decrease with distance from source (e.g. Engwell et al., 2014) as only smaller fragments can be transported long distances by volcanic updrafts or winds (Cai et al., 2016). In general, grain size and the amount of heavy minerals also decrease exponentially in thickness with increasing distance from source due to aeolian fractionation as observed by Königer et al. (2002). For example, they suggest a maximum travel distance of volcanic ash which settled down in the Saar-Nahe Basin of less than 300 km, based on the maximum grain sizes of occurring pyroclasts, which are 440 µm for zircon and 400 µm for apatite. Maximum zircon grain sizes from this study are < 150 µm. Thus, the volcanic source can potentially be within the Variscan Belt at 1250 km distance to Ireland.

Early-Variscan I-type plutons (c. 370 - 340 Ma) occur in the Odenwald within the Saxothuringian zone, Northern Vosges and Northern Black Forest, in the Central Bohemian Batholith and along the Alpine front (Finger et al., 1997) (see section 2.4). The Odenwald granitoids include a few gabbro bodies, diorites, tonalites and normal to high K-granitoids (Liew and Hofmann, 1988; Henes-Klaiber, 1989; Henes-Klaiber, 1992). The Early Carboniferous central Bohemian plutonic complex is a composite granitoid body, that ranges from mafic to acidic and from calc-alkaline to ultrapotassic (Holub et al., 1997; Janousek and Gerdes, 2003). The Sázava suite and Blatna granodiorites yield zircon ages at 349 ± 12 and 346 ± 10 Ma, respectively (Holub et al., 1997). Most of the other granitoids of the Central Bohemian Batholith are approximately 350 Ma old (Finger et al., 1997). Younger, Viséan granitoid plutons (c. 340 Ma) are all S-type granites and are reported as deformed granites in the southeastern Bohemian Massif (Finger et al., 1997).

In the southern part of the Black Forest, Viséan magmatism started with andesitic basalt flows and finished with effusive rhyolites at the top of the volcanic sequence, which yield a U-Pb zircon age of 340 ± 2 Ma (Schaltegger, 2000). In the Southern Black Forest, there are sub-alkaline high-K shoshonitic dacitic and rhyolitic tuffs, pyroclastic breccias and lava flows (Gueldenpfennig and Loeschke, 1991; Schaltegger, 2000). Mafic and felsic plutonic intrusions in the Central and Southern Vosges Mountains can be assigned to an Early Viséan Mg-K event at c. 345 - 332 Ma (Tabaud et al., 2015). While the lowermost rhyolite flows yielded an age of 345 ± 2 Ma, the age of an ignimbrite, which terminated the volcanic activity in Southern Vosges was roughly 5 Ma younger (340 ± 2 Ma) (Schaltegger et al., 1996). The volcanic strata within the southern Vosges Basin, which is dated between 345 - 342 Ma (Schaltegger et al., 1996) is comprised of sub-alkaline, andesitic lavas and pyroclastics (Coulon et al., 1975; Lefevre et al., 1994; Lakhrissi, 1996).

The younger volcanic rocks (342 - 340 Ma) (Schaltegger et al., 1996) are trachyandesitic to trachytic in composition as well as subaerial lavas and ignimbrites of quartz latitic and rhyolitic composition (Coulon et al., 1979). Volcanic rocks were intruded by granitoid dykes, monzogabbroic to dioritic stocks and large granite plutons between 339.5 and 340 Ma (Schaltegger et al., 1996). Due to similar eruption ages, it is very likely that Southern Black Forest and Southern Vosges share a similar magmatic evolution (Schaltegger, 2000).

The Irish Mississippian tuffs investigated in this study plot mainly in the comendite/pantellerite field, but also in the phonolite, rhyolite and the upper part of the trachyte fields (Figure 4-19). Further trace element diagrams suggest also an evolved volcanic source (e.g. Figure 4-17). Thus, the trachytic and rhyolitic composition of the volcanic rocks from the southern Vosges Basin and the Southern Black Forest, as well as the granitoids of the Central Bohemian Batholith are closest in composition and age to the Irish Mississippian tuffs. There are also Lower Viséan andesitic lavas, which match the intermediate composition of samples Slievedart_3470/15_HK 237 and Slievedart_3471/4_HK 238. However, there could be a more proximal Irish volcanic source for these two samples. These samples are most likely Lower Viséan in age and plot in the lower edge of the trachyandesite field in the Winchester & Floyd diagram (Figure 4-19). Thus, the chemical composition as well as the age matches with the eruptions of the Knockroe Volcanic Unit in the Limerick area, which consisted of trachyandesite flows and tuffs and yields eruption ages between 345 and 339 Ma (Strogen, 1983, 1988; Somerville et al., 1992; Sevastopulo & Wyse Jackson, 2009).

If tuff layers were deposited as primary fall deposits, only thin tuff layers (up to several cm thickness) are normally preserved at distances > 1000 km (e.g. Engwell et al., 2014). But Matthews et al. (2012) observed that distal secondary deposits can still reach thicknesses up to 3 m. These deposits are developed by processes like local reworking, slumping of previously deposited ash or syn-depositional turbidity currents. The Marker Tuffs, which are up to 2.5 m thick, do not show major indications of reworking on the applied diagrams. However, they are also rather thin tuff layers (c 2 cm thick), interlaminated with carbonaceous mud than one massive horizon. Some tuff samples from this study, which are > 10 cm thick show sharp upper and lower contacts with their host lithology (see Table 3-1). This also suggests rather a rapid precipitation of carbonate than reworking. However, tuff samples of similar age cannot be correlated in between the study sites (bulk-rock sample Lisheen_mine sample_HK 203 does not match bulk-rock sample Stonepark_G11-2638-01_HK 197 and Stonepark_G11-2654-01_HK 212). This should be possible if the source was a super-eruption that caused these primary ashfall deposits > 1000 km from its source. Thus, at this stage an Irish evolved volcanic center, which has not yet been discovered, cannot be excluded.

Commonly employed tectonic discrimination diagrams are problematic as most of them either use absolute elemental ratios, which can easily be rendered during alteration (e.g. through relative enrichments of immobile elements due to element mobility), or are based on limited data sets. However, these diagrams can potentially help elucidate the tectonic settings of magmatic rocks. Sample trace element data from the tuff samples of this study are plotted on the Th/Hf *vs* Ta/Hf diagram of Schandl and Gorton (2002). All but seven samples plot within the within plate volcanic zones field where 62 tuff samples form a cluster (Figure 6-5). All samples, which plot outside the cluster have REE concentrations which are similar to shales (Figure 4-8B). Additionally, *matchograms*, which are used for tuff correlations also suggest a non-volcanic origin for these samples. Thus it is questionable, if this plot actually shows the tectonic setting of these 17 samples.

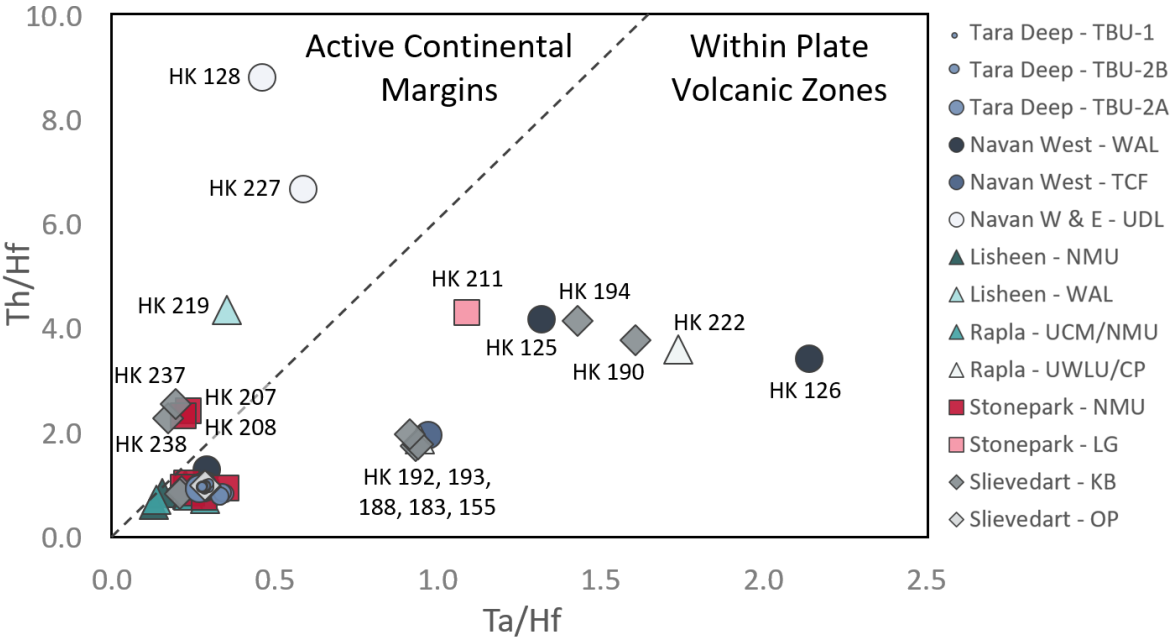

Figure 6-5: Tectonic discrimination diagram of Schandl and Gorton (2002), using Th/Hf and Ta/Hf ratios. Most samples build a cluster in the 'Within Plate Volcanic Zone'. All samples, which are outside that cluster have REE concentrations which are similar to shale.

6.6 Eruption History of Irish Early Carboniferous Tuffs

The bulk-rock and apatite trace element data, U-Pb zircon ages and the relative stratigraphic position of the tuff samples support the following eruption history for the investigated tuffs (Figure 6-6A-E):

The first eruptions took place around 350 Ma and led to the deposition of several volcanic ash layers within the Nodular Micrite Unit in the Stonepark area and in Lisheen (Figure 6-6B). The tuff samples from the Stonepark area show inconsistent bulk-rock and apatite trace element patterns, with mafic chemistries based on apatite data, while the bulk-rock data are not diagnostic. A plausible source is the Central Bohemian Batholith of the Variscan Belt as it consists of felsic and more mafic granitoid bodies of the same age as the Irish tuff layers. It is therefore possible that

the apatite crystals crystallised first in a less evolved magma chamber and were subsequently mixed into a more evolved magma chamber. Bulk-rock trace element analyses show an evolved character for the Lisheen tuffs. Therefore, the tuff layers cannot be correlated across the two study sites. Thus, there is the possibility that there were two different eruption centres around 350 Ma, which led to the deposition of geographically separated ash layers: in Stonepark and in Lisheen. A more widespread deposition is expected for a magmatic source within the Variscan Belt as discussed in the previous section. Although it is currently the closest known evolved volcanic centre to Ireland, a more proximal source than the Variscan Belt has to be taken into consideration, and may yet to have been discovered yet.

The ash layers in the Lisheen area may have had poor preservation potential, as up to five tuff layers can be geochemically distinguished, although only two have been observed in the same drill core. The different preservation across the area is probably due to different erosion rates, sedimentary reworking and/or slow settlement of ash from the ash cloud, which is accompanied by quick precipitation/sedimentation rate of limestone. There is clear evidence that the Lisheen eruption sequence took place over a longer significant period of time (e.g. tens of thousands of years), as this tuff package also contain two ash layers, which were taken from the same drill core (LK-1915) and are separated by 2 m of limestone. A similar eruption history is observed in the Stonepark area. However, the two tuff layers from the same drill core which are 5 m apart (samples Stonepark_G11-2638-01_HK 197 and Stonepark_G11-2638-01_HK 198) can still be assigned to the same tuff horizon. Thus, the volcanic source that produced the tuff layers from Stonepark had overall a more heterogeneous chemistry, but did not change significantly between each eruption. The magma source for the Lisheen ashes may have changed significantly between each eruption with each layer having its unique fingerprint.

Samples HK 125, 126 and 169 from Navan West have most likely a big detrital input. The lack of tephra deposits in the Waulsortian Limestone Formation in the remaining three study areas is probably also caused by the nature of this formation. Steep depositional slopes are mapped, which can range from zero to over 40° and depositional relief from zero to 200 m (Sevastopulo and Wyse Jackson, 2009). Probably the failure of these slopes led to the redeposition of ash layers from an intra mound-facies down to the flank facies and thus dilution, so that the tuff layers will either be mixed with surrounding mud or are no longer recognised in drill cores anymore.

The Waulsortian Limestone Formation is followed by the Kilbryan Limestone Formation in Slievedart and the Lough Gur Formation in Stonepark. The stratigraphically lowest tuff layer in both formations have a common eruption age of c. 346.4 Ma and show the same apatite trace element chemistry, indicating an evolved volcanic source. There are known volcanic centres of similar age and composition in the Black Forest and Vosges. Due to the occurrence of this ash

layer across Ireland, they could have been deposited as part of a bigger volcanic eruption based in the Variscan Belt.

Another three ash layers occur in the Kilbryan Limestone Formation in Slievedart and one in the overlying Lower Viséan Oakport Limestone Formation, while no further layers are detected in Lisheen. Tuff four layers in Slievedart could be dated and yielded an average U-Pb zircon age of 347.2 Ma and thus, show a very similar eruption age to tuff one samples in the same drill cores. The bulk-rock chemistry of the second, fourth and fifth tuffs show an evolved character, while tuff three layers have an intermediate (trachyandesitic) composition. This implies either different volcanic sources or one magma chamber that changed its composition from an evolved to an intermediate and back to an evolved character in between successive eruptions. Volcanic rocks of the Knockroe Volcanic Formation in the Limerick area are similar in age and composition to tuff three layers. However, to date, there are no evolved volcanics known in the Limerick area. The latter also show a distinct appearance, and thus are classified as sand-grade tuffs, while the remaining sample set consists of very fine grained ashes. Bulk-rock data indicate a chemical fractionation between tuff two, four and five from rhyolitic to phonolitic and finally comenditic composition (Figure 4-23). However, there were some breaks during this eruption phase as there is up to 90 m of limestone between these ash layers. These magmatic breaks would have allowed the deposition of tuff three from a different magmatic source, suggesting two different volcanic sources for the evolved (tuff two, four and five layers) and intermediate tuff layer three.

Finally, there are three successive tuff layers in the New Bedded Unit in Tara Deep. Based on the U-Pb zircon age of one Upper Tuff sample, they were erupted around the same time as the Slievedart samples were deposited. All three ash layers have an evolved composition and can only be observed in the Navan area. The stratigraphically highest layer in Tara Deep, the Marker Tuffs, have a distinctive appearance (interlaminated tuffs with calcareous mudstone bands), which cannot be observed in any other region except sample HK 117, which occurs in the second lowest stratigraphic unit of the Upper Dark Limestone Formation in Navan East. The Marker Tuffs and sample HK 117 can also be correlated based on their bulk-rock chemistry. Thus, the Marker Tuffs and sample HK 117 were likely deposited from the same eruption and represent the same ash layer (Figure 6-6E). The Tara Deep Upper or Lower Tuff also matches the bulk-rock chemistry of one tuff layer in the Tober Colleen Formation.

Thus, there was maybe one bigger eruption, whose source was in the Variscan belt and led to the deposition of tuff one layers in Slievedart and one layer in the Lough Gur Formation in Stonepark. This was followed by many small-scale volcanic eruptions, having multiple volcanic centres in Ireland around 345 Ma, which led to the deposition of very local ash beds in Slievedart and Navan.

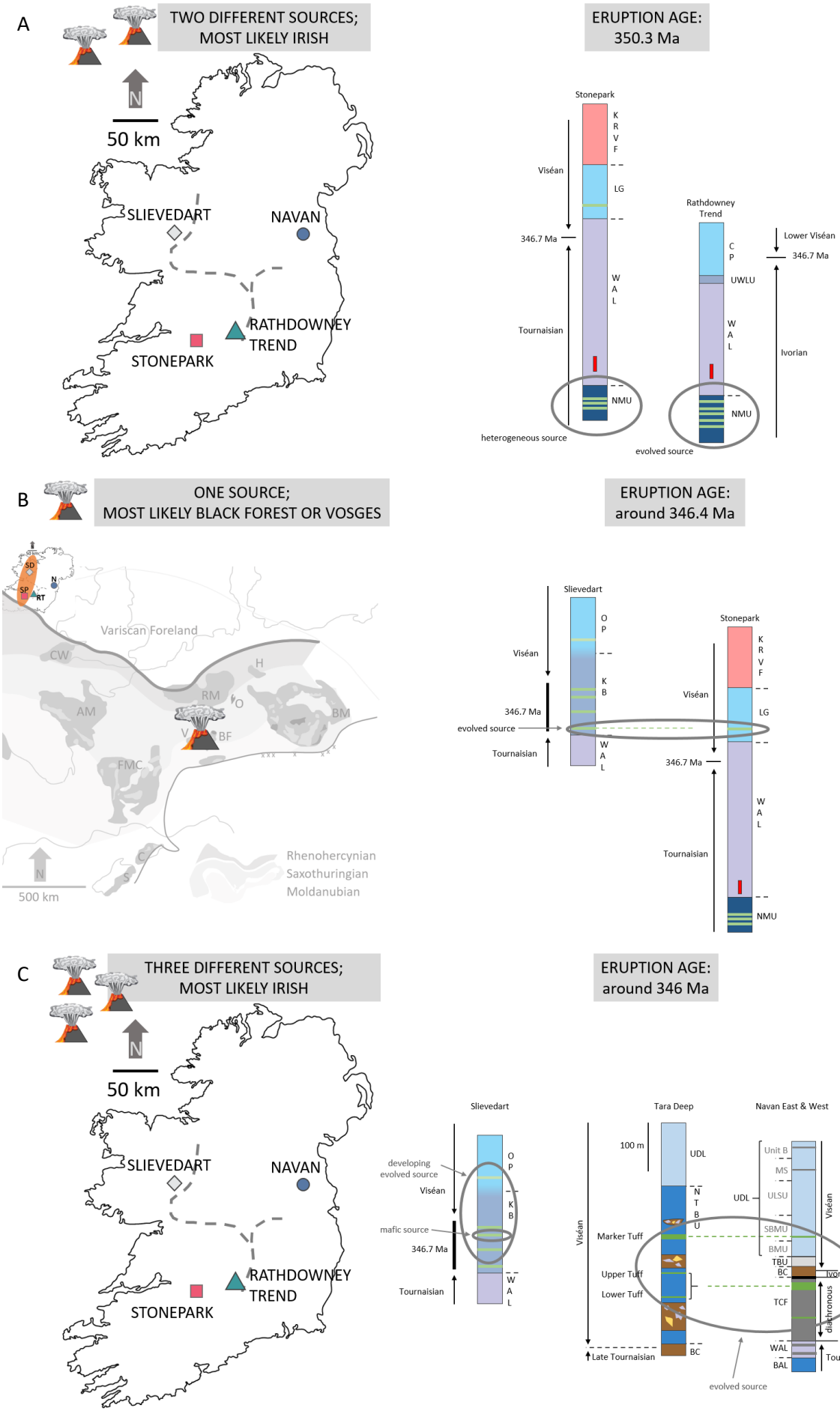
A
TWO DIFFERENT SOURCES;
MOST LIKELY IRISH
ERUPTION AGE:
350.3 Ma
N
50 km
SLIEVEDART
NAVAN
RATHDOWNEY
TREND
STONEPARK
Stonepark
K
R
V
F
Viséan
LG
346.7 Ma
W
A
L
Tournaisian
NMU
heterogeneous source
Rathdowney
Trend
C
P
UWLU
Lower Viséan
346.7 Ma
Ivorian
evolved source
B
ONE SOURCE;
MOST LIKELY BLACK FOREST OR VOSGES
ERUPTION AGE:
around 346.4 Ma
SD
SP
RT
N
Variscan Foreland
CW
H
RM
O
AM
BM
V
BF
FMC
Rhenohercynian
Saxothuringian
Moldanubian
500 km
Slievedart
O
P
K
B
Viséan
346.7 Ma
evolved source
Tournaisian
W
A
L
Stonepark
K
R
V
F
Viséan
LG
346.7 Ma
W
A
L
Tournaisian
NMU
C
THREE DIFFERENT SOURCES;
MOST LIKELY IRISH
ERUPTION AGE:
around 346 Ma
N
50 km
SLIEVEDART
NAVAN
RATHDOWNEY
TREND
STONEPARK
Slievedart
developing
evolved source
Viséan
O
P
K
B
mafic source
346.7 Ma
Tournaisian
W
A
L
Tara Deep
Navan East & West
100 m
UDL
N
T
B
U
Viséan
Marker Tuff
Upper Tuff
Lower Tuff
BC
Late Tournaisian
Unit B
MS
UDL
ULSU
SBMU
BMU
TBU
BC
Ivorian
TCF
diachronous
WAL
BAL
Tournaisian
evolved source

Figure 6-6 A-E: Eruption history in chronological order of the Irish Mississippian tuff samples. On the left: most likely source area for associated deposited tuff layers (on the right). Orange shaded area indicates a more specific area (if known). Stratigraphic columns show ash layers in relation to their host rocks. Circled ash layers have the same magmatic source A) Two unknown magmatic centers, which are most likely in Ireland. One led to the deposition of several ash layers in Stonepark of similar chemical composition. The other event led to the deposition of a tuff package in Lisheen. These tuff layers can be clearly distinguished. B) Tuff layers can be traced across Slievedart and Stonepark (indicted by dashed line). Their source could be within the Variscan Belt. C) Multiple volcanic sources within Ireland, that led to the deposition of ash layers in Slievedart and Navan. AM = Armorican Massif, BC = Boulder Conglomerate, BF = Black Forest, BM = Bohemian Massif, BMM = Ballynamona Member, C = Corsica Massif, CP = Crosspatrick Formation, CW = Cornwall, FG = Fingal Group, FMC = French Massif Central, H = Harz, IM = Iberian Massif, KB = Kilbryan Limestone Formation, LG = Lough Gur Formation, N = Navan, NMU = Nodular Micrite Unit, NTBU = New Thin Bedded Unit, O = Odenwald, OP = Oakport Limestone Formation, RM = Rhenish Massif, RT = Rathdowney Trend, S = Sardinia Massif, SD = Slievedart, SB = Sedimentary Breccia, SP = Stonepark, TBU = Thin Bedded Unit, TCF = Tober Colleen Formation, UCM = Upper Calcarenite Member, UWLU = Upper Wavy Laminated Unit, V = Vosges, WAL = Waulsortian Limestone Formation.

Chapter 7:

Strontium Isotope Stratigraphy as a Secondary Stratigraphic Tool using Carbonates from the Irish Mississippian – a Pilot Study Introducing a Novel *In Situ* Laser-Sampling Technique

---

7.1 Introduction

At present, the Mississippian limestones of Ireland are often biostratigraphically poorly constrained. As a result, Sr isotopes and trace elements of the host carbonates will be analysed to examine whether they can be employed as a secondary independent tool for checking age, in addition to investigating the chemical stratigraphy of the volcanogenic clay bands (investigated in Chapters 3 to 6).

Strontium isotope stratigraphy (SIS) is commonly used as an additional control for stratigraphic correlations. The concept of SIS, which uses the $^{87}Sr/^{86}Sr$ composition of past seawater, is a valuable complementary technique for correlation and dating of sedimentary sequences (DePaolo and Ingram, 1985; Veizer, 1989; McArthur, 1994; Howarth and McArthur, 1997; McArthur et al., 2012), especially for sequences where biostratigraphy is not diagnostic due to a lack of fossil assemblages or their limited biostratigraphic utility (Veizer et al., 1999). Strontium isotope stratigraphy rests on the assumption that the world's oceans are homogeneous with respect to $^{87}Sr/^{86}Sr$. Such uniformity of $^{87}Sr/^{86}Sr$ ratio of seawater on a global scale (to the fifth decimal place) is expected at any given time, because the residence time of Sr in the ocean (c. 1 million years) greatly exceeds the oceanic mixing rate (c. 1000 years) (Veizer, 1989; McArthur, 1994). This means the oceans are thoroughly mixed on time scales that are short relative to the rates of gain and loss of Sr. Consequently, by measuring the Sr isotopic ratios in limestones or shells from geological units in deep time it is possible to record temporal Sr isotopic variations in seawater. The temporal variation of marine $^{87}Sr/^{86}Sr$ variations reflect changes in the riverine sources of Sr (continental erosion, isotopically heavy strontium) *vs* Sr input from submarine hydrothermal exchange ('mantle' flux, isotopically light strontium) (Faure, 1986; Palmer and Edmond, 1989; Veizer, 1989; Martin and Macdougall, 1995; Taylor and Lasaga, 1999; Veizer et al., 1999). The SIS calibration curve is based on the measurement of $^{87}Sr/^{86}Sr$ in samples from different localities dated by biostratigraphy, magnetostratigraphy and astrochronology.

The database used herein is from McArthur et al. (2012) and uses 4119 data pairs. Comparison of the measured $^{87}Sr/^{86}Sr$ ratio in marine carbonate (e.g. a shell or cement) with these calibration curves can then yield an absolute age for the carbonate. The curves will inherit uncertainties that are inherent in the limitations of the constituent calibrating techniques. According to McArthur (1994), the quality of the match of a sample with the SIS calibration curve depends on

- the preservation state of the sample
- the quality of the analytical data
- the accuracy of the age model used to calibrate the isotope curve
- the slope of the seawater $^{87}Sr/^{86}Sr$ curve at the given time interval

The slope of the calibration curve rarely exceeds a value of 0.000 060 per Ma, which will result in a minimum dating precision about ± 0.1 Ma (McArthur et al., 2012). For example, Bruckschen et al. (1995) attained a resolution for the Tournaisian (Hastarian) to lower Viséan interval of c. 1 Ma, while the rate of change in the Sr curve over the Brigantian substage results in a resolution in the order of ± 0.3 Ma (Cummins and Elderfield, 1994). The European Carboniferous $^{87}Sr/^{86}Sr$ record commences with values of 0.70820 in the Tournaisian and declines continuously until it reaches a mid-Viséan minimum around 0.707690 (Figure 7-1). The rapid rise during the upper Viséan and Serpukhovian is followed by a plateau in the Sr isotope record during the Bashkirian to Moscovian at 0.708260 (Bruckschen et al., 1999). However, the Sr isotope data show a large spread at certain time windows, especially for Serpukhovian and Viséan times: values of $^{87}Sr/^{86}Sr$ around 332 Ma range from 0.707637 to 0.707805 even when extreme outliers are ignored (McArthur et al., 2012). The considerable degree of scatter, particularly during the Viséan, results in part from partial diagenetic alteration of some samples, which overprint the original marine isotope signal but is also due to biostratigraphic uncertainties (Bruckschen et al., 1995; Bruckschen et al., 1999; McArthur et al., 2001).

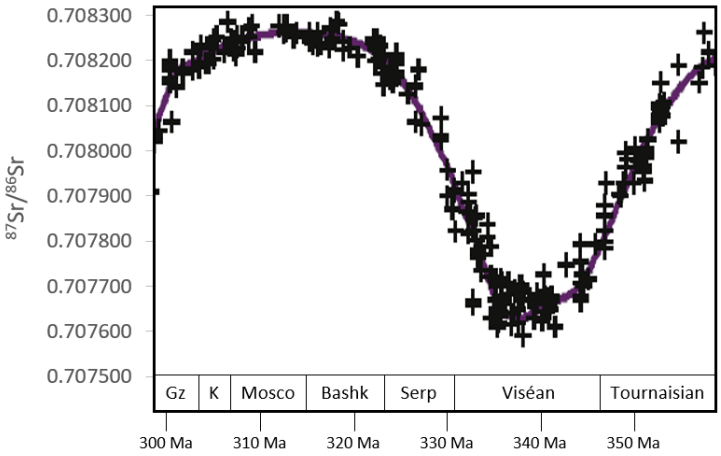

Figure 7-1: Strontium isotopic curve for the Carboniferous. The $^{87}Sr/^{86}Sr$ values range between 0.70769 and 0.70826. Serp=Serpukhovian, Bashk=Bashkirian, Mosco=Moscovian, K=Kasimovian, Gz=Gzhelian. Figure adapted from Figure 7.2 in McArthur et al. (2012).

In an optimum scenario (e.g. a well preserved sample which yields precise analytical data is matched to a well calibrated SIS curve for a time window with a rapidly changing $^{87}Sr/^{86}Sr$ ratio), the precision of SIS calibration can surpass foraminiferal and ammonite biostratigraphy in the Cenozoic and Mesozoic, respectively (McArthur et al., 2012). For the Palaeozoic, it is already a valuable tool for correlating marine sediments, but more samples that are well preserved and well constrained in age are required. Consequently, the application of SIS on Irish samples may improve the data set and provide a new useful tool for the chronostratigraphic control of the Irish Carboniferous (Tournaisian and Viséan), especially in combination with trace element patterns. In particular, the rare earth elements plus Y (REE+Y) have a characteristic distribution in seawater (an increase from La to Lu with large Y and Ce anomalies; Elderfield et al., 1990), which potentially allows the reconstruction of the marine REE+Y chemistry in Ireland during the Carboniferous. As far as the author is aware, a study employing a combination of Sr isotopes and carbonate trace elements for general stratigraphic correlations in the Mississippian has not been reported before. To improve and realise the true potential for correlating rocks using SIS and a chemostratigraphic approach, it is crucial to use only clean and well-preserved samples, which are free from diagenetic alteration and contamination from non-carbonate mineral phases. Thus, several studies have employed sequential leaching experiments to minimise contributions from contaminant Sr from non-carbonate minerals, secondary carbonate overgrowths and organic matter (e.g. Bailey et al., 2000; Li et al., 2011; Zhang et al., 2015). This study compares $^{87}Sr/^{86}Sr$ values as well as trace element contents from sequentially leached limestones and crinoids to those derived from bulk leaching analyses of single-digested limestones as well as brachiopods, crinoids and corals with the ultimate goal of finding which material best preserves the original marine chemistry signal. Furthermore, micrites were used as a sampling target as the chemostratigraphic trend between micrites from two different locations can potentially still be used to achieve correlation if an equivalent amount of diagenetic modification happened in between those two. If even the amount of diagenetic modification that has taken place can be established, everything could be normalised back to the original pristine values.
However, sampling of the target material poses a risk to contaminate the samples by the surrounding matrix. In order to minimise the risk of sample contamination, a new laser-micro sampling method guided by elemental maps was established. This new method enables shallow sampling depths, which avoids sampling unwanted material such as veins, infiltrated sulphides, deformation-related features and other diagenetic artefacts. Ablated sample material is then collected in a test tube containing weak acid. The bulk of the solution remains for elemental analysis, while an aliquot is used for analysis of Sr isotope ratios. Thus, the same material can be used to screen the carbonate sample for potential contamination, as well as for trace element and

Sr isotopic correlations. The ultimate goal is to create a split-stream approach, that one part of the sample gets guided directly into a multi collector inductively coupled plasma mass spectrometry (MC-ICP-MS) and the remaining part into a solution inductively coupled plasma mass spectrometry (ICP-MS), avoiding any further treatment of the samples.

7.2 Geological Setting

Samples from this study were taken from drill hole 2666-02, which is located in the Irish Midlands Province (Figure 7-2A). During the Early Carboniferous time period, the sample site was part of an extensive carbonate platform (Long et al., 2005; Pracht et al., 2004), which led to the deposition of the Micrite Unit, followed by the Mixed Beds, the Upper Sandstone, the Shaley Pales, the Ballysteen Limestone Formation and the Oakport Limestone Formation (Figure 7-2B). Analysed samples include micritic limestones, brachiopods, corals and crinoids (Figure 7-2C-H). The micrites as well as one brachiopod were sampled from the Micrite Unit. The other brachiopods as well as two corals and two crinoids were sampled from the Ballysteen Limestone Formation. Both stratigraphic units are Tournaisian in age (Figure 7-2B).

The exact sampling depth, stratigraphic position, sampling method and dissolution protocol for each sample is listed in **Error! Reference source not found.**, Appendix 3.

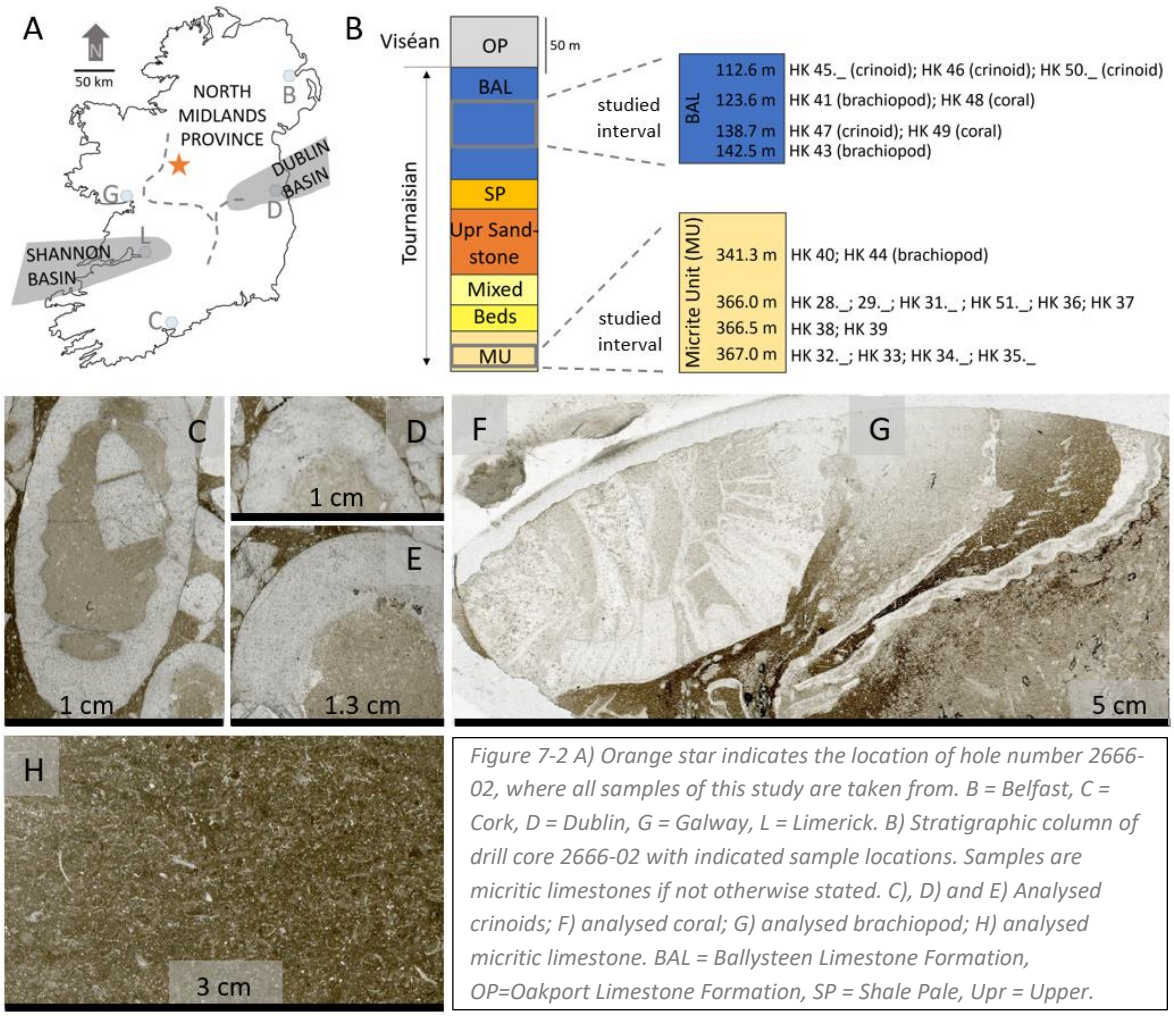

Figure 7-2 A) Orange star indicates the location of hole number 2666-02, where all samples of this study are taken from. B = Belfast, C = Cork, D = Dublin, G = Galway, L = Limerick. B) Stratigraphic column of drill core 2666-02 with indicated sample locations. Samples are micritic limestones if not otherwise stated. C), D) and E) Analysed crinoids; F) analysed coral; G) analysed brachiopod; H) analysed micritic limestone. BAL = Ballysteen Limestone Formation, OP=Oakport Limestone Formation, SP = Shale Pale, Upr = Upper.

7.3 Wet Chemistry

Micritic limestones and fossils were either digested using three-stage sequential leaches or single-step digestions. The different approaches were compared to see which samples give primary seawater signals in trace element patterns, as well as in Sr isotopes, without being influenced by non-carbonate minerals or other secondary processes.

7.3.1 Method

This section includes the description of milling, leaching and trace element analyses of samples as well as the column chemistry and thermal ionisation mass spectrometry (TIMS) analyses to obtain Sr isotope data. The schematic workflow used to obtain trace element as well as Sr isotope data is shown in Figure 7-3.

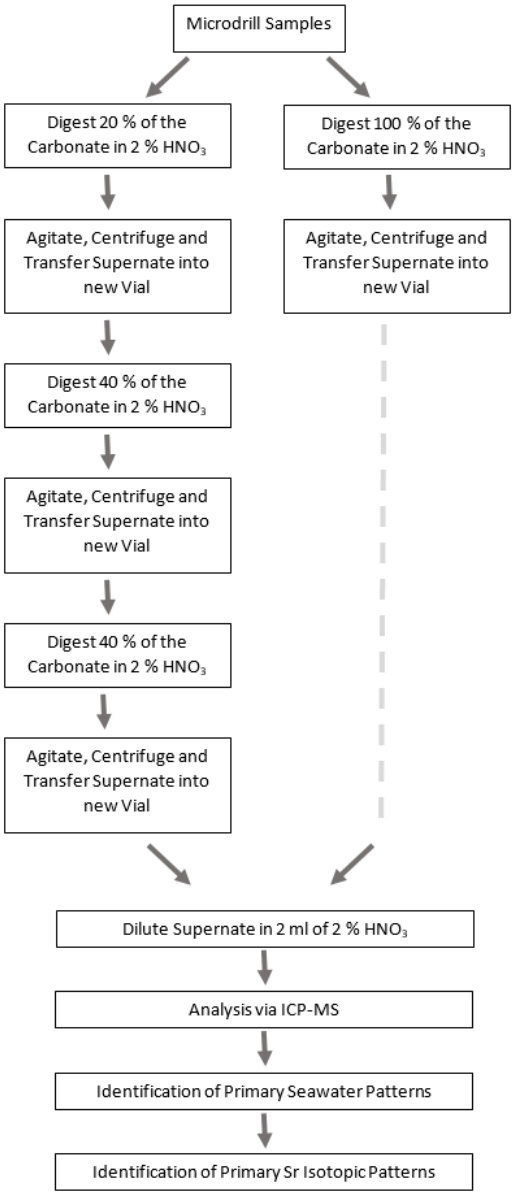

Figure 7-3: Applied workflow for sequential leaching experiments as well as single-step digestions. ICP-MS = inductively coupled mass spectrometry.

7.3.1.1 Milling

A hand-operated microdrill, equipped with 0.3 to 0.5 mm Ø tungsten drill bits was used to obtain sample powder from micritic limestones for geochemical analyses. Areas of micritic limestone were targeted, while bioclasts, secondary veins, and cement were avoided.
The high-precision milling of the fossils was conducted at University College Dublin (UCD), using a micro-mill, which was equipped with 0.3 mm Ø tungsten drill bits. The combination of computer-controlled sub-micron stage resolution and positional accuracy enabled the physical separation from brachiopods, crinoids and corals from the surrounding matrix. Furthermore, two micritic limestones (16HK-011 and 16HK-013) were crushed and powdered using a tungsten-carbide mill.

7.3.1.2 Trace Element Chemistry and Analyses

Powdered carbonate samples were dissolved by adding a sufficient volume of 2% nitric acid to dissolve 20% of the sample. This calculation is based on a theoretical purity of 100% $CaCO_3$. Before being centrifuged, the sample was agitated on a shaker for 15 min at room temperature. Then, the supernatant was transferred and the solution was diluted to 2% for analysis. The procedure was repeated twice with sufficient acid to get a central leach (20–60%) and a final leach (60-100%). Moreover, three different leaching procedures were applied: 1) the precipitate was cleaned in deionised water between each leaching step, discarding the water. 2) deionised water was kept and analysed together with the supernatant. 3) no cleaning steps were performed between the different leaching stages. As there were no obvious differences between the cleaning procedures, they are not further mentioned.

All samples were analysed using the quadrupole inductively couple plasma mass spectrometry (ICP-Q-MS) in the Geology Department, Trinity College Dublin using the methodology already described in Chapter 4, section 4.2.1. However, due to the leaching steps that were performed, concentrations cannot be recalculated based on the sample weight as was undertaken for the tuff samples. Therefore, based on a theoretical purity of 100% $CaCO_3$, it is assumed that all samples contain 40.04 wt% Ca and the relative signal intensities from all elements were recalculated in relation to Ca, the internal standard element.

7.3.1.3 Strontium Isotope Chemistry and Analyses

Samples for Sr isotope analyses were prepared at Trinity College Dublin and subsequently analysed at UCD, Ireland. All reagents were prepared using triple-distilled HNO_3 and ultrapure water. Remaining stock solutions (between 300 and 600 µl; see section 7.3.1.2) from single-step digested and sequentially leached samples were dried down and subsequently re-dissolved in 2 ml 1 M HNO_3 for the separation of Sr using micro-columns filled with Eichrom Sr-spec resin (AG® 50 W-X8 (200-400 mesh, Bio-Rad)). Prior to the loading of the samples on the resin, columns were

cleaned with 3 ml 0.05 M HNO_3 and preconditioned with 6 ml 1 M HNO_3. After the samples were carefully loaded onto the columns without disturbing the resin, the columns were washed again with 3 ml 8 M HNO_3. The elution medium to collect Sr and Ba was 0.05 mol/L HNO_3. Subsequently, collected fractions were evaporated and redissolved in 1 ml 1 M HNO_3. The same procedure was repeated, using new columns to purify Sr from Ba.

One µl of a tantalum oxide emitter solution was loaded onto the outgassed Re double filaments to enhance Sr ionisation (Birck, 1986). Approximately 200 ng of the collected Sr was subsequently loaded on the dried Ta-emitter solution. The samples were then analysed using a Thermo Scientific Triton TIMS. A single analysis consisted of minimum of 200 ratios (8 blocks of 25 cycles). The analytical uncertainties on Sr isotope ratios are reported at 1 standard deviation (SD). A $^{87}Sr/^{86}Sr$ ratio of 0.710262 ± 0.000032 SD (n=5) was determined for the NBS SRM 987 Sr international standard during different runs, which is in agreement with the long-term mean value of this standard in UCD of 0.710260 ± 0.000009 SD (March 2019). The ratios were recalculated according to a NIST SRM 987 value of 0.710248 as recommended by Weis et al. (2006). Within-run mass fractionation was corrected using an exponential law to a $^{86}Sr/^{88}Sr$ ratio of 0.1194. Total procedural blanks for Sr were < 1 ng.

7.3.2 Results

Magnesium, Al, P, Ca, Sc, Fe, Mn, Rb, Sr, Y, Nb, Cd, Ba, Hf, Th concentrations, the complete rare earth elements (REE) data set as well as Sr isotopic data of the leaching experiments and the single-step digested samples are reported in Table A3-1, Appendix 3.

7.3.2.1 Results – Trace Elements

Magnesium and Mn concentrations for all micrites, single-step digested corals and crinoids as well as one central and both final leaches of the crinoids range between 2 309 to 16 947 µg/g and 85 to 704 µg/g, respectively. Brachiopods, one first and one central leach of the crinoids show the lowest Mg concentrations (632 to 2 809 µg/g), while all brachiopods and both first crinoid leaches show the lowest Mn content (6 to 36 µg/g). The P content for one final micrite leach, both final crinoid leaches and both single-step digested crinoids range between 242 and 660 µg/g. The other samples have lower P concentrations (5 and 215 µg/g). All but four samples (first micrite leaches; Rb content = 3.22 – 4.42 µg/g) yield Rb concentrations between 0.02 and 1.79 µg/g. Single-step digested micrites, final leaches of the micrites and one coral (HK 48) have constantly higher concentrations in Sc, Al, Fe, Hf, Th and REE+Y in comparison to the remaining samples (first and central leached micrites, all brachiopods, all crinoids and coral HK 49), with threshold values of 0.79, 141, 1596, 0.16, 0.002, 0.33 and 22.09 µg/g, respectively. Cadmium concentrations are very similar. However, seven out of eight central leaches show

similar Cd values to single-step digested micrites, final micrite leaches and the one coral, ranging between 0.01 and 0.03 µg/g. Strontium and Ba contents are lowest for all micrite samples, one central (HK 45.2) and one final crinoid leach (HK 45.3) with values below 502 µg/g and 49.3 µg/g, respectively. The other fossils have Sr contents between 980 and 4744 µg/g. Barium concentrations for the brachiopods and corals are also low (between 2.6 to 3.6 µg/g), while the crinoid samples yield high Ba concentrations, ranging from 195.9 to 516.6 µg/g.

7.3.2.2 Results – Sr Isotopes

Sr isotopic results are presented in Figure 7-4. Five analyses of NIST SRM 987 show $^{87}Sr/^{86}Sr$ values of 0.710266, 0.710263, 0.710256, 0.710260 and 0.710263. $^{87}Sr/^{86}Sr$ values for both single-step digested micrite samples, all central leaches of the micrites, both single-step digested crinoids as well as one final crinoid leach (HK 50.3) yield the highest values (0.708338 to 0.708599). The second highest group of $^{87}Sr/^{86}Sr$ values comprise the central crinoid leach (HK 45.2; 0.708121) and the other final crinoid leach (HK 45.3; 0.708095). Single-step digested brachiopods and corals yield $^{87}Sr/^{86}Sr$ values between 0.707816 and 0.707945.

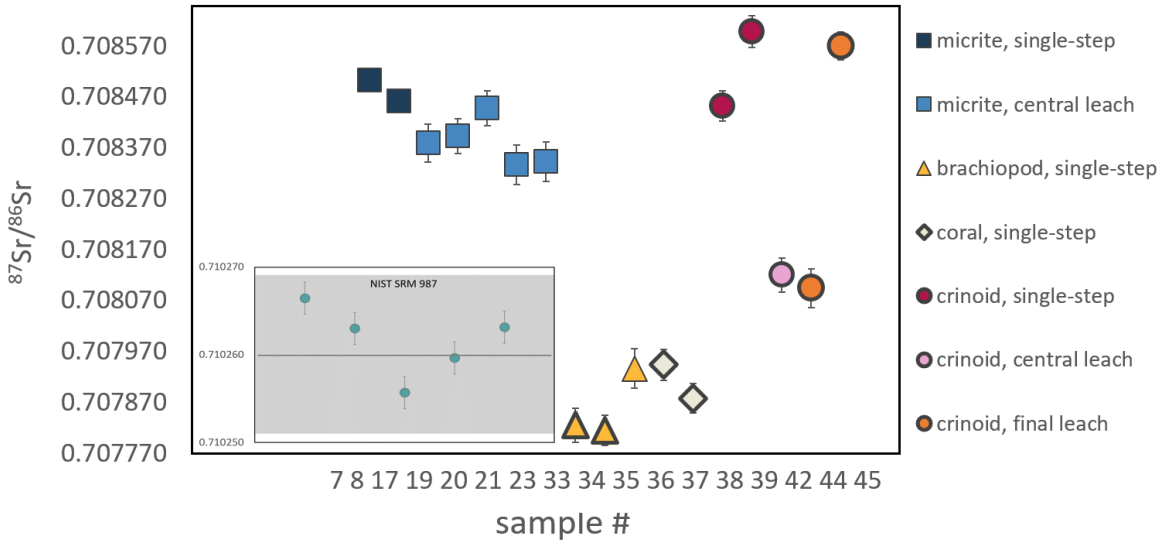

Figure 7-4: Individual $^{87}Sr/^{86}Sr$ Thermal ionisation mass spectrometry (TIMS) analyses of micritic limestones, NIST SRM 987 standard, crinoids, brachiopods and corals. Samples with a thin outline were sampled within the Micrite Unit, while samples with a thick outline come from the stratigraphically higher Ballysteen Limestone Formation. One standard deviation error bars are also plotted. Error bars correspond to the standard deviation on the measured isotopic ratio. Sample # refers to the sample number listed in ***Error! Reference source not found.****, Appendix 3.*

7.3.3 Discussion

It has proven challenging to find limestones and fossils, which can reliably preserve seawater Sr isotopes and REE signatures. However, to ensure that the sampled materials can serve as reliable proxies for Early Carboniferous seawater, possible contaminants should be ruled out. Therefore, fossils (brachiopods, corals and crinoids) were characterised first using thin section petrography to ensure that samples were pristine.

The most likely type of contaminant is fine-grained clastic detritus (Goldstein and Jacobsen, 1988; Elderfield et al., 1990), volcanic ash (Zhou et al., 2000), hydroxides of Fe and Mn (Bau et al., 1996) and phosphates (German and Elderfield, 1990; Byrne et al., 1996). Diagenetic alteration of samples can also overprint primary seawater signatures and thus needs to be constrained in every SIS study (Brand and Veizer, 1980; Banner and Hanson, 1990; Banner, 1995; Brand, 2004). Contaminated limestones can show unusual non-seawater-like REE patterns, as the REE concentrations in carbonates are low but the level of REEs in contaminants is high (Nothdurft et al., 2004). The sequential leaching method allows effective isolation of the least-altered carbonate fraction from each sample, which is most likely to retain a pristine marine $^{87}Sr/^{86}Sr$ signature (Bailey et al., 2000; Li et al., 2011).

7.3.3.1 Acetic *vs* Nitric Acid

Different studies use different methods for carbonate dissolution. All samples of this study were leached in nitric acid as recommended by Tostevin et al. (2016).

7.3.3.2 Identification of Contaminants

Elements such as Al, Th, Sc and Hf are excellent monitors of clastic and volcanic detritus, because of their much greater concentrations in average shale than in marine carbonates (e.g. Webb and Kamber, 2000). For example, the post-Archaean average Australian shale (PAAS) has Al, Th, Sc and Hf concentrations of 10 wt%, 14.6 µg/g, 16 µg/g and 5.8 µg/g, respectively (McLennan, 2001), while all samples from this study contain very low concentrations of Al (< 0.2 wt%), Th (< 2.16 µg), Sc (< 2.77 µg) and Hf (< 0.015 µg). However, there is a positive correlation between these elements for the micrite samples. For example, the correlation coefficient R^2 between Th and Sc concentration is 0.9396 (Figure 7-5A). As the final leaches have the highest concentrations in Al, Th, Sc and Hf, followed by the single-step digested samples, they likely contain the highest amounts of either clastic or volcanic detritus.

The Y/Ho ratio is often used as a discriminator between altered and unaltered seawater REE+Y patterns in the marine rock record. Yttrium is removed less efficient from seawater than Ho, due to different surface complex stabilities of Y and Ho. Therefore, preserved unaltered carbonates should show supra-chondritic marine Y/Ho ratios > 36 (e.g. Bau, 1996). However, contamination of carbonate by a small amount of shale can strongly reduce the Y/Ho ratio, pushing it towards the chondritic ratio of impure carbonate (Webb and Kamber, 2000; Kamber and Webb, 2001; Nothdurft et al., 2004) while also increasing the total REE concentration (e.g. Bau and Dulski, 1996). Single-step digested samples and final leaches have Y/Ho ratios < 36, while having the highest REE contents, which again supports some minor shale contamination in these samples (Figure 7-5B).

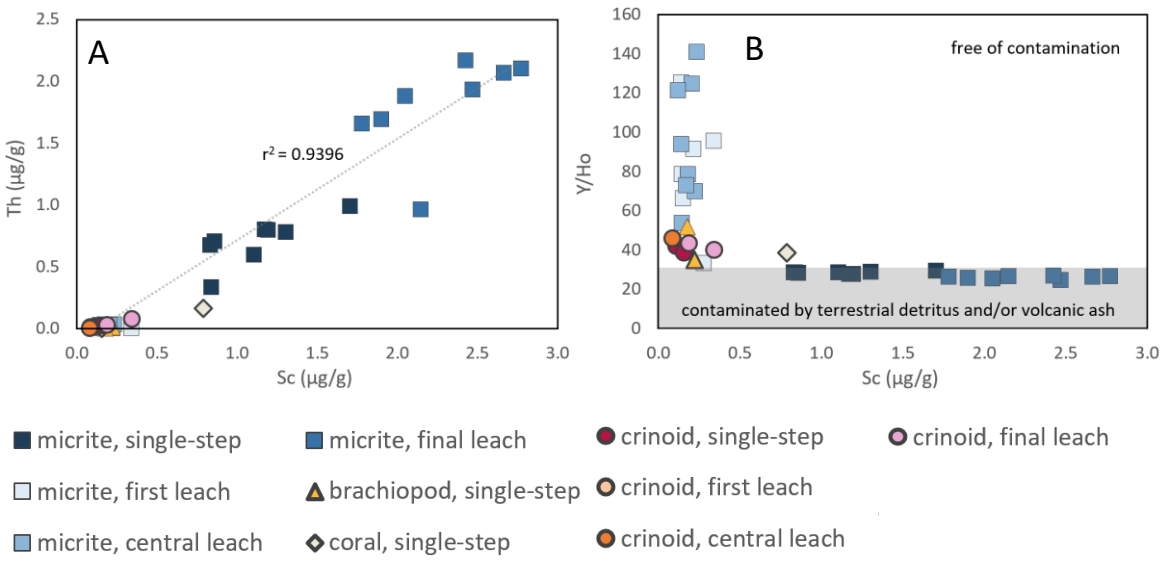

Figure 7-5: Th vs Sc and Y/Ho vs Sc values of micrites, brachiopods, corals and crinoids from the Irish Midlands are plotted for the identification of possibly contaminated samples. A) Strong positive correlation in Th and Sc concentrations for final leaches and single step digested micritic samples. Both sample suits likely contain high amounts of either volcanic or clastic detritus. B) Final leaches and single-step digestions show Y/Ho ratios lower than 36, coinciding with the highest REE concentrations, which could be due to small degrees of contamination by detrital or volcaniclastic sediments. All other samples show ratios above 36, suggesting that the carbonates have preserved primary seawater signals. Samples with a thin outline were sampled within the Micrite Unit, while samples with a thick outline come from the stratigraphically higher Ballysteen Limestone Formation.

While the Al content is a reliable tool to track the dissolution of detrital phases, Rb concentrations can be used as a proxy for the dissolution of detrital phases but also the leaching of weak clay surface bound ions during several leaching steps (Banner et al., 1988; Bailey et al., 2000). Normally, the weak clay surface bound ions should be removed during the first leaching step (e.g. Li et al., 2011). The highest Rb/Ca ratio is observed in samples of the first leachates, a minor amount in the last 40% and the lowest ratio is within the central leachate for both materials (limestones and crinoids), although to a much lower extent within the crinoid samples (Figure 7-6A). Thus, the pre-cleaning step effectively removed the majority of adsorbed ions and weak clay surface bound ions on easily exchangeable sites, while the increase in the final leach could arise from the attack of the non-carbonate phases such as clays and oxides as suggested by Zhang et al. (2015) and Tostevin et al. (2016).

The majority of the Rb and Al seen in the single-step digested micrites seems to be caused by the dissolution of non-carbonate materials, as the first leachate contains a negligible amount of Al compared to the final leachates (Figure 7-6B). All fossils, except one coral, have low Rb/Ca as well as Al/Ca ratios, suggesting they are non-contaminated samples (Figure 7-6A, B).

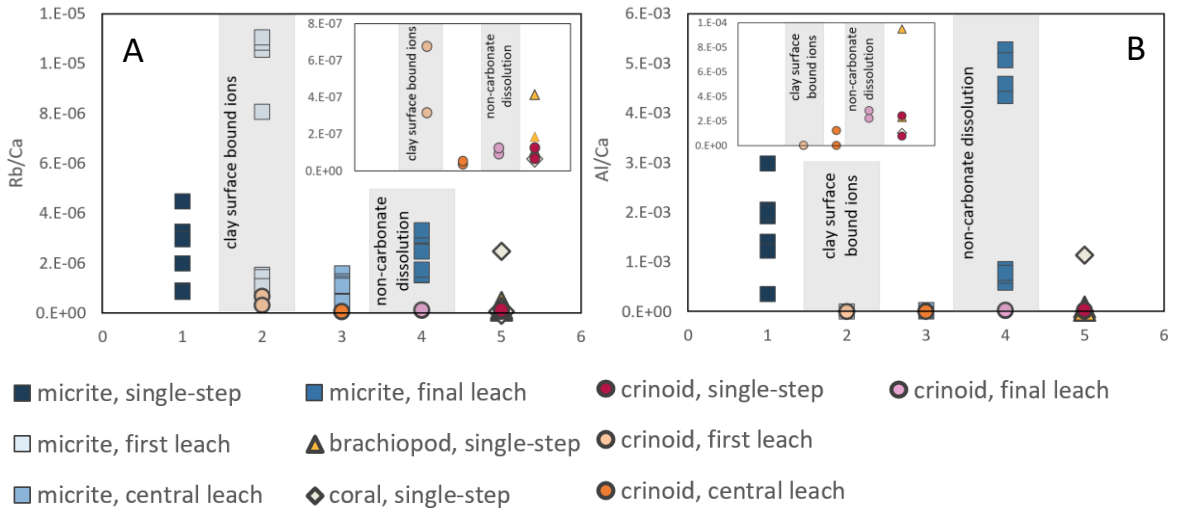

Figure 7-6: A) Rb/Ca and B) Al/Ca ratios for all samples of this study. High Rb/Ca and Al/Ca ratios in final leaches indicate contamination with clay surface bound ions, while high Rb/Ca and Al/Ca ratios in the final leaches suggest contamination of these samples by non-carbonate phases. Samples with a thin outline were sampled within the Micrite Unit, while samples with a thick outline come from the stratigraphically higher Ballysteen Limestone Formation.

Iron *vs* ΣREE and P *vs* ΣREE show positive correlations within the sequentially leached micrite and crinoid samples (Figure 7-7A, B). First and central leaches have very low Fe and P concentrations while final leaches show the highest Fe and P content. This suggests that Fe-Mn oxyhydroxides as well as phosphates cause REE contamination in the final leaches of the samples as observed by Zhang et al. (2015).

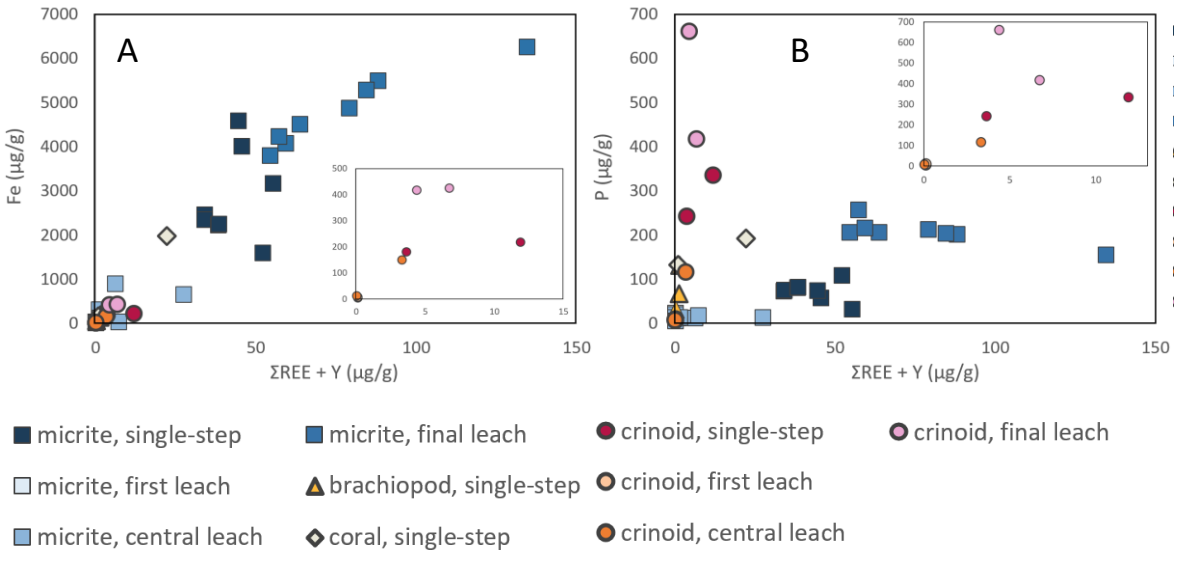

Figure 7-7: The strong positive correlation between Fe and REE+Y concentrations (A) and P vs REE+Y contents (B) in single-step digested micrites/crinoids and final leaches of the micrites/crinoids is most likely caused by Fe-Mn oxyhydroxides and phosphates. Samples with a thin outline were sampled within the Micrite Unit, while samples with a thick outline come from the stratigraphically higher Ballysteen Limestone Formation.

Marine calcites are typically Sr-rich and Mn-poor (Banner and Hanson, 1990). Diagenetic alteration usually leads to an increase in Mn and Fe contents, which coincides with a decline in Sr concentrations (Brand and Veizer, 1980; Popp et al., 1986; Banner, 1995). Thus, Sr/Mn ratios are used as a proxy to track diagenesis from meteoric fluids (Brand and Veizer, 1980). Values above 15 indicate samples free of diagenetic effects (Montañez et al., 1996). Most of the samples in this data set have Sr/Mn ratios below 15, while the single-step digested brachiopods and both first leaches of the crinoid samples show a spread between 59 and 340 (Figure 7-8A). Furthermore, negative correlations are not observed in Fe *vs* Sr (Figure 7-8B) nor in Mn *vs* Sr biplots (Figure 7-8C). However, it was shown earlier that especially single-step digested and final leached micrites are highly influenced by Fe-Mn oxyhydroxides (Figure 7-7A). Nevertheless, single-step digested brachiopods and first leaches of the crinoid samples contain the lowest Mn and low Fe, but high Sr concentrations (Figure 7-8B, C). Thus, they are most likely the least diagenetically overprinted samples in this sample suite.

Samples were also screened for dolomitisation using Mg/Ca ratios. In the study of Fantle and Higgins (2014), the molar Mg/Ca ratios of limestones vary between 0.0265 and 0.0360, while the average dolostone Mg/Ca value is 0.78 ± 0.04. Mg/Ca values for samples of this study are well within the limestone values, ranging between 0.0017 and 0.0449 (Figure 7-8A). Thus, a significant impact from a dolomite component can be excluded.

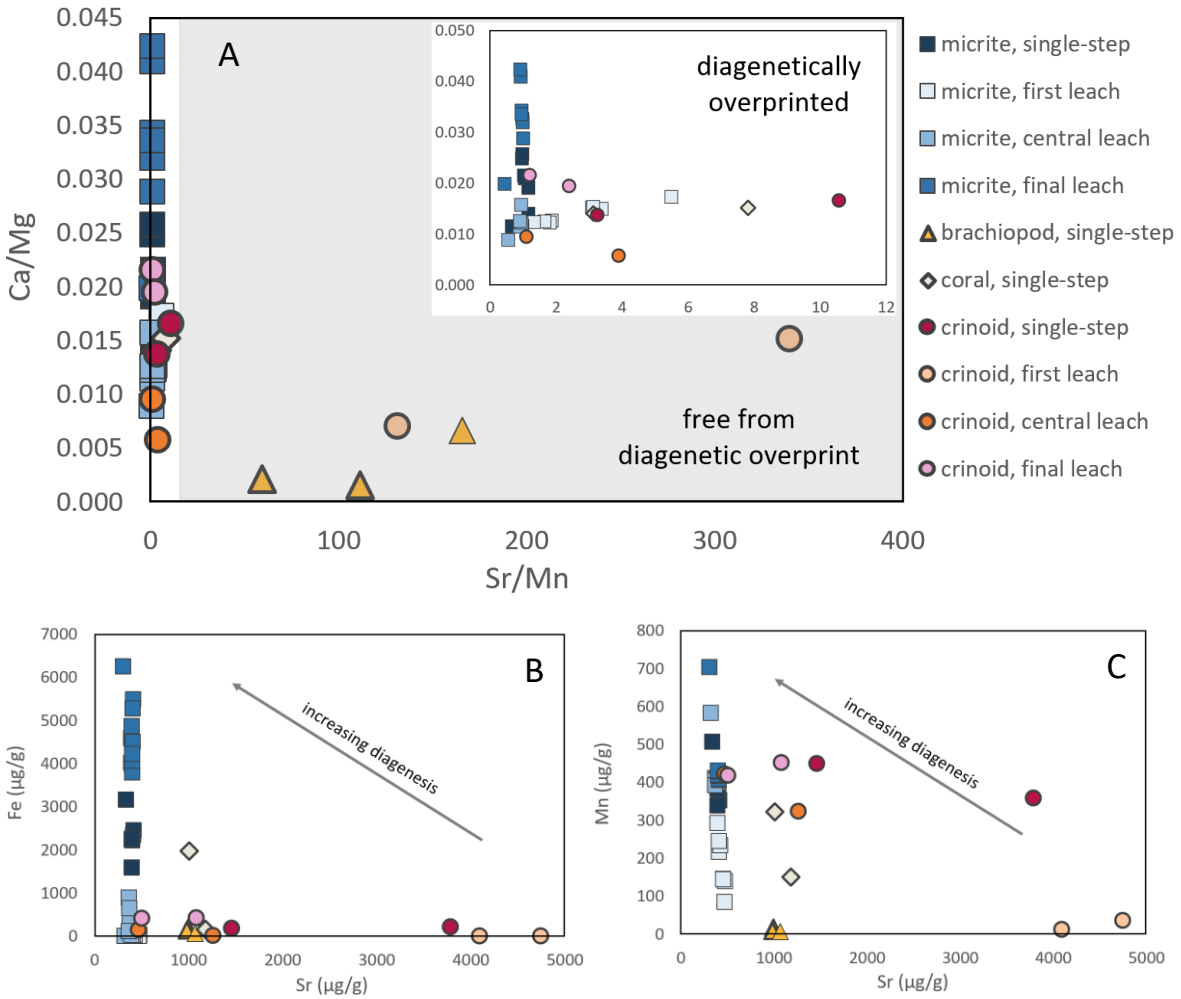

Figure 7-8: A) Sr/Mn vs Ca/Mg biplots of micrites, brachiopods, corals and crinoids from the Irish Midlands. Ca/Mg ratios of all samples indicate that samples are not influenced by dolomitisation, whereas all samples, whose Sr/Mn ratio are below 15 are probably diagenetically overprinted. B) Fe vs Sr and C) Mn vs Sr biplots. There is no obvious negative correlation within this sample suite, which is typical for diagenetically overprinted samples. Samples with a thin outline were sampled within the Micrite Unit, while samples with a thick outline come from the stratigraphically higher Ballysteen Limestone Formation.

Many studies (e.g. Denison et al., 1994; Derry et al., 1994, Montañez et al., 1996; Van Geldern et al., 2006) use the occurrence of specific element concentrations as an additional technique to screen carbonate samples for diagenetic effects and contamination from non-carbonate phases. Therefore, the abundance of Al, Fe, Mn, Rb, Sr and Sr/Mn, Rb/Sr as well as Y/Ho ratios are used with threshold values of < 10 µg/g, < 400 µg/g, < 100 µg/g, < 0.5 µg/g, > 500 µg/g and ≥ 15, < 0.001 as well as > 36, respectively. The limits for Al, Rb, Sr/Mn and Rb/Sr are chosen following Montañez et al. (1996), while the Fe, Mn and Sr threshold values stem from the study from Van Geldern et al. (2006) and the Y/Ho threshold ratios from Bau et al. (1996). Figure 7-9 summarises the result of the screening test separated by the different digestion/leaching approaches. Single-step digested brachiopods and first leaches of the crinoid samples pass the screening test, while single-step digested and final leaches of the micrite fail the test for any chosen parameter (Figure 7-9). The remaining samples show a mixed result (Figure 7-9).

	Σ Analyses	Al < 10 µg/g	Fe < 400 µg/g	Mn < 100 µg/g	Rb < 0.5 µg/g	Sr > 500 µg/g	Sr/Mn > 15	Rb/Sr < 0.001	Y/Ho > 36
Micrite - Single-Step	8				2			2	
Micrite - First Leach	8								
Micrite - Central Leach	8	6	6		6			4	
Micrite - Final Leach	8								
Brachiopods - Single-Step	3	2							
Coral - Single-Step	2	1	1		1				
Crinoid - Single-Step	2								
Crinoid - First Leach	2								
Crinoid - Central Leach	2					1			
Crinoid - Final Leach	2	1							

Figure 7-9: Summary of screening test to evaluate the degree of diagenetic effects and contamination from non-carbonate phases, performed on micrites, brachiopods, corals and crinoids from the Irish Midlands, using the threshold values from Montañez et al. (1996) (Rb, Al, Sr/Mn, Rb/Sr), Van Geldern et al. (2006) (Mn, Fe, Sr) and Bau et al. (1996) (Y/Ho). Either all or the majority of the analysed samples passed the screening test if boxes are green and vice versa if boxes are orange. Exactly half of the samples passed the screening test if boxes are grey. Numbers within the boxes indicate the amount of samples which passed the screening test. All or none of the samples passed the screening test if boxes are empty.

In summary, low Th, Sc, Hf, Al, Rb, P and Fe concentrations, but high Y/Ho ratios, indicate a low degree of contamination from non-carbonate phases like detritus, phosphates and Fe-Mn-oxyhydroxides for the central leaches of micrites and crinoids as well as for most of the single-step digested fossils. Final leaches of the micrites have the highest concentrations of these elements. This suggests that the highest contribution of contaminants in single-step digested micrites stem from non-carbonate materials, which are dissolved in the final dissolution step. Furthermore, Sr/Mn ratios as well as the relatively high Sr and low Fe and Mn content for single-step digested brachiopods and first leaches of the crinoid samples indicate a low diagenetic overprint for these samples.

7.3.3.3 Chemostratigraphic Correlations

If the preserved seawater REE+Y signature in chosen samples represent the seawater chemistry during the Early Carboniferous times, they can be used for chemostratigraphic approaches.

The REE+Y are displayed as shale (PAAS) normalised patterns as it removes the Oddo-Harkins effect on the absolute concentrations of REE+Y and provides a genetic link to the upper crust, for which shale is a proxy. The typical shale normalised seawater and microbialite REE+Y profile shows a smooth, progressive enrichment in heavier REE with a large positive Y and a large negative Ce anomaly, along with more weakly positive La, Eu, Gd and Lu anomalies (Elderfield et al., 1990) (blue and dark green line, respectively, Figure 7-10). Deviations from this pattern can occur where the REE is either removed during sedimentation via particle scavenging, for example onto Fe-Mn (oxyhydroxides), organic matter and clay particles or added to the ocean through rivers, aeolian input or hydrothermal vents (Elderfield et al., 1990). Owing to the relatively high concentration of REEs in shale, even small (e.g. 1–2%) REE contributions from shale can greatly reduce the La and Ce anomalies in carbonates, while also decreasing the degree of light rare earth element (LREE) depletion (Nothdurft et al., 2004). Any mixing with non-carbonate phases thus

usually results in this type of pattern together with a decrease in the Y/Ho ratio and the development of a small Eu anomaly (brown line, Figure 7-10).

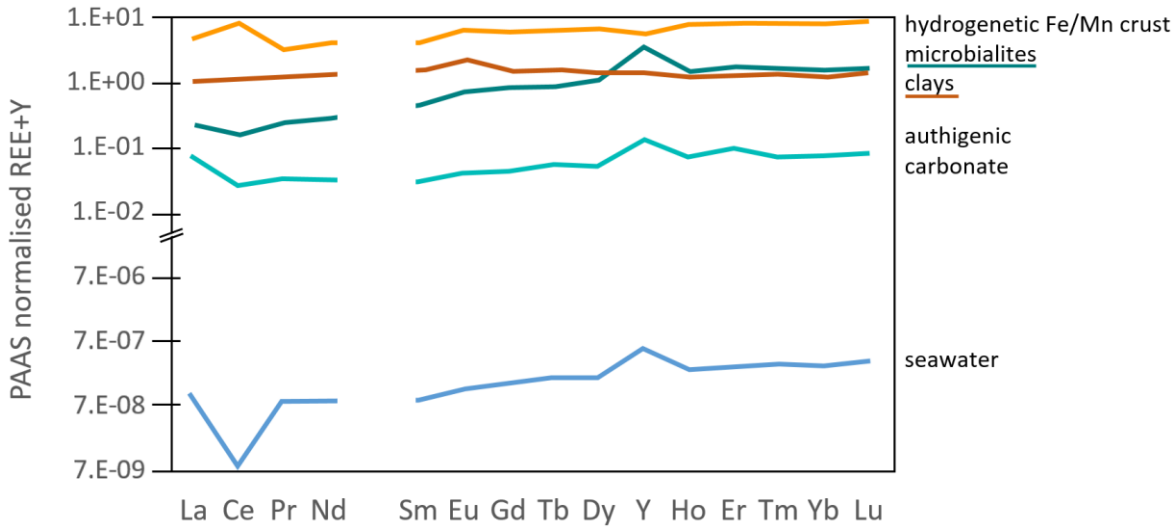

Figure 7-10: Shale-normalised REE+Y patterns showing typical features such as La, Ce, Eu and Y anomalies for different natural environments and minerals. Data are based on reported REE+Y concentrations in the literature. Data for marine hydrogenetic Fe-Mn crusts are from Bau and Dulski (1996), modern seawater from James et al. (1995), authigenic carbonate and clays from Zebra River are from Tostevin et al. (2016) and microbialites from Webb and Kamber (2000).

The clay contamination in the single-step digested samples as well as the final leaches of the micrites (see previous section, 7.3.3.2), is also reflected in the REE+Y pattern of these samples, which is more similar to clay than to typical seawater (Figure 7-11A, B). Their REEs show very comparable patterns, gradually decreasing from La to Lu with no obvious La and Ce anomalies, but either exhibiting a weak positive or negative Eu anomaly, as well as either positive or negative Y anomalies (Figure 7-11A, B). First leaches of micrites and crinoids as well as one out of two central leaches of the crinoids show low REE concentrations and chaotic REE+Y patterns (Figure 7-11C, D), which are probably caused by secondary carbonate phases, adsorbed ions and easily exchangeable ions (see previous section, 7.3.3.2). However, the single-step digestions, one out of two central leaches and all final leaches of the crinoid samples show comparable REE patterns (Figure 7-11D, E). Therefore, sequential leaching is not necessary for sampled crinoids as it seems that the partial leachings have no effect on their REE+Y patterns (Figure 7-11D, E). Central leaches of the micrites, single-step digested fossils, one central and both final leaches of the crinoids show positive La and Y anomalies as expected from seawater-like patterns (Figure 7-11D-F). Although most of these samples show neither negative Ce anomalies nor heavy rare earth element (HREE) enrichments, they still show the most seawater-like patterns of all samples of this study.

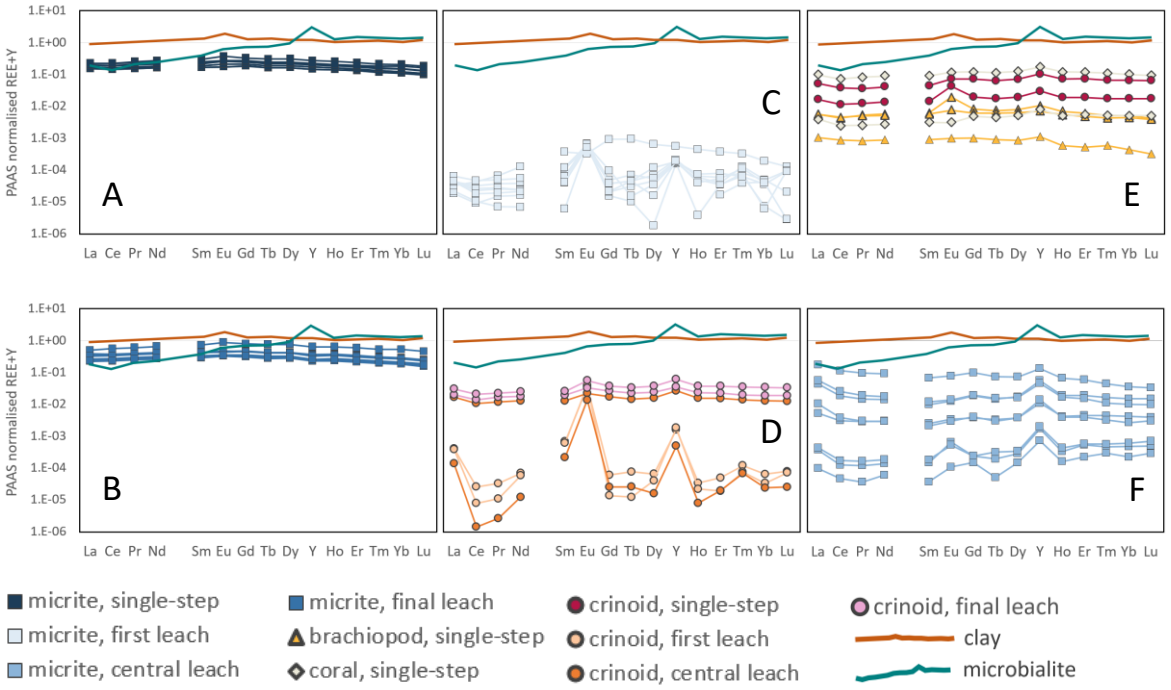

Figure 7-11: PAAS-normalised REE+Y patterns of micrites, brachiopods, corals and crinoids from the Irish Midlands Province. A) and B) REE+Y patterns of single-step digested samples and final leaches of micrite resemble clay-like patterns. C) Chaotic REE+Y patterns of final leaches from micrites are probably caused by adsorbates on easily exchangeable sites. D) Chaotic REE+Y patterns in both first leaches and one central leach of crinoids, while the other central leach and both final leaches show seawater-like patterns. E) and F) Most similar seawater like REE+Y patterns in central leaches of micrites and single-step digested brachiopods, corals and crinoids. Brown and green REE+Y patterns are shown for comparison.

According to Webb and Kamber (2000), microbial and other non-skeletal carbonate may provide a more reliable proxy for seawater REE+Y geochemistry than skeletal carbonate, as they directly precipitate carbonate without the use of complex mineralisation pathways which may cause fractionation. Furthermore, most non-skeletal carbonate is free from associated ferromanganese crusts. On the other hand, most publications (e.g. Popp et al., 1986) argue, that brachiopods are best for isotopic and elemental analyses, as they are mainly composed of low-magnesium calcite (LMC). This form of calcite has the greatest potential to reliably maintain the primary seawater isotopic values as it is more resistant to diagenetic alteration and inversion than other carbonate components (Popp et al., 1986). Furthermore, they are large enough to be separated from their enclosing matrix/cement while they are also abundant in rocks of Palaeozoic age. However, this study shows that brachiopods show very similar REE patterns to crinoids, corals and the central leaches of micrites (Figure 7-11C, E, F). Therefore, the basin in which the carbonates were deposited could also contain a regional, rather than a global (open ocean) REE+Y signal. Furthermore, Ba/Ca and Cd/Ca ratios are commonly used in foraminiferal studies as it is assumed that foraminiferal Cd and Ba concentrations reflect the nutrient distribution in oceans and thus can serve as proxies of changes in the chemical composition of seawater (e.g. Lea and Martin, 1996; Hönisch et al., 2011).

Thus, samples which resemble seawater REE+Y patterns can ideally be assigned to either the Micrite Unit or the Ballysteen Limestone Formation based on their REE+Y patterns as well as Ba/Ca and Cd/Ca ratios. Four central leaches of the micrites and brachiopod sample HK 44 were collected in the Micrite Unit and indeed show lower REE+Y normalised ratios than the remaining samples (Figure 7-12A). However, the other five central leached micrites as well as single-step digested corals, crinoids, brachiopods HK 41 and 43, one central leached crinoid and both final leached crinoid were either sampled within the Micrite Unit or the Ballysteen Limestone Formation and show the same REE+Y pattern (Figure 7-12B). Moreover, these samples also show a big spread in Ba/Ca and Cd/Ca ratios and cannot be separated according to their stratigraphic unit (Figure 7-12B, C). However, brachiopod HK 44, which was sampled in the Micrite Unit and brachiopods HK 41 and 43, which come from the Ballysteen Limestone Formation (Figure 7-2B) can be separated based on their REE+Y patterns, Ba/Ca and Cd/Ca ratios (Figure 7-12C, E, F). Thus, there is the possibility that brachiopods, which are the least contaminated and diagenetically altered material, show local REE+Y seawater distributions typical for the Early Carboniferous in the Irish Midlands.

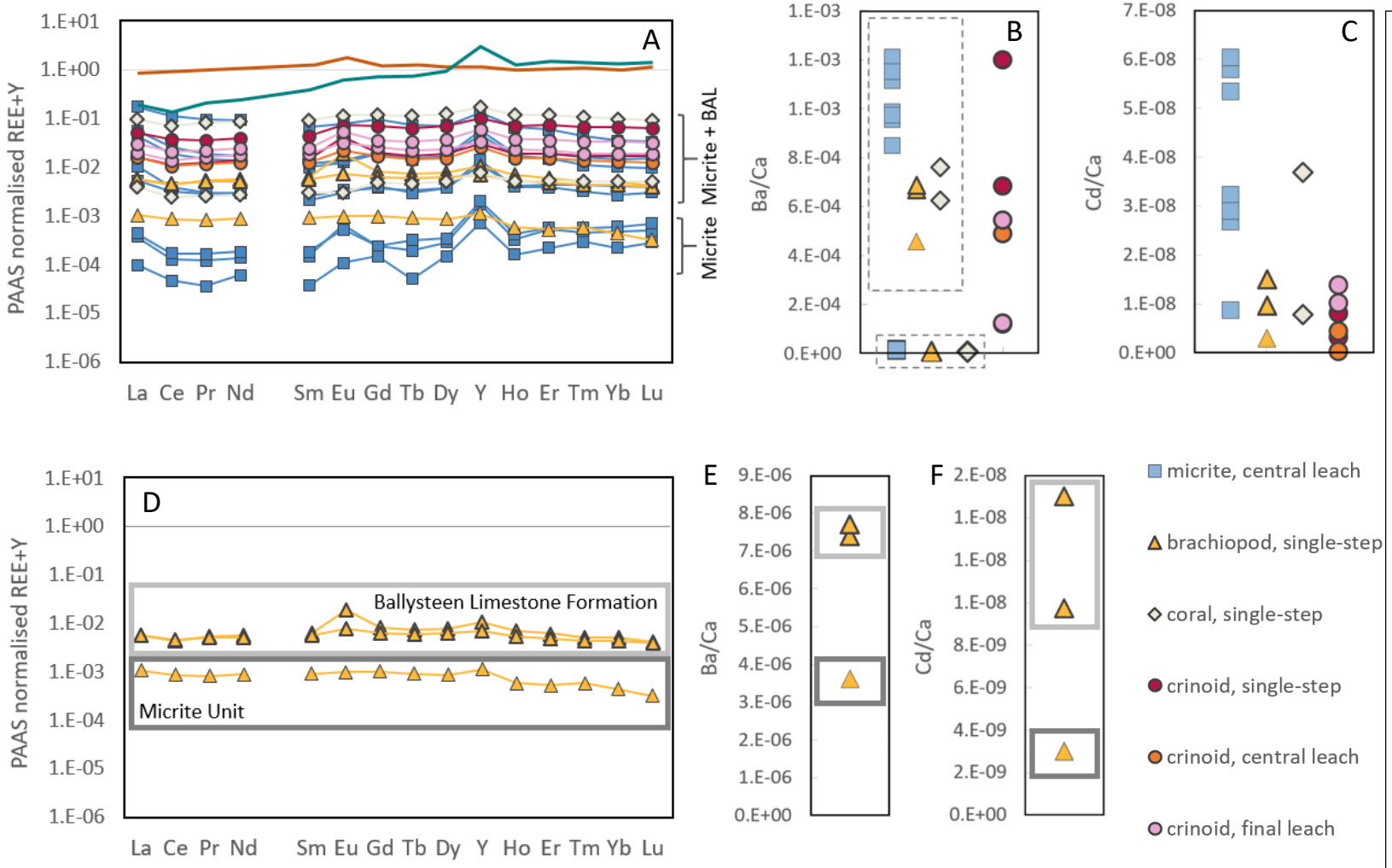

Figure 7-12: Central leach micrites, single-step digested crinoids and corals as well as central and final leach crinoids cannot be split in samples from the Micrite Unit and the Ballysteen Limestone Formation based on PAAS-normalised REE+Y patterns (A), Cd/Ca (B) as well as Cd/Ca (C) ratios, while PAAS normalised REE+Y (D) as well as Ba/Ca (E) and Cd/Ca (F) data from three analysed brachiopods of this study allows the separation of the three samples into the Micrite Unit (HK 44) and the Ballysteen Limestone Formation (HK41 and 43). Samples with a thin outline were sampled within the Micrite Unit, while samples with a thick outline come from the stratigraphically higher Ballysteen Limestone Formation.

7.3.3.4 Sr Isotopic Correlations

Only samples revealing minor contamination along with two single-step digested micrites were used for Sr isotopic analysis.

All samples from this study were deposited either within the Ballysteen Limestone Formation or in the Micrite Unit, which are Tournaisian in age. Courceyan $^{87}Sr/^{86}Sr$ values, which are reported in literature, range from c. 0.70820 to 0.70780 (McArthur et al., 2012). Single-step digested and central leaches of the micrites, single-step digested crinoids as well as one final leach (HK 50.3) of the crinoid samples plot close together, but outside the Tournaisian range (Figure 7-13A), showing higher $^{87}Sr/^{86}Sr$ isotopic ratios.

Strontium is mainly incorporated into calcite by substitution at Ca structural sites, with only minimal incorporation by sorption (< 3%; Zachara et al., 1991), occlusion or in undetected trace phases (Pingitore Jr et al., 1992). However, Rb is a potential source of radiogenic ^{87}Sr in limestones (Denison et al., 1994), which subsequently leads to an increase in ^{87}Sr due to the decay of ^{87}Rb to ^{87}Sr. Radiogenic ^{87}Sr can also be leached from detrital siliciclastics. Late diagenesis can also change Sr isotope ratios to either higher or lower values (Brand et al., 2010).

The elevated $^{87}Sr/^{86}Sr$ ratios of single-step digested micrites could be either caused by contamination from non-carbonate 'input' from detrital material or diagenesis as both samples failed any screening test (Figure 7-9). However, the central leaches of the micrites, single-step digested and one final-leach crinoid samples reveal seawater-like REE+Y patterns (Figure 7-11C, E, F), while no sample appears contaminated by clays (Figure 7-5) and Fe-Mn oxyhydroxites nor by phosphates (Figure 7-7A, B). Nevertheless, all samples show elevated Mn concentrations (> 100 µg/g; Figure 7-8C), and Sr/Mn ratios < 15 (Figure 7-8A). Both parameters are indicative for a diagenetic overprint of these samples as shown in Figure 7-13B.

This suggests that the first sequential leaching step can remove the contribution from non-carbonate mineral phases in micrites, while diagenetic carbonates are probably too hard being dissolved during this step as proposed by Gorokhov et al. (1995). The influence of cementation within the skeletal pore space and diagenetic alteration of high-Mg calcite to low-Mg calcite seems to be sufficient enough to overprint the original Sr signature of the crinoids.

The remaining samples yield $^{87}Sr/^{86}Sr$ values which are representative of the Courceyan (Figure 7-13A). The Courceyan SIS curve published by McArthur et al. (2012) decreases with time and thus the stratigraphically lowest sample should reveal the highest $^{87}Sr/^{86}Sr$ ratios. However the samples in this study which fit within the Courceyan $^{87}Sr/^{86}Sr$ ratio range still show a large spread in $^{87}Sr/^{86}Sr$ values when plotted on the McArthur et al. (2012) SIS curve based on stratigraphic position (Figure 13C). The sequentially leached crinoid samples HK 45.2 and 45.3 show the highest deviation from the SIS curve (Figure 7-13C). Both coral samples (HK 48 and 49)

and one brachiopod sample (HK 43) scatter around the SIS curve, while single-step digested brachiopod samples HK 41 and 44 plot on the SIS (Figure 7-13C).

Brachiopod samples HK 41 and 44 are free of contamination and diagenetic alteration. Sample HK 44 was deposited in the stratigraphically lower Micrite Unit and reveals a slightly older $^{87}Sr/^{86}Sr$ age correlation than sample HK 41, which comes from the Ballysteen Limestone Formation (Figure 7-13D). Thus, the stratigraphic position as well as determined ages match for these brachiopod samples.

Sample HK 48 (coral) and HK 45.3 (final crinoid leachate) show elevated Sc, Hf, Th (Figure 7-5A), P (Figure 7-7B) and Fe (Figure 7-7A) values, which suggest minor contamination by detrital material and phosphates. Sample HK 48 (coral) shows additionally an elevated Rb content (not shown), which supports contamination by a non-carbonate phase. The elevated Al concentrations from the single-step digested brachiopod (sample HK 43) also indicates contamination by detritus. Sample HK 45.2 (central crinoid leachate) has a lower Sr concentration (Figure 7-8B, C). Furthermore, both coral samples (HK 48 and 49) and both crinoid samples (HK 45.2, second leachate; HK 45.3, third leachate) have elevated Mn contents and decreased Sr/Mn ratios implying diagenetic alteration, which is a stronger effect in the crinoid compared to coral samples (Figure 7-13B). Thus, a combination of incorporation of non-carbonate materials and increasing diagenetic alteration could have shifted the $^{87}Sr/^{86}Sr$ isotopic values of the crinoid and coral samples towards higher values, while detrital contamination of the brachiopod sample (HK 43) lead to a decrease in the $^{87}Sr/^{86}Sr$ ratio.

Thus, this work shows that central leached micritic limestone samples as well as single-step digested crinoids cannot be used for SIS, while corals and brachiopods, provided they are free from contamination and diagenetic overprints are suitable geomaterials. Future work is necessary in order to establish the potential of sequentially leached crinoids from the Irish Midlands for SIS.

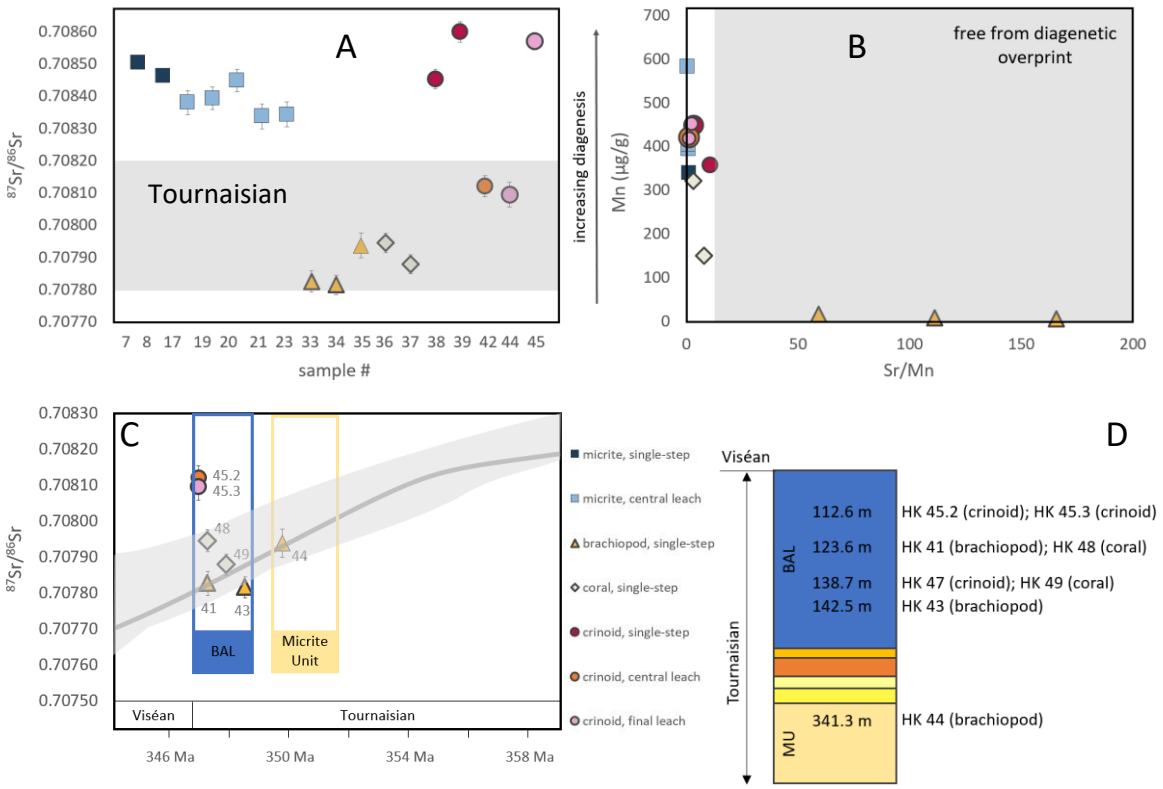

Figure 7-13: A) Single-step digested brachiopods and corals as well as one central and one final leach of the crinoid samples yield $^{87}Sr/^{86}Sr$ values which fall within the literature range for the Tournsaisian. B) Sr/Mn vs Mn biplot. Brachiopod samples show no diagenetic overprint while crinoid samples show the highest diagenetic alteration. C) Seven samples of this study can be plotted on the Sr isotope curve of the Tournaisian. Samples which have a thick outline symbol come from the Ballysteen Limestone Formation (BAL) while the remaining samples come from the Micrite Unit (MU). The Sr isotope curve is taken from McArthur et al. (2012). Grey line shows the best-fit curve through the data while the bright grey area shows the actual scatter of used data. D) Simplified stratigraphic column highlighting the position of the sample, which are plotted on the Strontium Isotope Stratigraphy curve. Full stratigraphic column is shown in Figure 7-2B.

7.4 *In Situ* Sampling

Clean physical extraction of fossils from their surrounding matrix is a prerequisite to gain reliable Sr isotopic data, as contaminated and diagenetically altered material potentially shows higher $^{87}Sr/^{86}Sr$ ratios in comparison to pristine samples (Figure 7-13A, B). Although micro-drilling was used to extract sample material, potential contamination of powdered materials cannot be excluded, as seen in this study, where especially one coral (sample HK 48) seems to be highly contaminated by surrounding material based on trace element screening (e.g. Figure 7-9). Therefore, this part of the study comprises a pilot study using a laser ablation system as a clean and precise spatial sampling tool. Using the laser ablation unit as a milling device comes with the advantage of high spatial-resolution (2 x 2 µm, which is the minimum size of the laser beam) and shallow sampling depths and thus surpasses the spatial resolution of micro-drilling. Ahead of laser micro-sampling, potential sampling targets (identifiable bioclasts such as brachiopods, crinoids and corals *vs* micrite) are mapped by laser ablation inductively coupled plasma mass spectrometry (LA-ICP-MS) for their trace element distribution, which permits spatial characterisation of heterogeneities in the sample and identifies areas of constant chemistry devoid of diagenetic features or extraneous matter. Extracted material is subsequently collected in acid-filled test tubes before analysing the dissolved aerosol using a mass spectrometer.

Although conventional LA-ICP-MS is a well-established analytical technique for *in situ* trace element and isotope ratio analysis, it is typically less precise when using the same analyte list, dwell times and volume of mapped sample in comparison to solution mass spectrometry due to the transient nature of laser ablation signals. Both LA-ICP-MS and solution ICP-MS analysis require a minimum amount of sample to obtain high-precision data. However, obtaining a larger sample volume by LA-ICP-MS can only be realistically achieved by increasing the spot size, which results in decreasing spatial resolution. At the same time, decoupling the laser from the mass spectrometer provides the possibility of collecting sample material even from very fine features using small spot-sizes, as the ablated material will be accumulated in the test tubes ahead of the analysis, until the required sample volume is obtained. This way, irregular shaped ablation areas and different sample areas of interest can be combined. Overall, this method allows for high spatial resolution sampling while still resulting in low detection limits and precise data even when a long analyte lists is required. Furthermore, the collected aerosol can be split into multiple aliquots. For example, this allows for an aliquot be analysed for trace elements by solution ICP-MS and another aliquot to be analysed for Sr isotope ratios by MC-ICP-MS without requiring both instruments to be connected to the same laser. As the sample is effectively devoid of any contaminants, there is no need for any further chemical preparation. Therefore, it is potentially a very fast and clean method compared to any micro-drilling technique.

However, the most crucial step using this method is to ablate enough material for both high-precision trace element as well as Sr isotopic analyses. Therefore, this study introduces a protocol which links the total amount of laser shots to the volume of ablated material received and the expected signal intensities on the mass spectrometer. Furthermore, the experiment design is briefly outlined but the main focus is on the impact of different laser parameters like spot size, scan speed, repetition rate, fluence and flow rates on the final amount of ablated material. Although this experiment was undertaken on carbonates, it can easily be applied to a variety of geomaterials.

7.4.1 Experiment Design

This method is split into three main parts. Elemental maps are first made on pre-defined areas of petrographic interest. Subsequently, contamination and diagenesis-free areas are chosen and sampled based on these trace element maps. Finally, the sample-acid mix is analysed and the ablated area is examined using white light interferometry.

7.4.1.1 Elemental Maps

Ahead of laser ablation micro-sampling, potential sampling targets were screened first by optical petrography and then mapped by LA-ICP-MS for their trace element distribution. Elemental maps were acquired using a Teledyne Photon Machines Analyte G2 193 nm ArF Excimer laser-ablation system with a HelEx II active 2-volume ablation cell coupled to a Thermo Scientific iCAP-Q ICP-MS at the Department of Geology, Trinity College Dublin. The ablation cell was retrofitted with a Teledyne Photon Machines Aerosol Rapid Introduction System (ARIS), which connects the ablation cell directly to the ICP-Q-MS torch with narrow bore PEEK (Polyetheretherketone) tubing. Ten analyte masses (^{25}Mg, ^{43}Ca, ^{55}Mn, ^{58}Fe, ^{66}Zn, ^{87}Sr, ^{137}Ba, ^{208}Pb, ^{232}Th and ^{238}U) and mass 248 (^{232}Th^{16}O) were measured by ablating line scans employing a 25 Hz laser repetition rate and a fluence of 0.75 J/cm^2. Relatively large maps (0.45 x 0.2 cm) were produced in less than an hour, using a 100 x 100 µm spot size and a scan speed of 50 µm/sec (Figure 7-14). A washout time of 25 seconds was used between lines to avoid any carry-over of material from standards to samples, and vice versa. Data was calibrated using line scans of NIST SRM 610 glass reference material, ablated using the same parameters as the sample**.** Three NIST SRM 610 lines were analysed at the beginning and end of each experiment. NIST SRM 612 and BHVO-2 glass standards were used as external quality control standards. The ICP-Q-MS was tuned using NIST SRM 612 standard glass to minimise fractionation (Th/U ratios > 0.9) and to minimise oxide production rates (ThO^+ < 0.2%). Data reduction was performed using the Iolite software v2.4 (Paton et al., 2011), using the 'trace element' data reduction scheme in 'Quantitative' mode. Following data reduction, trace element distribution maps were produced with the Iolite module

'Images from Integrations'. A Ca concentration of 40.04 wt% is used as the internal standard. On average, the experiment duration was one hour and required 20 minutes of data analysis.

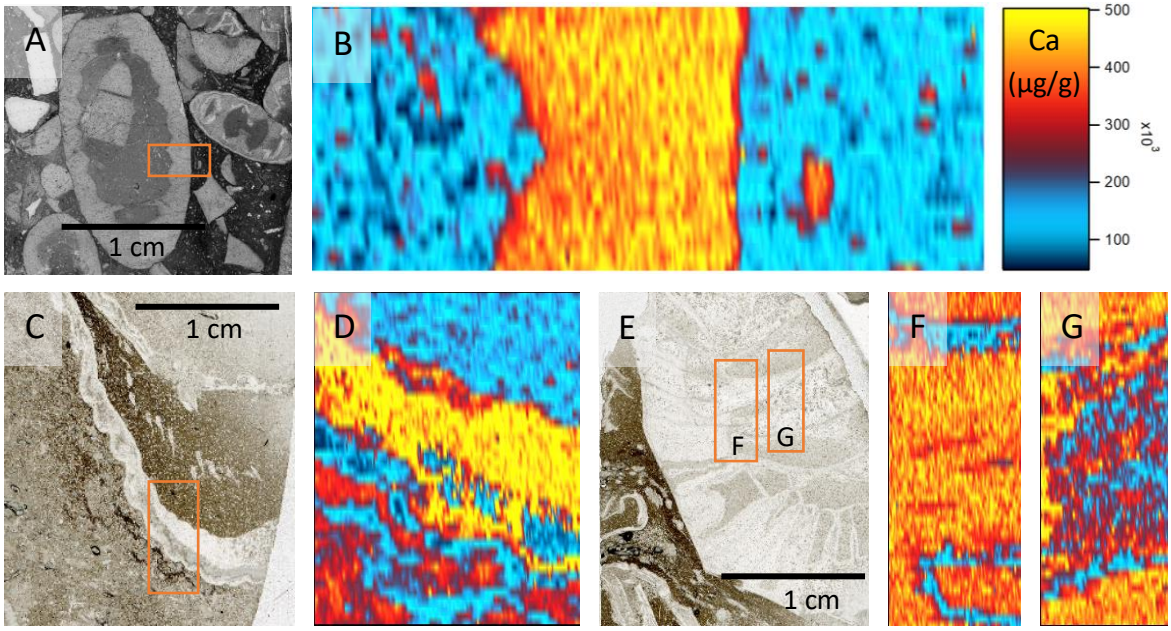

Figure 7-14: Thin section images of fossils and semi-quantitative elemental maps are used to visualise the distribution of Ca in µg/g. The yellow-red area represents the fossil shell whereas the blue part represents the matrix infill. A) Thin section image of a crinoid. B) Semi-quantitative map of the orange part of the crinoid shown in (A). C) Thin section image of a brachiopod. D) Semi-quantitative map of the orange part of the brachiopod shown in (C). E) Thin section image of a coral. F) and G) Semi-quantitative maps of the orange parts of the coral shown in (E).

7.4.1.2 Sampling

A 193 nm UV excimer laser ablation system was used for the ablation experiments to extract material. To facilitate sample collection, the aerosol transfer tube (ARIS) was disconnected from the ICP-Q-MS and the sample aerosol was instead transported with He directly into test tubes containing dilute HNO_3 spiked with an enriched isotope and elemental internal standard mixture (^{6}Li, Rh, Re, Bi, ^{235}U). Sampled material is subsequently analysed using a Thermo Scientific iCAP-Q quadrupole ICP-MS. Spiked HNO_3 was measured independently and its signal intensity (in counts per second; cps) subtracted from the spiked HNO_3 – sample mixture as a form of background correction. Either Ca or La background-corrected signals (in cps) are shown in the subsequent figures.

7.4.1.3 Examination of Sample Volume

White light interferometry is a non-destructive optical method, where the micro-topography of surface features can be characterised with excellent precision. The basic principle is that a beam splitter divides a beam of light into two beams, with one beam reflected from a reference mirror and the other directly onto the sample (the measurement beam). These two beams are then recombined to create an interference pattern which is analysed to determine the phase difference which is directly related to the path travelled by the two beams. A Filmetrics Profilm 3D Profilometer is used to examine and subsequently calculate the volume of removed

sample using the following parameters and settings: backscan: 45 µm; scan length: 50 µm; vertical scanning interferometry and envelope peak.

7.4.1.4 Laser as a Sampling Tool - Theory

In laser sampling, the sampling depth and thus the volume of sampled material increases with increasing shots by the laser. Therefore, the maximum amount of shots per unit area and the maximum sampling depth are directly linked. Consequently, two new terms, called *Maximum Shot Density* (equation 2) and *Total Shots* (equation 3) are introduced, which define the maximum number and the total number of shots the target area receives, respectively.

The beam aperture employed in this study is square. The repetition rate defines how many times the laser fires per second and thus is given in Hz. Therefore, if the selected area is the size of the laser spot (i.e. there is no stage movement), the repetition rate defines the amount of 'removed layers' (Figure 7-15).

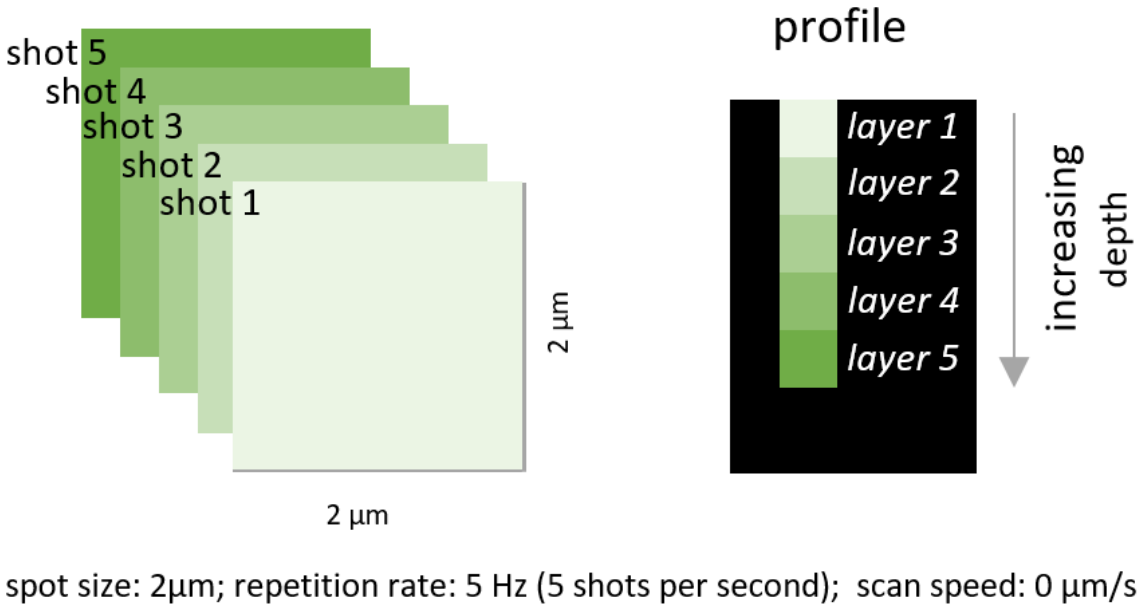

Figure 7-15: The size of the laser beam is 2 x 2 µm. With each shot, a thin layer of targeted sample gets removed thus increasing the sampling depth.

However, the sample must be moved under the laser beam (e.g. a line scan or raster), as soon as the experimental area is bigger than the spot size. The distance the laser covers between every single shot is independent of the spot size (although it should not be larger than the spot size to ensure complete sampling). The distance moved between each shot is defined by the scan speed and the repetition rate:

$$x = distance\ moved\ between\ each\ shot\ [\mu m/shot] = \frac{scan\ speed\ \left[\frac{\mu m}{s}\right]}{repetition\ rate\ \left[\frac{1}{s}\ per\ shot\right]} \quad (1)$$

The *Maximum Shot Density* coincides with the maximum amount of removed 'layers' and is calculated as follow (Figure 7-16E):

$$Maximum\ Shot\ Density = max.shots\ per\ subdivided\ area = \frac{spot\ size}{x} = \frac{spot\ size}{scan\ speed} * rep\ rate \quad (2)$$

The total amount of shots is calculated by dividing the target area by the spot-size and subsequent multiplication by the *Maximum Shot Density* (equation 2), which is a simplified approach as the start and end of each constituent laser line scan will not receive the *Maximum Shot Density* (Figure 7-16). However, that caveat is a minor effect when the line scans are significantly longer than the width of the spot size, or the *Maximum Shot Density* is low.

$$Total\ Shots\ per\ Area = \frac{mapped\ area\ [\mu m^2]}{spot\ size\ [\mu m^2]} * Maximum\ Shot\ Density \quad (3)$$

Figure 7-16 illustrates the volume of material removed during five successive shots in a line scan / raster, using the following parameters: spot size: 2 µm; scan speed: 2 µm/s, repetition rate: 5 Hz.

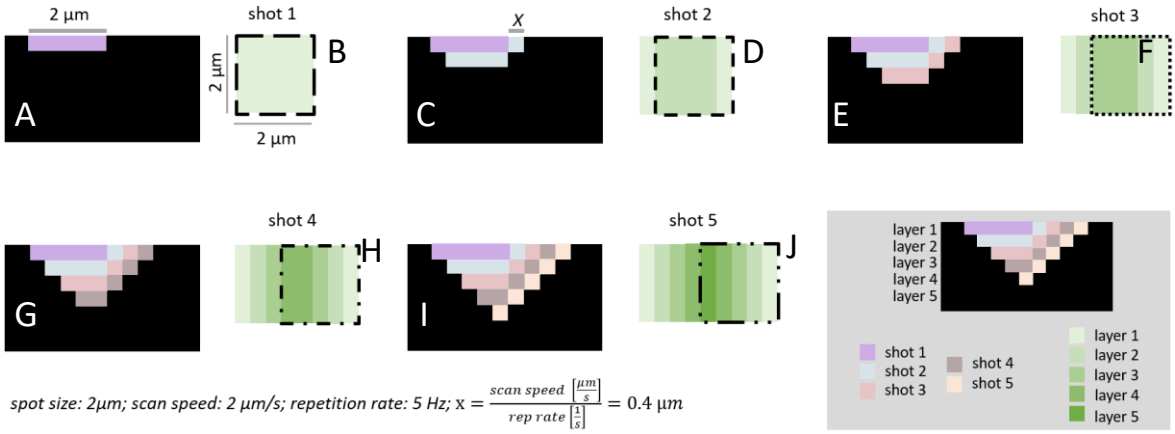

Figure 7-16: A, C, E, G, I show profiles of the sample removed using a laser for the first five successive shots. B, D, F, H, J shows the accompanying ablated areas in plan view. The different colours in the profiles (A, C, E, G, I) represent individual shots, whereas the deeper green shades in plan view correspond to more sample material removed.

Thus, an increase in *Maximum Shot Density* coincides with deeper sampling depths, while an increase in the total amount of shots results in an increased sample volume. Both coincide with increased sample signals in the mass spectrometer, provided that parameters like fluence and flow rates are kept constant. The micrite samples analysed within this study show the expected increasing linear relationship between signal intensity and either *Total Shots* or *Maximum Shot Density* (Figure 7-17A-D).

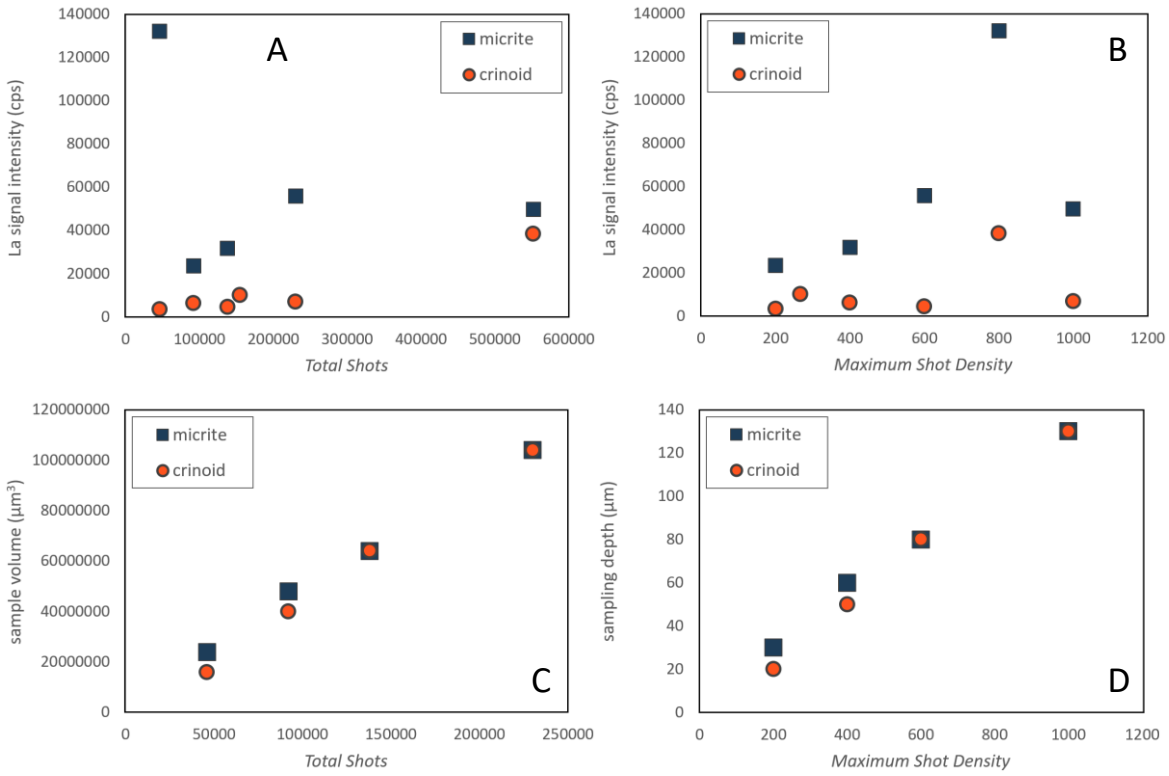

Figure 7-17: The Maximum Shot Density is calculated using the spot size, scan speed and repetition rate of the laser, while total shot calculations take the size of the mapped area, spot size and the Maximum Shot Density into account. The La intensity is analysed using inductively coupled plasma mass-spectrometry. A) Biplot of calculated Total Shots vs La signal intensities. B) Biplot of calculated Total Shots vs Maximum Shot Density. C) Biplot of sample volume vs Total Shots. D) Biplot of sampling depth vs Maximum Shot Density. There is a crude positive correlation in A) and B), while samples in C) and D) show a clear positive correlation.

7.4.2 Sample Volume

Getting high-precision data on an inductively-coupled quadrupole mass-spectrometer requires a critical sample load so that the sample signal is significantly higher than the background noise on the mass spectrometer. The dilution factor defines how much sample material is dissolved in a given volume of acid:

$$\text{dilution factor} = \frac{\text{amount of acid (ml)}}{\text{amount of sample (g)}} \quad (4)$$

However, the same dilution factor can produce different signal-to-background ratios on different mass-spectrometers due to the sensitivity of individual mass-spectrometers and differing tuning, different experimental parameters and different sample types. As the weight of sample material introduced is known in whole-rock digestions, the dilution factor can be adjusted depending on the likely concentration of the elements of interest within the sample (Table 7-1). For example, if the concentration of the element of interest and its analytical sensitivity is low, the dilution factor should be lowered and vice versa. It is also advantageous if the likely element concentrations are

known from the literature or previous analyses on similar samples to provide a better estimate of amount of sample needed for optimal signal-to-noise ratios.

The micrite samples employed in this laser ablation micro-sampling study were previously analysed using whole-rock HF-HNO_3 digestions (see Chapter 4). Approximately 0.1 mg of micrite sample dissolved in 2 ml of acid was required to produce sufficient signal for high-precision trace element analysis, with lowest signal intensities of c. 1 500 cps for the HREE, while 100 000 cps were obtained for the LREE. Thus, the low HREE content defines the final dilution factor for this specific sample.

Table 7-1: Sample material (micritic limestone from the Ballysteen Limestone Formation in the Irish Midlands Province), the amount of sample in the final solution, the total sample concentration, concentration for chosen elements (Ca, Y, La, Lu) and the concentration of chosen elements in the analysed solution are listed together with resulting raw counts for single-step digested micrites.

Sample material	***Amount of sample in 2 ml solution [µg]***	***Total sample conc.** [µg/g]***	***Analysed Element conc. (ICP-Q-MS)***	***Conc. in final solution*** [µg/g]***	***Counts per second 44Ca 89Y 139La 175Lu***
Micritic limestone	133.3	66.67	40 wt% (Ca)	26.66 (Ca)	32,000,000 (Ca)
			4.3 µg/g (Y)	0.27 (Y)	80,000 (Y)
			6.5 µg/g (La)	4.7 (La)	148,000 (La)
			0.06 µg/g (Lu)	0.04 (Lu)	1,500 (Lu)
Micritic limestone	100	50	40 wt% (Ca)	20 (Ca)	23,000,000 (Ca)
			4.3 µg/g (Y)	2.0 (Y)	59,000 (Y)
			6.5 µg/g (La)	3.5 (La)	117,000 (La)
			0.06 µg/g (Lu)	0.03 (Lu)	1,700 (Lu)

$*dilution\ factor = \frac{amount\ of\ acid\ (ml)}{amount\ of\ sample\ (g)}$

$**total\ sample\ conc.\ (\mu g/g) = \frac{amount\ of\ sample\ (mg)}{amount\ of\ acid\ (l)}$

$***conc.element_A\ in\ final\ solution\ (\mu g/g) = total\ sample\ concentration\ (\mu g/g) * proportion\ of\ element_A$

However, the total volume of ablated material in the laser ablation micro-sampling is too low to obtain a reliable mass determination using a balance. Therefore, it will be estimated using the density of the sample material (e.g. calcite: 2.7 g/cm^3) and the volume of the ablated map, assuming total recovery.

$$amount\ of\ sample\ (g) = ablated\ volume\ (cm^3) * density\ (\frac{g}{cm^3}) \quad (5)$$

The length and width of the ablation area is known, while the depth is dependent on the laser settings and can be determined using white light interferometry. However, most of the samples of this study were not reflective enough to achieve high-resolution white light interferometry images. Depth calculations using white light interferometry were thus difficult, even when gold coating was applied, which normally enhances reflections. Thus an optical microscope with a high-precision z-stage was additionally used to obtain approximate depth estimates by focusing on both the sample surface and then the base of the rectangular ablated area. Determining the ablated sample volume can also employ the count of *Total Shots*, as total shot counts and sample volume are also directly linked when the mapped volume is quantified by white light interferometry or depth measurements using an optical microscope (Figure 7-17C).
The following experiments were designed to keep all parameters (spot size, scan speed, repetition rate, fluence, flow rate) constant but for one parameter, to investigate their influence on the sampling depth and thus the total sample volume. Results are presented on total shot (≈ signal intensity) *vs* the investigated laser parameter in question.

7.4.2.1 Spot Size

The spot size determines the x and y-resolution of a single spot or line scan. Using small spot sizes is time consuming; if small features need sampling then small spot sizes can be used while large spot sizes are recommended for shallow ablation of large areas.

7.4.2.2 Scan Speed

Slowing down the scan speed coincides with a shorter distance in between each shot and an increase in the *Maximum Shot Density* which follows a power law, provided that the repetition rate and spot size is kept constant (see equation 2). This coincides with an increasing sampling depth. The experiment undertaken in this study used areas of identical size, the same repetition rate and spot size, but two different scan speeds (30 µm/s and 20 µm/s). As the sample area was kept constant, a lower scan speed results in higher *Total Shots* and thus higher La signal intensities, while higher scan speeds lead to the opposite result. The calculated *Total Shots* and obtained La signal intensities from both experiments followed the expected potential growth (Figure 7-18).
However, the choice of spot size, repetition rate and scan speed needs to be adjusted to ensure that the *Maximum Shot Density* is > 1 (i.e. material is continually ablated along the line scan with no gaps).

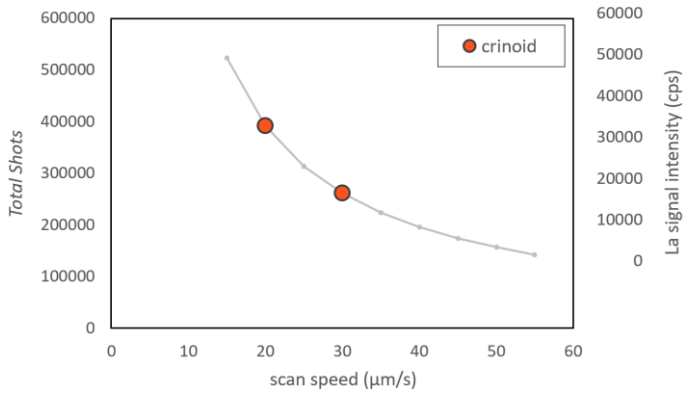

Figure 7-18: Biplot of scan speed vs Total Shots and La signal intensities for crinoidal material from the Ballysteen Limestone Formation in the Irish Midlands Province. Crinoid samples plot on the grey line, which follows the potential law. The following parameters were applied for these experiments: Spot Size: 100 µm; Fluence: 0.75 J/cm²; Repetition Rate: 80 Hz; Cell/Cup He Flow Rate: 0.3 L/min each; Scan Speed: varied.

7.4.2.3 Repetition Rate

A change in repetition rate should result in a linear increase of the *Maximum Density Factor* and the amount of *Total Shots*, which subsequently leads to a greater sampling depth. The La signal intensities in the micrite samples rise for repetition rates 50, 100 and 150 Hz, but unexpectedly falls for 250 Hz (Figure 7-19A), while the La intensities first rise between 50 and 100 Hz, drop for 150 Hz and increase again for 250 Hz for the crinoid sample (Figure 7-19B). At the same time there is a gradual increase in the maximum sampling depth (Table 7-2).
However, the white light interferometry images show uneven ablation of the material for most samples (not shown). A homogeneous ablation can only be observed in the sample which was ablated at 50 Hz (Figure 7-20A). The ablated line scans in the other samples resemble funnel shaped lines, instead of sharp rastered areas (Figure 7-20B). The laser gets more out of focus with increasing sampling depth, which coincides with reducing laser energy on the sample. With deepening profiles, the gas may also become less efficient in transporting the material out of the sample chamber. Both cases would lead to the collection of lower amounts of sample material, which is subsequently seen in lower signal intensities than expected at high repetition rates (Figure 7-19A, B).

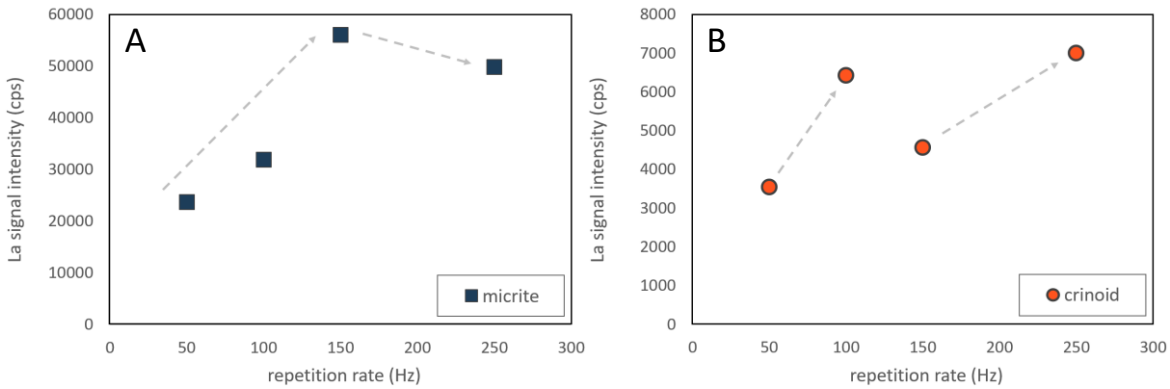

Figure 7-19: Biplot of repetition rate vs La signal intensities of micritic and crinoidal sample material from the Ballysteen Formation in the Irish Midlands Province . (A) Blue squares represent micritic limestone samples whereas the orange dots in (B) represent crinoid samples. The following parameters were applied for these experiments: Spot Size: 80 µm; Scan Speed: 20 µm/s; Fluence: 1.5 J/cm²; Cell/Cup He Flow Rate: 0.3 L/min each; Repetition Rate: Varied.

Table 7-2: Maximum depth of ablated areas for crinoidal and micritic sample material from the Ballysteen Limestone Formation in the Irish Midlands Province estimated using an optical microscope. Maps were ablated using identical parameters but varying repetition rates.

	50 Hz	*100 Hz*	*150 Hz*	*200 Hz*
Crinoid; depth in µm	**20**	**50**	**80**	**130**
Micrite; depth in µm	**30**	**60**	**80**	**130**

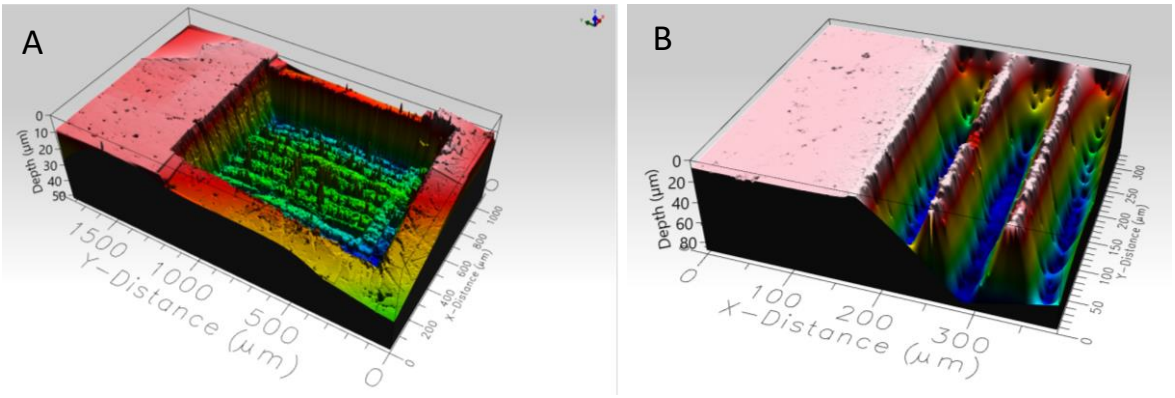

Figure 7-20: Ablated areas investigated using white light spectrometry. The following parameters were applied for these experiments: Spot Size: 80 µm; Scan Speed: 20 µm/s; Fluence: 1.5 J/cm²; Cell/Cup He Flow Rate: 0.3 L/min each; Repetition Rate = 50 Hz (A); Repetition Rate = 200 Hz (B)

7.4.2.4 Fluence

The fluence is the energy density of the laser acting on the sample. Thus, although the fluence has no direct impact on the *Total Shots*, there should be an increase in signal intensity and sampling depth with increasing fluence, which is observed (Figure 7-21; Table 7-3). Nevertheless, the low signal intensity for crinoid samples up to a fluence of 1.3 J/cm^2 implies that the ablation threshold for crinoids is only reached between a fluence of 1.3 J/cm^2 and 1.7 J/cm^2, when the laser starts ablating the material properly. However, these experiments were conducted at 200 Hz. The previous section showed that samples seemed to be strongly influenced by high repetition rates, changing their ablation behaviour (see section 7.4.2.3), possibly as a result of

defocussing and the difficulty in transporting the sample – carrier gas aerosol from the deeper raster pits. To eliminate the effects of employing a high repetition rate, these experiments should be performed again at lower repetition rates. The ideal fluence for these experiments should comfortably exceed the ablation threshold for the material, while not causing melting.

Table 7-3: Maximum depth of ablated areas, in micritic and crinoidal samples from the Irish Midlands Province, which are estimated using an optical microscope. Maps were ablated using identical parameters (Spot Size: 80 µm; Scan Speed: 20 µm/s; Repetition Rate: 200 Hz; Cell/Cup He Flow Rate: 0.3 L/min each), but with a varying fluence.

Fluence (*J/cm²*)	*0.9*	*1.1*	*1.3*	*1.7*
Crinoid; depth in µm	**75**	**80**	**90**	**110**
Micrite; depth in µm	**75**	**85**	**95**	**95**

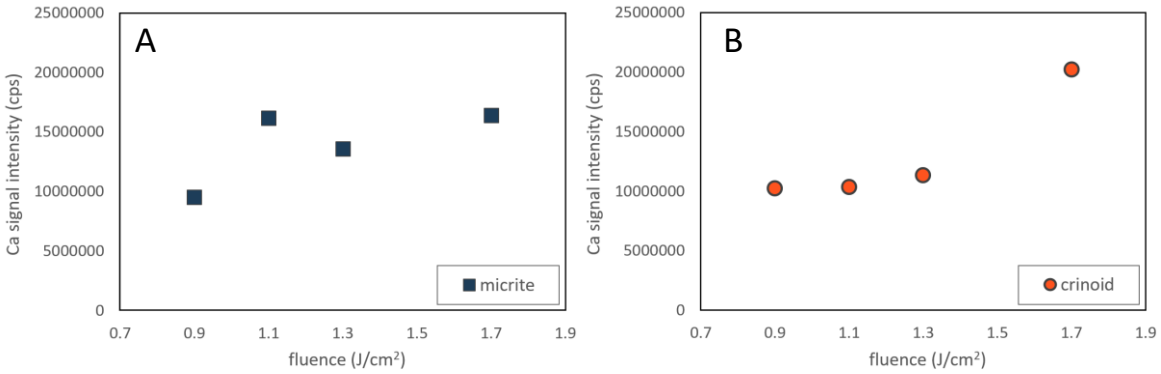

Figure 7-21: Fluence vs La signal intensity for (A) crinoid and (B) micrite sample materials, from the Ballysteen Limestone Formation and Micrite Unit, respectively sampled in the Irish Midlands Province. A positive correlation between both parameters is evident in both plots. The following parameters were applied for these experiment: Spot Size: 80 µm; Scan Speed: 20 µm/s; Repetition Rate: 200 Hz; Cell/Cup He Flow Rate: 0.3 L/min each; Fluence: varied.

7.4.2.5 Flow Rate

The flow rate of the He carrier gas in the laser cup and cell neither changes the amount of *Total Shots*, nor changes the sampling depth. However, the flow rates directly influence the transportation of the ablated material from the cup and chamber, through the sample transfer tubing to the test tube. The sample cell and cup is a HelEx cell with a proprietary two-volume design. The total He flow rate into the cell and cup was kept constant at 0.6 l / minute. A continuous increase in La signal intensities coincide with increasing He flow rates into the cell and decreasing He flow rate into the cup (Figure 7-22A). The flow rates into the cell and cup were also split equally using a total flow rate of 0.5, 0.6 and 0.7 L/min during a second experiment design. This results in lower La signal intensities with a minimum intensity when both flow rates were at 0.3 L/min (Figure 7-22B).

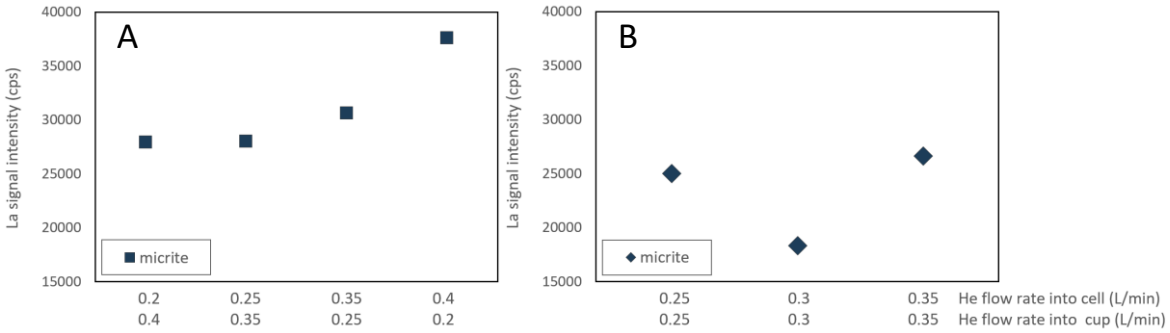

Figure 7-22: A) Increasing La signal intensities are detected with increasing He flow rates into the cell and decreasing He flow rates into the cup. B) Low La signal intensities when the cell and cup He flow rates are approximately equal, with the lowest La signal intensities seen for equal He flow rates of 0.3 l/Min in the cup and cell. The following parameters were applied for these experiments: Spot Size: 80 µm; Scan Speed: 20 µm/s; Repetition Rate: 200 Hz; Fluence: 200 Hz; Cell/Cup He flow rate: Varied.

7.4.2.6 Particle Size and Sample Material

The particle size of the ablated material is also important to consider as the smaller the particle size, the more likely that complete dilution occurs in the acid-filled test tube for aerosol collection.

The 266 nm Nd:YAG laser produces a particle size distribution which is significantly larger in comparison with aerosols produced using a laser wavelength of 193 nm (Guillong and Günther, 2002). Furthermore, the laser-sample interaction/absorption behaviour of the material is also responsible for the particle size distribution, with optically transparent samples producing particle size distributions dominated by particle sizes above 1 µm, whereas the particle size distributions measured from opaque samples show a large proportion of particles below 0.2 µm (Guillong and Günther, 2002). Another option to create different particle sizes is the ablation of a single hole compared to a scanning ablation. Ablated particles become smaller with increasing depth in single hole ablations for a 266 nm Nd:YAG laser, and therefore, particle sizes are smaller in single hole ablations when compared to rastered areas (Guillong and Günther, 2002).

However, the particle size distribution for shallow rastered areas is relatively constant and therefore should not be a major factor in this study. As the same laser and same laser parameters were used to map identical sized areas for the micrite *vs* crinoid sample, a consistent particle size distribution should be expected and the resulting difference in signal intensities (Figure 7-19, Figure 7-21) is most likely caused by differing absorption behaviour of the laser energy as the laser couples better with the dark micritic samples, in comparison to the optically transparent fossils.

7.4.2.7 Elemental Fractionation

In LA-ICP-MS analysis, the signal intensities cannot be directly related to the actual concentration of the analysed material if elemental fractionation occurs (Fryer et al., 1995). Employing matrix-matched calibration standards can surmount this problem. However, elemental fractionation remains one of the major limitations of LA-ICP-MS analysis, especially for the precise

element ratio determinations such as in U-Th-Pb dating, where shallow pits and rasters have been shown to produce less fractionation (Eggins et al., 1998; Mank and Mason, 1999; Košler et al., 2002).

Elemental fractionation has been ascribed to different processes in LA-ICP-MS analysis, including the aerosol formation process, the transport of the aerosol into the ICP, and the conversion of the aerosol into ions within the ICP-MS. Another possibility is depth related mechanical fractionation. Guillong and Günther (2002) consider elemental fractionation in LA-ICP-MS analysis to be dominantly an ICP-enhanced process, as the particles produced by laser ablation are probably not completely vaporised and ionised. However, there are also a large number of parameters that influence the ablation process itself like wavelength, energy, ablation diameter, ablation time, pulse duration, repetition rate, etc. as well as background gas conditions and mechanical characteristics of the sample (Rodushkin et al., 2002; Hattendorf et al., 2003; Claverie et al., 2009). Furthermore, it is important for this study to avoid a laser-material-interaction that results in ejected molten material which causes a heat transfer beyond the ablated area. This could potentially contribute to the alteration of the stoichiometric composition of the laser-generated aerosol, resulting in unknown elemental or isotopic fractionation effects.

7.4.3 Future Work

If the analyte list is reduced, less analysis time and hence less sample (and also less acid if the dilution factor is kept constant) is required to produce high-precision trace element data. This should permit even higher spatial resolution sampling.

Once the optimal laser parameters are confirmed, materials in this study, such as brachiopods, corals and crinoids (see section 7.3.2.1), could be sampled using this novel method. Ideally, samples HK 43 (brachiopod) and HK 48 (coral), which show contamination in the micro-drilled powders, would reveal contaminant-free trace element data (Figure 7-9). This would prove the superiority of this method compared to the micro-drilling technique. Ultimately the goal would be to undertake Sr isotopic analysis on these materials.

For Sr isotope analyses, two maps of the same size and material, using the same parameters should be ablated first. During the first experiment, the laser would be coupled to a MC-ICP-MS and directly analysed, while the ablated material from the second experiment could be collected in a test tube, and treated conventionally using column chemistry and subsequently analysed by TIMS. The latter experiment would show if this new sampling technique is able to produce high-precision and high spatial resolution $^{87}Sr/^{86}Sr$ TIMS data which can be directly compared with the LA-MC-ICP-MS $^{87}Sr/^{86}Sr$ results.

7.5 Conclusions

The micritic limestone is variably contaminated with detritus. The contaminants are mainly dissolved in the first and final leaching step (e.g. Figure 7-6A, B). As a result, the REE+Y pattern of the central leaching steps, which predominantly dissolves 20-60% of the sample, resembles that of modern seawater (Figure 7-11C). This finding confirms the conclusions of Tostevin et al. (2016), that sequential leaching of micritic limestones is necessary to minimise the influence of contamination. However, the micritic limestones do not show expected Early Carboniferous (Courceyan) $^{87}Sr/^{86}Sr$ values (Figure 7-13A). Single-step digested crinoid samples seem to be free of contamination (e.g. Figure 7-9), show seawater-like REE+Y patterns but they also do not reflect $^{87}Sr/^{86}Sr$ ratios typical for the Courceyan (Figure 7-13A).

Single-step digested brachiopods, corals, one central and one final crinoid leach have REE+Y patterns which are close to modern seawater (Figure 7-11E, F) and plot within uncertainty on the global Tournaisian Sr isotope range (Figure 7-13A, C). However, only the two brachiopods (sample HK 41 and 44), which are free of contamination and diagenetic overprinting can be assigned to their stratigraphic position (sampled in two different formations - Figure 7-13D), based on their REE+Y pattern, Ba/Ca and Cd/Ca ratios (Figure 7-12) and on their Sr isotopic compositions (Figure 7-13). A combination of contamination by non-carbonate materials and increasing diagenetic alteration could have increased the $^{87}Sr/^{86}Sr$ isotopic values of crinoid and coral samples towards higher values, while detrital contamination of the brachiopod sample (HK 43) lead to a decrease in the $^{87}Sr/^{86}Sr$ ratio. Thus, brachiopods still seem to be the best material as suggested by Popp et al. (1986) or Brand et al. (2012).

Summarising, central micrite leaches and single-step digested crinoids cannot be applied for trace element or Sr isotopic correlation approaches. Corals and central or final crinoid leaches can be used with caution, but more data is required to test if this biogenic component can yield reliable SIS data, while brachiopods seem to be the optimum material to sample and process. However, the REE+Y patterns of brachiopods reflect a local source signal, typical of the Irish Early Carboniferous rather than open ocean chemistry. More brachiopod samples from different stratigraphic units are needed to assess Early Carboniferous seawater REE+Y distributions and thereby provide information on Early Carboniferous paleoocean chemistry.

To be able to exclude potential contamination during sampling that may affect REE+Y patterns or $^{87}Sr/^{86}Sr$ ratios, a novel *in situ* sampling technique was devised. The targeted material was sampled using the laser ablation unit as a milling device, which allows high-spatial resolution sampling down to 2 x 2 µm. Potential sampling targets (identifiable bioclasts such as brachiopods, crinoids and corals *vs* micrite) were first examined by optical petrography and then mapped by LA-ICP-MS for their trace element distributions. The maps reveal internal features which allow for

the identification of areas of constant chemistry, devoid of diagenetic features or extraneous matter. Results of the preliminary study show that total shot calculations, which were introduced in this study provide a good approach to obtain volume estimates and elemental signal intensities for different scan speeds and repetition rates. For a given sample area, more material is ablated with decreasing scan speeds, increased repetition rate and increased fluence at otherwise constant laser conditions. However, increasing repetition rates can lead to lower signal intensities at appreciable pit depths than otherwise expected and thus repetition rates have to be carefully monitored. Maximum signal intensities were obtained by having a higher He carrier gas in the cup compared to the sample cell. The volume of material sampled and the resultant signal intensities are also influenced by the nature of the targeted material. Micrites couple better with the laser than crinoids (which are more optically transparent) as micrites yield higher signal intensities when using identical laser parameters (Figure 7-19, Figure 7-21). Once the total shot count required to produce a good signal to noise ratios has been established, the repetition rate, spot size and scan speed can be adjusted for different samples as appropriate. This *in situ* sampling technique is now ready to be used on brachiopods, corals and crinoids for trace element and SIS analysis.

Chapter 8:

Conclusions

Multi-element, high-precision solution ICP-Q-MS trace element analyses using the method originally developed by Eggins et al. (1997) and employing further refinements (Babechuk et al., 2010) have successfully been used to identify, fingerprint and correlate Irish volcanic ash layers. Alteration, weathering or mineralisation does not seem to hamper the use of bulk-rock trace element data for chemostratigraphic correlations. Thus, whole-rock trace element geochemistry complements the chemistry of apatite and zircon grains, which are generally seen as more robust tephrochronological tools (Sell and Samson, 2011a; Harvey, 2014; Nicklen et al., 2015).

Overall, six distinct tuff packages were deposited across the Irish Midlands and were sampled in Navan (Tara Deep, Navan East & West), along the Rathdowney Trend (Lisheen and Rapla), in Stonepark and Slievedart. The first two eruptions led to the deposition of two distinct ash sequences in Stonepark and Lisheen with a U-Pb zircon age of c. 350 Ma most likely having an Irish source. A slightly younger eruption event led to the deposition of one evolved ash layer in Slievedart and Lisheen around 346 Ma ago. The Variscan Belt is a possible source for this ash layer, due to the more widespread deposition of these ashes, and a matching composition and eruption age with the volcanics of the Black Forest and the Vosges. The next volcanic event led to the deposition of several ash layers in Slievedart and Navan at around 345 Ma. The tuff chemistry in between these two areas cannot be matched. Four different ash layers were deposited in Slievedart from most likely two different Irish sources. The mafic source could be the Knockroe Volcanic Formation, while the evolved magmatic centre of the remaining three ash layers is unknown to date. The third eruption sequence of similar age resulted in the deposition of three distinct ash layer in the New Thin Bedded Unit in Tara Deep, called the Marker Tuff, Upper Tuff and Lower Tuff. As the tuff layer in the Tober Colleen Formation in Navan West can be correlated with the Marker Tuff in Tara Deep, there is the possibility that the New Thin Bedded Unit and the Tober Colleen Formation are time-equivalent.

Furthermore, according to U-Pb zircon ages of this study, the Tournaisian-Viséan boundary in the Kilbryan Limestone Formation in Slievedart can be moved close to the tuff one to four layers.

This work also suggests that mineralisation in Slievedart took place after the deposition of the host rock as overlying tuff samples seem to be influenced by mineralisation. Thus, this study supports an epigenetic origin for the sediment-hosted deposits in Slievedart, while tuff layers in other areas do not provide clear evidence for an either syn- or epigenetic nature of the deposits.

Brachiopods from Irish Tournaisian, which are free of contamination and diagenetic overprinting plot within Early Carboniferous $^{87}Sr/^{86}Sr$ values and show the most reliable Sr isotope data. Thus, they show greatest potential as a secondary stratigraphic tool for the refinement of the Irish Mississippian stratigraphy. The newly introduced *in situ* sampling technique employs the laser ablation unit as a milling device. It guarantees clean physical extraction of fossils from their surrounding matrix and high spatial resolution sampling down to 2 x 2 µm. This method also allows targeted sampling, as samples can be examined by optical petrography and LA-ICP-MS mapping prior to *in situ* sampling.

Appendices

Appendix 1: Solution ICP-MS Geochemistry Data of Rock Standards & Tuffs

Table A1-1 Long-term averages of six rock standards; AGV-2, BCR-2, BHVO, BIR-1, JA-2, W-2a

Table A1-2 Comparison of bulk-rock geochemical data of tuff replicates

Table A1-3 Bulk-rock geochemical data of analysed rock standards

Table A1-4 Comparison of bulk-rock geochemical data of samples HK 184 and 223

Table A1-5 Bulk-rock geochemical data of 79 Irish tuff samples

Appendix 2: LA-ICP-MS Data from Irish Tuff samples

Table A2-1 U-Pb zircon LA-ICP-MS data

Table A2-2 U-Pb apatite LA-ICP-MS data

Table A2-3 Apatite trace element LA-ICP-MS data

Appendix 3: Bulk-Rock Geochemistry Data of Limestones and Fossils

Table A3-1 Trace element and and Sr isotopic data of micritic limestones, brachiopods, crinoids and corals

9.1 Appendix 1 – Solution ICP-MS Bulk-Rock Geochemistry Data

Table A1 - 1: Long-term averages of multiple analyses of certified reference materials AGV-2, JA-2 (andesites) and BCR-2, BHVO-2, BIR-1 (basalts) along with their standard deviations (SD), relative standard deviation in percent (%RSD) and the W-2a calibration values employed. Preferred concentrations of W-2a are based on an assessment of published standard data. Sample bias is calculated by comparing standards to values taken from the GeoReM database and were published in Jochum et al. (2016). Standards were prepared in-house and deployed as quality control standards to measure the quality of the experiment and data reduction. Elements are ordered according to their atomic number. Calibration values, average concentrations, SD and GeoReM values are given in ng/g. RSD and bias are expressed in percent.

	AGV-2					JA-2					W-2a
	Digestions = 1, Analyses = 5					Digestions = 1, Analyses = 6					
	Average	SD	%RSD	GeoReM	Bias	Average	SD	%RSD	GeoReM	Bias	
Li	10714	55	0.5	10800	-0.8	28708	78	0.3	29180	-1.6	9158
Be	2096	38	1.8	2209	-5.1	2064	52	2.5	2260	-8.7	617
Mg	10741417	840941	7.8	10855144	-1.0	45841081	1216799	2.7	47286214	-3.1	38414000
Al	88538021	2379390	2.7	90129664	-1.8	81627303	2267513	2.8	82085208	-0.6	81771000
P	2351316	32635	1.4	2107698	11.6	737118	13451	1.8	662856	11.2	611000
Ca	36754714	401442	1.1	36806747	-0.1	44702289	428647	1.0	44732704	-0.1	77616000
Sc	12640	138	1.1	13110	-3.6	19182	71	0.4	18930	1.3	36074
Ti	6112417	66045	1.1	6300581	-3.0	3981545	80792	2.0	4013548	-0.8	6354611
V	111317	4548	4.1	118500	-6.1	116130	4669	4.0	119700	-3.0	261597
Cr	15795	157	1.0	16220	-2.6	468338	2286	0.5	424800	10.2	92791
Fe	46114774	481511	1.0	47422536	-2.8	43290437	523909	1.2	43988249	-1.6	75748000
Mn	758157	6521	0.9	777571	-2.5	819522	9903	1.2	845725	-3.1	1293000
Co	15677	100	0.6	15460	1.4	29368	304	1.0	28330	3.7	44526
Ni	18033	224	1.2	18870	-4.4	138644	1052	0.8	136000	1.9	69993
Cu	48540	1329	2.7	51510	-5.8	26845	929	3.5	29000	-7.4	103000
Zn	88584	535	0.6	86700	2.2	62670	841	1.3	64500	-2.8	77000
Ga	19859	149	0.8	20420	-2.7	16277	62	0.4	16850	-3.4	17424
As	868	59	6.8	670	29.5	953	18	1.9	710	34.2	1260
Rb	67462	336	0.5	67790	-0.5	70034	505	0.7	69800	0.3	19803
Sr	653457	2769	0.4	659500	-0.9	242969	1329	0.5	245800	-1.2	194828
Y	18199	53	0.3	19140	-4.9	15754	83	0.5	19890	-20.8	20113
Zr	220902	2603	1.2	232000	-4.8	105063	1064	1.0	108500	-3.2	87866
Nb	13953	117	0.8	14120	-1.2	9114	124	1.4	9300	-2.0	7275
Mo	1968	23	1.2	2000	-1.6	548	11	1.9	581	-5.7	423
Cd	116	11	9.5	184	-36.8	74	5	7.4	69	7.3	77
In	49	1	1.4	48	1.5	44	1	2.1	37	20.0	65
Sn	2197	43	1.9	1830	20.1	1731	25	1.5	1690	2.4	1950
Sb	420	14	3.4	458	-8.4	147	6	4.4	150	-1.9	800
Cs	1166	5	0.5	1173	-0.6	4766	18	0.4	4780	-0.3	888
Ba	1156697	13663	1.2	1134000	2.0	311890	1001	0.3	308400	1.1	169680
La	37968	186	0.5	38210	-0.6	15646	61	0.4	15460	1.2	10521
Ce	70074	150	0.2	69430	0.9	32817	117	0.4	32860	-0.1	23216
Pr	8256	18	0.2	8165	1.1	3722	11	0.3	3691	0.9	3025
Nd	30430	96	0.3	30490	-0.2	14116	47	0.3	14040	0.5	12911
Sm	5519	38	0.7	5509	0.2	3041	10	0.3	3032	0.3	3266
Eu	1517	14	0.9	1553	-2.3	883	6	0.7	893	-1.2	1094
Tb	631	5	0.7	651	-3.1	477	3	0.6	479	-0.5	615
Gd	4496	26	0.6	4678	-3.9	2996	15	0.5	3013	-0.6	3708
Dy	3429	15	0.4	3549	-3.4	2877	8	0.3	2851	0.9	3808
Ho	677	5	0.7	682	-0.8	607	3	0.6	591	2.7	803
Er	1797	15	0.8	1825	-1.5	1707	10	0.6	1676	1.9	2222
Tm	261	2	0.9	262	-0.5	257	3	1.1	255	0.8	327
Yb	1631	8	0.5	1653	-1.3	1643	8	0.5	1645	-0.1	2058
Lu	244	2	0.8	251	-2.9	246	2	0.7	255	-3.4	301
Hf	4944	46	0.9	5137	-3.8	2707	33	1.2	2838	-4.6	2356
Ta	834	2	0.3	865	-3.5	642	13	2.1	652	-1.6	454
W	480	13	2.6	553	-13.2	1334	49	3.7	1150	16.0	260
Pb	12541	180	1.4	13140	-4.6	18198	532	2.9	18880	-3.6	7528
Tl	277	3	1.1	275	0.9	339	6	1.8	330	2.7	94
Th	5969	55	0.9	6174	-3.3	4669	69	1.5	4800	-2.7	2104
U	1890	14	0.8	1885	0.3	2247	16	0.7	2182	3.0	505

Continue Table A1 - 1

	BCR-2 Digestions = 1, Analyses = 5					BHVO-2 Digestions = 1, Analyses = 8					BIR-1 Digestions = 1, Analyses = 6				
	Average	SD	%RSD	GeoReM	Bias	Average	SD	%RSD	GeoReM	Bias	Average	SD	%RSD	GeoReM	Bias
Li	9221	70	0.9	9130	1.0	4476	41	0.9	4500	-0.5	3104	37	1.2	3203	-3.1
Be	2318	61	2.9	2170	6.8	1035	41	4.0	1076	-3.8	89	5	5.6	102	-12.7
Mg	21024134	647323	3.4	21704258	-3.1	42482162	1482511	3.5	43764323	-2.9	56032692	2154175	3.8	58430829	-4.1
Al	70209102	2209770	3.5	71341625	-1.6	70993918	2352759	3.3	71129929	-0.2	81160748	2713794	3.3	82085208	-1.1
P	1755475	28379	1.8	1567900	12.0	1315603	31261	2.4	1171670	12.3	102508	6005	5.9	130913	-21.7
Ca	50145884	656369	1.5	50843339	-1.4	81075428	1055596	1.3	81475129	-0.5	94316512	1206394	1.3	94982847	-0.7
Sc	33378	115	0.4	33530	-0.5	32178	171	0.5	31830	1.1	44951	1326	3.0	43210	4.0
Ti	13187566	711627	6.0	13578323	-2.9	16376460	858053	5.2	16371920	0.0	5754057	47866	0.8	5747257	0.1
V	413355	5119	1.4	417600	-1.0	319793	8679	2.7	318200	0.5	323010	4364	1.4	320600	0.8
Cr	15232	133	1.0	15850	-3.9	302259	1826	0.6	287200	5.2	410001	2081	0.5	392900	4.4
Fe	95647990	394018	0.5	96313912	-0.7	86215180	1080655	1.3	86661537	-0.5	79632679	845457	1.1	79737008	-0.1
Mn	1515866	10270	0.8	1522615	-0.4	1304001	18062	1.4	1308860	-0.4	1334285	8521	0.6	1340613	-0.5
Co	37639	343	1.0	37330	0.8	44862	458	1.0	44890	-0.1	52819	563	1.1	52220	1.1
Ni	11699	150	1.4	12570	-6.9	117973	459	0.4	119800	-1.5	170639	1602	0.9	168900	1.0
Cu	14777	4143	31.3	19660	-24.8	123188	3261	2.6	129300	-4.7	120610	1414	1.2	120700	-0.1
Zn	131642	1625	1.4	129500	1.7	97605	4407	4.5	103900	-6.1	71002	820	1.2	70400	0.9
Ga	21402	142	0.7	22070	-3.0	20976	141	0.7	21370	-1.8	15452	163	1.1	15460	0.0
As	1105	60	6.0	860	28.5	1344	154	11.5	700	92.0	66	11	17.1	170	-61.0
Rb	46811	279	0.7	46020	1.7	9175	53	0.6	9261	-0.9	193	5	2.5	210	-8.1
Sr	337215	2123	0.7	337400	-0.1	394410	1942	0.5	394100	0.1	108904	747	0.7	108600	0.3
Y	33242	191	0.6	36070	-7.8	24292	127	0.5	24910	-2.5	14718	103	0.7	15600	-5.7
Zr	177628	1094	0.7	186500	-4.8	163924	1614	1.0	171200	-4.3	14177	174	1.2	14800	-4.2
Nb	12386	49	0.4	12440	-0.4	18364	234	1.3	18100	1.5	543	8	1.4	553	-1.7
Mo	261298	1126	0.5	250600	4.3	4435	1044	23.5	4070	9.0	40	1	3.2	68	-41.3
Cd	178	98	61.3	690	-74.2	119	8	7.1	152	-21.9	63	5	7.7	77	-18.2
In	96	2	2.7	70	36.6	89	1	1.4	117	-24.1	56	1	2.2	58	-3.4
Sn	2356	32	1.5	2280	3.3	1962	28	1.4	1776	10.5	1019	87	8.5	701	45.4
Sb	270	7	2.8	302	-10.7	99	5	4.7	103	-4.2	688	100	14.6	462	49.0
Cs	1154	4	0.4	1160	-0.5	99	1	1.0	100	-1.1	5	0	8.8	7	-21.5
Ba	686912	4316	0.7	683900	0.4	131499	775	0.6	130900	0.5	6476	68	1.1	6750	-4.1
La	25069	43	0.2	25080	0.0	15234	60	0.4	15200	0.2	605	3	0.5	647	-6.5
Ce	53515	159	0.3	53120	0.7	37842	151	0.4	37530	0.8	1902	11	0.6	1920	-0.9
Pr	6895	24	0.4	6827	1.0	5389	15	0.3	5339	0.9	379	2	0.5	372	1.8
Nd	28662	119	0.5	28260	1.4	24391	119	0.5	24270	0.5	2383	20	0.8	2397	-0.6
Sm	6565	33	0.6	6547	0.3	6073	29	0.5	6023	0.8	1101	12	1.0	1113	-1.1
Eu	1948	13	0.8	1989	-2.0	2052	13	0.6	2043	0.5	524	5	0.9	520	0.7
Tb	1053	8	0.8	1077	-2.2	931	2	0.3	939	-0.9	365	3	0.7	362	0.9
Gd	6690	35	0.6	6811	-1.8	6204	38	0.6	6207	0.0	1877	12	0.6	1809	3.7
Dy	6303	41	0.7	6424	-1.9	5221	26	0.5	5280	-1.1	2544	22	0.9	2544	0.0
Ho	1312	4	0.4	1313	-0.1	994	3	0.3	989	0.5	583	2	0.3	572	1.8
Er	3629	31	1.0	3670	-1.1	2496	13	0.5	2511	-0.6	1701	14	0.8	1680	1.2
Tm	532	2	0.5	534	-0.3	337	2	0.5	335	0.5	259	2	0.6	256	1.0
Yb	3348	15	0.5	3392	-1.3	1972	15	0.8	1994	-1.1	1662	10	0.6	1631	1.9
Lu	498	4	0.9	505	-1.4	272	1	0.5	275	-1.0	248	2	0.8	248	0.2
Hf	4680	30	0.7	4972	-5.9	4205	41	1.0	4470	-5.9	559	6	1.1	582	-4.0
Ta	768	3	0.4	785	-2.2	1137	19	1.7	1154	-1.4	37	1	3.6	41	-8.7
W	456	16	4.0	465	-1.9	212	11	5.0	251	-15.7	6	4	62.5	27	-77.9
Pb	9604	173	2.0	10590	-9.3	1601	53	3.3	1653	-3.1	3979	535	13.4	3037	31.0
Tl	267	2	0.9	267	0.0	20	1	4.0	22	-9.6	1	0	5.2	2	-30.1
Th	5767	62	1.2	5828	-1.0	1178	11	0.9	1224	-3.8	31	2	6.3	33	-7.6
U	1692	8	0.5	1683	0.5	421	2	0.5	412	2.1	13	1	9.5	11	15.6

Table A1 - 2: Stock solutions from nine tuff samples diluted and analysed twice during two different experiments to monitor the external precision and accuracy of the analytical method and data reduction protocol in this study. Elements are ordered according to their atomic number. Concentrations and deviations (Dev) are given in ng/g and in percent (%), respectively. Gaps are left when no data is available. Deviations, which are > 3% are highlighted in grey.

Sample ID	HK 119			HK 116			HK 114			HK 117			HK 184		
	Analysis 1	Analysis 2	%Dev	Analysis 1	Analysis 2	%Dev	Analysis 1	Analysis 2	%Dev	Analysis 1	Analysis 2	%Dev	Analysis 1	Analysis 2	%Dev
Li	29912	31207	4.1	31013	32034	3.2	36339	37693	3.6	37911	39138	3.1	98491	97661	0.9
Be	8442	8775	3.8	7145	7423	3.7	4796	5060	5.2	11168	11475	2.7	2433	2464	1.2
Mg	16964183	10935015	55.1	11471101	11634691	1.4	15000266	15222383	1.5	12115604	11997189	1.0	18410796	17937116	2.6
Al	163143731	93131319	75.2	94165920	95162499	1.0	84267257	84815363	0.6	99663970	97784826	1.9	84874843	83108779	2.1
P	190069	164521	15.5	265857	224535	18.4	231432	209785	10.3	150272	126634	18.7	84868	92400	8.2
Ca	8281219	8183470	1.2	8414725	8453163	0.5	18157783	17990965	0.9	14034389	13897495	1.0	111865688	108851465	2.8
Sc	2606	1611	61.8	2775	1841	50.7	2936	2016	45.7	3631	2234	62.6	1314	1326	0.9
Ti	3215440	2001174	60.7	2104918	2089612	0.7	1941888	1898353	2.3	2912177	2850907	2.1	1865741	1866379	0.0
V	7582	7842	3.3	11138	11498	3.1	13083	13464	2.8	5499	5573	1.3	5395	5360	0.7
Cr	4018	3727	7.8	4600	4483	2.6	8198	7823	4.8	4817	4548	5.9	4302	4202	2.4
Fe	21255676	13134765	61.8	21339475	21834314	2.3	19548717	19749572	1.0	19301302	19326712	0.1	17516395	16790624	4.3
Mn	89735	93675	4.2	51990	53823	3.4	246291	246874	0.2	351395	349445	0.6	191067	209301	8.7
Co	1125	1052	6.9	1350	1316	2.7	2151	2063	4.3	1118	1036	7.9	11186	10984	1.8
Ni	5160	5040	2.4	7743	7794	0.7	8431	8402	0.3	4210	4042	4.2	56023	55281	1.3
Cu	4489	3145	42.7	6055	4601	31.6	5689	4539	25.3	5475	3491	56.9	4704	4630	1.6
Zn	8745	6836	27.9	8543	6566	30.1	7010	5335	31.4	11893	9506	25.1	509406	513491	0.8
Ga	51801	52678	1.7	49110	49115	0.0	44803	44399	0.9	53930	53798	0.2	30616	30024	2.0
As	4520	4091	10.5	7457	6981	6.8	5682	5081	11.8	4659	4108	13.4	10560	10022	5.4
Rb	349044	211671	64.9	237374	244536	2.9	174461	176732	1.3	203524	206883	1.6	189826	187048	1.5
Sr	69849	69695	0.2	83327	83133	0.2	90431	89893	0.6	78614	77713	1.2	330851	323270	2.3
Y	345759	218451	58.3	229934	232302	1.0	211029	210447	0.3	302362	304453	0.7	55311	54337	1.8
Zr	3763746	2566439	46.7	2376082	2450029	3.0	2313805	2361541	2.0	3625523	3645221	0.5	976610	972584	0.4
Nb	367048	228224	60.8	202970	208882	2.8	204352	206805	1.2	348232	351194	0.8	69891	70217	0.5
Mo	1155	1199	3.7	1306	1375	5.0	1143	1188	3.7	2359	2403	1.9	643	649	0.9
Cd	1008	548	83.9	979	513	91.0	948	503	88.5	1458	808	80.5	622	651	4.4
In	292	282	3.5	229	217	5.4	236	231	2.3	335	325	2.8	322	331	2.7
Sn	18473	18319	0.8	16492	16657	1.0	10208	10162	0.5	16494	16883	2.3	10108	9928	1.8
Sb	452	455	0.6	1099	1102	0.3	541	574	5.7	289	291	0.6	486	498	2.5
Cs	217048	127905	69.7	203682	201312	1.2	102634	102896	0.3	131951	133242	1.0	13307	13358	0.4
Ba	13522	13393	1.0	14035	14277	1.7	21644	21705	0.3	28945	28900	0.2	114986	113765	1.1
La	185339	110095	68.3	149017	149034	0.0	150796	150812	0.0	108717	111551	2.5	23643	23636	0.0
Ce	393491	252628	55.8	338786	341062	0.7	334442	336220	0.5	253513	253876	0.1	59930	59636	0.5
Pr	31241	31088	0.5	40866	40686	0.4	40021	39987	0.1	30949	31055	0.3	8391	8318	0.9
Nd	118749	119702	0.8	147989	149000	0.7	145091	145983	0.6	120709	120548	0.1	36832	36582	0.7
Sm	31650	31713	0.2	33795	34104	0.9	32265	32578	1.0	38478	38367	0.3	11919	11865	0.5
Eu	1244	1233	0.9	1379	1372	0.5	1264	1259	0.3	1688	1683	0.3	1007	1015	0.8
Tb	6188	6203	0.2	6383	6359	0.4	5855	5907	0.9	8673	8670	0.0	2027	2017	0.5
Gd	33752	33961	0.6	34918	34962	0.1	32242	32569	1.0	46811	46873	0.1	12675	12677	0.0
Dy	39652	39824	0.4	40571	40767	0.5	37437	37821	1.0	54904	55206	0.5	11101	11021	0.7
Ho	8647	8632	0.2	8765	8733	0.4	8125	8198	0.9	11893	11891	0.0	2035	2007	1.4
Er	25281	25165	0.5	25498	25120	1.5	23797	23797	0.0	34734	34422	0.9	4917	4893	0.5
Tm	3902	3917	0.4	3847	3853	0.2	3651	3692	1.1	5382	5366	0.3	629	613	2.6
Yb	25190	25519	1.3	24543	24597	0.2	23439	23784	1.5	34020	34447	1.2	3469	3460	0.2
Lu	3616	3660	1.2	3496	3507	0.3	3374	3391	0.5	4898	4893	0.1	455	453	0.3
Hf	60017	59416	1.0	61811	60583	2.0	55218	54388	1.5	87546	85649	2.2	25503	25159	1.4
Ta	16908	17133	1.3	17764	17825	0.3	15521	15636	0.7	25099	24979	0.5	5947	5927	0.3
W	2192	2320	5.5	4505	4751	5.2	2227	2359	5.6	2817	2913	3.3	132	134	1.5
Tl	2132	2111	1.0	1610	1591	1.2	1376	1365	0.8	2160	2135	1.2	884	901	1.9
Pb	8595	8673	0.9	29166	29644	1.6	9334	9407	0.8	7698	7734	0.5	22011	22352	1.5
Th	57232	59064	3.1	60380	62103	2.8	53182	54539	2.5	84914	87373	2.8	20675	20800	0.6
U	10358	10347	0.1	8407	8416	0.1	11998	11890	0.9	19469	19399	0.4	1145	1155	0.9

Continue Table A1 - 2

Sample ID	HK 198			HK 197			HK 190			HK 192		
	Analysis 1	Analysis 2	%Dev	Analysis 1	Analysis 2	%Dev	Analysis 1	Analysis 2	%Dev	Analysis 1	Analysis 2	%Dev
Li	55735	55152	1.1	48577	48545	0.1	117387	117775	0.3	171547	164444	4.3
Be	8896	8982	1.0	10532	10822	2.7	1757	1721	2.1	7263	6901	5.2
Mg	9747196	10952625	11.0	9590060	10809329	11.3	23488573	23515488	0.1	23401633	22580360	3.6
Al	137674254	137855256	0.1	156179548	155616207	0.4	116508998	116768364	0.2	113145378	109630788	3.2
P	638581	637861	0.1	445808	449485	0.8	90827	92895	2.2	85782	78637	9.1
Ca	7839329	7841539	0.0	2787379	2867456	2.8	1765752	1787401	1.2	1472420	1413745	4.2
Sc	4803	4812	0.2	3146	3204	1.8	6610	6609	0.0	1157	1179	1.8
Ti	3830052	3802480	0.7	3491962	3522476	0.9	744719	750743	0.8	1182799	1145123	3.3
V	34065	33937	0.4	16026	16084	0.4	8301	8403	1.2	1630	1561	4.4
Cr	21332	21635	1.4	9462	9536	0.8	2081	1993	4.4	1459	1492	2.2
Fe	18929995	19090584	0.8	17225135	17382831	0.9	19612342	19575300	0.2	27397677	26829632	2.1
Mn	38725	44695	13.4	15730	18315	14.1	148135	148278	0.1	22796	25304	9.9
Co	8998	8906	1.0	3478	3478	0.0	4454	4448	0.1	3347	3232	3.5
Ni	194156	192423	0.9	81282	80627	0.8	36287	36366	0.2	64843	62861	3.2
Cu	9086	9051	0.4				11046	10985	0.6	12916	12568	2.8
Zn	11990	13261	9.6	8786	10059	12.7	59117	58836	0.5	154852	157628	1.8
Ga	57429	57738	0.5	49507	49699	0.4	29428	29401	0.1	50780	49730	2.1
As	1055	1117	5.5	4382	4408	0.6	12532	12710	1.4	9592	9303	3.1
Rb	331493	323770	2.4	302082	302287	0.1	198094	198594	0.3	236930	233337	1.5
Sr	86009	85745	0.3	48658	48694	0.1	68508	68561	0.1	36836	36519	0.9
Y	204899	190582	7.5	201798	198875	1.5	13943	13958	0.1	99817	99048	0.8
Zr							109006	109359	0.3	671176	663385	1.2
Nb	214235	209483	2.3	172984	169979	1.8	31438	31460	0.1	364004	312408	16.5
Mo	581	590	1.6	277	275	0.8	4978	4957	0.4	9619	9657	0.4
Cd	615	648	5.1	437	452	3.4	268	255	5.2	502	498	0.8
In	128	128	0.1	94	93	0.5	88	87	0.6	319	326	1.9
Sn	28652	28665	0.0	18698	18803	0.6	7040	6909	1.9	32482	32347	0.4
Sb	331	342	3.2	892	915	2.5	706	716	1.5	644	689	6.6
Cs	25724	25581	0.6	21546	21422	0.6	40974	40999	0.1	17262	17201	0.4
Ba	441312	440382	0.2	337165	334229	0.9	75609	75787	0.2	52974	52952	0.0
La	134625	135852	0.9	28882	28736	0.5	9694	9737	0.4	46959	46720	0.5
Ce	283048	251451	12.6	61948	61832	0.2	21384	21447	0.3	103748	103795	0.0
Pr	31870	31851	0.1	6783	6803	0.3	2553	2538	0.6	11808	11790	0.2
Nd	106166	106183	0.0	22791	22738	0.2	9346	9359	0.1	38407	38396	0.0
Sm	21415	21376	0.2	8687	8732	0.5	2076	2090	0.7	8765	8750	0.2
Eu	734	737	0.4	945	943	0.1	114	114	0.1	608	614	0.9
Tb	4514	4545	0.7	4162	4150	0.3	381	381	0.1	2197	2212	0.7
Gd	21194	21261	0.3	15428	15329	0.6	2024	2025	0.0	8924	8889	0.4
Dy	33198	33054	0.4	32803	32762	0.1	2487	2481	0.3	16318	16219	0.6
Ho	8071	8011	0.8	7965	7906	0.8	523	521	0.3	3786	3768	0.5
Er	25435	25604	0.7	24469	24468	0.0	1534	1512	1.5	12035	12132	0.8
Tm	4170	4122	1.1	3887	3844	1.1	239	239	0.1	2038	2008	1.5
Yb	27492	27452	0.1	25213	25117	0.4	1486	1477	0.6	13471	13452	0.1
Lu	3935	3938	0.1	3579	3580	0.0	204	206	1.0	1839	1836	0.1
Hf	64078	63883	0.3	45307	44760	1.2	4793	4769	0.5	31008	30723	0.9
Ta	14627	14604	0.2	10990	10922	0.6	7699	7677	0.3	28318	28169	0.5
W	1871	1846	1.3	1470	1461	0.6	33	32	2.8	143	139	2.8
Tl	1868	1874	0.3	1550	1559	0.6	9730	9711	0.2	2009	2025	0.8
Pb	2384	2432	1.9	1510	1509	0.0	35398	35178	0.6	37727	38258	1.4
Th	67312	66970	0.5	39119	39117	0.0	18157	18161	0.0	61565	61633	0.1
U	11252	11243	0.1	6363	6424	0.9	2387	2381	0.3	8132	8154	0.3

Table A1 - 3: Trace element data in ng/g for the standards BHVO-2 (basalt), JA-2 (andesite) and OU-6 (slate), which were digested and analysed in an identical fashion as the unknown samples and used to test the reliability of the preparation and digestion method. Data are presented along with their preferred GeoReM values; BHVO-2 and JA-2: Jochum et al. (2016); OU-6: Potts and Kane (2005).

	BHVO-2					JA-2					OU-6				
	Digestions and Analyses = 8					Digestions and Analyses = 8									
	Average	SD	%RSD	GeoReM	Bias	Average	SD	%RSD	GeoReM	Bias	Digestion 1	Digestion 2	% DEV	GeoReM	Bias
Li	4505	69	1.6	4500	0.10	28991	504	1.7	29180	0.65	99956	100825	0.86	95300	5.34
Be	1070	54	5.4	1076	0.60	2126	131	6.2	2260	5.91	2709	2701	0.31	2530	6.92
Mg	42818794	1461016	3.6	43764323	2.16	46111652	1574750	3.4	47286214	2.48	14052217	14077238	0.18	14533832	3.23
Al	71217298	2150368	3.2	71129929	0.12	81524396	2921385	3.6	82085208	0.68	107358314	107489303	0.12	108229690	0.74
P	1339382	47456	3.8	1171670	14.31	749813	27236	3.6	662856	13.12	584870	595826	1.84	523652	12.74
Ca	81652505	1266141	1.7	81475129	0.22	44980217	737639	1.6	44732704	0.55	5215503	5174981	0.78	5288736	1.77
Sc	32472	346	1.1	31830	2.02	19317	184	1.0	18930	2.04	23910	23934	0.10	23100	3.56
Ti	16503680	866188	5.6	16371920	0.80	4005731	85307	2.1	4013548	0.19	6067977	6099157	0.51	5934896	2.51
V	323762	7675	2.5	318200	1.75	115588	5021	4.3	119700	3.43	116378	116529	0.13	129800	10.28
Cr	305147	3260	1.1	287200	6.25	473558	6004	1.3	424800	11.48	73156	72820	0.46	70700	3.24
Fe	86578893	1214053	1.5	86661537	0.10	43348732	595572	1.4	43988249	1.45	60121119	60288838	0.28	62530601	3.72
Mn	1313752	23317	1.9	1308860	0.37	825058	13484	1.6	845725	2.44	2107985	2108415	0.02	2168525	2.78
Co	45173	650	1.5	44890	0.63	29488	398	1.3	28330	4.09	29165	29436	0.92	29200	0.34
Ni	118862	1802	1.6	119800	0.78	139424	1934	1.4	136000	2.52	40098	40094	0.01	40200	0.26
Cu	124481	1979	1.7	129300	3.73	27210	572	2.1	29000	6.17	53833	45022	19.57	40400	22.34
Zn	101316	6672	7.0	103900	2.49	64499	5914	9.2	64500	0.00	125879	128028	1.68	111400	13.96
Ga	21102	250	1.3	21370	1.25	16304	150	0.9	16850	3.24	23852	23740	0.47	24170	1.55
As	887	120	14.5	700	26.67	843	172	20.4	710	18.76	17418	14057	23.91	13230	18.96
Rb	9184	102	1.2	9261	0.83	70069	789	1.1	69800	0.39	122926	122660	0.22	121300	1.23
Sr	395847	4814	1.3	394100	0.44	242901	2376	1.0	245800	1.18	131885	131509	0.29	131700	0.00
Y	24386	268	1.2	24910	2.10	15804	120	0.8	19890	20.55	26017	25995	0.09	27750	6.28
Zr	164694	1637	1.1	171200	3.80	104954	1233	1.2	108500	3.27	147657	146936	0.49	174200	15.44
Nb	18381	265	1.5	18100	1.55	9085	173	1.9	9300	2.31	14524	14570	0.31	14490	0.39
Mo	3915	704	19.2	4070	3.81	553	23	4.1	581	4.75	486	455	6.68		
Cd	122	9	7.6	152	19.58	77	5	6.0	69	11.11	67	67	0.00		
In	86	2	3.0	117	26.21	45	3	6.6	37	22.54	85	90	5.48		
Sn	811	403	53.1	1776	54.34	1698	81	4.8	1690	0.50	652	2075	68.58	2670	48.94
Sb	84	16	20.8	103	18.12	129	14	10.6	150	13.84	523	495	5.77	560	9.10
Cs	98	2	1.8	100	1.82	4770	31	0.6	4780	-0.22	8246	8235	0.13	8100	1.73
Ba	131878	1380	1.1	130900	0.75	312326	2909	0.9	308400	1.27	482122	483008	0.18	480000	0.53
La	15288	135	0.9	15200	0.58	15673	122	0.8	15460	1.38	34280	34048	0.68	33200	2.90
Ce	37922	337	0.9	37530	1.05	32806	232	0.7	32860	0.16	80893	80246	0.81	77100	4.50
Pr	5396	57	1.1	5339	1.08	3723	21	0.6	3691	0.87	8297	8263	0.42	7910	4.68
Nd	24478	227	1.0	24270	0.86	14123	93	0.7	14040	0.59	30889	30739	0.49	30200	2.03
Sm	6073	48	0.8	6023	0.84	3036	26	0.9	3032	0.13	6088	6073	0.25	6010	1.17
Eu	2060	20	1.1	2043	0.81	882	8	0.9	893	1.20	1359	1349	0.68	1360	0.44
Tb	935	8	0.9	939	0.45	475	4	0.8	479	0.78	840	840	0.08	860	2.33
Gd	6245	33	0.6	6207	0.61	2998	16	0.5	3013	0.48	5345	5340	0.09	5300	0.80
Dy	5242	43	0.9	5280	0.72	2874	16	0.5	2851	0.81	5048	5042	0.13	5060	0.29
Ho	998	6	0.7	989	0.92	607	4	0.6	591	2.76	1044	1049	0.43	1040	0.64
Er	2505	14	0.6	2511	0.23	1706	10	0.6	1676	1.78	2962	2966	0.15	2930	1.16
Tm	339	3	0.9	335	1.24	257	2	0.7	255	0.72	458	460	0.36	450	2.06
Yb	1981	15	0.8	1994	0.65	1649	7	0.4	1645	0.23	3034	3086	1.69	2980	2.69
Lu	274	2	0.9	275	0.22	246	1	0.5	255	3.56	456	458	0.33	450	1.56
Hf	4220	50	1.3	4470	5.59	2712	36	1.3	2838	4.45	4056	4051	0.12	4700	13.75
Ta	1140	21	1.9	1154	1.18	640	18	2.7	652	1.77	921	925	0.47	1020	9.48
W	203	4	2.0	251	19.08	1292	48	3.7	1150	12.39	1346	1356	0.73		
Pb	1641	97	6.3	1653	0.75	18547	674	3.6	18880	1.76	28333	28671	1.18	28800	1.04
Tl	20	0	2.6	22	7.42	346	5	1.4	330	4.98	563	565	0.27	540	4.48
Th	1180	10	0.9	1224	3.62	4665	68	1.4	4800	2.82	10928	10959	0.29	11300	3.15
U	423	3	0.7	412	2.69	2253	31	1.4	2182	3.25	1998	1990	0.40	1920	3.87

Table A1 - 4: Analyses of samples HK 223 and 184 which were digested twice and analysed by solution ICP-MS to test the reproducibility of the tuff sample analyses. Low deviations (< 3%) indicate high reproducibility. Concentrations are given in ng/g. Deviations, which are > 3% are highlighted in grey.

	HK 223			HK 184		
	Analysis 1	Analysis 2	%DEV	Analysis 1	Analysis 2	%DEV
Li	60	59	1.6	98	102	3.1
Be	5	5	0.2	2	3	16.0
Mg	11959553	11965764	0.1	18410796	33304495	44.7
Al	85213037	88925457	4.2	84874843	151880616	44.1
P	344612	345884	0.4	84868	118296	28.3
Ca	104371799	105219293	0.8	111865688	112345670	0.4
Sc	9	9	0.4	1	2	22.2
Ti	2382	2358	1.0	1866	1674	11.5
V	47	47	0.3	5	5	5.7
Cr	57	57	0.1	4	4	3.7
Fe	14050272	14198161	1.0	17516395	31779286	44.9
Mn	256185	261948	2.2	191067	177614	7.6
Co	9	9	0.1	11	11	1.7
Ni	50	51	0.3	56	58	2.8
Cu	10	10	1.5	5	5	0.7
Zn	95	97	2.5	509	647	21.3
Ga	25	25	0.2	31	31	0.9
As	9	8	19.0	11	12	10.5
Rb	230	243	5.5	190	250	24.2
Sr	627	622	0.8	725	734	1.2
Y	48	48	0.7	55	55	0.9
Zr	585	594	1.5	977	979	0.2
Nb	34	35	2.9	70	68	2.8
Mo	0	0	6.2	1	1	0.6
Cd	0	0	15.8	1	1	22.4
In	0	0	2.9	0	0	1.4
Sn	9	9	2.0	10	9	10.1
Sb	1	1	4.3	0	0	14.5
Cs	20	20	0.5	13	13	1.5
Ba	155	157	0.9	115	114	1.1
La	21	21	1.0	24	23	3.6
Ce	39	39	0.9	60	58	3.5
Pr	5	5	0.3	8	8	3.4
Nd	20	20	0.1	37	36	2.1
Sm	5	5	0.6	12	12	1.7
Eu	1	1	0.8	1	1	0.1
Tb	1	1	0.4	2	2	0.9
Gd	5	5	0.3	13	13	0.5
Dy	8	8	0.2	11	11	0.7
Ho	2	2	1.3	2	2	0.9
Er	5	6	0.8	5	5	1.7
Tm	1	1	1.2	1	1	0.6
Yb	6	6	0.8	3	3	0.4
Lu	1	1	1.8	0	0	0.6
Hf	23	23	0.1	26	25	2.1
Ta	3	3	2.3	6	6	6.5
W	1	1	0.8	0	0	0.2
Pb	2	1	8.8	1	1	2.4
Tl	14	14	0.3	22	22	1.7
Th	17	17	0.9	21	20	1.3
U	2	2	0.6	1	1	2.3

Table A1 - 5: Trace element data of 79 tuff and one shale sample. Concentrations are given in µg/g and are arranged by atomic number. Chondrite values are taken from McDonough and Sun (1995).

	TARA DEEP - MARKER TUFF																					
sample ID	HK 115	HK 116	HK 118	HK 122	HK 121	HK 120	HK 119	HK 245	HK 130	HK 114	HK 161	HK 163	HK 162	HK 186	HK 232	HK 196	HK 247	HK 234	HK 235	HK 236	HK 251	HK 250
drill core	N-2250	N-2259	N-2319	N-2332	N-2332	N-2332	N-2332	N-2360	N-2373	N-2373	N-2415	N-2444	N-2444	N-2451	N-2457	N-2464	N-2467	N-2477	N-2479	N-2480	N-2494	N-2494
sample number	1	2	3	4	5	6	7	8	9	10	11	12	13	14	15	16	17	18	19	20	21	22
stratigraphic level	TBU-1	TBU -1	TBU-1	TBU-1	TBU-1	TBU-1	TBU-1	TBU -1	TBU-1	TBU-1	TBU-1	TBU-1	TBU-1	TBU-1	TBU-1	TBU-1	TBU -1	TBU-1	TBU-1	TBU-1	TBU-1	TBU-1
Li	78	31	32	33	32	28	30	29	31	36	41	47	85	54	27	37	37	44	81	36	33	36
Be	11.0	7.1	10.8	8.7	8.9	9.1	8.4	11.7	5.2	4.8	14.1	8.9	9.5	6.1	8.6	9.8	18.8	9.1	12.6	10.4	12.8	6.5
Mg	9885	11471	9722	12097	12111	10693	16964	11925	12336	15000	10539	12757	15620	11792	13764	10020	10259	12471	11693	16395	12228	13914
Al	99681	94166	102781	94833	97202	99634	163144	124093	83776	84267	112294	113135	112737	118850	124087	95576	113966	132535	134059	144997	130906	117147
P	328	266	186	226	168	177	190	232	389	231	185	169	196	470	203	163	199	164	313	170	225	444
Ca	30734	8415	2294	17166	20446	16100	8281	6568	21140	18158	8511	6647	9151	2525	10438	1153	2068	1689	12901	7218	7307	11875
Sc	3.8	2.8	3.6	4.1	3.6	2.6	2.6	3.0	3.1	2.9	2.0	2.5	3.2	4.8	2.6	1.7	2.7	2.4	3.0	2.6	2.5	3.2
Ti	2398	2105	2626	2720	2579	2125	3215	2371	2071	1942	2392	2565	2587	3020	1970	2054	2359	2085	2213	2134	2154	2417
V	19.4	11.1	11.3	22.1	19.8	4.4	7.6	13.2	18.5	13.1	5.5	11.2	24.6	49.6	9.9	8.4	7.8	5.6	13.7	10.2	7.6	11.7
Cr	11.1	4.6	5.7	10.1	7.5	2.1	4.0	7.1	11.2	8.2	2.6	6.2	10.5	28.6	5.1	4.3	4.7	3.4	8.9	4.9	3.3	8.3
Fe	15419	21339	10763	17961	17345	33193	21256	23230	16962	19549	25829	16007	35103	21994	18357	11666	12670	14693	17311	20607	13265	12771
Mn	159	52	27	172	172	72	90	67	185	246	52	108	60	80	118	19	21	16	85	97	36	50
Co	3.9	1.4	1.6	2.5	1.9	1.5	1.1	2.4	3.7	2.2	1.6	1.6	2.4	8.7	1.8	1.2	1.4	1.2	3.1	1.5	1.3	2.5
Ni	15.2	7.7	7.1	10.1	7.7	11.1	5.2	10.8	13.4	8.4	9.7	6.9	10.9	34.2	7.8	5.3	5.9	5.4	12.4	6.2	6.4	9.5
Cu	8.7	6.1	6.3	7.1	5.8	4.9	4.5	6.7	7.4	5.7	3.5	4.4	5.9	18.8	4.0	3.5	3.8	3.2	6.0	3.3	3.2	5.3
Zn	10.4	8.5	8.6	11.6	15.7	10.4	8.7	16.0	6.1	7.0	7.0	4.2	9.3	7.7	4.0	5.4	13.9	5.4	7.5	7.3	18.2	5.9
Ga	50.2	49.1	57.5	50.9	54.3	56.3	51.8	51.9	40.7	44.8	62.9	60.2	59.6	55.9	49.1	52.4	64.1	57.2	55.4	52.0	62.0	61.2
As	12.8	7.5	4.8	6.0	4.5	25.0	4.5	6.7	9.1	5.7	17.0	4.9	5.8	14.7	9.2	2.9	4.9	3.0	13.7	4.2	5.9	4.5
Rb	200	237	202	213	218	240	349	264	213	174	262	255	211	236	241	212	263	300	299	303	314	304
Sr	140	83	37	78	75	102	70	234	64	90	86	61	72	65	84	39	83	39	121	68	88	89
Y	259	230	290	273	237	245	346	366	189	211	274	279	263	276	313	238	303	324	345	384	319	297
Zr	2820	2376	3303	3022	2753	2859	3764	3944	2064	2314	3294	3232	2973	3208	3496	2721	3642	3704	3706	4371	3678	3419
Nb	251	203	308	222	201	250	367	338	183	204	308	286	219	319	307	260	339	366	354	390	315	316
Mo	2.1	1.3	1.8	1.8	1.6	1.6	1.2	2.0	1.8	1.1	1.3	1.2	5.0	4.5	1.2	1.3	2.2	1.5	1.9	1.1	1.6	1.6
Cd	1.1	1.0	1.3	1.1	1.1	1.1	1.0	1.1	0.8	0.9	0.9	0.9	0.9	0.8	0.9	0.6	1.1	1.1	1.0	1.0	1.1	1.1
In	0.3	0.2	0.3	0.3	0.3	0.3	0.3	0.3	0.2	0.2	0.3	0.4	0.3	0.3	0.3	0.3	0.3	0.3	0.3	0.3	0.3	0.3
Sn	20.7	16.5	22.6	18.9	18.8	19.7	18.5	19.6	17.6	10.2	17.1	24.0	16.6	24.1	19.4	20.9	23.0	23.1	22.4	20.1	21.4	23.2
Sb	1.0	1.1	0.6	0.7	0.5	0.8	0.5	0.7	1.2	0.5	0.5	0.5	0.5	2.1	0.5	0.4	0.5	0.3	1.0	0.4	0.5	0.5
Cs	174.5	203.7	107.0	128.5	134.1	164.3	217.0	163.1	180.6	102.6	181.7	220.9	207.8	154.7	119.5	152.4	148.5	265.3	270.0	175.5	210.9	201.4
Ba	29.8	14.0	19.8	22.2	18.6	14.2	13.5	21.8	29.5	21.6	15.1	20.4	25.9	55.6	21.4	16.8	47.0	14.9	23.9	16.1	13.9	21.6
La	191.5	149.0	98.7	134.5	86.9	90.6	185.3	165.7	64.9	150.8	104.0	105.1	118.9	195.5	149.5	118.1	118.3	97.6	225.4	96.4	153.4	220.7
Ce	420.7	338.8	237.9	286.2	192.3	216.7	393.5	348.1	143.7	334.4	254.8	239.6	255.8	467.1	342.6	272.8	280.5	297.0	459.8	344.1	337.4	487.6
Pr	50.4	40.9	29.2	34.2	23.5	27.1	31.2	32.5	18.3	40.0	31.6	28.9	30.6	56.1	31.7	33.4	32.0	28.6	46.9	26.7	35.5	53.5
Nd	183.4	148.0	112.8	129.9	94.0	107.3	118.7	124.9	74.5	145.1	122.7	114.0	119.5	201.1	120.4	125.4	123.3	111.5	173.8	104.0	134.8	189.2
Sm	42.2	33.8	36.1	37.2	32.0	33.4	31.7	39.3	22.6	32.3	35.2	38.1	37.2	45.1	33.9	33.8	36.5	33.9	43.1	31.2	37.2	41.5
Eu	1.6	1.4	1.6	1.6	1.4	1.4	1.2	1.6	1.2	1.3	1.4	1.7	1.7	2.1	1.4	1.2	1.5	1.3	1.7	1.2	1.5	2.0
Gd	42.0	34.9	44.4	43.0	38.1	37.8	33.8	46.4	27.0	32.2	40.4	43.0	41.0	44.0	37.9	37.2	43.1	39.4	44.4	36.7	41.3	41.8
Tb	7.4	6.4	8.3	7.6	6.8	7.0	6.2	8.3	5.1	5.9	7.6	7.7	7.2	7.9	6.8	6.7	8.0	7.3	7.8	6.8	7.5	7.7
Dy	46.3	40.6	52.5	48.0	42.7	44.8	39.7	51.8	32.9	37.4	49.4	48.7	45.2	51.0	43.1	43.2	50.7	47.0	49.4	43.8	48.5	48.9
Ho	10.0	8.8	11.3	10.3	9.2	9.7	8.6	11.1	7.1	8.1	10.8	10.6	9.7	11.0	9.3	9.3	11.0	10.2	10.7	9.5	10.6	10.7
Er	29.1	25.5	32.6	30.0	26.6	28.6	25.3	31.9	20.8	23.8	31.4	30.5	28.1	32.0	26.7	27.0	31.9	29.8	31.1	27.6	30.9	31.1
Tm	4.5	3.8	5.0	4.6	4.1	4.4	3.9	4.9	3.2	3.7	4.9	4.7	4.3	5.0	4.2	4.2	5.0	4.7	4.8	4.3	4.8	4.9
Yb	28.3	24.5	31.8	28.9	26.1	28.4	25.2	31.0	20.1	23.4	31.6	30.0	27.1	32.5	26.5	27.1	31.6	29.9	31.0	27.5	31.0	31.3
Lu	4.1	3.5	4.6	4.2	3.7	4.1	3.6	4.5	2.9	3.4	4.5	4.3	3.8	4.6	3.8	3.9	4.6	4.3	4.5	4.0	4.5	4.6
Hf	67.7	61.8	79.2	77.7	74.1	67.7	60.0	75.8	53.4	55.2	73.1	73.7	71.9	73.1	63.0	62.2	77.6	70.3	70.9	69.5	72.7	73.0
Ta	19.2	17.8	22.4	23.0	21.9	19.1	16.9	20.9	15.4	15.5	20.9	21.3	21.2	20.9	17.4	17.7	21.2	19.2	19.4	19.4	19.8	20.1
W	3.4	4.5	3.1	3.7	3.2	2.1	2.2	3.4	6.0	2.2	2.3	2.7	3.3	2.2	2.1	2.6	2.9	2.3	3.2	1.9	2.4	1.7
Tl	2.4	1.6	2.5	2.2	2.1	2.2	2.1	2.2	1.8	1.4	3.1	1.3	1.3	5.6	1.6	2.2	3.8	3.0	2.2	1.5	2.4	2.7
Pb	26.0	29.2	13.1	12.2	10.0	15.6	8.6	16.4	22.0	9.3	13.0	8.6	18.4	56.5	10.2	7.3	14.6	5.9	18.9	7.8	8.6	6.9
Th	65.3	60.4	75.3	77.5	71.9	63.3	57.2	75.3	52.6	53.2	74.1	75.9	75.9	74.2	62.7	62.2	76.0	68.8	70.6	69.8	71.6	72.3
U	11.9	8.4	16.5	10.1	8.7	11.6	10.4	14.2	8.3	12.0	14.7	12.7	7.2	21.7	12.5	14.1	15.2	15.5	13.4	12.3	11.3	15.3
La_{CN}/Sm_{CN}	2.83	2.75	1.71	2.26	1.69	1.69	3.66	2.63	1.80	2.92	1.84	1.73	1.99	2.71	2.75	2.19	2.02	1.80	3.27	1.93	2.58	3.32
Gd_{CN}/Lu_{CN}	1.28	1.23	1.21	1.28	1.26	1.15	1.15	1.28	1.17	1.18	1.11	1.24	1.32	1.18	1.22	1.19	1.16	1.12	1.23	1.14	1.14	1.13
La_{CN}/Lu_{CN}	4.91	4.42	2.25	3.35	2.41	2.31	5.32	3.84	2.35	4.64	2.39	2.54	3.21	4.38	4.05	3.18	2.68	2.34	5.25	2.52	3.55	5.03
Eu anomaly	0.12	0.12	0.12	0.12	0.12	0.12	0.12	0.11	0.15	0.12	0.11	0.12	0.13	0.14	0.11	0.10	0.12	0.11	0.12	0.11	0.11	0.14
ΣREE+Y	1321	1090	997	1074	825	886	1254	1268	634	1053	1005	986	993	1431	1151	981	1081	1067	1480	1147	1198	1473
TiO_2/Al_2O_3	0.02	0.02	0.02	0.03	0.02	0.02	0.02	0.02	0.02	0.02	0.02	0.02	0.02	0.02	0.01	0.02	0.02	0.01	0.01	0.01	0.01	0.02

Continue Table A1 - 5

	TARA DEEP - UPPER TUFF				TARA DEEP - LOWER TUFF								NAVAN WEST							NAVAN EAST		SHALE
sample ID	HK 158	HK 228	HK 230	HK 252	HK 166	HK 165	HK 159	HK 170	HK 229	HK 231	HK 233	HK 248	HK 169	HK 126	HK 125	HK 155	HK 156	HK 157	HK 128	HK 117	HK 227	HK 164
hole number	N-2444	N-2455	N-2461	N-2494	N-2406	N-2406	N-2444	N-2454	N-2455	N-2461	N-2469	N-2495	N-2441	N-2411	N-2411	N-2441	N-2441	N-2441	N-2412	N-2317	N-2376	N-2406
sample number	23	24	25	26	27	28	29	30	31	32	33	34	35	36	37	38	39	40	41	42	43	44
Stratigraphic level	TBU-2	TBU-2	TBU-2	TBU-2	TBU-2	TBU-2	TBU-2	TBU-2	TBU-2	TBU-2	TBU -2	TBU-2	WAL Eq.	WAL	WAL	TCF	TCF	TCF	FG	FG	FG	TBU-2
Li	36	51	31	32	38	44	53	54	66	61	40	33	54	29	46	31	31	28	43	38	36	68
Be	4.3	4.2	3.3	5.2	5.2	5.1	5.1	4.4	5.1	3.8	6.7	4.6	5.0	2.0	3.3	3.0	9.7	9.1	1.2	11.2	1.2	3.5
Mg	13246	11796	7969	9916	12741	12780	14519	13052	13402	19420	12582	11714	20294	16697	19259	16367	17569	18248	10275	12116	17343	11331
Al	91816	104941	64097	96125	108128	101963	135991	110276	91488	188520	130398	107059	121564	103491	110545	116546	117756	112820	136078	99664	245718	71123
P	570	491	4719	242	439	264	430	313	525	468	669	487	258	249	258	90	154	67	1372	150	1106	1004
Ca	27210	18368	59784	6861	15220	17395	2641	45429	69244	30518	3542	11288	32195	10115	20045	54921	13896	9233	38065	14034	9787	47173
Sc	8.2	10.2	6.8	9.4	8.4	6.1	8.2	6.6	9.2	7.7	10.9	6.8	6.1	5.4	6.7	2.0	2.1	1.9	5.4	3.6	8.8	13.6
Ti	3024	4064	2145	3883	3745	3183	4251	3404	3476	5275	4807	3321	2737	549	1058	1152	2461	2376	2893	2912	2332	3701
V	28.9	41.8	44.3	26.1	25.5	13.6	20.5	13.6	56.7	19.5	42.6	15.7	31.4	7.8	10.6	8.3	6.8	1.8	45.1	5.5	41.3	175.0
Cr	14.3	24.7	25.7	14.8	13.9	10.2	15.0	10.9	44.7	15.3	33.0	12.0	16.9	2.2	3.9	5.7	3.0	1.3	29.4	4.8	14.7	115.3
Fe	42930	34457	60452	65861	28731	20266	22114	18470	29953	34281	28491	18452	17911	4546	15527	24092	20220	14269	14735	19301	20259	31958
Mn	397	231	553	151	190	149	88	314	648	427	140	120	129	24	42	100	270	275	289	351	204	575
Co	3.6	5.9	6.5	4.6	6.3	1.9	2.7	1.8	6.8	3.0	5.6	2.4	17.5	0.7	7.3	4.2	1.8	0.6	13.2	1.1	8.0	15.3
Ni	17.4	26.0	29.1	22.2	19.6	8.9	13.6	8.6	37.3	14.3	32.2	11.1	77.0	4.2	25.1	60.1	17.6	4.8	116.6	4.2	32.4	94.8
Cu	7.9	12.4	16.2	11.4	6.7	4.7	6.1	4.8	17.6	4.7	13.5	5.1	18.3	2.5	12.0	16.8	7.3	4.4	15.8	5.5	12.6	40.1
Zn	9.8	15.9	27.0	12.3	6.6	3.7	3.7	5.5	15.3	6.9	10.6	13.6	61.6	2.8	8.5	22.3	3.1	0.6	65.1	11.9	40.5	70.5
Ga	48.4	48.9	31.3	45.1	44.7	46.9	58.7	53.0	31.7	45.6	45.5	47.7	28.9	31.3	31.9	39.1	62.0	63.9	19.6	53.9	21.1	17.6
As	14.6	13.4	39.2	29.3	26.7	16.2	17.0	5.8	65.2	15.6	38.6	20.5	53.9	2.3	22.7	29.4	4.8	2.8	10.7	4.7	11.6	21.0
Rb	149	213	110	145	211	227	287	230	186	387	272	236	267	188	195	227	215	223	118	204	113	170
Sr	79	81	232	59	296	351	93	597	135	128	160	285	89	90	114	539	100	86	79	79	594	160
Y	174	224	112	229	250	239	306	254	188	405	310	274	105	22	33	102	317	245	13	302	12	14
Zr	2196	2761	1405	2711	2971	2802	3668	3007	2031	4570	3380	3114	1031	74	114	619	3534	3213	147	3626	103	93
Nb	311	412	149	398	299	299	400	322	190	504	335	330	50	44	41	167	306	331	7	348	16	11
Mo	2.0	2.5	4.8	2.7	9.4	1.8	1.7	1.1	5.6	2.3	4.6	1.9	1.6	0.4	3.4	9.1	11.1	2.5	2.6	2.4	5.3	4.6
Cd	0.7	1.0	0.7	1.0	0.9	0.8	1.0	0.9	0.7	1.1	1.1	1.0	0.4	0.0	0.1	0.2	1.1	1.0	0.3	1.5	0.2	0.2
In	0.5	0.4	0.2	0.3	0.4	0.3	0.4	0.3	0.2	0.3	0.3	0.3	0.1	0.1	0.1	0.3	0.3	0.4	0.1	0.3	0.0	0.0
Sn	7.2	9.6	6.1	13.0	15.3	18.2	25.4	14.9	7.4	20.7	18.2	20.5	16.4	24.6	19.3	49.1	20.6	25.5	14.8	16.5	6.0	2.0
Sb	1.3	1.5	2.7	1.5	0.8	0.5	0.6	0.4	1.7	0.9	8.9	4.1	8.4	0.3	1.2	1.0	1.2	0.4	3.7	0.3	1.2	1.6
Cs	134.6	234.4	90.9	82.6	147.0	256.2	301.2	375.1	95.4	529.5	182.5	204.6	150.2	134.0	49.0	100.3	29.0	34.3	30.3	132.0	18.7	60.9
Ba	36.2	54.8	72.9	36.5	449.6	991.0	49.3	2230.8	115.6	142.7	435.6	399.2	48.5	55.8	59.1	1028.3	50.0	40.0	101.0	28.9	267.2	359.9
La	95.3	110.6	94.1	123.1	171.4	191.8	242.0	206.6	123.7	385.8	272.3	285.9	10.7	6.6	19.3	33.6	122.2	183.2	14.7	108.7	12.9	22.2
Ce	227.4	276.7	254.1	305.7	378.2	412.4	534.3	449.2	281.2	848.3	625.0	614.7	21.1	15.8	45.5	77.9	307.3	393.8	39.2	253.5	28.5	39.1
Pr	26.2	29.8	28.9	33.6	43.9	47.7	61.8	51.9	31.2	65.6	68.5	66.8	3.0	2.0	5.5	9.8	37.5	47.7	5.2	30.9	3.6	4.6
Nd	91.5	103.5	99.7	116.8	159.1	168.7	222.6	183.3	109.0	228.2	236.8	234.5	13.8	7.6	19.9	33.5	141.4	176.4	20.5	120.7	14.5	16.6
Sm	23.5	27.6	18.3	27.3	40.7	38.5	52.1	40.3	24.2	45.7	45.9	46.4	6.1	2.3	4.8	7.7	36.2	39.8	3.9	38.5	3.2	3.1
Eu	2.8	3.8	2.0	4.1	2.1	1.7	2.6	1.5	2.4	2.6	3.0	2.2	1.7	0.1	0.2	1.4	1.4	1.4	0.4	1.7	0.4	0.6
Gd	23.2	28.6	16.0	28.2	41.2	36.8	49.8	38.5	25.4	41.9	43.1	40.6	9.0	2.7	4.7	8.9	39.5	40.0	3.1	46.8	2.9	2.7
Tb	4.4	5.4	3.0	5.4	7.3	6.6	8.7	7.0	4.7	7.4	7.9	7.2	2.1	0.6	1.0	2.1	8.0	7.2	0.4	8.7	0.4	0.4
Dy	28.4	34.6	18.8	35.3	44.6	41.9	54.3	44.9	30.4	46.6	50.2	45.0	15.6	4.1	6.4	16.5	53.6	46.5	2.5	54.9	2.4	2.5
Ho	6.2	7.6	4.1	7.7	9.5	9.1	11.7	9.8	6.5	10.0	10.8	9.8	3.5	0.8	1.3	3.8	12.0	9.9	0.5	11.9	0.5	0.5
Er	18.6	22.5	11.9	22.6	27.4	26.8	34.4	28.8	19.0	29.4	31.2	28.6	10.1	2.4	3.8	11.5	34.9	28.8	1.3	34.7	1.3	1.5
Tm	3.0	3.6	1.9	3.5	4.3	4.2	5.4	4.5	2.9	4.7	4.9	4.5	1.4	0.4	0.6	1.8	5.4	4.6	0.2	5.4	0.2	0.2
Yb	19.4	23.4	12.0	22.8	27.5	27.6	35.1	29.4	18.9	30.5	31.5	29.2	8.4	2.5	3.9	11.2	34.0	29.6	1.2	34.0	1.2	1.6
Lu	2.9	3.5	1.8	3.4	4.0	4.0	5.2	4.3	2.8	4.5	4.7	4.3	1.1	0.3	0.5	1.4	4.9	4.3	0.2	4.9	0.2	0.2
Hf	51.6	62.0	33.1	60.4	64.1	61.1	79.6	65.4	44.3	69.0	71.6	65.2	35.3	3.7	4.8	32.4	79.2	71.8	7.9	87.5	4.7	2.5
Ta	17.9	20.5	11.2	20.0	18.1	17.1	22.1	18.3	12.0	18.7	19.1	17.4	10.2	7.9	6.3	31.4	22.7	20.6	3.6	25.1	2.7	0.7
W	1.7	2.4	1.2	2.4	4.1	3.4	4.7	3.8	1.7	3.7	2.9	4.0	0.2	0.3	0.4	0.1	0.7	0.9	1.2	2.8	4.3	1.2
Tl	17.1	9.2	48.2	11.5	8.9	7.3	5.3	4.7	11.6	8.1	10.3	7.5	2.9	3.9	6.1	4.8	1.9	1.6	0.5	2.2	0.8	13.5
Pb	22.5	19.6	30.3	25.6	35.4	22.6	16.2	11.8	41.9	21.2	32.0	17.4	66.1	2.6	16.4	36.5	33.8	12.6	39.2	7.7	32.3	24.9
Th	43.2	49.3	28.5	48.0	61.1	59.9	78.2	63.9	43.2	65.6	68.1	61.4	46.0	12.7	20.0	63.7	80.1	72.6	69.5	84.9	31.1	8.7
U	6.7	8.6	5.9	8.4	12.8	12.7	17.7	15.7	10.6	13.9	16.3	13.8	5.0	7.8	3.3	8.4	21.6	20.0	9.1	19.5	9.5	4.0
La_{CN}/Sm_{CN}	2.53	2.50	3.21	2.81	2.63	3.11	2.90	3.20	3.19	5.27	3.70	3.85	1.09	1.79	2.51	2.74	2.10	2.88	2.37	1.76	2.53	4.40
Gd_{CN}/Lu_{CN}	1.00	1.01	1.12	1.02	1.28	1.13	1.18	1.10	1.14	1.16	1.14	1.16	0.98	0.97	1.13	0.77	1.00	1.16	2.14	1.18	1.98	1.40
La_{CN}/Lu_{CN}	3.44	3.28	5.52	3.76	4.46	4.96	4.82	4.96	4.65	8.93	6.07	6.87	0.98	2.01	3.88	2.44	2.61	4.45	8.63	2.30	7.52	9.76
Eu anomaly	0.37	0.41	0.36	0.44	0.15	0.13	0.15	0.12	0.29	0.18	0.20	0.15	0.68	0.13	0.10	0.50	0.11	0.10	0.30	0.12	0.36	0.65
ΣREE+Y	747	905	679	969	1212	1257	1626	1355	870	2156	1746	1694	213	70	150	322	1155	1259	106	1058	84	110
TiO_2/Al_2O_3	0.03	0.03	0.03	0.04	0.03	0.03	0.03	0.03	0.03	0.02	0.03	0.03	0.02	0.00	0.01	0.01	0.02	0.02	0.02	0.03	0.01	0.05

Continue Table A1 - 5

						LISHEEN								**RAPLA**			
sample ID	HK 215	HK 218	HK 180.1	HK 221	HK 214	HK 216	HK 220	HK 181.1	HK 182	HK 203	HK 219	HK 217	HK 185	HK 223	HK 184	HK 222	HK 183
hole number	LK-669	LK-1585	LK-1722	LK-1773	LK-1874	LK-1915	LK-1915	LK-2180	LK-1040	LK-0721	LK-1432	3312-62	3667-04	3667-04	3312-78	3312-54	3312-62
sample number	45	46	47	48	49	50	51	52	53	54	55	56	57	58	59	60	61
Stratigraphic level	NMU	NMU	NMU	NMU	NMU	NMU	NMU	S-ABL	S-ABL	S-ABL	WAL	UCM	UCM	UCM/NMU	NMU	UWLU	CP
Li	42	49	45	27	35	43	42	28	30	30	121	218	40	60	98	54	588
Be	3.0	4.0	2.9	5.0	2.5	5.9	5.1	4.1	5.4	3.0	4.8	5.6	3.4	5.0	2.4	3.7	7.0
Mg	26988	23496	23402	16444	17819	16318	30032	19074	15078	10865	17447	18334	16973	11960	18411	25144	32085
Al	162065	112015	97178	119684	110552	118158	193616	90261	133199	77192	99012	94718	105916	85213	84875	195320	85276
P	156	257	712	320	228	338	328	199	248	1021	648	570	244	345	85	175	119
Ca	63718	51986	65644	27341	49267	32071	32121	109206	15185	76284	9294	66565	58667	104372	111866	3453	37874
Sc	2.6	2.4	1.3	3.2	2.8	4.0	4.8	1.9	3.4	3.7	15.9	6.6	2.8	8.9	1.3	8.7	1.3
Ti	2392	2620	2086	2506	1411	2584	1784	2483	2921	1899	4831	4677	2356	2382	1866	873	823
V	12.3	8.1	5.3	18.0	15.1	19.0	14.9	6.8	18.0	20.5	83.4	24.9	12.3	47.0	5.4	14.1	15.8
Cr	5.2	3.7	4.5	10.6	23.4	11.8	19.5	3.0	11.1	17.1	113.5	10.6	9.7	57.4	4.3	13.0	3.7
Fe	50201	22853	29606	22468	25239	20563	46112	17053	15426	68302	39909	33247	21809	14050	17516	36418	22151
Mn	161	150	383	253	441	190	167	391	114	215	97	115	196	256	191	38	147
Co	39.8	11.0	7.8	56.9	27.6	31.2	18.8	7.3	21.1	93.3	105.6	15.5	22.5	9.2	11.2	5.3	2.0
Ni	201.1	70.5	71.9	241.0	93.3	90.7	144.5	52.2	124.8	386.4	132.4	159.5	84.4	50.4	56.0	67.0	30.2
Cu	11.0	9.4	5.9	14.8	4.6	23.8	44.5	6.2	20.8	23.1	6.9	18.4	6.8	9.8	4.7	43.3	9.3
Zn	22.4	181.9	17.3	408.4	55.5	51.6	601.0	32.3	2422.2	84.6	130.1	12.4	17.9	94.6	509.4	19.5	331.8
Ga	35.6	39.7	39.9	39.8	31.2	41.6	37.3	34.2	46.6	25.1	24.9	41.8	36.7	25.3	30.6	39.1	45.5
As	83.3	8.4	2.6	92.9	4.5	14.8	25.0	5.9	43.4	142.4	198.6	41.1	9.2	9.2	10.6	40.4	14.3
Rb	371	200	196	203	229	240	402	189	233	168	324	237	232	230	190	316	174
Sr	229	299	111	38	172	157	115	207	14	140	39	99	132	81	331	13	104
Y	94	136	113	103	57	110	345	137	92	69	12	111	85	48	55	12	81
Zr	2348	2524	1143	1378	529	1376	3521	2036	1448	803	95	1787	1185	585	977	128	582
Nb	93	137	102	100	30	94	109	136	97	67	16	200	86	34	70	63	236
Mo	2.2	4.1	0.3	2.6	0.3	0.7	0.4	2.5	1.5	6.2	0.2	0.9	0.6	0.2	0.6	1.3	12.2
Cd	0.4	1.0	0.3	0.5	0.2	0.7	6.6	0.6	1.4	0.4	0.1	0.6	0.3	0.3	0.6	0.1	1.5
In	0.2	0.2	0.3	0.2	0.2	0.2	0.2	0.2	0.3	0.1	0.1	0.2	0.3	0.1	0.3	0.1	0.4
Sn	10.3	18.5	10.6	10.0	10.4	12.0	14.2	16.4	13.1	4.1	1.7	17.5	10.9	8.7	10.1	16.8	35.3
Sb	4.2	0.7	0.3	3.5	0.3	0.5	0.3	0.8	1.2	4.3	0.6	1.2	0.7	0.6	0.5	1.4	1.2
Cs	16.4	21.1	23.8	19.9	39.5	29.5	32.1	14.1	24.7	22.7	41.1	19.4	23.1	20.5	13.3	7.8	15.3
Ba	503.5	113.5	127.9	352.8	329.4	1015.4	1868.9	111.8	1861.2	168.5	346.3	94.3	114.0	155.4	115.0	428.9	38.3
La	17.3	81.3	87.3	79.5	45.9	84.2	67.8	50.9	61.5	56.2	17.1	34.2	97.9	20.5	23.6	12.8	60.9
Ce	44.4	214.3	181.1	192.7	110.5	202.8	298.2	119.4	147.1	133.7	31.9	89.1	225.7	39.1	59.9	32.5	131.2
Pr	6.1	25.0	25.6	22.7	13.5	24.5	20.4	14.6	18.7	16.9	4.2	11.8	28.5	5.2	8.4	3.5	14.1
Nd	26.8	94.5	96.4	83.4	48.6	91.7	75.3	55.8	71.8	64.3	15.4	50.1	104.9	19.7	36.8	12.7	44.1
Sm	9.7	24.4	20.4	16.8	11.6	19.9	21.0	15.0	17.0	13.8	2.8	14.9	20.9	5.0	11.9	2.9	9.7
Eu	0.9	1.5	0.8	1.0	1.0	1.0	1.4	1.0	0.9	0.9	0.5	1.3	1.0	0.6	1.0	0.1	0.5
Gd	13.1	25.0	18.3	14.2	10.5	17.6	22.9	17.1	14.5	11.6	2.3	16.3	15.9	5.2	12.7	2.4	8.8
Tb	2.7	4.3	3.4	2.6	1.9	3.2	4.9	3.5	2.7	2.0	0.3	3.2	2.7	1.0	2.0	0.4	1.9
Dy	17.8	25.3	22.1	18.2	11.7	20.8	35.3	24.1	17.2	12.8	2.0	21.4	16.8	7.6	11.1	2.4	13.5
Ho	3.7	5.1	4.7	4.1	2.3	4.5	7.8	5.3	3.7	2.8	0.4	4.8	3.6	1.8	2.0	0.5	3.0
Er	10.2	14.2	13.4	12.5	6.1	12.8	23.3	15.7	10.5	8.1	1.3	14.3	10.2	5.5	4.9	1.4	9.1
Tm	1.4	2.2	2.0	2.0	0.9	2.0	3.7	2.4	1.6	1.3	0.2	2.3	1.6	0.9	0.6	0.2	1.5
Yb	8.8	14.0	13.3	12.9	5.1	12.5	23.9	16.1	10.0	8.1	1.4	14.4	10.3	5.6	3.5	1.6	9.1
Lu	1.2	2.0	1.9	1.9	0.7	1.8	3.3	2.3	1.4	1.2	0.2	2.0	1.5	0.8	0.5	0.2	1.2
Hf	34.2	60.9	29.0	35.0	24.4	35.3	67.2	52.4	38.0	21.3	2.8	42.4	31.6	23.3	25.5	6.0	29.3
Ta	7.9	13.7	6.8	8.1	3.8	8.3	8.7	11.8	8.9	5.0	1.0	12.1	7.3	3.2	5.9	10.4	27.7
W	0.2	0.2	0.2	0.3	0.2	0.3	0.3	0.2	0.2	0.5	1.8	1.2	0.2	0.5	0.1	0.2	0.1
Tl	1.9	1.4	6.3	17.3	4.6	32.4	49.8	1.5	41.9	10.1	31.9	1.0	1.6	1.6	0.9	2.3	1.7
Pb	64.6	43.0	13.1	166.5	17.4	124.6	7583.0	35.7	63.7	254.7	43.9	58.7	25.5	14.1	22.0	19.5	70.5
Th	28.0	61.0	24.5	29.0	21.1	30.0	42.1	52.5	32.2	18.7	12.3	31.8	26.4	16.9	20.7	21.5	55.2
U	4.0	10.8	6.0	6.7	2.7	6.4	5.4	10.3	30.7	5.9	2.2	5.2	6.2	1.9	1.1	3.8	5.7
La_{CN}/Sm_{CN}	1.11	2.08	2.67	2.96	2.47	2.65	2.02	2.12	2.26	2.55	3.84	1.43	2.92	2.59	1.24	2.80	3.93
Gd_{CN}/Lu_{CN}	1.33	1.59	1.19	0.94	1.94	1.23	0.87	0.94	1.29	1.24	1.33	0.99	1.34	0.83	3.45	1.34	0.91
La_{CN}/Lu_{CN}	1.48	4.33	4.77	4.41	7.15	4.93	2.16	2.34	4.58	5.05	8.44	1.74	6.95	2.74	5.40	5.96	5.25
Eu anomaly	0.24	0.19	0.13	0.19	0.26	0.16	0.20	0.18	0.17	0.22	0.55	0.26	0.17	0.35	0.25	0.13	0.15
ΣREE+Y	258	669	604	567	327	609	954	480	470	402	92	391	626	167	234	85	390
TiO_2/Al_2O_3	0.01	0.02	0.02	0.02	0.01	0.02	0.01	0.02	0.02	0.02	0.04	0.04	0.02	0.02	0.02	0.00	0.01

Continue Table A1 - 5

	STONEPARK								SLIEVEDART										
sample ID	HK 198	HK 197	HK 209	HK 208	HK 207	HK 210	HK 212	HK 211	HK 190.1	HK 194.1	HK 189	HK 195	HK 237	HK 238	HK 188	HK 193.1	HK 192	HK 187	HK 191
hole number	2638-01	2638-01	2638-02	2638-02	2638-02	450-02	2654-01	2654-01	3470/15	3471/4	3470/15	3471/4	3470/15	3471/4	3470/15	3471/4	3471/4	3470/15	3471/4
sample number	62	63	64	65	66	67	68	69	70	71	72	73	74	75	76	77	78	79	80
Stratigraphic level	NMU	NMU	NMU	NMU	NMU	NMU	NMU	LG	KB	KB	KB	KB	KB	KB	KB	KB	KB	OP	OP
Li	56	49	48	110	113	11	64	36	117	113	100	92	27	32	155	176	172	84	69
Be	8.9	10.5	6.7	7.7	5.7	2.8	6.5	2.8	1.8	3.5	2.1	2.9	0.8	0.6	3.9	7.3	7.3	3.5	4.1
Mg	9747	9590	11101	9664	9668	13815	13838	22385	23489	21558	20119	17441	8752	10463	22995	23280	23402	19069	18234
Al	137674	156180	143673	91573	90206	149700	125461	205629	116509	119596	105715	95217	80285	82470	111026	110462	113145	113528	118250
P	639	446	1051	1088	1306	240	827	358	91	151	238	220	1054	1095	48	45	86	81	139
Ca	7839	2787	14708	17764	15190	14956	26400	4229	1766	3037	2167	21622	47216	36086	14358	1130	1472	8209	4918
Sc	4.8	3.1	8.9	13.0	11.9	3.1	7.9	8.5	6.6	7.2	5.0	5.1	4.0	4.8	1.3	1.7	1.2	1.6	1.8
Ti	3830	3492	7191	5328	5647	3174	6032	1531	745	921	3575	3718	1882	1900	1072	1189	1183	2414	2505
V	34.1	16.0	50.4	76.4	81.1	9.4	28.7	8.7	8.3	10.6	47.4	22.1	30.4	23.7	4.1	3.3	1.6	10.0	7.4
Cr	21.3	9.5	34.2	113.3	102.9	3.7	9.2	3.2	2.1	2.8	18.2	11.7	9.5	5.5	2.7	2.0	1.5	3.7	3.2
Fe	18930	17225	7521	20990	15281	14568	17352	18934	19612	16254	70136	94787	28120	27016	30163	18645	27398	58161	59159
Mn	39	16	52	107	510	88	119	7	148	118	376	493	155	128	325	49	23	913	1013
Co	9.0	3.5	1.6	10.3	9.3	17.8	48.8	35.3	4.5	4.3	9.0	12.0	13.4	12.5	4.1	2.8	3.3	0.3	0.3
Ni	194.2	81.3	47.9	77.4	77.9	107.1	325.4	367.0	36.3	37.2	104.3	128.3	61.3	71.2	41.4	41.7	64.8	19.3	17.2
Cu	9.1	-0.7	1.1	13.2	4.8	4.6	22.2	14.5	11.0	10.2	18.5	24.8	10.0	13.0	11.5	11.1	12.9	3.9	6.3
Zn	12.0	8.8	491.5	954.3	952.6	5.4	49.7	71.0	59.1	31.9	502.8	122.0	59.7	91.6	198.8	368.7	154.9	148.4	103.2
Ga	57.4	49.5	50.3	23.1	21.8	53.4	54.4	36.7	29.4	30.2	27.2	26.8	13.6	14.1	42.3	50.6	50.8	47.7	38.2
As	1.1	4.4	4.1	53.6	19.1	8.6	385.0	161.8	12.5	25.9	34.7	24.4	8.5	6.3	7.1	3.0	9.6	12.1	12.8
Rb	331	302	256	248	236	284	213	169	198	225	189	165	83	95	179	237	237	129	140
Sr	86	49	26	25	28	44	46	8	69	51	83	45	534	338	196	33	37	1049	141
Y	205	202	151	10	12	351	179	32	14	10	121	174	8	9	89	123	100	106	153
Zr	2592	1804	1850	162	190	4143	2477	187	109	129	1601	2045	101	97	668	804	671	3352	3518
Nb	214	173	268	17	18	287	313	69	31	41	40	91	6	8	287	307	364	255	248
Mo	0.6	0.3	0.7	0.2	0.2	1.6	0.5	6.5	5.0	4.2	17.6	16.7	3.8	3.3	13.4	5.5	9.6	15.5	15.7
Cd	0.6	0.4	0.5	0.1	0.9	0.9	0.8	0.7	0.3	0.2	3.3	1.0	0.1	0.2	0.6	0.9	0.5	1.2	1.4
In	0.1	0.1	0.1	0.0	0.0	0.2	0.3	0.1	0.1	0.1	0.2	0.1	0.0	0.0	0.3	0.4	0.3	0.2	0.1
Sn	28.7	18.7	19.6	3.0	2.8	23.9	23.4	17.1	7.0	8.3	4.3	4.5	0.5	0.7	24.6	49.1	32.5	8.9	7.1
Sb	0.3	0.9	0.3	1.4	1.1	0.8	2.3	1.8	0.7	1.2	2.8	1.8	0.4	0.3	0.7	0.4	0.6	2.5	2.8
Cs	25.7	21.5	22.6	35.0	33.2	4.5	17.3	17.9	41.0	30.0	47.6	19.1	4.7	3.5	26.7	17.9	17.3	27.9	17.1
Ba	441.3	337.2	191.5	248.1	271.9	75.3	128.8	78.6	75.6	83.0	45.3	42.1	1439.2	1329.5	39.8	44.6	53.0	32.9	36.3
La	134.6	28.9	51.9	41.8	46.4	20.3	200.0	27.0	9.7	6.5	113.3	70.3	8.4	6.9	27.2	16.9	47.0	57.9	101.9
Ce	283.0	61.9	111.6	51.6	55.6	45.8	475.8	60.9	21.4	14.0	259.8	154.3	15.9	14.2	59.3	38.2	103.7	170.6	272.0
Pr	31.9	6.8	12.2	4.9	5.6	6.4	55.6	7.3	2.6	1.7	33.2	19.8	2.2	2.2	6.7	4.7	11.8	25.3	35.1
Nd	106.2	22.8	43.4	12.0	14.9	36.8	203.8	26.9	9.3	6.3	121.2	76.6	8.9	9.0	21.6	16.9	38.4	111.7	134.1
Sm	21.4	8.7	11.9	1.5	1.8	24.1	41.0	5.9	2.1	1.4	27.0	23.0	1.8	2.0	5.5	5.9	8.8	31.3	36.0
Eu	0.7	0.9	1.1	0.2	0.3	1.9	3.1	0.1	0.1	0.1	2.9	2.1	0.7	0.7	0.4	0.6	0.6	1.2	1.6
Gd	21.2	15.4	15.0	1.4	1.7	35.0	36.1	5.6	2.0	1.4	25.3	28.0	1.6	1.9	6.6	8.4	8.9	26.3	33.9
Tb	4.5	4.2	3.3	0.2	0.3	7.2	6.3	1.0	0.4	0.3	4.0	5.2	0.2	0.3	1.8	2.4	2.2	4.2	5.7
Dy	33.2	32.8	24.3	1.6	1.9	49.7	37.9	6.5	2.5	1.9	22.3	32.1	1.4	1.6	13.8	19.1	16.3	23.1	32.5
Ho	8.1	8.0	5.7	0.4	0.4	10.9	7.4	1.3	0.5	0.4	4.3	6.4	0.3	0.3	3.3	4.7	3.8	4.4	6.2
Er	25.4	24.5	17.8	1.2	1.4	32.1	19.1	3.9	1.5	1.4	10.6	16.1	0.7	0.9	10.3	16.0	12.0	11.2	15.7
Tm	4.2	3.9	2.8	0.2	0.2	4.9	2.7	0.6	0.2	0.3	1.4	2.2	0.1	0.1	1.7	2.9	2.0	1.6	2.1
Yb	27.5	25.2	18.2	1.5	1.6	31.7	15.5	4.1	1.5	1.8	7.6	11.9	0.6	0.7	10.3	20.1	13.5	9.1	11.8
Lu	3.9	3.6	2.6	0.2	0.3	4.5	2.0	0.6	0.2	0.3	1.0	1.6	0.1	0.1	1.4	2.9	1.8	1.2	1.6
Hf	64.1	45.3	48.4	4.6	5.1	72.7	57.4	7.2	4.8	5.4	47.3	48.5	2.8	2.7	32.1	39.1	31.0	83.2	86.1
Ta	14.6	11.0	16.9	1.1	1.1	15.8	16.3	7.9	7.7	7.7	10.1	10.1	0.5	0.5	29.8	36.6	28.3	24.0	24.6
W	1.9	1.5	2.2	3.6	3.7	0.8	2.2	0.3	0.0	0.0	0.3	0.2	0.1	0.1	0.3	0.2	0.1	0.2	0.2
Tl	1.9	1.6	2.4	4.8	5.4	1.2	1.0	9.6	9.7	2.3	7.2	2.0	2.9	0.7	4.8	1.6	2.0	4.4	3.7
Pb	2.4	1.5	5.1	21.6	143.7	15.8	107.2	15.9	35.4	40.4	89.4	90.3	30.3	29.3	81.8	29.2	37.7	115.6	119.1
Th	67.3	39.1	46.4	11.1	12.0	71.1	44.4	31.3	18.2	22.3	41.8	41.2	6.4	6.8	56.6	70.0	61.6	82.6	86.7
U	11.3	6.4	9.8	1.7	1.7	34.5	12.8	13.4	2.4	8.8	8.0	9.5	1.6	1.5	4.6	9.7	8.1	5.4	8.4
La_{CN}/Sm_{CN}	3.93	2.08	2.72	17.75	16.09	0.53	3.04	2.87	2.92	2.84	2.62	1.91	2.84	2.12	3.07	1.79	3.35	1.15	1.77
Gd_{CN}/Lu_{CN}	0.67	0.53	0.71	0.68	0.83	0.96	2.20	1.22	1.23	0.67	3.08	2.23	2.14	2.22	0.59	0.37	0.60	2.63	2.68
La_{CN}/Lu_{CN}	3.55	0.84	2.08	17.80	18.61	0.47	10.20	4.96	4.94	2.63	11.58	4.70	9.20	6.72	2.03	0.61	2.65	4.87	6.78
Eu anomaly	0.10	0.25	0.24	0.52	0.51	0.20	0.24	0.06	0.17	0.29	0.33	0.26	1.14	1.02	0.21	0.24	0.21	0.12	0.14
ΣREE+Y	911	449	473	129	144	662	1285	184	68	48	755	623	51	50	259	282	371	585	843
TiO_2/Al_2O_3	0.02	0.02	0.04	0.05	0.06	0.02	0.04	0.01	0.01	0.01	0.03	0.03	0.02	0.02	0.01	0.01	0.01	0.02	0.02

9.2 Appendix 2 – LA-ICP-MS Geochemistry Data

Table A2 - 1: Zircon LA-ICP-MS U-Pb analytical results. Concentrations are in µg/g. P = correlation coefficient for $^{206}Pb/^{238}U$ vs $^{207}Pb/^{235}U$. P** = correlation coefficient for $^{238}U/^{206}Pb$ vs $^{207}Pb/^{206}Pb$ All errors are propagated errors at the 2SE level.*

							isotopic ratios										ages						
Grain-ID	Lab ID	# exp	U	Th	Pb	U/Th	$^{207}Pb/^{235}U$	± 2SE	$^{206}Pb/^{238}U$	± 2SE	ρ*	$^{238}U/^{206}Pb$	± 2SE	$^{207}Pb/^{206}Pb$	± 2SE	ρ**	$^{207}Pb/^{235}U$	± 2SE	$^{206}Pb/^{238}U$	± 2SE	$^{207}Pb/^{206}Pb$	± 2SE	Disc. %
Z_91500_0		1	80	30	15	2.63	1.837	0.079	0.180	0.006	0.553	5.552	0.188	0.075	0.003	0.312	1056	28	1067	33	1059	72	-4.5
Z_91500_1		1	80	30	15	2.69	1.793	0.084	0.181	0.006	0.215	5.540	0.187	0.072	0.003	0.344	1040	31	1069	33	966	88	18.0
Z_91500_2		1	79	30	14	2.69	1.854	0.086	0.174	0.006	0.167	5.744	0.185	0.077	0.003	0.330	1062	31	1034	31	1107	85	0.1
Z_91500_3		1	80	30	15	2.69	1.860	0.080	0.178	0.006	0.192	5.634	0.187	0.076	0.003	0.354	1065	29	1053	32	1078	78	-1.2
Z_91500_4		1	79	30	15	2.66	1.891	0.090	0.182	0.006	0.371	5.491	0.193	0.075	0.003	0.278	1074	32	1078	35	1073	79	-6.9
Z_91500_5		1	80	30	15	2.67	1.882	0.083	0.182	0.006	0.189	5.485	0.178	0.075	0.003	0.352	1072	29	1079	32	1048	80	-7.3
Z_91500_6		1	80	30	15	2.64	1.883	0.086	0.181	0.006	0.246	5.528	0.186	0.075	0.003	0.310	1072	30	1071	33	1065	84	-5.1
Z_91500_7		1	82	31	16	2.65	1.904	0.082	0.181	0.006	0.076	5.513	0.191	0.076	0.003	0.500	1080	29	1074	34	1083	84	-3.1
Z_91500_8		1	81	30	16	2.70	1.814	0.082	0.181	0.006	0.232	5.540	0.181	0.073	0.003	0.285	1048	30	1069	32	1010	76	13.0
Z_91500_9		1	80	30	15	2.69	1.767	0.078	0.176	0.006	0.115	5.682	0.184	0.073	0.003	0.445	1031	29	1045	31	997	93	13.0
Z_91500_10		1	80	30	15	2.66	1.838	0.085	0.180	0.006	0.069	5.571	0.180	0.074	0.003	0.401	1056	30	1064	32	1031	85	10.6
Z_91500_11		1	79	29	15	2.69	1.856	0.081	0.178	0.006	0.247	5.605	0.185	0.076	0.003	0.323	1063	29	1058	32	1068	79	-2.1
Z_91500_12		1	80	30	15	2.66	1.858	0.079	0.180	0.006	0.092	5.549	0.179	0.075	0.003	0.405	1064	28	1068	31	1050	78	-5.5
Z_91500_13		1	81	30	15	2.67	1.875	0.077	0.182	0.006	0.558	5.491	0.172	0.075	0.002	0.046	1070	27	1078	31	1051	63	-3.7
Z_91500_14		1	81	30	15	2.68	1.868	0.086	0.180	0.006	0.442	5.568	0.183	0.075	0.003	0.132	1067	30	1065	32	1066	74	-4.0
Z_91500_15		1	80	30	16	2.66	1.839	0.074	0.178	0.006	0.194	5.612	0.186	0.075	0.003	0.480	1058	26	1057	32	1056	73	-2.8
Z_91500_16		1	80	30	14	2.66	1.821	0.085	0.176	0.006	0.336	5.679	0.187	0.075	0.003	0.154	1055	29	1046	32	1052	83	-4.2
Z_91500_17		1	79	30	14	2.64	1.870	0.080	0.178	0.006	0.197	5.612	0.176	0.076	0.003	0.322	1073	26	1057	31	1078	77	0.5
Z_91500_0		2	78	29	16	2.65	1.934	0.068	0.181	0.004	0.084	5.534	0.116	0.078	0.003	0.376	1091	23	1070	21	1140	75	5.3
Z_91500_1		2	78	29	14	2.70	1.868	0.061	0.179	0.004	0.271	5.574	0.115	0.076	0.003	0.503	1069	22	1063	20	1083	73	-1.7
Z_91500_2		2	75	29	14	2.63	1.878	0.067	0.180	0.004	0.426	5.571	0.109	0.076	0.003	0.161	1074	23	1064	19	1084	73	-1.4
Z_91500_3		2	79	29	15	2.67	1.853	0.065	0.180	0.004	0.074	5.565	0.115	0.075	0.003	0.466	1065	22	1065	20	1082	74	0.2
Z_91500_4		2	78	29	14	2.66	1.839	0.063	0.177	0.003	0.370	5.637	0.108	0.075	0.003	0.236	1061	22	1052	18	1067	70	0.1
Z_91500_5		2	77	29	15	2.69	1.838	0.069	0.182	0.004	0.203	5.488	0.105	0.073	0.003	0.342	1057	25	1079	19	1004	78	-7.8
Z_91500_6		2	76	29	14	2.68	1.877	0.072	0.181	0.003	0.364	5.522	0.095	0.075	0.003	0.008	1071	25	1073	17	1053	77	-1.9
Z_91500_7		2	78	30	14	2.62	1.929	0.070	0.180	0.003	0.145	5.559	0.093	0.078	0.003	0.251	1089	24	1066	16	1133	74	3.2
Z_91500_8		2	84	31	16	2.67	1.881	0.068	0.179	0.003	0.144	5.599	0.100	0.076	0.003	0.187	1072	24	1059	18	1074	79	0.0
Z_91500_9		2	82	31	16	2.64	1.841	0.059	0.177	0.003	0.081	5.656	0.109	0.076	0.003	0.496	1059	21	1049	19	1077	79	0.8
Z_91500_10		2	83	31	15	2.61	1.803	0.057	0.177	0.003	0.195	5.640	0.105	0.074	0.003	0.425	1045	21	1052	18	1046	73	-2.3
Z_91500_11		2	81	30	15	2.69	1.840	0.062	0.178	0.004	0.347	5.627	0.120	0.075	0.003	0.407	1061	23	1054	21	1066	71	0.3
Z_91500_12		2	80	31	15	2.63	1.850	0.066	0.179	0.003	0.294	5.574	0.096	0.075	0.003	0.222	1062	24	1063	17	1060	72	-2.9
Z_91500_13		2	81	31	16	2.67	1.830	0.060	0.180	0.004	0.070	5.552	0.108	0.074	0.003	0.434	1058	22	1067	19	1047	75	-3.9
Z_91500_14		2	79	30	15	2.68	1.831	0.064	0.182	0.003	0.216	5.504	0.100	0.073	0.003	0.332	1055	23	1076	18	1011	71	-5.9
Z_91500_15		2	81	30	16	2.67	1.813	0.066	0.178	0.003	0.036	5.627	0.108	0.074	0.003	0.430	1051	25	1054	19	1053	83	-2.9
Z_91500_16		2	81	31	15	2.69	1.879	0.068	0.178	0.003	0.044	5.615	0.101	0.077	0.003	0.350	1072	24	1056	18	1109	82	5.2
Z_91500_17		2	79	30	14	2.67	1.837	0.057	0.178	0.003	0.019	5.609	0.101	0.074	0.003	0.495	1060	21	1057	18	1042	73	-2.0
Z_91500_18		2	81	30	15	2.67	1.825	0.060	0.180	0.003	0.310	5.559	0.096	0.073	0.003	0.167	1053	21	1066	17	1034	64	-3.2
Z_91500_19		2	85	32	16	2.69	1.895	0.066	0.180	0.003	0.187	5.543	0.101	0.076	0.003	0.336	1077	23	1069	18	1087	75	1.3
Z_91500_20		2	83	31	16	2.71	1.861	0.066	0.180	0.004	0.402	5.571	0.112	0.074	0.003	0.282	1068	24	1066	21	1057	75	-3.4
Z_91500_21		2	85	33	16	2.63	1.875	0.068	0.178	0.003	0.050	5.618	0.101	0.077	0.003	0.165	1070	24	1056	18	1091	81	2.1
Z_91500_22		2	85	32	16	2.67	1.851	0.072	0.179	0.003	0.063	5.599	0.103	0.075	0.003	0.249	1061	26	1059	18	1058	83	-2.0
Z_91500_23		2	87	32	15	2.70	1.822	0.061	0.176	0.003	0.110	5.688	0.110	0.075	0.003	0.347	1055	21	1044	18	1061	72	2.5
Z_91500_24		2	86	33	17	2.65	1.798	0.063	0.179	0.003	0.222	5.574	0.106	0.073	0.003	0.403	1048	24	1063	19	1004	77	-5.5
Z_91500_25		2	88	33	16	2.62	1.857	0.078	0.177	0.003	0.315	5.637	0.105	0.076	0.003	0.132	1073	28	1053	18	1105	84	1.1
Z_91500_26		2	85	32	16	2.66	1.814	0.064	0.181	0.004	0.048	5.531	0.116	0.073	0.003	0.518	1051	24	1071	21	985	82	-9.9
Z_91500_27		2	86	32	16	2.67	1.799	0.063	0.176	0.004	0.154	5.675	0.113	0.074	0.003	0.424	1043	23	1046	19	1028	79	-4.8
Z_91500_28		2	87	33	17	2.67	1.812	0.061	0.178	0.003	0.400	5.605	0.107	0.074	0.003	0.196	1048	22	1058	19	1022	70	-5.4
Z_91500_29		2	87	33	16	2.68	1.859	0.066	0.178	0.004	0.367	5.631	0.111	0.075	0.003	0.237	1067	23	1056	19	1076	73	-1.2
Z_91500_30		2	69	25	12	2.79	1.905	0.081	0.182	0.004	0.290	5.501	0.106	0.076	0.003	0.116	1079	28	1077	19	1086	83	-0.5
Z_91500_31		2	70	25	13	2.83	1.788	0.067	0.180	0.004	0.379	5.559	0.117	0.072	0.003	0.184	1039	24	1066	21	980	79	10.3
Z_91500_32		2	72	26	13	2.76	1.855	0.061	0.180	0.004	0.313	5.571	0.118	0.076	0.003	0.254	1067	20	1064	21	1101	76	-0.1
Z_91500_33		2	73	28	14	2.69	1.856	0.069	0.182	0.003	0.317	5.491	0.103	0.074	0.003	0.175	1066	25	1079	19	1035	75	-8.3
Z_91500_34		2	75	29	14	2.65	1.832	0.066	0.182	0.004	0.377	5.498	0.109	0.073	0.003	0.089	1055	24	1077	20	1006	76	-6.4
Z_91500_35		2	76	29	14	2.65	1.850	0.070	0.179	0.003	0.358	5.602	0.100	0.075	0.003	0.080	1061	25	1059	18	1048	77	-5.8
Z_91500_36		2	77	28	14	2.67	1.890	0.064	0.178	0.004	0.183	5.634	0.114	0.077	0.003	0.381	1076	22	1053	20	1116	71	4.1
Z_91500_37		2	78	30	15	2.63	1.877	0.069	0.180	0.003	0.222	5.549	0.099	0.076	0.003	0.297	1071	24	1068	17	1070	77	-1.9
Z_91500_38		2	81	31	15	2.60	1.840	0.061	0.180	0.003	0.430	5.571	0.106	0.075	0.003	0.147	1061	23	1066	18	1046	69	-3.1
Z_91500_39		2	82	32	16	2.63	1.847	0.084	0.177	0.004	0.268	5.653	0.112	0.076	0.003	0.192	1061	30	1050	19	1100	85	-0.2
Z_91500_40		2	85	32	16	2.64	1.857	0.062	0.179	0.004	0.549	5.602	0.129	0.076	0.003	0.174	1064	22	1059	22	1084	70	1.3
Z_91500_41		2	86	33	16	2.59	1.910	0.075	0.180	0.004	0.233	5.568	0.112	0.078	0.003	0.149	1082	26	1064	20	1117	80	5.3
Z_91500_42		2	84	32	17	2.63	1.906	0.066	0.181	0.004	0.028	5.537	0.107	0.077	0.003	0.481	1086	24	1072	19	1110	81	2.0
Z_91500_0		3	84	31	16	2.64	1.956	0.096	0.184	0.006	0.290	5.438	0.163	0.078	0.003	0.070	1097	33	1088	30	1118	83	2.9
Z_91500_1		3	83	31	16	2.70	1.795	0.085	0.175	0.005	0.581	5.721	0.157	0.074	0.003	0.062	1041	31	1038	26	1024	75	-4.2
Z_91500_2		3	81	30	15	2.71	1.855	0.078	0.180	0.005	0.197	5.565	0.149	0.075	0.003	0.496	1066	28	1065	26	1073	71	-1.5
Z_91500_3		3	82	31	15	2.62	1.844	0.079	0.181	0.005	0.523	5.540	0.141	0.075	0.002	0.254	1062	29	1070	25	1057	65	-4.9
Z_91500_4		3	79	30	15	2.64	1.816	0.080	0.180	0.005	0.440	5.549	0.163	0.074	0.003	0.335	1050	28	1067	29	1016	74	-7.7
Z_91500_5		3	78	28	14	2.69	1.833	0.088	0.180	0.005	0.450	5.565	0.146	0.074	0.003	0.112	1058	32	1065	26	1030	82	-8.4
Z_91500_6		3	84	32	15	2.62	1.910	0.130	0.182	0.006	0.805	5.498	0.178	0.075	0.004	0.413	1079	43	1077	32	1054	97	-1.9
Z_91500_7		3	90	34	16	2.65	1.796	0.100	0.178	0.007	0.603	5.605	0.220	0.074	0.004	0.232	1041	37	1058	38	1033	98	-3.1
Z_91500_8		3	79	29	15	2.67	1.812	0.083	0.179	0.005	0.187	5.593	0.156	0.074	0.003	0.493	1048	30	1060	27	1028	80	-5.4
Z_91500_9		3	79	29	15	2.68	1.842	0.079	0.181	0.005	0.338	5.540	0.157	0.074	0.003	0.300	1062	30	1069	28	1048	75	-3.8
Z_91500_10		3	81	30	15	2.66	1.814	0.081	0.176	0.005	0.501	5.672	0.161	0.075	0.003	0.282	1051	30	1047	28	1077	65	1.0
Z_91500_11		3	87	33	18	2.68	1.948	0.092	0.180	0.005	0.207	5.546	0.157	0.079	0.003	0.320	1104	32	1068	28	1182	86	6.8
Z_91500_12		3	88	33	17	2.66	1.813	0.087	0.176	0.006	0.276	5.682	0.181	0.075	0.003	0.352	1052	30	1045	31	1057	83	0.5
Z_91500_13		3	64	23	11	2.83	1.914	0.092	0.180	0.005	0.318	5.556	0.151	0.077	0.003	0.306	1083	32	1067	27	1120	83	1.2
Z_91500_14		3	65	25	12	2.81	1.833	0.080	0.181	0.005	0.363	5.540	0.150	0.074	0.003	0.296	1056	29	1069	27	1029	72	-7.5
Z_91500_15		3	72	30	15	2.53	1.871	0.083	0.182	0.005	0.443	5.507	0.152	0.074	0.003	0.352	1069	30	1075	27	1045	71	-7.1
Z_91500_16		3	84	37	20	2.47	1.856	0.087	0.176	0.005	0.391	5.682	0.152	0.077	0.003	0.115	1063	31	1045	26	1130	85	6.9
Z_91500_17		3	77	29	15	2.92	1.862	0.090	0.181	0.005	0.477	5.516	0.152	0.074	0.003	0.174	1071	32	1077	26	1040	78	-8.9
Z_91500_18		3	82	31	15	2.72	1.863	0.076	0.179	0.004	0.329	5.602	0.135	0.075	0.002	0.324	1067	27	1059	24	1066	66	-2.5
Z_91500_19		3	82	31	16	2.71	1.847	0.085	0.175	0.005	0.435	5.701	0.150	0.076	0.003	0.223	1060	30	1042	25	1109	71	5.4
Z_91500_20		3	78	30	14	2.68	1.871	0.081	0.180	0.005	0.275	5.552	0.154	0.075	0.003	0.472	1069	29	1067	27	1065	75	-4.3
Z_91500_21		3	80	30	15	2.70	1.825	0.089	0.177	0.005	0.193	5.643	0.146	0.075	0.003	0.319	1055	31	1051	25	1051	83	-2.5
Z_91500_22		3	82	30	15	2.66	1.816	0.082	0.177	0.005	0.262	5.637	0.146	0.074	0.003	0.320	1054	30	1053	26	1063	77	-1.2
Z_91500_23		3	82	31	15	2.65	1.865	0.090	0.179	0.005	0.429	5.583	0.150	0.075	0.003	0.218	1066	32	1062	27	1066	78	0.3
Z_91500_24		3	82	31	17	2.65	1.951	0.093	0.181	0.005	0.134	5.540	0.166	0.079	0.003	0.422	1096	32	1069	30	1165	72	7.9
Z_91500_25		3	85	32	16	2.65	1.792	0.076	0.179	0.005	0.376	5.602	0.157	0.073	0.002	0.429	1041	28	1058	28	1008	71	-6.3
Z_91500_26		3	83	31	15	2.69	1.858	0.077	0.179	0.005	0.502	5.596	0.141	0.075	0.002	0.232	1065	27	1060	25	1068	65	-1.4
Z_91500_27		3	82	31	16	2.63	1.877	0.084	0.179	0.005	0.377	5.590	0.147	0.076	0.003	0.434	1071	30	1061	26	1088	72	1.9
Z_91500_28		3	83	30	15	2.69	1.818	0.089	0.178	0.005	0.378	5.624	0.161	0.074	0.003	0.269	1049	32	1054	28	1052	82	-1.9
Z_91500_29		3	83	31	15	2.71	1.873	0.089	0.180	0.005	0.206	5.565	0.142	0.075	0.003	0.281	1072	32	1065	25	1078	84	-1.3
Z_91500_30		3	82	31	15	2.65	1.881	0.082	0.184	0.005	0.216	5.450	0.143	0.075	0.003	0.435	1073	29	1086	26	1066	71	-5.0
Z_91500_31		3	82	30	15	2.72	1.888	0.085	0.183	0.005	0.387	5.456	0.158	0.075	0.003	0.400	1075	30	1085	29	1086	78	-0.7
Z_91500_32		3	79	30	15	2.62	1.917	0.086	0.182	0.005	0.408	5.507	0.152	0.077	0.003	0.308	1088	31	1075	27	1107	71	-0.6
Z_91500_33		3	73	28	14	2.63	1.877	0.090	0.185	0.006	0.553	5.417	0.161	0.075	0.003	0.122	1073	31	1091	30	1060	73	-7.3
Z_91500_34		3	86	32	16	2.70	1.793	0.080	0.176	0.005	0.383	5.682	0.149	0.073	0.003	0.212	1044	30	1045	25	1023	68	-4.0
Z_91500_35		3	79	29	15	2.68	1.800	0.075	0.175	0.005	0.353	5.708	0.163	0.075	0.003	0.403	1044	27	1040	27	1070	70	-0.4
Z_91500_0		4	76	29	14	2.67	1.843	0.060	0.179	0.003	0.359	5.583	0.097	0.075	0.002	0.253	1058	21	1062	17	1070	64	0.4
Z_91500_1		4	91	34	17	2.67	1.841	0.046	0.181	0.004	0.548	5.531	0.125	0.074	0.002	0.341	1059	17	1071	22	1053	52	0.5
Z_91500_2		4	82	31	15	2.60	1.848	0.053	0.179	0.004	0.363	5.590	0.112	0.074	0.003	0.402	1066	19	1060	20	1036	66	0.4
Z_91500_3		4	87	33	17	2.62	1.869	0.051	0.180	0.004	0.201	5.552	0.126	0.077	0.003	0.489	1071	18	1067	22	1110	69	0.2
Z_91500_4		4	77	28	14	2.81	1.880	0.051	0.178	0.004	0.383	5.615	0.120	0.077	0.003	0.365	1075	19	1056	21	1108	64	0.4
Z_91500_5		4	83	35	17	2.48	1.861	0.061	0.178	0.003	0.239	5.618	0.085	0.076	0.003	0.212	1064	22	1056	15	1085	67	0.2
Z_91500_6		4	73	27	13	2.76	1.832	0.051	0.178	0.003	0.329	5.605	0.107	0.074	0.002	0.423	1055	18	1061	19	1031	61	0.3
Z_91500_7		4	70	26	13	2.77	1.838	0.051	0.180	0.003	0.440	5.556	0.102	0.074	0.002	0.259	1060	19	1067	18	1053	60	0.4
Z_91500_8		4	81	31	16	2.66	1.818	0.050	0.179	0.004	0.552	5.593	0.116	0.074	0.002	0.301	1052	18	1060	20	1047	53	0.6
Z_91500_9		4	86	33	16	2.66	1.854	0.043	0.180	0.003	0.322	5.556	0.086	0.075	0.002	0.290	1063	15	1067	15	1067	51	0.3
Z_91500_10		4	76	28	14	2.71	1.863	0.052	0.180	0.004	0.444	5.568	0.115	0.075	0.002	0.335	1066	18	1064	20	1073	54	0.4
Z_91500_11		4	89	34	18	2.59	1.877	0.053	0.180	0.003	0.473	5.562	0.105	0.076	0.002	0.321	1074	19	1065	19	1116	63	0.5
Z_91500_12		4	80	30	14	2.68	1.827	0.054	0.178	0.004	0.518	5.605	0.116	0.074	0.002	0.104	1053	19	1058	20	1056	60	0.5

Continue Table A2 - 1

							isotopic ratios										ages						
Grain-ID	Lab ID	# exp	U	Th	Pb	U/Th	$^{207}Pb/^{235}U$	± 2SE	$^{206}Pb/^{238}U$	± 2SE	ρ*	$^{238}U/^{206}Pb$	± 2SE	$^{207}Pb/^{206}Pb$	± 2SE	ρ**	$^{207}Pb/^{235}U$	± 2SE	$^{206}Pb/^{238}U$	± 2SE	$^{207}Pb/^{206}Pb$	± 2SE	Disc. %
WRS_0		1	87	92	22	0.94	0.681	0.040	0.085	0.003	0.215	11.710	0.411	0.058	0.003	0.269	530	22	528	18	490	120	-48
WRS_1		1	91	96	22	0.95	0.668	0.036	0.083	0.003	0.181	12.107	0.440	0.059	0.003	0.340	517	22	512	18	540	120	-19
WRS_2		1	106	122	28	0.86	0.687	0.030	0.086	0.003	0.359	11.614	0.391	0.058	0.002	0.229	533	20	532	17	521	85	-32
WRS_3		1	92	100	24	0.93	0.665	0.041	0.085	0.003	0.029	11.820	0.433	0.057	0.004	0.345	515	25	524	18	460	130	60
WRS_4		1	99	116	28	0.85	0.703	0.037	0.087	0.003	0.341	11.561	0.401	0.059	0.003	0.177	539	22	535	18	559	90	-24
WRS_5		1	86	94	24	0.92	0.677	0.040	0.088	0.003	0.054	11.390	0.389	0.056	0.003	0.415	527	26	543	18	440	130	4
WRS_6		1	89	94	23	0.94	0.667	0.037	0.083	0.003	0.006	12.048	0.450	0.059	0.003	0.497	517	22	514	19	510	120	-8
WRS_7		1	84	89	22	0.94	0.688	0.038	0.085	0.003	0.312	11.765	0.401	0.059	0.003	0.125	530	22	526	17	526	100	-29
WRS_8		1	87	93	23	0.94	0.670	0.043	0.084	0.003	0.077	11.933	0.384	0.058	0.004	0.338	518	26	519	16	490	130	-9
WRS_9		1	102	116	28	0.88	0.668	0.039	0.083	0.003	0.281	12.048	0.435	0.058	0.003	0.139	521	26	514	18	530	120	18
WRS_10		1	88	96	23	0.92	0.651	0.041	0.085	0.003	0.159	11.834	0.434	0.056	0.003	0.309	506	25	523	19	420	130	-31
WRS_11		1	86	91	22	0.94	0.655	0.040	0.086	0.003	0.365	11.682	0.423	0.056	0.003	0.043	509	25	529	18	400	110	-110
WRS_12		1	83	89	23	0.93	0.686	0.036	0.086	0.003	0.212	11.655	0.394	0.058	0.003	0.256	528	22	531	17	506	110	57
WRS_13		1	83	90	23	0.93	0.666	0.040	0.085	0.003	0.170	11.765	0.429	0.057	0.003	0.267	516	25	526	18	450	130	97
WRS_14		1	81	88	21	0.92	0.682	0.038	0.086	0.003	0.096	11.669	0.422	0.058	0.003	0.361	526	23	530	19	500	120	14
WRS_0		2	36	30	7	1.22	0.682	0.041	0.085	0.002	0.236	11.751	0.304	0.058	0.004	0.224	528	26	526	13	510	140	80
WRS_1		2	37	29	7	1.25	0.676	0.049	0.085	0.002	0.113	11.751	0.276	0.058	0.004	0.156	524	29	526	12	480	150	68
WRS_2		2	43	36	9	1.19	0.682	0.035	0.086	0.003	0.184	11.669	0.340	0.058	0.003	0.313	527	21	530	15	521	110	-47
WRS_3		2	40	33	8	1.20	0.660	0.041	0.084	0.002	0.233	11.933	0.313	0.058	0.004	0.105	517	27	519	13	520	140	-70
WRS_4		2	92	114	27	0.81	0.685	0.044	0.085	0.003	0.045	11.765	0.401	0.059	0.004	0.496	528	26	526	17	550	150	-7
WRS_5		2	45	41	10	1.13	0.697	0.040	0.087	0.002	0.203	11.534	0.239	0.058	0.003	0.166	534	24	536	11	480	120	22
WRS_6		2	38	32	7	1.23	0.678	0.044	0.085	0.002	0.298	11.710	0.329	0.057	0.004	0.133	526	27	528	14	500	140	60
WRS_7		2	49	39	9	1.26	0.683	0.056	0.086	0.003	0.104	11.669	0.408	0.058	0.005	0.473	526	34	530	18	590	160	33
WRS_8		2	41	33	9	1.25	0.689	0.038	0.086	0.002	0.232	11.614	0.297	0.058	0.003	0.254	530	23	532	13	490	120	23
WRS_9		2	38	31	7	1.24	0.666	0.038	0.085	0.002	0.186	11.710	0.302	0.056	0.003	0.324	526	24	528	13	420	120	24
WRS_10		2	40	33	8	1.25	0.686	0.053	0.086	0.003	0.026	11.696	0.342	0.060	0.005	0.349	532	33	529	15	530	180	88
WRS_11		2	39	31	8	1.23	0.682	0.055	0.085	0.002	0.077	11.710	0.329	0.057	0.005	0.320	524	33	528	14	530	180	80
WRS_12		2	39	31	8	1.25	0.678	0.048	0.085	0.002	0.259	11.751	0.318	0.057	0.004	0.136	525	28	526	14	460	150	14
WRS_13		2	48	39	10	1.21	0.669	0.040	0.084	0.003	0.096	11.876	0.367	0.057	0.004	0.337	519	25	521	15	510	150	53
WRS_14		2	32	27	7	1.24	0.679	0.080	0.084	0.002	0.198	11.862	0.267	0.058	0.007	0.023	521	49	522	12	460	240	-10
WRS_15		2	40	32	7	1.25	0.677	0.048	0.086	0.002	0.201	11.696	0.274	0.058	0.004	0.181	528	29	529	12	460	140	107
WRS_16		2	43	34	8	1.27	0.670	0.045	0.085	0.002	0.025	11.737	0.303	0.056	0.004	0.374	523	28	527	13	450	150	27
WRS_17		2	43	35	8	1.23	0.669	0.057	0.085	0.004	0.008	11.737	0.496	0.055	0.005	0.399	526	32	527	21	430	210	10
WRS_18		2	39	33	8	1.20	0.674	0.047	0.084	0.003	0.209	11.919	0.369	0.060	0.004	0.211	519	28	519	15	570	150	20
WRS_19		2	42	34	9	1.22	0.677	0.035	0.085	0.003	0.149	11.751	0.345	0.058	0.004	0.334	527	22	526	15	540	130	50
WRS_20		2	40	33	8	1.21	0.675	0.037	0.085	0.002	0.182	11.792	0.306	0.059	0.004	0.187	529	25	524	13	510	130	36
WRS_21		2	34	28	7	1.23	0.694	0.062	0.086	0.002	0.210	11.628	0.311	0.058	0.005	0.042	532	37	532	14	480	190	130
WRS_22		2	46	37	9	1.23	0.678	0.038	0.084	0.002	0.242	11.862	0.324	0.059	0.004	0.224	527	22	524	13	560	120	1
WRS_23		2	45	38	9	1.19	0.679	0.057	0.084	0.002	0.116	11.905	0.269	0.058	0.005	0.157	522	35	520	12	480	180	140
WRS_24		2	44	36	9	1.23	0.660	0.046	0.083	0.002	0.318	12.019	0.289	0.058	0.004	0.075	519	27	515	12	540	140	24
WRS_25		2	40	34	8	1.18	0.685	0.048	0.086	0.002	0.105	11.641	0.271	0.058	0.004	0.212	530	30	531	12	500	160	29
WRS_26		2	46	37	9	1.23	0.686	0.036	0.086	0.003	0.157	11.655	0.435	0.059	0.004	0.533	529	21	530	19	560	130	-10
WRS_27		2	42	34	8	1.23	0.683	0.039	0.086	0.002	0.117	11.682	0.273	0.058	0.004	0.206	529	24	529	12	490	140	50
WRS_28		2	44	35	9	1.25	0.674	0.047	0.085	0.002	0.057	11.806	0.335	0.058	0.004	0.383	520	29	524	15	510	170	-60
WRS_29		2	42	34	9	1.23	0.683	0.047	0.085	0.002	0.266	11.751	0.318	0.058	0.004	0.109	525	28	526	14	520	140	21
WRS_30		2	49	41	10	1.20	0.683	0.040	0.086	0.003	0.085	11.655	0.340	0.058	0.004	0.497	532	26	531	15	490	160	80
WRS_31		2	43	36	9	1.18	0.675	0.050	0.085	0.003	0.259	11.765	0.401	0.058	0.004	0.113	521	30	526	17	480	160	80
WRS_32		2	47	39	10	1.21	0.684	0.052	0.085	0.003	0.058	11.792	0.417	0.061	0.005	0.352	527	31	524	18	600	190	39
WRS_33		2	36	29	7	1.25	0.699	0.050	0.086	0.003	0.048	11.655	0.367	0.057	0.004	0.446	536	30	531	16	470	150	-170
WRS_34		2	42	34	8	1.24	0.689	0.048	0.085	0.002	0.042	11.751	0.318	0.057	0.004	0.389	528	29	526	14	480	160	30
WRS_35		2	44	36	8	1.23	0.663	0.038	0.084	0.003	0.394	11.976	0.402	0.057	0.003	0.215	514	23	517	17	500	120	-90
WRS_36		2	45	35	9	1.27	0.693	0.048	0.086	0.002	0.261	11.682	0.328	0.058	0.004	0.105	532	29	529	15	510	170	42
WRS_37		2	54	43	10	1.25	0.676	0.068	0.084	0.002	0.069	11.976	0.330	0.058	0.006	0.254	520	41	517	14	520	220	43
WRS_38		2	51	41	10	1.23	0.669	0.058	0.086	0.003	0.433	11.669	0.354	0.058	0.005	0.136	531	39	530	15	510	180	80
WRS_39		2	73	80	19	0.94	0.657	0.038	0.083	0.002	0.305	12.034	0.304	0.056	0.003	0.078	515	22	514	13	490	130	38
WRS_40		2	53	45	12	1.20	0.648	0.050	0.083	0.002	0.108	11.990	0.345	0.058	0.005	0.252	517	30	516	15	470	180	96
WRS_41		2	53	41	10	1.27	0.664	0.041	0.083	0.003	0.010	12.019	0.477	0.059	0.005	0.479	516	25	515	20	510	170	80
WRS_42		2	48	39	9	1.26	0.659	0.046	0.083	0.002	0.159	12.092	0.322	0.056	0.004	0.209	511	28	512	13	450	140	22
WRS_43		2	48	39	9	1.24	0.672	0.038	0.083	0.002	0.093	11.990	0.316	0.058	0.003	0.304	520	23	516	13	500	130	80
WRS_44		2	44	36	9	1.25	0.686	0.045	0.085	0.002	0.292	11.765	0.263	0.058	0.004	0.027	526	27	526	11	510	130	56
WRS_0		3	41	32	8	1.24	0.673	0.041	0.084	0.002	0.063	11.848	0.337	0.058	0.003	0.308	520	25	522	14	480	120	-2
WRS_1		3	40	34	8	1.20	0.687	0.048	0.086	0.003	0.008	11.682	0.368	0.060	0.004	0.479	532	30	529	16	550	160	39
WRS_2		3	39	32	9	1.22	0.701	0.048	0.086	0.003	0.089	11.669	0.368	0.059	0.004	0.285	536	29	530	16	520	150	50
WRS_3		3	43	35	9	1.23	0.681	0.044	0.085	0.002	0.223	11.765	0.332	0.056	0.004	0.120	530	28	526	14	490	130	29
WRS_4		3	43	35	9	1.22	0.676	0.043	0.085	0.003	0.143	11.723	0.371	0.057	0.004	0.465	522	26	527	16	490	140	44
WRS_5		3	44	36	10	1.21	0.698	0.045	0.086	0.003	0.215	11.628	0.352	0.058	0.003	0.224	535	27	532	15	550	120	34
WRS_6		3	44	36	9	1.20	0.682	0.040	0.084	0.002	0.337	11.891	0.339	0.059	0.003	0.058	526	24	521	14	583	93	-6
WRS_7		3	39	32	8	1.24	0.686	0.051	0.085	0.003	0.170	11.820	0.377	0.059	0.004	0.247	527	31	524	16	530	160	21
WRS_8		3	40	33	8	1.20	0.682	0.063	0.085	0.003	0.297	11.710	0.452	0.059	0.005	0.173	531	41	528	19	580	190	64
WRS_9		3	43	36	9	1.19	0.670	0.041	0.085	0.002	0.229	11.792	0.334	0.057	0.003	0.259	521	24	524	14	430	130	89
WRS_10		3	39	32	8	1.22	0.674	0.049	0.085	0.003	0.747	11.710	0.425	0.057	0.004	0.229	520	30	523	13	500	150	42
WRS_11		3	43	36	9	1.19	0.689	0.041	0.085	0.002	0.201	11.710	0.315	0.059	0.003	0.156	530	24	529	14	560	110	28
WRS_12		3	39	33	8	1.18	0.702	0.045	0.087	0.002	0.046	11.481	0.316	0.059	0.004	0.297	538	27	538	14	560	130	29
WRS_13		3	39	31	8	1.21	0.696	0.048	0.086	0.003	0.073	11.587	0.363	0.059	0.004	0.307	537	28	533	16	540	150	73
WRS_14		3	40	32	7	1.22	0.684	0.044	0.085	0.003	0.185	11.820	0.349	0.059	0.004	0.512	527	26	523	15	550	140	-1
WRS_15		3	42	35	9	1.18	0.683	0.041	0.087	0.002	0.065	11.561	0.321	0.059	0.004	0.294	530	26	535	14	570	120	32
WRS_16		3	41	35	9	1.19	0.673	0.051	0.085	0.003	0.070	11.737	0.427	0.060	0.005	0.478	526	33	527	18	570	170	-1
WRS_17		3	39	32	9	1.24	0.686	0.056	0.085	0.003	0.048	11.710	0.466	0.059	0.005	0.355	528	34	528	20	570	180	-120
WRS_18		3	42	34	8	1.24	0.686	0.046	0.086	0.002	0.298	11.696	0.328	0.057	0.003	0.129	527	28	529	14	460	130	30
WRS_19		3	44	37	9	1.28	0.684	0.055	0.087	0.003	0.245	11.561	0.374	0.057	0.004	0.117	532	32	535	16	440	150	120
WRS_20		3	40	33	8	1.29	0.667	0.049	0.085	0.003	0.045	11.820	0.349	0.058	0.004	0.357	521	31	524	15	490	160	92
WRS_21		3	38	31	8	1.31	0.676	0.042	0.085	0.002	0.274	11.751	0.318	0.059	0.003	0.051	525	25	528	14	510	110	28
WRS_22		3	43	33	8	1.34	0.675	0.042	0.085	0.003	0.112	11.834	0.350	0.058	0.004	0.277	524	25	523	15	510	140	41
WRS_23		3	39	32	8	1.27	0.678	0.064	0.086	0.003	0.218	11.669	0.381	0.057	0.005	0.148	531	42	530	17	500	210	54
WRS_24		3	40	33	8	1.30	0.686	0.046	0.086	0.003	0.172	11.655	0.340	0.058	0.004	0.291	532	27	530	15	480	130	-9
WRS_25		3	40	32	7	1.25	0.662	0.053	0.084	0.003	0.306	11.933	0.384	0.059	0.004	0.000	524	32	523	16	510	150	60
WRS_26		3	39	31	7	1.28	0.686	0.040	0.085	0.003	0.065	11.779	0.375	0.059	0.003	0.345	528	24	525	16	530	130	15
WRS_27		3	43	35	8	1.24	0.673	0.053	0.084	0.003	0.414	11.891	0.382	0.058	0.004	0.030	519	32	521	16	480	150	62
WRS_28		3	41	33	9	1.23	0.671	0.041	0.084	0.002	0.133	11.862	0.338	0.058	0.003	0.284	519	25	522	14	500	130	440
WRS_29		3	41	34	8	1.22	0.665	0.044	0.086	0.003	0.029	11.614	0.351	0.057	0.004	0.412	528	27	532	16	460	140	96
WRS_30		3	39	32	7	1.23	0.669	0.047	0.085	0.003	0.141	11.737	0.344	0.058	0.004	0.196	526	29	529	14	500	130	66
WRS_31		3	44	35	8	1.24	0.687	0.039	0.086	0.002	0.134	11.655	0.326	0.058	0.003	0.348	529	24	531	14	540	120	2
WRS_32		3	43	35	9	1.22	0.695	0.061	0.085	0.003	0.151	11.737	0.386	0.060	0.005	0.167	530	37	527	17	540	180	39
WRS_33		3	39	31	7	1.26	0.687	0.054	0.085	0.003	0.192	11.710	0.343	0.057	0.004	0.242	527	32	530	16	490	160	0
WRS_34		3	39	31	7	1.25	0.669	0.049	0.085	0.003	0.384	11.806	0.376	0.056	0.003	0.014	521	29	524	16	470	140	-16
WRS_35		3	46	37	9	1.24	0.664	0.036	0.084	0.003	0.146	11.919	0.455	0.058	0.003	0.461	516	22	519	19	510	120	-60
WRS_36		3	40	32	8	1.26	0.665	0.047	0.084	0.003	0.007	11.848	0.365	0.057	0.004	0.397	523	26	522	15	470	150	55
WRS_37		3	45	36	9	1.21	0.673	0.045	0.084	0.002	0.124	11.848	0.323	0.057	0.004	0.210	523	27	522	14	470	130	89
WRS_38		3	44	35	8	1.21	0.654	0.045	0.085	0.003	0.262	11.820	0.377	0.057	0.003	0.158	515	27	523	16	490	120	37
WRS_39		3	40	32	8	1.23	0.672	0.047	0.085	0.002	0.058	11.806	0.321	0.056	0.004	0.350	522	29	524	14	450	150	190
WRS_40		3	41	33	8	1.25	0.707	0.039	0.084	0.002	0.105	11.919	0.327	0.062	0.003	0.297	544	24	519	14	636	110	80
WRS_41		3	41	33	8	1.24	0.674	0.050	0.084	0.002	0.223	11.848	0.323	0.058	0.004	0.039	518	30	522	14	500	140	56
WRS_42		3	39	31	7	1.24	0.688	0.041	0.086	0.002	0.015	11.641	0.325	0.057	0.004	0.381	529	25	531	14	490	130	62
WRS_0		4	58	49	11	1.15	0.662	0.034	0.084	0.001	0.415	11.947	0.200	0.057	0.003	0.132	518	20	518	9	450	120	0.4
WRS_1		4	49	41	10	1.18	0.665	0.042	0.084	0.002	0.189	11.947	0.328	0.057	0.004	0.227	517	25	518	14	490	130	0.2
WRS_2		4	53	45	10	1.16	0.697	0.031	0.086	0.002	0.113	11.614	0.243	0.058	0.003	0.346	535	19	534	11	529	100	0.1
WRS_3		4	52	39	10	1.29	0.696	0.039	0.086	0.002	0.234	11.641	0.257	0.059	0.003	0.155	532	24	531	11	550	130	0.2
WRS_4		4	50	40	10	1.26	0.687	0.036	0.086	0.002	0.232	11.628	0.297	0.059	0.003	0.288	531	21	531	13	550	120	0.2
WRS_5		4	52	40	10	1.27	0.683	0.028	0.085	0.002	0.262	11.806	0.265	0.057	0.002	0.353	527	17	524	11	491	93	0.3
WRS_6		4	52	42	9	1.23	0.664	0.036	0.083	0.002	0.152	11.990	0.230	0.058	0.004	0.328	514	22	516	10	480	130	-0.2
WRS_7		4	47	40	9	1.20	0.697	0.047	0.085	0.002	0.259	11.723	0.330	0.059	0.004	0.139	534	28	527	14	520	150	0.3
WRS_8		4	47	37	9	1.26	0.659	0.039	0.083	0.002	0.035	12.034	0.261	0.057	0.004	0.394	511	24	515	11	470	140	0.0
WRS_9		4	52	46	10	1.13	0.683	0.032	0.084	0.002	0.073	11.876	0.254	0.058	0.003	0.323	526	20	521	11	520	120	0.1
WRS_10		4	49	44	10	1.12	0.682	0.039	0.085	0.002	0.047	11.723	0.261	0.058	0.004	0.301	524	24	527	11	490	130	0.0
WRS_11		4	52	46	11	1.14	0.677	0.042	0.083	0.002	0.079	11.990	0.230	0.059	0.004	0.303	522	26	517	9	550	130	0.1
WRS_12		4	44	38	9	1.23	0.672	0.036	0.085	0.002	0.012	11.737	0.234	0.058	0.004	0.318	524	21	527	10	500	130	0.0
WRS_13		4	49	41	10	1.24	0.683	0.026	0.086	0.002	0.199	11.628	0.257	0.057	0.002	0.272	527	16	532	11	489	100	0.2
WRS_14		4	47	38	9	1.29	0.656	0.029	0.084	0.002	0.150	11.962	0.300	0.055	0.003	0.221	514	19	518	13	420	120	0.1
WRS_15		4	43	33	8	1.31	0.680	0.044	0.084	0.002	0.160	11.862	0.253	0.057	0.004	0.168	527	28	522	11	510	150	0.2

Continue Table A2 - 1

							isotopic ratios										ages						
Grain-ID	Lab ID	# exp	U	Th	Pb	U/Th	$^{207}Pb/^{235}U$	± 2SE	$^{206}Pb/^{238}U$	± 2SE	ρ*	$^{238}U/^{206}Pb$	± 2SE	$^{207}Pb/^{206}Pb$	± 2SE	ρ**	$^{207}Pb/^{235}U$	± 2SE	$^{206}Pb/^{238}U$	± 2SE	$^{207}Pb/^{206}Pb$	± 2SE	Disc. %
Z_Plesovice_0		1	1122	146	22	7.67	0.401	0.016	0.054	0.002	0.611	18.484	0.615	0.054	0.002	0.216	342	12	340	11	349	67	-17
Z_Plesovice_1		1	1085	145	82	7.47	0.651	0.026	0.058	0.002	0.409	17.153	0.618	0.081	0.003	0.434	508	16	365	13	1212	66	69
Z_Plesovice_2		1	1065	138	22	7.70	0.396	0.016	0.054	0.002	0.629	18.553	0.654	0.053	0.002	0.378	339	12	338	12	319	70	-20
Z_Plesovice_3		1	1040	136	22	7.60	0.398	0.014	0.054	0.002	0.238	18.584	0.587	0.054	0.002	0.557	340	10	338	11	349	67	-16
Z_Plesovice_4		1	906	113	100	7.99	0.823	0.039	0.057	0.002	0.544	17.443	0.548	0.103	0.004	0.112	608	22	359	11	1681	78	78
Z_Plesovice_5		1	878	107	17	8.17	0.395	0.016	0.055	0.002	0.569	18.282	0.602	0.052	0.002	0.148	338	12	343	11	308	74	-13
Z_Plesovice_6		1	1115	143	22	7.80	0.393	0.015	0.053	0.002	0.347	18.939	0.646	0.054	0.002	0.514	336	11	332	11	363	71	-23
Z_Plesovice_7		1	1081	140	22	7.71	0.397	0.016	0.055	0.002	0.585	18.328	0.571	0.053	0.002	0.197	339	11	342	11	320	67	-29
Z_Plesovice_8		1	981	123	19	7.95	0.407	0.016	0.056	0.002	0.519	17.947	0.580	0.053	0.002	0.239	346	11	350	11	320	68	51
Z_Plesovice_9		1	1142	149	23	7.62	0.392	0.015	0.053	0.002	0.383	18.914	0.608	0.054	0.002	0.363	335	11	332	10	351	71	27
Z_Plesovice_10		1	1050	141	96	7.43	0.701	0.039	0.056	0.002	0.379	17.889	0.576	0.091	0.004	0.007	537	23	351	11	1417	91	75
Z_Plesovice_11		1	1098	151	23	7.29	0.387	0.015	0.054	0.002	0.408	18.591	0.588	0.052	0.002	0.202	332	11	338	10	284	70	-110
Z_Plesovice_12		1	842	101	16	8.33	0.389	0.016	0.053	0.002	0.308	18.709	0.595	0.053	0.002	0.303	333	12	336	11	311	75	-5
Z_Plesovice_13		1	960	121	19	8.02	0.392	0.015	0.055	0.002	0.465	18.182	0.628	0.052	0.002	0.415	335	11	345	12	278	72	80
Z_Plesovice_14		1	1085	147	24	7.37	0.393	0.014	0.054	0.002	0.510	18.505	0.548	0.053	0.001	0.055	336	10	339	10	320	61	-34
Z_Plesovice_0		2	539	50	8	10.74	0.394	0.012	0.053	0.001	0.157	18.904	0.347	0.054	0.002	0.508	338	9	332	6	341	73	-15
Z_Plesovice_1		2	604	58	9	10.48	0.391	0.014	0.054	0.001	0.351	18.539	0.378	0.053	0.002	0.232	335	10	339	7	309	83	-29
Z_Plesovice_2		2	506	46	7	10.81	0.394	0.014	0.053	0.001	0.369	18.748	0.351	0.054	0.002	0.219	338	10	335	6	366	79	-12
Z_Plesovice_3		2	510	47	7	10.87	0.399	0.014	0.054	0.001	0.343	18.608	0.381	0.053	0.002	0.206	340	10	337	7	322	81	-42
Z_Plesovice_4		2	488	44	7	10.86	0.393	0.013	0.054	0.001	0.002	18.580	0.325	0.053	0.002	0.505	337	9	338	6	328	81	-26
Z_Plesovice_5		2	517	48	8	10.81	0.391	0.014	0.054	0.001	0.376	18.660	0.383	0.053	0.002	0.225	335	10	337	7	324	78	-16
Z_Plesovice_6		2	522	48	8	10.70	0.397	0.015	0.054	0.001	0.315	18.474	0.321	0.053	0.002	0.162	339	11	340	6	335	78	16
Z_Plesovice_7		2	489	46	7	10.61	0.395	0.013	0.054	0.001	0.282	18.605	0.346	0.053	0.002	0.256	338	10	338	6	333	78	-17
Z_Plesovice_8		2	555	53	8	10.78	0.399	0.012	0.054	0.001	0.401	18.529	0.336	0.054	0.002	0.342	341	9	339	6	352	71	3
Z_Plesovice_9		2	571	53	9	10.81	0.392	0.013	0.054	0.001	0.343	18.643	0.348	0.053	0.002	0.283	335	10	337	6	322	77	30
Z_Plesovice_10		2	527	49	8	10.75	0.387	0.013	0.054	0.001	0.350	18.650	0.348	0.052	0.002	0.185	332	9	337	6	295	85	-60
Z_Plesovice_11		2	560	54	8	10.55	0.389	0.015	0.053	0.001	0.310	18.861	0.356	0.052	0.002	0.173	333	11	333	6	290	84	33
Z_Plesovice_12		2	559	53	8	10.55	0.397	0.013	0.054	0.001	0.276	18.467	0.341	0.052	0.002	0.359	340	10	340	6	299	83	-27
Z_Plesovice_13		2	485	45	7	10.66	0.392	0.015	0.053	0.001	0.210	18.769	0.387	0.054	0.002	0.336	337	11	335	6	351	87	42
Z_Plesovice_14		2	473	45	8	10.63	0.393	0.014	0.054	0.001	0.553	18.657	0.348	0.053	0.002	0.014	338	10	337	6	304	81	-40
Z_Plesovice_15		2	536	50	8	10.70	0.396	0.013	0.054	0.001	0.331	18.505	0.377	0.053	0.002	0.410	339	10	339	7	318	81	-23
Z_Plesovice_16		2	555	53	9	10.64	0.391	0.012	0.054	0.001	0.255	18.612	0.346	0.053	0.002	0.419	336	9	337	6	333	79	-4
Z_Plesovice_17		2	579	55	9	10.53	0.396	0.014	0.053	0.001	0.364	18.720	0.385	0.054	0.002	0.157	340	11	335	6	373	87	30
Z_Plesovice_18		2	591	55	8	10.82	0.395	0.014	0.054	0.001	0.411	18.498	0.376	0.053	0.002	0.166	338	10	339	7	305	77	-10
Z_Plesovice_19		2	620	59	9	10.51	0.393	0.012	0.054	0.001	0.185	18.460	0.334	0.053	0.002	0.315	336	9	340	6	303	73	-45
Z_Plesovice_20		2	474	43	7	10.96	0.390	0.013	0.053	0.001	0.028	18.829	0.355	0.052	0.002	0.527	334	10	334	6	283	85	20
Z_Plesovice_21		2	423	39	6	10.83	0.399	0.015	0.054	0.001	0.040	18.488	0.376	0.054	0.002	0.522	341	11	340	7	348	99	10
Z_Plesovice_22		2	548	51	8	11.03	0.395	0.015	0.053	0.001	0.465	18.723	0.386	0.054	0.002	0.093	338	11	335	7	355	89	-18
Z_Plesovice_23		2	520	48	8	10.89	0.385	0.014	0.053	0.001	0.034	18.961	0.360	0.053	0.002	0.438	330	10	331	6	307	92	130
Z_Plesovice_24		2	496	46	8	10.82	0.389	0.014	0.053	0.001	0.152	18.702	0.322	0.052	0.002	0.305	334	10	336	6	289	82	39
Z_Plesovice_25		2	570	52	8	10.96	0.394	0.014	0.053	0.001	0.502	18.723	0.386	0.053	0.002	0.235	337	10	335	7	332	72	-16
Z_Plesovice_26		2	606	56	9	10.73	0.398	0.013	0.054	0.001	0.428	18.608	0.381	0.053	0.002	0.277	340	10	337	7	322	75	-18
Z_Plesovice_27		2	502	46	7	11.01	0.389	0.013	0.054	0.001	0.433	18.692	0.328	0.052	0.002	0.147	333	9	336	6	303	74	-55
Z_Plesovice_28		2	410	36	6	11.30	0.401	0.014	0.054	0.001	0.059	18.450	0.374	0.053	0.002	0.484	343	11	340	7	333	85	0
Z_Plesovice_29		2	456	41	6	11.30	0.397	0.014	0.054	0.001	0.196	18.580	0.380	0.053	0.002	0.387	339	10	338	7	326	89	47
Z_Plesovice_30		2	500	45	7	11.12	0.392	0.015	0.053	0.001	0.405	19.011	0.470	0.054	0.002	0.258	335	11	331	8	364	81	-7
Z_Plesovice_31		2	473	44	7	10.82	0.401	0.014	0.054	0.001	0.351	18.508	0.377	0.053	0.002	0.348	342	10	339	7	328	82	-32
Z_Plesovice_32		2	476	43	7	11.10	0.399	0.014	0.054	0.001	0.251	18.437	0.374	0.053	0.002	0.370	341	10	341	7	302	83	6
Z_Plesovice_33		2	561	51	8	11.04	0.394	0.014	0.053	0.001	0.259	18.871	0.356	0.054	0.002	0.341	337	10	333	6	348	81	86
Z_Plesovice_34		2	583	54	9	10.79	0.391	0.012	0.053	0.001	0.293	18.808	0.350	0.053	0.002	0.331	335	9	334	6	315	74	20
Z_Plesovice_35		2	588	53	8	11.05	0.390	0.014	0.053	0.001	0.197	18.929	0.394	0.054	0.002	0.465	334	10	332	7	357	87	-62
Z_Plesovice_36		2	553	51	8	10.85	0.385	0.013	0.053	0.001	0.308	19.011	0.398	0.053	0.002	0.445	331	10	330	7	299	81	-52
Z_Plesovice_37		2	608	56	8	11.00	0.387	0.014	0.053	0.001	0.153	18.864	0.391	0.053	0.002	0.484	332	10	333	7	312	98	8
Z_Plesovice_38		2	709	68	11	10.60	0.394	0.016	0.053	0.001	0.552	18.797	0.459	0.053	0.002	0.163	337	12	334	8	315	86	-39
Z_Plesovice_39		2	679	62	10	10.69	0.392	0.012	0.053	0.001	0.506	18.716	0.385	0.053	0.002	0.679	335	9	336	7	324	77	59
Z_Plesovice_40		2	583	55	9	10.73	0.386	0.013	0.052	0.001	0.352	19.102	0.350	0.054	0.002	0.195	332	10	329	6	353	70	-6
Z_Plesovice_41		2	561	51	8	11.11	0.392	0.013	0.053	0.001	0.399	18.822	0.333	0.054	0.002	0.181	335	10	334	6	363	73	-6
Z_Plesovice_42		2	626	57	9	11.10	0.387	0.016	0.053	0.001	0.573	18.975	0.468	0.053	0.002	0.195	332	12	331	8	324	89	10
Z_Plesovice_43		2	551	51	8	11.08	0.391	0.015	0.053	0.001	0.392	18.993	0.397	0.054	0.002	0.163	335	11	331	7	358	85	-49
Z_Plesovice_44		2	572	51	8	11.23	0.383	0.013	0.053	0.001	0.412	19.008	0.397	0.053	0.002	0.321	329	10	331	7	332	79	7
Z_Plesovice_45		2	505	45	8	11.16	0.392	0.013	0.054	0.001	0.143	18.681	0.384	0.053	0.002	0.459	335	10	336	7	322	89	0
Z_Plesovice_46		2	551	50	8	11.07	0.390	0.012	0.053	0.001	0.096	18.847	0.391	0.053	0.002	0.523	334	9	333	7	334	83	-61
Z_Plesovice_47		2	672	64	10	10.50	0.395	0.012	0.053	0.001	0.338	18.755	0.295	0.054	0.002	0.204	338	9	335	5	353	71	-13
Z_Plesovice_0		3	510	47	8	10.75	0.401	0.016	0.055	0.001	0.361	18.222	0.465	0.054	0.002	0.483	344	12	344	9	354	71	-15
Z_Plesovice_1		3	1022	154	25	6.58	0.398	0.016	0.054	0.001	0.694	18.386	0.439	0.053	0.002	0.140	340	11	341	8	313	65	-26
Z_Plesovice_2		3	1006	150	24	6.52	0.396	0.015	0.054	0.001	0.583	18.440	0.442	0.054	0.002	0.372	339	11	340	8	363	66	-19
Z_Plesovice_3		3	612	61	9	9.98	0.392	0.016	0.054	0.001	0.370	18.580	0.483	0.053	0.002	0.354	336	12	338	8	312	73	-4
Z_Plesovice_4		3	554	53	9	10.28	0.396	0.017	0.054	0.001	0.467	18.413	0.475	0.052	0.002	0.101	339	13	341	9	289	80	-60
Z_Plesovice_5		3	657	62	10	10.43	0.391	0.016	0.054	0.001	0.332	18.605	0.450	0.053	0.002	0.288	335	12	338	8	314	75	-17
Z_Plesovice_6		3	606	57	9	10.69	0.394	0.016	0.054	0.001	0.329	18.501	0.479	0.053	0.002	0.492	337	12	339	9	318	79	-20
Z_Plesovice_7		3	818	106	16	7.84	0.396	0.016	0.054	0.001	0.414	18.615	0.450	0.053	0.002	0.388	339	12	337	8	347	72	-12
Z_Plesovice_8		3	533	50	8	10.80	0.397	0.016	0.054	0.001	0.441	18.525	0.480	0.053	0.002	0.386	339	12	339	8	332	69	-5
Z_Plesovice_9		3	566	53	8	10.48	0.397	0.018	0.054	0.002	0.353	18.355	0.505	0.052	0.002	0.312	340	13	342	9	288	80	-45
Z_Plesovice_10		3	605	57	9	10.66	0.389	0.015	0.053	0.001	0.323	18.836	0.497	0.053	0.002	0.377	334	11	334	9	347	81	-3
Z_Plesovice_11		3	636	62	9	10.31	0.401	0.018	0.055	0.001	0.420	18.302	0.469	0.054	0.002	0.163	342	13	343	9	350	83	-3
Z_Plesovice_12		3	628	60	10	10.42	0.392	0.016	0.053	0.001	0.369	18.864	0.463	0.053	0.002	0.386	336	12	333	8	343	72	-41
Z_Plesovice_13		3	577	55	9	10.46	0.397	0.017	0.055	0.001	0.341	18.288	0.435	0.053	0.002	0.297	339	12	343	8	322	71	-13
Z_Plesovice_14		3	679	69	11	9.87	0.402	0.016	0.054	0.001	0.398	18.372	0.439	0.054	0.002	0.288	343	12	342	8	351	77	-33
Z_Plesovice_15		3	445	41	6	11.08	0.401	0.018	0.055	0.001	0.307	18.349	0.471	0.054	0.002	0.241	342	13	343	9	354	90	-100
Z_Plesovice_16		3	428	39	6	11.19	0.399	0.017	0.054	0.001	0.443	18.454	0.477	0.053	0.002	0.313	341	12	340	9	308	76	-59
Z_Plesovice_17		3	490	45	7	11.06	0.398	0.017	0.054	0.001	0.558	18.505	0.479	0.053	0.002	0.156	340	12	339	9	325	72	-27
Z_Plesovice_18		3	495	46	8	11.68	0.405	0.018	0.055	0.001	0.098	18.235	0.466	0.053	0.002	0.470	345	13	344	9	345	83	78
Z_Plesovice_19		3	550	51	7	11.71	0.394	0.017	0.054	0.001	0.398	18.556	0.448	0.053	0.002	0.309	337	12	338	8	339	77	-44
Z_Plesovice_20		3	543	51	8	11.50	0.400	0.017	0.055	0.001	0.403	18.258	0.433	0.053	0.002	0.207	342	12	344	8	332	74	-34
Z_Plesovice_21		3	574	54	8	11.35	0.387	0.016	0.052	0.001	0.170	19.066	0.509	0.053	0.002	0.637	332	12	330	9	330	75	-52
Z_Plesovice_22		3	525	48	7	11.79	0.390	0.017	0.053	0.001	0.288	19.040	0.508	0.055	0.002	0.296	334	13	330	8	380	83	23
Z_Plesovice_23		3	477	43	6	10.97	0.383	0.017	0.052	0.001	0.424	19.113	0.475	0.052	0.002	0.222	330	13	329	8	306	72	-12
Z_Plesovice_24		3	488	45	7	10.92	0.398	0.017	0.054	0.001	0.281	18.546	0.447	0.054	0.002	0.330	341	13	339	8	338	77	-39
Z_Plesovice_25		3	510	45	7	11.11	0.394	0.017	0.053	0.001	0.058	18.843	0.497	0.054	0.002	0.652	337	12	333	8	349	90	27
Z_Plesovice_26		3	507	46	7	11.08	0.394	0.018	0.054	0.001	0.520	18.508	0.445	0.053	0.002	0.035	337	13	339	8	318	77	-19
Z_Plesovice_27		3	537	48	7	11.03	0.384	0.017	0.053	0.001	0.356	18.850	0.497	0.054	0.002	0.286	332	12	333	8	349	80	-38
Z_Plesovice_28		3	530	48	8	10.94	0.393	0.017	0.054	0.001	0.388	18.471	0.444	0.052	0.002	0.078	336	12	340	8	275	78	-40
Z_Plesovice_29		3	544	50	8	10.90	0.401	0.017	0.054	0.001	0.375	18.646	0.452	0.054	0.002	0.266	342	12	337	8	371	75	-27
Z_Plesovice_30		3	541	49	7	10.88	0.396	0.018	0.055	0.001	0.185	18.339	0.471	0.053	0.002	0.328	338	13	342	9	321	91	-2
Z_Plesovice_31		3	504	45	7	11.17	0.392	0.016	0.053	0.001	0.409	18.786	0.494	0.054	0.002	0.388	336	12	334	9	345	75	-21
Z_Plesovice_32		3	472	41	6	11.53	0.387	0.016	0.053	0.001	0.351	18.871	0.463	0.053	0.002	0.185	332	12	333	8	320	81	38
Z_Plesovice_33		3	524	47	7	11.03	0.393	0.016	0.053	0.001	0.221	18.932	0.502	0.054	0.002	0.533	337	12	332	8	371	73	-17
Z_Plesovice_34		3	528	47	7	11.01	0.392	0.017	0.054	0.002	0.422	18.484	0.513	0.053	0.002	0.325	337	12	340	9	330	80	38
Z_Plesovice_35		3	551	50	8	10.77	0.387	0.016	0.053	0.001	0.564	18.786	0.459	0.053	0.002	0.026	332	12	334	8	342	73	-31
Z_Plesovice_36		3	579	52	9	10.97	0.383	0.017	0.053	0.001	0.415	19.008	0.470	0.053	0.002	0.234	329	12	331	8	307	79	-160
Z_Plesovice_37		3	586	53	8	10.90	0.387	0.017	0.053	0.001	0.404	19.037	0.507	0.054	0.002	0.358	333	12	330	9	369	82	120
Z_Plesovice_38		3	568	52	8	10.71	0.387	0.017	0.053	0.001	0.417	18.839	0.461	0.053	0.002	0.250	333	12	333	8	307	78	-180
Z_Plesovice_39		3	458	38	6	11.78	0.396	0.017	0.054	0.001	0.453	18.443	0.476	0.053	0.002	0.280	338	12	340	9	333	78	-16
Z_Plesovice_40		3	573	52	9	10.88	0.396	0.018	0.053	0.001	0.517	18.734	0.491	0.054	0.002	0.234	339	13	335	9	351	79	-25
Z_Plesovice_41		3	505	45	7	11.09	0.396	0.016	0.054	0.001	0.312	18.519	0.446	0.054	0.002	0.254	338	12	339	8	348	75	6
Z_Plesovice_42		3	505	46	7	10.87	0.397	0.016	0.054	0.001	0.217	18.584	0.449	0.054	0.002	0.466	340	12	338	8	352	73	80
Z_Plesovice_43		3	671	62	9	10.69	0.390	0.017	0.053	0.001	0.603	18.943	0.502	0.054	0.002	0.036	334	13	332	8	365	76	-24
Z_Plesovice_0		4	682	65	11	10.15	0.389	0.008	0.053	0.001	0.159	18.790	0.339	0.053	0.002	0.538	333	6	334	6	311	67	0.2
Z_Plesovice_1		4	1124	173	26	6.33	0.390	0.009	0.053	0.001	0.344	18.850	0.298	0.053	0.001	0.351	334	7	333	5	337	52	0.3
Z_Plesovice_2		4	1082	165	28	6.50	0.391	0.009	0.053	0.001	0.451	18.808	0.223	0.053	0.001	0.115	335	7	334	4	321	60	0.5
Z_Plesovice_3		4	1080	143	21	7.44	0.386	0.008	0.053	0.001	0.525	18.769	0.328	0.053	0.001	0.443	331	6	335	6	310	50	0.5
Z_Plesovice_4		4	748	66	11	11.06	0.399	0.010	0.054	0.001	0.341	18.692	0.349	0.054	0.002	0.343	341	8	336	6	375	62	0.3
Z_Plesovice_5		4	746	69	11	10.75	0.393	0.008	0.054	0.001	0.351	18.580	0.217	0.053	0.001	0.398	336	6	338	4	325	53	0.4
Z_Plesovice_6		4	1130	169	27	6.65	0.387	0.008	0.054	0.001	0.141	18.643	0.275	0.052	0.002	0.600	332	6	337	5	291	66	0.1
Z_Plesovice_7		4	868	99	15	9.05	0.391	0.007	0.054	0.001	0.213	18.488	0.219	0.053	0.001	0.321	335	5	340	4	301	55	0.2
Z_Plesovice_8		4	1155	180	27	6.58	0.385	0.007	0.052	0.001	0.500	19.099	0.215	0.054	0.001	0.138	331	5	329	4	357	47	0.5
Z_Plesovice_9		4	735	74	11	10.24	0.391	0.008	0.054	0.001	0.447	18.657	0.230	0.053	0.001	0.242	335	6	337	4	333	52	0.4
Z_Plesovice_10		4	709	72	11	9.75	0.392	0.008	0.053	0.001	0.483	18.818	0.237	0.054	0.001	0.199	336	6	334	4	372	53	0.5
Z_Plesovice_11		4	687	66	11	9.99	0.394	0.009	0.053	0.001	0.256	18.854	0.277	0.054	0.002	0.351	337	7	334	5	374	61	0.3
Z_Plesovice_12		4	989	156	25	6.71	0.390	0.006	0.052	0.001	0.174	19.088	0.211	0.054	0.001	0.474	334	5	329	4	354	56	0.2
Z_Plesovice_13		4	868	105	16	8.73	0.384	0.008	0.053	0.001	0.291	18.871	0.231	0.053	0.001	0.377	330	6	333	4	333	54	0.3
Z_Plesovice_14		4	747	70	11	11.07	0.387	0.007	0.054	0.001	0.337	18.653	0.219	0.053	0.001	0.360	333	5	337	4	310	52	0.3
Z_Plesovice_15		4	1069	154	27	7.16	0.386	0.008	0.052	0.001	0.357	19.172	0.254	0.054	0.001	0.328	331	6	328	4	358	54	0.4
Z_Plesovice_16		4	622	56	10	11.53	0.401	0.011	0.054	0.001	0.467	18.664	0.338	0.054	0.002	0.045	342	8	336	6	370	62	0.5

Continue Table A2 – 1

							isotopic ratios										ages						
Grain-ID	Lab ID	# exp	U	Th	Pb	U/Th	$^{207}Pb/^{235}U$	± 2SE	$^{206}Pb/^{238}U$	± 2SE	ρ*	$^{238}U/^{206}Pb$	± 2SE	$^{207}Pb/^{206}Pb$	± 2SE	ρ**	$^{207}Pb/^{235}U$	± 2SE	$^{206}Pb/^{238}U$	± 2SE	$^{207}Pb/^{206}Pb$	± 2SE	Disc. %
GZ7_0		1	1239	1505	375	0.82	0.689	0.024	0.087	0.003	0.320	11.494	0.344	0.058	0.002	0.444	532	14	538	16	519	56	-8.3
GZ7_1		1	1231	1515	379	0.81	0.701	0.024	0.088	0.003	0.478	11.412	0.339	0.058	0.002	0.275	539	14	541	15	523	55	-7.8
GZ7_2		1	1249	1539	380	0.81	0.704	0.025	0.088	0.003	0.416	11.416	0.339	0.058	0.002	0.337	541	15	543	14	540	56	-5.7
GZ7_3		1	1261	1549	375	0.81	0.680	0.023	0.084	0.003	0.186	11.947	0.357	0.059	0.002	0.593	527	14	518	15	550	56	3.9
GZ7_4		1	1231	1493	370	0.82	0.690	0.023	0.086	0.003	0.583	11.574	0.362	0.058	0.001	0.462	533	14	534	16	522	54	-6.4
GZ7_5		1	1235	1508	367	0.82	0.691	0.023	0.085	0.003	0.376	11.710	0.356	0.059	0.002	0.424	533	14	528	15	558	60	2.3
GZ7_6		1	1190	1475	371	0.80	0.709	0.025	0.089	0.003	0.455	11.274	0.343	0.058	0.002	0.414	544	15	548	16	525	57	-10.4
GZ7_7		1	1202	1493	367	0.80	0.689	0.023	0.087	0.003	0.111	11.494	0.344	0.057	0.002	0.657	532	14	538	16	502	60	-13.3
GZ7_8		1	1229	1502	369	0.82	0.680	0.025	0.087	0.003	0.658	11.547	0.360	0.057	0.002	0.090	527	15	535	16	485	56	-16.7
GZ7_9		1	1173	1440	361	0.81	0.702	0.024	0.088	0.003	0.414	11.390	0.350	0.058	0.002	0.515	540	14	542	16	526	57	-5.0
GZ7_10		1	1176	1446	360	0.81	0.697	0.025	0.087	0.003	0.537	11.455	0.341	0.058	0.002	0.154	537	15	539	16	521	58	-5.2
GZ7_11		1	1167	1424	357	0.82	0.693	0.024	0.087	0.003	0.481	11.468	0.355	0.058	0.002	0.479	535	14	539	16	515	57	-10.3
GZ7_12		1	1159	1422	355	0.81	0.699	0.024	0.087	0.003	0.364	11.547	0.360	0.059	0.002	0.458	538	14	535	16	546	60	0.2
GZ7_13		1	1180	1455	359	0.81	0.685	0.024	0.086	0.003	0.545	11.655	0.367	0.058	0.002	0.246	530	15	531	16	522	60	-6.2
GZ7_14		1	1140	1410	353	0.80	0.690	0.024	0.088	0.003	0.336	11.375	0.336	0.057	0.002	0.357	533	14	543	15	486	58	-20.0
GZ7_0		2	562	529	137	1.07	0.697	0.020	0.087	0.002	0.318	11.534	0.200	0.058	0.002	0.424	537	12	536	9	525	69	-12.0
GZ7_1		2	548	518	129	1.06	0.710	0.021	0.087	0.001	0.411	11.446	0.183	0.059	0.002	0.247	544	13	540	9	550	66	-2.1
GZ7_2		2	537	511	127	1.06	0.704	0.021	0.088	0.002	0.494	11.351	0.193	0.057	0.002	0.277	541	12	544	9	499	67	-16.6
GZ7_3		2	452	420	113	1.08	0.699	0.021	0.087	0.001	0.015	11.452	0.184	0.057	0.002	0.470	538	12	540	8	497	72	-2.0
GZ7_4		2	480	448	121	1.08	0.705	0.022	0.088	0.001	0.515	11.339	0.180	0.057	0.002	0.081	541	13	545	8	505	70	-13.0
GZ7_5		2	567	523	134	1.08	0.697	0.019	0.087	0.001	0.203	11.537	0.186	0.058	0.002	0.537	537	11	536	8	540	67	-3.5
GZ7_6		2	556	520	129	1.07	0.693	0.021	0.087	0.001	0.414	11.482	0.185	0.057	0.002	0.098	534	13	538	9	491	72	-17.0
GZ7_7		2	505	472	122	1.07	0.709	0.022	0.088	0.002	0.390	11.429	0.209	0.058	0.002	0.253	544	13	541	10	541	70	-5.5
GZ7_8		2	524	494	126	1.06	0.699	0.019	0.088	0.001	0.411	11.395	0.169	0.058	0.002	0.124	539	11	542	8	509	66	-6.6
GZ7_9		2	510	479	126	1.06	0.708	0.023	0.088	0.002	0.258	11.351	0.193	0.058	0.002	0.266	543	14	544	9	527	73	-9.0
GZ7_10		2	534	503	128	1.07	0.698	0.021	0.087	0.001	0.120	11.467	0.184	0.058	0.002	0.535	537	12	539	8	527	74	-11.0
GZ7_11		2	557	522	132	1.07	0.696	0.020	0.088	0.001	0.433	11.409	0.182	0.057	0.002	0.271	536	12	542	8	505	66	-6.7
GZ7_12		2	603	565	138	1.07	0.694	0.019	0.087	0.002	0.542	11.523	0.199	0.058	0.002	0.241	535	12	536	9	509	64	-8.3
GZ7_13		2	587	551	140	1.07	0.707	0.020	0.088	0.002	0.505	11.328	0.192	0.058	0.002	0.187	543	12	545	9	537	57	-3.1
GZ7_14		2	664	619	154	1.07	0.685	0.020	0.086	0.001	0.535	11.632	0.189	0.058	0.002	0.270	530	12	532	8	540	63	-1.9
GZ7_15		2	608	572	144	1.08	0.688	0.019	0.087	0.001	0.144	11.554	0.187	0.057	0.002	0.499	532	12	535	8	497	66	-12.5
GZ7_16		2	680	631	155	1.07	0.697	0.020	0.087	0.002	0.454	11.442	0.196	0.058	0.002	0.289	537	12	540	9	516	67	-8.0
GZ7_17		2	612	569	145	1.07	0.707	0.019	0.088	0.001	0.152	11.353	0.168	0.058	0.002	0.435	543	11	544	8	516	67	-13.1
GZ7_18		2	608	572	140	1.07	0.702	0.021	0.087	0.001	0.405	11.478	0.184	0.058	0.002	0.192	540	12	539	8	530	68	-14.0
GZ7_19		2	613	573	142	1.08	0.690	0.019	0.087	0.001	0.472	11.533	0.186	0.057	0.002	0.365	533	12	536	9	507	67	-8.6
GZ7_20		2	610	574	146	1.07	0.712	0.020	0.088	0.002	0.465	11.351	0.206	0.058	0.002	0.356	546	12	545	9	545	67	-5.7
GZ7_21		2	571	533	135	1.08	0.706	0.021	0.088	0.002	0.574	11.312	0.192	0.058	0.002	0.134	543	12	546	9	523	66	-7.0
GZ7_22		2	597	555	142	1.08	0.694	0.019	0.086	0.002	0.255	11.633	0.203	0.058	0.002	0.488	535	11	533	9	535	66	0.1
GZ7_23		2	627	582	146	1.07	0.689	0.020	0.086	0.001	0.264	11.610	0.175	0.058	0.002	0.234	532	12	533	8	516	66	-10.5
GZ7_24		2	624	589	145	1.06	0.690	0.020	0.086	0.001	0.289	11.578	0.174	0.058	0.002	0.299	532	12	534	8	515	66	-10.2
GZ7_25		2	627	586	147	1.07	0.697	0.020	0.087	0.001	0.271	11.539	0.173	0.058	0.002	0.314	537	12	536	8	532	62	-1.7
GZ7_26		2	628	595	149	1.07	0.700	0.020	0.088	0.001	0.388	11.373	0.168	0.057	0.002	0.217	540	12	543	8	503	61	-9.8
GZ7_27		2	631	584	145	1.08	0.689	0.020	0.086	0.001	0.385	11.665	0.190	0.058	0.002	0.298	532	12	530	8	545	65	0.0
GZ7_28		2	642	598	153	1.08	0.698	0.020	0.087	0.001	0.507	11.502	0.172	0.058	0.002	0.089	537	12	537	8	542	65	-3.3
GZ7_29		2	632	596	145	1.08	0.693	0.020	0.087	0.001	0.425	11.506	0.185	0.058	0.002	0.170	535	12	537	8	519	69	-10.0
GZ7_30		2	629	590	146	1.08	0.695	0.021	0.087	0.002	0.310	11.545	0.200	0.057	0.002	0.324	536	12	536	9	519	68	-10.1
GZ7_31		2	688	638	161	1.08	0.699	0.019	0.088	0.002	0.275	11.422	0.196	0.058	0.002	0.506	538	12	541	9	537	67	-4.3
GZ7_32		2	706	665	162	1.07	0.694	0.021	0.087	0.001	0.548	11.553	0.187	0.058	0.002	0.028	535	13	535	9	531	64	-10.0
GZ7_33		2	649	607	152	1.09	0.698	0.021	0.087	0.001	0.442	11.525	0.186	0.058	0.002	0.176	537	13	536	9	531	69	-6.5
GZ7_34		2	648	609	152	1.08	0.695	0.020	0.086	0.001	0.069	11.606	0.189	0.058	0.002	0.428	537	12	533	8	526	67	-4.9
GZ7_35		2	703	657	162	1.08	0.701	0.020	0.087	0.002	0.391	11.561	0.214	0.059	0.002	0.330	539	12	535	9	552	70	0.7
GZ7_36		2	638	585	153	1.09	0.692	0.020	0.087	0.002	0.519	11.482	0.198	0.057	0.002	0.201	535	12	538	9	501	66	-10.7
GZ7_37		2	681	630	159	1.09	0.690	0.020	0.087	0.002	0.426	11.534	0.200	0.058	0.002	0.445	533	12	536	9	514	66	-2.4
GZ7_38		2	669	625	156	1.09	0.686	0.018	0.086	0.001	0.196	11.563	0.187	0.057	0.002	0.539	530	11	535	8	500	66	-11.4
GZ7_39		2	668	616	157	1.08	0.692	0.020	0.086	0.001	0.224	11.648	0.190	0.058	0.002	0.333	534	12	531	8	546	69	-0.3
GZ7_40		2	687	640	160	1.08	0.703	0.020	0.087	0.001	0.156	11.517	0.186	0.058	0.002	0.426	540	12	537	9	518	68	-12.0
GZ7_41		2	612	574	149	1.08	0.685	0.022	0.086	0.002	0.398	11.614	0.202	0.057	0.002	0.223	530	13	533	9	511	74	-14.0
GZ7_42		2	670	616	158	1.09	0.693	0.020	0.087	0.001	0.235	11.547	0.173	0.058	0.002	0.366	534	12	535	8	529	67	-7.2
GZ7_43		2	628	588	146	1.09	0.681	0.020	0.086	0.001	0.172	11.598	0.175	0.057	0.002	0.403	529	12	533	8	480	74	-20.0
GZ7_0		3	585	546	137	1.08	0.682	0.027	0.086	0.003	0.657	11.628	0.352	0.057	0.002	0.429	528	16	532	15	496	70	-11.0
GZ7_1		3	567	530	135	1.05	0.688	0.028	0.087	0.002	0.673	11.534	0.306	0.057	0.002	0.315	531	17	536	14	503	61	-7.6
GZ7_2		3	511	483	120	1.05	0.710	0.028	0.088	0.002	0.284	11.412	0.260	0.059	0.002	0.420	544	16	542	12	548	69	-2.8
GZ7_3		3	455	424	112	1.07	0.695	0.030	0.087	0.002	0.393	11.455	0.302	0.057	0.002	0.320	536	18	540	13	496	79	-12.0
GZ7_4		3	437	405	105	1.08	0.706	0.029	0.088	0.002	0.096	11.351	0.271	0.058	0.002	0.496	542	17	544	13	544	72	-10.0
GZ7_5		3	466	432	108	1.07	0.702	0.027	0.088	0.002	0.406	11.425	0.261	0.058	0.002	0.188	540	16	541	12	527	64	-7.6
GZ7_6		3	363	336	90	1.07	0.696	0.032	0.087	0.002	0.461	11.431	0.261	0.057	0.002	0.155	536	19	541	12	497	81	-20.0
GZ7_7		3	434	408	102	1.06	0.712	0.028	0.089	0.002	0.215	11.279	0.267	0.059	0.002	0.378	546	17	548	12	546	70	-10.0
GZ7_8		3	485	458	115	1.06	0.695	0.027	0.087	0.002	0.468	11.521	0.292	0.058	0.002	0.442	536	16	536	13	527	66	-2.9
GZ7_9		3	465	424	110	1.09	0.707	0.030	0.088	0.002	0.262	11.364	0.271	0.058	0.002	0.368	543	18	544	12	533	77	-7.0
GZ7_10		3	459	418	106	1.09	0.710	0.028	0.089	0.002	0.319	11.249	0.266	0.059	0.002	0.424	545	16	549	12	556	66	-3.7
GZ7_11		3	543	499	128	1.17	0.709	0.028	0.088	0.002	0.411	11.364	0.284	0.059	0.002	0.440	544	17	543	13	555	69	-0.1
GZ7_12		3	552	521	132	1.13	0.707	0.029	0.088	0.002	0.448	11.429	0.287	0.059	0.002	0.318	543	17	541	13	554	71	1.2
GZ7_13		3	575	528	133	1.19	0.698	0.031	0.087	0.002	0.060	11.442	0.314	0.058	0.002	0.580	537	18	540	14	499	96	-19.0
GZ7_14		3	489	448	114	1.18	0.707	0.029	0.088	0.002	0.504	11.338	0.270	0.058	0.002	0.164	544	18	545	13	531	68	-8.2
GZ7_15		3	495	455	116	1.18	0.707	0.027	0.088	0.002	0.078	11.358	0.271	0.059	0.002	0.509	543	16	544	12	554	69	-22.0
GZ7_16		3	572	529	132	1.10	0.685	0.029	0.086	0.002	0.483	11.628	0.284	0.058	0.002	0.139	529	18	532	12	537	73	-11.0
GZ7_17		3	555	508	133	1.10	0.706	0.029	0.088	0.002	0.520	11.377	0.285	0.059	0.002	0.181	542	17	543	13	551	66	-3.6
GZ7_18		3	538	497	126	1.09	0.702	0.029	0.088	0.002	0.551	11.377	0.298	0.057	0.002	0.377	541	17	543	14	501	67	-11.3
GZ7_19		3	556	504	125	1.10	0.684	0.028	0.087	0.002	0.421	11.547	0.307	0.058	0.002	0.358	529	17	535	14	519	68	-3.3
GZ7_20		3	491	445	112	1.09	0.703	0.028	0.088	0.002	0.220	11.382	0.259	0.058	0.002	0.418	540	17	543	12	513	71	-9.0
GZ7_21		3	484	449	112	1.08	0.702	0.028	0.088	0.002	0.219	11.390	0.272	0.058	0.002	0.428	539	16	542	12	532	65	-8.0
GZ7_22		3	448	412	104	1.09	0.704	0.028	0.089	0.002	0.210	11.299	0.268	0.058	0.002	0.519	541	17	546	12	510	70	-10.0
GZ7_23		3	473	430	113	1.10	0.695	0.028	0.088	0.002	0.272	11.403	0.273	0.057	0.002	0.324	536	17	542	12	511	69	-9.0
GZ7_24		3	424	394	97	1.09	0.688	0.027	0.087	0.002	0.309	11.547	0.267	0.057	0.002	0.407	531	17	536	12	504	72	-14.0
GZ7_25		3	558	511	124	1.09	0.700	0.028	0.087	0.002	0.538	11.547	0.293	0.058	0.002	0.330	539	17	536	13	543	65	-4.0
GZ7_26		3	594	544	138	1.09	0.701	0.029	0.088	0.002	0.460	11.429	0.313	0.059	0.002	0.305	539	18	541	14	559	68	0.3
GZ7_27		3	569	520	131	1.08	0.706	0.029	0.089	0.002	0.576	11.299	0.281	0.058	0.002	0.267	543	17	547	13	544	64	-3.1
GZ7_28		3	569	524	126	1.08	0.691	0.028	0.087	0.002	0.254	11.507	0.278	0.058	0.002	0.439	533	17	537	13	507	71	-9.0
GZ7_29		3	563	517	128	1.09	0.696	0.028	0.088	0.002	0.245	11.429	0.274	0.058	0.002	0.562	536	17	541	13	512	70	-14.0
GZ7_30		3	567	520	131	1.08	0.699	0.029	0.088	0.002	0.409	11.429	0.274	0.058	0.002	0.314	538	17	541	13	533	71	-7.4
GZ7_31		3	609	559	137	1.08	0.694	0.032	0.087	0.002	0.481	11.547	0.293	0.059	0.002	0.069	535	19	536	13	544	83	0.0
GZ7_32		3	455	415	103	1.09	0.694	0.027	0.087	0.002	0.176	11.481	0.250	0.057	0.002	0.378	535	16	538	12	518	70	-5.2
GZ7_33		3	477	442	110	1.07	0.699	0.028	0.088	0.002	0.251	11.421	0.261	0.058	0.002	0.307	538	17	541	12	547	62	-10.0
GZ7_34		3	444	411	109	1.08	0.701	0.028	0.088	0.002	0.076	11.403	0.273	0.058	0.002	0.488	539	17	542	12	530	73	-6.0
GZ7_35		3	496	455	111	1.08	0.697	0.027	0.086	0.002	0.357	11.562	0.254	0.059	0.002	0.343	538	17	535	11	546	63	-0.6
GZ7_36		3	467	434	106	1.07	0.706	0.028	0.088	0.002	0.207	11.396	0.247	0.059	0.002	0.298	542	17	542	12	559	70	0.6
GZ7_37		3	464	429	106	1.08	0.706	0.028	0.088	0.002	0.291	11.377	0.272	0.058	0.002	0.355	542	16	543	12	548	67	-8.0
GZ7_0		4	688	681	160	1.00	0.693	0.012	0.086	0.001	0.450	11.601	0.161	0.058	0.001	0.325	534	7	533	7	531	50	0.4
GZ7_1		4	661	651	160	1.01	0.689	0.010	0.086	0.001	0.291	11.601	0.161	0.058	0.001	0.568	533	5	533	7	518	48	0.3
GZ7_2		4	650	640	156	1.00	0.700	0.012	0.087	0.001	0.527	11.468	0.171	0.058	0.001	0.324	538	8	539	8	536	48	0.5
GZ7_3		4	709	625	151	1.12	0.694	0.010	0.087	0.001	0.292	11.534	0.160	0.058	0.001	0.554	535	6	536	7	519	51	0.3
GZ7_4		4	689	606	146	1.11	0.694	0.012	0.087	0.001	0.363	11.468	0.184	0.058	0.001	0.549	537	8	539	8	528	54	0.4
GZ7_5		4	663	587	144	1.11	0.691	0.013	0.086	0.001	0.623	11.613	0.134	0.058	0.001	0.145	534	7	533	6	522	43	0.6
GZ7_6		4	732	738	176	1.01	0.685	0.014	0.086	0.002	0.445	11.587	0.201	0.058	0.001	0.414	531	9	533	9	519	53	0.4
GZ7_7		4	648	641	154	1.00	0.694	0.014	0.087	0.001	0.476	11.547	0.147	0.058	0.001	0.154	535	9	535	6	538	52	0.5
GZ7_8		4	645	610	150	1.09	0.689	0.012	0.086	0.001	0.427	11.655	0.136	0.058	0.001	0.315	532	7	531	6	532	45	0.4
GZ7_9		4	626	580	146	1.10	0.703	0.014	0.088	0.002	0.258	11.429	0.196	0.058	0.002	0.426	540	8	541	9	526	52	0.3
GZ7_10		4	612	559	141	1.12	0.708	0.017	0.089	0.002	0.484	11.287	0.204	0.057	0.002	0.211	543	10	547	9	492	57	0.5
GZ7_11		4	632	572	142	1.11	0.710	0.013	0.088	0.001	0.604	11.377	0.155	0.059	0.001	0.280	545	7	543	7	563	38	0.6
GZ7_12		4	597	526	131	1.13	0.721	0.014	0.090	0.001	0.490	11.148	0.124	0.058	0.001	0.153	552	9	554	6	533	47	0.5

Continue Table A2 – 1

							isotopic ratios										ages						
Grain-ID	Lab ID	# exp	U	Th	Pb	U/Th	$^{207}Pb/^{235}U$	± 2SE	$^{206}Pb/^{238}U$	± 2SE	ρ*	$^{238}U/^{206}Pb$	± 2SE	$^{207}Pb/^{206}Pb$	± 2SE	ρ**	$^{207}Pb/^{235}U$	± 2SE	$^{206}Pb/^{238}U$	± 2SE	$^{207}Pb/^{206}Pb$	± 2SE	Disc %
Navan Area																							
Tara Deep																							
X18HK005_0	HK 158	1	52	90	14	0.58	0.418	0.041	0.053	0.002	0.118	18.797	0.848	0.057	0.006	0.235	350	29	334	15	420	190	69
X18HK005_1	HK 158	1	61	112	19	0.56	0.412	0.037	0.055	0.003	0.086	18.215	0.863	0.055	0.005	0.415	347	26	344	16	350	190	140
X18HK005_2	HK 158	1	135	229	36	0.60	0.405	0.050	0.054	0.002	0.141	18.382	0.777	0.054	0.006	0.306	342	33	341	14	320	190	180
X18HK005_3	HK 158	1	68	170	28	0.49	0.413	0.035	0.054	0.003	0.370	18.553	0.895	0.056	0.004	0.183	348	25	338	16	380	160	77
X18HK005_4	HK 158	1	66	108	17	0.61	0.391	0.033	0.055	0.003	0.286	18.248	0.832	0.052	0.004	0.214	333	24	344	15	240	150	91
X18HK005_5	HK 158	1	119	229	36	0.52	0.405	0.087	0.057	0.003	0.170	17.668	0.812	0.052	0.011	0.251	343	50	355	16	250	260	700
X18HK005_6	HK 158	1	89	137	23	0.65	0.435	0.034	0.056	0.003	0.395	17.825	0.858	0.056	0.004	0.196	364	24	351	16	420	140	77
X18HK005_7	HK 158	1	238	272	41	0.93	0.439	0.030	0.057	0.004	0.181	17.668	1.217	0.057	0.004	0.589	368	21	355	24	450	160	102
X18HK005_8	HK 158	1	48	88	13	0.55	0.437	0.039	0.055	0.003	0.256	18.083	0.850	0.058	0.005	0.190	364	27	347	16	440	170	46
X18HK005_9	HK 158	1	312	236	172	1.36	4.390	nan	0.302	nan	0.726	3.312		0.105	nan	0.441	1707	nan	1699	nan	1714	nan	0.1
X18HK005_10	HK 158	1	242	218	49	1.12	0.573	nan	0.076	nan	0.364	13.123		0.055	nan	0.422	459	nan	473	nan	390	nan	-10
X18HK005_11	HK 158	1	52	112	15	0.46	0.420	0.051	0.054	0.004	0.280	18.587	1.278	0.058	0.010	0.611	352	37	338	23	460	290	94
X18HK005_12	HK 158	1	38	52	8	0.74	0.414	0.170	0.057	0.003	0.089	17.544	0.954	0.055	0.021	0.595	349	89	357	19	300	360	400
X18HK005_13	HK 158	1	67	120	19	0.56	0.404	0.034	0.053	0.002	0.151	18.762	0.810	0.055	0.004	0.245	342	24	334	14	370	170	180
X18HK005_14	HK 158	1	89	216	31	0.42	0.405	0.030	0.056	0.003	0.105	17.986	1.100	0.054	0.006	0.471	343	22	349	21	300	190	172
X18HK005_15	HK 158	1	69	110	18	0.62	0.403	0.025	0.054	0.002	0.153	18.450	0.783	0.054	0.004	0.589	342	18	340	14	380	160	128
Kells																							
X18HK_001_0	HK 155	3	174	100	17	1.80	0.435	0.029	0.059	0.002	0.157	17.065	0.524	0.055	0.004	0.221	371	22	367	11	380	150	-10
X18HK_001_1	HK 155	3	325	189	31	2.07	0.409	0.019	0.055	0.002	0.284	18.116	0.525	0.054	0.002	0.347	348	14	346	10	359	92	-40
X18HK_001_2	HK 155	3	371	267	25	3.01	0.388	0.020	0.048	0.003	0.467	20.921	1.182	0.061	0.003	0.650	332	15	301	17	608	110	33
X18HK_001_0	HK 155	4	384	504	63	0.73	0.870	0.120	0.052	0.002	0.049	19.305	0.894	0.123	0.017	0.184	628	64	326	15	1930	230	0.0
X18HK_001_1	HK 155	4	889	136	22	6.36	0.415	0.010	0.055	0.001	0.448	18.054	0.264	0.055	0.001	0.253	353	7	348	5	402	57	0.4
X18HK_001_2	HK 155	4	439	187	30	2.36	0.410	0.009	0.056	0.001	0.199	17.944	0.254	0.053	0.001	0.416	350	6	350	5	313	62	0.2
X18HK_001_3	HK 155	4	475	314	130	2.61	1.610	0.360	0.065	0.003	0.860	15.385	0.639	0.162	0.032	0.787	850	140	405	16	1860	390	0.9
X18HK_039_0	HK 169	3	500	470	71	1.12	0.409	0.022	0.055	0.002	0.068	18.215	0.597	0.054	0.003	0.514	348	15	345	11	350	120	-90
X18HK_039_1	HK 169	3	194	121	19	1.60	0.407	0.022	0.055	0.002	0.031	18.175	0.496	0.055	0.003	0.318	349	17	345	9	380	110	22
X18HK_039_2	HK 169	3	183	162	18	1.15	0.446	0.030	0.052	0.002	0.394	19.084	0.656	0.063	0.003	0.183	374	21	329	11	680	120	41
X18HK_039_3	HK 169	3	167	89	14	1.98	0.398	0.018	0.054	0.002	0.091	18.553	0.516	0.053	0.002	0.459	340	13	338	9	339	93	9
X18HK_039_4	HK 169	3	220	292	27	0.75	0.427	0.023	0.049	0.001	0.056	20.371	0.581	0.065	0.003	0.409	360	17	309	9	730	110	47
X18HK_039_5	HK 169	3	308	187	30	1.61	0.408	0.020	0.056	0.002	0.262	17.794	0.570	0.054	0.002	0.566	351	13	352	11	347	87	-49
X18HK_039_6	HK 169	3	171	90	15	1.89	0.400	0.021	0.055	0.002	0.047	18.328	0.504	0.051	0.003	0.331	341	16	343	9	270	120	110
X18HK_039_7	HK 169	3	144	168	15	0.84	0.452	0.036	0.050	0.001	0.001	20.056	0.563	0.065	0.005	0.362	377	25	314	9	830	150	55
X18HK_039_8	HK 169	3	234	139	21	1.68	0.398	0.018	0.054	0.001	0.402	18.376	0.439	0.053	0.002	0.057	342	14	342	8	332	90	-20
X18HK_039_9	HK 169	3	237	170	22	1.40	0.420	0.025	0.052	0.002	0.051	19.120	0.622	0.058	0.004	0.478	356	18	328	11	560	110	32
X18HK_039_10	HK 169	3	146	87	13	1.72	0.384	0.021	0.054	0.002	0.015	18.580	0.518	0.053	0.002	0.345	331	15	338	9	297	99	-40
X18HK_039_11	HK 169	3	196	121	18	1.63	0.411	0.023	0.054	0.002	0.329	18.450	0.545	0.055	0.003	0.127	349	16	340	10	410	100	8
X18HK_039_12	HK 169	3	163	123	17	1.40	0.412	0.023	0.053	0.002	0.185	19.026	0.543	0.057	0.003	0.290	349	17	330	9	480	120	40
X18HK_039_13	HK 169	3	203	117	18	1.81	0.417	0.021	0.053	0.001	0.095	18.706	0.490	0.057	0.003	0.370	353	15	336	8	445	110	37
X18HK_039_14	HK 169	3	194	244	26	0.78	0.457	0.035	0.049	0.002	0.372	20.619	0.638	0.071	0.006	0.059	381	25	305	9	950	150	64
X18HK_039_15	HK 169	3	173	192	22	0.89	0.501	0.025	0.053	0.002	0.048	18.904	0.572	0.070	0.003	0.496	411	17	332	10	944	92	62
X18HK_039_16	HK 169	3	394	370	49	1.05	0.494	0.031	0.055	0.002	0.270	18.335	0.504	0.066	0.004	0.535	406	20	342	9	770	130	46
X18HK_039_17	HK 169	3	197	220	30	0.88	0.444	0.025	0.052	0.001	0.198	19.183	0.515	0.062	0.003	0.320	372	18	328	9	683	93	45
X18HK_039_18	HK 169	3	165	102	15	1.60	0.382	0.025	0.053	0.002	0.335	18.762	0.634	0.052	0.003	0.093	328	18	335	11	270	130	-80
X18HK_039_19	HK 169	3	217	91	14	2.39	0.404	0.021	0.054	0.001	0.153	18.454	0.477	0.054	0.003	0.263	344	15	340	9	358	100	14
Rathdowney																							
Trend																							
Rapla																							
X18HK_128_0	HK 185	2	185	134	22	1.42	0.443	0.020	0.053	0.001	0.283	18.861	0.427	0.060	0.003	0.178	373	14	333	7	591	96	29
X18HK_128_1	HK 185	2	81	69	8	1.22	0.424	0.026	0.051	0.002	0.230	19.569	0.613	0.060	0.004	0.228	358	19	323	10	620	140	62
X18HK_128_2	HK 185	2	102	58	9	1.84	0.406	0.026	0.055	0.001	0.003	18.349	0.471	0.054	0.004	0.316	345	19	342	8	370	150	69
X18HK_128_3	HK 185	2	65	31	4	2.20	0.396	0.032	0.054	0.002	0.053	18.692	0.559	0.054	0.005	0.366	337	23	336	10	360	190	150
X18HK_128_4	HK 185	2	91	49	8	1.86	0.393	0.026	0.055	0.001	0.097	18.298	0.368	0.053	0.004	0.327	342	19	343	7	310	160	68
X18HK_128_5	HK 185	2	212	160	24	1.36	0.401	0.022	0.055	0.002	0.111	18.116	0.492	0.054	0.003	0.415	345	16	346	9	330	140	103
X18HK_128_6	HK 185	2	118	103	13	1.11	0.427	0.027	0.051	0.002	0.255	19.531	0.610	0.060	0.004	0.346	360	19	322	10	560	140	33
X18HK_128_7	HK 185	2	71	49	9	1.46	0.532	0.030	0.052	0.001	0.269	19.268	0.483	0.073	0.005	0.645	431	20	326	8	1000	140	62
X18HK_128_8	HK 185	2	707	471	137	1.54	0.831	0.027	0.100	0.002	0.610	10.000	0.180	0.060	0.002	0.093	615	15	614	11	608	67	-0.3
X18HK_128_9	HK 185	2	118	133	14	0.88	0.516	0.032	0.049	0.001	0.068	20.243	0.574	0.075	0.005	0.449	426	23	311	8	1070	140	67
X18HK_128_10	HK 185	2	123	72	10	1.74	0.397	0.025	0.054	0.001	0.315	18.484	0.478	0.053	0.003	0.170	341	17	340	9	310	120	40
X18HK_128_11	HK 185	2	81	39	6	2.15	0.407	0.040	0.054	0.002	0.076	18.416	0.543	0.053	0.005	0.165	344	29	341	10	330	200	65
X18HK_128_12	HK 185	2	111	86	13	1.30	0.589	0.028	0.049	0.002	0.223	20.619	0.638	0.090	0.005	0.271	469	18	305	9	1432	110	79
X18HK_128_13	HK 185	2	206	273	36	0.77	0.416	0.024	0.049	0.002	0.380	20.367	0.622	0.061	0.004	0.148	353	17	309	9	610	130	15
X18HK_128_14	HK 185	2	134	108	13	1.24	0.408	0.025	0.051	0.002	0.193	19.763	0.742	0.058	0.004	0.520	347	18	318	11	530	140	37
X18HK_128_15	HK 185	2	113	88	14	1.30	0.431	0.024	0.053	0.002	0.208	19.048	0.544	0.059	0.003	0.291	363	17	330	9	540	130	-1.0
X18HK_128_16	HK 185	2	107	108	15	1.02	0.431	0.030	0.052	0.002	0.391	19.231	0.629	0.061	0.004	0.126	363	21	327	10	640	130	39
X18HK_128_17	HK 185	2	203	132	21	1.56	0.394	0.016	0.054	0.001	0.132	18.692	0.419	0.054	0.003	0.382	337	11	336	8	349	100	40
X18HK_128_18	HK 185	2	116	98	17	1.23	0.411	0.027	0.057	0.001	0.094	17.668	0.437	0.054	0.004	0.260	355	19	355	9	350	150	10
X18HK_128_19	HK 185	2	107	57	9	1.90	0.390	0.022	0.054	0.001	0.243	18.674	0.384	0.053	0.003	0.156	333	16	336	7	320	120	54
X18HK_128_20	HK 185	2	116	76	10	1.57	0.424	0.020	0.052	0.001	0.156	19.380	0.488	0.060	0.003	0.382	360	15	324	8	562	110	62
X18HK_128_21	HK 185	2	74	37	6	2.00	0.395	0.024	0.053	0.001	0.064	18.748	0.422	0.054	0.003	0.241	336	17	335	7	350	130	67
X18HK_128_22	HK 185	2	70	34	6	2.08	0.406	0.027	0.055	0.001	0.240	18.215	0.431	0.053	0.003	0.110	347	20	344	8	340	130	57
X18HK_128_23	HK 185	2	204	182	21	1.13	0.412	0.016	0.051	0.001	0.266	19.724	0.506	0.058	0.002	0.357	350	11	319	8	550	88	23
X18HK_128_24	HK 185	2	167	130	21	1.32	0.404	0.019	0.054	0.001	0.246	18.416	0.441	0.056	0.003	0.206	344	14	341	8	410	120	91
Lisheen																							
X18HK_112_0	HK 180	2	62	83	21	0.75	1.642	0.061	0.122	0.004	0.453	8.170	0.240	0.095	0.004	0.371	984	24	744	21	1517	77	50
X18HK_112_1	HK 180	2	155	109	24	1.42	0.534	0.049	0.057	0.001	0.112	17.553	0.370	0.067	0.006	0.071	430	32	357	7	800	190	33
X18HK_112_2	HK 180	2	129	122	20	1.15	0.404	0.028	0.055	0.001	0.147	18.182	0.397	0.053	0.004	0.463	343	20	345	8	330	170	78
X18HK_112_3	HK 180	2	114	71	11	1.62	0.394	0.021	0.054	0.001	0.133	18.556	0.413	0.053	0.003	0.426	338	15	338	7	310	120	170
X18HK_112_4	HK 180	2	158	98	42	1.59	1.595	0.064	0.146	0.004	0.229	6.845	0.197	0.078	0.003	0.444	967	25	879	24	1145	94	20
X18HK_112_5	HK 180	2	120	26	12	4.63	1.739	0.063	0.171	0.003	0.341	5.841	0.106	0.073	0.003	0.243	1026	25	1019	17	1005	82	-2
X18HK_112_6	HK 180	2	97	53	9	1.84	0.426	0.028	0.055	0.001	0.062	18.215	0.464	0.056	0.004	0.289	359	20	344	8	470	160	34
X18HK_112_7	HK 180	2	124	74	12	1.69	0.408	0.027	0.056	0.002	0.357	17.762	0.505	0.053	0.004	0.020	350	20	353	10	320	140	-50
X18HK_112_8	HK 180	2	203	140	22	1.45	0.408	0.017	0.055	0.001	0.483	18.116	0.394	0.054	0.002	0.038	347	12	346	7	347	91	-70
X18HK_112_9	HK 180	2	189	157	20	1.24	0.448	0.023	0.050	0.001	0.058	20.040	0.522	0.067	0.004	0.458	375	16	314	8	810	130	61
X18HK_112_10	HK 180	2	113	108	12	1.06	0.411	0.023	0.047	0.002	0.235	21.368	0.685	0.064	0.004	0.319	351	16	295	9	740	120	51
X18HK_112_11	HK 180	2	79	45	7	1.75	0.404	0.039	0.055	0.002	0.230	18.051	0.717	0.051	0.006	0.550	343	28	347	14	200	250	40
X18HK_112_12	HK 180	2	112	62	10	1.87	0.392	0.028	0.055	0.001	0.189	18.215	0.431	0.052	0.004	0.179	334	20	344	8	280	150	94
X18HK_112_13	HK 180	2	109	108	15	1.01	0.639	0.029	0.047	0.001	0.186	21.142	0.626	0.097	0.005	0.431	500	18	298	9	1560	91	80
X18HK_112_14	HK 180	2	107	58	13	1.82	0.611	0.052	0.055	0.001	0.430	18.332	0.336	0.079	0.006	0.216	478	32	342	6	1110	160	61
X18HK_112_15	HK 180	2	68	40	7	1.76	0.423	0.026	0.053	0.002	0.125	18.797	0.601	0.057	0.004	0.523	357	19	334	10	470	170	65
X18HK_112_16	HK 180	2	69	39	16	1.80	1.080	0.300	0.064	0.003	0.825	15.625	0.830	0.129	0.032	0.671	750	150	400	21	1990	440	76
X18HK_112_17	HK 180	2	281	160	27	1.77	0.408	0.016	0.055	0.001	0.106	18.051	0.391	0.054	0.002	0.437	347	11	347	8	346	97	0.0
X18HK_112_18	HK 180	2	239	158	26	1.53	0.410	0.017	0.055	0.001	0.346	18.139	0.362	0.054	0.002	0.111	348	12	346	7	363	89	1.0
X18HK_112_19	HK 180	2	71	33	5	2.18	0.410	0.031	0.056	0.002	0.127	17.986	0.518	0.053	0.004	0.244	347	22	349	10	350	170	54
X18HK_112_20	HK 180	2	104	64	12	1.68	0.587	0.062	0.055	0.001	0.045	18.282	0.468	0.075	0.008	0.168	462	38	343	8	1120	220	68
X18HK_112_21	HK 180	2	654	849	396	0.79	1.731	0.053	0.171	0.004	0.478	5.862	0.137	0.073	0.003	0.327	1020	20	1015	22	1019	70	1.0
X18HK_112_22	HK 180	2	70	60	7	1.46	0.435	0.024	0.049	0.002	0.052	20.325	0.744	0.065	0.004	0.521	365	17	310	11	750	140	66
X18HK_112_23	HK 180	2	45	25	13	1.83	2.180	0.120	0.199	0.006	0.298	5.038	0.162	0.079	0.005	0.352	1169	41	1167	35	1200	120	1.0
X18HK_112_24	HK 180	2	85	44	7	1.96	0.398	0.029	0.054	0.002	0.139	18.450	0.681	0.053	0.004	0.265	339	21	340	12	370	160	-13
X18HK_112_25	HK 180	2	650	68	42	9.80	1.998	0.100	0.172	0.005	0.685	5.807	0.155	0.085	0.003	0.244	1117	35	1024	25	1305	76	23
X18HK_112_26	HK 180	2	324	188	99	1.77	1.893	0.062	0.181	0.004	0.552	5.519	0.113	0.075	0.002	0.278	1077	22	1073	20	1084	65	-1
X18HK_112_27	HK 180	2	112	94	16	1.22	0.589	0.062	0.054	0.001	0.344	18.416	0.441	0.081	0.009	0.180	463	37	341	8	1140	200	54
X18HK_112_28	HK 180	2	138	99	16	1.46	0.410	0.021	0.055	0.001	0.094	18.100	0.360	0.053	0.003	0.282	348	15	347	7	312	110	82
X18HK_112_29	HK 180	2	217	204	25	1.08	0.424	0.021	0.048	0.001	0.026	20.730	0.473	0.064	0.004	0.390	358	15	304	7	750	110	-10
X18HK_117_0	HK 181	2	204	269	113	0.77	2.520	0.240	0.064	0.002	0.805	15.649	0.563	0.276	0.018	0.167	1267	66	399	14	3326	100	87
X18HK_117_1	HK 181	2	38	29	18	1.37	2.170	0.180	0.175	0.004	0.428	5.714	0.137	0.091	0.007	0.143	1159	56	1039	23	1410	160	25
X18HK_121_0	HK 182	2	179	129	20	1.40	0.569	0.035	0.028	0.001	0.107	35.894	1.185	0.149	0.009	0.076	455	21	177	6	2295	96	92
X18HK_121_1	HK 182	2	93	57	8	1.68	0.408	0.026	0.037	0.001	0.340	27.248	1.039	0.085	0.006	0.439	346	19	232	9	1310	130	80
X18HK_121_2	HK 182	2	241	164	24	1.48	0.482	0.026	0.049	0.002	0.651	20.408	0.916	0.070	0.004	0.118	399	18	308	13	952	93	67
X18HK_121_3	HK 182	2	353	254	32	1.44	0.411	0.024	0.041	0.001	0.522	24.331	0.503	0.071	0.004	0.068	349	17	260	5	940	120	71
X18HK_121_4	HK 182	2	170	104	17	1.63	0.407	0.017	0.055	0.001	0.336	18.169	0.363	0.054	0.002	0.125	350	13	345	7	385	99	-10
X18HK_121_5	HK 182	2	171	110	18	1.55	0.432	0.023	0.050	0.001	0.483	20.202	0.571	0.064	0.003	0.017	364	16	312	9	702	110	50
X18HK_121_6	HK 182	2	149	68	26	2.24	1.439	0.057	0.129	0.006	0.378	7.764	0.368	0.081	0.004	0.799	904	24	780	35	1202	100	33
X18HK_121_7	HK 182	2	127	86	12	1.49	0.462	0.035	0.023	0.001	0.598	42.735	2.374	0.144	0.009	0.214	389	23	149	8	2282	96	93
X18HK_121_8	HK 182	2	159	116	32	1.40	1.051	0.060	0.045	0.001	0.188	22.361	0.475	0.168	0.010	0.123	726	30	282	6	2535	95	89
X18HK_121_9	HK 182	2	85	53	9	1.61	0.413	0.023	0.056	0.001	0.054	17.986	0.421	0.054	0.003	0.290	350	16	349	8	350	120	91
X18HK_121_10	HK 182	2	255	83	53	3.07	2.824	0.100	0.235	0.007	0.719	4.263	0.127	0.088	0.003	0.356	1361	27	1358	37	1377	64	2

Continue Table A2 – 1

							isotopic ratios										ages						
Grain-ID	Lab ID	# exp	U	Th	Pb	U/Th	$^{207}Pb/^{235}U$	± 2SE	$^{206}Pb/^{238}U$	± 2SE	ρ*	$^{238}U/^{206}Pb$	± 2SE	$^{207}Pb/^{206}Pb$	± 2SE	ρ**	$^{207}Pb/^{235}U$	± 2SE	$^{206}Pb/^{238}U$	±SE	$^{207}Pb/^{206}Pb$	± 2SE	Disc. %
X18HK_121_11	HK 182	2	193	160	15	1.22	0.390	0.025	0.025	0.001	0.406	40.486	2.131	0.116	0.007	0.472	333	18	157	8	1870	120	91
X18HK_121_12	HK 182	2	504	212	139	2.42	2.568	0.076	0.229	0.004	0.753	4.367	0.084	0.082	0.002	0.126	1294	20	1329	23	1234	57	-8
X18HK_121_13	HK 182	2	95	59	10	1.65	0.409	0.018	0.056	0.001	0.185	17.992	0.388	0.053	0.003	0.322	348	13	349	7	348	110	28
X18HK_121_14	HK 182	2	113	74	12	1.53	0.413	0.020	0.055	0.001	0.161	18.051	0.456	0.054	0.003	0.311	350	14	347	8	327	110	30
X18HK_121_15	HK 182	2	141	111	18	1.28	0.440	0.028	0.058	0.001	0.155	17.271	0.418	0.054	0.004	0.281	369	20	363	9	360	150	37
X18HK_121_16	HK 182	2	141	87	13	1.69	0.478	0.022	0.034	0.003	0.416	29.499	2.175	0.109	0.008	0.793	396	15	215	16	1770	130	87
X18HK_121_17	HK 182	2	155	95	15	1.63	0.408	0.019	0.055	0.001	0.072	18.315	0.335	0.054	0.003	0.252	347	14	343	6	369	110	60
X18HK_121_18	HK 182	2	196	105	21	1.88	0.524	0.036	0.056	0.002	0.219	17.857	0.542	0.069	0.006	0.532	425	23	351	10	830	160	36
X18HK_121_19	HK 182	2	82	42	7	1.98	0.444	0.027	0.055	0.001	0.259	18.083	0.458	0.059	0.004	0.164	371	19	347	8	510	130	53
X18HK_121_20	HK 182	2	89	54	9	1.64	0.419	0.023	0.056	0.001	0.100	17.953	0.419	0.055	0.003	0.287	354	17	350	8	370	120	33
X18HK_121_21	HK 182	2	461	318	69	1.53	0.543	0.017	0.071	0.001	0.222	14.061	0.237	0.055	0.002	0.379	440	11	443	7	412	77	-41
X18HK_121_22	HK 182	2	154	84	13	1.84	0.411	0.020	0.055	0.001	0.274	18.248	0.400	0.055	0.003	0.208	349	14	344	8	404	110	-9
X18HK_121_23	HK 182	2	96	50	8	1.99	0.453	0.026	0.054	0.002	0.122	18.692	0.559	0.062	0.003	0.208	381	17	336	10	681	110	52
X18HK_121_24	HK 182	2	381	174	116	2.18	2.925	0.083	0.240	0.004	0.579	4.167	0.076	0.088	0.003	0.411	1388	21	1386	23	1369	55	-1
X18HK_121_25	HK 182	2	134	129	23	1.17	0.476	0.037	0.054	0.002	0.243	18.416	0.509	0.065	0.005	0.055	393	26	341	9	710	170	29
X18HK_121_26	HK 182	2	92	56	8	1.65	0.412	0.031	0.055	0.002	0.208	18.215	0.498	0.053	0.004	0.157	348	22	345	9	350	150	70
X18HK_121_27	HK 182	2	12	16	8	0.76	1.650	0.120	0.165	0.005	0.143	6.061	0.169	0.073	0.006	0.315	994	47	984	25	950	160	-21
X18HK_157_0	HK 203	3	454	255	136	1.75	3.860	0.210	0.255	0.011	0.879	3.922	0.169	0.112	0.004	0.121	1602	43	1464	58	1824	58	21
X18HK_157_1	HK 203	3	101	58	9	1.78	0.418	0.035	0.056	0.002	0.317	17.889	0.768	0.055	0.004	0.139	353	25	351	15	430	180	77
X18HK_157_2	HK 203	3	205	146	24	1.40	0.417	0.020	0.055	0.002	0.128	18.182	0.496	0.055	0.002	0.409	354	14	345	9	408	93	3
X18HK_157_3	HK 203	3	386	81	32	6.03	2.171	0.094	0.199	0.006	0.775	5.038	0.142	0.079	0.002	0.076	1170	30	1167	30	1167	61	0
X18HK_157_4	HK 203	3	111	66	11	1.76	0.412	0.024	0.057	0.002	0.081	17.575	0.556	0.053	0.003	0.388	352	17	357	11	296	110	60
X18HK_157_5	HK 203	3	76	40	7	1.88	0.405	0.025	0.056	0.001	0.199	17.960	0.452	0.054	0.003	0.151	349	17	349	9	340	120	70
X18HK_157_6	HK 203	3	127	80	14	1.60	0.451	0.035	0.056	0.002	0.378	17.731	0.534	0.057	0.004	0.215	376	24	354	10	540	160	22
X18HK_157_7	HK 203	3	180	120	19	1.49	0.404	0.020	0.055	0.001	0.110	18.067	0.457	0.053	0.002	0.298	344	14	347	8	328	99	1.0
X18HK_157_8	HK 203	3	76	38	7	1.97	0.421	0.028	0.056	0.002	0.099	17.960	0.484	0.055	0.003	0.318	355	20	349	9	390	120	43
X18HK_157_9	HK 203	3	226	150	25	1.54	0.416	0.021	0.054	0.001	0.163	18.653	0.452	0.057	0.003	0.135	353	15	337	8	470	98	42
X18HK_157_10	HK 203	3	107	63	10	1.75	0.418	0.023	0.055	0.001	0.027	18.106	0.459	0.054	0.003	0.401	354	16	347	9	360	120	-11
X18HK_157_11	HK 203	3	43	39	21	1.08	1.889	0.093	0.181	0.006	0.781	5.528	0.171	0.075	0.003	0.246	1074	32	1071	30	1075	74	-3
X18HK_157_12	HK 203	3	122	85	13	1.47	0.418	0.025	0.057	0.002	0.179	17.690	0.469	0.053	0.003	0.214	356	17	355	9	320	120	14
X18HK_157_13	HK 203	3	212	159	24	1.44	0.400	0.020	0.054	0.002	0.519	18.416	0.543	0.053	0.002	0.071	341	15	341	10	314	87	-23
X18HK_157_14	HK 203	3	147	42	29	3.56	3.318	0.130	0.259	0.006	0.499	3.861	0.094	0.093	0.003	0.204	1484	32	1485	32	1483	56	-2
X18HK_157_15	HK 203	3	79	39	7	2.01	0.408	0.024	0.055	0.002	0.069	18.051	0.489	0.053	0.003	0.282	346	17	348	9	310	110	51
X18HK_157_16	HK 203	3	87	51	8	1.70	0.410	0.023	0.056	0.002	0.201	17.737	0.472	0.054	0.003	0.184	348	16	354	9	345	110	-3
X18HK_157_17	HK 203	3	218	159	26	1.37	0.413	0.021	0.055	0.001	0.115	18.064	0.457	0.054	0.002	0.374	350	15	347	9	346	97	78
X18HK_157_18	HK 203	3	303	255	40	1.18	0.407	0.020	0.056	0.002	0.362	17.848	0.478	0.053	0.002	0.143	347	15	351	9	300	98	160
X18HK_157_19	HK 203	3	271	186	31	1.46	0.406	0.021	0.056	0.002	0.455	17.746	0.472	0.052	0.002	0.522	346	15	353	9	277	100	40
X18HK_157_20	HK 203	3	114	60	10	1.88	0.399	0.026	0.054	0.002	0.122	18.450	0.681	0.053	0.003	0.390	340	19	341	12	310	120	-48
X18HK_157_21	HK 203	3	133	73	12	1.83	0.408	0.030	0.054	0.001	0.030	18.457	0.477	0.054	0.004	0.232	347	22	340	9	420	150	16
X18HK_157_22	HK 203	3	127	49	22	2.54	1.516	0.064	0.156	0.004	0.510	6.423	0.169	0.071	0.002	0.168	936	26	933	23	943	68	-0.4
X18HK_157_23	HK 203	3	137	90	15	1.53	0.417	0.026	0.057	0.002	0.676	17.452	0.487	0.053	0.003	0.184	353	19	359	10	302	110	50
X18HK_157_24	HK 203	3	97	64	10	1.51	0.419	0.026	0.056	0.002	0.312	17.857	0.510	0.054	0.003	0.135	354	18	351	10	360	120	60
X18HK_157_25	HK 203	3	186	122	31	1.52	0.746	0.032	0.092	0.002	0.286	10.858	0.271	0.058	0.002	0.339	565	18	568	14	547	76	-19
X18HK_157_26	HK 203	3	73	33	6	2.19	0.419	0.038	0.056	0.002	0.163	17.731	0.534	0.055	0.005	0.424	353	27	354	10	340	190	85
X18HK_157_27	HK 203	3	134	81	14	1.58	0.406	0.020	0.056	0.002	0.204	17.921	0.514	0.053	0.003	0.314	345	14	350	10	312	99	100
X18HK_157_28	HK 203	3	164	101	17	1.58	0.411	0.025	0.056	0.002	0.688	17.928	0.482	0.052	0.003	0.173	348	18	350	9	269	100	70
X18HK_157_29	HK 203	3	88	46	8	1.92	0.419	0.027	0.057	0.002	0.142	17.668	0.499	0.054	0.003	0.337	356	19	355	10	360	130	63
X18HK_157_30	HK 203	3	96	58	9	1.69	0.414	0.023	0.056	0.002	0.293	18.018	0.552	0.053	0.003	0.117	351	17	348	10	355	110	70
X18HK_157_31	HK 203	3	196	119	19	1.65	0.413	0.030	0.057	0.002	0.659	17.699	0.689	0.054	0.003	0.039	350	22	354	14	360	120	-16
X18HK_157_32	HK 203	3	186	116	19	1.61	0.404	0.022	0.055	0.002	0.439	18.051	0.586	0.054	0.003	0.028	344	16	348	11	370	100	22
X18HK_157_33	HK 203	3	234	174	27	1.32	0.409	0.020	0.056	0.002	0.056	18.018	0.487	0.054	0.002	0.428	348	14	348	9	349	99	90
X18HK_157_34	HK 203	3	75	38	6	1.96	0.413	0.024	0.056	0.002	0.026	17.857	0.510	0.054	0.003	0.343	350	17	351	10	330	110	98
X18HK_157_35	HK 203	3	7380	1943	13	3.66	0.013	0.001	0.002	0.000	0.227	493.583	14.130	0.049	0.002	0.339	14	1	13	0	138	93	103
X18HK_157_36	HK 203	3	97	54	9	1.79	0.410	0.022	0.055	0.002	0.302	18.116	0.525	0.055	0.003	0.457	348	16	346	10	385	110	31
X18HK_157_37	HK 203	3	73	41	7	1.81	0.428	0.030	0.057	0.002	0.505	17.422	0.637	0.054	0.003	0.070	364	20	360	13	370	130	-21
X18HK_157_38	HK 203	3	43	37	18	1.14	1.790	0.092	0.177	0.004	0.313	5.643	0.140	0.074	0.003	0.234	1042	32	1052	24	1052	90	-7
X18HK_157_39	HK 203	3	115	66	10	1.71	0.403	0.022	0.054	0.002	0.362	18.382	0.507	0.055	0.002	0.125	343	16	341	9	394	98	64
X18HK_157_40	HK 203	3	254	92	46	2.74	1.825	0.074	0.180	0.005	0.566	5.552	0.139	0.074	0.002	0.388	1053	27	1067	25	1035	57	-4
X18HK_157_41	HK 203	3	90	52	9	1.76	0.420	0.023	0.056	0.002	0.076	17.794	0.507	0.055	0.003	0.483	355	17	353	10	405	100	58
X18HK_157_42	HK 203	3	58	25	4	2.30	0.396	0.031	0.057	0.002	0.306	17.699	0.564	0.051	0.004	0.023	337	23	355	11	220	160	138
X18HK_157_43	HK 203	3	188	124	20	1.61	0.433	0.022	0.059	0.002	0.146	17.082	0.438	0.054	0.002	0.342	366	16	367	9	373	98	49
X18HK_157_44	HK 203	3	80	40	6	1.97	0.415	0.026	0.056	0.002	0.027	17.857	0.542	0.053	0.003	0.387	354	19	351	10	340	130	109
X18HK_157_45	HK 203	3	26	29	15	0.91	1.748	0.099	0.169	0.005	0.207	5.910	0.189	0.074	0.004	0.466	1030	34	1007	30	1049	100	-1.0
X18HK_157_46	HK 203	3	97	60	10	1.62	0.443	0.027	0.059	0.002	0.195	17.077	0.437	0.055	0.003	0.159	371	19	367	9	403	110	38
X18HK_157_47	HK 203	3	48	45	22	1.10	1.693	0.091	0.166	0.005	0.209	6.017	0.174	0.074	0.004	0.279	1006	33	991	26	1025	98	-10
X18HK_157_48	HK 203	3	80	38	6	2.06	0.408	0.021	0.055	0.001	0.010	18.175	0.462	0.054	0.003	0.374	348	15	345	9	396	110	170
X18HK_157_49	HK 203	3	65	30	5	2.16	0.407	0.025	0.055	0.002	0.070	18.051	0.554	0.053	0.004	0.411	345	18	348	11	300	140	62
X18HK_157_50	HK 203	3	82	40	6	2.02	0.432	0.026	0.056	0.002	0.118	17.828	0.477	0.056	0.003	0.255	363	19	352	9	430	120	104
Stonepark																							
X18HK_151_0	HK 197	3	95	150	72	0.63	1.639	0.071	0.167	0.004	0.515	6.006	0.159	0.072	0.002	0.233	984	28	992	25	994	67	-2
X18HK_151_1	HK 197	3	375	289	48	1.28	0.418	0.020	0.057	0.002	0.491	17.489	0.459	0.053	0.002	0.084	354	14	358	9	318	83	-8
X18HK_151_2	HK 197	3	67	32	5	2.04	0.403	0.032	0.055	0.002	0.093	18.149	0.494	0.054	0.004	0.145	342	23	346	9	370	150	132
X18HK_151_3	HK 197	3	145	89	14	1.65	0.417	0.026	0.056	0.002	0.051	17.828	0.477	0.054	0.003	0.267	353	19	352	9	320	140	50
X18HK_151_4	HK 197	3	120	112	15	1.10	0.389	0.024	0.053	0.002	0.303	19.011	0.578	0.055	0.003	0.129	332	17	331	10	380	120	24
X18HK_151_5	HK 197	3	211	150	26	1.37	0.399	0.023	0.053	0.002	0.124	18.797	0.671	0.054	0.003	0.329	340	17	334	11	360	120	40
X18HK_151_6	HK 197	3	236	151	25	1.60	0.438	0.027	0.057	0.002	0.465	17.699	0.658	0.055	0.003	0.123	368	19	354	13	388	110	130
X18HK_151_7	HK 197	3	153	86	14	1.78	0.424	0.021	0.057	0.002	0.075	17.603	0.465	0.054	0.003	0.550	358	15	356	9	351	100	54
X18HK_151_8	HK 197	3	90	45	7	2.00	0.419	0.028	0.056	0.002	0.183	17.921	0.578	0.055	0.004	0.271	354	20	350	11	360	140	120
X18HK_151_9	HK 197	3	100	63	10	1.61	0.408	0.025	0.055	0.002	0.117	18.083	0.523	0.054	0.003	0.208	346	18	347	10	355	110	74
X18HK_151_10	HK 197	3	81	42	7	1.89	0.409	0.026	0.058	0.002	0.402	17.391	0.575	0.052	0.003	0.122	352	19	361	12	270	120	180
X18HK_151_11	HK 197	3	55	19	9	2.87	1.596	0.079	0.161	0.005	0.541	6.207	0.189	0.074	0.003	0.278	968	31	963	27	1030	90	4
X18HK_151_12	HK 197	3	161	156	21	1.04	0.410	0.025	0.055	0.002	0.089	18.315	0.604	0.054	0.003	0.491	348	18	343	11	370	140	6
X18HK_151_13	HK 197	3	130	80	14	1.61	0.417	0.028	0.056	0.002	0.026	17.762	0.599	0.054	0.004	0.345	353	20	353	11	340	140	-70
X18HK_151_14	HK 197	3	133	84	16	1.64	0.415	0.028	0.053	0.003	0.450	18.868	0.890	0.059	0.004	0.327	356	18	333	15	530	140	22
X18HK_151_15	HK 197	3	748	363	210	2.04	2.243	0.088	0.207	0.005	0.724	4.838	0.115	0.080	0.002	0.421	1195	28	1211	26	1186	55	-3
X19HK_004_0	HK 207	4	193	85	74	2.34	5.030	0.150	0.329	0.007	0.251	3.039	0.064	0.112	0.004	0.281	1821	24	1839	32	1813	53	0.3
X19HK_004_1	HK 207	4	6	1	3	5.90	4.720	0.730	0.185	0.021	0.424	5.405	0.614	0.175	0.029	0.127	1730	140	1090	110	2550	320	0.4
X19HK_004_2	HK 207	4	644	179	156	3.56	4.491	0.070	0.304	0.007	0.654	3.295	0.075	0.108	0.003	0.619	1732	14	1715	36	1758	42	0.7
X19HK_004_3	HK 207	4	593	135	114	4.37	4.740	0.150	0.322	0.010	0.576	3.106	0.096	0.108	0.004	0.568	1772	26	1800	49	1754	65	0.6
X19HK_004_4	HK 207	4	101	59	32	1.68	2.262	0.042	0.204	0.004	0.273	4.897	0.094	0.080	0.002	0.534	1200	13	1197	21	1200	58	0.3
X19HK_004_5	HK 207	4	954	377	365	2.56	5.170	0.260	0.332	0.015	0.233	3.012	0.136	0.114	0.005	0.485	1844	42	1846	71	1850	76	0.2
X19HK_004_6	HK 207	4	114	40	22	2.86	2.283	0.058	0.208	0.005	0.551	4.812	0.113	0.080	0.002	0.448	1205	18	1216	26	1181	57	0.6
X19HK_005_0	HK 208	4	340	288	57	1.23	0.539	0.013	0.070	0.001	0.449	14.347	0.268	0.056	0.002	0.365	437	8	435	8	436	59	0.4
X19HK_005_1	HK 208	4	456	317	64	1.66	0.592	0.019	0.076	0.002	0.012	13.158	0.312	0.056	0.002	0.558	472	12	472	11	451	89	0.0
X19HK_005_2	HK 208	4	526	67	35	8.41	1.310	0.035	0.134	0.003	0.691	7.468	0.184	0.071	0.002	0.271	849	15	810	19	952	44	0.7
X19HK_005_3	HK 208	4	56	46	10	1.23	0.512	0.036	0.068	0.002	0.332	14.815	0.395	0.055	0.004	0.102	424	22	421	11	450	150	0.3
X19HK_005_4	HK 208	4	145	176	132	0.85	4.640	0.140	0.312	0.009	0.493	3.210	0.091	0.107	0.003	0.432	1754	25	1747	43	1749	49	0.5
X19HK_005_5	HK 208	4	1507	738	264	2.13	3.630	0.110	0.246	0.009	0.626	4.072	0.148	0.107	0.004	0.281	1556	24	1415	46	1747	59	0.6
X19HK_005_6	HK 208	4	413	147	102	2.89	4.775	0.098	0.317	0.009	0.839	3.154	0.091	0.109	0.003	0.664	1779	17	1774	44	1790	38	0.8
X19HK_005_7	HK 208	4	1341	287	162	4.79	2.240	0.120	0.161	0.008	0.907	6.231	0.318	0.102	0.003	0.148	1191	37	959	45	1656	46	0.9
X19HK_005_8	HK 208	4	754	533	178	1.49	2.386	0.074	0.192	0.005	0.816	5.219	0.144	0.091	0.002	0.151	1237	22	1130	29	1445	43	0.8
X19HK_005_9	HK 208	4	1283	141	86	10.00	1.986	0.063	0.187	0.005	0.891	5.356	0.152	0.078	0.002	0.005	1109	21	1103	29	1147	40	0.9
X19HK_005_10	HK 208	4	156	133	29	1.13	1.735	0.091	0.149	0.010	0.444	6.707	0.436	0.086	0.005	0.654	1020	33	895	54	1350	110	0.4
X19HK_005_11	HK 208	4	164	70	32	2.53	2.186	0.053	0.195	0.005	0.531	5.128	0.139	0.081	0.002	0.474	1175	17	1148	28	1223	58	0.5
X19HK_015_0	HK 211	3	272	74	12	3.66	0.422	0.027	0.056	0.002	0.224	17.857	0.542	0.054	0.003	0.345	357	19	351	10	370	130	120
X19HK_015_1	HK 211	3	445	101	14	4.85	0.402	0.018	0.055	0.001	0.435	18.172	0.462	0.054	0.002	0.106	343	13	345	9	344	76	-19
X19HK_015_2	HK 211	3	79	48	9	1.71	0.489	0.033	0.061	0.002	0.016	16.420	0.620	0.059	0.004	0.440	403	22	381	14	510	150	-30
X19HK_015_3	HK 211	3	60	122	19	0.51	0.376	0.036	0.053	0.002	0.133	19.011	0.614	0.051	0.005	0.143	322	26	330	10	210	180	128
X19HK_015_4	HK 211	3	633	81	13	8.01	0.405	0.018	0.055	0.002	0.583	18.198	0.497	0.054	0.002	0.073	345	13	345	9	349	73	6
X19HK_015_5	HK 211	3	367	92	15	4.25	0.388	0.019	0.050	0.001	0.243	20.040	0.562	0.057	0.003	0.247	332	14	314	9	479	96	24
X19HK_015_6	HK 211	3	297	300	35	1.13	0.562	0.046	0.051	0.002	0.142	19.608	0.769	0.081	0.007	0.449	449	29	320	12	1200	180	67
X19HK_015_7	HK 211	3	213	74	11	2.90	0.414	0.028	0.056	0.002	0.102	18.018	0.682	0.055	0.004	0.317	351	20	348	13	420	160	66
X19HK_015_8	HK 211	3	124	59	10	2.20	0.448	0.026	0.058	0.001	0.027	17.280	0.418	0.057	0.003	0.326	375	18	363	8	466	110	28
X19HK_015_9	HK 211	3	160	96	13	2.00	0.476	0.046	0.054	0.002	0.020	18.416	0.543	0.062	0.006	0.410	392	31	341	10	630	180	170
X19HK_015_10	HK 211	3	219	132	29	1.76	0.920	0.089	0.074	0.003	0.820	13.441	0.578	0.086	0.005	0.289	673	47	463	19	1380	110	63
X19HK_015_11	HK 211	3	23	13	2	1.92	0.456	0.048	0.056	0.002	0.190	17.794	0.633	0.057	0.006	0.070	382	35	352	12	510	220	65
X19HK_015_12	HK 211	3	343	84	15	4.42	0.401	0.022	0.054	0.001	0.267	18.574	0.483	0.055	0.003	0.129	342	16	338	8	378	110	60

Continue Table A2- 1

							isotopic ratios										ages						
Grain-ID	Lab ID	# exp	U	Th	Pb	U/Th	$^{207}Pb/^{235}U$	± 2SE	$^{206}Pb/^{238}U$	± 2SE	ρ*	$^{238}U/^{206}Pb$	± 2SE	$^{207}Pb/^{206}Pb$	± 2SE	ρ**	$^{207}Pb/^{235}U$	± 2SE	$^{206}Pb/^{238}U$	±SE	$^{207}Pb/^{206}Pb$	± 2SE	Disc. %
X19HK_015_13	HK 211	3	161	80	13	2.46	0.437	0.022	0.058	0.002	0.310	17.271	0.477	0.056	0.002	0.192	369	16	363	10	412	98	48
X19HK_015_14	HK 211	3	176	50	8	3.95	0.417	0.020	0.055	0.001	0.198	18.169	0.462	0.055	0.002	0.314	353	15	345	9	407	89	-2
X19HK_015_15	HK 211	3	85	62	11	1.59	0.417	0.024	0.056	0.002	0.362	17.794	0.507	0.054	0.003	0.101	353	17	353	10	355	100	-36
X19HK_015_16	HK 211	3	297	53	9	6.09	0.417	0.022	0.057	0.002	0.041	17.587	0.464	0.053	0.003	0.350	353	16	357	9	297	110	41
X19HK_015_17	HK 211	3	344	205	33	1.84	0.399	0.022	0.055	0.002	0.274	18.349	0.572	0.053	0.002	0.337	341	16	342	10	325	95	-20
X19HK_015_18	HK 211	3	121	45	7	2.86	0.443	0.026	0.056	0.002	0.201	18.018	0.519	0.057	0.003	0.196	372	18	348	10	480	120	31
X19HK_015_19	HK 211	3	119	47	8	3.14	0.399	0.029	0.055	0.002	0.013	18.282	0.568	0.054	0.004	0.327	339	21	343	10	340	160	110
X19HK_015_20	HK 211	3	351	59	9	6.60	0.439	0.019	0.056	0.001	0.315	17.924	0.450	0.057	0.002	0.347	369	14	350	9	492	77	0.0
X19HK_015_21	HK 211	3	136	81	15	1.86	0.540	0.044	0.060	0.002	0.255	16.750	0.561	0.065	0.006	0.351	436	28	374	12	740	170	38
X19HK_015_22	HK 211	3	149	54	8	2.92	0.412	0.022	0.056	0.001	0.189	17.883	0.448	0.053	0.003	0.251	350	16	351	9	314	100	37
X19HK_015_23	HK 211	3	315	81	13	4.13	0.429	0.022	0.057	0.002	0.329	17.455	0.457	0.055	0.002	0.199	362	16	359	9	402	97	-18
X19HK_015_24	HK 211	3	511	74	12	7.21	0.412	0.019	0.056	0.002	0.533	17.854	0.478	0.053	0.002	0.118	352	13	351	9	343	82	-23
X19HK_015_25	HK 211	3	168	98	16	1.83	0.430	0.022	0.057	0.001	0.152	17.541	0.431	0.055	0.003	0.245	363	16	357	9	388	100	-45
X19HK_015_26	HK 211	3	479	104	12	4.86	0.435	0.020	0.058	0.002	0.516	17.182	0.590	0.054	0.002	0.397	369	16	364	12	371	76	5
X19HK_015_27	HK 211	3	187	105	12	1.94	0.556	0.030	0.057	0.002	0.300	17.575	0.494	0.071	0.003	0.124	448	20	357	10	958	91	62
X19HK_015_28	HK 211	3	110	51	8	2.21	0.416	0.024	0.057	0.002	0.428	17.699	0.564	0.054	0.003	0.141	352	17	354	11	350	110	64
X19HK_015_29	HK 211	3	304	66	10	4.77	0.386	0.018	0.054	0.002	0.655	18.450	0.545	0.052	0.002	0.071	331	13	340	10	293	82	-1.0
X19HK_015_30	HK 211	3	241	55	9	4.67	0.393	0.020	0.053	0.001	0.260	18.734	0.456	0.054	0.002	0.249	336	14	335	8	346	89	9
X19HK_015_31	HK 211	3	186	83	13	2.13	0.399	0.020	0.054	0.001	0.121	18.372	0.473	0.053	0.002	0.279	342	15	342	8	308	91	-12
X19HK_015_32	HK 211	3	179	43	7	4.38	0.403	0.023	0.055	0.002	0.107	18.051	0.521	0.052	0.002	0.292	344	16	348	10	284	100	34
X19HK_015_33	HK 211	3	95	90	14	1.06	0.412	0.026	0.056	0.002	0.676	17.857	0.574	0.054	0.003	0.183	349	19	351	11	381	110	0.0
X19HK_015_34	HK 211	3	192	129	18	1.55	0.430	0.025	0.054	0.002	0.257	18.587	0.622	0.057	0.003	0.378	363	17	338	11	515	99	-5
X19HK_015_35	HK 211	3	106	62	11	1.97	0.456	0.028	0.060	0.002	0.583	16.694	0.613	0.055	0.003	0.264	380	20	375	13	370	120	28
X19HK_016_0	HK 212	4	192	118	17	1.55	0.461	0.023	0.052	0.002	0.120	19.231	0.740	0.064	0.004	0.664	385	16	327	13	750	130	0.1
X19HK_016_1	HK 212	4	139	65	11	2.04	0.418	0.032	0.057	0.001	0.165	17.668	0.437	0.054	0.004	0.140	353	23	355	9	380	180	0.2
X19HK_016_2	HK 212	4	176	97	16	1.77	0.405	0.024	0.055	0.004	0.045	18.248	1.265	0.054	0.005	0.595	345	18	344	23	430	220	0.0
X19HK_016_3	HK 212	4	103	46	7	2.19	0.420	0.024	0.056	0.002	0.171	17.825	0.604	0.054	0.003	0.430	355	17	352	12	320	130	0.2
X19HK_016_4	HK 212	4	339	275	44	1.19	0.397	0.011	0.053	0.001	0.336	18.797	0.353	0.054	0.002	0.393	339	8	334	6	385	71	0.3
X19HK_016_5	HK 212	4	119	69	13	1.78	0.447	0.020	0.061	0.001	0.160	16.474	0.380	0.054	0.003	0.407	374	14	380	8	340	110	0.2
X19HK_016_6	HK 212	4	118	96	21	1.26	0.658	0.065	0.060	0.002	0.405	16.667	0.639	0.080	0.008	0.026	510	39	376	14	1260	190	0.4
X19HK_016_7	HK 212	4	224	186	27	1.29	0.404	0.016	0.053	0.001	0.366	18.727	0.386	0.055	0.002	0.090	343	11	335	7	414	86	0.4
X19HK_016_8	HK 212	4	198	132	21	1.49	0.401	0.012	0.055	0.001	0.158	18.282	0.468	0.055	0.002	0.605	342	9	344	9	397	94	0.2
X19HK_016_9	HK 212	4	127	67	10	1.89	0.423	0.032	0.056	0.002	0.502	18.018	0.617	0.054	0.005	0.013	357	23	348	11	370	160	0.5
Slievedart Area																							
X18KH133_0	HK 187	1	109	78	14	1.26	0.456	0.033	0.058	0.003	0.332	17.331	0.811	0.058	0.004	0.303	379	23	361	16	470	140	83
X18KH133_1	HK 187	1	296	430	62	0.84	0.426	0.030	0.055	0.003	0.240	18.051	0.815	0.055	0.004	0.693	358	21	348	15	400	160	6
X18KH133_2	HK 187	1	168	140	23	1.20	0.440	0.020	0.059	0.002	0.186	17.036	0.580	0.054	0.002	0.374	370	14	368	12	371	89	80
X18KH133_3	HK 187	1	339	289	37	1.22	0.402	0.020	0.053	0.003	0.439	18.904	0.929	0.057	0.004	0.214	343	15	332	16	460	140	68
X18KH133_4	HK 187	1	66	51	8	1.34	0.456	0.039	0.054	0.005	0.326	18.484	1.674	0.062	0.006	0.073	378	29	339	30	590	190	56
X18KH133_5	HK 187	1	83	80	11	1.09	0.448	0.069	0.059	0.002	0.419	16.949	0.661	0.055	0.008	0.206	374	41	369	14	370	210	120
X18KH133_6	HK 187	1	146	109	18	1.41	0.407	0.024	0.056	0.002	0.179	18.018	0.682	0.053	0.003	0.339	346	17	348	13	320	120	54
X18KH133_7	HK 187	1	397	1290	347	0.32	3.110	0.290	0.079	0.004	0.863	12.658	0.641	0.280	0.018	0.617	1406	78	490	24	3320	120	85
X18KH133_8	HK 187	1	343	300	44	1.14	0.404	0.029	0.055	0.002	0.318	18.116	0.689	0.053	0.004	0.535	344	20	346	13	320	120	60
X18KH133_9	HK 187	1	408	279	43	1.52	0.407	0.020	0.055	0.002	0.417	18.182	0.661	0.054	0.002	0.230	346	14	345	12	339	91	12
X18KH133_10	HK 187	1	866	1550	245	0.60	0.425	0.095	0.055	0.003	0.405	18.116	1.017	0.056	0.008	0.408	359	52	346	19	430	190	44
X18KH133_11	HK 187	1	151	205	31	0.76	0.420	0.029	0.056	0.002	0.227	18.018	0.682	0.054	0.003	0.218	354	21	348	13	350	130	62
X18KH133_12	HK 187	1	488	451	64	1.08	0.415	0.310	0.057	0.003	0.914	17.699	0.877	0.053	0.021	0.288	351	84	355	17	322	300	-35
X18KH133_13	HK 187	1	352	220	35	1.60	0.418	0.019	0.056	0.002	0.389	17.731	0.660	0.054	0.002	0.365	354	13	354	13	351	86	94
X18KH133_14	HK 187	1	525	258	42	2.02	0.412	0.017	0.056	0.002	0.270	18.018	0.649	0.054	0.002	0.483	350	12	348	12	355	82	-17
X18KH133_15	HK 187	1	454	645	100	0.72	0.437	0.021	0.055	0.002	0.363	18.282	0.668	0.058	0.002	0.333	367	15	343	12	520	89	8
X18KH133_16	HK 187	1	260	247	42	1.05	0.418	0.018	0.055	0.002	0.381	18.051	0.717	0.055	0.003	0.496	354	13	348	14	400	95	-27
X18KH133_17	HK 187	1	538	561	74	1.04	0.498	0.035	0.053	0.002	0.530	18.904	0.750	0.068	0.004	0.143	408	23	332	13	830	110	52
X18KH133_18	HK 187	1	1176	800	130	1.44	0.404	0.017	0.054	0.002	0.708	18.382	0.642	0.054	0.002	0.100	345	13	341	12	361	69	-7
X18KH133_19	HK 187	1	225	233	34	0.96	0.553	0.071	0.052	0.007	0.658	19.120	2.632	0.076	0.004	0.264	442	48	328	44	1040	110	61
X18KH133_20	HK 187	1	452	299	49	1.52	0.431	0.020	0.058	0.002	0.337	17.301	0.629	0.054	0.002	0.417	363	14	362	13	347	89	10
X18KH133_21	HK 187	1	75	50	7	1.58	0.456	0.520	0.059	0.005	0.215	16.949	1.321	0.054	0.042	0.459	378	170	369	28	400	460	85
X18KH133_22	HK 187	1	651	560	91	1.23	0.421	0.018	0.054	0.002	0.416	18.416	0.644	0.056	0.002	0.329	356	13	341	11	449	78	-6
X18KH133_23	HK 187	1	822	816	135	1.03	0.439	0.019	0.058	0.002	0.611	17.241	0.624	0.055	0.002	0.210	369	13	363	13	398	72	-21
X18KH133_24	HK 187	1	391	355	58	1.20	0.418	0.021	0.056	0.002	0.487	17.921	0.674	0.054	0.002	0.178	354	15	350	13	354	89	40
X18KH133_25	HK 187	1	260	252	39	1.06	0.407	0.023	0.055	0.002	0.285	18.149	0.725	0.054	0.003	0.287	345	17	346	13	330	110	130
X18KH133_26	HK 187	1	399	340	51	1.37	0.423	0.017	0.057	0.002	0.410	17.422	0.607	0.053	0.002	0.602	358	12	360	12	332	75	-10
X18KH133_27	HK 187	1	304	193	30	1.62	0.405	0.018	0.055	0.002	0.357	18.083	0.752	0.053	0.002	0.601	345	13	347	14	329	94	48
X18KH133_28	HK 187	1	540	340	51	1.59	0.405	0.019	0.054	0.002	0.431	18.657	0.627	0.055	0.002	0.085	344	14	337	11	382	86	-37
X18KH133_29	HK 187	1	451	930	42	0.70	0.361	0.039	0.048	0.005	0.888	21.053	2.039	0.055	0.003	0.024	311	29	299	29	394	110	17
X18KH133_30	HK 187	1	193	392	28	0.57	0.467	0.029	0.053	0.002	0.232	19.011	0.867	0.065	0.004	0.415	387	20	331	15	720	130	39
X18KH133_31	HK 187	1	1371	806	126	1.69	0.408	0.016	0.055	0.002	0.598	18.149	0.692	0.054	0.002	0.458	347	12	345	13	354	71	-13
X18HK135_0	HK 190	1	647	333	54	2.08	0.427	0.020	0.057	0.002	0.598	17.422	0.637	0.054	0.002	0.037	360	14	360	13	354	79	-12
X18HK135_1	HK 190	1	527	272	37	2.01	0.424	0.017	0.058	0.002	0.314	17.391	0.575	0.054	0.002	0.265	361	11	360	12	351	83	80
X18HK135_2	HK 190	1	417	243	35	1.69	0.435	0.022	0.057	0.002	0.448	17.575	0.587	0.055	0.002	0.120	366	15	356	12	390	99	160
X18HK135_3	HK 190	1	385	166	28	2.31	0.424	0.018	0.057	0.002	0.037	17.556	0.616	0.054	0.002	0.445	359	13	357	12	364	81	6
X18HK135_4	HK 190	1	481	1070	69	0.46	0.512	0.024	0.047	0.002	0.296	21.368	0.867	0.080	0.004	0.494	419	16	295	12	1168	90	74
X18HK135_5	HK 190	1	638	596	77	1.06	0.565	0.026	0.067	0.003	0.444	14.837	0.616	0.061	0.002	0.558	454	17	420	17	621	87	22
X18HK135_6	HK 190	1	351	112	19	3.17	0.415	0.020	0.056	0.002	0.142	17.794	0.602	0.054	0.003	0.337	352	14	352	11	333	95	0.0
X18HK135_7	HK 190	1	198	188	29	1.09	0.423	0.024	0.057	0.002	0.300	17.575	0.741	0.054	0.005	0.278	357	17	356	14	350	150	38
X18HK135_8	HK 190	1	518	111	18	4.79	0.411	0.017	0.056	0.002	0.402	17.857	0.606	0.054	0.002	0.288	350	12	352	12	345	77	-25
X18HK135_9	HK 190	1	694	253	22	2.96	0.429	0.016	0.058	0.002	0.121	17.123	0.557	0.054	0.002	0.512	363	12	366	12	345	69	-40
X18HK135_10	HK 190	1	288	345	56	0.83	0.392	0.037	0.053	0.002	0.151	18.797	0.707	0.054	0.005	0.191	335	25	334	12	340	180	140
X18HK135_11	HK 190	1	80	77	12	1.05	0.448	0.036	0.059	0.003	0.022	16.978	0.922	0.056	0.004	0.359	373	25	369	20	380	150	80
X18HK135_12	HK 190	1	288	230	38	1.29	0.417	0.017	0.057	0.002	0.172	17.699	0.595	0.054	0.002	0.436	354	13	354	12	355	83	-7
X18HK135_13	HK 190	1	606	307	41	2.10	0.468	0.018	0.058	0.002	0.462	17.361	0.633	0.059	0.002	0.148	390	13	361	13	571	70	35
X18HK135_14	HK 190	1	781	397	60	2.08	0.419	0.015	0.057	0.002	0.388	17.513	0.644	0.053	0.002	0.437	358	11	358	13	338	75	44
X18HK135_15	HK 190	1	246	237	35	1.05	0.411	0.320	0.059	0.019	0.397	17.094	5.552	0.051	0.007	0.490	349	130	366	110	240	190	590
X18HK135_16	HK 190	1	590	76	20	7.60	0.510	0.170	0.060	0.014	0.712	16.667	3.889	0.061	0.003	0.119	410	76	376	78	610	77	2.0
X18HK135_17	HK 190	1	372	1920	131	0.20	0.628	0.045	0.052	0.002	0.079	19.380	0.751	0.089	0.006	0.652	494	28	324	12	1380	130	75
X18HK135_18	HK 190	1	531	1439	63	0.37	0.526	0.023	0.050	0.002	0.073	19.960	0.956	0.077	0.004	0.650	429	15	315	15	1093	100	69
X18HK135_19	HK 190	1	220	196	31	1.15	0.405	0.260	0.054	0.002	0.360	18.657	0.801	0.055	0.035	0.134	344	120	337	14	370	380	69
X18HK135_20	HK 190	1	582	490	32	1.54	0.456	0.022	0.054	0.002	0.087	18.671	0.662	0.061	0.003	0.312	381	15	336	11	640	96	37
X18HK135_21	HK 190	1	553	902	44	0.62	0.427	0.022	0.049	0.002	0.591	20.325	0.785	0.063	0.003	0.014	360	15	310	12	684	92	50
X18HK135_22	HK 190	1	348	356	41	0.95	0.455	0.021	0.054	0.002	0.232	18.622	0.624	0.061	0.003	0.378	380	14	337	11	626	89	38
X18HK135_23	HK 190	1	392	320	48	1.29	0.401	0.018	0.054	0.002	0.275	18.450	0.613	0.054	0.002	0.300	342	13	340	11	350	90	-5
X18HK135_24	HK 190	1	358	1340	62	0.38	0.558	0.039	0.044	0.003	0.639	22.523	1.319	0.097	0.011	0.901	447	25	280	16	1400	210	70
X18HK135_25	HK 190	1	380	144	17	2.64	0.435	0.023	0.056	0.003	0.670	17.921	0.931	0.057	0.002	0.027	366	16	350	18	460	89	-7
X18HK135_26	HK 190	1	215	233	38	0.90	0.424	0.093	0.056	0.002	0.421	17.762	0.694	0.055	0.009	0.012	358	53	353	13	400	230	41
X18HK135_27	HK 190	1	329	280	48	1.17	0.434	0.022	0.057	0.002	0.376	17.513	0.583	0.055	0.003	0.161	365	16	358	12	382	99	220
X18HK135_28	HK 190	1	894	1030	150	0.88	0.429	0.016	0.058	0.002	0.678	17.391	0.665	0.054	0.002	0.587	362	11	361	14	385	71	-13
X18HK135_29	HK 190	1	854	1072	83	0.79	0.446	0.018	0.053	0.002	0.294	18.762	0.704	0.061	0.003	0.212	374	12	335	12	613	85	40
X18HK_137_0	HK 192	2	323	130	21	2.47	0.404	0.016	0.055	0.002	0.440	18.116	0.525	0.053	0.002	0.214	344	11	346	10	331	100	-150
X18HK_137_1	HK 192	2	77	55	9	1.38	0.393	0.027	0.055	0.001	0.096	18.215	0.431	0.052	0.004	0.156	341	21	345	8	290	150	119
X18HK_137_2	HK 192	2	121	55	10	2.20	0.427	0.028	0.054	0.002	0.175	18.450	0.545	0.056	0.004	0.340	360	20	340	10	430	150	34
X18HK_137_3	HK 192	2	171	99	14	1.74	0.424	0.030	0.051	0.001	0.298	19.493	0.494	0.058	0.003	0.096	358	21	323	8	559	110	39
X18HK_137_4	HK 192	2	193	82	13	2.33	0.407	0.020	0.056	0.002	0.069	18.018	0.617	0.054	0.003	0.640	346	15	348	12	350	140	0.0
X18HK_137_5	HK 192	2	142	126	19	1.16	0.395	0.021	0.053	0.001	0.020	18.832	0.426	0.054	0.003	0.347	337	16	333	7	350	120	25
X18HK_137_6	HK 192	2	84	46	7	1.86	0.403	0.025	0.054	0.001	0.197	18.352	0.404	0.053	0.003	0.080	345	19	342	7	300	130	70
X18HK_137_7	HK 192	2	264	102	17	2.55	0.410	0.014	0.056	0.001	0.144	17.902	0.320	0.053	0.002	0.375	351	10	350	6	342	81	-27
X18HK_137_8	HK 192	2	476	251	39	1.91	0.404	0.014	0.055	0.001	0.317	18.285	0.368	0.053	0.002	0.179	345	10	343	7	320	80	-10
X18HK_137_9	HK 192	2	158	140	26	1.15	0.630	0.110	0.058	0.002	0.359	17.361	0.452	0.081	0.013	0.230	483	60	361	9	1040	280	54
X18HK_137_10	HK 192	2	136	108	21	1.29	0.532	0.034	0.057	0.001	0.529	17.699	0.407	0.068	0.004	0.248	430	22	354	8	840	120	45
X18HK_137_11	HK 192	2	114	132	22	0.90	0.912	0.074	0.057	0.002	0.349	17.575	0.525	0.113	0.009	0.040	654	39	357	11	1880	140	81
X18HK_137_12	HK 192	2	274	152	25	1.83	0.418	0.019	0.056	0.002	0.320	17.762	0.536	0.055	0.003	0.665	354	14	353	10	390	130	37
X18HK_137_13	HK 192	2	286	180	29	1.61	0.404	0.018	0.055	0.001	0.343	18.159	0.330	0.053	0.002	0.128	344	13	346	6	333	98	-12
X18HK_137_14	HK 192	2	90	63	10	1.44	0.418	0.025	0.056	0.001	0.360	17.921	0.418	0.053	0.003	0.029	354	18	350	8	340	130	67
X18HK_137_15	HK 192	2	232	173	29	1.33	0.419	0.036	0.057	0.002	0.587	17.668	0.593	0.055	0.005	0.296	355	26	355	11	400	180	29
X18HK_137_16	HK 192	2	275	132	20	2.07	0.424	0.025	0.054	0.002	0.080	18.587	0.622	0.056	0.003	0.436	358	18	338	11	440	130	6
X18HK_137_17	HK 192	2	514	322	62	1.62	0.624	0.037	0.057	0.002	0.657	17.544	0.492	0.080	0.004	0.439	491	23	358	10	1181	99	71
X18HK_137_18	HK 192	2	38	21	4	1.84	0.451	0.034	0.056	0.002	0.221	17.921	0.514	0.057	0.004	0.093	375	24	350	10	490	160	87
X18HK_137_19	HK 192	2	178	144	25	1.23	0.490	0.056	0.057	0.002	0.303	17.637	0.498	0.063	0.008	0.121	402	36	356	10	640	230	60
X18HK_137_20	HK 192	2	104	70	12	1.48	0.386	0.028	0.054	0.002	0.157	18.587	0.518	0.051	0.004	0.600	331	21	338	9	270	190	-40
X18HK_137_21	HK 192	2	101	68	10	1.48	0.417	0.046	0.056	0.002	0.345	17.986	0.647	0.055	0.006	0.079	353	33	349	12	370	240	80
X18HK_137_22	HK 192	2	209	218	35	0.96	0.424	0.018	0.057	0.001	0.415	17.513	0.429	0.055	0.002	0.158	361	13	358	8	395	91	-15

Continue Table A2- 1

							isotopic ratios										ages						
Grain-ID	Lab ID	# exp	U	Th	Pb	U/Th	$^{207}Pb/^{235}U$	± 2SE	$^{206}Pb/^{238}U$	± 2SE	ρ*	$^{238}U/^{206}Pb$	± 2SE	$^{207}Pb/^{206}Pb$	± 2SE	ρ**	$^{207}Pb/^{235}U$	± 2SE	$^{206}Pb/^{238}U$	±SE	$^{207}Pb/^{206}Pb$	± 2SE	Disc. %
X18HK_138_0	HK 193	2	269	1030	42	0.27	0.434	0.020	0.045	0.002	0.544	22.321	0.797	0.072	0.003	0.374	370	13	283	10	980	88	68
X18HK_138_1	HK 193	2	94	242	220	0.37	11.800	1.700	0.143	0.015	0.966	6.993	0.734	0.597	0.033	0.670	2590	130	858	87	4494	84	81
X18HK_138_2	HK 193	2	292	123	20	2.39	0.406	0.013	0.055	0.001	0.169	18.159	0.330	0.054	0.002	0.345	346	10	346	6	338	83	36
X18HK_138_3	HK 193	2	623	279	44	2.26	0.405	0.013	0.055	0.002	0.335	18.149	0.527	0.053	0.002	0.539	345	10	346	10	337	81	-8
X18HK_138_4	HK 193	2	160	522	26	0.32	0.325	0.022	0.042	0.001	0.377	23.866	0.740	0.057	0.004	0.070	285	17	265	8	440	150	56
X18HK_138_5	HK 193	2	178	80	14	2.25	0.410	0.015	0.056	0.001	0.190	17.950	0.322	0.053	0.002	0.582	350	11	349	6	315	90	53
X18HK_138_6	HK 193	2	191	118	19	1.61	0.413	0.030	0.057	0.002	0.042	17.637	0.498	0.053	0.004	0.412	351	22	355	10	330	170	0.0
X18HK_138_7	HK 193	2	61	42	6	1.47	0.403	0.027	0.054	0.001	0.183	18.450	0.408	0.053	0.004	0.122	342	20	340	8	320	140	24
X18HK_138_8	HK 193	2	82	63	10	1.31	0.415	0.032	0.056	0.001	0.222	18.018	0.422	0.054	0.004	0.069	351	23	348	8	330	160	60
X18HK_138_9	HK 193	2	40	93	9	0.44	0.718	0.060	0.054	0.002	0.096	18.587	0.656	0.095	0.009	0.390	551	37	338	12	1540	170	75
X18HK_138_10	HK 193	2	107	46	8	2.29	0.447	0.035	0.060	0.002	0.136	16.584	0.523	0.053	0.004	0.202	374	25	378	12	320	180	170
X18HK_138_11	HK 193	2	225	99	17	2.28	0.404	0.016	0.055	0.001	0.347	18.315	0.403	0.053	0.002	0.347	344	11	343	8	338	94	-1
X18HK_138_12	HK 193	2	195	108	20	1.81	0.404	0.035	0.055	0.003	0.776	18.051	0.880	0.052	0.003	0.422	352	30	348	17	380	140	25
X18HK_138_13	HK 193	2	493	348	44	1.45	0.408	0.017	0.055	0.001	0.411	18.192	0.397	0.054	0.002	0.068	347	12	345	7	350	90	-31
X18HK_138_14	HK 193	2	415	414	66	1.02	0.401	0.016	0.055	0.002	0.442	18.215	0.498	0.053	0.002	0.366	342	12	345	9	302	88	-26
X18HK_138_15	HK 193	2	385	240	26	1.58	0.404	0.018	0.055	0.002	0.406	18.248	0.499	0.055	0.002	0.097	345	13	344	9	395	99	16
X18HK_138_16	HK 193	2	138	172	18	0.82	0.405	0.036	0.055	0.002	0.138	18.282	0.635	0.054	0.005	0.462	344	26	343	12	330	210	63
X18HK_138_17	HK 193	2	81	32	8	2.54	0.595	0.034	0.055	0.001	0.233	18.159	0.396	0.077	0.004	0.130	472	21	346	7	1116	110	66
X18HK_138_18	HK 193	2	78	69	9	1.11	0.387	0.034	0.053	0.002	0.103	18.939	0.717	0.056	0.005	0.544	331	25	332	12	460	200	-130
X18HK_138_19	HK 193	2	147	97	16	1.51	0.401	0.024	0.056	0.001	0.326	17.986	0.421	0.054	0.003	0.063	345	16	349	8	340	120	42
X18HK_138_20	HK 193	2	333	155	24	2.20	0.407	0.017	0.055	0.001	0.209	18.073	0.327	0.053	0.002	0.285	349	12	347	6	330	91	40
X18HK_138_21	HK 193	2	340	326	52	1.04	0.400	0.013	0.055	0.001	0.150	18.188	0.364	0.052	0.002	0.421	343	10	345	7	291	83	0.0
X18HK_138_22	HK 193	2	192	162	26	1.39	0.399	0.018	0.054	0.001	0.240	18.457	0.409	0.053	0.003	0.231	340	13	340	7	306	100	50
X18HK_139_0	HK 194	2	124	52	5	2.42	0.376	0.019	0.040	0.002	0.364	24.752	1.470	0.068	0.005	0.627	323	14	255	15	830	130	67
X18HK_139_1	HK 194	2	158	105	17	1.57	0.431	0.036	0.057	0.001	0.238	17.422	0.395	0.055	0.005	0.081	362	26	360	8	360	180	35
X18HK_139_2	HK 194	2	160	94	15	1.85	0.570	0.048	0.055	0.003	0.344	18.149	0.889	0.076	0.008	0.695	457	31	346	17	1030	230	61
X18HK_139_3	HK 194	2	287	290	48	1.02	0.409	0.028	0.056	0.001	0.363	18.018	0.422	0.053	0.003	0.060	347	20	348	8	300	140	80
X18HK_139_4	HK 194	2	190	52	9	3.60	0.438	0.028	0.058	0.001	0.181	17.173	0.354	0.055	0.003	0.143	368	19	365	7	370	130	14
X18HK_139_5	HK 194	2	170	104	17	1.61	0.453	0.035	0.057	0.002	0.763	17.422	0.668	0.058	0.004	0.326	378	24	360	13	500	150	20
X18HK_139_6	HK 194	2	186	41	7	4.48	0.436	0.024	0.054	0.001	0.041	18.605	0.415	0.058	0.003	0.323	367	17	338	7	560	130	60
X18HK_139_7	HK 194	2	170	41	7	4.14	0.401	0.018	0.055	0.001	0.107	18.232	0.319	0.053	0.003	0.173	344	14	344	6	332	100	33
X18HK_139_8	HK 194	2	194	121	22	1.59	0.432	0.019	0.058	0.001	0.222	17.391	0.393	0.054	0.003	0.599	364	14	360	8	360	120	-50
X18HK_139_9	HK 194	2	249	47	8	5.56	0.427	0.023	0.057	0.001	0.564	17.637	0.435	0.055	0.003	0.115	360	16	356	9	407	100	-22
X18HK_139_10	HK 194	2	81	51	8	1.64	0.516	0.036	0.057	0.002	0.268	17.637	0.591	0.066	0.004	0.120	421	24	355	12	790	130	72
X18HK_139_11	HK 194	2	205	145	115	1.36	4.450	0.330	0.288	0.017	0.959	3.472	0.205	0.112	0.004	0.407	1725	59	1631	88	1832	60	12
X18HK_139_12	HK 194	2	114	76	12	1.56	0.413	0.030	0.056	0.002	0.147	17.857	0.606	0.054	0.004	0.353	350	21	351	11	330	140	15
X18HK_139_13	HK 194	2	176	188	15	0.93	0.560	0.026	0.053	0.003	0.524	18.975	0.900	0.077	0.005	0.829	451	17	331	15	1100	140	67
X18HK_139_14	HK 194	2	235	71	23	3.86	0.831	0.049	0.097	0.005	0.820	10.277	0.549	0.062	0.003	0.197	613	28	599	31	663	92	12
X18HK_139_15	HK 194	2	228	101	17	2.32	0.406	0.020	0.054	0.001	0.361	18.365	0.371	0.054	0.003	0.013	345	14	342	7	367	110	-130
X18HK_139_16	HK 194	2	135	59	11	2.63	0.473	0.026	0.056	0.001	0.384	17.879	0.384	0.061	0.003	0.041	392	18	351	7	617	100	29
X18HK_139_17	HK 194	2	218	220	42	1.02	0.758	0.042	0.075	0.001	0.184	13.364	0.250	0.074	0.004	0.137	577	26	465	8	1040	110	53
X18HK_139_18	HK 194	2	22	13	2	1.81	0.425	0.053	0.057	0.002	0.160	17.513	0.705	0.052	0.007	0.296	355	39	358	14	240	250	61
X18HK_139_19	HK 194	2	51	43	7	1.22	0.414	0.034	0.056	0.002	0.192	17.825	0.699	0.053	0.004	0.173	350	24	352	13	350	190	100
X18HK_139_20	HK 194	2	294	188	53	1.58	0.765	0.026	0.094	0.002	0.492	10.627	0.181	0.059	0.002	0.115	576	15	580	10	569	67	-10
X18HK_139_21	HK 194	2	75	55	9	1.36	0.425	0.026	0.058	0.001	0.204	17.241	0.416	0.053	0.004	0.159	362	18	363	8	310	140	57

Table A2 - 2: LA-ICP-MS U-Pb apatite isotopic and age data. P = correlation coefficient for $^{206}Pb/^{238}U$ vs $^{207}Pb/^{235}U$. P** = correlation coefficient for $^{238}U/^{206}Pb$ vs $^{207}Pb/^{206}Pb$. All errors are propagated errors at the 2SE level.*

			isotopic ratios										ages			
Sample ID	Lab ID	#exp	$^{207}Pb/^{235}U$	± 2SE	$^{206}Pb/^{238}U$	± 2SE	ρ*	$^{238}U/^{206}Pb$	± 2SE	$^{207}Pb/^{206}Pb$	± 2SE	ρ**	$^{207}Pb/^{235}U$	± 2SE	$^{206}Pb/^{238}U$	± 2SE
A_MAD_0		1	0.609	0.021	0.0775	0.0042	0.02	12.90	0.70	0.057	0.000	0.19	483	13	480	25
A_MAD_1		1	0.605	0.020	0.0769	0.0038	-0.05	13.00	0.64	0.057	0.000	-0.08	480	13	477	23
A_MAD_2		1	0.620	0.021	0.0788	0.0043	-0.05	12.69	0.69	0.057	0.000	0.03	489	13	489	25
A_MAD_3		1	0.623	0.039	0.0743	0.0075	0.02	13.46	1.36	0.057	0.000	-0.14	481	12	460	46
A_MAD_4		1	0.592	0.019	0.0751	0.0040	-0.12	13.32	0.71	0.057	0.000	0.02	472	12	466	23
A_MAD_5		1	0.590	0.021	0.0750	0.0044	0.00	13.33	0.78	0.057	0.000	-0.13	470	14	466	26
A_MAD_6		1	0.607	0.022	0.0773	0.0052	0.01	12.94	0.87	0.057	0.000	0.03	481	14	479	30
A_MAD_7		1	0.604	0.021	0.0768	0.0046	-0.03	13.02	0.78	0.057	0.000	0.32	479	13	476	27
A_MAD_8		1	0.593	0.023	0.0753	0.0048	-0.01	13.28	0.85	0.057	0.000	0.02	472	14	467	28
A_MAD_9		1	0.590	0.027	0.0750	0.0053	-0.01	13.33	0.94	0.057	0.000	-0.20	469	17	465	31
A_MAD_10		1	0.593	0.022	0.0753	0.0049	0.05	13.28	0.86	0.057	0.000	-0.01	469	12	467	29
A_MAD_11		1	0.611	0.022	0.0775	0.0050	0.00	12.90	0.83	0.057	0.000	0.21	483	13	481	29
A_MAD_12		1	0.592	0.021	0.0749	0.0039	0.03	13.35	0.70	0.057	0.000	0.24	472	13	465	23
A_MAD_13		1	0.600	0.023	0.0760	0.0046	0.03	13.16	0.80	0.057	0.000	-0.05	477	14	472	27
A_MAD_14		1	0.577	0.022	0.0743	0.0058	0.01	13.46	1.05	0.057	0.000	-0.14	462	14	461	33
A_MAD_15		1	0.594	0.022	0.0753	0.0047	-0.05	13.28	0.83	0.057	0.000	-0.03	473	14	467	28
A_MAD_16		1	0.591	0.021	0.0747	0.0045	0.03	13.39	0.81	0.057	0.000	-0.13	471	13	464	26
A_MAD_17		1	0.606	0.022	0.0767	0.0047	-0.03	13.04	0.80	0.057	0.000	-0.24	480	14	476	27
A_MAD_18		1	0.606	0.026	0.0768	0.0053	-0.04	13.02	0.90	0.057	0.000	-0.12	480	16	476	31
A_MAD_19		1	0.602	0.025	0.0762	0.0054	-0.14	13.12	0.93	0.057	0.000	-0.10	477	16	473	31
A_MAD_20		1	0.611	0.021	0.0772	0.0045	-0.09	12.95	0.76	0.057	0.000	0.05	484	13	479	26
A_MAD_21		1	0.602	0.023	0.0763	0.0054	-0.06	13.11	0.93	0.057	0.000	-0.23	478	14	473	31
A_MAD_22		1	0.608	0.022	0.0768	0.0046	-0.05	13.02	0.78	0.057	0.000	-0.10	482	13	476	27
A_MAD_23		1	0.607	0.023	0.0768	0.0053	-0.09	13.02	0.90	0.057	0.000	-0.40	481	14	476	31
A_MAD_24		1	0.610	0.025	0.0772	0.0053	0.01	12.95	0.89	0.100	1.000	-0.11	483	15	479	31
A_MAD_25		1	0.603	0.023	0.0770	0.0054	0.10	12.99	0.91	0.057	0.000	0.09	478	14	477	31
A_MAD_0		2	0.596	0.026	0.0756	0.0032	1.00	13.23	0.56	0.057	0.000	-0.5	475	16	470	19
A_MAD_1		2	0.586	0.022	0.0743	0.0028	1.00	13.46	0.51	0.057	0.000	-0.2	468	14	462	17
A_MAD_2		2	0.615	0.027	0.078	0.0034	1.00	12.82	0.56	0.057	0.000	0.05	487	17	484	20
A_MAD_3		2	0.614	0.026	0.0779	0.0033	1.00	12.84	0.54	0.057	0.000	-0.2	486	16	483	20
A_MAD_4		2	0.601	0.026	0.0763	0.0033	1.00	13.11	0.57	0.057	0.000	-0	478	16	474	20
A_MAD_5		2	0.611	0.027	0.0774	0.0035	1.00	12.92	0.58	0.057	0.000	-0.1	484	17	481	21
A_MAD_6		2	0.621	0.025	0.0787	0.0032	1.00	12.71	0.52	0.057	0.000	-0.1	490	16	488	19
A_MAD_7		2	0.6	0.024	0.0761	0.0031	1.00	13.14	0.54	0.057	0.000	0.3	477	15	473	18
A_MAD_8		2	0.604	0.023	0.0766	0.0029	1.00	13.05	0.49	0.057	0.000	0.3	480	14	476	17
A_MAD_9		2	0.589	0.026	0.0747	0.0033	1.00	13.39	0.59	0.057	0.000	-0.1	470	17	464	20
A_MAD_10		2	0.594	0.026	0.0753	0.0033	1.00	13.28	0.58	0.057	0.000	0.03	473	17	468	20
A_MAD_11		2	0.606	0.024	0.0769	0.003	1.00	13.00	0.51	0.057	0.000	0.11	481	15	478	18
A_MAD_12		2	0.595	0.023	0.0754	0.0029	1.00	13.26	0.51	0.057	0.000	0	474	15	469	17
A_MAD_13		2	0.604	0.025	0.0766	0.0032	1.00	13.05	0.55	0.057	0.000	-0.2	479	16	476	19
A_MAD_14		2	0.627	0.028	0.0795	0.0036	1.00	12.58	0.57	0.057	0.000	0.22	494	18	493	21
A_MAD_15		2	0.585	0.023	0.0742	0.0029	1.00	13.48	0.53	0.057	0.000	0.05	467	14	461	17
A_MAD_16		2	0.609	0.025	0.0773	0.0031	1.00	12.94	0.52	0.057	0.000	0.4	483	16	480	19
A_MAD_17		2	0.604	0.025	0.0766	0.0032	1.00	13.05	0.55	0.057	0.000	-0	480	16	476	19
A_MAD_18		2	0.605	0.029	0.0767	0.0037	1.00	13.04	0.63	0.057	0.000	-0.1	480	18	476	22
A_MAD_19		2	0.61	0.025	0.0774	0.0032	1.00	12.92	0.53	0.057	0.000	-0	483	16	480	19
A_MAD_20		2	0.588	0.023	0.0746	0.003	1.00	13.40	0.54	0.057	0.000	-0	472	16	464	18
A_MAD_21		2	0.59	0.022	0.0748	0.0028	1.00	13.37	0.50	0.057	0.000	-0.1	471	14	465	17
A_MAD_22		2	0.596	0.024	0.0756	0.0031	1.00	13.23	0.54	0.057	0.000	0.01	475	15	470	18
A_MAD_23		2	0.601	0.026	0.0762	0.0033	1.00	13.12	0.57	0.057	0.000	0.19	477	17	473	20
A_MAD_24		2	0.611	0.024	0.0775	0.003	1.00	12.90	0.50	0.057	0.000	-0.2	484	15	481	18
A_MAD_25		2	0.633	0.029	0.0802	0.0037	1.00	12.47	0.58	0.057	0.000	-0.2	497	18	497	22
McC_0		1	1.535	0.091	0.0811	0.0023	0.72	12.33	0.35	0.136	0.007	-0.21	954	37	502	14
McC_1		1	2.240	0.140	0.0995	0.0024	0.35	10.05	0.24	0.157	0.009	0.11	1186	43	612	14
McC_2		1	2.930	0.140	0.1042	0.0035	0.29	9.60	0.32	0.198	0.010	0.28	1392	39	639	21
McC_3		1	1.850	0.110	0.0845	0.0024	-0.82	11.83	0.34	0.157	0.009	-0.09	1073	43	523	14
McC_4		1	2.300	0.150	0.0987	0.0025	0.19	10.13	0.26	0.165	0.010	0.29	1215	43	607	15
McC_5		1	2.370	0.120	0.0938	0.0024	0.36	10.66	0.27	0.180	0.009	0.26	1235	37	578	14
McC_6		1	3.190	0.200	0.1005	0.0039	0.02	9.95	0.39	0.227	0.018	0.62	1446	49	617	23
McC_7		1	2.730	0.140	0.0990	0.0025	0.23	10.10	0.26	0.196	0.012	0.40	1331	39	609	15
McC_8		1	2.610	0.190	0.0986	0.0024	-0.05	10.14	0.25	0.189	0.015	0.39	1295	54	606	14
McC_9		1	3.510	0.180	0.1026	0.0027	0.50	9.75	0.26	0.242	0.009	0.15	1532	41	629	16
McC_10		1	3.190	0.180	0.1009	0.0023	-0.02	9.91	0.23	0.226	0.014	0.44	1459	42	620	13
McC_11		1	2.450	0.180	0.0956	0.0027	0.45	10.46	0.30	0.185	0.016	0.33	1253	54	588	16
McC_12		1	1.926	0.090	0.0890	0.0018	0.28	11.24	0.23	0.151	0.007	0.14	1088	31	550	11
McC_13		1	2.300	0.140	0.0923	0.0024	0.18	10.83	0.28	0.176	0.010	0.23	1215	47	569	14
McC_14		1	1.650	0.091	0.0897	0.0015	-0.15	11.15	0.19	0.131	0.007	0.44	985	35	553	8.9
McC_15		1	2.660	0.140	0.0997	0.0030	0.57	10.03	0.30	0.190	0.008	0.17	1313	39	612	18
McC_16		1	3.107	0.110	0.0986	0.0026	0.73	10.14	0.27	0.221	0.008	0.14	1432	28	606	15
McC_17		1	1.890	0.120	0.0920	0.0025	0.51	10.87	0.30	0.145	0.009	0.08	1079	39	567	15
McC_18		1	2.390	0.130	0.0907	0.0025	0.24	11.03	0.30	0.190	0.010	0.23	1249	38	559	15
McC_19		1	1.868	0.100	0.0909	0.0024	0.20	11.00	0.29	0.144	0.007	0.17	1065	37	561	14
McC_20		1	3.730	0.150	0.1058	0.0025	0.15	9.45	0.22	0.248	0.011	0.51	1576	32	652	16
McC_21		1	2.070	0.120	0.0928	0.0020	0.28	10.78	0.23	0.159	0.009	0.23	1141	37	572	12
McC_0		2	2.69	0.16	0.0991	0.0042	0.53	10.09	0.43	0.192	0.007	0.06	1323	45	609	25
McC_1		2	3.95	0.22	0.123	0.0051	0.74	8.13	0.34	0.238	0.009	-0.2	1631	48	748	30
McC_2		2	2.98	0.18	0.1008	0.0049	0.17	9.92	0.48	0.211	0.011	0.49	1399	45	619	29
McC_3		2	3.09	0.22	0.1068	0.0047	0.5	9.36	0.41	0.208	0.010	-0.1	1434	58	654	27
McC_4		2	3.432	0.15	0.1101	0.0047	-0.1	9.08	0.39	0.224	0.010	0.7	1516	36	673	27
McC_5		2	2.146	0.095	0.1004	0.004	0.21	9.96	0.40	0.153	0.005	0.44	1163	31	617	23
McC_6		2	6.08	0.49	0.1294	0.0073	0.64	7.73	0.44	0.334	0.022	-0.2	1974	76	784	42
McC_7		2	2.497	0.11	0.1042	0.0042	0.27	9.60	0.39	0.178	0.007	0.37	1275	36	639	24
McC_8		2	2.94	0.2	0.103	0.0047	0.42	9.71	0.44	0.205	0.011	0.21	1387	52	632	27
McC_9		2	2.522	0.11	0.1037	0.0038	0.11	9.64	0.35	0.176	0.006	0.44	1277	32	636	22
McC_10		2	3.12	0.16	0.1078	0.0052	0.04	9.28	0.45	0.217	0.010	0.72	1448	43	660	30
McC_11		2	1.74	0.28	0.0907	0.0048	0.88	11.03	0.58	0.143	0.019	-0.8	1020	110	560	28
McC_12		2	1.928	0.078	0.0943	0.004	0.29	10.60	0.45	0.149	0.005	0.44	1090	27	581	23
McC_13		2	2.39	0.12	0.098	0.0037	0.35	10.20	0.39	0.175	0.007	0.17	1237	37	602	22

Continue Table A2 - 2

			isotopic ratios										ages			
Sample ID	Lab ID	#exp	$^{207}Pb/^{235}U$	± 2SE	$^{206}Pb/^{238}U$	± 2SE	ρ*	$^{238}U/^{206}Pb$	± 2SE	$^{207}Pb/^{206}Pb$	± 2SE	ρ**	$^{207}Pb/^{235}U$	± 2SE	$^{206}Pb/^{238}U$	± 2SE
McC_14		2	2.108	0.12	0.098	0.004	0.5	10.20	0.42	0.158	0.007	-0.1	1155	41	602	23
McC_15		2	2.84	0.15	0.1018	0.004	0.37	9.82	0.39	0.201	0.008	0.18	1364	40	625	23
McC_16		2	2.54	0.14	0.0989	0.0042	0.6	10.11	0.43	0.185	0.006	0.04	1282	39	608	25
McC_17		2	2.192	0.12	0.0966	0.0038	0.26	10.35	0.41	0.165	0.006	0.34	1176	37	594	22
McC_18		2	2.64	0.15	0.1027	0.0044	0.7	9.74	0.42	0.188	0.006	-0.1	1308	41	634	24
DUR_0		1	0.216	0.043	0.0062	0.0007	0.62	161.03	18.93	0.295	0.080	0.25	193	36	40	4.7
DUR_1		1	0.198	0.040	0.0066	0.0005	0.25	151.98	10.39	0.224	0.051	0.07	179	33	42	2.9
DUR_2		1	0.174	0.040	0.0066	0.0006	0.00	151.98	13.17	0.200	0.049	0.36	158	34	42	3.7
DUR_3		1	0.229	0.048	0.0064	0.0008	0.18	156.01	20.44	0.239	0.047	0.57	203	40	41	5.4
DUR_4		1	0.237	0.043	0.0067	0.0007	0.09	149.70	15.01	0.277	0.057	0.55	210	35	43	4.3
DUR_5		1	0.261	0.034	0.0070	0.0006	0.27	143.27	12.11	0.276	0.040	0.46	237	29	45	3.8
DUR_6		1	0.214	0.046	0.0059	0.0006	0.35	169.20	17.75	0.284	0.057	0.09	191	38	38	4
DUR_7		1	0.197	0.029	0.0059	0.0005	0.15	170.94	13.15	0.241	0.036	0.30	185	26	38	2.9
DUR_8		1	0.210	0.041	0.0069	0.0008	0.38	144.93	16.17	0.226	0.043	0.22	189	34	44	5
DUR_9		1	0.204	0.031	0.0059	0.0006	0.13	169.49	17.24	0.254	0.043	0.41	186	26	38	3.8
DUR_10		1	0.350	0.094	0.0074	0.0009	0.30	135.32	16.11	0.325	0.069	0.08	269	53	48	5.6
DUR_11		1	0.185	0.044	0.0058	0.0006	0.15	173.31	17.12	0.252	0.069	0.71	166	38	37	3.7
DUR_12		1	0.226	0.041	0.0058	0.0007	0.26	173.61	19.89	0.314	0.062	0.40	208	36	37	4.2
DUR_13		1	0.247	0.047	0.0061	0.0006	-0.34	165.29	15.57	0.310	0.059	0.45	225	40	39	3.6
DUR_14		1	0.215	0.042	0.0064	0.0007	-0.11	156.99	16.51	0.253	0.057	0.69	212	34	41	4.3
DUR_15		1	0.213	0.037	0.0058	0.0005	-0.22	173.61	15.07	0.268	0.053	0.47	199	29	37	3.2
DUR_16		1	0.200	0.039	0.0057	0.0005	0.15	174.22	16.39	0.280	0.072	0.65	181	34	37	3.4
DUR_17		1	0.184	0.028	0.0064	0.0007	-0.81	157.48	16.37	0.231	0.056	0.99	169	24	41	4.2
DUR_18		1	0.215	0.046	0.0062	0.0005	0.19	162.34	13.97	0.247	0.058	0.27	192	38	40	3.4
DUR_19		1	0.204	0.034	0.0065	0.0005	-0.22	154.32	12.86	0.256	0.061	0.67	185	28	42	3.5
DUR_20		1	0.186	0.033	0.0059	0.0005	0.12	170.65	13.10	0.246	0.038	0.06	176	27	38	2.9
DUR_21		1	0.219	0.038	0.0066	0.0007	-0.35	151.06	14.83	0.269	0.055	0.26	197	31	43	4.1
DUR_22		1	0.270	0.049	0.0058	0.0006	-0.43	172.71	17.60	0.373	0.087	0.68	236	39	37	3.8
DUR_23		1	0.216	0.047	0.0065	0.0005	-0.09	153.14	12.66	0.234	0.054	0.45	192	40	42	3.4
DUR_24		1	0.215	0.040	0.0063	0.0006	-0.20	159.49	13.99	0.265	0.062	0.79	200	36	40	3.5
DUR_25		1	0.264	0.046	0.0072	0.0008	-0.06	139.08	14.70	0.274	0.058	0.55	239	35	46	4.9
DUR_0		2	0.217	0.026	0.0067	0.0005	-0.1	149.25	10.25	0.229	0.030	0.56	198	22	43	3
DUR_1		2	0.238	0.027	0.0071	0.0006	0.27	140.45	11.84	0.247	0.035	0.41	216	22	45.8	3.9
DUR_2		2	0.357	0.064	0.0084	0.0009	0.23	119.47	12.99	0.297	0.053	0.17	312	50	53.7	5.8
DUR_3		2	0.405	0.07	0.0077	0.0006	0.82	130.38	10.54	0.388	0.060	-0.2	338	50	49.2	4
DUR_4		2	0.206	0.024	0.0063	0.0005	-0.2	158.73	12.85	0.213	0.037	0.65	189	20	40.5	3.2
DUR_5		2	0.214	0.028	0.0068	0.0005	-0.2	147.06	10.38	0.233	0.036	0.71	201	25	43.7	3.1
DUR_6		2	0.294	0.035	0.0073	0.0007	0.34	137.36	12.45	0.29	0.040	0.06	260	28	46.8	4.2
DUR_7		2	0.217	0.033	0.0062	0.0005	-0.3	160.51	13.91	0.249	0.040	0.68	202	28	40	3.4
DUR_8		2	0.232	0.019	0.0070	0.0005	-0.1	143.47	10.91	0.248	0.028	0.79	211	16	44.8	3.4
DUR_9		2	0.198	0.018	0.0064	0.0005	-0.2	156.74	11.79	0.241	0.026	0.69	183	15	41	3.1
DUR_10		2	0.184	0.035	0.0064	0.0005	-0.3	155.52	10.88	0.214	0.045	0.52	175	31	41.3	2.9
DUR_11		2	0.252	0.039	0.0068	0.0006	0.21	146.63	13.11	0.289	0.050	0.37	225	32	43.8	3.9
DUR_12		2	0.181	0.032	0.0070	0.0006	0.19	143.06	12.08	0.189	0.034	0.27	167	27	44.9	3.8
DUR_13		2	0.18	0.027	0.0068	0.0004	-0	146.63	9.46	0.195	0.031	0.52	166	23	43.8	2.8
DUR_14		2	0.323	0.088	0.0072	0.0008	0.58	138.12	16.03	0.32	0.069	-0.2	276	63	46.5	5.4
DUR_15		2	0.223	0.025	0.0065	0.0005	0.06	154.80	11.74	0.249	0.027	0.66	204	20	41.5	3.2
DUR_16		2	0.381	0.07	0.0077	0.0012	0.57	129.87	20.24	0.352	0.070	0.15	325	52	49.6	7.9
DUR_17		2	0.24	0.041	0.0072	0.0008	0.55	139.28	16.10	0.264	0.047	0.1	217	33	46.1	5.3
DUR_18		2	0.197	0.019	0.0064	0.0005	0.35	155.28	11.09	0.221	0.021	0.31	185	15	41.3	2.9
DUR_19		2	0.185	0.025	0.0061	0.0005	0.19	163.13	12.77	0.218	0.026	0.52	171	21	39.4	3.1
Navan Area																
Tara Deep																
X18HK_005_0	HK 158	1	4.480	0.170	0.2337	0.0064	0.58	4.28	0.12	0.137	0.005	0.16	1724	32	1353	33
X18HK_006_0	HK 159	1	85.300	2.800	0.7670	0.0220	0.40	1.30	0.04	0.783	0.024	0.62	4524	34	3667	81
X18HK_006_1	HK 159	1	11.260	0.650	0.1444	0.0056	0.40	6.93	0.27	0.554	0.025	0.37	2547	50	869	31
X18HK_006_2	HK 159	1	15.500	1.000	0.1732	0.0064	0.08	5.77	0.21	0.626	0.047	0.54	2838	65	1029	35
X18HK_006_3	HK 159	1	13.000	0.800	0.1544	0.0065	0.35	6.48	0.27	0.603	0.039	0.44	2691	57	925	36
X18HK_006_4	HK 159	1	25.600	1.400	0.2570	0.0100	0.33	3.89	0.15	0.722	0.041	0.47	3330	56	1472	52
X19HK_009_0	HK 235	1	9.840	0.400	0.3322	0.0058	0.43	3.01	0.05	0.211	0.007	0.10	2416	38	1849	28
Stonepark																
X19HK_004_0	HK 207	1	22.000	1.300	0.4410	0.0180	-0.94	2.27	0.09	0.355	0.021	0.32	3197	49	2356	79
X19HK_004_1	HK 207	1	4.160	0.220	0.1704	0.0040	-0.14	5.87	0.14	0.174	0.010	0.53	1658	44	1014	22
X19HK_006_0	HK 209	1	2.930	0.470	0.0738	0.0075	0.20	13.55	1.38	0.310	0.063	0.57	1410	110	458	45
X19HK_014_0	HK 210	1	7.060	0.710	0.1060	0.0150	0.08	9.43	1.33	0.480	0.075	0.80	2114	91	647	85
X19HK_014_1	HK 210	1	9.620	0.520	0.1201	0.0064	0.00	8.33	0.44	0.556	0.039	0.75	2391	50	731	37
X19HK_014_2	HK 210	1	4.160	0.180	0.0970	0.0029	0.66	10.31	0.31	0.299	0.010	0.04	1668	34	599	18
X19HK_014_3	HK 210	1	8.700	1.200	0.1190	0.0110	0.05	8.40	0.78	0.526	0.091	0.43	2290	130	725	61
X19HK_014_4	HK 210	1	9.820	0.570	0.1268	0.0052	0.40	7.89	0.32	0.546	0.032	0.38	2416	52	774	28
X19HK_014_5	HK 210	1	8.600	3.800	0.1360	0.0580	-0.11	7.35	3.14	0.461	0.068	-0.40	2210	360	810	320
X19HK_014_6	HK 210	1	14.500	1.900	0.1500	0.0190	0.96	6.67	0.84	0.681	0.025	-0.08	2780	140	900	110
X19HK_014_7	HK 210	1	9.450	0.710	0.1183	0.0080	0.40	8.45	0.57	0.560	0.046	0.56	2371	67	720	46
X19HK_015_0	HK 211	1	10.680	0.770	0.1519	0.0082	0.92	6.58	0.36	0.491	0.014	-0.39	2478	67	910	46
X19HK_015_1	HK 211	1	16.040	0.610	0.1833	0.0057	-0.82	5.46	0.17	0.616	0.020	0.12	2875	36	1084	31
X19HK_015_2	HK 211	1	13.330	0.690	0.1567	0.0070	0.69	6.38	0.29	0.585	0.022	0.26	2712	50	937	39
X19HK_015_3	HK 211	1	14.610	0.530	0.1745	0.0047	-0.74	5.73	0.15	0.594	0.021	0.22	2786	34	1037	26
X19HK_015_4	HK 211	1	8.680	0.760	0.1248	0.0083	0.85	8.01	0.53	0.491	0.019	-0.34	2279	77	756	47
X19HK_015_5	HK 211	1	13.530	0.490	0.1620	0.0042	0.32	6.17	0.16	0.598	0.023	0.51	2726	35	967	24
X19HK_015_6	HK 211	1	21.100	1.700	0.2330	0.0160	0.87	4.29	0.29	0.643	0.041	-0.01	3137	78	1348	86
X19HK_015_7	HK 211	1	11.450	0.550	0.1492	0.0063	0.77	6.70	0.28	0.539	0.013	0.13	2556	45	896	36
X19HK_015_8	HK 211	1	4.340	0.200	0.0843	0.0035	0.55	11.86	0.49	0.369	0.013	0.24	1710	33	521	21
X19HK_015_9	HK 211	1	17.340	0.560	0.1999	0.0044	0.19	5.00	0.11	0.619	0.018	0.56	2952	32	1175	24

Continue Table A2 – 2

			isotopic ratios										ages			
Sample ID	Lab ID	#exp	$^{207}Pb/^{235}U$	± 2SE	$^{206}Pb/^{238}U$	± 2SE	ρ*	$^{238}U/^{206}Pb$	± 2SE	$^{207}Pb/^{206}Pb$	± 2SE	ρ**	$^{207}Pb/^{235}U$	± 2SE	$^{206}Pb/^{238}U$	± 2SE
X19HK_015_10	HK 211	1	28.000	1.200	0.3030	0.0100	0.64	3.30	0.11	0.639	0.022	0.27	3415	43	1706	51
X19HK_015_11	HK 211	1	13.220	0.590	0.1650	0.0058	-0.77	6.06	0.21	0.575	0.021	0.03	2690	42	984	32
X19HK_015_12	HK 211	1	12.760	0.920	0.1552	0.0079	0.81	6.44	0.33	0.574	0.030	-0.31	2654	72	929	44
X19HK_015_13	HK 211	1	13.470	0.950	0.1574	0.0085	0.76	6.35	0.34	0.601	0.018	-0.20	2696	70	941	48
X19HK_015_14	HK 211	1	7.120	0.270	0.1108	0.0033	0.62	9.03	0.27	0.457	0.013	0.28	2123	34	677	19
X19HK_015_15	HK 211	1	8.270	0.450	0.1176	0.0054	0.89	8.50	0.39	0.502	0.014	-0.13	2263	50	716	31
X19HK_015_16	HK 211	1	15.160	0.650	0.1795	0.0050	-0.65	5.57	0.16	0.595	0.017	0.16	2826	38	1064	27
X19HK_015_17	HK 211	1	16.300	0.510	0.1834	0.0043	0.38	5.45	0.13	0.632	0.017	0.48	2896	29	1085	23
X19HK_015_18	HK 211	1	12.960	0.550	0.1617	0.0055	0.32	6.18	0.21	0.578	0.029	0.45	2675	40	966	30
X19HK_015_19	HK 211	1	4.630	0.280	0.0893	0.0032	0.92	11.20	0.40	0.369	0.012	-0.61	1763	56	551	19
X19HK_015_20	HK 211	1	12.520	0.460	0.1534	0.0035	0.17	6.52	0.15	0.577	0.019	0.56	2640	35	920	20
X19HK_015_21	HK 211	1	10.260	0.390	0.1370	0.0037	0.63	7.30	0.20	0.535	0.013	0.27	2466	35	827	21
X19HK_015_22	HK 211	1	13.860	0.520	0.1637	0.0054	0.69	6.11	0.20	0.603	0.019	0.16	2762	38	977	30
X19HK_015_23	HK 211	1	17.480	0.680	0.2008	0.0052	0.20	4.98	0.13	0.616	0.025	0.59	2958	38	1179	28
X19HK_015_24	HK 211	1	11.870	0.790	0.1580	0.0130	-0.89	6.33	0.52	0.538	0.016	0.41	2587	63	945	70
X19HK_016_0	HK 212	1	5.340	0.580	0.0937	0.0050	0.32	10.67	0.57	0.404	0.035	0.28	1868	88	577	30
X19HK_016_1	HK 212	1	2.900	1.500	0.0740	0.0100	-0.02	13.51	1.83	0.290	0.160	0.26	1300	360	457	61
X19HK_016_2	HK 212	1	3.140	0.450	0.0766	0.0045	-0.02	13.05	0.77	0.308	0.046	0.41	1450	110	476	27
X19HK_016_3	HK 212	1	1.940	0.350	0.0677	0.0079	0.46	14.77	1.72	0.204	0.036	0.16	1120	100	422	48
X19HK_016_4	HK 212	1	2.160	0.270	0.0643	0.0035	0.50	15.55	0.85	0.232	0.033	0.19	1151	84	402	21
X19HK_016_5	HK 212	1	1.810	0.220	0.0694	0.0037	0.03	14.41	0.77	0.188	0.025	0.40	1053	85	433	23
X19HK_016_6	HK 212	1	4.050	0.590	0.0870	0.0100	0.06	11.49	1.32	0.349	0.062	0.55	1620	120	536	62
X19HK_016_7	HK 212	1	11.660	0.850	0.1399	0.0086	0.20	7.15	0.44	0.577	0.055	0.65	2564	71	843	49
X19HK_016_8	HK 212	1	4.110	0.440	0.0804	0.0055	-0.02	12.44	0.85	0.373	0.044	0.56	1666	85	498	33
X19HK_016_9	HK 212	1	1.440	0.300	0.0619	0.0033	-0.19	16.16	0.86	0.159	0.035	0.54	880	120	387	20
X19HK_016_10	HK 212	1	3.300	0.440	0.0726	0.0054	0.02	13.77	1.02	0.333	0.049	0.56	1477	97	451	33
Slievedart Area																
X18HK_132_0	HK 187	1	2.720	0.160	0.0249	0.0008	0.16	40.14	1.34	0.773	0.045	0.41	1336	46	158.6	5.2
X18HK_135_0	HK 190	1	10.180	0.350	0.1423	0.0089	-0.07	7.03	0.44	0.525	0.011	0.43	2448	32	856	48
X18HK_135_1	HK 190	1	13.970	0.520	0.1697	0.0047	0.12	5.89	0.16	0.581	0.022	0.59	2744	35	1010	26
X18HK_135_2	HK 190	1	16.210	0.750	0.1904	0.0073	-0.77	5.25	0.20	0.618	0.019	-0.15	2890	46	1123	39
X18HK_138_0	HK 193	1	11.820	0.550	0.1560	0.0038	0.17	6.41	0.16	0.553	0.027	0.54	2587	43	934	21
X18HK_139_0	HK 194	1	12.930	0.430	0.1635	0.0099	0.02	6.12	0.37	0.585	0.016	0.23	2672	31	952	27
X18HK_139_1	HK 194	1	9.480	0.350	0.1389	0.0095	0.01	7.20	0.49	0.493	0.011	-0.18	2382	34	836	52
X18HK_139_2	HK 194	1	14.930	0.840	0.1774	0.0081	0.78	5.64	0.26	0.584	0.021	0.47	2806	52	1052	45
X18HK_139_3	HK 194	1	15.020	0.490	0.1761	0.0042	0.81	5.68	0.14	0.607	0.018	0.08	2818	30	1046	23
X18HK_139_4	HK 194	1	10.200	0.440	0.1390	0.0046	0.52	7.19	0.24	0.522	0.019	0.16	2459	37	839	26
X18HK_139_5	HK 194	1	14.350	0.700	0.1680	0.0060	0.66	5.95	0.21	0.594	0.021	0.00	2767	47	1001	33
X18HK_158_0	HK 237	2	17.52	0.73	0.1933	0.0083	0.52	5.17	0.22	0.654	0.02	0.33	2962	40	1139	45
X18HK_158_1	HK 237	2	19.29	0.79	0.2138	0.0098	0.44	4.68	0.21	0.662	0.021	0.73	3055	40	1249	52
X18HK_158_2	HK 237	2	19.57	0.88	0.214	0.0092	0.54	4.67	0.20	0.667	0.020	0.36	3075	47	1249	49
X18HK_158_3	HK 237	2	19.34	0.78	0.2068	0.0085	0.45	4.84	0.20	0.671	0.017	0.63	3057	38	1211	45
X18HK_158_4	HK 237	2	21.18	0.92	0.2219	0.009	0.46	4.51	0.18	0.697	0.019	0.22	3151	45	1292	47
X18HK_158_5	HK 237	2	17.06	0.7	0.191	0.0078	0.33	5.24	0.21	0.648	0.017	0.69	2947	35	1127	42
X18HK_158_6	HK 237	2	21.65	0.91	0.2294	0.0087	0.5	4.36	0.17	0.685	0.016	0.44	3171	42	1331	46
X18HK_158_7	HK 237	2	21.77	1.1	0.2269	0.011	0.94	4.41	0.21	0.693	0.021	0.25	3170	48	1317	60
X18HK_158_8	HK 237	2	20.09	0.8	0.2145	0.0083	0.68	4.66	0.18	0.682	0.015	0.07	3094	39	1252	44
X18HK_158_9	HK 237	2	18.48	0.82	0.2051	0.0099	0.49	4.88	0.24	0.656	0.022	0.63	3012	43	1202	53
X18HK_158_10	HK 237	2	19.79	0.8	0.2136	0.0094	0.74	4.68	0.21	0.674	0.013	0.61	3080	39	1247	50
X18HK_158_11	HK 237	2	17.83	0.85	0.1931	0.0093	0.58	5.18	0.25	0.667	0.022	0.49	2977	46	1137	51
X18HK_158_12	HK 237	2	21.69	0.84	0.2284	0.01	0.54	4.38	0.19	0.689	0.017	0.66	3174	41	1325	54
X18HK_158_13	HK 237	2	21.63	0.9	0.2236	0.0098	0.58	4.47	0.20	0.695	0.018	0.48	3165	41	1300	52
X18HK_158_14	HK 237	2	16.01	0.75	0.181	0.008	0.88	5.52	0.24	0.639	0.017	-0.5	2875	45	1072	44
X18HK_158_15	HK 237	2	19.27	0.87	0.2108	0.0092	0.72	4.74	0.21	0.666	0.018	0.41	3061	40	1233	49
X18HK_158_16	HK 237	2	21.26	0.89	0.221	0.0095	0.28	4.52	0.19	0.692	0.025	0.63	3148	41	1287	50
X18HK_158_17	HK 237	2	21.63	0.9	0.2288	0.0091	0.39	4.37	0.17	0.684	0.018	0.59	3165	40	1328	47
X18HK_158_18	HK 237	2	19.41	0.78	0.2088	0.0083	0.43	4.79	0.19	0.679	0.015	0.53	3061	39	1222	44
X18HK_158_19	HK 237	2	23.95	1.1	0.2406	0.01	0.32	4.16	0.17	0.709	0.025	0.49	3264	44	1389	52
X18HK_158_20	HK 237	2	19.72	0.83	0.2062	0.0088	0.51	4.85	0.21	0.695	0.022	0.53	3082	43	1208	47
X18HK_158_21	HK 237	2	18.46	0.73	0.1993	0.0082	0.58	5.02	0.21	0.664	0.017	0.69	3012	38	1171	44
X18HK_159_0	HK 238	2	20.94	0.97	0.2207	0.01	0.6	4.53	0.21	0.689	0.017	0.43	3133	44	1285	53
X18HK_159_1	HK 238	2	20.51	0.92	0.2174	0.0094	0.46	4.60	0.20	0.668	0.017	0.49	3113	43	1267	50
X18HK_159_2	HK 238	2	22.32	0.99	0.2371	0.011	0.67	4.22	0.20	0.679	0.017	0.4	3195	43	1371	57
X18HK_159_3	HK 238	2	22.16	0.94	0.2287	0.0094	0.55	4.37	0.18	0.710	0.018	0.4	3189	41	1327	49
X18HK_159_4	HK 238	2	18.54	0.74	0.2008	0.0079	0.36	4.98	0.20	0.661	0.019	0.61	3017	39	1180	42
X18HK_159_5	HK 238	2	23.39	1	0.2379	0.0097	0.67	4.20	0.17	0.698	0.014	0.13	3241	43	1375	51
X18HK_159_6	HK 238	2	21.37	0.88	0.2218	0.0095	0.62	4.51	0.19	0.700	0.015	0.49	3159	42	1291	50
X18HK_159_7	HK 238	2	19.02	0.78	0.206	0.0079	0.5	4.85	0.19	0.666	0.016	0.42	3041	39	1207	42
X18HK_159_8	HK 238	2	15.2	0.68	0.1795	0.0074	0.83	5.57	0.23	0.621	0.011	0.02	2833	47	1064	41
X18HK_159_9	HK 238	2	21.78	0.85	0.2339	0.0095	0.48	4.28	0.17	0.688	0.014	0.59	3173	38	1354	50
X18HK_159_10	HK 238	2	17.66	0.76	0.1952	0.0082	0.83	5.12	0.22	0.653	0.019	-0.4	2970	42	1149	44
X18HK_159_11	HK 238	2	19.83	0.89	0.2186	0.0095	0.61	4.57	0.20	0.657	0.018	0.34	3081	43	1274	50
X18HK_159_12	HK 238	2	20.77	0.92	0.2232	0.0096	0.54	4.48	0.19	0.679	0.015	0.59	3131	41	1298	51
X18HK_159_13	HK 238	2	21.07	0.95	0.2233	0.0098	0.48	4.48	0.20	0.680	0.021	0.47	3145	46	1299	52
X18HK_159_14	HK 238	2	22.07	0.82	0.2264	0.009	0.46	4.42	0.18	0.707	0.017	0.62	3186	36	1315	47
X18HK_159_15	HK 238	2	20.8	0.89	0.2176	0.0083	0.29	4.60	0.18	0.704	0.018	0.48	3127	42	1269	44
X18HK_159_16	HK 238	2	22.09	1.1	0.2255	0.01	0.76	4.43	0.20	0.699	0.018	-0.1	3183	51	1310	54
X18HK_159_17	HK 238	2	22.53	0.94	0.2321	0.0091	0.14	4.31	0.17	0.705	0.024	0.59	3205	40	1345	48
X18HK_159_18	HK 238	2	20.42	0.86	0.2183	0.0089	0.41	4.58	0.19	0.688	0.022	0.44	3117	44	1273	47
X18HK_159_19	HK 238	2	20.95	0.8	0.2217	0.0094	0.35	4.51	0.19	0.684	0.019	0.67	3135	37	1290	49
X18HK_159_20	HK 238	2	29.6	1.5	0.298	0.014	0.81	3.36	0.16	0.710	0.018	0.1	3469	51	1680	71

Table A2 - 3: Apatite trace element data in µg/g and U-Pb apatite ages. Grey samples: U-Pb ages are outside the Mississippian (Tournaisian and Viséan) time window or reveal high analytical uncertainties. Bold grey numbers: deviation is bigger than 20% from samples' median. LOD = limit of detection.

	Exp #	U-Pb age	95% conf.	V	± Int 2SE	Mn	± Int 2SE	Fe	± Int 2SE	Sr	± Int 2SE	Y	± Int 2SE	Zr	± Int 2SE	La	± Int 2SE	Ce	± Int 2SE	Pr	± Int 2SE	Nd	± Int 2SE	Sm	± Int 2SE	Eu	± Int 2SE	Gd	± Int 2SE
		Ma	Ma	µg/g	µg/g	µg/g	µg/g	µg/g	µg/g	µg/g	µg/g	µg/g	µg/g	µg/g	µg/g	µg/g	µg/g	µg/g	µg/g	µg/g	µg/g	µg/g	µg/g	µg/g	µg/g	µg/g	µg/g	µg/g	µg/g
NIST612																													
NIST612_0	1			185	5.5	205	9.4	270	41	357	10	173	5.0	171	5.4	163	5.3	177	5.9	166	6.5	165	7.9	170	7.5	157	4.8	161	6.6
NIST612_1	1			180	5.9	202	7.9	282	39	369	9	181	7.0	175	5.3	164	6.3	173	5.8	172	6.2	164	9.1	177	7.3	159	5.1	176	6.3
NIST612_2	1			183	6.4	198	8.4	231	38	363	9	176	5.1	178	5.6	165	5.3	180	5.4	172	5.2	162	8.2	179	6.0	162	4.3	166	6.2
NIST612_3	1			186	11.0	145	8.8	202	36	385	22	179	12.0	189	12.0	175	10.0	193	9.6	184	11.0	174	9.6	192	17.0	184	9.6	192	11.0
NIST612_4	1			191	6.4	153	10.0	226	42	382	13	185	6.1	190	4.6	181	7.1	197	6.3	187	6.1	185	10.0	188	8.2	182	5.6	188	8.7
NIST612_5	1			175	5.7	156	7.8	211	49	374	13	183	6.3	179	7.2	172	5.0	185	6.2	180	6.7	176	10.0	191	13.0	171	6.8	179	6.5
NIST612_6	1			186	6.2	162	11.0	215	31	393	11	187	5.9	185	7.1	181	5.6	195	6.2	184	6.4	180	12.0	191	8.1	176	6.4	185	8.6
NIST612_7	1			194	8.5	167	10.0	276	38	378	11	180	7.1	177	5.2	171	6.5	182	5.3	174	5.4	170	9.2	182	8.5	165	5.1	169	7.0
NIST612_8	1			189	7.7	177	11.0	254	34	375	11	184	6.1	176	6.7	168	6.5	186	5.8	179	5.2	173	10.0	185	9.7	167	4.9	173	8.1
NIST612_9	1			178	5.2	187	10.0	237	31	359	9	177	5.5	174	4.2	165	6.0	172	4.5	169	6.4	156	7.1	165	9.5	161	4.0	167	8.7
NIST612_10	1			185	6.8	204	12.0	230	33	359	7	177	5.4	183	7.1	163	3.9	182	6.6	171	5.1	175	10.0	175	9.5	161	3.9	170	7.5
NIST612_11	1			187	9.6	203	12.0	258	36	378	12	171	6.1	182	7.2	171	6.0	186	7.6	171	6.0	173	10.0	175	9.1	165	5.2	171	5.7
Σ Grains				12		11		11		12		12		12		12		12		12		12		12		12		12	
Average				185		183		237		373		179		180		170		184		176		171		181		167		175	
2SD				10.4		39.5		46.4		22.0		9.4		11.5		12.5		15.4		12.9		15.7		17.0		17.1		18.3	
NIST612_0	2			183	5.4	182	6.8	247	7.9	375	13.0	194	9.5	187	6.8	168	8.6	182	8.1	175	7.3	171	7.4	183	11.0	168	5.4	170	7.2
NIST612_1	2			178	5.6	173	6.3	242	9.9	358	11.0	172	8.4	169	6.1	163	6.7	176	7.9	170	7.0	169	8.5	180	7.3	163	6.6	171	9.3
NIST612_2	2			185	8.2	181	7.3	246	10.0	364	14.0	174	8.7	176	9.0	171	9.0	186	12.0	171	9.6	164	9.1	172	9.5	161	6.8	171	9.2
NIST612_3	2			187	5.1	186	4.7	241	10.0	382	12.0	180	8.3	183	6.0	178	7.7	181	8.4	182	6.1	184	10.0	186	9.5	171	4.0	176	7.1
NIST612_4	2			186	5.9	181	6.3	239	9.7	364	12.0	173	7.6	181	7.4	165	6.2	184	7.8	180	7.6	166	8.4	177	10.0	161	5.7	175	8.4
NIST612_5	2			186	6.3	177	6.5	235	8.7	368	15.0	178	7.5	174	7.8	168	7.2	182	7.4	167	8.4	167	10.0	176	10.0	157	5.3	173	7.1
NIST612_6	2			183	5.2	176	4.2	231	8.4	366	10.0	181	5.0	181	7.3	168	6.1	183	7.3	175	6.2	169	8.5	182	8.2	161	5.3	169	6.8
NIST612_7	2			184	5.1	184	5.1	236	8.8	375	12.0	176	8.4	178	8.1	171	10.0	184	6.7	171	7.8	172	11.0	180	10.0	167	7.7	172	6.5
NIST612_8	2			185	4.1	177	4.2	244	7.7	371	8.7	179	5.8	179	7.4	172	7.3	189	8.9	176	6.4	171	11.0	179	7.6	165	5.3	176	6.7
NIST612_9	2			185	5.0	176	5.4	230	9.2	375	11.0	181	6.0	182	8.1	174	8.9	182	8.2	182	5.4	166	7.5	186	8.6	169	7.7	176	6.9
NIST612_10	2			184	5.5	177	5.8	244	11.0	370	9.9	187	7.6	180	6.0	169	7.8	184	7.8	173	5.5	166	11.0	177	8.6	165	5.6	182	9.4
NIST612_11	2			183	4.7	176	5.9	250	8.5	375	12.0	177	7.7	184	6.6	175	8.0	186	8.2	176	6.9	164	7.0	178	6.7	167	6.9	173	7.7
NIST612_12	2			181	5.6	172	4.3	235	9.1	368	11.0	174	9.1	178	5.8	171	8.7	179	7.4	168	6.5	165	11.0	181	9.3	169	5.6	170	6.7
NIST612_13	2			186	3.3	187	4.5	238	11.0	369	6.4	179	6.5	179	5.1	171	6.6	181	7.0	174	5.5	176	9.6	183	6.4	164	6.8	175	5.2
NIST612_14	2			182	6.3	185	7.1	240	12.0	363	12.0	177	5.5	175	6.3	163	6.4	184	10.0	178	7.7	180	9.4	174	9.6	165	6.6	170	6.5
NIST612_15	2			180	5.6	177	5.6	248	10.0	366	12.0	183	8.7	179	7.1	164	7.0	179	8.6	177	7.8	167	6.9	177	9.0	162	5.8	168	7.2
Σ Grains				16		16		16		16		16		16		16		16		16		16		16		16		16	
Average				183		179		240		369		179		179		169		183		175		170		179		165		173	
2SD				2.4		4.4		5.6		5.8		5.3		4.1		4.3		3.0		4.4		5.7		3.8		3.6		3.5	
McClure																													
McC_0	1	*455*	*13*	*14.1*	*1.0*	*65*	*1.8*	*100.5*	*8.8*	*3710*	*110*	*349*	*18.0*	*11.0*	*1.2*	*2680*	*140*	*4340*	*180*	*405*	*20*	*1383*	*66*	*164*	*8.4*	*61.8*	*3.0*	*110.6*	*5.8*
McC_1	1	*540*	*14*	*22.1*	*1.2*	*73*	*1.8*	*111*	*8.3*	*3695*	*74*	*259*	*5.8*	*5.8*	*0.4*	*2051*	*45*	*3388*	*74*	*308*	*9*	*1042*	*18*	*124*	*3.5*	*47.0*	*1.4*	*80.8*	*2.1*
McC_2	1	*534*	*19*	*12.7*	*0.6*	*71*	*1.9*	*114*	*10.0*	*3801*	*81*	*191*	*4.6*	*4.0*	*1.0*	*1390*	*41*	*2314*	*53*	*212*	*5*	*749*	*14*	*92*	*3.2*	*30.2*	*0.9*	*60.0*	*2.0*
McC_3	1	*460*	*14*	*14.3*	*0.7*	*77*	*1.5*	*103*	*9.1*	*3921*	*97*	*228*	*6.2*	*4.5*	*0.3*	*1725*	*50*	*2851*	*80*	*273*	*9*	*936*	*21*	*115*	*3.0*	*37.9*	*1.1*	*78.3*	*2.4*
McC_4	1	*530*	*15*	*30.8*	*1.5*	*61*	*2.1*	*103*	*12.0*	*4210*	*100*	*278*	*9.2*	*5.0*	*0.3*	*2323*	*59*	*3730*	*130*	*335*	*10*	*1087*	*34*	*130*	*3.7*	*49.0*	*1.3*	*86.7*	*3.5*
McC_5	1	*494*	*14*	3.5	0.3	119	2.5	142	11.0	4166	71	400	9.7	11.6	0.6	2333	53	4480	100	433	10	1602	44	219	5.9	59.9	1.6	145.6	4.5
McC_6	1	493	23	9.6	0.6	109	2.5	122	8.8	4210	100	178	5.0	5.9	0.3	1596	55	2528	66	226	7	786	19	92	3.4	32.8	1.0	63.3	2.5
McC_7	1	509	15	16.4	1.0	66	2.1	95	10.0	3696	93	204	5.5	3.0	0.3	1696	44	2819	83	254	8	881	23	105	3.0	43.4	1.4	68.2	2.1
McC_8	1	512	16	5.7	0.5	123	3.5	122	7.7	4050	110	272	8.9	14.9	0.8	2427	96	4000	160	366	12	1286	43	153	3.9	51.2	1.7	105.7	3.8
McC_9	1	492	15	15.1	1.1	66	2.2	90	11.0	4186	96	263	7.6	4.7	0.3	1726	53	2889	59	271	6	982	31	123	3.0	39.8	1.0	88.9	2.9
McC_10	1	*496*	*15*	*##*	*1.2*	*82*	*2.7*	*102*	*9.6*	*3625*	*94*	*144*	*4.8*	*3.1*	*0.3*	*1517*	*52*	*1683*	*53*	*108*	*3*	*328*	*10*	*31*	*1.2*	*18.7*	*0.6*	*22.2*	*1.1*
McC_11	1	*499*	*18*	*2.4*	*0.4*	*119*	*4.0*	*101*	*13.0*	*5600*	*310*	*465*	*22.0*	*##*	*1.2*	*2690*	*94*	*4910*	*190*	*493*	*24*	*1790*	*100*	*229*	*13.0*	*##*	*3.5*	*###*	*8.3*
McC_12	1	488	11	37.2	1.4	159	4.5	153	13.0	4040	120	198	4.2	4.9	0.4	1904	49	3111	89	266	6	901	30	101	4.1	40.8	1.1	66.3	2.7
McC_13	1	489	14	11.0	0.7	94	3.2	102	10.0	3950	110	170	6.3	5.7	0.4	1674	32	2503	61	221	5	802	25	99	3.7	31.3	0.8	67.8	2.0
McC_14	1	506	10	22.7	1.0	72	1.6	87	9.6	3654	93	248	7.6	4.9	0.5	1973	49	3247	84	286	7	1019	30	123	4.0	44.2	1.1	82.0	2.2
McC_15	1	*517*	*16*	*##*	*1.1*	*126*	*11.0*	*107*	*14.0*	*3909*	*98*	*342*	*8.9*	*5.7*	*0.4*	*2398*	*53*	*3326*	*86*	*244*	*6*	*764*	*25*	*87*	*2.3*	*38.1*	*1.0*	*64.4*	*2.0*
McC_16	1	488	14	23.7	1.0	92	2.4	87	7.9	3856	98	252	6.4	3.9	0.2	1974	53	3262	82	289	7	1033	26	117	3.7	50.7	1.4	80.2	2.3
McC_17	1	509	15	6.8	0.4	120	3.6	105	8.1	4153	79	279	6.5	8.7	0.4	2232	44	3756	59	332	6	1175	26	140	3.4	49.1	0.8	92.9	1.9
McC_18	1	*471*	*14*	*21.0*	*1.0*	*80*	*2.3*	*92*	*7.6*	*3900*	*100*	*96*	*2.5*	*2.4*	*0.2*	*1368*	*26*	*1845*	*41*	*139*	*4*	*466*	*16*	*47*	*1.9*	*19.7*	*0.6*	*31.0*	*1.1*
McC_19	1	503	14	38.4	1.3	148	3.6	129	8.5	3881	99	184	3.6	4.7	0.3	1837	43	2931	72	249	7	853	22	91	2.3	37.5	1.0	61.0	2.0
McC_20	1	502	15	24.3	1.0	68	2.4	77	7.7	4640	110	214	6.0	3.3	0.2	1944	50	2897	69	250	6	894	22	104	3.3	43.0	0.9	69.4	2.0
McC_21	1	503	12	21.7	0.9	141	4.0	129	9.2	3954	96	130	3.8	4.7	0.4	1600	46	2332	80	186	6	621	18	63	2.1	26.7	0.9	42.1	1.4
Σ Grains				4		8		11		15		9		7		12		10		10		10		10		10		9	
Average				19.0		112.8		101.7		3998		234.9		5.1		1806		2951		256		892		104		38.1		69.2	
2SD				6.5		24.5		22.9		502		66.0		0.8		397		275		43		181		25		17.1		13.7	

Continue Table A2 – 3

McC_0	2	512	22	20.4	1.0	62	2.9	93	4.0	3500	150	188	9.2	2.4	0.2	1658	98	2730	180	265	21.0	875	42	97	5.3	43.7	2.3	63.7	3.8
McC_1	2	*592*	*25*	*12.6*	*0.6*	*75*	*2.9*	*92*	*4.7*	*3920*	*210*	*79*	*4.6*	*2.4*	*0.2*	*1170*	*67*	*1730*	*110*	*140*	*7.5*	*436*	*30*	*48*	*2.6*	*##*	*1.2*	*31.0*	*2.2*
McC_2	2	507	25	35.7	1.8	78	3.4	99	7.5	3950	250	226	9.1	3.5	0.2	2130	210	3280	250	282	22.0	954	43	110	7.9	48.8	3.5	69.9	4.3
McC_3	2	539	24	7.5	1.0	131	5.3	122	5.8	4020	180	269	26.0	8.7	1.1	1930	150	3350	250	347	33.0	1140	110	139	13.0	43.7	3.5	95.6	9.3
McC_4	2	542	24	4.6	0.2	87	3.1	90	4.0	3720	170	211	14.0	6.8	0.4	1840	140	3100	200	294	23.0	923	44	111	6.4	44.3	2.6	74.0	4.6
McC_5	2	548	22	26.4	0.9	57	2.0	70	2.3	3430	120	218	10.0	5.1	0.3	2080	120	3330	210	292	12.0	902	49	102	4.8	63.5	2.9	64.5	2.4
McC_6	2	529	36	8.2	0.8	147	6.8	113	4.8	4280	200	300	32.0	7.6	1.0	1670	140	3290	400	317	30.0	1130	140	144	15.0	41.2	4.7	92.4	7.5
McC_7	2	549	22	13.4	0.6	74	2.6	79	2.9	3630	140	204	8.6	5.5	0.3	1780	87	2940	160	248	13.0	850	51	96	3.9	35.0	1.6	65.6	2.7
McC_8	2	522	25	8.3	0.4	122	5.3	114	5.9	3820	150	191	9.6	7.4	0.3	1687	86	2820	190	264	18.0	829	45	102	4.7	33.3	1.4	67.8	3.4
McC_9	2	548	20	15.6	0.6	93	3.7	98	4.5	3440	130	210	13.0	3.4	0.2	1807	77	3060	190	264	16.0	906	44	103	3.9	46.1	2.4	66.7	2.9
McC_10	2	536	27	11.1	0.7	93	5.8	95	5.2	4090	310	168	16.0	3.2	0.3	1381	92	2540	300	260	27.0	770	55	89	9.1	29.8	2.1	59.5	4.1
McC_11	2	503	29	24.1	1.0	99	4.1	85	3.7	3410	150	431	53.0	7.1	1.2	2390	240	3590	290	283	27.0	861	76	104	9.6	35.6	2.6	77.9	7.8
McC_12	2	518	22	13.5	0.5	97	3.7	94	4.7	3960	160	267	13.0	8.1	0.4	1989	97	3370	140	340	15.0	1105	71	135	8.0	44.5	2.4	89.2	4.3
McC_13	2	519	20	9.8	0.3	101	2.9	103	3.9	3860	110	115	7.0	5.2	0.4	1605	71	2320	110	185	8.1	618	29	66	2.8	26.0	1.6	44.5	2.0
McC_14	2	532	22	16.8	0.6	85	2.6	90	2.8	3590	120	88	4.5	3.2	0.2	1351	66	1910	100	160	8.4	517	18	58	3.6	24.5	1.1	37.2	1.8
McC_15	2	519	21	18.8	0.6	80	2.7	77	3.3	3830	130	227	12.0	4.1	0.2	1863	91	2860	160	258	11.0	851	46	103	4.4	40.3	2.2	68.7	3.6
McC_16	2	516	22	11.8	0.5	95	4.4	93	4.0	3940	140	162	10.0	5.7	0.5	1800	120	2870	170	250	16.0	772	48	89	4.9	37.8	2.6	58.3	3.5
McC_17	2	519	20	19.9	0.8	93	3.6	113	7.0	3820	100	173	9.0	5.2	0.4	1582	82	2510	130	218	11.0	713	39	80	4.8	34.8	1.6	55.2	2.7
McC_18	2	534	23	11.7	0.6	91	4.1	92	4.0	3760	170	179	8.2	3.9	0.3	1594	93	2650	160	245	18.0	780	45	95	5.1	42.2	2.3	60.8	3.1
Σ Grains				4		13		13		18		12		5		15		16		14		13		12		13		13	
Average				12.6		89.6		91.4		3781		196		5.3		1801		2939		267		845		100.0		40.2		65.6	
2SD				0.8		8.1		7.1		238		22		0.2		168		323		24		67		6.9		4.2		6.1	
Durango																													
DUR_0	1	27.4	5.2	28.8	0.9	87.9	2.5	281	14	522	12	818	22.0	0.5	0.1	3832	88	5390	130	467	13	1640	49	238	6.8	19.7	0.6	192	6.2
DUR_1	1	32.8	3.5	29.1	0.9	87.1	1.6	281	11	519	11	829	15	0.5	0.1	3860	110	5580	120	472	10	1638	43	240	7.1	20.2	0.6	193	5.1
DUR_2	1	34.1	3.9	28.1	0.9	88.4	2.0	265	14	509	12	818	19	0.4	0.1	3853	88	5400	110	472	9	1600	38	235	5.8	20.2	0.5	190	5.3
DUR_3	1	31.2	4.8	28.6	1.0	85.1	1.8	279	18	518	15	825	26	0.6	0.1	3850	120	5480	130	460	13	1620	37	234	6.6	19.9	0.6	190	4.7
DUR_4	1	30.4	4.3	28.2	1.2	85.1	2.4	261	14	518	13	838	25	0.4	0.1	3950	110	5640	150	483	13	1648	35	238	6.3	20.4	0.6	201	5.4
DUR_5	1	31.9	3.5	28.7	1.3	85.3	2.7	266	17	518	16	805	28	0.3	0.1	3940	120	5650	180	477	15	1698	45	245	6.7	20.8	0.7	197	6.6
DUR_6	1	26.6	3.9	28.7	1.2	87.9	2.4	281	16	531	11	852	20	0.5	0.1	4103	99	5930	160	508	11	1724	42	247	6.9	20.9	0.8	207	6.4
DUR_7	1	28.4	2.8	33.0	1.2	90.2	2.0	273	16	504	13	837	19	0.6	0.1	3950	83	5540	150	464	10	1678	43	238	6.5	20.8	0.6	193	5.0
DUR_8	1	34.3	4.5	31.7	1.3	92.2	3.2	263	13	522	12	839	24	0.6	0.1	4178	80	5923	96	499	10	1703	41	249	6.3	21.1	0.7	201	6.5
DUR_9	1	28.0	3.5	33.1	1.0	90.2	2.3	262	15	516	10	840	23	0.6	0.1	3977	92	5650	130	495	10	1707	38	248	6.3	20.5	0.6	198	4.7
DUR_10	1	30.8	5.5	29.6	1.2	94.0	2.8	261	15	532	13	846	21	0.4	0.1	4060	100	5780	110	480	11	1695	39	238	5.9	19.9	0.6	197	5.0
DUR_11	1	27.5	4.2	30.5	1.4	91.9	2.4	275	12	523	16	825	28	0.4	0.1	4030	120	5720	160	479	17	1643	55	236	8.3	19.6	0.7	191	7.1
DUR_12	1	24.5	4.0	30.2	1.1	89.9	2.4	237	12	520	12	830	23	0.7	0.1	3951	96	5420	140	438	10	1512	39	224	5.5	19.0	0.6	187	5.2
DUR_13	1	26.0	3.8	28.8	1.0	96.4	2.5	255	11	529	10	832	22	0.7	0.1	3941	96	5530	140	463	12	1643	45	234	6.0	19.3	0.8	191	5.3
DUR_14	1	30.3	4.3	28.0	1.0	93.9	2.1	257	14	507	11	795	20	0.8	0.1	3760	110	5350	120	452	11	1578	36	222	3.8	18.8	0.5	188	5.2
DUR_15	1	26.7	3.4	28.9	0.7	94.3	2.6	261	14	523	11	812	25	0.7	0.1	3860	110	5380	110	466	9	1595	42	231	5.5	19.0	0.6	190	4.6
DUR_16	1	26.0	4.2	28.8	1.1	98.2	2.5	261	13	514	11	807	19	0.8	0.1	3950	110	5510	140	457	13	1621	45	228	6.3	18.9	0.7	189	5.5
DUR_17	1	31.3	4.3	29.1	1.3	96.7	2.7	255	14	515	12	775	21	0.8	0.1	3777	93	5350	130	445	10	1590	28	226	6.0	18.4	0.5	186	4.1
DUR_18	1	29.6	3.9	29.0	0.8	99.3	2.4	248	11	513	12	808	22	0.4	0.1	3820	120	5430	150	468	14	1667	36	226	7.6	19.3	0.8	191	4.9
DUR_19	1	30.6	4.1	29.1	0.9	104.6	3.0	262	14	519	12	816	22	0.4	0.1	3910	100	5480	130	461	14	1671	46	227	5.7	19.7	0.7	189	6.5
DUR_20	1	28.2	2.8	27.7	1.1	101.3	2.0	265	17	510	9	793	17	0.4	0.1	3759	96	5420	120	446	11	1588	41	220	5.6	18.9	0.7	185	5.0
DUR_21	1	30.6	4.2	28.6	0.9	103.3	2.7	247	12	517	14	819	29	0.4	0.1	3830	110	5540	120	450	14	1638	47	229	6.6	19.1	0.5	184	4.5
DUR_22	1	21.9	4.7	29.7	1.3	107.4	1.9	266	14	509	10	792	21	0.4	0.1	3846	95	5420	150	456	12	1619	41	227	5.8	19.1	0.6	185	5.0
DUR_23	1	32.0	3.9	30.8	1.3	107.4	2.5	256	14	509	11	794	16	0.5	0.1	3833	82	5483	98	461	9	1626	36	223	3.6	19.3	0.5	180	3.8
DUR_24	1	29.2	4.1	28.9	0.9	107.6	2.4	270	14	512	10	795	16	0.4	0.1	3824	81	5430	120	451	8	1603	32	222	5.2	18.8	0.6	182	4.3
DUR_25	1	32.9	4.9	29.8	1.0	107.3	2.6	270	11	507	10	813	20	0.4	0.1	3834	66	5370	100	454	11	1592	26	226	5.7	19.4	0.4	185	4.9
Σ Grains				25		25		25		25		25		14		25		25		25		25		25		25		25	
Average				29.4		94.6		263.7		517.1		818.4		0.4		3905.3		5535.0		466.7		1636.7		232.9		19.7		191.0	
2SD				2.8		14.3		21.8		14.5		37.4		0.1		208.9		324.3		33.8		96.8		16.9		1.5		12.3	
DUR_0	2	33	3	30.9	1.1	94.9	3.0	325	12	545	19	812	29.0	0.6	0.1	3900	200	5650	320	484	25	1770	78	229	14	19.2	0.9	186	5.4
DUR_1	2	34	4	29.9	1.3	85.4	3.4	283	12	505	24	795	44.0	0.7	0.1	3600	190	5430	320	448	24	1409	62	191	10	18.4	0.7	165	6.3
DUR_2	2	37	5	27.8	1.2	91.7	2.9	318	11	513	18	809	41.0	0.4	0.1	3720	220	5550	280	465	27	1616	74	230	11	18.9	1.1	184	7.5
DUR_3	2	28	4	29.2	0.9	90.8	2.8	301	11	520	15	883	27.0	0.6	0.1	3760	140	5350	250	479	18	1655	77	232	7	19.3	0.8	189	6.6
DUR_4	2	32	3	31.3	1.6	89.9	4.8	293	14	517	26	816	45.0	0.7	0.1	3860	270	5610	390	443	26	1488	88	203	10	18.2	1.0	162	8.3
DUR_5	2	33	3	27.5	0.9	91.2	3.1	301	11	507	15	817	33.0	0.5	0.1	3550	120	5240	270	468	17	1576	69	217	7	18.3	0.9	177	4.2
DUR_6	2	32	4	28.1	0.9	95.9	3.6	312	10	524	17	829	33.0	0.5	0.1	3950	160	5670	380	494	22	1709	82	230	9	19.3	0.8	190	6.9
DUR_7	2	30	3	25.6	1.0	88.1	3.3	297	11	491	17	758	29.0	0.4	0.0	3370	150	5200	270	418	17	1449	64	213	8	17.3	0.7	170	7.1
DUR_8	2	33	3	30.9	1.0	90.8	2.7	287	11	518	19	795	39.0	0.8	0.1	3750	150	5040	260	424	24	1423	81	191	11	17.7	1.0	160	8.3
DUR_9	2	31	3	28.3	1.2	91.3	3.5	285	14	505	23	779	33.0	0.8	0.1	3780	220	5330	350	438	33	1473	95	202	7	16.9	1.0	166	6.4
DUR_10	2	33	3	26.4	0.8	92.1	2.3	315	9	523	16	778	39.0	0.4	0.1	3680	170	5520	280	480	25	1506	54	208	10	18.5	0.6	173	7.7

Continue Table A2 – 3

DUR_11	2	30	4	28.4	1.0	92.0	3.6	297	10	517	18	803	38.0	0.7	0.1	4060	140	5350	270	454	25	1516	69	211	9	17.6	0.8	179	5.9
DUR_12	2	*37*	*4*	*26.4*	*0.9*	*92.5*	*3.7*	*307*	*13*	*495*	*19*	*772*	*37.0*	*0.3*	*0.0*	*3630*	*210*	*5430*	*320*	*462*	*34*	*1644*	*91*	*211*	*8*	*18.8*	*0.9*	*182*	*9.2*
DUR_13	2	*36*	*3*	*30.2*	*0.8*	*93.2*	*2.8*	*308*	*10*	*523*	*16*	*808*	*36.0*	*0.8*	*0.1*	*3770*	*130*	*5480*	*300*	*454*	*25*	*1518*	*56*	*204*	*9*	*17.7*	*0.8*	*177*	*7.4*
DUR_14	2	30	5	26.7	1.2	94.2	5.1	308	18	510	27	793	55.0	0.5	0.1	3770	330	5560	440	477	26	1600	130	217	13	18.9	1.3	176	12.0
DUR_15	2	31	3	28.2	1.3	99.4	4.3	332	14	518	23	810	49.0	0.4	0.0	3770	170	5740	280	468	27	1668	79	231	12	19.3	0.9	182	7.2
DUR_16	2	30	6	30.4	1.4	101.3	3.1	332	10	546	21	828	38.0	0.4	0.1	4070	220	5890	430	512	25	1711	77	225	15	20.4	1.0	190	7.0
DUR_17	2	33	5	30.4	1.4	97.5	4.1	318	14	521	26	791	37.0	0.7	0.1	3930	150	5550	520	471	38	1480	120	218	12	17.6	1.2	180	8.6
DUR_18	2	32	3	26.0	1.1	95.3	3.8	314	13	504	22	778	41.0	0.4	0.0	3690	240	5340	300	483	31	1562	91	213	11	18.2	1.0	183	7.0
DUR_19	2	31	3	30.6	1.0	101.9	3.5	326	11	546	13	839	38.0	0.7	0.1	4060	220	5850	280	487	31	1617	74	226	8	19.4	0.9	186	7.7
Σ Grains				18.0		18.0		18.0		18.0		18.0		8.0		18.0		18.0		18.0		18.0		18.0		18.0		18.0	
Average				28.7		93.5		308		518		806		0.6		3793		5493		466		1568		216		19		178	
2SD				1.8		4.3		15.3		14.6		27.4		0.1		181		221		24		104		12.8		0.9		9.4	
Mao et al.,16		Σ Grains		206		217				217		217		63		217		217		217		161		217		217		217	
		Average		44.6		97.0				513		670		0.6		3879		4773		368		1174		162		15.6		149.2	
		2SD		9.6		7.6		0.0		29		98		0.2		325		395		26		106		22		1.7		20.6	
Madagascar																													
MAD_0	1	481	25	31.1	0.9	231	4.1	121	8.9	2138	37.0	297	6.5	17.8	0.6	2130	41	4280	100	436	9.5	1554	33	209	5.2	28.5	0.7	117	2.9
MAD_1	1	477	23	31.6	1.0	234	5.1	117	7.6	2161	54.0	296	7.5	18.0	0.5	2171	44	4361	94	446	10.0	1576	35	210	5.4	29.1	0.7	121	3.3
MAD_2	1	489	26	32.2	1.2	237	4.2	118	7.7	2176	50.0	303	7.7	18.4	0.7	2258	53	4440	120	462	10.0	1617	39	216	4.5	29.4	0.8	121	3.1
MAD_3	1	461	46	31.2	1.2	226	4.9	119	7.8	2101	49.0	296	5.5	17.6	0.5	2182	39	4368	92	451	10.0	1578	34	208	5.1	28.6	0.6	121	2.6
MAD_4	1	466	24	32.4	1.1	237	4.3	110	8.6	2246	38.0	310	6.6	18.6	0.7	2393	58	4760	120	475	10.0	1713	30	232	6.3	32.3	1.0	132	2.8
MAD_5	1	466	27	32.7	0.9	233	4.8	117	9.1	2215	47.0	306	9.4	19.1	0.6	2318	49	4700	110	470	12.0	1724	34	221	5.2	31.4	0.8	127	2.9
MAD_6	1	480	32	33.0	0.8	235	4.4	108	6.5	2263	56.0	314	6.8	19.3	0.6	2366	60	4680	120	471	12.0	1683	40	229	4.9	30.5	0.8	127	2.4
MAD_7	1	477	28	32.6	1.1	246	6.5	112	10.0	2239	72.0	309	8.1	18.2	0.7	2351	62	4760	120	470	13.0	1707	45	226	5.8	31.7	0.8	132	3.3
MAD_8	1	468	29	32.4	1.1	241	4.9	110	7.3	2252	55.0	313	9.1	19.5	0.7	2421	51	4880	110	478	11.0	1727	38	226	6.7	32.0	1.0	131	3.8
MAD_9	1	466	32	31.1	0.9	237	5.0	116	8.7	2162	60.0	297	8.2	18.6	0.5	2320	55	4700	130	466	10.0	1675	39	216	5.9	31.0	0.7	126	3.1
MAD_10	1	468	30	30.5	1.0	246	5.3	111	7.4	2200	63.0	304	9.4	18.1	0.9	2312	63	4650	130	462	13.0	1698	40	217	7.0	30.7	0.9	126	4.4
MAD_11	1	481	30	30.4	1.1	249	5.6	105	8.5	2187	52.0	305	7.3	17.9	0.8	2314	60	4570	100	459	13.0	1657	43	214	5.6	29.9	0.7	124	3.3
MAD_12	1	465	24	31.9	1.5	251	4.9	96	8.2	2219	45.0	309	6.3	18.8	0.6	2341	58	4700	130	461	15.0	1679	52	221	5.2	30.8	0.9	127	3.5
MAD_13	1	472	28	30.3	1.3	255	6.2	104	8.9	2218	60.0	305	8.5	18.4	0.7	2343	46	4650	120	458	9.7	1686	36	215	5.6	30.4	1.0	123	3.6
MAD_14	1	461	35	32.4	1.0	253	5.4	100	8.8	2189	49.0	295	6.7	17.8	0.6	2255	37	4500	100	449	9.5	1639	43	216	5.2	29.0	0.7	123	3.0
MAD_15	1	468	29	33.1	1.3	258	5.2	113	9.3	2155	48.0	299	5.8	17.9	0.6	2297	44	4580	130	463	13.0	1656	51	217	6.7	29.8	0.7	122	4.7
MAD_16	1	464	27	32.1	1.0	264	6.9	108	7.6	2263	41.0	308	6.2	18.2	0.5	2307	52	4666	88	460	13.0	1673	47	216	6.3	30.7	0.7	125	3.8
MAD_17	1	476	29	32.9	1.0	268	6.4	107	6.7	2191	53.0	299	8.6	18.7	0.6	2324	52	4590	120	448	9.1	1677	42	215	5.6	29.7	0.9	122	3.8
MAD_18	1	477	32	30.9	1.0	262	4.8	99	5.9	2214	50.0	297	7.0	17.8	0.6	2257	54	4489	91	446	11.0	1618	39	214	5.2	29.8	0.7	123	3.1
MAD_19	1	473	33	32.2	1.4	278	5.0	104	7.0	2189	49.0	296	6.8	18.5	0.6	2245	47	4424	89	445	9.2	1612	38	207	4.2	28.9	0.8	120	3.2
MAD_20	1	479	27	32.2	1.2	275	7.1	100	10.0	2199	56.0	297	7.5	17.2	0.7	2302	52	4485	90	446	11.0	1625	44	213	5.6	29.1	0.8	122	3.7
MAD_21	1	474	33	33.9	1.2	279	5.3	94	9.9	2243	48.0	299	7.3	17.9	0.7	2245	58	4610	100	445	10.0	1610	39	206	5.7	29.2	0.7	120	3.2
MAD_22	1	477	28	32.2	1.3	288	5.3	104	9.2	2226	55.0	285	6.9	18.2	0.7	2228	54	4440	100	440	12.0	1605	48	205	5.1	28.7	0.6	120	3.3
MAD_23	1	477	32	32.3	1.4	292	6.7	98	6.0	2187	55.0	292	8.3	17.9	0.8	2260	59	4390	110	435	11.0	1615	34	207	5.0	28.5	0.7	118	2.6
MAD_24	*1*	*454*	*581*	*31.1*	*1.0*	*289*	*4.4*	*99*	*8.7*	*2175*	*47.0*	*293*	*8.1*	*17.1*	*0.7*	*2237*	*60*	*4490*	*100*	*440*	*11.0*	*1606*	*44*	*205*	*5.9*	*29.3*	*0.9*	*121*	*3.5*
MAD_25	1	478	33	31.7	1.0	289	7.1	99	5.6	2234	58.0	295	9.0	18.0	0.8	2215	46	4424	91	431	8.1	1600	31	200	4.7	28.3	0.8	118	2.2
Σ Grains				25		25		25		25		25		25		25		25		25		25		25		25		25	
Average				32.0		255		107		2203		301		18		2286		4564		455		1648		215		30		123	
2SD				1.8		39		15.3		79		13.9		1.1		136		297		25.6		96		15.2		2.3		8.3	
MAD_0	2	469	19	30	0.8	241	6.8	112	4.3	2151	56	291	14	17.8	0.9	2100	110	4410	210	448	22	1551	76	199	8.3	28.3	1.4	118	3.1
MAD_1	2	461	17	29	0.97	237	9.8	102	4.1	2134	92	279	16	16.8	0.9	2110	130	4430	240	442	23	1489	62	198	10	27.9	1.5	113	5.3
MAD_2	2	484	21	29	1.4	233	10	107	5.4	2070	100	266	18	16.6	0.8	2010	140	4160	240	451	34	1498	95	189	11	26	1.3	106	6
MAD_3	2	483	20	30	1.4	231	9.5	99	4.1	2099	79	297	15	16.3	0.9	2100	130	4390	330	459	23	1600	71	210	8.2	29.9	1.7	119	5.8
MAD_4	2	474	20	30	0.73	246	5.5	104	2.6	2174	48	285	11	17.8	0.7	2118	91	4460	170	456	20	1524	73	198	9.1	28.7	1.2	116	3.7
MAD_5	2	480	21	30	1	235	8.5	96	3.5	2057	70	270.7	9.7	16.2	0.7	1948	73	4130	230	431	17	1515	72	196	9.2	26.9	1.4	111	5.1
MAD_6	2	488	19	30	1.4	249	9.9	99	4.9	2170	110	283	13	17.0	1.0	2040	140	3980	230	428	29	1619	99	193	12	26.5	1.3	111	5.4
MAD_7	2	472	19	30	0.82	233	7.2	89	2.3	2153	53	296	9.1	17.2	0.6	2151	97	4570	230	475	24	1676	85	215	10	29.2	0.63	120	4.5
MAD_8	2	475	18	30	0.93	255	7.4	98	3.3	2192	78	289	14	18.5	0.6	2090	100	4310	210	455	19	1571	91	199	9.7	28.8	1.2	116	5.4
MAD_9	2	464	20	31	0.99	251	11	91	3.4	2170	100	280	14	17.9	1.0	2140	110	4380	320	461	26	1583	86	198	8	27.7	1.1	114	5.2
MAD_10	2	468	20	30	1	248	9	101	3.3	2201	76	292	17	18.0	0.9	2160	120	4560	340	439	27	1561	91	195	12	28.9	1.9	116	6.5
MAD_11	2	477	18	30	1.2	236	11	82	4.7	2096	90	281	14	16.3	0.8	2050	120	4550	270	454	31	1610	120	198	9.8	28.6	1.3	115	4.5
MAD_12	2	468	18	30	1.2	253	10	95	3.8	2209	88	273	15	17.8	0.9	2136	98	4210	310	447	17	1562	90	190	10	27.7	1.4	113	5.9
MAD_13	2	475	19	30	1.1	251	10	86	4.3	2140	100	270	13	17.2	0.8	1980	110	4380	210	437	19	1491	72	191	11	27.1	1.5	109	5.8
MAD_14	2	493	22	29	1.4	243	10	89	3.4	2084	82	258	15	17.0	1.0	2020	100	4120	250	433	21	1466	63	185	11	26.3	1.6	109	4.9
MAD_15	2	461	18	31	0.9	242	9	77	3.4	2128	82	297	13	16.5	0.6	2210	130	4570	200	469	32	1669	79	205	8.9	29.5	1.2	119	4.5
MAD_16	2	480	19	30	1.2	254	11	90	4.2	2143	87	273	14	17.9	1.0	2110	110	4210	210	453	20	1510	87	192	11	26.9	1.5	110	5.6
MAD_17	2	475	19	31	1.3	257	12	87	4.1	2220	89	293	17	16.7	0.9	2140	150	4210	280	449	23	1475	73	190	9.6	28.2	1.4	119	5.4

Continue Table A2 – 3

	MAD_18	2	476	22	30	1.1	257	8.6	91	3.5	2221	73	264	13	17.4	0.8	2003	73	4340	220	450	23	1526	84	191	9	29.6	1.8	113	4.4
	MAD_19	2	480	19	31	1.4	245	10	79	3.7	2150	100	287	12	16.5	1.0	2150	120	4490	260	470	38	1580	100	206	11	29.9	1.6	120	5.8
	MAD_20	2	463	18	30	0.77	257	6.2	92	2.3	2201	66	297	9.7	19.2	0.8	2210	91	4370	190	464	19	1561	52	207	7.4	29.2	1	121	4.7
	MAD_21	2	465	17	30	1.3	258	13	86	3.9	2176	98	279	13	17.7	1.0	2076	81	4310	300	439	22	1565	73	201	10	28.6	1.6	116	6
	MAD_22	2	469	19	31	0.96	270	9.3	94	4.6	2235	88	303	18	18.1	0.9	2200	120	4370	220	446	23	1534	60	205	12	29.6	1.5	118	6.3
	MAD_23	2	473	20	30	1.2	250	8.6	77	3.3	2154	55	297	12	17.0	0.6	2260	120	4810	260	453	33	1621	75	207	9.3	30.3	1.4	121	6.2
	MAD_24	2	481	18	31	0.82	260	5.9	92	2.6	2188	63	304	10	18.5	0.7	2190	110	4120	180	434	17	1569	62	199	5.3	28.3	1.1	116	4
	MAD_25	2	497	22	31	1.1	258	10	83	3.5	2145	76	276	11	17.4	0.9	1983	94	4230	240	464	30	1520	83	193	11	28.1	1.5	111	5.7
	Σ Grains				26		26		25		26		26		26		26		26		26		26		26		26		26	
	Average				30.1		248.1		92.1		2156		283.9		17.4		2103		4349		450		1556		198		28.3		115	
	2SD				0.6		9.8		8.8		46.4		12.3		0.7		79		180		12.4		54		7.2		1.2		4.0	0.8
	Mao et al., 16		Σ Grains		216		230				230		230		230		230		230		230		174		230		230		230	
			Average		27.1		251				2001		276		16		2058		4309		435		1471		186		27		118	
			2SD		7.8		18.5		0.0		111.3		37.0		4.8		176		606		26.4		177		25.8		4.3		15.3	
Navan																														
HK 158	*X18HK_005_0*	1	*1276*	*34*	*6.9*	*0.6*	*288*	*7*	*103*	*11*	*317*	*9.5*	*430*	*13.0*	*0.1*	*0.0*	*79*	*3*	*456*	*19*	*91*	*3*	*532*	*16*	*124*	*5.0*	*16.3*	*0.8*	*104.7*	*4.2*
HK 159	*X18HK_006_0*	1	*509*	*145*	*23.0*	*1.3*	*1455*	*33*	*855*	*31*	*1564*	*32.0*	*658*	*15.0*	*5.2*	*0.3*	*3528*	*78*	*8400*	*160*	*1030*	*27*	*4290*	*120*	*628*	*18.0*	*62.7*	*1.6*	*346.2*	*9.6*
	X18HK_006_1	1	343	31	0.3	0.1	1699	34	1780	64	65	2.1	1166	27.0	11.7	0.5	1746	36	4140	100	519	12	2476	48	459	10.0	43.0	1.3	393.8	9.4
	X18HK_006_2	1	312	64	0.2	0.1	1630	53	1189	47	49	2.4	2330	100.0	12.9	0.9	4670	170	10310	480	1290	47	5610	220	936	40.0	36.6	1.5	###	21.0
	X18HK_006_3	1	306	49	0.1	0.1	1757	42	1730	44	51	1.5	1192	34.0	11.4	0.7	1830	61	4320	110	537	15	2575	62	465	13.0	36.5	0.8	391.0	11.0
	X18HK_006_4	1	*266*	*84*	*0.1*	*0.1*	*1382*	*26*	*1081*	*29*	*55*	*1.1*	*1726*	*56.0*	*9.5*	*0.5*	*3688*	*85*	*7950*	*150*	*935*	*18*	*4072*	*68*	*676*	*11.0*	*26.8*	*0.7*	*552.0*	*11.0*
	Σ Grains				1		3		2		2		2		3		2		2		2		2		2		3		2	
	Average				0.2		1695		1755		50.0		1179		12.0		1788		4230.0		528.0		2526		462		38.7		392.4	
	2SD				0.0		103.8		50.0		2.4		26.0		1.3		84.0		180		18.0		99.0		6.0		6.1		2.8	
HK 235	*X19HK_009_0*	1	*1642*	*31*	*0.4*	*0.2*	*487*	*11.0*	*202*	*17.0*	*169*	*6.6*	*1255*	*42.0*	*0.2*	*0.1*	*427*	*11.0*	*1212*	*41.0*	*175*	*5.6*	*962*	*31.0*	*279*	*10.0*	*21.9*	*0.5*	*285.3*	*9.1*
Stonepark Area																														
HK 207	*X19HK_004_0*	1	*1770*	*92*	*12.1*	*1.1*	*735*	*21*	*137*	*13*	*188*	*21.0*	*598*	*24.0*	*2.8*	*0.4*	*5050*	*190*	*6870*	*250*	*558*	*19*	*1846*	*60*	*218*	*11*	*50*	*2*	*155*	*9*
	X19HK_004_1	1	*895*	*23*	*4.4*	*0.4*	*333*	*8*	*237*	*10*	*352*	*8.7*	*88*	*3.9*	*0.2*	*0.1*	*739*	*22*	*1689*	*66*	*192*	*6*	*813*	*31*	*116*	*4*	*17*	*1*	*74*	*3*
HK 209	X19HK_006_0	1	316	48	1.1	0.2	893	19	1978	72	531	19.0	407	12.0	9.0	0.5	318	8	828	21	123	3	682	21	158	3	147	3	156	4
HK 210	X19HK_014_0	1	312	75	0.2	0.4	1160	100	1980	250	80	12.0	880	110	13.9	2.3	1170	150	2900	380	375	59	1840	120	371	18	42	4	307	37
	X19HK_014_1	1	282	40	0.1	0.1	1112	22	1996	67	175	4.9	630	18	9.6	0.5	752	23	1862	54	253	10	1240	41	243	8	59	2	219	7
	X19HK_014_2	1	*422*	*14*	*7.9*	*0.5*	*1190*	*28*	*191*	*12*	*246*	*8.5*	*184*	*7*	*1.1*	*0.2*	*3012*	*95*	*3840*	*110*	*251*	*8*	*730*	*22*	*71*	*4*	*18*	*1*	*50*	*2*
	X19HK_014_3	1	308	88	0.2	0.2	1194	40	1890	70	95	4.6	882	65	12.7	1.4	1142	58	2810	160	367	16	1735	86	355	20	48	3	295	11
	X19HK_014_4	1	308	34	< LOD	< LOD	1186	25	1756	47	46	1.3	837	20	9.5	0.5	1194	27	2824	60	367	9	1815	52	326	8	34	1	282	7
	X19HK_014_5	1	*423*	*190*	*0.1*	*0.4*	*1120*	*51*	*1875*	*69*	*124*	*5.6*	*1510*	*150*	*20.7*	*2.6*	*2340*	*130*	*5850*	*550*	*670*	*37*	*3400*	*300*	*694*	*54*	*43*	*3*	*558*	*36*
	X19HK_014_6	1	*200*	*40*	*0.3*	*0.4*	*1003*	*76*	*1340*	*220*	*50*	*7.3*	*1040*	*140*	*17.3*	*2.3*	*1620*	*140*	*3620*	*280*	*469*	*52*	*2210*	*220*	*436*	*49*	*26*	*3*	*364*	*46*
	X19HK_014_7	1	273	46	0.1	0.1	1238	34	1652	50	37	2.1	1172	42	12.7	0.9	1925	63	4450	190	569	19	2683	98	479	18	28	1	389	14
	Σ Grains						5		5		2		3		3		3		3		3		3		3		3		3	
	Average						1178		1855		88		866		13.1		1169		2845		370		1797		351		41		295	
	2SD						83		265		15		42		1.2		42		79		7		90		37		12		20	
HK 211	*X19HK_015_0*	1	*437*	*29*	*0.5*	*0.1*	*2171*	*36*	*3458*	*78*	*167*	*3.7*	*5320*	*150*	*0.7*	*0.1*	*824*	*21*	*2679*	*57*	*384*	*8*	*1976*	*51*	*726*	*17*	*13*	*0*	*921*	*19*
	X19HK_015_1	1	347	31	0.2	0.1	2230	40	3451	90	133	3.1	4960	120	0.6	0.1	787	19	2542	53	368	8	1821	44	642	16	10	0	826	17
	X19HK_015_2	1	334	31	2.3	0.5	2219	34	3412	82	135	2.9	4960	150	0.6	0.1	791	17	2519	59	377	10	1859	47	651	18	10	0	852	25
	X19HK_015_3	1	361	31	0.9	0.2	2309	44	3504	76	125	3.0	5190	110	0.7	0.1	808	18	2629	59	383	10	1936	38	672	13	10	0	879	16
	X19HK_015_4	1	358	30	0.3	0.1	2185	40	3393	90	144	3.0	5230	130	1.0	0.2	839	22	2664	59	397	10	1984	46	682	17	11	0	890	21
	X19HK_015_5	1	328	31	0.1	0.1	2255	32	3450	98	130	3.0	5230	150	0.6	0.1	837	14	2722	68	394	10	1973	45	693	15	11	0	907	23
	X19HK_015_6	1	395	78	1.1	0.2	2241	63	3298	61	128	6.5	4810	260	0.6	0.3	732	19	2460	150	359	13	1800	130	645	33	10	1	815	39
	X19HK_015_7	1	373	22	0.2	0.1	2470	52	3570	100	139	4.5	5380	120	0.5	0.1	873	23	2790	71	408	11	2067	51	731	20	12	1	931	23
	X19HK_015_8	1	322	16	0.2	0.1	2136	56	3260	99	189	6.3	5300	180	3.7	0.7	875	30	2880	110	423	15	2071	81	732	25	14	1	952	32
	X19HK_015_9	1	375	30	0.3	0.2	2313	40	3456	85	130	3.8	4720	110	0.5	0.1	771	20	2470	70	356	11	1797	42	624	15	9	0	796	22
	X19HK_015_10	1	*537*	*54*	*17.6*	*1.7*	*2345*	*78*	*3434*	*98*	*137*	*4.5*	*4780*	*200*	*2.2*	*0.2*	*781*	*30*	*2501*	*80*	*363*	*11*	*1833*	*62*	*638*	*27*	*10*	*1*	*840*	*31*
	X19HK_015_11	1	366	30	0.2	0.1	2735	52	3358	67	100	2.4	5530	120	0.8	0.1	767	16	2567	61	380	8	1916	45	685	18	9	0	903	17

Continue Table A2 – 3

HK 211	X19HK_015_12	1	344	40	0.4	0.2	2265	46	3500	130	132	4.9	4790	160	1.1	0.5	763	31	2470	110	364	12	1799	88	633	27	10	1	850	39
	X19HK_015_13	1	315	28	0.2	0.1	2293	40	3540	77	130	3.1	5290	160	0.6	0.1	814	26	2690	81	387	12	1913	72	681	22	10	0	898	31
	X19HK_015_14	1	347	15	0.3	0.2	2406	48	3637	80	129	4.6	7090	180	1.4	0.1	1071	30	3443	95	511	14	2495	69	923	27	14	1	1199	30
	X19HK_015_15	1	327	20	0.3	0.1	2681	48	3595	74	117	2.8	6570	240	1.0	0.2	973	41	3170	110	469	17	2360	100	840	27	12	1	1113	35
	X19HK_015_16	1	370	27	0.1	0.1	2370	43	3507	83	129	3.5	5170	130	0.5	0.1	783	21	2543	53	364	8	1855	42	652	13	10	0	860	19
	X19HK_015_17	1	323	27	1.6	0.3	2450	43	3540	81	130	3.0	5030	110	0.6	0.1	775	18	2512	65	364	8	1849	45	658	16	10	0	872	22
	X19HK_015_18	1	354	38	0.0	0.1	2321	49	3393	88	131	5.2	5080	190	0.7	0.2	803	16	2634	99	380	8	1951	54	681	21	10	1	883	26
	X19HK_015_19	1	341	15	0.2	0.1	2509	89	3147	98	187	19.0	5330	160	1.1	0.2	710	16	2367	47	355	11	1826	47	696	18	12	1	903	21
	X19HK_015_20	1	336	25	0.2	0.1	2386	44	3585	89	133	2.6	5470	120	0.8	0.1	848	20	2807	58	401	10	2026	60	701	19	11	0	918	23
	X19HK_015_21	1	346	17	0.5	0.1	2487	56	3630	110	136	4.4	5880	170	1.0	0.2	928	24	2902	78	432	14	2177	55	767	21	12	0	985	25
	X19HK_015_22	1	325	27	0.2	0.1	2670	54	3392	92	108	4.1	5260	130	0.7	0.2	817	19	2532	52	379	8	1887	43	666	15	10	0	874	21
	X19HK_015_23	1	382	40	0.0	0.1	2386	46	3480	51	132	3.2	4820	100	0.5	0.1	779	21	2485	52	363	10	1852	54	623	18	9	0	819	18
	X19HK_015_24	1	397	38	2.2	0.4	2233	71	3280	150	172	7.5	4940	200	2.1	0.4	807	33	2621	98	378	12	1893	76	690	28	13	1	867	35
	Σ Grains				6		23		23		19		21		9		21		21		21		21		21		22		21	
	Average				0.2		2372		3451		130		5160		0.7		805		2610		382		1917		676		10.7		880	
	2SD				0.0		317		245		15		553		0.1		98		284		42		201		72		2.5		90	
HK 212	X19HK_016_0	1	332	31	15.1	0.8	547	9.1	1986	34	639	14.0	492	13.0	17.8	0.7	384	14.0	983	33.0	133	4.2	691	20	162	5.4	37	1.0	161	5.5
	X19HK_016_1	1	*328*	*101*	*0.2*	*0.3*	*980*	*30.0*	*1640*	*130*	*104*	*4.8*	*639*	*30.0*	*15.8*	*2.5*	*583*	*30.0*	*1581*	*60.0*	*221*	*11.0*	*1239*	*70*	*290*	*22.0*	*95*	*6.9*	*271*	*14.0*
	X19HK_016_2	1	329	33	0.3	0.1	985	20.0	1800	49	308	9.1	412	9.6	8.4	0.6	331	6.0	886	22.0	127	2.3	688	16	161	5.3	122	3.1	157	3.4
	X19HK_016_3	1	345	44	0.8	0.3	1014	29.0	1915	87	201	9.0	519	26.0	9.1	1.0	435	17.0	1176	41.0	169	8.0	864	30	210	12.0	107	6.6	192	6.9
	X19HK_016_4	1	314	23	0.3	0.1	1016	17.0	1777	81	79	2.9	735	18.0	9.2	0.5	751	27.0	2024	83.0	293	8.9	1510	53	340	13.0	69	2.5	305	12.0
	X19HK_016_5	1	363	23	0.2	0.1	938	22.0	1466	63	49	2.3	647	30.0	11.5	1.1	574	24.0	1573	63.0	220	8.9	1185	56	273	11.0	75	2.9	242	12.0
	X19HK_016_6	1	346	57	1.0	0.3	915	13.0	1860	81	450	12.0	395	20.0	8.9	0.6	310	16.0	827	36.0	124	5.6	664	27	156	5.3	142	7.6	151	5.7
	X19HK_016_7	1	306	62	4.5	0.5	421	12.0	954	42	694	27.0	983	22.0	15.4	0.8	844	29.0	2144	64.0	276	8.3	1357	40	294	9.9	54	1.8	278	8.0
	X19HK_016_8	1	304	34	7.5	0.6	589	12.0	1983	56	679	15.0	527	12.0	17.0	0.6	424	12.0	1095	25.0	149	3.5	770	19	171	4.7	38	0.8	171	4.4
	X19HK_016_9	1	338	24	0.1	0.1	1089	35.0	1751	63	19	1.0	2191	70.0	8.3	0.6	3863	88.0	10060	370.0	1350	30.0	6860	280	1342	35.0	87	2.0	1106	28.0
	X19HK_016_10	1	297	35	0.4	0.1	989	20.0	1947	67	387	9.8	391	11.0	8.0	0.4	299	8.1	811	21.0	117	2.6	643	22	150	4.3	140	4.2	150	4.0
	Σ Grains						7		9		2		3		6		3		3		4		5		5		3		6	
	Average						992		1832		347		513		8.6		414		1085		144		735		172		77		164	
	2SD						105		307		79		30		0.9		44		158		32		147		39		15		29	
Slievedart Area																														
HK 187	*X18HK_132_0*	1	*13*	*9*	*77.6*	*2.5*	*499*	*7.5*	*302*	*21.0*	*7800*	*130*	*573*	*14.0*	*2.9*	*0.2*	*2926*	*68.0*	*6110*	*130*	*650*	*15.0*	*2369*	*49.0*	*357*	*8.1*	*87.2*	*2.3*	*248.6*	*4.9*
HK 190	X18HK_135_0	1	371	26	1.1	0.1	2256	42	3576	84	128	3.4	5710	170	1.1	0.1	871	22.0	2854	76.0	417	10.0	2058	55.0	750	17.0	11.1	0.4	972	25
	X18HK_135_1	1	368	31	1.1	0.1	2248	58	3460	130	131	4.1	5090	120	0.7	0.1	814	21.0	2632	77.0	385	7.7	1893	47.0	678	19.0	10.5	0.5	872	24
	X18HK_135_2	1	358	32	0.9	0.1	2170	51	3421	94	128	3.9	4700	120	0.6	0.1	770	22.0	2485	58.0	363	9.9	1790	51.0	623	17.0	9.6	0.4	815	23
	Σ Grains				3		3		3		3		3		2		3		3		3		3		3		3		3	
	Average				1.0		2225		3486		129		5167		0.6		818		2657		388.2		1914		684		10.4		886	
	2SD				0.2		77.6		132		2.6		831.8		0.1		82.7		303.4		44.3		221		104		1.2		130	
HK 193	X18HK_138_0	1	373	34	30.8	1.9	398	20.0	180.0	17.0	607.0	21.0	89.7	3.6	2.5	1.3	402.0	19.0	498.0	24.0	46.3	2.7	177.3	7.7	32.1	1.3	7.0	0.5	28.1	1.8
HK 194	X18HK_139_0	1	349	30	0.1	0.1	2212	44	3444	79	127	3.4	5100	120	0.8	0.1	811	21	2567	62	379	10.0	1873	49	672	16.0	10.2	0.4	843	18.0
	X18HK_139_1	1	397	29	0.3	0.1	2294	50	3570	100	159	6.8	5950	170	1.1	0.1	882	22	2811	80	414	10.0	2130	55	753	22.0	12.5	0.5	987	21.0
	X18HK_139_2	1	381	34	1.1	0.3	1932	97	3360	220	184	6.5	4380	270	3.5	1.2	706	31	2310	130	357	18.0	1656	81	597	28.0	10.5	0.5	741	29.0
	X18HK_139_3	1	345	27	< LOD	< LOD	2259	40	3578	84	132	4.0	4970	130	0.5	0.1	787	17	2575	56	377	8.7	1860	48	655	17.0	10.0	0.4	848	15.0
	X18HK_139_4	1	365	24	< LOD	< LOD	1831	87	2980	130	241	10.0	4430	160	2.2	0.3	752	23	2281	69	351	11.0	1663	89	592	17.0	11.9	0.7	760	30.0
	X18HK_139_5	1	347	31	< LOD	< LOD	1986	35	3119	69	179	5.6	4640	110	0.9	0.2	753	16	2405	45	358	5.9	1774	33	626	9.2	11.3	0.5	799	17.0
	Σ Grains				1		6		6		3		5		3		6		6		6		6		6		6		6	
	Average				0.3		2086		3342		174.0		4704		0.9		782		2492		373		1826		649		11.1		830	
	2SD				0.0		354		447		21.4		574		0.2		111		365		43		320		109		1.8		161	
HK 237	X18HK_158_0	2	306	34	2.94	0.17	1099	47	518	22	973	45	598	29	0.5	0.07	453	26	1281	94	194	12	930	52	214	12	36.9	1.7	192	11
	X18HK_158_1	2	326	39	3.15	0.13	1112	49	512	20	1025	37	665	27	0.553	0.07	428	22	1220	59	182.5	8.3	904	50	220	10	36.8	1.3	193.3	8.9
	X18HK_158_2	2	318	37	3.53	0.13	1097	53	495	20	793	37	635	31	0.543	0.07	349	18	1135	96	167	12	845	59	212	11	36.4	2.3	185.5	9.2
	X18HK_158_3	2	299	32	3.18	0.32	1142	50	498	29	938	45	609	27	0.478	0.1	348	14	1121	83	153	8.5	743	38	193	10	35	1.6	174.4	9.1

Continue Table A2 – 3

	X18HK_158_4	2	274	36	2.82	0.14	1046	51	460	22	632	28	677	40	0.2	0.04	215	12	753	50	118	6.8	648	36	202.4	9.8	31.2	1.7	192.4	7.3
	X18HK_158_5	2	312	30	3.37	0.16	1201	64	654	32	993	53	652	36	0.7	0.09	503	26	1500	100	216	14	1074	48	234	12	38.4	2.3	195	11
	X18HK_158_6	2	307	33	3.31	0.14	1031	35	473	21	924	45	565	24	0.7	0.07	350	17	1016	42	155.6	7.5	794	43	188.8	5.5	32.7	1.2	171.6	7.3
	X18HK_158_7	2	288	41	4.38	0.28	1104	20	940	260	714	13	703	15	1.8	0.2	271.1	6.8	850	28	133.7	3.1	723	18	203.8	5.6	32.89	0.92	195.8	5.3
	X18HK_158_8	2	291	29	3.73	0.23	1096	45	472	19	910	32	584	30	15	25	404	24	1144	68	166.2	9.1	874	41	205	11	33.7	1.5	173.2	6.8
	X18HK_158_9	2	322	39	3.11	0.17	1059	64	494	28	748	42	716	47	0.621	0.07	318	24	1045	63	163	11	848	52	226	16	37.7	2.8	205	14
	X18HK_158_10	2	304	27	3.15	0.1	1095	35	509	23	936	37	671	30	0.4	0.05	401	25	1307	79	179	11	897	41	220.1	9.4	37.9	2	199	8.2
	X18HK_158_11	2	284	37	2	0.075	1083	46	481	17	839	28	682	25	35	26	355	14	1053	79	164.7	9.2	767	35	208.8	9.4	32.5	1.4	188	6
	X18HK_158_12	2	298	35	4.16	0.7	1136	40	503	20	793	30	663	39	0.4	0.05	284	11	913	56	144.1	7.5	722	39	201	11	34.1	1.4	182.3	8.3
	X18HK_158_13	2	280	36	3.89	0.12	1175	40	558	21	1135	44	601	35	0.592	0.05	502	34	1443	88	213	12	994	35	215	12	37.6	1.5	192.1	8.2
	X18HK_158_14	2	308	29	2.69	0.18	1128	44	518	19	772	26	723	31	130	170	379	17	1170	57	179	9.1	890	31	232.4	9.2	36.1	1.5	214.5	8.2
	X18HK_158_15	2	314	34	2.53	0.2	1156	47	483	19	982	49	454	24	0.8	0.1	537	32	1580	130	209	13	988	51	198.6	9.6	31.8	1.6	156.2	7.5
	X18HK_158_16	2	282	46	3.33	0.18	1121	61	548	25	869	45	612	41	0.4	0.06	302	15	1040	110	146.8	8.8	745	48	196	11	33.5	2.2	184	12
	X18HK_158_17	2	308	36	3.25	0.15	1220	49	605	31	1056	61	613	33	0.4	0.04	389	20	1166	86	174	11	859	41	212.2	9.9	37.2	2.1	179	10
	X18HK_158_18	2	288	29	2.83	0.12	1083	45	530	25	951	41	657	39	0.4	0.05	410	20	1271	66	176.2	9.6	927	61	214	10	35.9	1.3	194.4	8.4
	X18HK_158_19	2	274	50	5.86	0.52	1101	38	539	20	979	34	594	25	1	0.14	286	13	953	62	132	7.2	689	31	179.7	8.7	34.2	1.5	156.5	6.9
	X18HK_158_20	2	256	39	2.44	0.13	1237	56	507	19	727	36	851	56	0.3	0.04	282	13	901	42	131	8.4	706	34	212	13	35.3	1.5	214.6	8.5
	X18HK_158_21	2	299	31	2.72	0.12	1214	43	623	22	956	39	681	40	22	7.6	410	19	1258	87	171.7	7.9	876	46	220	14	36.3	2	199.8	8.9
	Σ Grains				13		16		13		15		15		4		10		13		13		15		16		16		16	
	Average				3.1		1126.0		515.0		915.8		646.7		0.5		367.4		1125.0		164.9		830.2		209.5		35.5		186.5	
	2SD				0.3		50.5		32.7		94.1		46.1		0.1		38.7		120.3		16.8		86.1		15.3		2.0		15.7	
HK 238	X18HK_159_0	2	287	34	2.4	0.1	1047	43	475	22	809	44	586	34	0.3	0.1	332	26	1015	76	154	11.0	781	35	189	9.9	31	1.7	165	6.9
	X18HK_159_1	2	321	33	2.4	0.1	1124	47	566	29	889	47	663	30	0.3	0.0	379	27	1176	64	160	11.0	856	57	216	11.0	36	2.3	187	9.0
	X18HK_159_2	2	331	37	4.4	0.2	1038	32	472	20	759	22	730	36	0.7	0.1	312	16	1076	60	161	9.3	827	40	222	8.2	39	2.1	207	8.9
	X18HK_159_3	2	257	36	3.5	0.1	1085	32	513	15	984	40	627	36	0.4	0.0	350	17	1098	39	159	8.7	801	44	200	12.0	33	1.6	174	7.2
	X18HK_159_4	2	307	33	2.2	0.1	1139	39	530	20	800	25	790	48	0.3	0.0	292	15	938	54	145	7.2	779	29	218	10.0	35	1.5	211	6.1
	X18HK_159_5	2	293	31	3.3	0.2	1328	59	765	30	1005	52	668	45	0.5	0.0	312	20	1058	73	156	9.8	780	38	203	11.0	37	1.6	183	9.5
	X18HK_159_6	2	268	31	3.5	0.2	1022	48	457	22	812	35	596	29	0.5	0.1	361	22	1124	83	164	10.0	848	39	202	11.0	35	1.9	187	9.5
	X18HK_159_7	2	307	30	2.5	0.1	1092	46	497	22	990	48	523	24	0.4	0.1	410	29	1267	83	164	9.7	856	38	190	8.9	34	1.9	167	8.2
	X18HK_159_8	2	332	22	4.3	0.2	1116	50	490	22	898	45	672	43	1.0	0.1	592	40	1710	110	248	15.0	1230	72	257	16.0	44	2.4	199	12.0
	X18HK_159_9	2	308	31	4.6	0.2	1114	37	520	21	887	43	622	35	1.1	0.2	336	18	1002	65	152	6.6	755	34	198	10.0	34	2.0	182	8.9
	X18HK_159_10	2	311	33	3.3	0.2	1040	38	486	15	765	40	682	40	###	97.0	347	21	992	53	158	7.8	812	34	225	14.0	37	1.6	200	8.4
	X18HK_159_11	2	343	35	3.0	0.2	1099	66	523	31	999	63	553	27	0.9	0.2	439	35	1350	100	186	15.0	914	68	208	15.0	35	2.4	177	12.0
	X18HK_159_12	2	310	31	2.9	0.1	1140	32	552	14	1001	30	664	33	0.4	0.1	445	27	1381	84	188	9.3	961	46	222	14.0	37	1.6	196	9.4
	X18HK_159_13	2	308	40	3.3	0.2	1159	53	515	24	1009	37	593	37	0.4	0.0	382	26	1217	98	168	11.0	876	54	198	11.0	35	2.3	178	12.0
	X18HK_159_14	2	260	34	3.2	0.2	1148	59	525	31	937	54	590	26	0.4	0.1	362	20	1075	93	161	10.0	811	44	199	12.0	34	1.7	177	10.0
	X18HK_159_15	2	255	34	2.8	0.1	1036	39	465	19	790	38	537	29	7.7	5.0	312	15	1073	80	148	9.2	737	42	187	11.0	31	1.3	161	7.2
	X18HK_159_16	2	275	36	2.4	0.1	1101	42	509	24	951	40	644	44	0.6	0.1	485	37	1402	83	194	13.0	946	59	224	18.0	36	2.6	196	11.0
	X18HK_159_17	2	271	46	3.5	0.1	1075	48	494	21	956	40	553	34	0.6	0.1	387	28	1167	74	167	9.2	801	42	192	11.0	34	1.6	163	7.2
	X18HK_159_18	2	286	41	2.8	0.1	1070	52	557	24	1031	40	590	29	0.3	0.0	354	19	1117	72	150	8.0	791	29	199	10.0	33	1.5	165	9.9
	X18HK_159_19	2	298	37	2.9	0.1	1065	49	471	24	825	50	593	34	0.3	0.0	295	21	1003	69	142	10.0	722	46	188	9.4	32	1.5	178	12.0
	X18HK_159_20	2	345	47	4.3	0.3	1314	57	825	31	913	38	575	38	3.9	1.2	397	24	1107	58	165	9.8	862	59	197	11.0	34	2.2	162	7.8
	Σ Grains				7.0		13.0		12.0		14.0		13.0		4.0		11.0		11.0		13.0		13.0		13.0		13.0		14.0	
	Average				3.1		1116		515		912		625		0.4		347		1087		161		830		206		35.0		185	
	2SD				0.2		68		31		93		57		0.0		39		98		13.3		64		12.3		1.9		15.0	

Continue Table A2 – 3

	Exp #	U-Pb age Ma	95% conf. Ma	Tb µg/g	± Int 2SE µg/g	Dy µg/g	± Int 2SE µg/g	Ho µg/g	± Int 2SE µg/g	Er µg/g	± Int 2SE µg/g	Tm µg/g	± Int 2SE µg/g	Yb µg/g	± Int 2SE µg/g	Lu µg/g	± Int 2SE µg/g	Pb_204 µg/g	± Int 2SE µg/g	Pb_206 µg/g	± Int 2SE µg/g	Pb_207 µg/g	± Int 2SE µg/g	Pb_208 µg/g	± Int 2SE µg/g	Th µg/g	± Int 2SE µg/g	U µg/g	± Int 2SE µg/g
NIST612																													
NIST612_0	1			161	3.5	158	5.1	169	3.8	172	4.2	170	3.8	169	4.6	166	3.7	173	26.0	171	3.3	174	2.6	170	5.4	169	4.1	167	3.0
NIST612_1	1			169	4.3	168	5.0	175	4.4	175	5.0	176	4.1	184	4.2	166	3.7	178	17.0	175	4.1	177	3.5	173	8.0	173	4.6	169	3.4
NIST612_2	1			166	4.6	165	6.7	177	4.7	173	5.3	176	3.7	184	5.1	171	4.5	181	25.0	179	4.4	179	5.1	180	5.9	179	5.3	170	4.2
NIST612_3	1			186	7.8	186	9.5	194	9.7	188	9.5	194	8.6	207	8.6	189	8.2	184	38.0	201	6.8	200	6.7	191	8.8	198	11.0	197	6.6
NIST612_4	1			187	6.2	187	6.8	200	6.3	193	4.7	200	5.5	206	7.1	195	4.3	200	35.0	202	4.8	202	4.7	203	8.2	209	7.6	202	4.2
NIST612_5	1			178	5.2	179	7.2	186	4.2	186	7.3	186	4.5	197	6.7	181	5.9	197	34.0	195	4.1	198	4.3	192	5.4	192	7.8	191	3.8
NIST612_6	1			183	4.9	184	7.7	192	4.3	194	6.0	193	5.2	198	6.7	184	4.2	205	40.0	195	5.0	194	4.3	201	7.7	194	6.8	189	4.9
NIST612_7	1			173	5.6	170	5.2	180	5.1	182	5.5	180	4.0	182	6.3	175	4.2	192	31.0	183	4.8	182	5.0	182	6.1	180	7.2	176	5.1
NIST612_8	1			169	4.9	171	5.6	182	5.4	185	6.1	182	5.8	191	4.6	174	4.8	173	35.0	181	4.8	178	5.1	181	6.0	177	5.4	175	5.2
NIST612_9	1			162	3.7	162	5.1	172	4.3	171	4.2	175	4.0	173	5.5	166	4.4	190	31.0	175	4.4	172	3.9	173	6.5	165	5.5	168	3.5
NIST612_10	1			167	3.9	164	5.3	175	3.3	175	4.8	176	4.9	175	5.9	168	4.1	153	26.0	174	3.7	175	4.5	178	6.3	173	5.6	167	4.2
NIST612_11	1			169	5.8	173	7.6	175	5.8	175	5.8	171	4.2	182	8.7	169	4.8	190	27.0	176	5.5	177	5.6	170	7.9	180	6.8	172	4.4
Σ Grains				12		12		12		12		12		12		12		12		12		12		12		12		12	
Average				172.4		172.3		181.3		180.7		181.5		187.2		175.3		184.7		183.8		183.9		182.7		182.4		178.5	
2SD				17.2		18.6		18.4		15.8		18.3		23.8		18.6		27.4		21.2		21.1		22.0		25.4		24.1	
NIST612_0	2			168	4.9	176	6.8	184	6.4	182	5.8	180	6.9	184	5.9	176	5.9	198	26.0	187	6.8	186	7.1	183	10.0	178	7.8	177	4.7
NIST612_1	2			165	7.0	166	6.8	171	5.0	174	7.3	179	6.5	181	6.4	167	5.6	171	25.0	181	5.8	179	5.4	174	9.7	172	8.2	173	4.5
NIST612_2	2			167	7.5	167	6.6	180	8.5	172	10.0	177	8.5	182	10.0	172	7.0	172	28.0	179	7.1	178	6.7	180	12.0	175	9.6	176	5.9
NIST612_3	2			174	3.8	176	4.9	184	6.3	188	7.0	182	6.4	190	7.4	182	5.1	183	24.0	186	6.1	185	4.8	185	6.6	181	6.5	182	6.6
NIST612_4	2			168	5.8	169	7.1	181	6.7	174	6.5	180	6.1	191	7.5	174	6.0	183	26.0	182	6.1	182	6.8	181	8.1	177	7.6	181	5.3
NIST612_5	2			169	6.9	160	6.7	172	8.4	173	8.5	175	5.8	185	8.6	169	7.4	179	24.0	178	7.2	181	7.1	181	9.7	182	6.5	172	6.3
NIST612_6	2			167	4.8	167	6.6	182	6.3	180	7.6	179	6.2	181	7.1	169	5.6	181	26.0	181	4.9	180	5.0	181	7.0	179	6.7	174	5.4
NIST612_7	2			166	6.8	167	7.8	181	7.4	180	8.5	178	7.9	180	7.5	174	6.4	182	20.0	181	5.5	178	6.3	180	6.9	182	6.9	175	5.8
NIST612_8	2			175	5.5	171	5.9	182	5.3	180	6.8	178	6.8	191	8.1	175	4.7	178	21.0	179	3.8	183	3.8	182	6.2	173	6.1	177	5.2
NIST612_9	2			170	6.4	167	5.6	179	6.6	182	6.4	179	7.0	187	7.9	174	5.0	192	32.0	183	5.3	185	4.2	185	6.7	179	8.2	176	4.6
NIST612_10	2			170	4.9	172	6.9	177	5.4	183	5.8	181	7.6	183	6.7	174	4.8	190	22.0	183	4.1	180	5.8	183	8.8	176	7.0	175	5.5
NIST612_11	2			173	6.4	171	6.3	183	5.9	180	5.6	180	6.5	188	8.4	176	5.7	171	26.0	185	5.4	184	5.4	187	10.0	182	6.2	182	5.0
NIST612_12	2			165	7.1	173	7.6	175	6.6	175	7.2	178	6.2	184	9.8	176	5.9	193	23.0	182	6.1	185	6.2	187	10.0	185	8.2	176	5.2
NIST612_13	2			169	5.7	172	5.2	183	5.9	178	5.7	182	4.5	185	6.6	173	5.7	190	25.0	183	4.7	180	4.7	183	6.8	174	6.1	176	3.4
NIST612_14	2			169	5.9	172	8.3	177	8.5	175	7.9	174	7.2	184	8.6	169	6.0	167	19.0	178	8.0	178	5.6	176	6.3	176	8.9	176	5.7
NIST612_15	2			169	6.3	164	6.3	172	6.1	179	6.7	178	6.2	183	6.4	175	5.7	190	27.0	181	5.5	182	5.2	181	7.7	175	7.3	173	6.1
Σ Grains				16		16		16		16		16		16		16		16		16		16		16		16		16	
Average				168.9		169.3		179.0		178.4		178.7		184.9		173.5		182.5		181.7		181.5		181.8		177.9		176.1	
2SD				2.9		4.1		4.4		4.2		2.3		3.3		3.6		8.9		2.6		2.7		3.3		3.6		2.9	
McClure																													
McC_0	1	*455*	*13*	*11.8*	*0.6*	*63.6*	*3.0*	*11.9*	*0.5*	*31.0*	*1.8*	*4.1*	*0.2*	*25.2*	*1.5*	*3.4*	*0.2*	*2.6*	*1.1*	*9.3*	*0.5*	*1.4*	*0.1*	*4.1*	*0.2*	*88.5*	*5.6*	*32.3*	*2.1*
McC_1	1	*540*	*14*	*9.1*	*0.3*	*48.1*	*1.7*	*8.9*	*0.2*	*23.3*	*0.7*	*3.1*	*0.1*	*19.3*	*0.7*	*2.6*	*0.1*	*2.5*	*1.1*	*8.0*	*0.2*	*1.4*	*0.1*	*4.3*	*0.3*	*78.2*	*3.1*	*22.8*	*0.5*
McC_2	1	*534*	*19*	*6.8*	*0.2*	*36.4*	*1.1*	*6.7*	*0.2*	*17.5*	*0.5*	*2.3*	*0.1*	*13.0*	*0.5*	*1.9*	*0.1*	*2.3*	*1.2*	*4.7*	*0.2*	*1.0*	*0.1*	*2.4*	*0.3*	*37.5*	*1.5*	*12.8*	*0.3*
McC_3	1	*460*	*14*	*8.6*	*0.3*	*46.2*	*1.6*	*8.3*	*0.3*	*21.3*	*0.8*	*2.9*	*0.1*	*16.6*	*0.6*	*2.3*	*0.1*	*1.4*	*1.0*	*5.7*	*0.2*	*1.0*	*0.1*	*3.0*	*0.3*	*61.5*	*1.8*	*19.3*	*0.5*
McC_4	1	*530*	*15*	*9.7*	*0.4*	*52.3*	*2.5*	*9.9*	*0.5*	*27.4*	*1.1*	*3.8*	*0.2*	*24.4*	*1.4*	*3.5*	*0.2*	*2.9*	*1.6*	*10.7*	*0.4*	*1.9*	*0.1*	*5.2*	*0.4*	*91.4*	*3.4*	*30.1*	*0.9*
McC_5	1	*494*	*14*	16.7	0.6	87.7	2.1	15.3	0.5	39.8	1.0	4.9	0.2	27.0	1.0	3.2	0.1	3.1	1.3	6.4	0.2	1.3	0.1	2.8	0.2	49.6	1.7	19.4	0.4
McC_6	1	493	23	6.9	0.2	37.7	1.4	6.7	0.2	16.9	0.4	2.3	0.1	13.1	0.7	1.9	0.1	1.6	1.1	4.1	0.1	1.0	0.1	2.3	0.2	31.5	1.3	11.5	0.2
McC_7	1	509	15	7.3	0.3	40.6	1.5	7.2	0.3	19.3	0.6	2.6	0.1	15.1	0.7	2.0	0.1	0.2	0.4	6.4	0.2	1.4	0.1	3.4	0.2	55.0	1.9	18.5	0.5
McC_8	1	512	16	10.8	0.4	60.1	2.2	10.5	0.4	26.7	1.1	3.2	0.2	18.0	1.1	2.4	0.1	2.0	1.4	7.7	0.4	1.6	0.1	3.6	0.3	56.3	3.5	21.1	1.1
McC_9	1	492	15	9.5	0.3	53.6	1.8	9.9	0.4	25.2	0.9	3.4	0.2	20.5	0.8	3.0	0.1	2.5	1.3	4.6	0.2	1.2	0.0	2.6	0.3	37.6	1.3	##	0.3
McC_10	1	*496*	*15*	*2.6*	*0.1*	*15.9*	*0.8*	*3.7*	*0.2*	*12.9*	*0.6*	*2.3*	*0.1*	*17.2*	*0.6*	*3.1*	*0.2*	*2.6*	*1.3*	*5.8*	*0.2*	*1.5*	*0.1*	*4.8*	*0.3*	*##*	*2.6*	*16.2*	*0.3*
McC_11	1	*499*	*18*	*##*	*1.3*	*95.4*	*4.9*	*##*	*0.6*	*42.3*	*2.1*	*5.2*	*0.2*	*##*	*1.3*	*3.1*	*0.2*	*1.4*	*1.5*	*5.4*	*0.3*	*1.1*	*0.1*	*2.5*	*0.3*	*40.2*	*2.5*	*16.0*	*0.7*
McC_12	1	488	11	7.1	0.3	36.9	1.1	6.9	0.2	18.5	0.7	2.5	0.1	15.2	0.8	2.1	0.1	2.1	1.2	7.3	0.2	1.2	0.0	3.2	0.3	58.4	2.2	22.7	0.7
McC_13	1	489	14	6.9	0.2	34.8	1.2	6.4	0.3	15.2	0.6	1.9	0.1	11.4	0.7	1.8	0.1	1.8	1.1	6.9	0.2	1.4	0.1	3.5	0.3	56.4	1.8	20.9	0.5
McC_14	1	506	10	9.2	0.3	48.3	1.3	9.1	0.2	24.9	0.9	3.4	0.2	20.3	0.7	3.0	0.1	2.4	1.1	7.7	0.2	1.1	0.1	4.0	0.3	79.0	2.7	##	0.6
McC_15	1	*517*	*16*	*8.0*	*0.2*	*50.1*	*1.7*	*##*	*0.4*	*33.4*	*0.9*	*5.0*	*0.2*	*##*	*1.1*	*5.9*	*0.2*	*3.9*	*1.9*	*15.2*	*0.6*	*3.2*	*0.2*	*12.7*	*1.0*	*##*	*11.0*	*##*	*1.3*
McC_16	1	488	14	8.5	0.3	46.9	1.7	8.6	0.2	23.5	0.7	3.0	0.1	17.6	0.7	2.6	0.1	1.1	0.8	6.6	0.2	1.6	0.1	4.4	0.3	71.5	2.1	18.7	0.5
McC_17	1	509	15	10.1	0.3	54.7	1.5	10.1	0.2	26.6	0.8	3.4	0.1	19.8	0.6	2.6	0.1	1.8	1.0	6.8	0.2	1.1	0.1	3.4	0.2	58.9	1.4	20.2	0.4
McC_18	1	*471*	*14*	*3.1*	*0.1*	*16.5*	*0.7*	*3.2*	*0.1*	*8.5*	*0.4*	*1.1*	*0.1*	*7.3*	*0.4*	*1.1*	*0.0*	*0.7*	*0.7*	*4.7*	*0.1*	*1.0*	*0.1*	*2.5*	*0.2*	*40.9*	*1.2*	*14.2*	*0.3*
McC_19	1	503	14	6.5	0.2	33.8	0.9	6.2	0.2	16.7	0.6	2.2	0.1	13.0	0.4	1.9	0.1	1.2	0.9	6.7	0.2	1.1	0.1	2.9	0.2	55.5	2.0	20.9	0.6
McC_20	1	502	15	7.4	0.3	40.3	1.5	7.2	0.2	19.5	0.6	2.4	0.1	15.0	0.7	2.1	0.1	2.0	1.2	7.2	0.2	2.0	0.1	4.7	0.3	62.5	1.9	18.7	0.5
McC_21	1	503	12	4.4	0.2	22.8	1.0	4.4	0.2	11.8	0.6	1.5	0.1	9.1	0.5	1.5	0.1	1.2	0.9	6.1	0.2	1.1	0.1	3.1	0.2	55.7	2.0	18.2	0.5
Σ Grains				9		8		7		7		9		9		8		6		13		12		9		9		12	
Average				7.5		42.0		7.4		21.1		2.6		17.6		2.5		1.9		6.7		1.2		3.3		56.5		19.3	
2SD				1.6		10.7		1.9		6.2		0.8		4.2		0.7		0.3		1.3		0.3		0.7		6.6		3.8	

Continue Table A2 – 3

McC_0	2	512	22	7.1	0.4	36.6	2.1	6.8	0.3	17.0	1.0	2.2	0.1	12.8	0.8	1.8	0.1	1.0	0.7	5.7	0.3	1.2	0.1	3.1	0.2	46.4	3.5	17.2	0.8
McC_1	2	*592*	*25*	*3.2*	*0.2*	*15.3*	*0.9*	*3.0*	*0.2*	*7.1*	*0.4*	*0.8*	*0.1*	*5.4*	*0.5*	*0.7*	*0.0*	*3.1*	*1.2*	*4.5*	*0.2*	*1.2*	*0.1*	*2.5*	*0.2*	*##*	*1.7*	*##*	*0.5*
McC_2	2	507	25	7.6	0.6	42.4	2.5	8.1	0.5	20.2	1.2	2.8	0.2	15.9	1.3	2.3	0.2	1.6	0.8	8.3	0.3	2.0	0.2	4.2	0.4	69.3	5.1	##	1.5
McC_3	2	539	24	10.2	1.0	56.1	5.3	10.1	1.0	26.2	2.6	3.1	0.3	18.2	1.9	2.4	0.2	1.3	0.8	5.0	0.4	1.2	0.1	2.5	0.2	34.9	2.5	13.8	1.0
McC_4	2	542	24	8.0	0.4	42.1	2.0	7.7	0.4	19.7	0.9	2.5	0.2	13.9	0.7	1.9	0.1	1.3	0.5	5.7	0.4	1.4	0.1	2.8	0.3	37.9	2.4	15.3	0.7
McC_5	2	548	22	7.0	0.3	38.6	1.3	7.2	0.4	18.7	0.8	2.6	0.2	15.9	0.8	2.2	0.1	2.2	0.8	10.4	0.5	1.8	0.1	5.1	0.3	78.9	3.4	##	1.2
McC_6	2	529	36	10.1	0.9	55.9	5.3	10.4	1.0	26.2	2.8	3.2	0.3	18.8	1.8	2.3	0.2	1.7	0.8	4.2	0.4	1.6	0.1	2.4	0.3	25.7	3.7	9.4	1.2
McC_7	2	549	22	6.9	0.2	36.2	1.7	6.9	0.3	18.7	0.9	2.4	0.1	15.0	0.7	2.3	0.1	1.4	0.6	6.7	0.2	1.3	0.1	3.4	0.3	54.5	2.3	19.1	0.5
McC_8	2	522	25	7.1	0.4	39.2	2.1	7.4	0.3	18.3	1.0	2.4	0.1	14.2	0.8	1.9	0.1	0.7	0.5	4.2	0.2	1.0	0.1	1.9	0.2	30.8	2.6	12.0	0.7
McC_9	2	548	20	7.4	0.4	38.1	1.6	7.3	0.3	18.7	0.8	2.4	0.1	13.9	0.7	1.9	0.1	1.0	0.6	6.4	0.3	1.3	0.1	3.2	0.2	58.0	2.4	18.5	0.8
McC_10	2	536	27	6.7	0.5	35.0	2.6	6.8	0.6	17.0	1.4	2.0	0.2	11.8	1.0	1.6	0.1	0.8	0.6	4.2	0.3	1.0	0.1	2.4	0.2	35.7	3.7	11.6	0.7
McC_11	2	503	29	9.6	1.1	61.6	6.7	12.8	1.5	38.4	4.4	6.0	0.7	42.5	5.4	6.4	0.8	1.9	0.8	21.0	4.6	2.9	0.3	48.0	13.0	###	350.0	##	16.0
McC_12	2	518	22	9.6	0.5	53.4	1.4	9.9	0.6	25.9	1.4	3.5	0.2	20.7	1.1	2.8	0.1	0.6	0.5	7.0	0.3	1.2	0.1	3.6	0.2	66.1	4.4	##	0.9
McC_13	2	519	20	4.2	0.3	22.1	1.3	4.2	0.3	10.6	0.5	1.2	0.1	7.4	0.5	1.2	0.1	0.9	0.5	5.6	0.3	1.0	0.1	2.6	0.3	44.8	2.4	16.3	0.8
McC_14	2	532	22	3.7	0.2	18.3	1.1	3.1	0.2	8.1	0.3	0.9	0.0	5.4	0.3	0.8	0.1	0.3	0.4	5.3	0.3	0.9	0.1	2.9	0.3	48.7	2.3	15.8	0.5
McC_15	2	519	21	7.5	0.4	41.1	1.9	7.9	0.4	20.4	0.9	2.8	0.1	18.3	0.7	2.5	0.1	0.9	0.5	6.5	0.2	1.5	0.1	3.5	0.4	61.4	3.5	18.6	0.7
McC_16	2	516	22	6.1	0.4	32.6	2.4	6.0	0.5	16.1	1.0	2.0	0.1	12.4	0.8	1.9	0.1	0.5	0.4	5.5	0.4	1.2	0.1	3.2	0.3	48.5	3.8	16.0	1.0
McC_17	2	519	20	5.9	0.3	30.6	1.5	5.9	0.3	15.9	0.6	2.2	0.1	13.9	0.7	2.3	0.1	0.8	0.5	5.3	0.2	1.0	0.1	2.7	0.3	49.4	2.1	16.5	0.5
McC_18	2	534	23	6.2	0.4	35.5	2.0	6.4	0.3	16.2	0.7	2.2	0.1	13.1	0.5	1.8	0.1	1.3	0.7	5.8	0.2	1.2	0.1	3.2	0.3	47.5	2.4	16.3	0.8
Σ Grains				12		12		12		12		12		11		9		5		11		12		12		8		12	
Average				7.0		37.3		7.0		18.1		2.4		13.9		1.9		0.9		5.8		1.2		3.1		49.7		16.3	
2SD				0.6		3.5		0.7		1.5		0.3		1.3		0.2		0.1		0.5		0.1		0.3		4.1		1.9	
Durango																													
DUR_0	1	27.4	5.2	23.7	0.7	142.2	4.3	27.3	0.7	72.0	1.5	9.3	0.3	48.2	1.5	5.3	0.1	1.8	1.0	0.3	0.0	0.1	0.0	0.8	0.1	255	7.4	13.4	0.3
DUR_1	1	32.8	3.5	23.6	0.5	137.7	3.6	27.1	0.7	72.3	2.3	9.3	0.2	49.6	1.5	5.5	0.2	1.2	0.9	0.3	0.0	0.1	0.0	0.7	0.1	255	5.8	13.3	0.3
DUR_2	1	34.1	3.9	23.9	0.6	143.3	3.8	27.4	0.8	72.9	1.8	9.3	0.3	48.2	1.2	5.5	0.2	2.0	1.0	0.3	0.0	0.1	0.0	0.6	0.1	253	4.9	13.2	0.3
DUR_3	1	31.2	4.8	24.0	0.5	141.6	3.8	27.5	0.6	71.9	1.4	9.0	0.2	49.2	1.2	5.3	0.1	1.1	0.8	0.3	0.0	0.1	0.0	0.6	0.1	259	7.4	13.4	0.3
DUR_4	1	30.4	4.3	24.3	0.7	146.7	3.6	28.4	0.8	74.1	2.0	9.3	0.3	50.2	1.7	5.5	0.2	0.8	0.7	0.3	0.0	0.1	0.0	0.7	0.1	263	6.6	14.0	0.4
DUR_5	1	31.9	3.5	25.1	0.8	144.7	4.3	27.7	0.9	74.4	2.3	9.4	0.3	49.2	1.6	5.6	0.2	1.9	1.0	0.3	0.0	0.1	0.0	0.7	0.1	261	7.1	13.9	0.3
DUR_6	1	26.6	3.9	25.4	0.7	147.3	4.1	29.4	0.7	76.5	2.0	9.4	0.2	50.7	1.6	5.8	0.2	0.4	0.5	0.3	0.0	0.1	0.0	0.7	0.1	265	6.6	14.3	0.3
DUR_7	1	28.4	2.8	24.5	0.8	146.2	3.4	27.6	0.7	75.4	1.9	9.5	0.2	50.9	1.8	5.6	0.2	1.1	0.8	0.4	0.0	0.1	0.0	1.0	0.2	330	8.7	##	0.4
DUR_8	1	34.3	4.5	25.4	0.7	152.2	4.8	29.1	0.7	76.0	2.4	9.6	0.3	52.5	1.9	5.9	0.2	1.4	1.0	0.4	0.0	0.1	0.0	0.9	0.1	304	8.7	16.1	0.5
DUR_9	1	28.0	3.5	24.9	0.6	148.2	3.6	28.2	0.8	76.4	2.2	9.8	0.2	52.3	1.9	5.9	0.2	0.4	0.6	0.4	0.0	0.1	0.0	0.8	0.1	325	9.2	##	0.4
DUR_10	1	30.8	5.5	25.0	0.7	144.7	3.9	28.0	0.8	76.1	1.8	9.4	0.2	50.4	1.4	5.6	0.2	1.1	0.9	0.4	0.0	0.1	0.0	0.9	0.2	263	5.1	13.7	0.3
DUR_11	1	27.5	4.2	23.7	0.8	141.9	4.0	26.8	0.8	75.1	2.1	9.2	0.2	49.7	1.7	5.4	0.2	0.2	0.4	0.3	0.0	0.1	0.0	0.6	0.1	260	7.6	13.5	0.3
DUR_12	1	24.5	4.0	23.6	0.6	135.7	2.8	26.8	0.7	72.1	1.6	9.0	0.2	48.0	1.4	5.4	0.1	0.6	0.7	0.3	0.0	0.1	0.0	0.8	0.1	253	6.3	14.3	0.4
DUR_13	1	26.0	3.8	23.5	0.6	140.1	3.7	27.1	0.7	72.6	1.9	9.2	0.3	47.4	1.2	5.2	0.2	2.2	1.1	0.3	0.0	0.1	0.0	0.8	0.1	246	7.5	13.6	0.3
DUR_14	1	30.3	4.3	23.5	0.8	137.7	3.4	26.1	0.8	71.5	2.0	8.8	0.2	45.9	1.7	5.2	0.2	0.7	0.6	0.3	0.0	0.1	0.0	0.8	0.1	250	5.9	13.2	0.3
DUR_15	1	26.7	3.4	23.4	0.6	137.4	2.5	26.8	0.6	72.6	1.6	8.9	0.2	46.3	1.5	5.4	0.2	0.2	0.4	0.3	0.0	0.1	0.0	0.6	0.1	246	8.1	13.5	0.3
DUR_16	1	26.0	4.2	23.3	0.6	135.3	3.5	26.8	0.7	72.9	2.0	9.1	0.3	46.4	1.2	5.2	0.2	0.6	0.7	0.3	0.0	0.1	0.0	0.8	0.1	242	6.5	13.2	0.3
DUR_17	1	31.3	4.3	23.2	0.5	136.1	4.0	26.1	0.7	71.7	1.4	9.0	0.3	47.2	1.4	5.2	0.2	1.5	0.9	0.3	0.0	0.1	0.0	0.7	0.1	244	6.8	13.2	0.3
DUR_18	1	29.6	3.9	23.0	0.5	134.5	4.0	26.9	0.7	73.2	1.9	9.1	0.3	46.7	1.2	5.4	0.2	< LOD	< LOD	0.3	0.0	0.1	0.0	0.6	0.1	239	6.2	13.0	0.3
DUR_19	1	30.6	4.1	23.1	0.7	136.1	3.7	26.3	0.7	71.2	1.8	9.0	0.3	46.0	1.4	5.3	0.1	1.0	0.8	0.3	0.0	0.1	0.0	0.7	0.1	237	6.7	12.8	0.3
DUR_20	1	28.2	2.8	22.7	0.7	134.2	3.0	26.1	0.7	71.7	1.8	8.8	0.3	47.3	1.3	5.2	0.1	0.7	0.7	0.3	0.0	0.1	0.0	0.7	0.1	232	6.3	12.5	0.3
DUR_21	1	30.6	4.2	22.5	0.7	134.6	3.6	26.2	0.8	71.0	1.8	8.9	0.3	45.9	1.2	5.2	0.2	< LOD	< LOD	0.3	0.0	0.1	0.0	0.6	0.1	232	7.0	12.3	0.3
DUR_22	1	21.9	4.7	22.2	0.6	132.2	3.8	25.7	0.8	69.4	1.6	8.8	0.3	45.3	1.4	5.2	0.2	1.2	0.9	0.3	0.0	0.1	0.0	0.6	0.1	227	6.8	12.1	0.3
DUR_23	1	32.0	3.9	22.7	0.5	133.4	3.2	26.4	0.6	70.6	1.7	8.7	0.3	46.1	1.5	5.3	0.2	1.8	1.1	0.3	0.0	0.1	0.0	0.6	0.1	228	5.9	12.2	0.2
DUR_24	1	29.2	4.1	22.7	0.6	130.4	2.8	25.8	0.5	70.7	1.6	8.9	0.2	44.5	1.4	5.4	0.2	1.2	0.9	0.3	0.0	0.1	0.0	0.7	0.1	230	4.9	12.3	0.3
DUR_25	1	32.9	4.9	22.6	0.7	132.4	3.1	25.5	0.6	69.7	1.8	8.5	0.2	45.0	1.2	5.1	0.1	0.8	0.8	0.3	0.0	0.1	0.0	0.6	0.1	230	4.7	12.2	0.2
Σ Grains				25		25		25		25		25		25		25		6		21		22		20		22		22	
Average				23.7		139.8		27.1		73.0		9.1		48.2		5.4		1.1		0.3		0.1		0.7		247.4		13.2	
2SD				1.7		11.3		1.9		3.9		0.6		4.4		0.4		0.1		0.0		0.0		0.1		23.8		1.2	
DUR_0	2	33	3	23.4	0.8	143.8	5.8	27.9	1.3	69.1	3.0	9.3	0.5	47.6	2.1	5.3	0.2	<LOD		0.3	0.0	0.1	0.0	0.7	0.1	237	11	13.4	0.5
DUR_1	2	34	4	21.5	1.2	128.4	6.5	25.9	1.3	67.5	2.5	8.5	0.4	47.8	3.0	5.5	0.2	<LOD		0.3	0.0	0.1	0.0	0.7	0.1	247	12	12.6	0.5
DUR_2	2	37	5	22.3	1.0	133.9	5.0	26.7	1.0	69.7	3.4	9.0	0.4	46.7	2.0	5.3	0.2	<LOD		0.4	0.0	0.1	0.0	0.8	0.1	232	12	12.5	0.5
DUR_3	2	28	4	23.4	0.8	137.5	4.5	27.7	1.1	72.3	3.1	9.1	0.3	48.0	1.9	5.4	0.2	<LOD		0.3	0.0	0.1	0.0	0.7	0.1	245	7	12.6	0.4
DUR_4	2	32	3	21.7	1.4	131.7	8.5	25.8	1.6	71.4	3.8	8.6	0.5	47.3	2.9	5.4	0.3	<LOD		0.3	0.0	0.1	0.0	0.7	0.1	256	12	13.1	0.7
DUR_5	2	33	3	21.0	0.7	126.6	4.1	25.4	1.0	67.3	2.7	8.4	0.4	45.2	1.5	5.1	0.2	<LOD		0.3	0.0	0.1	0.0	0.6	0.1	233	10	12.4	0.4
DUR_6	2	32	4	24.0	1.1	137.2	5.4	27.3	1.3	75.0	2.9	8.9	0.4	47.5	1.8	5.4	0.2	<LOD		0.3	0.0	0.1	0.0	0.8	0.1	241	11	12.5	0.4
DUR_7	2	30	3	20.3	0.8	124.4	5.7	23.6	1.0	64.7	2.9	8.0	0.3	42.1	2.5	4.9	0.3	<LOD		0.3	0.0	0.1	0.0	0.6	0.1	217	12	11.9	0.5
DUR_8	2	33	3	20.3	1.0	124.4	5.3	24.0	0.9	68.4	2.5	8.2	0.4	45.6	2.0	5.3	0.3	<LOD		0.3	0.0	0.1	0.0	0.7	0.1	243	12	12.2	0.5
DUR_9	2	31	3	21.5	0.9	129.9	6.0	25.0	1.2	68.1	2.4	8.4	0.4	43.4	1.8	5.0	0.2	<LOD		0.3	0.0	0.1	0.0	0.6	0.1	236	10	13.5	0.5
DUR_10	2	33	3	21.7	0.8	133.1	4.5	24.7	1.1	67.9	2.6	8.5	0.4	44.3	1.6	5.0	0.2	<LOD		0.3	0.0	0.1	0.0	0.6	0.1	224	8	12.4	0.3

Continue Table A2 – 3

DUR_11	2	30	4	22.2	0.6	127.5	5.7	25.9	0.9	67.6	2.8	8.2	0.4	45.2	1.8	5.2	0.2	<LOD		0.3	0.0	0.1	0.0	0.7	0.1	244	10	12.8	0.5
DUR_12	*2*	*37*	*4*	*21.1*	*1.2*	*125.6*	*5.3*	*24.7*	*1.0*	*66.5*	*3.0*	*8.3*	*0.4*	*44.7*	*2.6*	*4.9*	*0.2*	*<LOD*		*0.3*	*0.0*	*0.1*	*0.0*	*0.6*	*0.1*	*225*	*14*	*11.9*	*0.5*
DUR_13	*2*	*36*	*3*	*22.0*	*0.8*	*129.0*	*5.6*	*24.7*	*0.9*	*68.3*	*1.9*	*8.6*	*0.3*	*45.1*	*1.5*	*5.1*	*0.2*	*<LOD*		*0.3*	*0.0*	*0.1*	*0.0*	*0.8*	*0.1*	*250*	*13*	*13.6*	*0.4*
DUR_14	2	30	5	22.0	1.0	132.8	8.1	24.3	1.6	66.9	4.0	8.1	0.7	46.2	2.2	5.1	0.2	<LOD		0.3	0.0	0.1	0.0	0.6	0.1	225	15	12.3	0.6
DUR_15	2	31	3	22.4	1.0	130.8	5.9	25.2	1.2	68.9	3.4	8.7	0.3	47.3	2.6	5.3	0.2	<LOD		0.3	0.0	0.1	0.0	0.8	0.1	233	13	12.5	0.6
DUR_16	2	30	6	24.2	1.0	143.0	12.0	27.8	1.6	73.7	3.8	9.4	0.7	49.6	3.3	5.7	0.3	<LOD		0.3	0.0	0.1	0.0	0.8	0.1	259	18	12.8	0.5
DUR_17	2	33	5	22.0	1.4	125.9	5.8	25.8	1.1	68.5	3.2	8.7	0.3	44.6	2.8	5.2	0.3	<LOD		0.3	0.0	0.1	0.0	0.7	0.1	241	13	13.6	0.7
DUR_18	2	32	3	22.1	1.1	131.3	6.5	25.5	1.2	67.2	2.6	8.2	0.4	44.6	2.5	5.2	0.3	<LOD		0.3	0.0	0.1	0.0	0.7	0.1	228	12	12.2	0.5
DUR_19	2	31	3	23.7	1.1	137.6	6.3	27.8	1.2	73.7	3.3	9.5	0.4	49.2	2.0	5.5	0.2	<LOD		0.3	0.0	0.1	0.0	0.7	0.1	264	9	14.8	0.5
Σ Grains				18.0		18.0		18.0		18.0		18.0		18.0		18.0				18.0		13.0		18.0		18.0		18.0	
Average				22.2		132.2		25.9		69.3		8.6		46.2		5.3				0.3		0.1		0.7		239.1		12.8	
2SD				1.1		5.7		1.3		2.7		0.4		1.9		0.2				0.0		0.0		0.1		12.0		0.7	
Mao et al.,16		Σ Grains		23		217		23		23		23		217		161								91		217		217	
		Average		16.6		107.0		19.3		53.4		6.6		39.4		4.9								0.7		222.0		10.0	
		2SD		2.7		15.7		3.3		8.8		1.3		5.9		0.6								0.2		42.2		1.9	
Madagascar																													
MAD_0	1	481	25	12.0	0.3	62.1	1.4	10.2	0.3	24.6	0.6	3.0	0.1	17.4	0.5	2.2	0.1	1.4	0.8	7.5	0.2	1.0	0.0	26.3	1.1	663	20	26.1	0.5
MAD_1	1	477	23	12.3	0.4	64.2	1.8	10.4	0.3	25.6	0.8	3.0	0.1	17.9	0.7	2.3	0.1	1.6	0.9	7.6	0.2	1.0	0.0	26.0	0.8	692	14	27.1	0.5
MAD_2	1	489	26	12.7	0.4	64.9	2.0	10.8	0.4	25.6	0.8	3.2	0.1	18.3	0.6	2.3	0.1	1.7	1.0	8.0	0.2	1.1	0.1	27.6	1.0	698	18	27.3	0.7
MAD_3	1	461	46	12.3	0.3	62.2	1.3	10.2	0.3	25.4	0.6	3.1	0.1	17.6	0.6	2.3	0.1	1.7	0.9	7.8	0.2	1.1	0.1	26.8	1.0	679	14	26.9	0.5
MAD_4	1	466	24	13.3	0.3	69.0	1.7	11.7	0.3	27.5	0.8	3.5	0.1	19.9	0.8	2.5	0.1	1.1	0.8	8.6	0.2	1.2	0.1	29.7	0.8	774	16	30.5	0.5
MAD_5	1	466	27	13.4	0.3	68.1	1.7	11.1	0.3	27.3	0.6	3.4	0.1	19.2	0.6	2.5	0.1	1.2	0.9	8.3	0.2	1.0	0.1	28.1	0.9	751	21	29.7	0.6
MAD_6	1	480	32	13.3	0.3	66.7	1.8	11.2	0.3	27.4	0.9	3.4	0.1	19.5	0.8	2.5	0.1	1.5	0.9	8.5	0.2	1.0	0.0	29.0	1.1	752	18	30.2	0.5
MAD_7	1	477	28	13.6	0.5	67.9	1.9	11.7	0.3	27.2	0.7	3.4	0.1	18.9	0.7	2.6	0.1	0.7	0.7	8.4	0.2	1.1	0.1	29.4	1.1	742	19	29.8	0.6
MAD_8	1	468	29	13.4	0.4	68.3	2.0	11.1	0.3	28.0	0.9	3.3	0.1	19.1	0.7	2.6	0.1	1.2	1.0	8.5	0.3	1.1	0.1	29.5	1.1	758	21	30.4	0.7
MAD_9	1	466	32	13.5	0.3	67.0	1.7	11.2	0.3	26.5	0.9	3.3	0.1	18.9	0.6	2.5	0.1	1.1	0.9	8.3	0.2	1.1	0.1	28.1	0.8	744	20	29.5	0.6
MAD_10	1	468	30	12.9	0.3	65.9	1.8	10.8	0.3	26.9	1.0	3.2	0.1	18.3	0.7	2.5	0.1	1.0	0.8	8.1	0.2	1.1	0.1	27.3	1.1	727	22	29.0	0.7
MAD_11	1	481	30	12.8	0.3	63.7	2.1	10.6	0.2	26.6	0.7	3.2	0.1	18.5	0.6	2.4	0.1	1.2	0.8	7.9	0.2	1.0	0.1	27.9	0.9	709	17	28.0	0.5
MAD_12	1	465	24	13.4	0.4	65.9	1.8	11.3	0.4	27.2	0.9	3.2	0.2	19.2	0.7	2.5	0.1	1.3	0.9	7.9	0.3	1.0	0.1	28.1	1.0	736	23	28.8	0.6
MAD_13	1	472	28	12.9	0.3	64.5	1.3	10.9	0.3	26.4	0.7	3.2	0.1	17.9	0.7	2.3	0.1	0.6	0.6	7.9	0.2	1.1	0.1	27.4	1.1	707	18	27.5	0.6
MAD_14	1	461	35	12.9	0.4	63.4	1.4	10.8	0.3	26.2	0.6	3.1	0.1	17.6	0.7	2.4	0.1	1.6	0.9	7.7	0.2	1.1	0.0	25.5	0.7	704	16	27.2	0.5
MAD_15	1	468	29	12.6	0.4	64.1	2.3	10.7	0.3	25.8	0.8	3.2	0.1	18.3	0.6	2.4	0.1	1.7	0.9	7.7	0.2	1.0	0.0	26.1	1.2	691	22	27.5	0.6
MAD_16	1	464	27	13.0	0.3	65.5	1.7	11.0	0.4	27.6	0.7	3.3	0.1	18.3	0.7	2.5	0.1	1.2	0.9	7.8	0.3	1.0	0.1	27.8	1.0	694	16	27.9	0.7
MAD_17	1	476	29	12.9	0.4	64.3	1.7	10.6	0.3	26.3	0.8	3.2	0.1	17.9	0.6	2.4	0.1	1.9	1.2	7.8	0.2	0.9	0.1	26.4	1.2	691	22	27.6	0.6
MAD_18	1	477	32	12.8	0.4	63.8	1.5	10.8	0.3	26.4	0.9	3.1	0.1	18.3	0.6	2.4	0.1	1.0	0.8	7.7	0.2	0.9	0.0	26.6	0.9	684	18	27.0	0.5
MAD_19	1	473	33	12.6	0.3	63.5	1.6	10.5	0.2	25.9	0.5	3.1	0.1	16.5	0.6	2.2	0.1	1.5	0.9	7.5	0.2	1.0	0.0	25.9	0.9	671	17	26.5	0.4
MAD_20	1	479	27	12.6	0.4	62.6	1.7	10.7	0.3	25.8	0.7	3.1	0.2	17.2	0.8	2.3	0.1	1.3	0.8	7.5	0.2	0.9	0.0	24.8	0.9	653	16	26.0	0.5
MAD_21	1	474	33	12.3	0.3	60.9	1.4	10.2	0.3	25.5	0.9	3.0	0.1	17.4	0.5	2.3	0.1	1.8	0.9	7.5	0.2	0.9	0.0	26.3	0.9	662	18	25.8	0.5
MAD_22	1	477	28	12.7	0.4	61.3	1.8	10.3	0.3	25.5	0.6	3.0	0.1	16.8	0.7	2.3	0.1	< LOD	< LOD	7.3	0.2	0.9	0.0	25.3	0.9	658	14	25.7	0.4
MAD_23	1	477	32	12.1	0.4	59.6	1.2	9.8	0.2	25.8	0.7	2.9	0.1	16.3	0.6	2.2	0.1	1.1	0.8	7.3	0.2	0.8	0.0	24.7	0.8	651	15	25.4	0.6
MAD_24	*1*	*454*	*581*	*12.2*	*0.4*	*61.1*	*1.7*	*10.6*	*0.3*	*25.6*	*0.9*	*3.0*	*0.1*	*17.2*	*0.6*	*2.3*	*0.1*	*0.7*	*0.6*	*7.4*	*0.2*	*0.9*	*0.0*	*26.1*	*1.0*	*664*	*18*	*26.0*	*0.6*
MAD_25	1	478	33	12.2	0.3	60.8	1.7	10.2	0.3	24.6	0.8	2.9	0.1	16.4	0.6	2.2	0.1	2.2	1.0	7.1	0.2	0.8	0.0	24.9	0.8	634	17	25.3	0.5
Σ Grains				25		25		25		25		25		25		25		13		25		25		25		25		25	
Average				12.8		64.4		10.7		26.3		3.2		18.1		2.4		1.3		7.8		1.0		27.0		701.0		27.7	
2SD				0.9		5.0		0.9		1.8		0.3		1.9		0.2		0.3		0.8		0.2		2.9		75.2		3.2	
MAD_0	2	469	19	12.1	0.4	61.9	2.1	10.3	0.3	25.2	1.0	3.0	0.1	17.0	0.7	2.2	0.1	0.4	0.4	6.9	0.2	0.9	0.0	24.9	0.7	697	29	25.3	0.6
MAD_1	2	461	17	11.7	0.7	60.3	3.2	10.4	0.4	23.5	1.0	2.8	0.1	16.3	0.8	2.3	0.1	0.5	0.4	6.7	0.3	0.7	0.1	24.2	1.3	648	26	25.8	1.0
MAD_2	2	484	21	11.1	0.7	54.4	2.7	9.8	0.6	23.6	1.3	2.9	0.2	15.6	0.8	2.1	0.1	0.8	0.6	6.9	0.3	0.7	0.0	23.6	1.6	624	33	25.3	1.3
MAD_3	2	483	20	12.3	0.6	60.5	2.7	10.7	0.5	26.2	1.3	3.1	0.1	17.7	1.1	2.3	0.1	0.0	0.0	7.4	0.4	0.7	0.0	26.5	1.7	703	38	27.6	1.1
MAD_4	2	474	20	11.9	0.4	60.5	2.2	10.1	0.4	24.9	1.0	2.9	0.1	16.7	0.7	2.2	0.1	0.8	0.5	7.1	0.3	0.9	0.0	23.2	1.1	686	29	26.0	0.7
MAD_5	2	480	21	11.7	0.5	56.7	2.7	9.8	0.4	23.9	1.0	3.0	0.1	16.4	0.7	2.2	0.1	0.0	0.0	6.7	0.2	0.7	0.0	22.3	1.2	650	26	24.7	0.6
MAD_6	2	488	19	11.4	0.7	59.2	3.5	9.9	0.6	24.4	1.4	2.7	0.1	16.2	0.7	2.1	0.1	0.3	0.3	6.9	0.4	0.7	0.0	24.3	1.5	602	29	25.1	1.1
MAD_7	2	472	19	12.3	0.5	62.7	2.0	10.8	0.3	25.3	1.2	3.2	0.1	17.7	0.7	2.3	0.1	0.6	0.4	7.3	0.2	0.7	0.0	25.2	1.3	696	23	27.3	0.5
MAD_8	2	475	18	12.0	0.4	60.9	2.8	10.2	0.4	24.6	1.2	3.0	0.2	17.3	0.7	2.2	0.1	0.5	0.4	7.1	0.3	0.9	0.0	24.8	1.6	655	24	25.7	0.8
MAD_9	2	464	20	12.0	0.6	59.1	2.3	9.8	0.3	24.6	1.2	3.1	0.1	17.0	0.8	2.2	0.1	0.3	0.3	6.8	0.3	0.7	0.0	22.4	1.4	646	31	25.2	0.9
MAD_10	2	468	20	12.0	0.7	60.0	2.4	9.9	0.4	24.0	1.3	3.0	0.1	16.9	1.0	2.2	0.1	0.5	0.4	7.1	0.3	0.8	0.0	23.9	1.2	667	38	25.4	1.0
MAD_11	2	477	18	11.7	0.5	61.5	2.9	9.9	0.4	24.1	1.2	3.1	0.2	16.9	0.9	2.2	0.1	0.5	0.4	7.0	0.3	0.7	0.0	25.8	1.6	680	43	26.3	1.2
MAD_12	2	468	18	11.8	0.5	57.8	3.3	10.2	0.5	23.2	1.3	2.8	0.2	16.7	1.0	2.2	0.1	0.5	0.4	6.7	0.3	0.9	0.1	23.3	1.3	670	33	24.6	0.7
MAD_13	2	475	19	11.6	0.4	57.4	2.8	9.3	0.5	22.9	1.0	2.9	0.2	15.6	0.9	2.2	0.1	0.6	0.4	6.7	0.3	0.7	0.0	23.8	1.4	644	30	24.2	1.1
MAD_14	2	493	22	11.1	0.7	56.5	2.6	9.2	0.5	22.7	1.2	2.8	0.2	15.5	0.7	2.0	0.1	0.7	0.5	6.8	0.4	0.7	0.0	23.5	1.4	641	36	23.7	0.9
MAD_15	2	461	18	12.1	0.5	63.2	2.2	10.5	0.4	25.4	0.8	3.1	0.2	17.3	0.7	2.3	0.1	0.0	0.0	7.1	0.2	0.7	0.0	25.1	1.6	698	36	26.6	1.0
MAD_16	2	480	19	11.9	0.6	57.8	3.2	9.9	0.6	23.6	1.4	2.9	0.2	16.4	0.8	2.2	0.1	0.7	0.5	7.1	0.3	0.9	0.1	26.4	1.6	651	27	24.9	1.1
MAD_17	2	475	19	12.2	0.6	57.5	2.7	9.9	0.4	23.1	1.2	2.9	0.2	16.4	0.7	2.2	0.1	0.4	0.4	7.0	0.3	0.7	0.1	23.8	1.3	648	33	26.0	1.0

Continue Table A2 – 3

	MAD_18	2	476	22	12.0	0.5	59.4	2.7	10.2	0.5	24.0	1.1	2.9	0.2	16.6	0.9	2.2	0.1	0.1	0.2	7.1	0.3	0.7	0.0	25.6	1.8	655	29	25.8	0.8
	MAD_19	2	480	19	12.4	0.7	60.2	3.2	10.4	0.7	25.7	1.6	3.1	0.2	17.5	1.1	2.3	0.2	0.7	0.5	7.3	0.4	0.7	0.1	25.3	1.8	682	33	26.8	1.4
	MAD_20	2	463	18	12.3	0.4	61.1	1.9	10.5	0.5	25.5	0.9	3.1	0.2	17.4	0.8	2.3	0.1	0.5	0.5	7.1	0.3	0.8	0.0	26.4	1.2	676	30	25.9	0.9
	MAD_21	2	465	17	11.8	0.7	60.8	2.3	9.8	0.5	24.9	1.5	2.9	0.2	16.2	0.7	2.3	0.1	0.0	0.0	7.1	0.4	0.7	0.1	24.8	1.6	673	38	26.1	1.2
	MAD_22	2	469	19	12.1	0.6	61.2	2.4	10.2	0.4	25.8	1.3	2.9	0.2	17.3	1.0	2.3	0.1	0.4	0.4	7.4	0.4	0.9	0.1	25.5	1.3	641	27	26.6	1.1
	MAD_23	2	473	20	12.8	0.6	60.8	3.3	10.5	0.5	25.0	1.2	3.0	0.1	17.8	0.8	2.4	0.1	0.4	0.4	7.3	0.3	0.7	0.0	26.3	0.9	707	41	27.2	0.9
	MAD_24	2	481	18	12.1	0.5	59.2	2.1	10.1	0.4	24.8	0.9	3.0	0.1	17.2	0.8	2.2	0.1	1.1	0.7	7.1	0.3	0.9	0.1	25.1	1.1	667	21	24.7	0.7
	MAD_25	2	497	22	11.6	0.7	59.2	3.0	9.5	0.6	23.8	1.2	2.9	0.2	16.0	0.9	2.2	0.1	0.6	0.5	7.2	0.4	0.7	0.0	24.5	1.7	638	26	24.8	0.9
	Σ Grains				26		26		26		26		26		26		26		10		26		25		26		26		26	
	Average				11.9		59.6		10.1		24.4		3.0		16.7		2.2		0.5		7.0		0.8		24.6		663.3		25.7	
	2SD				0.4		2.0		0.4		0.9		0.1		0.7		0.1		0.1		0.2		0.1		1.2		25.5		1.0	
	Mao et al., 16		Σ Grains		37		230		37		37		37		229		142								220		230		230	
			Average		11.0		56.1		9.0		22.5		2.6		14.9		2.1								26		599		23	
			2SD		2.6		8.5		2.1		5.1		0.6		3.9		0.7								5		103		5.0	
Navan																														
HK 158	*X18HK_005_0*	1	*1276*	*34*	*12.6*	*0.4*	*73.9*	*2.2*	*13.9*	*0.5*	*40.8*	*1.2*	*5.4*	*0.2*	*35.6*	*1.4*	*5.4*	*0.2*	*2.2*	*1.2*	*22.2*	*1.3*	*3.4*	*0.2*	*2.2*	*0.2*	*4.8*	*0.5*	*26.4*	*1.2*
HK 159	*X18HK_006_0*	1	*509*	*145*	*35.0*	*1.1*	*163.3*	*4.6*	*25.6*	*0.8*	*56.6*	*1.6*	*6.3*	*0.2*	*31.8*	*1.2*	*3.8*	*0.1*	*8.3*	*3.1*	*9.5*	*0.3*	*8.3*	*0.3*	*9.5*	*0.6*	*25.6*	*0.8*	*3.4*	*0.1*
	X18HK_006_1	1	343	31	48.0	1.2	265.7	7.2	46.0	1.4	107.4	2.8	11.9	0.4	60.7	2.1	7.8	0.2	1.5	1.1	2.1	0.1	1.2	0.1	1.6	0.2	12.3	0.5	3.9	0.1
	X18HK_006_2	1	312	64	93.0	4.0	515.0	22.0	90.0	2.9	216.9	6.3	##	0.8	###	3.9	##	0.6	5.3	2.9	3.5	0.2	2.4	0.2	3.0	0.3	24.8	0.9	5.6	0.2
	X18HK_006_3	1	306	49	46.8	1.1	264.1	5.6	46.0	1.2	109.2	2.7	12.1	0.4	61.0	1.8	7.7	0.2	1.7	1.2	2.1	0.1	1.4	0.1	1.5	0.2	11.4	0.4	3.7	0.1
	X18HK_006_4	1	*266*	*84*	*66.1*	*1.5*	*369.3*	*8.8*	*64.9*	*1.3*	*154.1*	*3.4*	*16.4*	*0.3*	*82.8*	*1.8*	*9.6*	*0.2*	*2.6*	*1.3*	*3.3*	*0.1*	*2.6*	*0.1*	*2.9*	*0.2*	*11.6*	*0.5*	*3.5*	*0.1*
	Σ Grains				2		2		2		2		2		2		2		2		2		2		2		2		2	
	Average				47.4		264.9		46.0		108.3		12.0		60.9		7.7		1.6		2.1		1.3		1.6		11.9		3.8	
	2SD				1.2		1.6		0.0		1.8		0.2		0.3		0.1		0.2		0.0		0.1		0.2		0.9		0.1	
HK 235	*X19HK_009_0*	1	*1642*	*31*	*39.1*	*1.2*	*241.1*	*8.8*	*45.8*	*1.3*	*120.4*	*4.2*	*14.1*	*0.5*	*72.4*	*2.4*	*9.6*	*0.4*	*5.7*	*2.3*	*30.2*	*0.7*	*7.0*	*0.2*	*7.9*	*0.4*	*26.9*	*1.2*	*24.9*	*0.9*
Stonepark Area																														
HK 207	*X19HK_004_0*	1	*1770*	*92*	*17.0*	*1.1*	*94.0*	*4.2*	*18.4*	*1.2*	*49.4*	*2.7*	*6.4*	*0.3*	*38.0*	*2.4*	*6.0*	*0.3*	*5.3*	*2.8*	*17.5*	*1.1*	*6.8*	*0.3*	*13.9*	*1.0*	*115.0*	*13.0*	*11.6*	*1.0*
	X19HK_004_1	1	*895*	*23*	*6.4*	*0.3*	*25.6*	*1.1*	*3.2*	*0.2*	*5.6*	*0.3*	*0.5*	*0.0*	*2.1*	*0.2*	*0.2*	*0.0*	*4.4*	*1.5*	*23.2*	*1.9*	*4.2*	*0.2*	*2.9*	*0.2*	*2.2*	*0.3*	*37.2*	*2.8*
HK 209	X19HK_006_0	1	316	48	18.2	0.7	95.6	2.4	16.3	0.7	35.8	1.2	3.9	0.3	19.5	0.8	2.5	0.1	1.5	1.4	0.6	0.1	0.2	0.0	0.6	0.1	13.3	2.1	2.2	0.1
HK 210	X19HK_014_0	1	312	75	39.0	5.9	203	19.0	34.5	3.4	85.2	7.9	9.3	1.6	50.6	6.1	6.1	0.7	4.1	3.7	1.9	0.3	1.0	0.1	2.7	0.7	63.3	8.7	5.0	0.6
	X19HK_014_1	1	282	40	26.0	0.8	142	4.1	24.8	0.7	59.6	1.7	6.4	0.2	33.7	1.1	4.5	0.1	1.7	1.2	1.2	0.1	0.7	0.0	0.9	0.2	7.0	0.4	2.8	0.1
	X19HK_014_2	1	*422*	*14*	*5.2*	*0.2*	*29*	*1.2*	*6.0*	*0.3*	*16.8*	*0.6*	*2.4*	*0.1*	*17.5*	*0.9*	*3.6*	*0.2*	*4.5*	*2.2*	*13.3*	*0.4*	*4.4*	*0.2*	*5.9*	*0.4*	*58.3*	*2.9*	*38.5*	*1.3*
	X19HK_014_3	1	308	88	35.1	2.1	199	10.0	33.9	1.4	80.0	2.7	8.9	0.4	48.6	2.5	6.3	0.4	0.7	1.4	1.8	0.2	1.0	0.2	2.0	0.5	24.4	1.5	4.2	0.1
	X19HK_014_4	1	308	34	33.9	0.8	187	4.8	33.0	0.7	79.2	1.7	8.8	0.3	46.4	1.7	6.1	0.1	1.6	1.0	1.5	0.1	0.9	0.0	1.1	0.2	8.4	0.3	3.3	0.1
	X19HK_014_5	1	*423*	*190*	*65.4*	*3.7*	*363*	*26.0*	*59.1*	*3.7*	*134.0*	*10.0*	*15.4*	*1.2*	*81.8*	*7.0*	*10.4*	*0.3*	*<LOD*	*<LOD*	*2.0*	*0.3*	*1.0*	*0.1*	*2.0*	*0.3*	*33.7*	*2.8*	*5.9*	*0.4*
	X19HK_014_6	1	*200*	*40*	*40.8*	*6.3*	*249*	*39.0*	*41.7*	*5.1*	*91.0*	*12.0*	*10.6*	*1.6*	*55.1*	*9.7*	*7.0*	*0.8*	*3.8*	*4.7*	*2.1*	*0.3*	*1.5*	*0.3*	*2.1*	*0.2*	*14.6*	*2.0*	*3.8*	*0.2*
	X19HK_014_7	1	273	46	47.9	1.3	272	10.0	47.3	1.6	112.0	3.8	##	0.6	62.8	2.4	7.9	0.3	2.2	1.5	2.2	0.1	1.3	0.1	3.3	0.4	60.8	5.1	5.1	0.2
	Σ Grains				3		3		3		3		3		3		3		2		3		3		1		1		2	
	Average				36.0		196.2		33.8		81.5		9.0		48.5		6.2		1.7		1.7		1.0		2.0		24.4		4.6	
	2SD				4.4		14.1		1.3		5.3		0.4		3.4		0.2		0.1		0.4		0.1		0.0		0.0		0.8	
HK 211	*X19HK_015_0*	1	*437*	*29*	*171*	*3.2*	*1123*	*29.0*	*208*	*5.1*	*501*	*11.0*	*57.4*	*1.4*	*284*	*6.1*	*31.9*	*0.6*	*10.9*	*2.7*	*22.9*	*1.8*	*12.7*	*1.2*	*17.9*	*1.4*	*218.9*	*7.5*	*41.5*	*1.6*
	X19HK_015_1	1	347	31	150	3.6	1011	25.0	189	4.0	457	8.9	52.1	1.0	261	5.0	28.9	0.4	5.0	2.3	7.5	0.2	5.2	0.2	5.6	0.4	12.1	0.4	11.8	0.3
	X19HK_015_2	1	334	31	153	4.7	1021	30.0	194	5.7	470	9.9	53.9	1.5	267	7.3	30.4	0.9	3.9	1.4	7.5	0.3	4.9	0.2	5.6	0.4	14.7	1.1	13.2	0.7
	X19HK_015_3	1	361	31	159	4.0	1057	24.0	200	4.6	485	10.0	55.2	1.2	276	4.7	31.1	0.6	6.1	2.2	7.8	0.2	5.1	0.2	5.8	0.4	13.5	0.7	12.6	0.2
	X19HK_015_4	1	358	30	158	3.7	1073	27.0	204	5.4	497	13.0	56.9	1.8	284	7.4	31.9	0.8	6.2	2.8	11.9	0.8	6.4	0.4	10.0	0.8	###	20.0	##	2.8
	X19HK_015_5	1	328	31	164	4.3	1080	27.0	201	4.7	499	12.0	55.5	1.6	277	6.5	31.7	0.9	5.7	2.1	7.9	0.2	5.2	0.2	5.6	0.3	13.8	0.6	13.5	0.3
	X19HK_015_6	1	395	78	146	7.8	968	23.0	182	5.0	443	29.0	53.2	2.2	262	10.0	28.7	1.8	5.8	3.4	8.6	0.4	6.1	0.3	7.1	1.3	11.4	0.7	##	0.4
	X19HK_015_7	1	373	22	170	4.3	1119	33.0	213	7.5	503	16.0	56.8	1.7	284	9.5	32.7	1.2	8.9	2.4	10.9	0.4	6.5	0.2	7.8	0.5	49.2	2.6	##	0.7
	X19HK_015_8	1	322	16	169	5.9	1130	45.0	213	5.0	506	14.0	58.9	2.1	291	12.0	32.9	0.9	7.7	3.4	14.8	0.6	6.0	0.2	10.2	0.7	###	9.7	##	2.3
	X19HK_015_9	1	375	30	147	3.2	967	19.0	182	3.8	439	11.0	49.6	1.1	245	4.6	28.4	0.6	7.4	2.7	7.5	0.2	5.1	0.1	5.2	0.4	10.6	0.5	##	0.3
	X19HK_015_10	1	*537*	*54*	*148*	*4.3*	*990*	*37.0*	*189*	*6.5*	*463*	*13.0*	*51.5*	*2.1*	*252*	*9.4*	*29.5*	*1.1*	*10.3*	*4.2*	*11.1*	*0.6*	*7.9*	*0.4*	*9.1*	*0.9*	*28.6*	*3.1*	*10.1*	*0.5*
	X19HK_015_11	1	366	30	164	3.7	1147	24.0	210	3.9	515	10.0	59.2	1.5	299	6.7	33.2	0.7	4.5	1.8	8.2	0.2	5.2	0.2	5.5	0.3	15.5	0.6	14.1	0.3
	X19HK_015_12	1	344	40	151	3.6	1002	40.0	187	5.7	474	18.0	52.5	2.0	257	11.0	29.3	1.2	3.3	2.2	7.5	0.4	4.8	0.2	6.7	0.7	38.6	7.6	13.4	0.8
	X19HK_015_13	1	315	28	162	6.4	1087	41.0	205	8.6	500	20.0	55.6	2.2	283	12.0	31.6	1.3	4.5	2.0	7.6	0.3	5.1	0.1	5.0	0.4	15.4	1.5	13.7	1.0
	X19HK_015_14	1	347	15	217	6.6	1468	36.0	278	6.3	674	19.0	##	2.0	388	12.0	##	1.0	6.7	2.6	10.8	0.3	5.4	0.2	6.2	0.5	36.0	1.4	##	0.8
	X19HK_015_15	1	327	20	199	7.3	1337	44.0	257	8.2	623	19.0	##	2.3	357	11.0	##	1.3	6.9	2.5	9.4	0.4	5.3	0.2	6.3	0.3	30.7	1.4	##	1.4
	X19HK_015_16	1	370	27	158	3.4	1055	29.0	200	5.1	480	10.0	54.2	1.2	274	6.6	30.1	0.8	4.5	1.4	7.6	0.2	5.1	0.2	5.3	0.4	14.6	0.7	11.9	0.3
	X19HK_015_17	1	323	27	156	3.6	1025	23.0	194	4.0	472	8.3	53.2	1.2	263	4.6	30.1	0.5	5.7	2.2	7.3	0.2	5.3	0.2	5.9	0.3	10.4	0.4	11.3	0.3

Continue Table A2 – 3

HK 211	X19HK_015_18	1	354	38	156	4.6	1048	24.0	199	3.7	484	9.7	54.5	1.6	279	8.7	30.6	0.8	3.8	2.1	8.0	0.3	5.0	0.3	5.5	0.4	14.6	0.9	13.7	0.5
	X19HK_015_19	1	341	15	165	4.6	1102	33.0	202	5.5	491	15.0	56.6	1.6	286	7.1	34.0	0.7	8.5	2.4	16.6	1.1	6.8	0.4	17.1	1.7	###	56.0	##	4.1
	X19HK_015_20	1	336	25	163	3.4	1112	25.0	208	5.3	515	15.0	57.1	1.5	280	8.5	32.3	0.7	4.9	1.6	7.9	0.2	5.1	0.2	5.7	0.3	16.2	0.7	14.4	0.4
	X19HK_015_21	1	346	17	177	4.6	1197	33.0	225	5.6	561	15.0	62.6	1.4	311	9.7	35.4	1.0	7.2	2.2	8.8	0.3	5.2	0.2	5.7	0.4	20.9	1.3	##	0.7
	X19HK_015_22	1	325	27	158	4.1	1066	26.0	202	3.8	490	9.7	55.9	1.3	279	5.0	31.7	0.5	5.4	2.7	8.0	0.3	5.4	0.3	5.7	0.6	26.7	5.1	13.7	0.4
	X19HK_015_23	1	382	40	150	3.7	1001	25.0	184	4.1	460	11.0	50.6	1.2	249	4.5	29.0	0.6	4.8	2.2	7.8	0.3	5.3	0.2	5.7	0.4	11.9	0.7	##	0.2
	X19HK_015_24	1	397	38	155	4.3	1037	29.0	191	7.4	468	18.0	53.3	2.1	261	11.0	29.7	1.2	12.4	3.2	19.7	0.9	11.4	0.6	23.5	1.7	###	52.0	##	1.1
	Σ Grains				21		21		21		21		21		21		21		9		17		19		17		8		11	
	Average				158.6		1062		199.2		486.2		55.1		274.6		31.1		5.7		7.9		5.2		5.7		14.8		13.2	
	2SD				15.5		116		22.1		53.6		5.9		31.7		3.7		1.1		1.1		0.6		0.8		1.6		1.8	
HK 212	X19HK_016_0	1	332	31	19.4	0.6	107	3.9	18.2	0.5	42.2	1.7	4.3	0.2	23.9	1.1	2.9	0.1	1.3	1.0	0.8	0.1	0.4	0.0	0.6	0.1	6.2	0.4	2.4	0.1
	X19HK_016_1	1	*328*	*101*	*31.1*	*1.3*	*158*	*8.9*	*26.4*	*1.5*	*60.7*	*2.2*	*7.0*	*0.5*	*36.6*	*2.5*	*5.1*	*0.2*	*2.0*	*2.5*	*1.1*	*0.2*	*0.3*	*0.2*	*0.6*	*0.4*	*12.2*	*0.8*	*4.1*	*0.3*
	X19HK_016_2	1	329	33	18.2	0.4	98	2.5	16.5	0.4	37.6	1.0	4.1	0.2	21.7	0.8	2.7	0.1	0.5	0.7	0.6	0.0	0.2	0.0	0.4	0.1	5.4	0.3	2.2	0.1
	X19HK_016_3	1	345	44	23.8	0.8	121	7.2	20.6	0.9	48.1	3.1	5.2	0.3	27.0	2.2	3.5	0.1	<LOD	<LOD	0.9	0.1	0.2	0.0	0.6	0.2	9.7	0.9	3.9	0.1
	X19HK_016_4	1	314	23	35.8	0.9	195	7.0	31.3	1.1	72.2	2.5	7.9	0.3	40.7	1.9	5.3	0.2	<LOD	1.2	1.0	0.1	0.3	0.0	0.6	0.1	13.2	0.6	4.4	0.1
	X19HK_016_5	1	363	23	29.8	1.8	158	8.3	27.2	1.5	60.2	2.9	6.7	0.4	36.0	2.4	5.1	0.2	<LOD	<LOD	1.0	0.1	0.2	0.0	0.5	0.2	10.3	0.6	3.9	0.2
	X19HK_016_6	1	346	57	17.5	0.7	91	4.4	16.0	0.6	36.2	1.5	3.9	0.2	19.1	0.9	2.5	0.1	<LOD	<LOD	0.6	0.1	0.2	0.0	0.4	0.1	4.9	0.4	1.9	0.1
	X19HK_016_7	1	306	62	36.1	1.1	208	6.7	35.0	0.9	80.3	2.1	9.3	0.3	50.1	2.0	5.9	0.3	1.4	1.1	1.3	0.1	0.8	0.1	1.1	0.2	7.2	0.5	2.6	0.1
	X19HK_016_8	1	304	34	21.3	0.6	117	2.6	20.2	0.6	47.8	1.1	5.1	0.2	27.4	1.0	3.2	0.1	1.1	0.9	0.8	0.1	0.3	0.0	0.5	0.1	7.3	0.3	2.9	0.1
	X19HK_016_9	1	338	24	###	3.3	638	23.0	###	2.9	214.5	8.0	##	0.9	###	3.0	11.7	0.5	<LOD	<LOD	1.5	0.1	0.3	0.1	1.0	0.3	33.5	1.2	6.9	0.2
	X19HK_016_10	1	297	35	17.3	0.5	92	3.0	15.1	0.5	34.6	1.0	3.9	0.2	18.7	0.7	2.4	0.1	<LOD	<LOD	0.5	0.0	0.2	0.0	0.3	0.1	4.7	0.2	1.9	0.1
	Σ Grains				4		4		4		3		3		4		5		4		5		6		4		3		4	
	Average				20.6		110.7		18.9		46.0		4.9		25.0		2.9		1.3		0.9		0.2		0.5		6.9		2.6	
	2SD				4.2		18.2		3.3		5.4		0.8		4.7		0.8		0.3		0.2		0.1		0.1		1.0		0.5	
Slievedart Area																														
HK 187	*X18HK_132_0*	1	*13*	*9*	*29.2*	*0.7*	*151.3*	*4.4*	*24.3*	*0.8*	*54.7*	*1.4*	*6.2*	*0.3*	*30.5*	*0.9*	*3.2*	*0.1*	*2.4*	*1.7*	*2.0*	*0.1*	*1.7*	*0.1*	*2.0*	*0.2*	*167.9*	*5.2*	*21.9*	*0.4*
HK 190	X18HK_135_0	1	371	26	177	4.2	1197	22.0	221	4.9	545	12.0	62.3	1.8	309	8.8	35.1	1.0	5.3	1.6	8.9	0.2	5.1	0.1	7.2	0.4	69.6	4.6	##	0.5
	X18HK_135_1	1	368	31	156	4.0	1066	30.0	199	5.2	477	14.0	55.5	1.5	274	8.9	30.9	0.9	5.6	2.1	7.9	0.3	5.0	0.2	5.7	0.4	13.6	0.6	12.8	0.3
	X18HK_135_2	1	358	32	146	4.3	971	26.0	184	5.0	442	11.0	51.4	1.0	254	7.8	28.5	0.8	5.9	2.2	7.4	0.2	4.9	0.2	5.3	0.4	11.4	0.7	11.0	0.4
	Σ Grains				3		3		3		3		3		3		3		3		3		3		2		2		2	
	Average				159.4		1078.0		201.4		488.0		56.4		279.0		31.5		5.6		8.1		5.0		5.5		12.5		11.9	
	2SD				25.5		185.3		30.8		85.5		9.0		45.1		5.5		0.5		1.2		0.1		0.4		2.2		1.8	
HK 193	X18HK_138_0	1	373	34	3.4	0.2	18.5	1.2	3.6	0.1	8.9	0.5	1.1	0.1	6.9	0.5	1.0	0.1	< LOD	< LOD	4.9	0.2	2.9	0.1	3.5	0.3	25.2	1.4	8.7	0.3
HK 194	X18HK_139_0	1	349	30	156	4.2	1033	24.0	195.6	4.3	477	10.0	54.6	1.3	272	6.5	30.6	0.7	6.4	1.9	7.6	0.2	4.8	0.1	5.4	0.4	15.0	0.5	13.5	0.3
	X18HK_139_1	1	397	29	181	4.5	1193	31.0	###	5.0	544	12.0	##	1.2	311	7.5	##	0.9	4.9	1.9	9.4	0.2	5.2	0.2	7.9	0.5	###	9.7	##	0.6
	X18HK_139_2	1	381	34	140	6.1	906	37.0	168.7	6.5	400	15.0	46.9	2.8	232	12.0	25.1	0.9	7.0	3.8	8.4	0.5	5.4	0.2	10.7	1.0	###	16.0	13.0	0.7
	X18HK_139_3	1	345	27	155	3.4	1035	25.0	192.5	3.9	464	9.8	53.2	1.3	259	5.8	29.2	0.8	5.6	2.0	7.5	0.2	5.0	0.2	5.1	0.3	12.3	0.4	11.8	0.2
	X18HK_139_4	1	365	24	140	6.3	922	41.0	168.5	6.7	404	13.0	47.3	2.0	233	10.0	24.9	1.0	5.1	2.4	9.9	0.5	5.8	0.3	22.2	1.4	###	31.0	##	0.7
	X18HK_139_5	1	347	31	142	2.5	949	18.0	176.4	4.1	431	8.9	49.2	1.1	242	5.7	27.3	0.7	4.1	2.0	8.3	0.3	5.5	0.2	9.4	1.0	###	27.0	13.6	0.4
	Σ Grains				5		6		5		5		5		5		5		4		6		6		3		2		4	
	Average				146.5		1006.3		180.3		435.3		50.2		247.7		27.4		5.5		8.5		5.3		7.5		128.4		13.0	
	2SD				15.0		194.7		23.2		62.1		6.2		31.2		4.4		1.2		1.8		0.6		3.5		51.2		1.5	
HK 237	X18HK_158_0	2	306	34	24.4	1.3	141	7.6	24.1	1.3	57.8	3.4	6.84	0.4	36.3	1.9	4.36	0.26	5.6	1.3	8.04	0.38	5.84	0.3	6.37	0.48	19	1.7	12.2	0.59
	X18HK_158_1	2	326	39	24.9	1.4	147	7.6	25.4	1.2	61.5	3.3	7.24	0.32	38.4	1.9	4.52	0.2	5.9	1.1	8.53	0.38	6.2	0.23	6.52	0.34	11.94	0.75	11.7	0.46
	X18HK_158_2	2	318	37	24.4	1	140	7	24.9	1	61.7	2.5	6.8	0.33	37.8	2.5	4.63	0.25	4.9	1.4	8.44	0.38	6.19	0.32	6.83	0.62	11.79	0.76	11.6	0.53
	X18HK_158_3	2	299	32	22.7	1.2	134	6.6	24	1.4	57.8	3.3	6.95	0.41	36.3	1.8	4.47	0.26	7	1.5	8.44	0.46	6.35	0.38	6.21	0.46	10.9	1.2	12.2	0.64
	X18HK_158_4	2	274	36	25.4	1.2	149	8.6	25.5	1.1	62	2.6	6.99	0.36	37	1.8	4.38	0.23	6.7	1.9	7.87	0.34	6	0.28	6.41	0.38	8.1	0.47	10.4	0.4
	X18HK_158_5	2	312	30	24.5	1.2	137	6.3	24.3	1.1	59.3	3.6	6.95	0.36	37.2	2	4.59	0.22	7.1	1.6	9.09	0.41	6.46	0.33	6.86	0.53	29	1.9	14	0.72
	X18HK_158_6	2	307	33	21.26	0.89	122	5.3	21.16	0.95	51.4	2.1	5.97	0.28	30.9	1.6	3.75	0.15	5.11	0.95	7.64	0.34	5.73	0.2	6.26	0.47	24	2.3	9.91	0.36
	X18HK_158_7	2	288	41	25.55	0.79	148	4.1	26.51	0.73	63.2	1.8	7.25	0.22	39.1	1.4	4.81	0.13	6	1.6	8.21	0.35	6.38	0.33	7.17	0.51	33	1.7	10.7	0.3
	X18HK_158_8	2	291	29	22.6	1.1	128	5.2	21.7	0.8	54.5	2.3	6.14	0.3	32.6	1.7	3.98	0.23	5.09	0.92	8.08	0.41	5.97	0.24	6.56	0.5	11.14	0.51	11	0.54
	X18HK_158_9	2	322	39	26.3	1.6	153	9.1	28	1.9	67	3.5	7.75	0.42	41.1	2.5	4.9	0.26	5.66	0.85	8.18	0.57	5.96	0.41	5.98	0.52	15	0.94	11.6	0.67
	X18HK_158_10	2	304	27	24.8	1.1	150	7.2	25.5	1.1	62.2	2.8	7	0.26	37.4	1.9	4.53	0.18	5.6	1.1	7.91	0.32	5.9	0.17	6.14	0.42	10.9	0.6	11.1	0.35
	X18HK_158_11	2	284	37	24.58	0.94	148	7.1	25.9	1.1	62.8	2.5	7.16	0.28	36.9	1.1	4.58	0.16	5.7	1.3	8.25	0.3	6.03	0.18	6.04	0.37	10.29	0.52	12.3	0.53
	X18HK_158_12	2	298	35	24.21	0.92	141	6.5	24.67	0.75	60.7	1.9	6.99	0.26	36.5	1.7	4.52	0.18	5.1	1	8.47	0.38	6.48	0.25	6.45	0.44	9.66	0.53	11.1	0.4
	X18HK_158_13	2	280	36	23.3	1	129	5.4	23.5	1.1	55.1	2.7	6.25	0.3	33.9	1.8	4.13	0.18	5.5	1.4	8.09	0.3	6.32	0.25	6.54	0.49	11.44	0.56	10.8	0.31
	X18HK_158_14	2	308	29	28.2	1.1	157	5.7	29.6	1.1	69.7	3.4	8.4	0.34	42.5	2	5.25	0.3	7.9	1.7	8.79	0.4	6.25	0.32	6.62	0.54	21	2.1	14	0.75
	X18HK_158_15	2	314	34	18	1	100	6.1	17	0.86	40.8	2.9	5	0.33	25.3	1.7	3.2	0.17	5.8	1.3	8.5	0.36	6.3	0.23	8.37	0.8	61	14	11.7	0.59
	X18HK_158_16	2	282	46	23.5	1.2	136	6.9	23.5	1.3	56.3	3.2	6.67	0.37	34.3	1.9	4.25	0.25	5.4	1.2	7.87	0.42	6.06	0.36	6.07	0.4	8.7	0.66	10.5	0.63

Continue Table A2 – 3

HK 237	X18HK_158_17	2	308	36	23.9	1.4	136	7.9	24.6	1.3	58.8	3.9	6.72	0.36	37.1	1.8	4.51	0.27	5.5	1.2	8.38	0.47	6.49	0.36	6.61	0.54	9.75	0.53	11.3	0.49
	X18HK_158_18	2	288	29	24.6	1.3	137	6.4	23.63	0.87	59.3	3	6.97	0.36	36.2	1.8	4.28	0.19	7.8	1.6	7.83	0.4	5.88	0.3	5.84	0.45	10.05	0.61	11.3	0.45
	X18HK_158_19	2	274	50	21.07	0.99	124	6	22.2	1	55.6	2.4	6.56	0.34	35.9	1.3	4.26	0.17	6	1.2	7.67	0.33	6.19	0.25	5.92	0.44	8.5	0.35	9.36	0.38
	X18HK_158_20	2	256	39	28.8	1.2	175	9	31	1.3	77.9	3.7	9.1	0.4	47.6	2.3	5.8	0.21	5.6	1.3	8.9	0.42	6.78	0.28	7.14	0.65	8.2	0.45	12.7	0.63
	X18HK_158_21	2	299	31	25.8	1.1	151	7	27.2	1.4	66.1	3.4	7.97	0.38	42.6	1.9	5.04	0.24	5.3	1.2	8.66	0.43	6.33	0.33	6.47	0.45	11.57	0.65	12.6	0.55
	Σ Grains				15		15		15		15		14		15		15		13		16		16		15		7		14	
	Average				24.4		141		25.0		60.6		7.0		37.6		4.6		5.5		8.3		6.2		6.4		10.9		11.3	
	2SD				1.8		9.7		2.1		4.6		0.5		2.9		0.3		0.3		0.4		0.2		0.3		0.9		0.9	
HK 238	X18HK_159_0	2	287	34	21.5	1.0	125	5.9	22.8	1.0	55.7	3.4	6.3	0.4	34.0	2.0	3.9	0.2	6.1	1.7	8.0	0.4	6.3	0.3	6.3	0.4	8.7	0.6	10.8	0.4
	X18HK_159_1	2	321	33	24.7	1.3	146	8.5	25.8	1.3	60.1	3.7	7.3	0.5	37.0	2.6	4.3	0.2	4.9	1.4	8.2	0.5	6.2	0.3	6.2	0.5	9.3	0.4	11.4	0.5
	X18HK_159_2	2	331	37	26.2	1.3	154	8.7	27.1	1.5	64.9	3.0	7.8	0.4	41.5	2.2	4.9	0.3	6.3	1.2	8.3	0.4	6.3	0.3	6.3	0.5	11.2	0.6	10.4	0.4
	X18HK_159_3	2	257	36	23.0	1.0	130	5.6	23.9	1.2	55.8	2.3	6.5	0.3	33.8	1.7	4.2	0.2	6.0	1.1	7.9	0.4	6.2	0.3	6.2	0.4	8.8	0.6	10.2	0.3
	X18HK_159_4	2	307	33	29.9	1.2	168	7.0	30.4	1.6	76.3	3.5	8.5	0.3	46.0	2.1	5.4	0.3	7.5	1.3	8.7	0.4	6.5	0.3	6.0	0.4	8.7	0.6	12.8	0.4
	X18HK_159_5	2	293	31	24.1	1.1	139	7.4	25.9	1.3	63.4	2.8	7.6	0.4	41.0	2.3	4.9	0.2	6.0	1.6	9.0	0.4	7.1	0.5	7.1	0.5	10.0	0.6	11.4	0.6
	X18HK_159_6	2	268	31	24.1	1.5	132	8.4	23.6	1.4	56.0	3.5	6.5	0.4	36.0	2.0	4.1	0.2	5.0	1.0	7.9	0.4	6.2	0.3	6.3	0.4	11.2	0.9	10.6	0.5
	X18HK_159_7	2	307	30	20.9	1.2	129	7.3	21.6	1.4	51.3	2.6	6.0	0.3	31.4	1.7	3.8	0.2	5.6	1.7	8.0	0.4	5.9	0.3	5.6	0.5	9.4	0.6	11.5	0.5
	X18HK_159_8	2	332	22	25.1	1.3	144	8.4	26.2	1.9	64.8	4.2	8.1	0.5	41.9	2.3	5.3	0.3	5.6	1.3	9.2	0.4	6.4	0.3	7.0	0.5	34.2	1.6	##	0.8
	X18HK_159_9	2	308	31	22.5	1.2	133	4.7	24.5	1.0	55.9	2.0	6.8	0.3	36.3	1.7	4.2	0.2	5.3	1.4	8.5	0.3	6.5	0.2	6.8	0.4	15.5	1.2	11.0	0.4
	X18HK_159_10	2	311	33	25.0	1.2	146	4.1	25.9	1.3	64.9	2.4	7.5	0.4	38.5	1.3	4.8	0.2	7.1	1.7	8.9	0.3	6.5	0.2	6.8	0.4	17.2	2.1	##	0.5
	X18HK_159_11	2	343	35	22.0	1.5	126	8.6	21.8	1.5	52.2	3.5	5.9	0.4	33.6	2.2	3.9	0.3	5.9	1.6	8.6	0.6	6.2	0.4	6.5	0.6	14.7	1.5	11.6	0.8
	X18HK_159_12	2	310	31	25.9	1.0	145	5.4	25.8	1.0	63.4	2.9	7.2	0.4	38.6	2.1	4.6	0.2	7.9	1.4	8.5	0.3	6.4	0.2	6.1	0.3	11.6	0.6	11.4	0.3
	X18HK_159_13	2	308	40	22.9	1.1	130	6.9	24.7	1.4	57.1	3.8	6.7	0.4	35.9	1.6	4.1	0.2	6.6	1.7	8.1	0.4	6.3	0.3	6.7	0.5	10.2	0.6	11.1	0.5
	X18HK_159_14	2	260	34	23.4	1.4	135	7.2	24.4	1.4	58.5	2.5	6.3	0.3	35.1	1.9	4.3	0.3	5.8	1.0	8.1	0.5	6.4	0.4	6.0	0.6	12.0	1.8	10.6	0.6
	X18HK_159_15	2	255	34	21.0	1.0	119	5.4	20.9	1.1	50.5	2.6	5.9	0.3	30.8	1.9	3.7	0.2	6.3	1.2	7.4	0.3	5.8	0.3	5.9	0.5	11.5	0.7	10.3	0.5
	X18HK_159_16	2	275	36	24.8	1.5	141	11.0	23.6	1.3	57.9	3.2	6.7	0.5	35.2	2.3	4.2	0.2	5.9	1.1	8.2	0.4	6.4	0.3	6.5	0.5	15.8	2.0	10.6	0.5
	X18HK_159_17	2	271	46	21.0	1.0	122	4.8	21.4	1.1	51.2	2.7	6.0	0.3	32.0	1.9	3.8	0.2	5.4	1.2	7.4	0.4	6.0	0.3	6.2	0.3	9.2	0.6	9.8	0.3
	X18HK_159_18	2	286	41	22.3	1.3	132	7.9	23.6	1.4	57.4	3.3	6.9	0.5	34.4	2.6	4.1	0.2	5.8	1.4	8.3	0.4	6.2	0.4	6.2	0.5	8.7	0.5	11.2	0.4
	X18HK_159_19	2	298	37	23.5	1.3	131	8.3	23.7	1.3	58.3	3.4	6.9	0.3	35.1	1.8	4.3	0.2	5.7	0.9	7.8	0.4	5.9	0.2	5.4	0.4	8.5	0.5	10.5	0.5
	X18HK_159_20	2	345	47	20.8	1.0	119	5.8	21.2	1.1	52.9	3.0	6.2	0.4	32.6	1.7	4.1	0.2	9.3	1.9	9.3	0.4	7.4	0.4	7.4	0.5	18.3	1.5	9.5	0.4
	Σ Grains				13.0		13.0		13.0		13.0		13.0		13.0		12.0		11.0		14.0		14.0		14.0		6.0		12.0	
	Average				23.5		136		24.4		59.0		7.0		36.8		4.3		5.9		8.5		6.4		6.4		10.3		11.1	
	2SD				1.7		9.6		1.9		4.8		0.7		3.3		0.4		0.6		0.4		0.4		0.6		0.9		0.8	

9.3 Appendix 3 - Bulk-Rock Geochemistry Data of Limestones and Fossils

Table A3- 1: Twenty-seven trace elements are listed along with Ca, Sr/Mn, Rb/Sr and Y/Ho ratios as well as ΣREE+Y for all analysed samples of this study along with Sr isotopic ratios for 17 samples. The assumed calcium concentration is given in wt%, Mg, Al, P, Sc, Fe, Mn, Rb and Sr are presented in µg/g, while remaining element concentrations are shown in ng/g. Empty cells either signify concentrations below detection limits for trace element analyses or samples that were not chosen for $^{87}Sr/^{86}Sr$ analysis. TCM = tungsten-carbide mill; SSD = single-step digestion; SD = standard deviation.

sample #		1	2	3	4	5	6	7	8	9	10	11	12	13	14	15
		Micrite	Micrite	Micrite	Micrite	Micrite	Micrite	Micrite	Micrite	Micrite	Micrite	Micrite	Micrite	Micrite	Micrite	Micrite
sample ID		16 HK 013	16 HK 013	16 HK 012.3a	16 HK 011	16 HK 011	16 HK 011.2a	16 HK 011.2b	16 HK 009	16 HK 013	16 HK 013	16 HK 013	16 HK 012.3b	16 HK 011	16 HK 011	16 HK 011
Lab ID		HK 32.1	HK 32.2	HK 38	HK 28.1	HK 28.2	HK 36	HK 37	HK 40	HK 33.1	HK 34.1	HK 35.1	HK 39.1	HK 29.1	HK 30.1	HK 31.1
milling device		TCM	TCM	dentist drill	TCM	TCM	dentist drill	dentist drill	microdrill	TCM	TCM	TCM	dentist drill	TCM	TCM	TCM
dissolution method		SSD	SSD	SSD	SSD	SSD	SSD	SSD	SSD	first leach without rinsing	first leach keep rinsing	first leach discard rinsing	first leach without rinsing	first leach without rinsing	first leach keep rinsing	first leach discard rinsing
sampling depth (m)		367	367	366.5	366	366	366	366	341.3	367	367	367	366.5	366	366	366
stratigraphic formation		Micrite Unit	Micrite Unit	Micrite Unit	Micrite Unit	Micrite Unit	Micrite Unit	Micrite Unit	Micrite Unit	Micrite Unit	Micrite Unit	Micrite Unit	Micrite Unit	Micrite Unit	Micrite Unit	Micrite Unit
	unit															
Mg	µg/g	7641	7696	4650	8408	8636	9942	10314	5607	6103	5986	6161	6934	5070	4926	5024
Al	µg/g	822	770	565	142	141	799	1195	491.5	0.2	1.0	0.7	0.1	1.0	0.7	0.2
P	µg/g	73	75	32	80	82	57	74	108	13	22	12	8	12	23	12
Ca	wt%	40	40	40	40	40	40	40	40	40	40	40	40	40	40	40
Sc	µg/g	1.2	1.2	0.84	0.83	0.86	1.1	1.3	1.7	0.36	0.38	0.34	0.28	0.14	0.22	0.15
Fe	µg/g	2456	2342	3165	2225	2251	4011	4588	1596	16	26	29	11	31	29	28
Mn	µg/g	355	353	507	381	382	403	402	339	146	140	145	85	217	234	246
Rb	µg/g	1.3	1.3	0.79	0.36	0.34	1.18	1.8	0.80	4.2	4.3	4.4	3.2	0.60	0.61	0.58
Sr	µg/g	410	410	332	399	392	387	388	390	448	473	451	466	403	421	404
Y	ng/g	3955	3955	7299	4631	4619	5622	5389	6075	4.3	4.6	5.7	15.3	5.2	4.7	5.0
Cd	ng/g	13	12	14	17	16	17	18	31			0.07	0.13	0.01		0.23
Ba	ng/g	7849	7780	6160	6377	6294	8037	10020	7937	8076	7595	8345	6678	7853	7735	7812
La	ng/g	6300	6300	9170	7058	7114	8100	8114	9444	0.78	0.93	1.8	1.4	2.7	1.8	1.9
Ce	ng/g	12782	12823	19871	14311	14320	17049	16773	20094	0.82	0.95	2.9	3.9	4.2	2.1	2.4
Pr	ng/g	1500	1495	2513	1676	1680	1999	1955	2243	0.15	0.07	0.37	0.66	0.50	0.26	0.28
Nd	ng/g	5530	5551	9334	6183	6192	7338	7118	8319	0.56	0.24	1.3	4.4	1.9	0.84	0.83
Sm	ng/g	1024	1029	1828	1151	1152	1376	1327	1558	0.35	0.04	0.69	2.32	0.40	0.77	0.25
Eu	ng/g	196	197	423	237	242	299	292	310	0.71	0.65	0.61	0.38	0.77	0.72	0.76
Tb	ng/g	129	130	242	148	148	183	173	194	0.01	0.03	0.04	0.75	0.06	0.01	0.04
Gd	ng/g	876	886	1570	998	1002	1210	1156	1327	0.07	0.10	0.10	4.52	0.24	0.47	0.18
Dy	ng/g	723	728	1368	821	833	1039	971	1080	0.01	0.21	0.31	2.92	0.24	0.16	0.54
Ho	ng/g	143	143	258	163	164	197	188	208		0.004	0.06	0.46	0.07	0.05	0.08
Er	ng/g	373	378	665	416	420	515	494	550	0.05	0.10	0.12	1.08	0.17	0.10	0.23
Tm	ng/g	52	51	93	58	58	72	68	80	0.02	0.03	0.06	0.15	0.04	0.03	0.03
Yb	ng/g	302	305	573	338	341	427	406	499	0.12	0.02	0.14	0.54	0.14	0.02	0.10
Lu	ng/g	41	42	79	46	47	58	56	69		0.001	0.01	0.06	0.04	0.04	0.04
Hf	ng/g	4.3	5.0	2.7	4.1	4.1	4.1	5.2	1.9	0.01	0.04	0.05	0.01		0.07	0.03
Th	ng/g	796	797	332	670	704	596	777	987			0.002		0.14	0.003	0.01
Sr/Mn		1.2	1.2	0.7	1.0	1.0	1.0	1.0	1.2	3.1	3.4	3.1	5.5	1.9	1.8	1.6
Rb/Sr		0.00316	0.00318	0.00239	0.00090	0.00088	0.00306	0.00461	0.00204	0.00942	0.00917	0.00981	0.00692	0.00148	0.00145	0.00143
Y/Ho		28	28	28	28	28	28	29	29			95	33	78	91	66
ΣREE+Y	µg/g	33.93	34.01	55.29	38.24	38.33	45.49	44.48	52.05	0.01	0.01	0.01	0.04	0.02	0.01	0.01
$^{87}Sr/^{86}Sr$								0.708505	0.708463							
SD								0.000032	0.000034							

Continue Table A3- 1

sample #		16	17	18	19	20	21	22	23	24	25	26	27	28	29	30
		Micrite	Micrite	Micrite	Micrite	Micrite	Micrite	Micrite	Micrite	Micrite	Micrite	Micrite	Micrite	Micrite	Micrite	Micrite
sample ID		16 HK 011	16 HK 013	16 HK 013	16 HK 013	16 HK 012.3b	16 HK 011	16 HK 011	16 HK 011	16 HK 011	16 HK 013	16 HK 013	16 HK 013	16 HK 012.3b	16 HK 011	16 HK 011
Lab ID		HK 51.1	HK 33.2	HK 34.2	HK 35.2	HK 39.2	HK 29.2	HK 30.2	HK 31.2	HK 51.2	HK 33.3	HK 34.3	HK 35.3	HK 39.3	HK 29.3	HK 30.3
milling device		TCM	TCM	TCM	TCM	dentist drill	TCM	TCM	TCM	TCM	TCM	TCM	TCM	dentist drill	TCM	TCM
dissolution method		first leach without rinsing	central leach without rinsing	central leach keep rinsing	central leach discard rinsing	central leach without rinsing	central leach without rinsing	central leach discard rinsing	central leach discard rinsing	central leach without rinsing	final leach without rinsing	final leach keep rinsing	final leach discard rinsing	final leach without rinsing	final leach without rinsing	final leach discard rinsing
sampling depth (m)		366	367	367	367	366.5	366	366	366	366	367	367	367	366.5	366	366
stratigraphic formation		Micrite Unit	Micrite Unit	Micrite Unit	Micrite Unit	Micrite Unit	Micrite Unit	Micrite Unit	Micrite Unit	Micrite Unit	Micrite Unit	Micrite Unit	Micrite Unit	Micrite Unit	Micrite Unit	Micrite Unit
	unit															
Mg	µg/g	4941	4687	4675	4591	3561	4967	4910	5049	6309	11549	13099	12791	7952	13729	13448
Al	µg/g	0.3	7.9	1.2	0.8		11.1	3.9	0.7	13	1739	2114	2028	1838	233	290
P	µg/g	13	12	20	14	5.3	12	18	13	13	206	201	204	155	206	215
Ca	wt%	40	40	40	40	40	40	40	40	40	40	40	40	40	40	40
Sc	µg/g	0.14	0.23	0.23	0.21	0.12	0.18	0.17	0.14	0.14	2.47	2.77	2.67	2.15	1.78	1.90
Fe	µg/g	20	315	29	20	12	891	31	119	648	4504	5493	5283	6251	3796	4072
Mn	µg/g	292	395	400	411	583	404	409	405	392	406	415	409	704	418	420
Rb	µg/g	0.44	0.64	0.51	0.47	0.44	0.19	0.18	0.16	0.18	1.20	1.00	0.99	1.33	0.60	0.64
Sr	µg/g	388	370	387	366	316	364	386	362	365	404	405	403	302	397	396
Y	ng/g	5.2	300	48	55	20	1539	1256	381	3671	6895	9964	9478	17266	6159	6786
Cd	ng/g	0.37	13	11	12	3.5	24	23	21	24	16	23	23	35	20	21
Ba	ng/g	7081	6833	6148	6414	4243	5239	5008	5008	5128	8699	10225	10070	7542	6170	6658
La	ng/g	1.9	225	16	18	4.2	1862	2429	440	7465	11105	16188	15424	20914	9471	10178
Ce	ng/g	1.6	280	11	15	4.2	1698	2325	350	10291	24186	33399	32112	50032	20536	22254
Pr	ng/g	0.19	29	1.20	1.66	0.36	146	192	30	961	2926	3917	3784	6028	2481	2722
Nd	ng/g	0.73	103	4.8	6.4	2.1	491	605	101	3198	10877	14382	13856	22635	9120	9978
Sm	ng/g	0.26	16	0.92	1.15	0.23	62	76	13	426	2096	2682	2598	4502	1794	1956
Eu	ng/g	0.60	3.9	0.76	0.61	0.12	15	16	3.4	90	407	522	497	1012	376	411
Tb	ng/g	0.04	2.7	0.16	0.25	0.04	12	13	2.4	60	258	342	328	603	220	245
Gd	ng/g	0.18	18	1.16	1.16	0.73	90	95	20	480	1720	2295	2214	3843	1489	1630
Dy	ng/g	0.07	17	1.29	1.54	0.67	78	74	17	326	1435	1909	1832	3393	1252	1376
Ho	ng/g	0.04	4.3	0.34	0.44	0.16	20	17	4.1	68	277	377	362	652	237	262
Er	ng/g	0.16	13	1.54	1.65	0.64	56	44	11	171	713	976	944	1704	607	672
Tm	ng/g	0.05	2.0	0.21	0.26	0.13	7.4	4.9	1.5	20	102	136	133	237	86	92
Yb	ng/g	0.11	12	1.33	1.69	0.63	42	28	7.5	100	590	804	775	1461	510	566
Lu	ng/g	0.001	1.7	0.22	0.31	0.13	6.6	4.3	1.3	15	82	108	105	197	67	74
Hf	ng/g	0.04	0.04	0.51	0.76	0.20		0.3	0.6	0.8	14	10	11	5.1	10	8.1
Th	ng/g	0.01	2.1	30.67	28.09		0.1	31	24	28	1930	2100	2064	961	1655	1687
Sr/Mn		1.3	0.9	1.0	0.9	0.5	0.9	0.9	0.9	0.9	1.0	1.0	1.0	0.4	1.0	0.9
Rb/Sr		0.00112	0.00172	0.00130	0.00127	0.00139	0.00051	0.00047	0.00044	0.00049	0.00296	0.00247	0.00246	0.00439	0.00152	0.00162
Y/Ho		125	70	141	125	121	78	73	94	54	25	26	26	26	26	26
ΣREE+Y	µg/g	0.01	1.03	0.09	0.11	0.03	6.12	7.18	1.38	27.34	63.67	88.00	84.44	134.48	54.40	59.20
$^{87}Sr/^{86}Sr$			0.708380		0.708394	0.708449	0.708338		0.708344							
SD			0.000037		0.000034	0.000035	0.000039		0.000038							

Continue Table A3- 1

sample #		31	32	33	34	35	36	37	38	39	40	41	42	43	44	45
		Micrite	Micrite	Brachiopod	Brachiopod	Brachiopod	Coral	Coral	Crinoid	Crinoid	Crinoid	Crinoid	Crinoid	Crinoid	Crinoid	Crinoid
sample ID		16 HK 011	16 HK 011	brac	brac	brac	coral	coral	crinoid	crinoid	HK003 crin	HK 003 crin	HK003 crin	HK 003 crin	HK003 crin	HK 003 crin
Lab ID		HK 31.3	HK 51.3	HK 41	HK 43	HK 44	HK 48	HK 49	HK 46	HK 47	HK 45.1	HK 50.1	HK 45.2	HK 50.2	HK 45.3	HK 50.3
milling device		TCM	TCM	microdrill	microdrill	microdrill	microdrill	microdrill	microdrill	microdrill	micromill	micromill	micromill	micromill	micromill	micromill
dissolution method		final leach discard rinsing	final leach without rinsing	SSD	SSD	SSD	SSD	SSD	SSD	SSD	first leach without rinsing	first leach without rinsing	central leach without rinsing	central leach without rinsing	final leach without rinsing	final leach without rinsing
sampling depth (m)		366	366	123.6	142.5	341.3	123.6	138.7	112.55	138.7	112.55	112.55	112.55	112.55	112.55	112.55
stratigraphic formation		Micrite Unit	Micrite Unit	ABL	ABL	Micrite Unit	ABL	ABL	ABL	ABL	ABL	ABL	ABL	ABL	ABL	ABL
	unit															
Mg	µg/g	16390	16947	835	632	2639	5637	6083	5493	6635	6056	2809	3801	2309	8626	7797
Al	µg/g	344	314	9.1	38	9.3	456	4.2	3.1	9.7	0.1	0.1	4.9	0.04	9	11
P	µg/g	212	257	131	67	30	193	133	242	334	6.0	9.0	116	7.3	660	416
Ca	wt%	40	40	40	40	40	40	40	40	40	40	40	40	40	40	40
Sc	µg/g	2.05	2.43	0.18	0.22	0.18	0.79	0.16	0.11	0.16	0.09	0.09	0.08	0.08	0.34	0.19
Fe	µg/g	4872	4228	190	140	57	1972	156	181	218	4.1	7.2	150	12	417	425
Mn	µg/g	429	431	17	8.8	6.4	322	151	449	358	12	36	422	323	418	452
Rb	µg/g	0.62	0.70	0.04	0.17	0.07	0.99	0.03	0.03	0.05	0.27	0.13	0.02	0.02	0.04	0.05
Sr	µg/g	394	395	993	980	1069	1005	1178	1456	3782	4091	4744	466	1260	502	1080
Y	ng/g	8939	6892	290	193	31	4761	216	821	2873	43	49	726	13	949	1649
Cd	ng/g	26	21	3.9	6.0	1.2	3.1	14.8	1.3	3.2		0.1	1.8	0.1	5.5	4.1
Ba	ng/g	6761	6377	2959	3087	1448	3631	2648	273583	479646	489672	516573	47137	195875	49311	217471
La	ng/g	13557	9902	240	239	45	4133	167	694	2198	17	16	699	5.8	830	1268
Ce	ng/g	29822	21221	389	411	79	6527	223	1046	3432	2.3	0.7	954	0.1	1251	1880
Pr	ng/g	3642	2569	53	50	8.3	828	25	124	363	0.3	0.1	118	0.03	165	223
Nd	ng/g	13453	9510	198	178	31	3063	95	477	1409	2.4	2.0	442	0.4	613	852
Sm	ng/g	2610	1884	39	36	5.7	567	19	90	282	4.2	3.8	80	1.3	121	159
Eu	ng/g	544	393	22	8.7	1.1	135	3.5	49	84	41	45	25	16	37	64
Tb	ng/g	329	244	5.9	4.9	0.7	91	3.6	14	51	0.1	0.0	12	0.02	18	27
Gd	ng/g	2149	1566	40	30	4.8	581	24	95	350	0.3	0.1	83	0.1	126	178
Dy	ng/g	1824	1357	35	29	3.9	566	23	88	324	0.3	0.2	70	0.1	108	166
Ho	ng/g	350	258	7.1	5.5	0.6	124	5.2	19	74	0.0	0.0	16	0.01	24	38
Er	ng/g	889	659	18	14	1.5	345	16	55	212	0.1	0.1	44	0.1	64	106
Tm	ng/g	124	92	2.3	1.9	0.3	49	2.3	7.8	30	0.1	0.0	6.2	0.0	8.7	16
Yb	ng/g	739	558	14	12	1.2	280	14	49	184	0.2	0.1	36	0.1	53	95
Lu	ng/g	98	74	1.8	1.7	0.1	41	2.2	7.6	28	0.03	0.0	5.4	0.01	8.2	14
Hf	ng/g	12	15	0.3	0.9	0.4	2.8	0.1	0.2	1.0	0.1	0.3	0.3	0.1	1.7	0.3
Th	ng/g	1875	2164	10	12	5.4	163	3.2	14	25		5.0	12	0.6	77	31
Sr/Mn		0.9	0.9	59.2	111.1	165.8	3.1	7.8	3.2	10.6	339.6	131.1	1.1	3.9	1.2	2.4
Rb/Sr		0.00156	0.00177	0.00005	0.00017	0.00007	0.00098	0.00002	0.00002	0.00001	0.00007	0.00003	0.00003	0.00002	0.00007	0.00005
Y/Ho		26	27	41	35	52	39	42	42	39			46		40	43
ΣREE+Y	µg/g	79.07	57.18	1.36	1.21	0.21	22.09	0.84	3.64	11.90	0.11	0.12	3.32	0.04	4.37	6.74
$^{87}Sr/^{86}Sr$				0.707826	0.707816	0.707937	0.707945	0.707879	0.708454	0.708599			0.708121		0.708095	0.708571
SD				0.000034	0.000030	0.000039	0.000030	0.000029	0.000030	0.000031			0.000033		0.000038	0.000027

References

AITCHISON, J. 1982. The statistical analysis of compositional data. *Journal of the Royal Statistical Society: Series B (Methodological),* 44**,** 139-160.

AITCHISON, J. 1986. The statistical analysis of compositional data: Chapman Hall. *New York*.

ALLOWAY, B., LARSEN, G., LOWE, D., PAR, S. & WESTGATE, J. 2007. Tephrochronology. *Elias, SA (editor-in-chief) Encyclopaedia of Quaternary Science. Elsevier, London***,** 2869-2898.

ALTINOK, E. 2005. *Zn-Pb-Fe Mineralization process, evolution of sea water oxidation state in a restricted basin, and diagenesis of deep water calcareous sediments: geochemical and geological study of the Navan Deposit, Dublin Basin, Ireland.* PhD Thesis, Colorado School of Mines.

ANDERSON, I. K. 1990. *Ore depositional processes in the formation of the Navan zinc/lead deposit, Co. Meath, Ireland.* PhD Thesis, University of Strathclyde.

ANDREW, C. & ASHTON, J. 1985. Regional setting, geology and metal distribution patterns of Navan orebody, Ireland. *Transactions of the Institution of Mining and Metallurgy. Section B. Applied Earth Science,* 94**,** 66-93.

ANDREW, C. J. 1986. The tectono-stratigraphic controls to mineralization in the Silvermines area, County Tipperary, Ireland. *Geology and Genesis of Mineral Deposits in Ireland***,** 377-417.

ARCHER, J., SLEEMAN, A., SMITH, D., CLARINGBOLD, K., STANLEY, G. T. & WRIGHT, G. 1996. A Geological Description of Tipperary and Adjoining Parts of Laois Kilkenny, Offaly, Clare, and Limerick, to Accompany the Bedrock Geology 1: 100,000 scale Map Series, Sheet 18, Tipperary. *Claringbold, G. Stanley (Mineral Resources) and G. Wright (Groundwater Resources). Geological Survey Ireland,* 77.

ARETZ, M., HERBIG, H., WANG, X., GRADSTEIN, F., AGTERBERG, F. & OGG, J. 2020. The Carboniferous Period. *In:* GRADSTEIN, F. M., OGG, J. G., SCHMITZ, M. D. & OGG, G. M. (eds.) *Geologic Time Scale 2020.* Elsevier, Amsterdam, pp. 811-874.

ARSLAN, M., ABDİOĞLU, E. & KADİR, S. N. 2010. Mineralogy, geochemistry, and origin of bentonite in Upper Cretaceous pyroclastic units of the Tirebolu area, Giresun, northeast Turkey. *Clays and Clay Minerals,* 58**,** 120-141.

ASHTON, J., BEACH, A., BLAKEMAN, R., COLLER, D., HENRY, P., LEE, R., HITZMAN, M., HOPE, C., HULEATT-JAMES, S., O'DONOVAN, B. & PHILCOX, M. 2018. Discovery of the Tara Deep Zn-Pb Mineralization at the Boliden Tara Mine, Navan, Ireland: Success with Modern Seismic Surveys. *Society of Economic Geologists, Special Publication,* 21**,** 365-381.

ASHTON, J., BLACK, A., GERAGHTY, J., HOLDSTOCK, M. & HYLAND, E. 1992. The geological setting and metal distribution patterns of Zn-Pb-Fe mineralization in the Navan Boulder Conglomerate. *In:* BOWDEN, A. A., EARLS, G., O'CONNOR, P. G. & PYRNE, J. F. (eds.) *The Irish Minerals Industry 1980-1990.* Irish Association for Economic Geology, Dublin, 171-210

ASHTON, J., BLAKEMAN, R., GERAGHTY, J., BEACH, A., COLLER, D., PHILCOX, M., BOYCE, A. & WILKINSON, J. 2015. The giant Navan Carbonate-hosted Zn-Pb deposit: a review. *In:* ARCHIBALD, S. M. & PIERCEY, S. J. (eds.) *Current Perspectives on Zinc Deposits.* Irish Association for Economic Geology, Dublin, 85-122.

ASHTON, J., DOWNING, D. & FINLAY, S. 1986. The geology of the Navan Zn-Pb orebody. *Geology and Genesis of Mineral Deposits in Ireland: Dublin, Irish Association for Economic Geology***,** 243-280.

ASHTON, J., HOLDSTOCK, M., GERAGHTY, J., O'KEEFFE, W., MARTINEZ, N., PEACE, W. & PHILCOX, M. 2000. The Navan orebody discovery and geology of the SW extension. *Proceedings of the Irish Association of Economic Geology Millenium Conference on Europe's base metal deposits, Galway*.

ATANASOVA, P., MARKS, M. A., FRENZEL, M., GUTZMER, J., KRAUSE, J. & MARKL, G. 2020. Fractionation of geochemical twins (Zr/Hf, Nb/Ta and Y/Ho) and HREE-enrichment during magmatic and metamorphic processes in peralkaline nepheline syenites from Norra Kärr (Sweden). *Lithos,* 372**,** 105667.

BABECHUK, M. G., KAMBER, B. S., GREIG, A., CANIL, D. & KODOLÁNYI, J. 2010. The behaviour of tungsten during mantle melting revisited with implications for planetary differentiation time scales. *Geochimica et Cosmochimica Acta,* 74**,** 1448-1470.

BAILEY, T., MCARTHUR, J., PRINCE, H. & THIRLWALL, M. 2000. Dissolution methods for strontium isotope stratigraphy: whole rock analysis. *Chemical Geology,* 167**,** 313-319.

BAINBRIDGE, T. R. 1985. The committee on standards-precision and bias. *ASTM Standardization News,* 13**,** 44-46.

BANNER, J. L. 1995. Application of the trace element and isotope geochemistry of strontium to studies of carbonate diagenesis. *Sedimentology,* 42**,** 805-824.

BANNER, J. L., HANSON, G. & MEYERS, W. 1988. Determination of initial Sr isotopic compositions of dolostones from the Burlington-Keokuk Formation (Mississippian); constraints from cathodoluminescence, glauconite paragenesis and analytical methods. *Journal of Sedimentary Research,* 58**,** 673-687.

BANNER, J. L. & HANSON, G. N. 1990. Calculation of simultaneous isotopic and trace element variations during water-rock interaction with applications to carbonate diagenesis. *Geochimica et Cosmochimica Acta,* 54**,** 3123-3137.

BARHAM, M. 2010. *Controls on upper Viséan (Carboniferous) depositional environments in Ireland.* PhD Thesis, National University of Ireland Galway.

BATCHELOR, R. & JEPPSSON, L. 1999. Wenlock metabentonites from Gotland, Sweden: geochemistry, sources and potential as chemostratigraphic markers. *Geological Magazine,* 136**,** 661-669.

BAU, M. 1996. Controls on the fractionation of isovalent trace elements in magmatic and aqueous systems: evidence from Y/Ho, Zr/Hf, and lanthanide tetrad effect. *Contributions to Mineralogy and Petrology,* 123**,** 323-333.

BAU, M. & DULSKI, P. 1995. Comparative study of yttrium and rare-earth element behaviours in fluorine-rich hydrothermal fluids. *Contributions to Mineralogy and Petrology,* 119**,** 213-223.

BAU, M. & DULSKI, P. 1996. Distribution of yttrium and rare-earth elements in the Penge and Kuruman iron-formations, Transvaal Supergroup, South Africa. *Precambrian Research,* 79**,** 37-55.

BAU, M., KOSCHINSKY, A., DULSKI, P. & HEIN, J. R. 1996. Comparison of the partitioning behaviours of yttrium, rare earth elements, and titanium between hydrogenetic marine ferromanganese crusts and seawater. *Geochimica et Cosmochimica Acta,* 60**,** 1709-1725.

BAU, M., SCHMIDT, K., PACK, A., BENDEL, V. & KRAEMER, D. 2018. The European Shale: An improved data set for normalisation of rare earth element and yttrium concentrations in environmental and biological samples from Europe. *Applied Geochemistry,* 90**,** 142-149.

BEA, F. 1996. Residence of REE, Y, Th and U in granites and crustal protoliths; implications for the chemistry of crustal melts. *Journal of Petrology,* 37**,** 521-552.

BEA, F. & MONTERO, P. 1999. Behavior of accessory phases and redistribution of Zr, REE, Y, Th, and U during metamorphism and partial melting of metapelites in the lower crust: an example from the Kinzigite Formation of Ivrea-Verbano, NW Italy. *Geochimica et Cosmochimica Acta,* 63**,** 1133-1153.

BEA, F., MONTERO, P. & ORTEGA, M. 2006. A LA–ICP–MS evaluation of Zr reservoirs in common crustal rocks: Implications for Zr and Hf geochemistry, and zircon-forming processes. *The Canadian Mineralogist,* 44**,** 693-714.

BEGÉT, J., EDWARDS, M., HOPKINS, D., KESKINEN, M. & KUKLA, G. 1991. Old Crow tephra found at the Palisades of the Yukon, Alaska. *Quaternary Research,* 35**,** 291-297.

BELOUSOVA, E., GRIFFIN, W., O'REILLY, S. Y. & FISHER, N. 2002a. Apatite as an indicator mineral for mineral exploration: trace-element compositions and their relationship to host rock type. *Journal of Geochemical Exploration,* 76**,** 45-69.

BELOUSOVA, E., GRIFFIN, W. L., O'REILLY, S. Y. & FISHER, N. 2002b. Igneous zircon: trace element composition as an indicator of source rock type. *Contributions to Mineralogy and Petrology,* 143**,** 602-622.

BELOUSOVA, E., WALTERS, S., GRIFFIN, W. & O'REILLY, S. 2001. Trace-element signatures of apatites in granitoids from the Mt Isa Inlier, northwestern Queensland. *Australian Journal of Earth Sciences,* 48**,** 603-619.

BIRCK, J. L. 1986. Precision K-Rb-Sr isotopic analysis: application to Rb-Sr chronology. *Chemical Geology,* 56**,** 73-83.

BLANEY, D. 2019. Technical Report on the Irish Zinc Exploration Project of Minco Exploration Limited a subsidiary of Buchans Resources Limited, dated 29 October 2019.

BOHOR, B. F., PHILLIPS, R. E. & POLLASTRO, R. M. 1979. Altered volcanic ash partings in Wasatch Formation coal beds of the northern Powder River basin: Composition and geologic applications. US Geological Survey.

BOHOR, B. F. & TRIPLEHORN, D. M. 1993. *Tonsteins: altered volcanic ash layers in coal-bearing sequences*, Geological Society of America, Special Paper 285, 44 pp.

BONSON, C., WALSH, J. & CARBONI, V. 2012. The role of faults in localising mineral deposits in the Irish Zn-Pb orefield [extended abstract]. *Australian Institute of Geologists Bulletin,* 56**,** 8-11.

BOWRING, S. A., ERWIN, D., JIN, Y., MARTIN, M., DAVIDEK, K. & WANG, W. 1998. U/Pb zircon geochronology and tempo of the end-Permian mass extinction. *Science,* 280**,** 1039-1045.

BOWRING, S. A., SCHOENE, B., CROWLEY, J. L., RAMEZANI, J. & CONDON, D. J. 2006. High-precision U-Pb zircon geochronology and the stratigraphic record: Progress and promise. *The Paleontological Society Papers,* 12**,** 25-45.

BRAITHWAITE, C. & RIZZI, G. 1997. The geometry and petrogenesis of hydrothermal dolomites at Navan, Ireland. *Sedimentology,* 44**,** 421-440.

BRAND, U. 2004. Carbon, oxygen and strontium isotopes in Paleozoic carbonate components: an evaluation of original seawater-chemistry proxies. *Chemical Geology,* 204**,** 23-44.

BRAND, U., AZMY, K., TAZAWA, J.-I., SANO, H. & BUHL, D. 2010. Hydrothermal diagenesis of Paleozoic seamount carbonate components. *Chemical Geology,* 278**,** 173-185.

BRAND, U., JIANG, G., AZMY, K., BISHOP, J. & MONTAÑEZ, I. P. 2012. Diagenetic evaluation of a Pennsylvanian carbonate succession (Bird Spring Formation, Arrow Canyon, Nevada, USA)—1: Brachiopod and whole rock comparison. *Chemical Geology,* 308**,** 26-39.

BRAND, U. & VEIZER, J. 1980. Chemical diagenesis of a multicomponent carbonate system; 1, Trace elements. *Journal of Sedimentary Research,* 50**,** 1219-1236.

BRANDON, A. & HODSON, F. 1984. *The stratigraphy and palaeontology of the late Viséan and early Namurian rocks of north-east Connaught*, Geological Survey of Ireland, Special Paper Number 6.

BROWNE, M., DEAN, M., HALL, I. H., MCADAM, A., MONRO, S. & CHISHOLM, J. 1999. A lithostratigraphical framework for the Carboniferous rocks of the Midland Valley of Scotland. *British Geological Survey, Technical Report, RR/99/07*.

BRUAND, E., FOWLER, M., STOREY, C. & DARLING, J. 2017. Apatite trace element and isotope applications to petrogenesis and provenance. *American Mineralogist,* 102**,** 75-84.

BRÜCK, P., GARDINER, P., REEVES, T., SHANNON, P., COLTHURST, J., FEELY, M., PENNEY, S., SMITH, D. & VANGUESTAINE, M. 1979. South-east Ireland: Lower Palaeozoic stratigraphy and depositional history. *Geological Society, London, Special Publications,* 8**,** 533-544.

BRUCKSCHEN, P., BRUHN, F., VEIZER, J. & BUHL, D. 1995. 87Sr86Sr isotopic evolution of Lower Carboniferous seawater: Dinantian of western Europe. *Sedimentary Geology,* 100**,** 63-81.

BRUCKSCHEN, P., OESMANN, S. & VEIZER, J. 1999. Isotope stratigraphy of the European Carboniferous: proxy signals for ocean chemistry, climate and tectonics. *Chemical Geology,* 161**,** 127-163.

BURDA, J. & GAWĘDA, A. 2009. Shear-influenced partial melting in the Western Tatra metamorphic complex: geochemistry and geochronology. *Lithos,* 110**,** 373-385.

BYRNE, R. H., LIU, X. & SCHIJF, J. 1996. The influence of phosphate coprecipitation on rare earth distributions in natural waters. *Geochimica et Cosmochimica Acta,* 60**,** 3341-3346.

CABALLERO, E., REYES, E., DELGADO, A., HUERTAS, F. & LINARES, J. 1992. The formation of bentonite: mass balance effects. *Applied Clay Science,* 6**,** 265-276.

CAI, G., NOGUCHI, T., DEGÉE, H., ZHAO, J. & KITAGAKI, R. 2016. Volcano-related materials in concretes: a comprehensive review. *Environmental Science and Pollution Research,* 23**,** 7220-7243.

CALARGE, L. M., MEUNIER, A., LANSON, B. & FORMOSO, M. L. 2006. Chemical signature of two Permian volcanic ash deposits within a bentonite bed from Melo, Uruguay. *Anais da Academia Brasileira de Ciências,* 78**,** 525-541.

CALDWELL, W. G. E. 1959. The Lower Carboniferous rocks of the Carrick-on-Shannon syncline. *Quarterly Journal of the Geological Society,* 115**,** 163-188.

CARBONI, V., WALSH, J., STEWART, D., GÜVEN, J. & ELIOPOULOS, D. 2003. Timing and geometry of normal faults and associated structures at the Lisheen Zn/Pb deposit, Ireland—investigating their role in the transport and the trapping of metals. *Society for Geology Applied to Mineral Deposits Meeting, 7th biennial, Athens, Greece, Proceedings***,** 665-668.

CAREY, A., SAMSON, S. D. & SELL, B. 2009. Utility and limitations of apatite phenocryst chemistry for continent-scale correlation of Ordovician K-bentonites. *The Journal of Geology,* 117**,** 1-14.

CARRON, J.-P., DE KERNEIZON, M. L. G. & NACHIT, H. 1994. Variscan granites from Brittany. *Pre-Mesozoic geology in France and related areas.* Springer.

CERLING, T. E., BROWN, F. H. & BOWMAN, J. R. 1985. Low-temperature alteration of volcanic glass: hydration, Na, K, 18O and Ar mobility. *Chemical Geology: Isotope Geoscience Section,* 52**,** 281-293.

CHAKHMOURADIAN, A. R., REGUIR, E. P., ZAITSEV, A. N., COUËSLAN, C., XU, C., KYNICKÝ, J., MUMIN, A. H. & YANG, P. 2017. Apatite in carbonatitic rocks: Compositional variation, zoning, element partitioning and petrogenetic significance. *Lithos,* 274**,** 188-213.

CHEN, J., ALGEO, T. J., ZHAO, L., CHEN, Z.-Q., CAO, L., ZHANG, L. & LI, Y. 2015. Diagenetic uptake of rare earth elements by bioapatite, with an example from Lower Triassic conodonts of South China. *Earth-Science Reviews,* 149**,** 181-202.

CHERNIAK, D. & WATSON, E. 2001. Pb diffusion in zircon. *Chemical Geology,* 172**,** 5-24.

CHEW, D. 2009. Grampian orogeny. *In:* HOLLAND, C. & SANDERS, I. (eds.) *The Geology of Ireland, Second Edition. Dunedin Academic Press, Edinburgh, 69-93.*

CHEW, D., PETRUS, J. & KAMBER, B. 2014. U–Pb LA–ICPMS dating using accessory mineral standards with variable common Pb. *Chemical Geology,* 363**,** 185-199.

CHEW, D. M., BABECHUK, M. G., COGNÉ, N., MARK, C., O'SULLIVAN, G. J., HENRICHS, I. A., DOEPKE, D. & MCKENNA, C. A. 2016. (LA, Q)-ICPMS trace-element analyses of Durango and McClure Mountain apatite and implications for making natural LA-ICPMS mineral standards. *Chemical Geology,* 435**,** 35-48.

CHEW, D. M., SYLVESTER, P. J. & TUBRETT, M. N. 2011. U–Pb and Th–Pb dating of apatite by LA-ICPMS. *Chemical Geology,* 280**,** 200-216.

CHRISTIDIS, G. E. 1998. Comparative study of the mobility of major and trace elements during alteration of an andesite and a rhyolite to bentonite, in the islands of Milos and Kimolos, Aegean, Greece. *Clays and Clay minerals,* 46**,** 379-399.

CHU, M.-F., WANG, K.-L., GRIFFIN, W. L., CHUNG, S.-L., O'REILLY, S. Y., PEARSON, N. J. & IIZUKA, Y. 2009. Apatite composition: tracing petrogenetic processes in Transhimalayan granitoids. *Journal of Petrology,* 50**,** 1829-1855.

CHYI, L. L. 1986. Characteristics and genesis of zirconium and hafnium deposits. *Mineral Parageneses. Theophrastus Publications SA, Athens***,** 387-408.

CLAIBORNE, L. L., MILLER, C., WALKER, B., WOODEN, J., MAZDAB, F. & BEA, F. 2006. Tracking magmatic processes through Zr/Hf ratios in rocks and Hf and Ti zoning in zircons: an example from the Spirit Mountain batholith, Nevada. *Mineralogical Magazine,* 70**,** 517-543.

CLAVERIE, F., FERNÁNDEZ, B., PÉCHEYRAN, C., ALEXIS, J. & DONARD, O. F. 2009. Elemental fractionation effects in high repetition rate IR femtosecond laser ablation ICP-MS analysis of glasses. *Journal of Analytical Atomic Spectrometry,* 24**,** 891-902.

CLAYTON, G., HIGGS, K., GUEINN, K. J. & VAN GELDER, A. 1974. Palynological Correlations in the Cork Beds (Upper Devonian-?Upper Cabboniferous) of Southern Ireland. *Proceedings of the Royal Irish Academy,* 74**,** 145-155.

CLAYTON, G., JOHNSTON, I. & SMITH, D. 1980. Micropalaeontology of a Courceyan (Carboniferous) borehole section from Ballyvergin, County Clare, Ireland. *Journal of Earth Sciences***,** 81-100.

CLAYTON, T., FRANCIS, J., HILLIER, S., HODSON, F., SAUNDERS, R. & STONE, J. 1996. The implications of reworking on the mineralogy and chemistry of Lower Carboniferous K-bentonites. *Clay Minerals,* 31**,** 377-390.

CORYELL, C. D., CHASE, J. W. & WINCHESTER, J. W. 1963. A procedure for geochemical interpretation of terrestrial rare-earth abundance patterns. *Journal of Geophysical Research,* 68**,** 559-566.

COULON, M., FOURQUIN, C. & PAICHELER, J.-C. 1979. Contribution à la connaissance du tectorogène varisque dans les Vosges méridionales. Ill—Le Culm entre Bourbach-le-Haut et le Molkenrain (Vosges méridionales). *Sciences Géologiques, Bulletins et Mémoires,* 32**,** 117-129.

COULON, M., FOURQUIN, C., PAICHELER, J.-C. & POINT, R. 1975. Contribution à la connaissance du tectorogène varisque dans les Vosges méridionales—II. Le Culm de la région comprise entre Giromagny et Bourbach-le-Bas (partie occidentale de la feuille à 1/50 000 de Thann). *Sciences Géologiques, Bulletins et Mémoires,* 28**,** 109-140.

CUMMINS, D. & ELDERFIELD, H. 1994. The strontium isotopic composition of Brigantian (late Dinantian) seawater. *Chemical Geology,* 118**,** 255-270.

DAI, S., WARD, C. R., GRAHAM, I. T., FRENCH, D., HOWER, J. C., ZHAO, L. & WANG, X. 2017. Altered volcanic ashes in coal and coal-bearing sequences: A review of their nature and significance. *Earth-Science Reviews,* 175**,** 44-74.

DALY, J. S., MURPHY, M. D., STROGEN, P., HOELTTAE, P., VAASJOKI, M. & 1993. Sm–Nd dating of metamorphic garnet: case studies from contrasting settings. Terra Abstracts, Abstract Supplement No 1 to Terra Nova 5, 385.

DAVIS, D. W. 1982. Optimum linear regression and error estimation applied to U–Pb data. *Canadian Journal of Earth Sciences,* 19**,** 2141-2149.

DAVYDOV, V. I., CROWLEY, J. L., SCHMITZ, M. D. & POLETAEV, V. I. 2010. High-precision U-Pb zircon age calibration of the global Carboniferous time scale and Milankovitch band cyclicity in the Donets basin, eastern Ukraine. *Geochemistry, Geophysics, Geosystems,* 11.

DDANI, M., MEUNIER, A., ZAHRAOUI, M., BEAUFORT, D., EL WARTITI, M., FONTAINE, C., BOUKILI, B. & EL MAHI, B. 2005. Clay mineralogy and chemical composition of bentonites from the Gourougou volcanic massif (northeast Morocco). *Clays and Clay Minerals,* 53**,** 250-267.

DENISON, R., KOEPNICK, R., FLETCHER, A., HOWELL, M. & CALLAWAY, W. 1994. Criteria for the retention of original seawater 87Sr86Sr in ancient shelf limestones. *Chemical Geology,* 112**,** 131-143.

DEPAOLO, D. J. & INGRAM, B. L. 1985. High-resolution stratigraphy with strontium isotopes. *Science,* 227**,** 938-941.

DERRY, L., BRASIER, M., CORFIELD, R. E. A., ROZANOV, A. Y. & ZHURAVLEV, A. Y. 1994. Sr and C isotopes in Lower Cambrian carbonates from the Siberian craton: a paleoenvironmental record during the 'Cambrian explosion'. *Earth and Planetary Science Letters,* 128**,** 671-681.

DESPRAIRIES, A. & BONNOT-COURTOIS, C. 1980. Relation entre la composition des smectites d'altération sous-marine et leur cortège de terres rares. *Earth and Planetary Science Letters,* 48**,** 124-130.

DEVUYST, F.-X., HANCE, L., HOU, H., WU, X., TIAN, S., COEN, M. & SEVASTOPULO, G. 2003. A proposed global stratotype section and point for the base of the Visean stage (Carboniferous): the Pengchong section, Guangxi, South China. *Episodes,* 26**,** 105-115.

DICKSON, J., FORD, T. & SWIFT, A. 1987. The stratigraphy of the Carboniferous rocks around Castletown, Isle of Man. *Proceedings of the Yorkshire Geological Society,* 46**,** 203-228.

DILL, H. 1994. Can REE patterns and U-Th variations be used as a tool to determine the origin of apatite in clastic rocks? *Sedimentary Geology,* 92**,** 175-196.

DOEPKE, D. 2017. *Modelling the thermal history of onshore Ireland, Britain and its offshore basins using low-temperature thermochronology.* PhD Thesis, Trinity College Dublin.

EGGINS, S., WOODHEAD, J., KINSLEY, L., MORTIMER, G., SYLVESTER, P., MCCULLOCH, M., HERGT, J. & HANDLER, M. 1997. A simple method for the precise determination of≥ 40 trace elements in geological samples by ICPMS using enriched isotope internal standardisation. *Chemical Geology,* 134**,** 311-326.

EGGINS, S. M., KINSLEY, L. & SHELLEY, J. 1998. Deposition and element fractionation processes during atmospheric pressure laser sampling for analysis by ICP-MS. *Applied Surface Science,* 127**,** 278-286.

EL KORH, A., SCHMIDT, S. T., ULIANOV, A. & POTEL, S. 2009. Trace element partitioning in HP–LT metamorphic assemblages during subduction-related metamorphism, Ile de Groix, France: a detailed LA-ICPMS study. *Journal of Petrology,* 50**,** 1107-1148.

ELDERFIELD, H., UPSTILL-GODDARD, R. & SHOLKOVITZ, E. 1990. The rare earth elements in rivers, estuaries, and coastal seas and their significance to the composition of ocean waters. *Geochimica et Cosmochimica Acta,* 54**,** 971-991.

EMD Report 2006. "Zinc and Lead in Ireland"; Report from the Exploration and Mining Division Ireland of the Department of Communications, Climate Action and Environment.

EMERSON, N. R., SIMO, J. T., BYERS, C. W. & FOURNELLE, J. 2004. Correlation of (Ordovician, Mohawkian) K-bentonites in the upper Mississippi valley using apatite chemistry: implications for stratigraphic interpretation of the mixed carbonate-siliciclastic Decorah Formation. *Palaeogeography, Palaeoclimatology, Palaeoecology,* 210**,** 215-233.

ENGWELL, S. L., SPARKS, R. & CAREY, S. 2014. Physical characteristics of tephra layers in the deep sea realm: the Campanian Ignimbrite eruption. *Geological Society, London, Special Publications,* 398**,** 47-64.

ERSOY, Y., HELVACı, C., SÖZBILIR, H., ERKÜL, F. & BOZKURT, E. 2008. A geochemical approach to Neogene–Quaternary volcanic activity of western Anatolia: an example of episodic bimodal volcanism within the Selendi Basin, Turkey. *Chemical Geology,* 255**,** 265-282.

FALLICK, A. E., ASHTON, J. H., BOYCE, A. J., ELLAM, R. M. & RUSSELL, M. J. 2001. Bacteria were responsible for the magnitude of the world-class hydrothermal base metal sulfide orebody at Navan, Ireland. *Economic Geology,* 96**,** 885-890.

FALLON, P. & MURRAY, J. 2015. Conodont biostratigraphy of the mid-Carboniferous boundary in Western Ireland. *Geological Magazine,* 152**,** 1025-1042.

FANTLE, M. S. & HIGGINS, J. 2014. The effects of diagenesis and dolomitization on Ca and Mg isotopes in marine platform carbonates: implications for the geochemical cycles of Ca and Mg. *Geochimica et Cosmochimica Acta,* 142**,** 458-481.

FAULKNER, T. 1989. The early Carboniferous (Courceyan) Middle Hope volcanics of Weston-super-Mare: development and demise of an offshore volcanic high. *Proceedings of the Geologists' Association,* 100**,** 93-106.

FAURE, G. 1986. Principles of isotope geology. Wiley, New York, 589p.

FINGER, F., ROBERTS, M., HAUNSCHMID, B., SCHERMAIER, A. & STEYRER, H.-P. 1997. Variscan granitoids of central Europe: their typology, potential sources and tectonothermal relations. *Mineralogy and Petrology,* 61**,** 67-96.

FLEET, A. 1984. Aqueous and sedimentary geochemistry of the rare earth elements. *Developments in Geochemistry.* Elsevier.

FLEISCHER, M. & ALTSCHULER, Z. 1986. The lanthanides and yttrium in minerals of the apatite group-an analysis of the available data. *Neues Jahrbuch für Mineralogie, Monatshefte***,** 467-480.

FORD, C. V. 1996. *The integration of petrologic and isotopic data from the Boulder Conglomerate to determine the age of the Navan orebody, Ireland.* PhD Thesis, University of Glasgow.

FORD, D. & GOLONKA, J. 2003. Phanerozoic paleogeography, paleoenvironment and lithofacies maps of the circum-Atlantic margins. *Marine and Petroleum Geology,* 20**,** 249-285.

FRANCIS, E. 1991. Carboniferous-Permian igneous rocks. *In:* CRAIG, G. Y. (ed.) *Geology of Scotland.* 3rd edition, The Geological Society, London, 393-420.

FRANKE, W. 1989. Tectonostratigraphic units in the Variscan belt of central Europe. *Geological Society of America, Special Paper,* 230**,** 67-90.

FRANKE, W. 1992. Phanerozoic structures and events in Central Europe. *In:* BLUNDELL, D., FREEMAN, R. & MUELLER, S. (eds.) *A continent revealed: the European Geotraverse.* Cambridge University Press, Cambridge, 164-179.

FRASER, A. J. & GAWTHORPE, R. 1990. Tectono-stratigraphic development and hydrocarbon habitat of the Carboniferous in northern England. *In:* HARDMAN, R. & BROOKS, J. (eds.) *Tectonic events responsible for Britain's Oild and Gas Rserves.* Geological Society, London, Special Publications 55: 49-86.

FRASER, A. J. & GAWTHORPE, R. L. 2003. *An atlas of Carboniferous basin evolution in northern England*, Geological Society.

FRYER, B. J., JACKSON, S. E. & LONGERICH, H. P. 1995. The design, operation and role of the laser-ablation microprobe coupled with an inductively coupled plasma; mass spectrometer (LAM-ICP-MS) in the earth sciences. *The Canadian Mineralogist,* 33**,** 303-312.

FUSCIARDI, L., GUVEN, J., STEWART, D., CARBONI, V. & WALSH, J. 2003. The geology and genesis of the Lisheen Zn-Pb deposit, Co. Tipperary, Ireland. *In:* KELLY, J., ANDREW, C., ASHTON, J., BOLAND, M., EARLS, G., FUSCIARDI, L. & STANLEY, G. (eds.) *Europe's major base metal deposits.* Dublin, Irish Association for Economic Geology, 455-481.

GATLEY, S., SOMERVILLE, I., MORRIS, J., SLEEMAN, A. & EMO, G. 2004. Geology of Galway—Offaly, and Adjacent Parts of Westmeath, Tipperary, Laois, Clare and Roscommon: A Geological Description to Accompany the Bedrock Geology 1: 100 000 Scale Map Series, Sheet 15, Galway—Offaly. Geological Survey of Ireland Dublin.

GAWTHORPE, R., GUTTERIDGE, P. & LEEDER, M. 1989. Late Devonian and Dinantian basin evolution in northern England and North Wales. *In:* ARTHURTON, R., GUTTERIDGE, P. & NOLAN, S. (eds.) *The Role of Tectonics in Devonian and Carboniferous Sedimentation in the British Isles.* Yorkshire Geological Society, Occasional Publication, 6, 1-23.

GEORGE, T., JOHNSON, G., PRENTICE, J., MITCHELL, M., RAMSBOTTOM, W., SEVASTOPULO, G. & WILSON, R. 1976. A correlation of Dinantian rocks in the British Isles. *Special Report of the Geological Society, London***,** 7, 86 pp.

GERMAN, C. R. & ELDERFIELD, H. 1990. Application of the Ce anomaly as a paleoredox indicator: the ground rules. *Paleoceanography,* 5**,** 823-833.

GOLDMAN, D., MITCHELL, C. E., BERGSTROM, S. M., DELANO, J. W. & TICE, S. 1994. K-bentonites and graptolites biostratigraphy in the Middle Ordovician of New York State and Quebec; a new chronostratigraphic model. *Palaios,* 9**,** 124-143.

GOLDSCHMIDT, V. M. & BARTH, T. F. W. 1925. *Geochemische Verteilungsgesetze der Elemente. 5. 5,* Oslo, Kristiania, Ja. Dybwad.

GOLDSTEIN, S. J. & JACOBSEN, S. B. 1988. Rare earth elements in river waters. *Earth and Planetary Science Letters,* 89**,** 35-47.

GOLONKA, J. 2000. *Cambrian-Neogene plate tectonic maps*, Kraków: Wydawnictwo Uniwersytetu Jagiellońskiego.

GOLONKA, J. 2002. Plate-tectonic maps of the Phanerozoic. *In:* W. KIESSLING, W., FLÜGEL, E. & GOLONKA, J. (eds.) *Phanerozoic Reef Patterns.* Society for Sedimentary Geology, Special Publication, 72, 21–75.

GOLONKA, J. 2009. Phanerozoic paleoenvironment and paleolithofacies maps: Early Paleozoic. *Geologia/Akademia Górniczo-Hutnicza im. Stanisława Staszica w Krakowie,* 35**,** 589-654.

GOLONKA, J., KROBICKI, M., OSZCZYPKO, N., ŚLĄCZKA, A. & SŁOMKA, T. 2003. Geodynamic evolution and palaeogeography of the Polish Carpathians and adjacent areas during Neo-Cimmerian and preceding events (latest Triassic-earliest Cretaceous). *In:* MCCANN, T. & SAINTOT, A. (eds.) *Tracing tectonic deformation using the sedimentary record.* Geological Society, London, Special Publication, 208, 138-158.

GÖNCÜOGLU, M., GÜNAL-TÜRKMENOGLU, A., BOZKAYA, Ö., ÜNLÜCE-YÜCEL, Ö., OKUYUCU, C. & YILMAZ, İ. 2016. Geological features and geochemical characteristics of Late Devonian–Early Carboniferous K-bentonites from northwestern Turkey. *Clay Minerals,* 51**,** 539-562.

GORDON, P., KELLY, J. & VANLENTE, B. 2018. NI 43-101 Independent report on the zinc-lead exploration project at Stonepark, county Limerick, Ireland; Technical Report for Group Eleven Resources Corp. *SLR*.

GOROKHOV, I., SEMIKHATOV, M., BASKAKOV, A., KUTYAVIN, E., MEL'NIKOV, N., SOCHAVA, A. & TURCHENKO, T. 1995. Sr isotopic composition in Riphean, Vendian, and Lower Cambrian carbonates from Siberia. *Stratigraphy and Geological Correlation,* 3**,** 1-28.

GOVINDARAJU, K. 1989. 1989 compilation of working values and sample description for 272 geostandards. *Geostandards Newsletter,* 13**,** 1-113.

GRAHAM, J. 2009. Devonian. *In:* HOLAND, C. H. & SANDERS, I. S. (eds.) *The Geology of Ireland, second edition.* Dunedin Academic Press Ltd, Edinburgh, 175-214.

GREVENITZ, P., CARR, P. & HUTTON, A. 2003. Origin, alteration and geochemical correlation of Late Permian airfall tuffs in coal measures, Sydney Basin, Australia. *International Journal of Coal Geology,* 55**,** 27-46.

GRIMES, C., WOODEN, J., CHEADLE, M. & JOHN, B. 2015. "Fingerprinting" tectono-magmatic provenance using trace elements in igneous zircon. *Contributions to Mineralogy and Petrology,* 170**,** 46.

GROMET, L. P., HASKIN, L. A., KOROTEV, R. L. & DYMEK, R. F. 1984. The "North American shale composite": its compilation, major and trace element characteristics. *Geochimica et Cosmochimica Acta,* 48**,** 2469-2482.

GUDMUNDSSON, M. T., THORDARSON, T., HÖSKULDSSON, Á., LARSEN, G., BJÖRNSSON, H., PRATA, F. J., ODDSSON, B., MAGNÚSSON, E., HÖGNADÓTTIR, T. & PETERSEN, G. N. 2012. Ash generation and distribution from the April-May 2010 eruption of Eyjafjallajökull, Iceland. *Scientific reports,* 2**,** 1-12.

GUELDENPFENNIG, M. & LOESCHKE, J. 1991. Petrographie und Geochemie unterkarbonischer Grauwacken und Vulkanite der Zone von Badenweiler-Lenzkirch in der Umgebung von Präg (Südschwarzwald). *Jahreshefte des Geologischen Landesamtes in Baden-Württemberg,* 33**,** 5-32.

GUILLONG, M. & GÜNTHER, D. 2002. Effect of particle size distribution on ICP-induced elemental fractionation in laser ablation-inductively coupled plasma-mass spectrometry. *Journal of Analytical Atomic Spectrometry,* 17**,** 831-837.

GUION, P., GUTTERIDGE, P. & DAVIES, S. 2000. Carboniferous sedimentation and volcanism on the Laurussian margin. *In:* WOODCOCK, N. & STRACHAN, R. (eds.) *Geological History of Britain and Ireland.* Blackwell Science Oxford, 227-270.

HAMBLIN, R., COPPACK, B. & CALVER, M. 1995. *Geology of Telford and the Coalbrookdale Coalfield: Memoir for Parts of 1: 50 000 Geological Sheets 152 and 153 (England and Wales): 1: 25 000 Sheet SJ 60 with Parts of 61, 70, 71*, HM Stationery Office.

HAMILTON, L. 1992. The oldest abundant volcanic glass on Earth. *Australian Journal of Earth Sciences,* 39**,** 55-59.

HANCE, L., POTY, E. & DEVUYST, F.-X. 2006. Ivorian. *Geologica Belgica,* 9/1-2, 55-62.

HARVEY, J. C. 2014. Zircon age and oxygen isotopic correlations between Bouse Formation tephra and the Lawlor Tuff. *Geosphere,* 10**,** 221-232.

HATTENDORF, B., LATKOCZY, C. & GÜNTHER, D. 2003. Llaser ablation-ICPMS. *Analytical Chemistry,* 75 (15)**,** 341A-347A.

HAYNES, J. T. 1994. The Ordovician Deicke and Millbrig K-bentonite beds of the Cincinnati Arch and the southern Valley and Ridge Province. *Geological Society of America, Special Paper 290***,** 80 pp.

HEAMAN, L. M., BOWINS, R. & CROCKET, J. 1990. The chemical composition of igneous zircon suites: implications for geochemical tracer studies. *Geochimica et Cosmochimica Acta,* 54**,** 1597-1607.

HECKEL, P. H. & CLAYTON, G. 2006. The Carboniferous System. Use of the new official names for the subsystems, series, and stages. *Geologica Acta,* 4**,** 0403-407.

HENES-KLAIBER, U. 1989. Der Odenwald: Hinweise auf einen variszischen Arc-Magmatismus? *Berichte der Deutschen Mineralogischen Gesellschaft*.

HENES-KLAIBER, U. 1992. *Zur Geochemie der variskischen Granite des Bergstraesser Odenwalds.* PhD Thesis, University of Karlsruhe.

HENRICHS, I. A., O'SULLIVAN, G., CHEW, D. M., MARK, C., BABECHUK, M. G., MCKENNA, C. & EMO, R. 2018. The trace element and U-Pb systematics of metamorphic apatite. *Chemical Geology,* 483**,** 218-238.

HINTS, R., KIRSIMÄE, K., SOMELAR, P., KALLASTE, T. & KIIPLI, T. 2008. Multiphase Silurian bentonites in the Baltic palaeobasin. *Sedimentary Geology,* 209**,** 69-79.

HITZMAN, M. 1995. Mineralization in the Irish Zn-Pb-(Ba-Ag) orefield. *Society of Economic Geologists, Guidebook Series,* 21**,** 25-61.

HITZMAN, M. & BEATY, D. 1996. The Irish Zn-Pb-(Ba) orefield. *In:* SANGSTER, D. F. (ed.) *Carbonate-Hosted Lead-Zinc Deposits.* Society of Economic Geologists, Special Publication 4, 112-143.

HITZMAN, M., O'CONNOR, P., SHEARLEY, E., SCHAFFALITZKY, C., BEATY, D., ALLAN, J. & THOMPSON, T. 1992. Discovery and geology of the Lisheen Zn-Pb/Ag prospect, Rathdowney Trend, Ireland. *In:* BOWDEN, A. A., EARLS, G., O'CONNOR, P. G. & PYNE, J. F. (eds.) *The Irish Minerals Industry 1980-1990.* Irish Association for Economic Geology, Dublin, 227-246.

HITZMAN, M., REDMOND, P. & BEATY, D. 2002. The carbonate-hosted Lisheen Zn-Pb-Ag deposit, County Tipperary, Ireland. *Economic Geology,* 97**,** 1627-1655.

HITZMAN, M. W. & LARGE, D. 1986. A review and classification of the Irish carbonate-hosted base metal deposits. *In:* ANDREW, C., CROWE, R., FINLEY, S., PENNELL, W. & PYNE, J. (eds.) *Geology and genesis of mineral deposits in Ireland.* Irish Association of Economic Geologists, Dublin, 217-238.

HNATYSHIN, D., CREASER, R. A., WILKINSON, J. J. & GLEESON, S. A. 2015. Re-Os dating of pyrite confirms an early diagenetic onset and extended duration of mineralization in the Irish Zn-Pb ore field. *Geology,* 43**,** 143-146.

HODSON, M. E. 2002. Experimental evidence for mobility of Zr and other trace elements in soils. *Geochimica et Cosmochimica Acta,* 66**,** 819-828.

HOLUB, F. V., COCHERIE, A. & ROSSI, P. 1997. Radiometric dating of granitic rocks from the Central Bohemian Plutonic Complex (Czech Republic): constraints on the chronology of thermal and tectonic events along the Moldanubian-Barrandian boundary. *Comptes Rendus de L'Academie des Sciences-Series IIA-Earth and Planetary Science,* 325**,** 19-26.

HONG, H., ALGEO, T. J., FANG, Q., ZHAO, L., JI, K., YIN, K., WANG, C. & CHENG, S. 2019. Facies dependence of the mineralogy and geochemistry of altered volcanic ash beds: An example from Permian-Triassic transition strata in southwestern China. *Earth-Science Reviews,* 190**,** 58-88.

HONG, H., FANG, Q., WANG, C., GONG, N. & ZHAO, L. 2017. Constraints of parent magma on altered clay minerals: a case study on the ashes near the Permian-Triassic Boundary in Xinmin section, Guizhou Province. *Earth Science,* 42**,** 161-172.

HONG, H., FANG, Q., ZHAO, L., SCHOEPFER, S., WANG, C., GONG, N., LI, Z. & CHEN, Z.-Q. 2016. Weathering and alteration of volcanic ashes in various depositional settings during the Permian-Triassic transition in South China: Mineralogical, elemental and isotopic approaches. *Palaeogeography, Palaeoclimatology, Palaeoecology,* 486**,** 46-57.

HONG, H., WANG, C., ZENG, K., GU, Y., WU, Y., YIN, K. & LI, Z. 2013. Geochemical constraints on provenance of the mid-Pleistocene red earth sediments in subtropical China. *Sedimentary Geology,* 290**,** 97-108.

HONG, H., ZHANG, N., ZHAOHUI, L., XUE, H., XIA, W. & YU, N. 2008. Clay mineralogy across the PT boundary of the Xiakou section, China: Evidence of clay provenance and environment. *Clays and Clay Minerals,* 56**,** 131-143.

HÖNISCH, B., ALLEN, K. A., RUSSELL, A. D., EGGINS, S. M., BIJMA, J., SPERO, H. J., LEA, D. W. & YU, J. 2011. Planktic foraminifers as recorders of seawater Ba/Ca. *Marine Micropaleontology,* 79**,** 52-57.

HORSTWOOD, M. 2008. Data reduction strategies, uncertainty assessment and resolution of LA-(MC-) ICP-MS isotope data. *In:* SYLVESTER, P. (ed.) *Laser Ablation ICP-MS in the Earth Sciences: Current Practices and Outstanding issues.* Mineralogical Association of Canada, 40, 283-303.

HOSKIN, P. W. & IRELAND, T. R. 2000. Rare earth element chemistry of zircon and its use as a provenance indicator. *Geology,* 28**,** 627-630.

HOSKIN, P. W., KINNY, P. D., WYBORN, D. & CHAPPELL, B. W. 2000. Identifying accessory mineral saturation during differentiation in granitoid magmas: an integrated approach. *Journal of Petrology,* 41**,** 1365-1396.

HOSKIN, P. W. & SCHALTEGGER, U. 2003. The composition of zircon and igneous and metamorphic petrogenesis. *Reviews in Mineralogy and Geochemistry,* 53**,** 27-62.

HOWARTH, R. J. & MCARTHUR, J. M. 1997. Statistics for strontium isotope stratigraphy: A robust LOWESS fit to the marine Sr-isotope curve for 0 to 206 Ma, with look-up table for derivation of numeric age. *The Journal of Geology,* 105**,** 441-456.

HSIEH, P.-S., CHEN, C.-H., YANG, H.-J. & LEE, C.-Y. 2008. Petrogenesis of the Nanling Mountains granites from South China: constraints from systematic apatite geochemistry and whole-rock geochemical and Sr–Nd isotope compositions. *Journal of Asian Earth Sciences,* 33**,** 428-451.

HUANG, H., CAWOOD, P. A., HOU, M.-C., NI, S.-J., YANG, J.-H., DU, Y.-S. & WEN, H.-G. 2018. Provenance of Late Permian volcanic ash beds in South China: Implications for the age of Emeishan volcanism and its linkage to climate cooling. *Lithos,* 314**,** 293-306.

HUDSON, R. & PHILCOX, M. 1964. The Lower Carboniferous stratigraphy of the Buttevant area, Co. Cork. *Proceedings of the Royal Irish Academy. Section B: Biological, Geological, and Chemical Science,* 64**,** 65-79.

HUFF, W. D. 1983. Correlation of Middle Ordovician K-bentonites based on chemical fingerprinting. *The Journal of Geology,* 91**,** 657-669.

HUFF, W. D. 2016. K-bentonites: A review. *American Mineralogist,* 101**,** 43-70.

INANLI, F. Ö., HUFF, W. D. & BERGSTRÖM, S. M. 2009. The Lower Silurian (Llandovery) Osmundsberg K-bentonite in Baltoscandia and the British Isles: chemical fingerprinting and regional correlation. *GFF,* 131**,** 269-279.

ISAACSON, P., DIAZ-MARTINEZ, E., GRADER, G., KALVODA, J., BÁBEK, O. & DEVUYST, F. 2008. Late Devonian–earliest Mississippian glaciation in Gondwanaland and its biogeographic consequences. *Palaeogeography, Palaeoclimatology, Palaeoecology,* 268**,** 126-142.

JAMES, R., ELDERFIELD, H. & PALMER, M. 1995. The chemistry of hydrothermal fluids from the Broken Spur site, 29 N Mid-Atlantic Ridge. *Geochimica et Cosmochimica Acta,* 59**,** 651-659.

JANOUSEK, V. & GERDES, A. 2003. Timing the magmatic activity within the Central Bohemian Pluton, Czech Republic: conventional U-Pb ages for the Sázava and Tábor intrusions and their geotectonic significance. *Journal of Geosciences,* 48**,** 70-71.

JENSEN, B. J., PYNE-O'DONNELL, S., PLUNKETT, G., FROESE, D. G., HUGHES, P. D., SIGL, M., MCCONNELL, J. R., AMESBURY, M. J., BLACKWELL, P. G. & VAN DEN BOGAARD, C. 2014. Transatlantic distribution of the Alaskan white river ash. *Geology,* 42**,** 875-878.

JOCHUM, K., MCDONOUGH, W., PALME, H. & SPETTEL, B. 1989. Compositional constraints on the continental lithospheric mantle from trace elements in spinel peridotite xenoliths. *Nature,* 340**,** 548-550.

JOCHUM, K. P., WEIS, U., SCHWAGER, B., STOLL, B., WILSON, S. A., HAUG, G. H., ANDREAE, M. O. & ENZWEILER, J. 2016. Reference values following ISO guidelines for frequently requested rock reference materials. *Geostandards and Geoanalytical Research,* 40**,** 333-350.

JOCHUM, K. P., WEIS, U., STOLL, B., KUZMIN, D., YANG, Q., RACZEK, I., JACOB, D. E., STRACKE, A., BIRBAUM, K. & FRICK, D. A. 2011. Determination of reference values for NIST SRM 610–617 glasses following ISO guidelines. *Geostandards and Geoanalytical Research,* 35**,** 397-429.

JOHNSTON, J. 1999. Regional fluid flow and the genesis of Irish Carboniferous base metal deposits. *Mineralium Deposita,* 34**,** 571-598.

JOHNSTON, J., COLLER, D., MILLAR, G. & CRITCHLEY, M. 1996. Basement structural controls on Carboniferous-hosted base metal mineral deposits in Ireland. *In:* STROGEN, P., SOMERVILLE, I. D. & JONES, G. L. (eds.) *Recent advances in Lower Carboniferous Geology.* Geological Society, London, Special Publications, 107, 1-21.

JONES, G. L., SOMERVILLE, I. D. & STROGEN, P. 1988. The Lower Carboniferous (Dinantian) of the Swords area: sedimentation and tectonics in the Dublin Basin, Ireland. *Geological Journal,* 23**,** 221-248.

KACMAZ, H. 2016. Major, trace and rare earth element (REE) characteristics of tuffs in the Yenice-Saraycık area (Demirci, Manisa), Western Anatolia, Turkey. *Journal of Geochemical Exploration,* 168**,** 169-176.

KALSBEEK, F. & WENDT, I. 1992. The statistical distribution of the mean squared weighted deviation. Comment on isochrons, errorchrons, and the use of MSWD-values. Author reply. *Chemical Geology. Isotope Geoscience Section,* 94**,** 241-243.

KALVODA, J., BÁBEK, O., DEVUYST, F. X. & SEVASTOPULO, G. D. 2011. Biostratigraphy, sequence stratigraphy and gamma-ray spectrometry of the Tournaisian-Viséan boundary interval in the Dublin Basin. *Bulletin of Geosciences,* 86.

KAMBER, B., GREIG, A., SCHOENBERG, R. & COLLERSON, K. 2003. A refined solution to Earth's hidden niobium: implications for evolution of continental crust and mode of core formation. *Precambrian Research,* 126**,** 289-308.

KAMBER, B. S. & GLADU, A. H. 2009. Comparison of Pb purification by anion-exchange resin methods and assessment of long-term reproducibility of Th/U/Pb ratio measurements by quadrupole ICP-MS. *Geostandards and Geoanalytical Research,* 33**,** 169-181.

KAMBER, B. S., GREIG, A. & COLLERSON, K. D. 2005. A new estimate for the composition of weathered young upper continental crust from alluvial sediments, Queensland, Australia. *Geochimica et Cosmochimica Acta,* 69**,** 1041-1058.

KAMBER, B. S. & WEBB, G. E. 2001. The geochemistry of late Archaean microbial carbonate: implications for ocean chemistry and continental erosion history. *Geochimica et Cosmochimica Acta,* 65**,** 2509-2525.

KANE, J. S. 2004. Report of the International Association of Geoanalysts on the certification of Penrhyn Slate, OU-6. *Geostandards and Geoanalytical Research,* 28**,** 53-80.

KAWANO, M. & TOMITA, K. 2001. TEM-EDX study of weathered layers on the surface of volcanic glass, bytownite, and hypersthene in volcanic ash from Sakurajima volcano, Japan. *American Mineralogist,* 86**,** 284-292.

KIIPLI, T., HINTS, R., KALLASTE, T., VERŠ, E. & VOOLMA, M. 2017. Immobile and mobile elements during the transition of volcanic ash to bentonite–an example from the early Palaeozoic sedimentary section of the Baltic Basin. *Sedimentary Geology,* 347**,** 148-159.

KIIPLI, T., KALLASTE, T. & NESTOR, V. 2010. Composition and correlation of volcanic ash beds of Silurian age from the eastern Baltic. *Geological Magazine,* 147**,** 895-909.

KIIPLI, T., KIIPLI, E., KALLASTE, T., HINTS, R., SOMELAR, P. & KIRSIMÄE, K. 2007. Altered volcanic ash as an indicator of marine environment, reflecting pH and sedimentation rate–example from the Ordovician Kinnekulle bed of Baltoscandia. *Clays and Clay Minerals,* 55**,** 177-188.

KIIPLI, T., SOESOO, A., KALLASTE, T. & KIIPLI, E. 2008. Geochemistry of Telichian (Silurian) K-bentonites in Estonia and Latvia. *Journal of Volcanology and Geothermal Research,* 171**,** 45-58.

KIRTON, S. 1981. *Petrogenesis and tectonic relationships of Carboniferous lavas of the English Midlands.* PhD Thesis, University of Lancaster.

KOLATA, D. R., FROST, J. K. & HUFF, W. D. 1987. Chemical correlation of K-bentonite beds in the Middle Ordovician Decorah Subgroup, upper Mississippi Valley. *Geology,* 15**,** 208-211.

KÖNIGER, S., LORENZ, V., STOLLHOFEN, H. & ARMSTRONG, R. A. 2002. Origin, age and stratigraphic significance of distal fallout ash tuffs from the Carboniferous–Permian continental Saar–Nahe Basin (SW Germany). *International Journal of Earth Sciences,* 91**,** 341-356.

KOŠLER, J., FONNELAND, H., SYLVESTER, P., TUBRETT, M. & PEDERSEN, R.-B. 2002. U–Pb dating of detrital zircons for sediment provenance studies—a comparison of laser ablation ICPMS and SIMS techniques. *Chemical Geology,* 182**,** 605-618.

KRAMER, W., WEATHERALL, G. & OFFLER, R. 2001. Origin and correlation of tuffs in the Permian Newcastle and Wollombi Coal Measures, NSW, Australia, using chemical fingerprinting. *International Journal of Coal Geology,* 47**,** 115-135.

KUBANEK, F. & ZIMMERLE, W. 1986. Tuffe und kieselige Tonschiefer aus dem tieferen Unterkarbon der Bohrung Adlersberg (West-Harz). *Geologisches Jahrbuch. Reihe D. Mineralogie, Petrographie, Geochemie, Lagerstättenkunde***,** 207-268.

KYNE, R., TORREMANS, K., GÜVEN, J., DOYLE, R. & WALSH, J. 2019. 3-D modeling of the lisheen and silvermines deposits, County Tipperary, Ireland: insights into structural controls on the formation of Irish Zn-Pb deposits. *Economic Geology,* 114**,** 93-116.

LAKHRISSI, M. A. 1996. *Pétrologie, minéralogie, géochimie du volcanisme dévono-dinantien des Vosges méridionales (France): sa place dans le contexte géodynamique varisque.* Lille 1.

LANE, C. S., CHORN, B. T. & JOHNSON, T. C. 2013. Ash from the Toba supereruption in Lake Malawi shows no volcanic winter in East Africa at 75 ka. *Proceedings of the National Academy of Sciences,* 110**,** 8025-8029.

LANE, H. R., BRENCKLE, P. L., BAESEMANN, J. & RICHARDS, B. 1999. The IUGS boundary in the middle of the Carboniferous: Arrow Canyon, Nevada, USA. *Episodes,* 22**,** 272-283.

LAVIANO, R. & MONGELLI, G. 1996. Geochemistry and mineralogy as indicators of parental affinity for Cenozoic bentonites: a case study from S. Croce Di Magliano (southern Apennines, Italy). *Clay Minerals,* 31**,** 391-401.

LE BAS, M., LE MAITRE, R., STRECKEISEN, A., ZANETTIN, B. & ROCKS, I. S. O. T. S. O. I. 1986. A chemical classification of volcanic rocks based on the total alkali-silica diagram. *Journal of Petrology,* 27**,** 745-750.

LE MAITRE, R. 1976. The chemical variability of some common igneous rocks. *Journal of Petrology,* 17**,** 589-598.

LEA, D. W. & MARTIN, P. A. 1996. A rapid mass spectrometric method for the simultaneous analysis of barium, cadmium, and strontium in foraminifera shells. *Geochimica et Cosmochimica Acta,* 60**,** 3143-3149.

LEDRU, P., COSTA, S. & ECHTLER, H. 1994. The massif central: structure. *In:* KEPPIE, J. D. (ed.) *Pre-Mesozoic geology in France and related areas.* Berlin, Springer, 305-323.

LEE, J. K., WILLIAMS, I. S. & ELLIS, D. J. 1997. Pb, U and Th diffusion in natural zircon. *Nature,* 390**,** 159-162.

LEEDER, M. & MCMAHON, A. 1988. Upper Carboniferous (Silesian) bassin subsidence in northern Britain. *In:* BESLY, B. M. & KELUNG, G. (eds.) *Sedimentation in a synorogenic basin complex. The Upper Carboniferous of Northwest Europe.* Blackie, Glasgow and London, 43-52.

LEES, A. & MILLER, J. 1995. Waulsortian banks. *In:* MONTY, C. L. V., BOSENCE, D. W. J., BRIDGES, P. H. & PRATT, B. R. (eds.) *Carbonate Mud-Mounds: their origin and evolution.* Special Publication of the International Association of Sedimentologists, Blackwell Science, Oxford, 23, 191-271.

LEFEVRE, C., LAKHRISSI, M. & SCHNEIDER, J.-L. 1994. Les affinités magmatiques du volcanisme dinantien des Vosges méridionales (France); approche géochimique et interprétation. *Comptes Rendus de l'Académie des Sciences. Série 2. Sciences de la Terre et des Planètes,* 319**,** 79-86.

LEGG, I., JOHNSTON, T., MITCHELL, W. & SMITH, R. 1998. Geology of the country around Derrygonnelly and Marble Arch. *Sheets 44, 56 and 43, London, Memoir of the Geological Survey of Northern Ireland*.

LEWIS, D. 1986. *The Carboniferous Geology of the East Clare Syncline, incorporating a Study of the Gort G-1 Borehole.* PhD Thesis, University of Dublin.

LI, D., SHIELDS-ZHOU, G. A., LING, H.-F. & THIRLWALL, M. 2011. Dissolution methods for strontium isotope stratigraphy: Guidelines for the use of bulk carbonate and phosphorite rocks. *Chemical Geology,* 290**,** 133-144.

LIEW, T. & HOFMANN, A. 1988. Precambrian crustal components, plutonic associations, plate environment of the Hercynian Fold Belt of central Europe: indications from a Nd and Sr isotopic study. *Contributions to Mineralogy and Petrology,* 98**,** 129-138.

LIPPOLT, H. & HESS, J. 1985. 40Ar/39Ar dating of sanidines from Upper Carboniferous tonsteins. *Congrès International de Stratigraphie et de Géologie du Carbonifère,* 10**,** 175-181.

LONG, C., MCCONNELL, B. & PHILCOX, M. 2005. *Geology of South Mayo: A Geological Description of South Mayo, to Accompany the Bedrock Geology 1: 100.000 Scale Map Series, Sheet 11, South Mayo*, Geological Survey of Ireland.

LÓPEZ, J. G., BAULUZ, B., YUSTE, A., MAYAYO, M. & FERNÁNDEZ-NIETO, C. 2005. Mineralogical and trace element composition of clay-sized fractions from Albian siliciclastic rocks (Oliete Basin, NE Spain). *Clay Minerals,* 40**,** 565-580.

LOWE, D. J. 2011. Tephrochronology and its application: a review. *Quaternary Geochronology,* 6**,** 107-153.

LUDWIG, K. 2003. User's manual for isoplot 3.00, a geochronlogical toolkit for microsoft excel. *Berkeley Geochronology Center, Special Publication,* 4**,** 25-32.

LUDWIG, K. R. 1980. Calculation of uncertainties of U-Pb isotope data. *Earth and Planetary Science Letters,* 46**,** 212-220.

LUDWIG, K. R. 1998. On the treatment of concordant uranium-lead ages. *Geochimica et Cosmochimica Acta,* 62**,** 665-676.

LUX, D. & YATES, M. 2009. Apatite and granite petrogenesis. *Geological Society of America Abstracts with Programs,* 41**,** 33.

MACDONALD, R. 1976. Petrochemistry of the early Carboniferous (Dinantian) lavas of Scotland. *Scottish Journal of Geology,* 11**,** 269-314.

MACDONALD, R. & WALKER, B. 1984. Geochemistry and tectonic significance of the Lower Carboniferous Cockermouth lavas, Cumbria. *Proceedings of the Yorkshire Geological Society,* 45**,** 141-146.

MALLON, A. 1997. *Petrological and mineralogical characteristics of the Old Red Sandstone facies rocks beneath base metal deposits as a guide to the setting of mineralisation in the Irish Midlands.* PhD Thesis, University College Cork.

MANK, A. J. & MASON, P. R. 1999. A critical assessment of laser ablation ICP-MS as an analytical tool for depth analysis in silica-based glass samples. *Journal of Analytical Atomic Spectrometry,* 14**,** 1143-1153.

MAO, M., RUKHLOV, A. S., ROWINS, S. M., SPENCE, J. & COOGAN, L. A. 2016. Apatite trace element compositions: a robust new tool for mineral exploration. *Economic Geology,* 111**,** 1187-1222.

MARKWITZ, V. & KIRKLAND, C. 2018. Source to sink zircon grain shape: Constraints on selective preservation and significance for Western Australian Proterozoic basin provenance. *Geoscience Frontiers,* 9**,** 415-430.

MARTIN, E. & MACDOUGALL, J. 1995. Sr and Nd isotopes at the prmian/triassic boundary: A record of climate change. *Chemical Geology,* 125**,** 73-99.

MARTÍNEZ, F., CORRETGÉ, L., SUÁREZ, O. & DALLMEYER, R. 1990. Distribution, characteristics and evolution of metamorphism. *Pre-Mesozoic Geology of Iberia***,** 207-211.

MARX, S. K. & KAMBER, B. S. 2010. Trace-element systematics of sediments in the Murray–Darling Basin, Australia: Sediment provenance and palaeoclimate implications of fine scale chemical heterogeneity. *Applied Geochemistry,* 25**,** 1221-1237.

MARX, S. K., KAMBER, B. S. & MCGOWAN, H. A. 2005. Provenance of long-travelled dust determined with ultra-trace-element composition: a pilot study with samples from New Zealand glaciers. *Earth Surface Processes and Landforms: The Journal of the British Geomorphological Research Group,* 30**,** 699-716.

MASUDA, A. 1962. Regularities in variation of relative abundances of lanthanide elements and an attempt to analyze separation index patterns of some minerals. *The Journal of Earth Sciences, Nagoya University,* 10**,** 173-187.

MATTHEWS, N. E., SMITH, V. C., COSTA, A., DURANT, A. J., PYLE, D. M. & PEARCE, N. J. 2012. Ultra-distal tephra deposits from super-eruptions: examples from Toba, Indonesia and Taupo Volcanic Zone, New Zealand. *Quaternary International,* 258**,** 54-79.

MATTINSON, J. M., GRAUBARD, C. M., PARKINSON, D. L. & MCCLELLAND, W. C. 1996. U-Pb reverse discordance in zircons: the role of fine-scale oscillatory zoning and sub-micron transport of Pb. *Geophysical Monograph-American Geophysical Union,* 95**,** 355-370.

MCARTHUR, J. 1994. Recent trends in strontium isotope stratigraphy. *Terra Nova,* 6**,** 331-358.

MCARTHUR, J., HOWARTH, R. & SHIELDS, G. 2012. Strontium isotope stratigraphy. *The Geologic Time Scale,* 1**,** 127-144.

MCARTHUR, J. M., HOWARTH, R. & BAILEY, T. 2001. Strontium isotope stratigraphy: LOWESS version 3: best fit to the marine Sr-isotope curve for 0–509 Ma and accompanying look-up table for deriving numerical age. *The Journal of Geology,* 109**,** 155-170.

MCCONNELL, B. & PHILCOX, M. 1994. *Geology of Kildare-Wicklow: a geological description to accompany the bedrock geology 1: 100,000 Map Series, Sheet 16, Kildare-Wicklow with contributions by Sleeman, A.G., Stanley, G., Flegg, A.M., Daly, E.P. and Warren, W.P.*, Geological Survey of Ireland Dublin.

MCCONNELL, B., PHILCOX, M. & GERAGHTY, M. 2001. *Geology of Meath: A geological description to accompany the bedrock geology 1: 100,000 scale map series, Sheet 13, Meath with contributions by Morris, J., Cox, W. (Minerals), Wright, G. (Groundwater) and Meehan, R. (Quaternary)*, Geological Survey of Ireland Dublin.

MCCUSKER, J. & REED, C. 2013. The role of intrusions in the formation of Irish-type mineralisation. *Mineralium Deposita,* 48**,** 687-695.

MCDONOUGH, W. & SUN, S. 1995. The composition of the Earth. *Chemical Geology,* 120 (3-4)**,** 223-253.

MCDOWELL, F. W., MCINTOSH, W. C. & FARLEY, K. A. 2005. A precise 40Ar–39Ar reference age for the Durango apatite (U–Th)/He and fission-track dating standard. *Chemical Geology,* 214**,** 249-263.

MCHENRY, L. J. 2005. Phenocryst composition as a tool for correlating fresh and altered tephra, Bed I, Olduvai Gorge, Tanzania. *Stratigraphy,* 2**,** 101-115.

MCHENRY, L. J. 2009. Element mobility during zeolitic and argillic alteration of volcanic ash in a closed-basin lacustrine environment: Case study Olduvai Gorge, Tanzania. *Chemical Geology,* 265**,** 540-552.

MCKERROW, W., DEWEY, J. & SCOTESE, C. 1991. The Ordovician and Silurian development of the Iapetus ocean. *Special Papers in Palaeontology,* 44**,** 165-178.

MCKERROW, W. S. & SCOTESE, C. R. 1990. *Palaeozoic Palaeogeography and Biogeography*, Geological Society London.

MCLENNAN, S. M. 1989. Rare earth elements in sedimentary rocks: influence of provenance and sedimentary processes. *Geochemistry and Mineralogy of Rare Earth Elements, Reviews in Mineralogy 21***,** 169-200.

MCLENNAN, S. M. 2001. Relationships between the trace element composition of sedimentary rocks and upper continental crust. *Geochemistry, Geophysics, Geosystems,* 2 (4).

MCNESTRY, A. & REES, J. 1992. Environments and palynofacies of a Dinantian (Carboniferous) littoral sequence: the basal part of the Navan group, Navan, country Meath, Ireland. *Palaeogeography, Palaeoclimatology, Palaeoecology,* 96**,** 175-193.

MIKULÁŠ, R., RINDSBERG, A. K., SANTOS, A. & PAVELA, M. 2017. A Carboniferous chiton (Mollusca, Polyplacophora) at the end of its trail: a unique find from the Czech Republic. *Bollettino della Società Paleontologica Italiana,* 56**,** 171-179.

MILLER, B. V. 2006. Introduction to radiometric dating. *The Paleontological Society Papers,* 12**,** 1-23.

MITCHELL, C. E., ADHYA, S., BERGSTRÖM, S. M., JOY, M. P. & DELANO, J. W. 2004. Discovery of the Ordovician Millbrig K-bentonite Bed in the Trenton Group of New York State: implications for regional correlation and sequence stratigraphy in eastern North America. *Palaeogeography, Palaeoclimatology, Palaeoecology,* 210**,** 331-346.

MITCHELL, J. & MOHR, P. 1987. Carboniferous dikes of West Connacht, Ireland. *Earth and Environmental Science Transactions of The Royal Society of Edinburgh,* 78**,** 133-151.

MITCHELL, W. 2004. Carboniferous. *In: Mitchell, W.I. (eds). The Geology of Northern Ireland—Our Natural Foundation, 2nd. Geological Survey of Northern Ireland, Belfast***,** 79-116.

MOGHAZI, A. 2003. Geochemistry and petrogenesis of a high-K calc-alkaline Dokhan Volcanic suite, South Safaga area, Egypt: the role of late Neoproterozoic crustal extension. *Precambrian Research,* 125**,** 161-178.

MONAGHAN, A. & PRINGLE, M. 2004. High precision 40Ar–39Ar geochronology of Carboniferous–Permian volcanism in the Midland Valley. *In:* WILSON, M., NEUMANN, E.-R., DAVIES, G. R., TIMMERMAN, M. J., HEEREMANS, M. & LARSEN, B. T. (eds.) *Permo-Carboniferous Magmatism and Rifting in Europe.*: Geological Society, London, Special Publications, 223, 335-360.

MONTAÑEZ, I. P., BANNER, J. L., OSLEGER, D. A., BORG, L. E. & BOSSERMAN, P. J. 1996. Integrated Sr isotope variations and sea-level history of Middle to Upper Cambrian platform carbonates: Implications for the evolution of Cambrian seawater 87Sr/86Sr. *Geology,* 24**,** 917-920.

MORRIS, J. H., SOMERVILLE, I. D. & MCDERMOT, C. V. 2003. Geology of Longford and Roscommon: A geological description of Longford, Roscommon and part of Westmeath to accompany the bedrock Geology 1:100,000 Scale Map Series, Sheet 12. *Geological Survey of Ireland, Dublin***,** 99p.

MORTON, A. C. & HALLSWORTH, C. 2007. Stability of detrital heavy minerals during burial diagenesis. *Developments in Sedimentology,* 58**,** 215-245.

MORTON, A. C. & HALLSWORTH, C. R. 1999. Processes controlling the composition of heavy mineral assemblages in sandstones. *Sedimentary Geology,* 124**,** 3-29.

MURRAY, J. 2010. *Mid to Upper Viséan Facies and Palaeoenvironments of the Shannon Basin, Western Ireland.* PhD Thesis, Trinity College Dublin.

NAISH, T. R., NELSON, C. S. & HODDER, A. P. W. 1993. Evolution of Holocene sedimentary bentonite in a shallow-marine embayment, Firth of Thames, New Zealand. *Marine Geology,* 109**,** 267-278.

NASDALA, L., CORFU, F., SCHOENE, B., TAPSTER, S. R., WALL, C. J., SCHMITZ, M. D., OVTCHAROVA, M., SCHALTEGGER, U., KENNEDY, A. K. & KRONZ, A. 2018. GZ 7 and GZ 8–Two Zircon Reference Materials for SIMS U-Pb Geochronology. *Geostandards and Geoanalytical Research,* 42**,** 431-457.

NESBITT, H. W. 1979. Mobility and fractionation of rare earth elements during weathering of a granodiorite. *Nature,* 279**,** 206-210.

NESBITT, H. W. & MARKOVICS, G. 1980. Chemical processes affecting alkalis and alkaline earths during continental weathering. *Geochimica et Cosmochimica Acta,* 44**,** 1659-1666.

NEUBAUER, F. & RAUMER, J. V. 1993. The Alpine basement—linkage between Variscides and east-Mediterranean mountain belts. Pre-Mesozoic Geology in the Alps. Springer.

NICKLEN, B. L., BELL JR, G. L. & HUFF, W. D. 2015. A new shelf-to-basin timeline for the Middle Permian (Guadalupian) Capitan depositional system, west Texas and southeastern New Mexico, USA. *Stratigraphy,* 12**,** 109-122.

NISHIZAWA, M., TAKAHATA, N., TERADA, K., KOMIYA, T., UENO, Y. & SANO, Y. 2005. Rare-Earth element, lead, carbon, and nitrogen geochemistry of apatite-bearing metasediments from the∼ 3.8 Ga Isua Supracrustal Belt, West Greenland. *International Geology Review,* 47**,** 952-970.

NOTHDURFT, L. D., WEBB, G. E. & KAMBER, B. S. 2004. Rare earth element geochemistry of Late Devonian reefal carbonates, Canning Basin, Western Australia: confirmation of a seawater REE proxy in ancient limestones. *Geochimica et Cosmochimica Acta,* 68**,** 263-283.

NUTMAN, A. P. 2007. Apatite recrystallisation during prograde metamorphism, Cooma, southeast Australia: implications for using an apatite–graphite association as a biotracer in ancient metasedimentary rocks. *Australian Journal of Earth Sciences,* 54**,** 1023-1032.

O'REILLY, S. Y. & GRIFFIN, W. 2000. Apatite in the mantle: implications for metasomatic processes and high heat production in Phanerozoic mantle. *Lithos,* 53**,** 217-232.

O'SULLIVAN, G., CHEW, D., KENNY, G., HENRICHS, I. & MULLIGAN, D. 2020. The trace element composition of apatite and its application to detrital provenance studies. *Earth-Science Reviews,* 201**,** 103044.

ÖZDAMAR, Ş., ECE, Ö., UZ, B., BOYLU, F., ERCAN, H. & YANIK, G. 2014. Element mobility during the formation of the Uzunisa-Ordu bentonite, NE Turkey, and potential applications. *Clay Minerals,* 49(5)**,** 609-633.

PALMER, M. & EDMOND, J. 1989. The strontium isotope budget of the modern ocean. *Earth and Planetary Science Letters,* 92**,** 11-26.

PAPROTH, E., FEIST, R. & FLAJS, G. 1991. Decision on the Devonian-Carboniferous boundary stratotype. *Episodes Journal of International Geoscience,* 14**,** 331-336.

PATON, C., HELLSTROM, J., PAUL, B., WOODHEAD, J. & HERGT, J. 2011. Iolite: Freeware for the visualisation and processing of mass spectrometric data. *Journal of Analytical Atomic Spectrometry,* 26**,** 2508-2518.

PEACE, W. M. & WALLACE, M. W. 2000. Timing of mineralization at the Navan Zn-Pb deposit: A post-Arundian age for Irish mineralization. *Geology,* 28**,** 711-714.

PEARCE, J. A. 1996. A user's guide to basalt discrimination diagrams. Trace element geochemistry of volcanic rocks: applications for massive sulphide exploration. *Geological Association of Canada, Short Course Notes,* 12**,** 113.

PELL, S. D., WILLIAMS, I. S. & CHIVAS, A. R. 1997. The use of protolith zircon-age fingerprints in determining the protosource areas for some Australian dune sands. *Sedimentary Geology,* 109**,** 233-260.

PELLENARD, P., DECONINCK, J. F., HUFF, W. D., THIERRY, J., MARCHAND, D., FORTWENGLER, D. & TROUILLER, A. 2003. Characterization and correlation of Upper Jurassic (Oxfordian) bentonite deposits in the Paris Basin and the Subalpine Basin, France. *Sedimentology,* 50**,** 1035-1060.

PETRUS, J. A. & KAMBER, B. S. 2012. VizualAge: A novel approach to laser ablation ICP-MS U-Pb geochronology data reduction. *Geostandards and Geoanalytical Research,* 36**,** 247-270.

PHILCOX, M. E. 1984. *Lower Carboniferous lithostratigraphy of the Irish Midlands*, Irish Association for Economic Geology.

PHILCOX, M. E. 1989. The mid-Dinantian unconformity at Navan, Ireland. *In:* ARTHURTON, R. S., GUTTERIDGE, P. & NOLAN, S. C. (eds.) *The Role of Tectonics in Devonian and Carboniferous Sedimentation in the British Isles.* Yorkshire Geological Society, Occcasional Publication, 6, 67-81.

PHILCOX, M. E. 2016. The stratigraphic context of Dinantian tuffs in the Irish Midlands. *unpublished report*.

PHILLIPS, E. & MACPHERSON, K. 1996. *Petrology, Geochemistry and Classification of the Clyde Plateau Volcanic Formation, Kilmarnock District (Sheet 22), Midland Valley, Scotland*, British Geological Survey.

PHILLIPS, W. & SEVASTOPULO, G. D. 1986. The stratigraphic and structural setting of Irish mineral deposits. *Geology and Genesis of Mineral Deposits in Ireland***,** 1-30.

PHILLIPS, W. E. A., STILLMAN, C. J. & MURPHY, T. 1976. A Caledonian plate tectonic model. *Journal of the Geological Society,* 132**,** 579-605.

PICCOLI, P. M. & CANDELA, P. A. 2002. Apatite in igneous systems. *Reviews in Mineralogy and Geochemistry,* 48**,** 255-292.

PINGITORE JR, N. E., LYTLE, F. W., DAVIES, B. M., EASTMAN, M. P., ELLER, P. G. & LARSON, E. M. 1992. Mode of incorporation of Sr2+ in calcite: Determination by X-ray absorption spectroscopy. *Geochimica et Cosmochimica Acta,* 56**,** 1531-1538.

POINTON, M. A. 2012. *Constructing Global Carboniferous Climatic Fluctuations Using High Resolution Geochronology.* PhD Thesis, Trinity College Dublin.

POINTON, M. A., CHEW, D. M., OVTCHAROVA, M., DELCAMBRE, B. & SEVASTOPULO, G. D. 2021. Uranium-lead dates from Livian (middle Viséan) bentonites of the Namur-Dinant Basin, Belgium. *Newsletters on Stratigraphy*.

POINTON, M. A., CLIFF, R. A. & CHEW, D. M. 2012. The provenance of Western Irish Namurian Basin sedimentary strata inferred using detrital zircon U–Pb LA-ICP-MS geochronology. *Geological Journal,* 47**,** 77-98.

POLLARD, A., BLOCKLEY, S. & LANE, C. 2006. Some numerical considerations in the geochemical analysis of distal microtephra. *Applied Geochemistry,* 21**,** 1692-1714.

POPP, B. N., ANDERSON, T. F. & SANDBERG, P. A. 1986. Brachiopods as indicators of original isotopic compositions in some Paleozoic limestones. *Geological Society of America Bulletin,* 97**,** 1262-1269.

POTTS, P. J. & KANE, J. S. 2005. International association of geoanalysts certificate of analysis: certified reference material Ou-6 (Penrhyn Slate). *Geostandards and Geoanalytical Research,* 29**,** 233-236.

POTY, E., DEVUYST, F.-X. & HANCE, L. 2006. Upper Devonian and Mississippian foraminiferal and rugose coral zonations of Belgium and northern France: a tool for Eurasian correlations. *Geological Magazine,* 143**,** 829-857.

POUGET, S., BURSIK, M., CORTÉS, J. A. & HAYWARD, C. 2014. Use of principal component analysis for identification of Rockland and Trego Hot Springs tephras in the Hat Creek Graben, northeastern California, USA. *Quaternary Research,* 81**,** 125-137.

POURMAND, A., DAUPHAS, N. & IRELAND, T. J. 2012. A novel extraction chromatography and MC-ICP-MS technique for rapid analysis of REE, Sc and Y: Revising CI-chondrite and Post-Archean Australian Shale (PAAS) abundances. *Chemical Geology,* 291**,** 38-54.

PRACHT, M., LEES, A., LEAKE, B., FEELY, M., LONG, C. B., MORRIS, J. & MCCONNELL, B. J. 2004. Geology of Galway Bay: A geological description to accompany the bedrock geology, 1:100,000 scale map series, Sheet 14, Galway Bay. *Geological Survey of Ireland***,** 76pp.

PRACHT, M. & SOMERVILLE, I. D. 2015. A revised Mississippian lithostratigraphy of County Galway (western Ireland) with an analysis of carbonate lithofacies, biostratigraphy, depositional environments and palaeogeographic reconstructions utilising new borehole data. *Journal of Palaeogeography,* 4**,** 1-26.

PÜSPÖKI, Z., KOZÁK, M., KOVÁCS-PÁLFFY, P., SZEPESI, J., MCINTOSH, R., KÓNYA, P., VINCZE, L. & GYULA, G. 2008. Geochemical records of a bentonitic acid-tuff succession related to a transgressive systems tract–indication of changes in the volcanic sedimentation rate. *Clays and Clay Minerals,* 56**,** 23-38.

RAMSEY, C. B., HOUSLEY, R. A., LANE, C. S., SMITH, V. C. & POLLARD, A. M. 2015. The RESET tephra database and associated analytical tools. *Quaternary Science Reviews,* 118**,** 33-47.

REDMOND, P. 2010. The Limerick Basin: an important emerging subdistrict of the Irish Zn-Pb orefield. *SEG Newsletter,* 82**,** 20-25.

REED, C. P. & WALLACE, M. W. 2001. Diagenetic evidence for an epigenetic origin of the Courtbrown Zn–Pb deposit, Ireland. *Mineralium Deposita,* 36**,** 428-441.

REED, C. P. & WALLACE, M. W. 2004. Zn-Pb mineralisation in the Silvermines district, Ireland: a product of burial diagenesis. *Mineralium Deposita,* 39**,** 87-102.

REES, J. G. 1992. The Courceyan (Lower Carboniferous) succession at Slane, County Meath. *Irish Journal of Earth Sciences***,** 113-129.

RENOCK, D., LANDIS, J. D. & SHARMA, M. 2016. Reductive weathering of black shale and release of barium during hydraulic fracturing. *Applied Geochemistry,* 65**,** 73-86.

RICHARDS, B. 2009. Task Group 2010. *Report of the Task Group to establish a GSSP close to the existing Viséan-Serpukhovian boundary. Newsletter on Carboniferous Stratigraphy,* 28**,** 30-34.

RICHARDS, B. C. 2013. Current status of the international Carboniferous time scale. *The Carboniferous-Permian Transition, Bulletin,* 60**,** 348-353.

RIEGLER, T. & MCCLENAGHAN, S. 2017. Authigenic potassic silicates in the Rathdowney Trend, southwest Ireland: New perspectives for ore genesis from petrography of gangue phases in Irish-type carbonate-hosted Zn-Pb deposits. *Ore Geology Reviews,* 88**,** 140-155.

RILEY, N. 1990. Stratigraphy of the Worston Shale Group (Dinantian), Craven Basin, north-west England. *Proceedings of the Yorkshire Geological Society,* 48**,** 163-187.

RILEY, N. 1993. Dinantian (Lower Carboniferous) biostratigraphy and chronostratigraphy in the British Isles. *Journal of the Geological Society,* 150**,** 427-446.

RIZZI, G. 1992. *The sedimentology and petrography of Lower Carboniferous limestones and dolomites: host-rocks to the Navan zinc-lead deposit.* PhD Thesis, University of Glasgow.

RIZZI, G. & BRAITHWAITE, C. J. 1996. Cyclic emersion surfaces and channels within Dinantian limestones hosting the giant Navan Zn-Pb deposit, Ireland. *In:* STROGEN, P., SOMERVILLE, I. & JONES, G. (eds.) *Recent Advances in Carboniferous Geology.* Geological Society, London, Special Publications 107, 207-219.

RODUSHKIN, I., AXELSSON, M. D., MALINOVSKY, D. & BAXTER, D. C. 2002. Analyte-and matrix-dependent elemental response variations in laser ablation inductively coupled plasma mass spectrometry part 2. Implications for multi-element analyses. *Journal of Analytical Atomic Spectrometry,* 17**,** 1231-1239.

ROEDER, P. L., MACARTHUR, D., MA, X.-P., PALMER, G. R. & MARIANO, A. N. 1987. Cathodoluminescence and microprobe study of rare-earth elements in apatite. *American Mineralogist,* 72**,** 801-811.

ROLLINSON, H. 1993. Using Geochemical Data: Evaluation, Presentation, Interpretation. *Longman, London***,** 352 pp.

ROSS, C. S. & SHANNON, E. V. 1926. The minerals of bentonite and related clays and their physical properties 1. *Journal of the American Ceramic Society,* 9**,** 77-96.

ROSS, P.-S. & BÉDARD, J. H. 2009. Magmatic affinity of modern and ancient subalkaline volcanic rocks determined from trace-element discriminant diagrams. *Canadian Journal of Earth Sciences,* 46**,** 823-839.

SADLER, P. M. 2004. Quantitative biostratigraphy—achieving finer resolution in global correlation. *Annual Review of Earth and Planetary Science,* 32**,** 187-213.

SAMSON, S. D., MATTHEWS, S., MITCHELL, C. E. & GOLDMAN, D. 1995. Tephrochronology of highly altered ash beds: the use of trace element and strontium isotope geochemistry of apatite phenocrysts to correlate K-bentonites. *Geochimica et Cosmochimica Acta,* 59**,** 2527-2536.

SCHALTEGGER, U. 2000. U–Pb geochronology of the Southern Black Forest Batholith (Central Variscan Belt): timing of exhumation and granite emplacement. *International Journal of Earth Sciences,* 88**,** 814-828.

SCHALTEGGER, U., SCHNEIDER, J.-L., MAURIN, J.-C. & CORFU, F. 1996. Precise UPb chronometry of 345-340 Ma old magmatism related to syn-convergence extension in the Southern Vosges (Central Variscan Belt). *Earth and Planetary Science Letters,* 144**,** 403-419.

SCHANDL, E. S. & GORTON, M. P. 2002. Application of high field strength elements to discriminate tectonic settings in VMS environments. *Economic Geology,* 97**,** 629-642.

SCHOENE, B. & BOWRING, S. A. 2006. U–Pb systematics of the McClure Mountain syenite: thermochronological constraints on the age of the 40 Ar/39 Ar standard MMhb. *Contributions to Mineralogy and Petrology,* 151**,** 615.

SCHULMANN, K., KONOPÁSEK, J., JANOUŠEK, V., LEXA, O., LARDEAUX, J.-M., EDEL, J.-B., ŠTÍPSKÁ, P. & ULRICH, S. 2009. An Andean type Palaeozoic convergence in the Bohemian massif. *Comptes Rendus Geoscience,* 341**,** 266-286.

SCHULTZ, R. W. & SEVASTOPULO, G. D. 1965. Lower Carboniferous volcanic rocks near Tulla, Co. Clare, Ireland. *Scientific Proceedings of the Royal Dublin Society, 2A***,** 153-162.

SCOTESE, C. 2001. PALEOMAP Project.

SELL, B. K. & SAMSON, S. D. 2011a. Apatite phenocryst compositions demonstrate a miscorrelation between the Millbrig and Kinnekulle K-bentonites of North America and Scandinavia. *Geology,* 39**,** 303-306.

SELL, B. K. & SAMSON, S. D. 2011b. A tephrochronologic method based on apatite trace-element chemistry. *Quaternary Research,* 76**,** 157-166.

SELL, B. K., SAMSON, S. D., MITCHELL, C. E., MCLAUGHLIN, P. I., KOENIG, A. E. & LESLIE, S. A. 2015. Stratigraphic correlations using trace elements in apatite from Late Ordovician (Sandbian-Katian) K-bentonites of eastern North America. *Bulletin,* 127**,** 1259-1274.

SEVASTOPULO, G. D. 1982. The age and depositional setting of Waulsortian limestones in Ireland. In: Bolton, K., Lane, H. R., LeMone, D.V., (eds). Symposium on the Environmental Setting and Distribution of the Waulsortian Facies. *El Paso Geological Society and University of Texas at El Paso***,** 65-79.

SEVASTOPULO, G. D. & BARHAM, M. 2014. Correlation of the base of the Serpukhovian Stage (Mississippian) in NW Europe. *Geological Magazine,* 151**,** 244-253.

SEVASTOPULO, G. D. & WYSE JACKSON, P. N. 2001. Carboniferous (Dinantian). *In:* HOLLAND, C. H. (ed.) *The Geology of Ireland.*: Dunedin Academic Press.

SEVASTOPULO, G. D. & WYSE JACKSON, P. N. 2009. Carboniferous: Mississippian (Tournaisian and Viséan). *In:* HOLLAND, C. H. & SANDERS, I. S. (eds.) *The Geology of Ireland.* Academic Press Ltd., Edinburgh.

SHA, L.-K. & CHAPPELL, B. W. 1999. Apatite chemical composition, determined by electron microprobe and laser-ablation inductively coupled plasma mass spectrometry, as a probe into granite petrogenesis. *Geochimica et Cosmochimica Acta,* 63**,** 3861-3881.

SHEARLEY, E. 1988. *The Carboniferous geology of the Fermoy and Mitchelstown synclines.* PhD Thesis, Trinity College, Dublin.

SHEARLEY, E., REDMOND, P., KING, M. & GOODMAN, R. 1996. Geological controls on mineralization and dolomitization of the Lisheen Zn-Pb-Ag deposit, Co. Tipperary, Ireland. *In:* STROGEN, P., SOMERVILLE, I. D. & JONES, G. L. (eds.) *Recent advances in Lower Carboniferous Geology.* Geological Society, London, Special Publications, 107, 23-33.

SHEN, J. 2014. *Volcanic Effects to Marine Environments and Organisms Across the Permian–Triassic Transition in South China.* PhD Thesis, China University of Geosciences.

SHEPHARD-THORN, E. 1961. The Carboniferous limestone succession in north-west County Limerick, Ireland. *Proceedings of the Royal Irish Academy. Section B: Biological, Geological, and Chemical Science,* 62**,** 267-294.

SHILLER, A. M. & FRILOT, D. M. 1996. The geochemistry of gallium relative to aluminum in Californian streams. *Geochimica et Cosmochimica Acta,* 60**,** 1323-1328.

SIIR, S., KALLASTE, T., KIIPLI, T. & HINTS, R. 2015. Internal stratification of two thick Ordovician bentonites of Estonia: deciphering primary magmatic, sedimentary, environmental and diagenetic signatures. *Estonian Journal of Earth Sciences,* 64.

SINGER, D. A. 1995. World class base and precious metal deposits; a quantitative analysis. *Economic Geology,* 90**,** 88-104.

SLACK, J. F. & STEVENS, B. P. 1994. Clastic metasediments of the early Proterozoic Broken Hill group, new South Wales, Australia: geochemistry, provenance, and metallogenic significance. *Geochimica et Cosmochimica Acta,* 58**,** 3633-3652.

SLÁMA, J., KOŠLER, J., CONDON, D. J., CROWLEY, J. L., GERDES, A., HANCHAR, J. M., HORSTWOOD, M. S., MORRIS, G. A., NASDALA, L. & NORBERG, N. 2008. Plešovice zircon—a new natural reference material for U–Pb and Hf isotopic microanalysis. *Chemical Geology,* 249**,** 1-35.

SLEEMAN, A. & PRACHT, M. 1999. *Geology of the Shannon Estuary: A Geological Description of the Shannon Estuary Region Including Parts of Clare, Limerick and Kerry to Accompany the Bedrock Geology 1: 100,000 Scale Map Series, Sheet 17, Shannon Estuary, with contributions by Claringbold, K. and Stanley, G. (Minerals), Deakin, J. and Wright, G. (Groundwater), and Bloetjes, O. and Creighton, R. (Quaternary)*, Geological Survey of Ireland.

SMEDLEY, P. L. 1986. *Petrochemistry of Dinantian volcanism in Northern Britain.* PhD Thesis, University of Edinburgh.

SMEDLEY, P. L. 1988. Trace element and isotopic variations in Scottish and Irish Dinantian volcanism: evidence for an OIB-like mantle source. *Journal of Petrology,* 29**,** 413-443.

SMITH, D. 1967. The petrology and mineralogy of some lower Devonian bentonites from Gaspe, P. Q. *The Canadian Mineralogist,* 9**,** 141-165.

SOMERVILLE, I. D. & JONES, G. L. 1985. The Courceyan stratigraphy of the Pallaskenry Borehole, County Limerick, Ireland. *Geological Journal,* 20**,** 377-400.

SOMERVILLE, I. D. & STROGEN, P. 1992. Ramp sedimentation in the Dinantian limestones of the Shannon Trough, Co. Limerick, Ireland. *Sedimentary Geology,* 79**,** 59-75.

SOMERVILLE, I. D., STROGEN, P. & JONES, G. L. 1992. Biostratigraphy of Dinantian limestones and associated volcanic rocks in the Limerick Syncline, Ireland. *Geological Journal,* 27**,** 201-220.

SOMERVILLE, I. D. & WATERS, C. N. 2011. Western Ireland, Chapter 20. In: Waters, C.N., Somverville, I. D., *et al*., (eds). A Revised Correlation of Carboniferous Rocks in the British Isles. *Geological Society Special Report,* 26**,** 133-137.

SPEARS, D. & KANARIS-SOTIRIOU, R. 1976. Titanium in some Carboniferous sediments from Great Britain. *Geochimica et Cosmochimica Acta,* 40**,** 345-351.

SPEARS, D., KANARIS-SOTIRIOU, R., RILEY, N. & KRAUSE, P. 1999. Namurian bentonites in the Pennine Basin, UK: Origin and magmatic affinities. *Sedimentology,* 46**,** 385-401.

SPENCER, C. J., KIRKLAND, C. L. & TAYLOR, R. J. 2016. Strategies towards statistically robust interpretations of in situ U–Pb zircon geochronology. *Geoscience Frontiers,* 7**,** 581-589.

STACEY, J. T. & KRAMERS, J. 1975. Approximation of terrestrial lead isotope evolution by a two-stage model. *Earth and Planetary Science Letters,* 26**,** 207-221.

STEIGER, R. H. & JÄGER, E. 1977. Subcommission on geochronology: convention on the use of decay constants in geo-and cosmochronology. *Earth and Planetary Science Letters,* 36**,** 359-362.

STEPHENSON, D. 2003. *Carboniferous and Permian igneous rocks of Great Britain, north of the Variscan Front*, No. 27. Joint Nature Conservation Committee.

STRAETEN, C. A. V. 2004. K-bentonites, volcanic ash preservation, and implications for Early to Middle Devonian volcanism in the Acadian orogen, eastern North America. *Geological Society of America Bulletin,* 116**,** 474-489.

STROGEN, P. 1983. *The geology of the volcanic rocks of southeast County Limerick.* PhD Thesis, University College Dublin.

STROGEN, P. 1988. The Carboniferous lithostratigraphy of southeast County Limerick, Ireland, and the origin of the Shannon Trough. *Geological Journal,* 23**,** 121-137.

STROGEN, P., JONES, G. L. & SOMERVILLE, I. D. 1990. Stratigraphy and sedimentology of lower carboniferous (Dinantian) boreholes from West Co. Meath, Ireland. *Geological Journal,* 25**,** 103-137.

STROGEN, P., SOMERVILLE, I., PICKARD, N., JONES, G. L. & FLEMING, M. 1996. Controls on ramp, platform and basinal sedimentation in the Dinantian of the Dublin Basin and Shannon Trough, Ireland. *In:* STROGEN, P., SOMERVILLE, I. D. & JONES, G. L. (eds.) *Recent advances in Lower Carboniferous Geology.* Geological Society, London, Special Publications, 107, 263-279.

SUMMA, L. L. & VEROSUB, K. L. 1992. Trace element mobility during early diagenesis of volcanic ash: applications to stratigraphic correlation. *Quaternary International,* 13**,** 149-157.

SVERJENSKY, D. A. 1984. Europium redox equilibria in aqueous solution. *Earth and Planetary Science Letters,* 67**,** 70-78.

TABAUD, A.-S., JANOUŠEK, V., SKRZYPEK, E., SCHULMANN, K., ROSSI, P., WHITECHURCH, H., GUERROT, C. & PAQUETTE, J.-L. 2015. Chronology, petrogenesis and heat sources for successive Carboniferous magmatic events in the Southern–Central Variscan Vosges Mts (NE France). *Journal of the Geological Society,* 172**,** 87-102.

TANG, M., WANG, X.-L., XU, X.-S., ZHU, C., CHENG, T. & YU, Y. 2012. Neoproterozoic subducted materials in the generation of Mesozoic Luzong volcanic rocks: Evidence from apatite geochemistry and Hf–Nd isotopic decoupling. *Gondwana Research,* 21**,** 266-280.

TAYLOR, A. & LASAGA, A. 1999. The role of basalt weathering in the Sr isotope budget of the oceans. *Chemical Geology,* 161**,** 199-214.

TAYLOR, S. R. & MCLENNAN, S. M. 1985. The continental crust: its composition and evolution. *Blackwells Scientific, Oxford***,** 312 pp.

TERA, F. & WASSERBURG, G. 1972. U-Th-Pb systematics in three Apollo 14 basalts and the problem of initial Pb in lunar rocks. *Earth and Planetary Science Letters,* 14**,** 281-304.

THÓRARINSSON, S. 1944. Tephrochronological studies in Iceland. *Geografiska Annaler,* 26**,** 1-217.

TIMMERMAN, M. J. 2004. Timing, geodynamic setting and character of Permo-Carboniferous magmatism in the foreland of the Variscan Orogen, NW Europe. *In:* WILSON, M., NEUMANN, E. R., DAVIES, G. R., TIMMERMAN, M. J., HEEREMANS, M. & LARSEN, B. T. (eds.) *Permo-Carboniferous Magmatism and Rifting in Europe.* Geological Society, London, Special Publications, 223, 41-74.

TOLCIN, A. C. 2021. Mineral Commodity Summaries 2021: Zinc. *United States Geological Survey. Retrieved June 21*.

TORREMANS, K., KYNE, R., DOYLE, R., GÜVEN, J. F. & WALSH, J. J. 2018. Controls on Metal Distributions at the Lisheen and Silvermines Deposits: Insights into Fluid Flow Pathways in Irish-Type Zn-Pb Deposits. *Economic Geology,* 113**,** 1455-1477.

TOSTEVIN, R., SHIELDS, G. A., TARBUCK, G. M., HE, T., CLARKSON, M. O. & WOOD, R. A. 2016. Effective use of cerium anomalies as a redox proxy in carbonate-dominated marine settings. *Chemical Geology,* 438**,** 146-162.

ULRICH, T., KAMBER, B. S., WOODHEAD, J. D. & SPENCER, L. A. 2010. Long-term observations of isotope ratio accuracy and reproducibility using quadrupole ICP-MS. *Geostandards and Geoanalytical Research,* 34**,** 161-174.

VAN DEN BERG, R. 2005. *Granulite-facies lower crustal xenoliths from central Ireland.* PhD Thesis, University College Dublin.

VAN GELDERN, R., JOACHIMSKI, M., DAY, J., JANSEN, U., ALVAREZ, F., YOLKIN, E. & MA, X.-P. 2006. Carbon, oxygen and strontium isotope records of Devonian brachiopod shell calcite. *Palaeogeography, Palaeoclimatology, Palaeoecology,* 240**,** 47-67.

VEIZER, J. 1989. Strontium isotopes in seawater through time. *Annual Review of Earth and Planetary Sciences,* 17**,** 141-167.

VEIZER, J., ALA, D., AZMY, K., BRUCKSCHEN, P., BUHL, D., BRUHN, F., CARDEN, G. A., DIENER, A., EBNETH, S. & GODDERIS, Y. 1999. 87Sr/86Sr, δ13C and δ18O evolution of Phanerozoic seawater. *Chemical Geology,* 161**,** 59-88.

VELDE, B. & BRUSEWITZ, A. 1982. Metasomatic and non-metasomatic low grade metamorphism of Ordovician meta-bentonites in Sweden. *Geochimica et Cosmochimica Acta,* 46**,** 447-452.

WALKER, G. P. 1971. Grain-size characteristics of pyroclastic deposits. *The Journal of Geology,* 79**,** 696-714.

WALTERS, S. G. & INESON, P. R. 1981. A review of the distribution and correlation of igneous rocks in Derbyshire, England. *Mercian Geologist,* 8**,** 81-132.

WARTHO, J.-A., QUINN, D. & MEERE, P. 2006. The timing of Variscan deformation: UV laser 40Ar/39Ar dating of syn \ late-orogenic intrusions from SW Ireland. *Geochimica et Cosmochimica Acta,* 70**,** A690.

WATERS, C. N., SOMERVILLE, I., JONES, N., CLEAL, C., COLLINSON, J., WATERS, R., BESLY, B., DEAN, M., STEPHENSON, M., DAVIES, J., FRESHNEY, E. C., JACKSON, D. I., MITCHELL, W. I., POWELL, J. H., BARCLAY, W. J., BROWNE, M. A. E., LEVERIDGE, B. E., LONG, S. L. & MCLEAN, D. 2011. A revised correlation of Carboniferous rocks in the British Isles. 26**,** 186 pp.

WATSON, E., SWINDLES, G., STEVENSON, J., SAVOV, I. & LAWSON, I. 2016. The transport of Icelandic volcanic ash: Insights from northern European cryptotephra records. *Journal of Geophysical Research: Solid Earth,* 121**,** 7177-7192.

WATSON, E. B. 1979. Zircon saturation in felsic liquids: experimental results and applications to trace element geochemistry. *Contributions to Mineralogy and Petrology,* 70**,** 407-419.

WEAVER, C. 1963. Interpretive value of heavy minerals from bentonites. *Journal of Sedimentary Research,* 33**,** 343-349.

WEBB, G. E. & KAMBER, B. S. 2000. Rare earth elements in Holocene reefal microbialites: a new shallow seawater proxy. *Geochimica et Cosmochimica Acta,* 64**,** 1557-1565.

WEDEPOHL, K. 1978. Handbook of Geochemistry: Springr-Verlag. *Berlin, Heidelberg, New York*.

WEIS, D., KIEFFER, B., MAERSCHALK, C., BARLING, J., DE JONG, J., WILLIAMS, G., HANANO, D., PRETORIUS, W., MATTIELI, N. & SCOATES, J. 2006. Highprecision isotopic characterization of USGS reference materials by TIMS and MCICPMS. *Geochemistry, Geophysics, Geosystems,* 7(8).

WENDT, I. & CARL, C. 1991. The statistical distribution of the mean squared weighted deviation. *Chemical Geology: Isotope Geoscience Section,* 86**,** 275-285.

WETHERILL, G. W. 1956. Discordant uranium-lead ages, I. *Eos, Transactions American Geophysical Union,* 37**,** 320-326.

WIEDENBECK, M., ALLE, P., CORFU, F., GRIFFIN, W., MEIER, M., OBERLI, F. V., QUADT, A. V., RODDICK, J. & SPIEGEL, W. 1995. Three natural zircon standards for U-Th-Pb, Lu-Hf, trace element and REE analyses. *Geostandards Newsletter,* 19**,** 1-23.

WILDE, S. A., VALLEY, J. W., PECK, W. H. & GRAHAM, C. M. 2001. Evidence from detrital zircons for the existence of continental crust and oceans on the Earth 4.4 Gyr ago. *Nature,* 409**,** 175-178.

WILKINSON, J., BOYCE, A., EVERETT, C. & LEE, M. 2003. Timing and depth of mineralization in the Irish Zn-Pb orefield. *In:* KELLY, J. G., ANDREW, C. J., ASHTON, J. H., BOLAND, M. B., EARLS, G., FUSCIARDI, L. & STANLEY, G. (eds.) *Europe's major base metal deposits.* Irish Association for Economic Geology, 483–497.

WILKINSON, J., CROWTHER, H. & COLES, B. 2011. Chemical mass transfer during hydrothermal alteration of carbonates: Controls of seafloor subsidence, sedimentation and Zn–Pb mineralization in the Irish Carboniferous. *Chemical Geology,* 289**,** 55-75.

WILKINSON, J. & HITZMAN, M. 2015. The Irish Zn-Pb orefield: the view from 2014. *In:* ARCHIBALD, S. M. & PIERCEY, S. J. (eds.) *Current Perspectives on Zinc Deposits.* Irish Association for Economic Geology, 59-72.

WILKINSON, J. J., EVERETT, C., BOYCE, A., GLEESON, S. & RYE, D. 2005. Intracratonic crustal seawater circulation and the genesis of subseafloor zinc-lead mineralization in the Irish orefield. *Geology,* 33**,** 805-808.

WILLIAMS, I. S. 1998. U-Th-Pb geochronology by ion microprobe. *Reviews in Economic Geology,* 7**,** 1-35.

WILSON, H. E., ROBBIE, J. A. & SYMES, R. G. 1966. *Geology of the country around Ballycastle*, Memoir of the Geological Survey of Northern Ireland, Her Majesty's Stationery Office.

WILSON, L. & WALKER, G. 1987. Explosive volcanic eruptions-VI. Ejecta dispersal in plinian eruptions: the control of eruption conditions and atmospheric properties. *Geophysical Journal International,* 89**,** 657-679.

WINCHESTER, J. A. & FLOYD, P. A. 1977. Geochemical discrimination of different magma series and their differentiation products using immobile elements. *Chemical Geology,* 20**,** 325-343.

WOODCOCK, N. H. & STRACHAN, R. A. 2012. *Geological history of Britain and Ireland, 2nd Edition*, John Wiley & Sons.

WORTHINGTON, R. P. & WALSH, J. J. 2011. Structure of Lower Carboniferous basins of NW Ireland, and its implications for structural inheritance and Cenozoic faulting. *Journal of Structural Geology,* 33**,** 1285-1299.

WOUDLOPER 2008. Caledonides, Map, https://commons.wikimedia.org/w/index.php?curid=5038110.

WRAY, D. S. 1995. Origin of clay-rich beds in Turonian chalks from Lower Saxony, Germany—a rare-earth element study. *Chemical Geology,* 119**,** 161-173.

YORK, D. 1967. The best isochron. *Earth and Planetary Science Letters,* 2**,** 479-482.

YORK, D. 1968. Least squares fitting of a straight line with correlated errors. *Earth and Planetary Science Letters,* 5**,** 320-324.

ZACHARA, J., COWAN, C. & RESCH, C. 1991. Sorption of divalent metals on calcite. *Geochimica et Cosmochimica Acta,* 55**,** 1549-1562.

ZHANG, K., ZHU, X.-K. & YAN, B. 2015. A refined dissolution method for rare earth element studies of bulk carbonate rocks. *Chemical Geology,* 412**,** 82-91.

ZHOU, Y. 1992. Precise identification and correlation for coal seams using ziron features and trace elements in tonsteins. *Coal Geology Exploit,* 20**,** 18-23.

ZHOU, Y., BOHOR, B. F. & REN, Y. 2000. Trace element geochemistry of altered volcanic ash layers (tonsteins) in Late Permian coal-bearing formations of eastern Yunnan and western Guizhou Provinces, China. *International Journal of Coal Geology,* 44**,** 305-324.

ZIEGLER, P. 1989. Evolution of Laurussia. *Kluwer Academic Publishers, Dordrecht.*

ZIELINSKI, R. A. 1982. The mobility of uranium and other elements during alteration of rhyolite ash to montmorillonite: a case study in the Troublesome Formation, Colorado, USA. *Chemical Geology,* 35**,** 185-204.

ZIELINSKI, R. A. 1985. Element mobility during alteration of silicic ash to kaolinite—a study of tonstein. *Sedimentology,* 32**,** 567-579.

ZIRNER, A. L., MARKS, M. A., WENZEL, T., JACOB, D. E. & MARKL, G. 2015. Rare earth elements in apatite as a monitor of magmatic and metasomatic processes: The Ilímaussaq complex, South Greenland. *Lithos,* 228**,** 12-22.